Fluorescent Chemosensors for Exploring Zinc Metalloneurochemistry and Detecting Mercury in Aqueous Solution

by

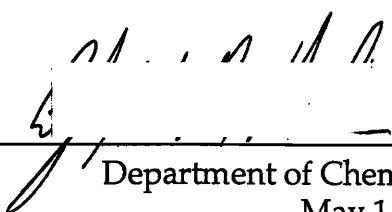Elizabeth M. Nolan
B. A. Chemistry
Smith College, 2000

SUBMITTED TO THE DEPARTMENT OF CHEMISTRY IN PARTIAL FULFILLMENT
OF THE REQUIREMENTS FOR THE DEGREE OF

DOCTOR OF PHILOSOPHY IN INORGANIC CHEMISTRY
AT THE
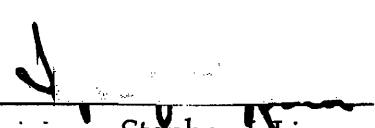MASSACHUSETTS INSTITUTE OF TECHNOLOGY

May 2006
[July, 2006]

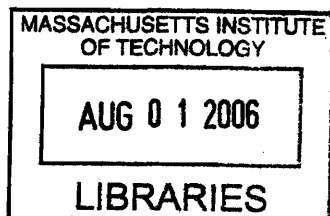© Massachusetts Institute of Technology, 2006

Signature of Author:_____

Department of Chemistry
May 1, 2006

Certified By:_____

Stephen J. Lippard
Arthur Amos Noyes Professor of Chemistry
Thesis Supervisor
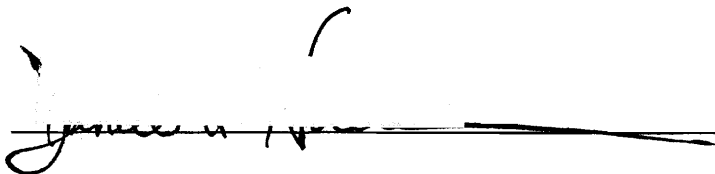
Accepted by:_____

Robert W. Field
Chairman, Departmental Committee on Graduate Studies

This doctoral thesis has been examined by a committee of the Department of Chemistry as follows:

_____

Daniel G. Nocera
Committee Chairman
W. M. Keck Professor of Energy and Professor of Chemistry

_____

Stephen J. Lippard
Arthur Amos Noyes Professor of Chemistry
Thesis Supervisor

_____

Joseph P. Sadighi
Assistant Professor of Chemistry

Fluorescent Chemosensors for Exploring Zinc Metalloneurochemistry and Detecting Mercury in Aqueous Solution

By
Elizabeth M. Nolan

Submitted to the Department of Chemistry on May 1, 2006 in partial fulfillment of the requirements for the Degree of Doctor of Philosophy in Inorganic Chemistry

Abstract

Chapter 1. An Introduction to Zinc Metalloneurochemistry and Zinc Detection in Biology

This chapter presents an overview of zinc neurophysiology and pathology, which provides motivation for the design of new tools and tactics for zinc detection in vivo. A historical account of biological zinc detection is also given, followed by a summary of recent progress in the development and use of fluorescent Zn(II) sensors for in vivo studies. A summary of project goals and thesis organization is also included.

Chapter 2. Zinc Sensors Based on Monosubstituted Fluorescein Platforms I: Routes to Electronic Variation, Syntheses and Spectroscopic Characterization

In this work, a convergent synthetic approach for the assembly of fluorescent zinc sensors from aniline-derivatized ligands and a fluroescein carboxaldehyde platform is presented. These sensors are based on the previously reported ZP4 motif and incorporate a di(2-picolyl)amine moiety in the aniline-based ligand framework. The effects of electronic variation, achieved by halogenation of either the zinc-binding unit

or the fluorophore platform, on the fluorescence properties and aniline nitrogen atom pK_a values are considered.

Chapter 3. Spectroscopic Characterization and Biological Applications of Halogenated Zinpyr Sensors

In this chapter, the effects of fluorescein halogenation on the photophysical properties and protonation equilbria of symmetrical Zinpyr derivatives, which contain two di(2-picolyl)amine-based ligand appendages, are considered. These sensors have sub-nM affinity for Zn(II) and are selective for Zn(II) over biologically relevant alkali and alkaline earth metals. Fluorescein halogenation influences background fluorescence, dynamic range, tertiary amine pK_a, and both excitation and emission wavelengths. Extensive biological work, including cytotoxicity assays and confocal imaging, are also presented. Studies in a number of cell lines, including neurons, show that ZP3 is a versatile Zn(II) imaging tool.

Chapter 4. Zinc Sensors Based on Monosubstituted Fluorescein Platforms II: Modulation of Zinc Affinity and Biological Applications

To access ZP sensors with lower Zn(II) affinity, pyrrole moieties were incorporated into an aniline-based ligand unit to give sensors ZP9 and ZP10. The photophysical characterization and metal binding properties of these sensors are described. The pyrrole-for-pyridyl substitution affords Zn(II) sensors with improved Zn(II) selectivity and sub-μM dissociation constants. Biological imaging studies revealed that asymmetrical ZP probes, including ZP4, are cell permeable and Zn(II) responsive in vivo. Both ZP4 and ZP9 detect endogenous Zn(II) in acute hippocampal slices from the adult rat.

Chapter 5. The Zinspy Family of Fluorescent Zinc Sensors: Syntheses and Spectroscopic Investigations

Four fluorescent sensors designed for Zn(II) detection and which contain a fluorescein reporting group and a pyridyl-amine-thioether derivatized ligand moiety were prepared and their photophyiscal properties characterized. These "Zinspy" sensors are water soluble and generally display ~1.4 to ~4.5-fold fluorescence enhancement upon Zn(II) coordination, depending upon fluorescein halogenation and the number and nature of the Zn(II)-binding appendages. The Zinspy sensors exhibit improved selectivity and lower affinity for Zn(II) compared to the di(2-picolyl)amine-based Zinpyr family members.

Chapter 6. Zinspy Sensors with Enhanced Dynamic Range: Imaging Zinc Uptake and Mobilization with a Low Affinity Probe

This chapter describes the preparation and characterization of Zinspy sensors containing non-coordinating thiophene heterocycles in the metal-binding unit. These probes show improved dynamic range relative to thioether-containing ZS sensors, low μM dissociation constants for Zn(II) and improved Zn(II) selectivity. Stopped-flow kinetics investigations indicate fast association rates and reversible Zn(II) coordination with $k_{on} > 1.8 \times 10^6$ M^{-1}s^{-1} and $k_{off} > 3$ s^{-1} at 25 °C. ZS5 is cell permeable, Zn(II)-responsive in vivo and localizes to the mitochondria of certain cell types. ZS5 can detect Zn(II) released from neurons following nitrosative stress.

Chapter 7. QZ1 and QZ2, Rapid Reversible Quinoline Derivatized Fluoresceins for Sensing Biological Zinc

Two fluorescein-based dyes derivatized with 8-aminoquinoline were prepared and their photophysical, thermodynamic and zinc-binding kinetic properties determined. Because of their low background fluorescence and highly emissive Zn(II) complexes,

QZ1 and QZ2 display a large dynamic range, with ~42- and ~150-fold fluorescence enhancements upon Zn(II) coordination, respectively. These sensors have micromolar dissociation constants for Zn(II), improved selectivity and bind Zn(II) rapidly and reversibly with k_{on} values $>10^6$ M^{-1}s^{-1} and k_{off} values of ~150 s^{-1}. Biological imaging studies with ZP3 and QZ2 show that binding affinity is an important parameter for metal ion detection in vivo. QZ1 and QZ2 also respond to two-photon excitation and two-photon microscopy was used to visualize Zn(II) with QZ2 in live HeLa cells.

Chapter 8. A "Turn-On" Fluorescent Sensor for the Selective Detection of Mercuric Ion in Aqueous Media

This chapter describes the synthesis, photophysical characterization and metal-binding properties of mercury sensor 1 (MS1). This sensor is based on a fluorescein platform and has a thioether-rich metal-binding unit, which conveys high selectivity for Hg(II). To the best of our knowledge, MS1 was the first reversible fluorescent Hg(II) sensor to give fluorescence turn-on in water. MS1 can detect low ppb levels of Hg(II) in aqueous solution at neutral pH.

Chapter 9. Selective Hg(II) Detection in Aqueous Solution with Thiol Derivatized Fluoresceins

The syntheses and photophysical properties of MS2 and MS3, two asymmetrically derivatized fluorescein-based dyes designed for Hg(II) detection, are described. These sensors each contain a single pyridyl-amine-thiol metal-binding moiety, form 1:1 complexes with Hg(II) and exhibit selectivity for Hg(II) over other Group 12 metals, alkali and alkaline earth metals, and most divalent first-row transition metals. Both dyes display superior brightness (Φ x ε) and fluorescence enhancement following Hg(II) coordination in aqueous solution. At neutral pH, the fluorescence turn-on derives from greater brightness due to increased molar absorptivity. At higher pH, photoinduced

electron transfer (PET) quenching of the free dye is enhanced, and the Hg(II)-induced turn-on also benefits from alleviation of this pathway. MS2 can detect ppb levels of Hg(II) in aqueous solution, demonstrating its ability to identify environmentally relevant concentrations of Hg(II).

Chapter 10. MS4, A Seminaphthofluorescein-Based Chemosensor for the Ratiometric Detection of Hg(II)

The synthesis and photophysical characterization of MS4, an aniline-derivatized seminaphthofluorescein-based dye that contains a pyridyl-amine-thioether ligand analogous to that employed in the Zinspy Zn(II) sensor family (Chapter 5) are reported. Sensor MS4 provides single-excitation, dual-emission ratiometric detection of Hg(II) in aqueous solution. An ~4-fold ratiometric change $(\lambda_{624}/\lambda_{524})$ is observed upon introduction of Hg(II) to an aqueous chloride-containing solution of MS4 at pH 8. In this milieu, MS4 shows selectivity for Hg(II) over a background of alkali and alkaline earth metals, a number of divalent first-row transition metals and its Group12 congeners Zn(II) and Cd(II).

Chapter 11. Turn-On and Ratiometric Mercury Sensing in Water with a Seminaphthofluorescein-Based Probe

The synthesis and characterization of MS5 are presented in this chapter. This sensor incorporates the aniline-derivatized thioether ligand used in the preparation of MS1 and the seminaphthofluorescein platform described in the design of MS4. MS5 gives selective fluorescence turn-on for Hg(II) at pH > 7. At pH > 8, single-excitation dual-emission ratiometric Hg(II) detection is possible by comparison of the $(\lambda_{624}/\lambda_{524})$ ratio before and after Hg(II) coordination. Studies of the pH dependence suggest that the seminaphthofluorescein dianion is critical for generating the ratiometric response. X-ray crystallographic studies with a salicylaldehyde-based model complex are presented to

help elucidate the nature of Hg(II) coordination to MS1 and MS5. MS5 can respond to Hg(II) added to natural water samples, which points to its potential utility in the field.

Appendix 1. Miscellenous Fluorescein-Based Ligands

This appendix details the preparation and, in some cases, characterization of potential fluorescein based sensors for either Zn(II) or Hg(II) detection that were not described in earlier chapters. Many of these compounds give fluorescence turn-off or no fluorescence change with analyte binding. Sensors ZP11 and MS6 are lower-affinity probes that give fluorescence turn-on for Zn(II) and Hg(II), respectively.

Appendix 2. Theoretical Investigations of Fluorescein Derivatives

In this chapter, we present the results from DFT and TDDFT calculations on fluorescein and its derivatives. These studies include establishing protocols for fluorescein pK_a determination and TDDFT analysis. The absorption spectra of the fluorescein dianion and monoanion were assigned and a detailed molecular orbital analysis for a fluorescein dianion analog was conducted. These studies indicate that oxygen atoms in the xanthenone moiety influence the amount of C_1 character in the donor and acceptor molecular orbitals responsible for fluorescein absorption.

Appendix 3. Miscellaneous NMR Spectra

Thesis Supervisor: Professor Stephen J. Lippard

Title: Arthur Amos Noyes Professor of Chemistry

To Mom, Dad and Gram

Acknowledgements

Sometimes it's a bit hard for me to believe that almost five years have passed since I ventured onto this Ph.D. journey, let alone that this period is coming to very a quick close. I'm grateful for the chance to thank the people who have contributed to my experiences and growth during this time.

My advisor, Steve, receives a bundle of thanks for his guidance, training and support, and for the opportunities he has given to me and to his group. Looking back on the Building 18 renovations and what I'll call "The Year of the Grants," I conclude that I've encountered few people with as much dedication and loyalty to their lab, projects and people as Steve shows. There are few places in this world where someone can mount a crystal, image cells and run a stopped-flow experiment all in one afternoon. I feel privileged to have worked in such a dynamic environment. I appreciate Steve's willingness to take me on and allow me to pursue a synthetic project as a first-year, and also thank him for endless ideas and suggestions, and for accepting nothing short of my best effort.

I've had the pleasure to interact with many fellow graduate students and post-docs in the Lippard Lab, and thank former and current members for providing an intriguing and stimulating workplace. Edna welcomed me into the group and entertained many questions about stability constants and kinetics. Emily, Katie and Jane have provided guidance and encouragement, especially during the vicissitudes of oral exams. Over five years, I've watched Subgroup II evolve from a mix of unrelated projects to a genuine sensing subgroup and I look forward to seeing the outcomes of current and future endeavors. Early on, Shawn helped me set up my first Schlenk line and Carolyn and I ultimately became pals while working with the "pink stuff." I was lucky to learn many tricks from synthetic guru Matt Clark and had fun investigating halogenated ZPs with Chris #1. I thank my fellow "sensor girl," Mi Hee, for good times and her insights on chemistry, life and the typical Korean way. More recent additions to the neurochemistry subgroup include Andy, Rhett, Chris #2, Brian, Todd, Xiao-an and Lindsey. I wish them all the best. I appreciate Todd's sound experimental advice, Brian's inquisitive nature, Xiao-an's enthusiasm and Lindsey's thoughtfulness. I'll always remember some of Andy and Rhett's comedy acts.

Kudos to Scott for his aldehyde synthesis and for capturing the IR computer burglar and to Leslie for saving my PC from viruses and coffee spills. I also thank Leslie and Laurance for keeping the aqueous stopped-flow system in tip-top shape. Jeremy gave me many useful suggestions for organic reactions and the lab's official entertainer, Dong, shared many early morning stories and cell culture tips. I thank Evan for his cheerful outlook, daily "good morning!" and iBook help. Datong solved my Hg(II) crystal structures and Rodney provided much needed crystallographic assistance during my thesis preparation. I appreciate Erik's willingness to partake in almost any adventure. Professor Tom Smith played a significant role in the early Raman sagas and, looking back, I realize he helped ease my transition from a small to a big place.

I've had the opportunity to work with a number of talented Lippard Lab undergraduates. Jessica helped with ZP5 and kept my French from getting rusty, and Kathryn was a great lab companion. I enjoyed mentoring my two UROPs, Maryann and Dugan, very much and I commend them both for their efforts.

Significant portions of my thesis work were possible because of our collaboration with Prof. Morgan Sheng's group. I thank Morgan for his interest and for sharing his lab space and resources. Jacek deserves special recognition. He taught me about cell work, lab animals, imaging and Polish history, and gave me complete freedom on the Sheng Lab scope. We also had fun placing bets on experiments and sharing travel stories. Jubin has been my recent Sheng Lab cohort and I appreciate his scientific thoughts and benevolence.

I also acknowledge Prof. Hayashi for our two-photon microscopy collaboration and Ken-Ichi for his assistance and humor. Prof. Mookie Baik provided resources for theoretical work and I thank him for his hospitality during my Bloomington stay in 2004. Profs. Dan Nocera and Joseph Sadighi served on my thesis committee and offered insights and suggestions for improvement. David and Mark helped me overcome my silly fear of the NMR and, although unrelated to my thesis research, Joseph Gardecki taught me some basics about lasers and Raman systems. I thank Susan Brighton for her kindness and smiles and Rich for sorting out a variety of matters.

Although this fact might be a surprise to some, I didn't like high school chemistry very much and registered for the subject as a first-year undergraduate because I was determined to find some redeeming feature in the discipline. I did and I thank members of the Chemistry Department at Smith College for sparking my interest in this field. In particular, Mr. Linck introduced me to the joys of research and prepared me for the rigors of graduate school, and Mrs. Burk's warmth has touched my life on many occasions. My old lab buddies Catherine, Laurel and Marina hold a special place in my heart and I can always count on them. Along these lines, I thank Marina and Catherine for helping out last minute with the CSD fiasco.

I thank the Tylerites for our yearly reunions, Ruth for our Cambridge adventures, Kelly and Bill for wonderful dinner parties, Evie for well-timed phone calls and Lara for coffee. Most importantly, I recognize my family for their love and support. My four siblings all offer their own unique perspectives on my career as a graduate student and my life as a city dweller, and all look out for me. I thank Bridgit for her emails, Cathy for help with my disaster apartment, John for his teenager-like affection, and Megan for sharing some of her crazy high school stories. Gram equipped my kitchen with a variety of gadgets and I'm always happy to find one of her sticker-covered letters in my mailbox. Lastly, I thank Mom and Dad for more than words can ever express. Their devotion, encouragement and inspiration mean so much to me. I couldn't have asked for better role models and I dedicate this work to them.

Table of Contents

Chapter 8. A "Turn-On" Fluorescent Sensor for the Selective Detection of

Chapter 9. Selective Hg(II) Detection in Aqueous Solution with Thiol

List of Tables

Appendix 2

List of Schemes

Chapter 2

Chapter 3

Chapter 4

Chapter 5

Chapter 6

Chapter 7

Chapter 8

Chapter 9

Chapter 10

Chapter 11

Appendix 1

List of Figures

Chapter 7

Chapter 8

Chapter 9

Chapter 10

Chapter 11

List of Equations

Chapter 1

An Introduction to Zinc Metalloneurochemistry and Zinc Detection in Biology

Zinc in Biology

The primary motivation of this work is to design and use tools for exploring zinc metalloneurochemistry, but first the importance of zinc in human physiology warrants brief discussion.[1] Zinc is a trace element required for growth and development, proper immune function and good health.[2] Over 300 metalloproteins contain one or more Zn(II) centers, which play both structural and catalytic roles.[1] Examples include carbonic anhydrase, liver alcohol dehydrogenase, superoxide dismutase, and nitric oxide synthase. Zinc also regulates processes including DNA repair,[3,4] caspase activity and apoptosis,[5,6] and is thus a signaling agent. Various pathologies, including diabetes,[7] immune system dysfunction[2] and prostrate cancer,[8] have been associated with failure to maintain Zn(II) homeostasis.

Zinc Metalloneurochemistry

Metalloneurochemistry[9] defines an emerging field at the intersection of inorganic chemistry and neuroscience and includes explorations of metal ions as neurotransmitters, as co-factors in neuroproteins and as neurotoxins. Most early investigations of metal ions in the brain and central nervous system (CNS) focused on the neuromodulatory roles of K(I) and Ca(II). More recently, the importance of both redox active and inactive d-block metal ions, including Fe(II), Cu(II) and Zn(II), in both neurophysiology and pathology has come to light.

Zinc is the second most abundant d-block metal ion in the human brain and its distribution varies, with relatively high concentrations found in the hippocampus and neocortex.[10] Brain zinc is generally divided into two types, protein-bound and loosely bound, the latter also termed histochemically observable, chelatable or mobile zinc. The loosely bound pool constitutes 5-10% of total brain zinc[11] and its physiological and pathological significance remains enigmatic despite numerous investigations. Of particular interest is the loosely bound zinc found in the hippocampus, a region of the

mammalian forebrain involved in learning and memory formation. Moblie zinc is housed in the synaptic vesicles of glutamatergic mossy fiber synapses (Figures 1.1 and 1.2).[10,11] Although co-localization of zinc and glutamate in this subset of synaptic vesicles was assumed for approximately 30 years, only recently were experiments conducted that provided proof of such mutual uptake by showing that both the Zn(II) transporter ZnT3 and the glutamate transporter Vglut1 are targeted to and expressed in this vesicle population.[12]

Synaptic vesicles release neurotransmitters and neuromodulatory agents into the synaptic cleft following fusion with the presynaptic membrane, which allows for signaling cascades between neurons.[13] This process is illustrated in Figure 1.2. The notion of synaptically released Zn(II), in conjunction with glutamate release and in accord with the idea that Zn(II) may be a neurotransmitter,[14] presumably originates from this central dogma. Multiple neuromodulatory effects for Zn(II) have been documented including down-regulation of the NMDA[15-18] and GABA[19-21] receptors and inhibition of Ca(II) channels.[22] Zinc has also been implicated in long-term potentiation (LTP), or memory formation, in DG→CA3 mossy fiber synapses.[23] Despite these observations, the concept of zinc release into the synapse remains controversial.[24-27] This debate stems, in part, from differences in tissue handling, neuron stimulation and Zn(II) detection protocols, which can significantly influence experimental outcomes.[24,28] Early work demonstrated Zn(II) release into the extracellular space following electrophysiological stimulation, but the frequencies applied to the mossy fiber synapses were generally high, of long duration and not physiologically relevant.[29-33] For instance, one early study[30] applied a train of 750 pulses at 12.5 Hz (60 s duration) and frequencies up to 100 Hz have been employed.[32] These values contrast with those obtained from recordings of neuronal activity in live rats, which suggest that hippocampal granule cells generally fire at frequencies of <2.5[34] and even ≤ 0.5 Hz.[35]

In a separate report where high frequency and prolonged stimulation (100 Hz, 10 s) was employed, essentially no Zn(II) signal was detected and the authors hypothesized that zinc is not released and remains bound to the presynaptic membrane following vesicle exocytosis.[36] More recently, Zn(II) release was observed in the stratum ludicum region of the hippocampus after the mossy fibers were stimulated with lower frequency pulses of shorter duration (5 Hz, 1 sec).[28] Parallel experiments with brain tissue from ZnT3 knock-out mice, which lack the transporter that loads Zn(II) into vesicles, showed a 3-fold reduction in the zinc signal, which confirms its vesicular origin.[28] This study offers the most convincing evidence that synaptic Zn(II) release occurs and is physiologically meaningful. Nevertheless, detailed investigations directed at elucidating its functional significance are needed.

Related questions concern Zn(II) concentrations both in the vesicles and in the synapse following release under physiological conditions. Although 0.3 mM is a number often cited as the concentration of Zn(II) in synaptic vesicles or in the synapse, this value is only a calculated[10] estimate and no experimental evidence for this concentration exists. In some recent studies, reported concentrations of released Zn(II) range from 1 to 10 μM.[31,33,37,38] In a separate account, two micromolar affinity Zn(II) sensors failed to detect extracellular Zn(II) following stimulation whereas a nanomolar affinity sensor did, although the authors suggested this result could reflect poor sensor performance and not low extracellular Zn(II) levels.[28] Recently, a series of fluorescent Zn(II) sensors with varying affinity were employed to monitor Zn(II) release from hippocampal slices stimulated with K(I).[37] A moderate affinity probe ($K_d \sim 25$ μM) showed no response whereas higher affinity sensors did.[37] These investigations may point towards lower concentrations of released Zn(II) than the 0.3 mM estimate; however, they do not provide definitive proof since extracellular and non-localized sensors were used and, given the smaller volume of vesicles relative to the synapse and

extracellular space, dilution of Zn(II) following its release occurs. More work is clearly needed to resolve these discrepancies.

Zinc pathophysiology is also an area of substantial current interest since high concentrations of Zn(II) are neurotoxic.[39] A number of zinc transporter proteins[40-43] and metallothionein[44-46] maintain zinc homeostasis in the brain under normal physiological conditions, but these mechanisms can fail during periods of stress. For instance, uncontrolled Zn(II) release occurs following blunt head trauma and as a result of stroke or seizure, and is implicated in subsequent neurodegeneration.[47,48] Significant evidence exists for a role of Zn(II) in the onset and pathogenesis of Alzheimer's disease.[49-52] Failure of Zn(II) homeostasis has been correlated to many other neurological problems including poor cognitive and motor development resulting from dietary Zn(II) deficiency in children[53] and depression.[54]

Several mechanisms exist to explain Zn(II) neurotoxicity, including rapid influx into the mitochondria following uncontrolled release.[55,56] Many of the details of these mechanisms need further elaboration. Of particular relevance to some of the work described here is the growing link between Zn(II) toxicity and oxidative stress.[55,57-59] For instance, both nitric oxide (NO), a putative signaling molecule in the CNS, and Zn(II) have been implicated in neurodegeneration resulting from stroke and in other pathological conditions.[60,61] NO can cause Zn(II) release from native protein stores,[62,63] and a recent study established that Zn(II) entry into the mitochondria following NO-induced intracellular release causes respiratory block, ROS production, p38 MAP kinase activation and K(I) influx, which ultimately results in apoptotic-like neuronal death.[64]

Many avenues for exploring zinc metalloneurochemistry exist. Some pressing questions include: (i) Is zinc a neurotransmitter? (ii) What factors govern Zn(II) release in both physiological and pathological contexts? (iii) What is the chemical structure of Zn(II) in the vesicles and following release into the extracellular milieu? (iv) How and why does Zn(II) influence signaling cascades and synaptic plasticity? Further studies of

these phenomena require a combination of biology, chemistry, electrophysiology and optical imaging. In what follows, we discuss recent progress in the design and biological application of fluorescent Zn(II) sensors, some of which have addressed problems in neurobiology.

Zinc Detection in Biological Samples

Historical Perspective. The concept of using fluorescent probes for in vivo metal ion detection is relatively new. Early histochemical studies relied on other techniques, including silver amplification (Timm's staining) and colorimetric methods, to visualize metal ions. Histochemically observable Zn(II) was serendipitously discovered in brain tissue by Maske in 1955 and subsequently located in other tissues including the pancreas, prostrate, salivary glands and retina.[10] The generally accepted procedure to prove the existence of Zn(II) in a tissue sample involves a combination of Timm's staining and dithizone treatment.[65] Silver amplification is extremely sensitive, but can label other transition metal ions including Cu(II) and Fe(II). Dithizone is a Zn(II)-selective colorimetric indicator, but it affords poor sensitivity and resolution. Although this combined approach is invaluable for unambiguously detecting new Zn(II) pools, silver amplification is tedious and irreversible, and both procedures are limited to samples of fixed tissue (i.e. post-mortem). These deficiencies prompted the search for other Zn(II) imaging reagents and, as early as 1970, fluorescence techniques were employed for studying Zn(II) distribution in mammalian tissues.[65-67]

Considerations and Challenges. Because of its closed-shell configuration, Zn(II) has no facile spectroscopic signature, which limits the kinds of methods that can be readily applied to its study. As a result, fluorescence is arguably the best suited method for investigating Zn(II) distribution and movement in biological contexts. Many factors must be considered in the design of fluorescent Zn(II) sensors for use in vivo.[68] First and foremost, the probe should be highly selective for Zn(II) over all other constituents in

the biological milieu, including millimolar concentrations of Na(I), K(I), Ca(II) and Mg(II). The probe affinity must also be considered. In general, this value should approach the median concentration of Zn(II) in the sample to allow the monitoring of both increases and decreases in analyte concentration. If the concentration of Zn(II) is unknown, then a suite of sensors with varying affinity might be required. An immediate, bright and readily detectable response to Zn(II) is necessary and reversibility is also important, both for monitoring Zn(II) flux and for attributing a signal to Zn(II) and not some other phenomena such as high local dye concentration. Ideally, excitation and emission wavelengths should be in the visible range with $\lambda_{ex} >$ 400 nm to avoid irradiating live cells or tissues with high energy light and $\lambda_{em} > 500$ to avoid autofluorescence from native species. Additionally, the excitation wavelength should be compatible with laser lines and/or commercially available filter sets for laser scanning confocal and epifluorescence microscopy. Photostability is another factor, and it is important that the sensor not suffer from photobleaching or photoactivation during the course of an imaging experiment. For experiments involving live cells or animals, the sensor must be non-toxic. Depending on the experimental objective, an extracellular or intracellular probe might be required, which necessitates firm understanding of sensor uptake and distribution in cells and tissues.

Some of these desired attributes are easy to address in the design of a sensor. Excitation and emission wavelengths can be obtained by the choice of fluorophore. The affinity and selectivity can both be tuned through modifications of the Zn(II) binding unit. Other factors are less readily predictable. For instance, a given probe may be permeable or cytotoxic to one type of cell and not to another. Unintended compartmentalization, or the localization of sensor to a given subcellular organelle, has been described as problematic in the Ca(II) sensor literature.[69] We maintain that this feature is not problematic, and can even be beneficial, if it is well understood in the cell type under study. These considerations point to a need for extensive investigations of

Zn(II) sensor behavior in a variety of biological contexts. In what follows, we summarize recent approaches to fluorescence-based Zn(II) detection.

Fluorescent Zn(II) Sensors Based on Biomolecules

Although the focus of this work concerns small-molecule fluorescent Zn(II) sensors, many approaches to Zn(II) sensing rely on proteins,[31,70,71] peptides[72-76] and nucleic acids[77,78] and warrant some discussion. In general, these sensors are not as readily applicable to biological studies as small molecule probes. Often microinjection is required for intracellular work and, for systems relying on proteins and peptides, the possibility of degradation by proteases exists.

The most well-developed protein-based Zn(II) sensors employ carbonic anhydrase (CA),[31,70] an enzyme that binds Zn(II) through three histidine residues and with picomolar affinity. Aryl sulfonamides can coordinate to the Zn(II) center of the holoenzyme, which results in enhanced fluorescence intensity, lifetime and anisotropy. Additionally, modification of CA with a second fluorophore allows for FRET and ratiometric Zn(II) detection. In the biological context, these sensors are generally limited to extracellular applications and hence have been used to monitor extracellular Zn(II) release from hippocampal slices.[31] Recently, a CA biosensor was modified with a cell-penetrating peptide and used to quantify endogenous Zn(II) concentrations in rat pheochromocytoma cells.[79] In another protein-based strategy, metallothionein was appended with the FRET pair Alexa 448 and 546.[71] Zinc coordination resulted in a conformational change and fluorescence response.

Numerous peptide-based approaches to Zn(II) sensing have been documented. Zinc finger peptides bind Zn(II) with picomolar affinity and are selective for Zn(II) over Cu(II). These motifs were modified to incorporate dansyl and coumarin fluorophores and used for Zn(II) detection.[72,73] Unnatural amino acids containing the 8-hydroxyquinoline fluorophore have been installed adjacent to a β-turn sequence in

peptides that bind Zn(II) with varying affinities and give a chelation enhanced fluorescence (CHEF) response.[76] Peptide-based systems that give FRET with Zn(II) coordination have also been described.[75]

Small Molecule Fluoresent Zinc Sensors

The small molecule fluorescent Zn(II) sensing field is currently undergoing a renaissance. In this section, we summarize noteworthy Zn(II) sensors and discuss strengths and weaknesses of selected probes in a biological context. We limit our discussion to sensors that operate in aqueous solution and give either fluorescence enhancement or a ratiometric change with Zn(II) coordination. Several detailed review articles on Zn(II) sensing have appeared in recent years, which can be consulted for further information.[68,80-84]

Mechanisms. Mechanisms commonly invoked to explain the response of fluorescent sensors to Zn(II) include photoinduced electron transfer (PET)[85,86] and, for ratiometric sensing, excited state intramolecular proton transfer (ESIPT).[87] Other mechanisms, such as internal charge transfer (ICT) and electronic energy transfer (EET), are less relevant to the work described below.[81,86] Chelation enhanced fluorescence (CHEF), sometimes used synonymously with PET, generally refers to generation of a new fluorescent signal with metal ion coordination. PET-based probes are most frequently encountered in the Zn(II) sensing literature. These sensors consist of a reporter fluorophore (acceptor) linked to a receptor (donor), often via a spacer. The receptor generally contains an amine group that is considered the donor or off/on switch, although properties of the entire receptor determine the degree of PET quenching and fluorescence turn-on following analyte detection. If the donor is of appropriate energy, it can transfer an electron into the fluorophore excited state (acceptor) following photoexcitation and thereby quench emission. Zinc coordination lowers the energy of the donor orbital involved in this interaction and blocks PET, which results in fluorescence enhancement.

The ESIPT mechanism has been used in the design of several ratiometric Zn(II) sensors based on the benzimidazole chromophore. In these systems, intramolecular proton transfer in the excited state lowers the emission energy of the free probe and zinc coordination disrupts this process, causing blue-shifted emission.[87] Figure 1.3 includes diagrams for PET and ESIPT.

TSQ and Related Derivatives. Fluorescence-based approaches to Zn(II) imaging emerged in the late 1980s with the discovery that TSQ, *N*-(6-methoxy-8-quinolyl)-para-toluenesulfonamide (**1**, Figure 1.4), gives appreciable fluorescence enhancement in the presence of Zn(II) and can reproduce the Zn(II) staining patterns established by silver amplification and dithizone in biological tissues.[65] In solution, TSQ gives up to ~300-fold fluorescence enhancement following Zn(II) coordination and has a lower detection limit of 4 pM.[83] It is also selective for Zn(II) over biologically relevant Ca(II) and Mg(II) ions, and it does not fluoresce in the presence of Cu(II) and Fe(II), two metal ions that give positive Timm's staining.[65] Nevertheless, limitations of TSQ are numerous and include its incompatibility with live cell imaging and poor solubility, high energy excitation ($\lambda_{ex} \sim 350$ nm) and dim fluorescence, even in the Zn(II)-bound form, resulting from a weakly emitting fluorophore, and complicated solution stoichiometry.[88] These shortcomings motivated the search for new and improved imaging tools. A number of TSQ derivatives, including 2-Me-TSQ, **2**, and Zinquin sensors **3** and **4** were subsequently reported and are also shown in Figure 1.4.[89,90] Zinquin-E has an ester moiety that hydrolyzes in vivo and has been employed in biological imaging applications, including studies of Zn(II)-induced apoptosis.[91,92]

Other Small Molecule Zn(II) Sensors with UV Excitation. Although high-energy excitation is undesirable from the standpoint of biological imaging, this feature may become less problematic as two-photon microscopy becomes more commonly accessible. A number of Zn(II) sensors that employ anthracene, dansyl and coumarin reporters are shown in Figure 1.5.[93-96] Sensors **5-9** have macrocycle-based receptors and

afford fluorescence enhancement with Zn(II) coordination; however, the slow binding kinetics[95,96] of macrocyclic chelates for Zn(II) may prohibit their use in biological contexts, and the reporter fluorophores all suffer from relatively dim emission. Dansyl **6** binds Zn(II) with sub-pM affinity, is cell permeable and stains apoptotic cells.[6,93] Despite its slow (~1 h in vitro) response time, coumarin **8** is cell permeable and can detect exogenously added Zn(II) in rat tumor cells.[96] A di(2-picolyl)amine analog, **10**, binds Zn(II) more rapidly with an ~29-fold increase in quantum yield.[97]

Most ratiometric Zn(II) sensors reported to date, depicted in Figure 1.6, employ benzofuran or indole chromophores and require UV excitation. Commercially available FuraZin-1, **11**, and IndoZin-2, **12**, are excitation and emission ratiometric Zn(II) sensors, respectively, that exhibit low micromolar affinity for Zn(II), dim emission and a relatively small dynamic range.[98] The ZnAF-R1, **13**, and ZnAF-R2, **14**, probes use a di(2-picolyl)amine ligand, bind Zn(II) with sub-nM affinity and afford a blue shift in excitation wavelength following Zn(II) coordination.[99] These sensors, however, have dim emission and Zn(II) coordination results in a 2.8-fold decrease in quantum yield. Zinbo-5, **15**, is based on the 2-arylbenzoxazole chromophore, contains a pyridyl-based ligand and binds Zn(II) with low-nM affinity.[100] Zinbo-5 gives single-excitation dual-emission ratiometric detection of Zn(II) and was used for biological Zn(II) imaging by two-photon microscopy.[100] Benzimidazole-based probes **16-18**, which operate by ESIPT and exhibit a blue-shift in emission wavelength following Zn(II) coordination, were reported shortly after Zinbo-5.[87]

Small Molecule Zinc Sensors with Visible Excitation. Several Zn(II) probes requiring visible excitation employ naphthalimide, coumarin and BODIPY fluorophores (Figure 1.7). Sensor **19** gives >50-fold fluorescence enhancement with Zn(II) coordination following excitation at 442 nm. Coumarin **20** affords a ratiometric response to Zn(II) in MeOH ($\lambda_{484}/\lambda_{505}$), but not in aqueous solution, making it poorly suited for biological investigations.[97] BODIPY **21** has many desirable features including insensitivity to pH in

the physiological range, an ~11-fold increase in quantum yield following Zn(II) complexation (K_d = 1 nM), and cell permeability.[101]

Most Zn(II) sensors that require visible excitation employ xanthene-based reporters, including fluorescein, fluorone derivatives and rhodamine. Figure 1.7 includes the ACF probes, **22** and **23**, two early examples of xanthenone-based Zn(II) sensors that afford 14- and 26-fold fluorescence enhancement following Zn(II) coordination.[102] Invitrogen sells a number of xanthenone- and rhodamine-based probes for Zn(II) detection where the chelates are linked to the fluorophore through the "bottom" benzoate or phenyl moiety (Figure 1.8). Despite the resulting low background fluorescence, one general limitation of this design feature is that Zn(II) coordination does not afford full emission and these sensors generally exhibit Φ_{Zn} < 0.4. The FluoZin family, **24-26**, comprises modified calcium sensors that have carboxylate-rich metal-binding units and afford low nM (FluoZin-3) to μM (FluoZin-1 and 2) affinity for Zn(II). FluoZin-3 gives greater than 100-fold fluorescence enhancement following Zn(II) coordination and has been employed to monitor Zn(II) release from both pancreatic β–cells[103] and hippocampal mossy fibers[28] following stimulation. One potential limitation of FluoZin-3, **27**, is its sensitivity to Ca(II) and Fe(II). The rhodamine-based analog RhodZin-3 displays 75-fold fluorescence turn-on with Zn(II) addition and a K_d value of 65 nM.[104] Other RhodZin species **28** and **29** are included in Figure 1.8. RhodZin-3 has been used to visualize Zn(II) in mitochondria, but it apparently does not localize there reliably.[105] Newport Greens **30** and **31** represent another class of commercially available Zn(II) sensors. These sensors use the DPA chelate, have low to mid-μM affinity for Zn(II) and relatively poor dynamic range.[28,102]

The ZnAF sensor family, comprising sensors **32-40**, is depicted in Figure 1.9.[37,106,107] These sensors generally give rapid Zn(II) complexation and ~10- to ~60-fold fluorescence enhancement with Zn(II) coordination. The DPA-based sensors have low nM affinity for Zn(II). More recently, lower affinity ZnAF probes were described, which

have K_d values that range from the low nM to sub-mM.[37] This sensor suite was used to estimate the concentration of released zinc from hippocampal slices following depolarization. They hold much promise for future biological work and quantification.

Zinpyr Sensors and Related Compounds. The Zn(II) sensing initiative began in our laboratory in the late 1990s. In contrast to the xanthenone-based systems described above where the metal binding units are linked to the phenyl or benzoate ring, our approach was to install amine-based chelates on the "top" xanthenone unit of fluorescein. This design feature is similar to the one used in the preparation of Calcein,[108] a high-pH calcium ion sensor, and we chose fluorescein as the reporter because of its excellent photophysical properties ($\Phi \sim 1$, high ε) and biological compatibility. Figure 1.10 includes ZP1, **41**, and ZP2, **42**, the first fluorescein-based Zn(II)-responsive probes prepared by our group and, independently, by the Tsien laboratory at UCSD.[109,110] These sensors are symmetric and contain DPA units linked to the 4' and 5' positions of the xanthenone ring. ZP1 and ZP2 give modest ~3- to ~6-fold fluorescence enhancement following Zn(II) coordination, bind Zn(II) with dissociation constants of 0.7 ± 0.1 and 0.5 ± 0.1 nM, are selective for Zn(II) over the biologically relevant cations K(I), Na(I), Ca(II), and Mg(II) and exhibit substantial brightness ($\Phi \times \varepsilon$). These sensors, however, bind other divalent first-row transition metals with greater affinity and also fluoresce brightly in the presence of Cd(II). Major limitations of ZP1 and ZP2 are their pH sensitivity and high background fluorescence, which stem from the nature of the PET switch. Protonation of the tertiary amine nitrogen atom responsible PET occurs at neutral pH, which alleviates this quenching pathway and results in fluorescence emission. As a result, ZP1 and ZP2 have quantum yields of 0.38 and 0.25, respectively, at pH 7, which accounts for their modest dynamic range and can possibly complicate the interpretation of results from biological imaging experiments. Subsequently, trappable versions of ZP1, were prepared where an ethyl ester moiety was installed in the 5 or 6 position of the benzoate group (**43** and **44**, Figure 1.10), which

is hydrolyzed by intracellular esterases to afford sensors **45** and **46** that exhibit improved intracellular retention.[111]

ZP4, **47**, also depicted in Figure 1.10, was designed both to achieve lower background fluorescence and to afford a monofunctional Zn(II)-binding unit.[112] Because anilines have lower pK_a values than tertiary amines, and it was hypothesized that this group would be less susceptible to protonation at physiological pH than the tertiary amines of ZP1 and ZP2 and thereby afford lower background fluorescence. ZP4 has Φ_{free} = 0.06 and exhibits ~5-fold fluorescence enhancement immediately after Zn(II) coordination. Although emission from the Zn(II) complex is bright, the binding event fails to restore full fluorescein-like emission and Φ_{Zn} is only 0.33. The Zn(II) selectivity and sub-nM affinity of ZP4 (K_d = 0.65 nM) are similar to those of ZP1, which was anticipated given the DPA-appended metal-ion chelate.

The ZP1 and ZP4 platforms also provided a basis for ratiometric Zn(II) sensor design. Dual-excitation dual-emission ratiometric detection was achieved by linking a Zn(II)-insensitive coumarin 343 to ZP1 through an alkyl-amidoester (CZ1, **48**) or di-ester (CZ2, **49**) linkage.[113,114] CZ1 and CZ2, depicted in Figure 1.11, both exhibit weak emission (Φ_{free} < 0.05) under simulated physiological conditions. Hydrolysis of the ester bonds in vitro results in emission enhancement from both the ZP1 and coumarin chromophores with ~8- (CZ1) and ~4-fold (CZ2) increases in the ratio of ZP1/coumarin 343 integrated emission following Zn(II) addition. These sensors are cell permeable and a small ratiometric change was observed in cultured HeLa cells treated with CZ2 following Zn(II)/pyrithione addition.

Single fluorophore ratiometric Zn(II) sensors were also considered and are shown in Figure 1.11. RF-2, **50**, has a pyridine-derivatized cyclen linked to a hybrid fluorescein/rhodamine chromophore.[115] Although RF-2 shows some fluorescence enhancement with Zn(II) binding (K_d ~ 15 μM), the change is not ratiometric. Subsequently, the ZP4 analog ZNP1, **51**, was prepared (Figure 1.11).[116] The

seminaphthofluorescein chromophore affords single-excitation dual-emission ratiometric detection of Zn(II) (λ_{624} / λ_{524}) when excited at 499 nm. The ~18-fold ratio change results from selective enhancement of the 624 nm emission band following Zn(II) addition. Given the conserved aniline-based ligand, ZNP1 exhibits similar Zn(II) affinity (K_d = 0.50 nM) and selectivity as ZP4.

Goals and Organization of this Thesis

The ZP sensors described above provided a solid foundation for the design and implementation of new small-molecule Zn(II) imaging tools. The studies described in this thesis were intended to accomplish several important objectives. From a synthetic perspective, the primary goals were to prepare and characterize Zn(II) sensors that (i) span a wider range of K_d values, (ii) have improved Zn(II) selectivity, (iii) display lower background fluorescence and improved dynamic range, and (iv) bind Zn(II) rapidly and reversibly on the biological (millisecond) timescale. Through modifications of the fluorophore and ligand units, we obtained Zn(II) sensors that (i) have K_d values that cover approximately six orders of magnitude, from the sub-nM to mid-μM; (ii) exhibit Zn(II)-selective fluorescence enhancement, binding Zn(II) over many other species including its Group 12 congeners, biologically relevant cations and many divalent first-row transition metal ions; (iii) give up to ~150-fold fluorescence enhancement resulting from an ~76-fold reduction in background fluorescence relative to parent ZP1; and (iv) display rapid and reversible Zn(II) coordination with association and dissociation rates on the sub-millisecond timescale. Some of these Zn(II) sensors were successfully applied in multiple biological contexts with the following aims: (i) understanding sensor uptake, distribution and Zn(II) response in cultured cells and biological tissues; (ii) illustrating that the K_d value is an important parameter for Zn(II) detection in vivo; (iii) imaging endogenous Zn(II), including Zn(II) release and mobilization in neuronal

cultures; and (iv) using probes of varying affinity to provide information about Zn(II) concentration in both hippocampal tissue and following release from native stores.

The details of these investigations are included in Chapters 2 – 7. These chapters are generally organized in terms of the synthetic goals listed above. Chapters 2 and 3 include studies of new DPA-derivatized ZP family members, **52-59**, depicted in Figure 1.12. The main objective of these studies was to learn how substituent effects influence the fluorescence properties of the ZP platforms. In Chapters 4-7, we depart from the DPA ligand motif with the primary aim of varying Zn(II) affinity. We first present ZP9, **60**, and ZP10, **61** (Figure 1.12). These probes are ZP4 (Figure 1.10) analogs, in which one pyridyl group is replaced by a pyrrole moiety. These substitutions lower Zn(II) binding affinity and improve Zn(II) selectivity relative to DPA-containing ZP. Chapters 5 and 6 detail our investigations of fluorescein-based "Zinspy" sensors **62-71** (Figure 1.12), which contain sulfur moieties in the Zn(II) binding unit. Originally, this work was inspired by the occurrence of Zn—S linkages, including the Cys_2His_2 binding motif of Zn(II) finger peptides, in biology. As a result, these studies began with consideration of thiol donors (Appendix 1), but sensors with thioether (Chapter 5) and thiophene (Chapter 6) groups proved more useful for turn-on Zn(II) detection. The Zinspy probes also display lower Zn(II) affinity and improved Zn(II) selectivity relative to DPA-containing ZP sensors. Chapter 7 details our most significant departures from the ZP sensor motifs. In this work, we present the QZ family, comprised of sensors **72** and **73** (Figure 1.12), which have one or two aminoquinoline units installed on the fluorescein moiety. These sensors exhibit micromolar K_d values, readily reversible Zn(II) binding and up to ~150-fold fluorescence enhancement with Zn(II) coordination. Biological imaging studies are included throughout these chapters and are organized according to the sensor being utilized. Chapters 8-11 discuss our Hg(II) sensing initiative.

References

(1)   Vallee, B. L.; Falchuk, K. H. *Physiol. Rev.* **1993**, *73*, 79-118.

(2)   Walker, C. F.; Black, R. E. *Annu. Rev. Nutr.* **2004**, *24*, 255-275.

(3)   Diayasu, H.; Osaka, K.; Ishino, Y.; Toh, H. *FEBS Lett.* **2001**, *503*, 1-6.

(4)   Ho, E.; Ames, B. N. *Proc. Natl. Acad. Sci. USA* **2002**, *99*, 16770-16775.

(5)   Trúong-Tran, A. Q.; Carter, J.; Ruffin, R. E.; Zalewski, P. D. *Biometals* **2001**, *14*, 315-330.

(6)   Kimura, E.; Aoki, S.; Kikuta, E.; Koike, T. *Proc. Natl. Acad. Sci. USA* **2003**, *100*, 3731-3736.

(7)   Chausmer, A. B. *J. Am. Coll. Nutr.* **1998**, *17*, 109-115.

(8)   Henshall, S. M. et. al. *Oncogene* **2003**, *22*, 6005-6012.

(9)   Burdette, S. C.; Lippard, S. J. *Proc. Natl. Acad. Sci. USA* **2003**, *100*, 3605-3610.

(10)   Frederickson, C. J. *Int. Rev. Neurobiol.* **1989**, *31*, 145-238.

(11)   Frederickson, C. J.; Suh, S. W.; Silva, D.; Thompson, R. B. *J. Nutr.* **2000**, *130*, 1471S-1483S.

(12)   Salazar, G.; Craige, B.; Love, R.; Kalman, D.; Faundez, V. *J. Cell Sci.* **2005**, *118*, 1911-1921.

(13)   Sudhof, T. C. *Annu. Rev. Neurosci.* **2004**, *27*, 509-547.

(14)   Li, Y. V.; Hough, C. J.; Sarvey, J. M. *Science STKE* **2003**, pe19.

(15)   Kim, T. Y.; Hwang, J. J.; Yun, S. H.; Jung, M. W.; Koh, J. Y. *Synapse* **2002**, *46*, 49-56.

(16)   Molhar, P.; Nadler, J. V. *Brain Res.* **2001**, *910*, 205-207.

(17)   Williams, K. *Neurosci. Lett.* **1996**, *215*, 9-12.

(18)   Paoletti, P.; Ascher, P.; Neyton, J. *J. Neurosci.* **1997**, *17*, 5711-5725.

(19)   Smart, T. G.; Xie, X.; Krishek, B. J. *Prog. Neurobiol.* **1994**, *42*, 339-341.

(20)   Casagrande, S.; Valle, L.; Cupello, A.; Robello, M. *Eur. Biophys. J.* **2003**, *32*, 40-46.

(21)   Xie, X.; Smart, T. G. *Eur. J. Neurosci.* **1993**, *4*, 430-436.

(22)   Davies, P. A.; Wang, W.; Hales, T. G.; Kirkness, E. F. *J. Biol. Chem.* **2003**, *278*, 712-717.

(23)   Li, Y.; Hough, J. H.; Frederickson, C. J.; Sarvey, J. M. *Neuroscience* **2001**, *21*, 8015-8025.

(24)   Frederickson, C. J.; Giblin, L. J.; Rengarajan, B.; Masalha, R.; Frederickson, C. J.; Zeng, Y.; Lopez,
        E. V.; Koh, J. Y.; Chorin, U.; Besser, L.; Hershfinkel, M.; Li, Y.; Thompson, R. B.; Krezel, A. *J.
        Neurosci. Meth.* **2006**, *ASAP*.

(25)   Kay, A. R.; Toth, K. *J. Neurophys.* **2005**, *95*, 1956-2006.

(26)   Kay, A. R. *Trends Neurosci.* **2006**, *29*, 200-206.

(27)   Frederickson, C. J.; Bush, A. I. *Biometals* **2001**, *14*, 353-366.

(28)   Qian, J.; Noebels, J. L. *J. Physiol.* **2005**, *566*, 747-758.

(29)   Assaf, S. Y.; Chung, S. H. *Nature* **1984**, *308*, 734-736.

(30)   Howell, G. A.; Welch, M. G.; Frederickson, C. J. *Nature* **1984**, *308*, 736-738.

(31)   Thompson, R. B.; Whetsell, W. O.; Maliwal, B. P.; Fierke, C. A.; Frederickson, C. J. *J. Neurosci. Meth.* **2000**, *96*, 35-45.

(32)   Ureno, S.; Tsukamoto, M.; Hirano, T.; Kikuchi, K.; Yamada, M. K.; Niskiyama, N.; Nagano, T.; Matsuki, N.; Ikegaya, Y. *J. Cell. Biol.* **2002**, *158*, 215-220.

(33)   Li, Y.; Hough, C. J.; Suh, S. W.; Sarvey, J. M.; Frederickson, C. J. *J. Neurophysiol.* **2001**, *86*, 2597-2604.

(34)   Gothard, K. M.; Hoffman, K. L.; Battaglia, F. P.; McNaughton, B. L. *J. Neurosci.* **2001**, *21*, 7284-7292.

(35)   Jung, M. W.; McNaughton, B. L. *Hippocampus* **1993**, *3*, 165-182.

(36)   Kay, A. R. *J. Neurosci.* **2003**, *23*, 6847-6855.

(37)   Komatsu, K.; Kikuchi, K.; Kojima, H.; Urano, Y.; Nagano, T. *J. Am. Chem. Soc.* **2005**, *127*, 10197-10204.

(38)   Takeda, A.; Yamada, K.; Minami, A.; Nagano, T.; Oku, N. *Epilepsy Res* **2005**, *63*, 77-84.

(39)   Frederickson, C. J.; Koh, J. Y.; Bush, A. I. *Nature Neurosci* **2005**, *6*, 449-4462.

(40)   Liuzzi, J. P.; Cousins, R. J. *Annu. Rev. Nutr.* **2004**, *24*, 151-172.

(41)   Valente, T.; Auladell, C. *Mol. Cell Neurosci* **2002**, *21*, 189-204.

(42)   Cole, T. B.; Wenzel, H. J.; Kafer, K. E.; Schwartzkroin, P. A.; Palmiter, R. D. *Proc. Natl. Acad. Sci. USA* **1999**, *96*, 1716-1721.

(43)   Lee, J.-Y.; Cole, T. B.; Palmiter, R. D.; Koh, J. Y. *J. Neurosci.* **2000**, *20*, RC791-RC795.

(44)   Jacob, C.; Maret, W.; Vallee, B. L. *Proc. Natl. Acad. Sci. USA* **1998**, *95*, 3489-3494.

(45)   Ebadi, M.; Iversen, P. L.; Hao, R.; Cerutis, D. R.; Rojas, P.; Happe, H. K.; Murrin, L. C.; Pfeiffer, R. F. *Neurochem Int.* **1995**, *27*, 1-22.

(46)   Maret, W. *Biometals* **2001**, *14*, 187-190.

(47)   Choi, D. W.; Koh, J. Y. *Annu. Rev. Neurosci.* **1998**, *21*, 347-375.

(48)   Frederickson, C. J.; Maret, W.; Cuajungco, M. P. *The Neuroscientist* **2004**, *10*, 18-25.

(49)   Cuajungco, M. P.; Lees, G. J. *Neurobiol. Dis.* **1997**, *4*, 137-169.

(50)   Bush, A. I. *Trends Neurosci.* **2003**, *26*, 207-214.

(51)   Bush, A. I. *Alzheimer Dis. Assoc. Disord.* **2003**, *17*, 147-150.

(52)   Suh, S. W.; Jensen, K. B.; Jensen, M. S.; Silva, D. S.; Kesslak, P. J.; Danscher, G.; Frederickson, C. J. *J. Brain Res.* **2000**, *852*, 274-278.

(53)   Mocchegiani, E.; Bertoni-Freddari, C.; Marcellini, F.; Malavolta, M. *Prog. Neurobiol.* **2005**, *75*, 367-390.

(54)   Garcia-Colunga, J.; Vazquez-Gomez, E.; Miledi, R. *Pharmacogenomics J.* **2004**, *4*, 388-393.

(55)   Sensi, S. L.; Yin, H. Z.; Carriedo, S. G.; Rao, S. S.; Weiss, J. H. *Proc. Natl. Acad. Sci. USA* **1999**, *96*, 2414-2419.

(56)   Sensi, S. L.; Yin, H. Z.; Weiss, J. H. *Eur. J. Neurosci.* **2000**, *12*, 3813-3818.

(57)   Kim, E. Y. et. al. *Eur. J. Neurosci.* **1999**, *11*, 327-334.

(58)   Sensi, S. L.; Yin, H. Z.; Weiss, J. H. *Neuroreport* **1999**, *10*, 1723-1727.

(59)   Cuajungco, M. P.; Lees, G. J. *Brain Res.* **1998**, *799*, 118-129.

(60)   Huang, Z.; Huang, P. L.; Panahian, N.; et. al. *Science* **1994**, *265*, 1883-1885.

(61)   Koh, J. Y.; Suh, S. W.; Gwag, B. J.; He, Y. Y.; Hsu, C. Y.; Choi, D. W. *Science* **1996**, *272*, 1013-1016.

(62)   Che, Y.; Irie, Y.; Keung, W. M.; Maret, W. *Biochemistry* **2002**, *41*, 8360-8367.

(63)   Spahl, D. U.; Berendji-Grun, D.; Suschek, C. V.; Kolb-Bachofen, V.; Kroncke, K. D. *Proc. Natl. Acad. Sci. USA* **2003**, *100*, 13952-13957.

(64)   Bossy-Wetzel, E.; Talantova, M. V.; Lee, W. D.; Scholzke, M. N.; Harrop, A.; Mathews, E.; Gotz, T.; Han, J.; Ellisman, M. H.; Perkins, G. A.; Lipton, S. A. *Neuron* **2004**, *41*, 351-365.

(65)   Frederickson, C. J.; Kasarskis, E. J.; Ringo, D.; Frederickson, R. E. *J. Neurosci. Meth.* **1987**, *20*, 91-103.

(66)   Toroptsev, I. V.; Eshchenko, V. A. *Tsitologiya* **1970**, *12*, 1481-1484.

(67)   Toroptsev, I. V.; Eshchenko, V. A. *Bull. Exp. Biol. Med.* **1971**, *72*, 118-120.

(68)   Kimura, E.; Koike, T. *Chem. Soc. Rev.* **1998**, *27*, 179-184.

(69)   Takahashi, A.; Camacho, P.; Lechleiter, J. D.; Herman, B. *Physiol. Rev.* **1999**, *79*, 1089-1125.

(70)   Thompson, R. B.; Cramer, M. L.; Bozym, R.; Fierke, C. A. *J. Biomed. Opt.* **2002**, *7*, 550-560.

(71)   Hong, S.-H.; Maret, W. *Proc. Natl. Acad. Sci. USA* **2003**, *100*, 2255-2260.

(72)   Walkup, G. K.; Imperiali, B. *J. Org. Chem.* **1996**, *63*, 6727-6731.

(73)   Walkup, G. K.; Imperiali, B. *J. Am. Chem. Soc.* **1996**, *118*, 3053-3054.

(74)   Jotterand, M.; Pearce, D. A.; Imperiali, B. *J. Org. Chem.* **2001**, *66*, 3224-3228.

(75)   Godwin, H. A.; Berg, J. M. *J. Am. Chem. Soc.* **1996**, *118*, 6514-6515.

(76)   Shults, M. D.; Pearce, D. A.; Imperiali, B. *J. Am. Chem. Soc.* **2003**, *125*, 10591-10597.

(77)   Lu, Y. *Chem. Eur. J.* **2002**, *8*, 4589-4596.

(78)   Liu, J.; Lu, Y. *J. Am. Chem. Soc.* **2002**, *124*, 15208-15216.

(79)   Bozym, R.; Thompson, R. B.; Stoddard, A. K.; Fierke, C. A. *ACS Chem. Biol.* **2006**, *1*, 103-111.

(80)   Chang, C. J.; Lippard, S. J. *Metal Ions in Life Sciences* **2006**, *1*, 321-370.

(81)   Jiang, P.; Guo, Z. *Coor. Chem. Rev.* **2004**, *248*, 205-229.

(82)   Kikuchi, K.; Komatsu, K.; Nagano, T. *Cur. Opin. Chem. Biol.* **2004**, *8*, 182-191.

(83)   Lim, N. C.; Freake, H. C.; Bruckner, C. *Chem. Eur. J.* **2005**, *11*, 38-49.

(84)   Frederickson, C. J. *Science STKE* **2003**, pe18.

(85)   de Silva, A. P.; Gunaratne, N.; Gunnlaugsson, T.; Huxley, A. J. M.; McCoy, C. P.; Rademacher, J. T.; Rice, T. E. *Chem. Rev.* **1997**, *97*, 1515-1566.

(86)   Callan, J. F.; de Silva, A. P.; Magri, D. C. *Tetrahedron* **2005**, *61*, 8551-8588.

(87)   Henary, M. M.; Wu, Y.; Fahrni, C. J. *Chem. Eur. J.* **2004**, *10*, 3015-3025.

(88)   Fahrni, C. J.; O'Halloran, T. V. *J. Am. Chem. Soc.* **1999**, *121*, 11448-11458.

(89)   Nasir, M. S.; Fahrni, C. J.; Suhy, D. A.; Kolodsick, K. J.; Singer, C. P.; O'Halloran, T. V. *J. Biol. Inorg. Chem.* **1999**, *4*, 775-783.

(90)   Zalewski, P. D.; Millard, S. H.; Forbes, I. J.; Kapaniris, O.; Slavotinek, A.; Betts, W. H.; Ward, A. D.; Lincoln, S. F.; Mahadevan, I. B. *J. Histochem. Cytochem.* **1994**, *42*, 877-884.

(91)   Zalewski, P. D.; Forbes, I. J.; Seamark, R. F.; Borlinghaus, R.; Betts, W. H.; Lincoln, S. F.; Ward, A. D. *Chem. Biol.* **1994**, *1*, 153-161.

(92)   Zalewski, P. D.; Forbes, I. J.; Betts, W. H. *Biochem. J.* **1993**, *296*, 403-408.

(93)   Koike, T.; Watanabe, T.; Aoki, S.; Kimura, E.; Shiro, M. *J. Am. Chem. Soc.* **1996**, *118*, 12696-12703.

(94)   Koike, T.; Abe, T.; Takahashi, M.; Ohtani, K.; Kimura, E.; Shiro, M. *J. Chem. Soc. Dalton Trans.* **2002**, 176-1768.

(95)   Aoki, S.; Kaido, S.; Fujioka, H.; Kimura, E. *Inorg. Chem.* **2003**, *42*, 1023-1030.

(96)   Lim, N. C.; Yao, L.; Freake, H. C.; Bruckner, C. *Bioorg. Med. Chem. Lett.* **2003**, *13*, 2251-2254.

(97)   Lim, N. C.; Bruckner, C. *Chem. Commun.* **2004**, 1094-1095.

(98)   Gee, K. R.; Zhou, Z.-L.; Ton-That, D.; Sensi, S. L.; Weiss, J. H. *Cell Calcium* **2003**, *31*, 245-251.

(99)   Maruyama, S.; Kikuchi, K.; Hirano, T.; Urano, Y.; Nagano, T. *J. Am. Chem. Soc.* **2002**, *124*, 10650-10651.

(100)   Taki, M.; Wolford, J. L.; O'Halloran, T. V. *J. Am. Chem. Soc.* **2004**, *126*, 712-713.

(101)   Wu, Y.; Peng, X.; Guo, B.; Fan, J.; Zhang, Z.; Wang, J.; Cui, A.; Gao, Y. *Org. Biomol. Chem.* **2005**, *3*, 1387-1392.

(102)   Hirano, T.; Kikuchi, K.; Urano, Y.; Higuchi, T.; Nagano, T. *Angew. Chem. Int. Ed.* **2000**, *39*, 1052-1054.

(103)   Gee, K. R.; Zhou, Z.-L.; Qian, J.; Kennedy, R. *J. Am. Chem. Soc.* **2002**, *124*, 776-778.

(104)   Sensi, S. L.; Ton-That, D.; Weiss, J. H.; Rothe, A.; Gee, K. R. *Cell Calcium* **2003**, *34*, 281-284.

(105)   Sensi, S. L. *Personal communication*, November 2005.

(106)   Hirano, T.; Kikuchi, K.; Urano, Y.; Higuchi, T.; Nagano, T. *J. Am. Chem. Soc.* **2000**, *122*, 12399-12400.

(107)   Hirano, T.; Kikuchi, K.; Urano, Y.; Nagano, T. *J. Am. Chem. Soc.* **2002**, *124*, 6555-6562.

(108)   Diehl, H.; Ellingboe, J. L. *Anal. Chem.* **1956**, *28*, 882-884.

(109)   Walkup, G. K.; Burdette, S. C.; Lippard, S. J.; Tsien, R. Y. *J. Am. Chem. Soc.* **2000**, *122*, 5644-5645.

(110)   Burdette, S. C.; Walkup, G. K.; Spingler, B.; Tsien, R. Y.; Lippard, S. J. *J. Am. Chem. Soc.* **2001**, *123*, 7831-7841.

(111)   Woodroofe, C. C.; Masalha, R.; Barnes, K. R.; Frederickson, C. J.; Lippard, S. J. *Chem. Biol.* **2004**, *11*, 1659-1666.

(112)   Burdette, S. C.; Frederickson, C. J.; Bu, W.; Lippard, S. J. *J. Am. Chem. Soc.* **2003**, *125*, 1778-1787.

(113)   Woodroofe, C. C.; Lippard, S. J. *J. Am. Chem. Soc.* **2003**, *125*, 11458-11459.

(114)   Woodroofe, C. C.; Won, A. C.; Lippard, S. J. *Inorg. Chem.* **2005**, *44*, 3112-3120.

(115)   Burdette, S. C.; Lippard, S. J. *Inorg. Chem.* **2002**, *31*, 6816-6823.

(116)   Chang, C. J.; Jaworski, J.; Nolan, E. M.; Sheng, M.; Lippard, S. J. *Proc. Natl. Acad. Sci. USA* **2004**, *101*, 1129-1134.

(117)   Nolan, E. M.; Jaworski, J.; Sheng, M.; Lippard, S. J. *Unpublished results*.

(118)   Dubrun, L. E.; Garner, C. C. *Nature* **2002**, *415*, 277-278.
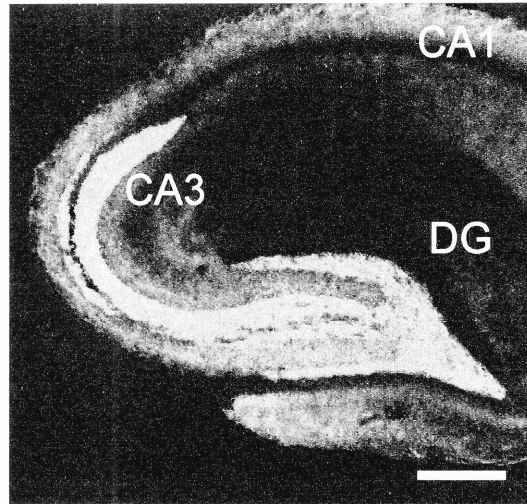
Figure 1.1. Confocal image of an acute hippocampal slice from adult rat treated with a ZP sensor illustrating the Zn(II) rish mossy fiber circuit (light grey).[117] Axons originating from the dentate gyrus (DG) synapse with dendrites in the CA3 region. The scale bar represents ~0.5 mm.
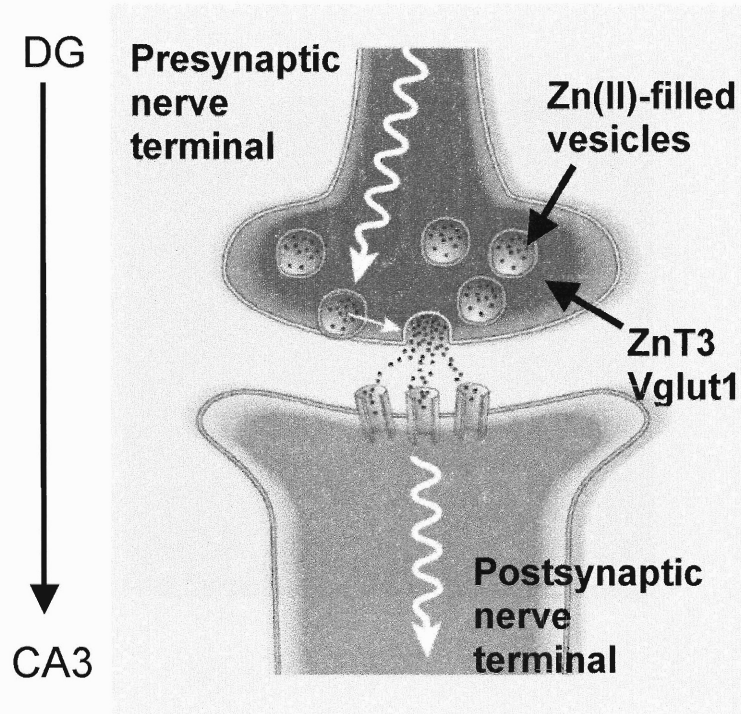
Figure 1.2. Representation of a synapse in the DG → CA3 circuit. Vesicles located in the presynaptic nerve terminal dock and release their contents into the synaptic cleft. In the Zn(II)-rich mossy fiber synapses of the DG region, the Zn(II)-filled vesicles co-express ZnT3 and Vglut1 and also house glutamate. The image was adapted from a figure taken from ref. 118.

A. Photoinduced Eelectron Transfer (PET)

acceptor   donor

fluorescence OFF   fluorescence ON
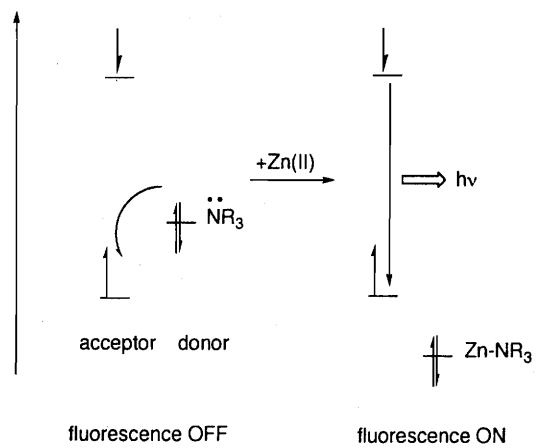
B. Excited State Intramolecular Proton Transfer (ESIPT)

L = solvent
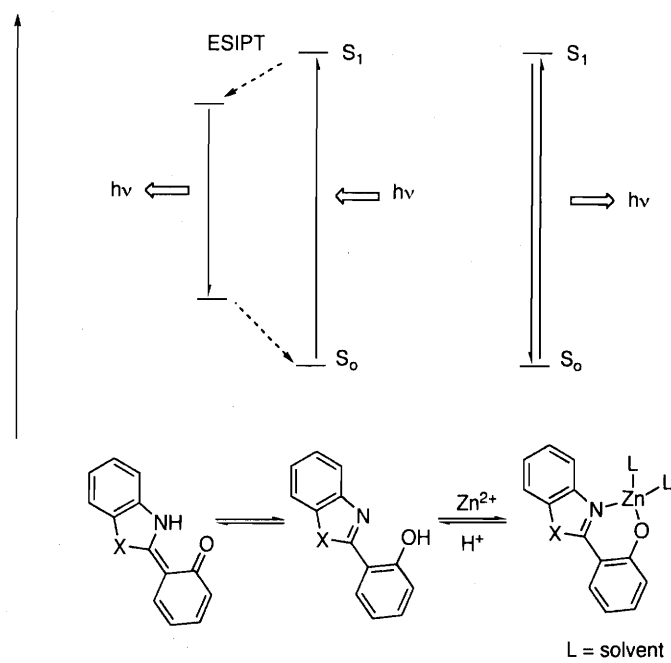
Figure 1.3. PET and ESIPT mechanisms.

1, TSQ

2, 2-Me-TSQ

3, Zinquin-A
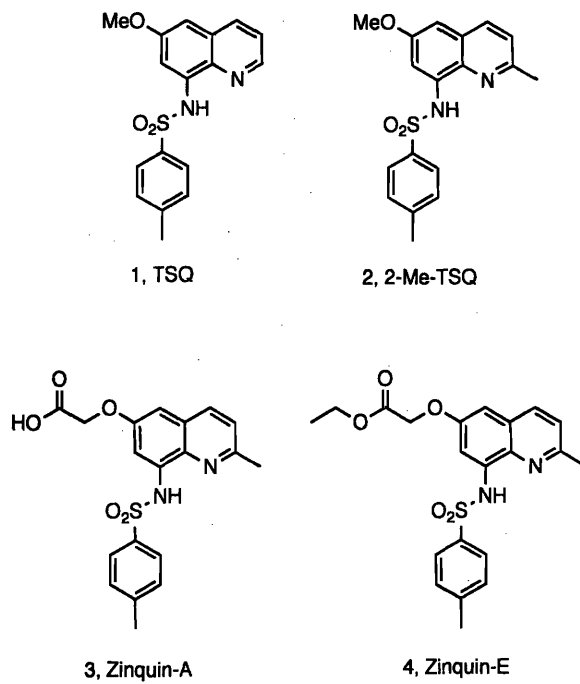
4, Zinquin-E

Figure 1.4. Aryl sulfonamide Zn(II) sensors, including TSQ and Zinquin.
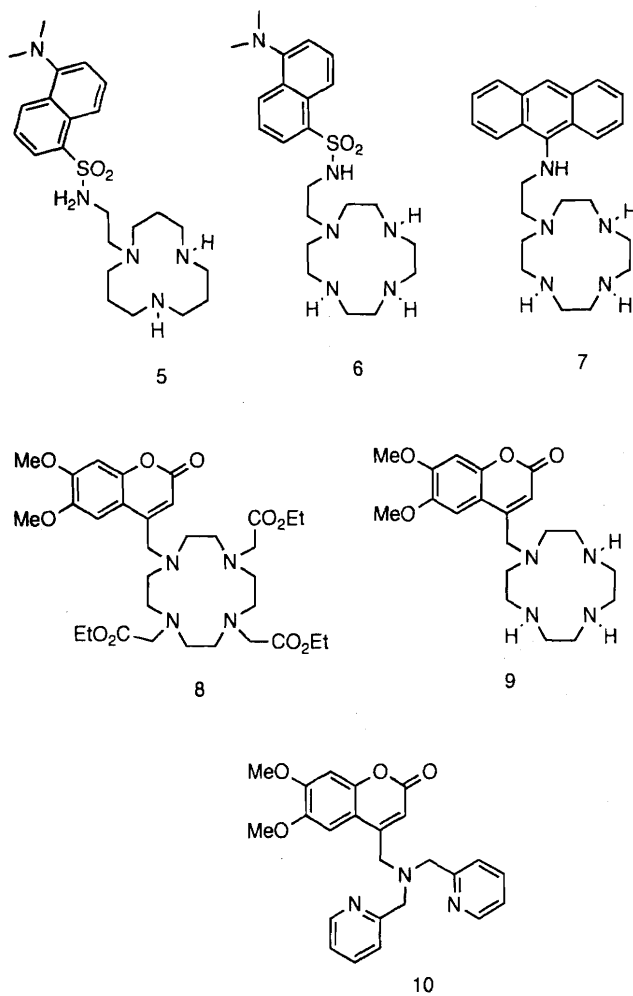
Figure 1.5. Other fluorescent Zn(II) sensors that require UV excitation.

11, FuraZin-1   12, IndoZin-1   13, ZnAF-R1   14, ZnAF-R2

16   17   18

R = H, Et

15, Zinbo-5
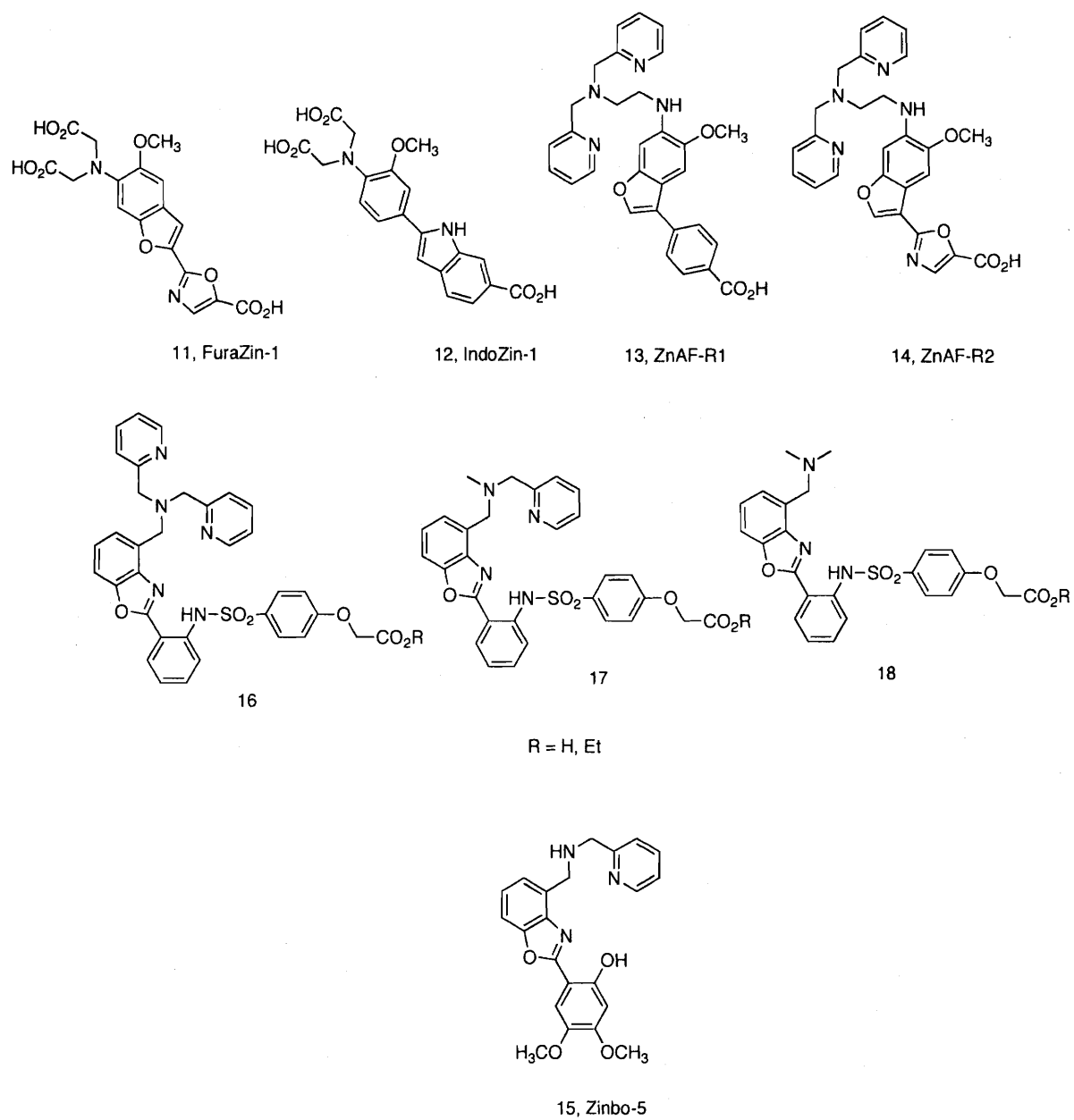
Figure 1.6. Ratiometric Zn(II) sensors that require UV excitation.
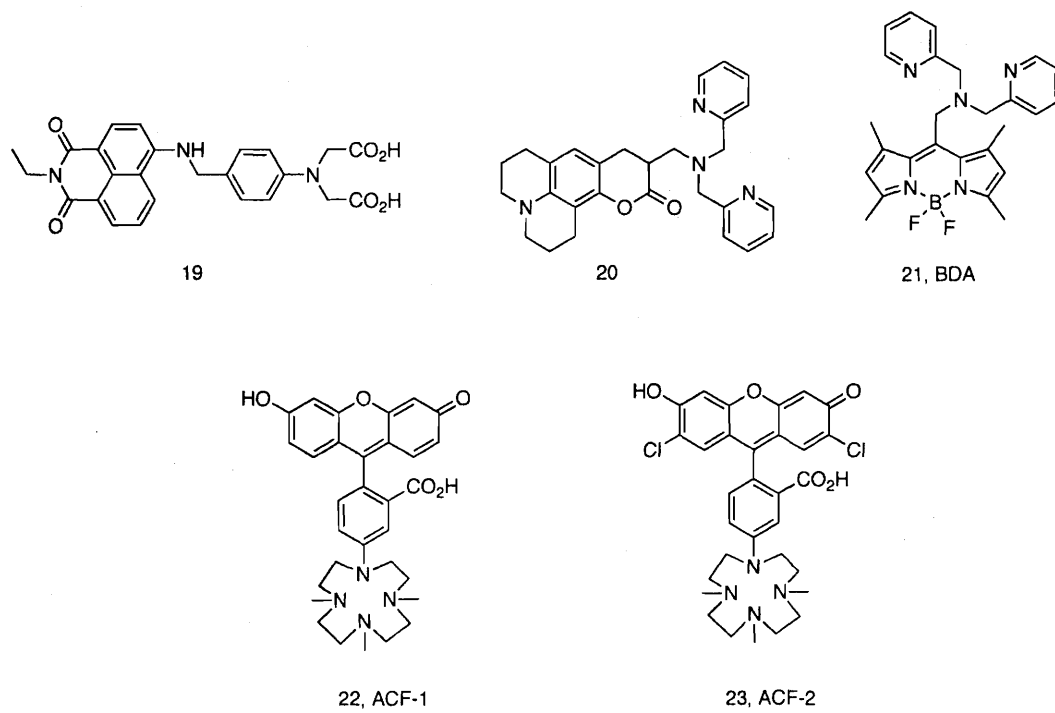
Figure 1.7. Fluorescent Zn(II) sensors that require visible excitation.

24, FluoZin-1

25, FluoZin-2

26, FluoZin-3

27, RhodZin-3

28, RhodZin

29, X-RhodZin

30, Newport Green

31, Newport Green DCF
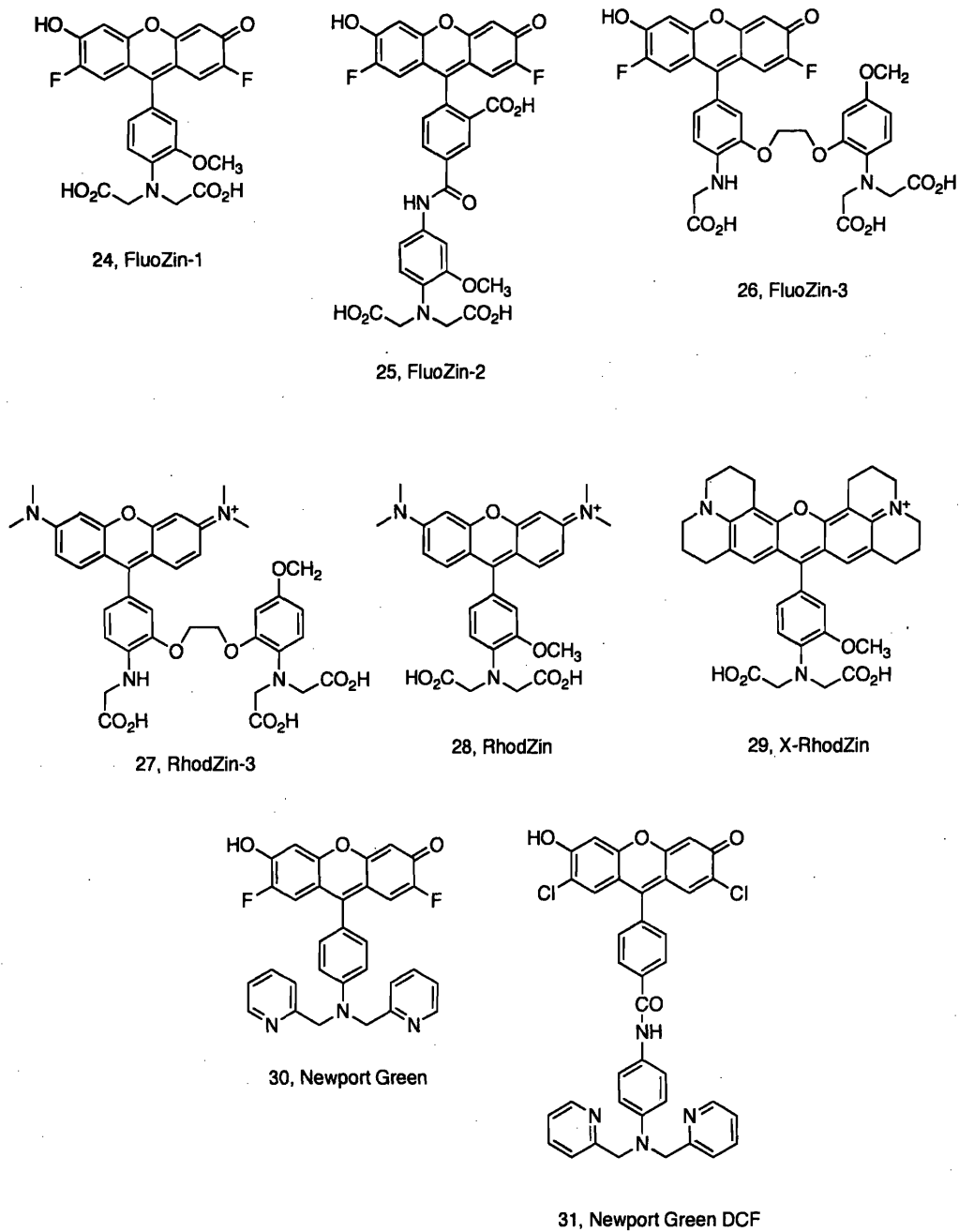
Figure 1.8. Fluorescent Zn(II) sensors that require visible excitation sold by Invitrogen.
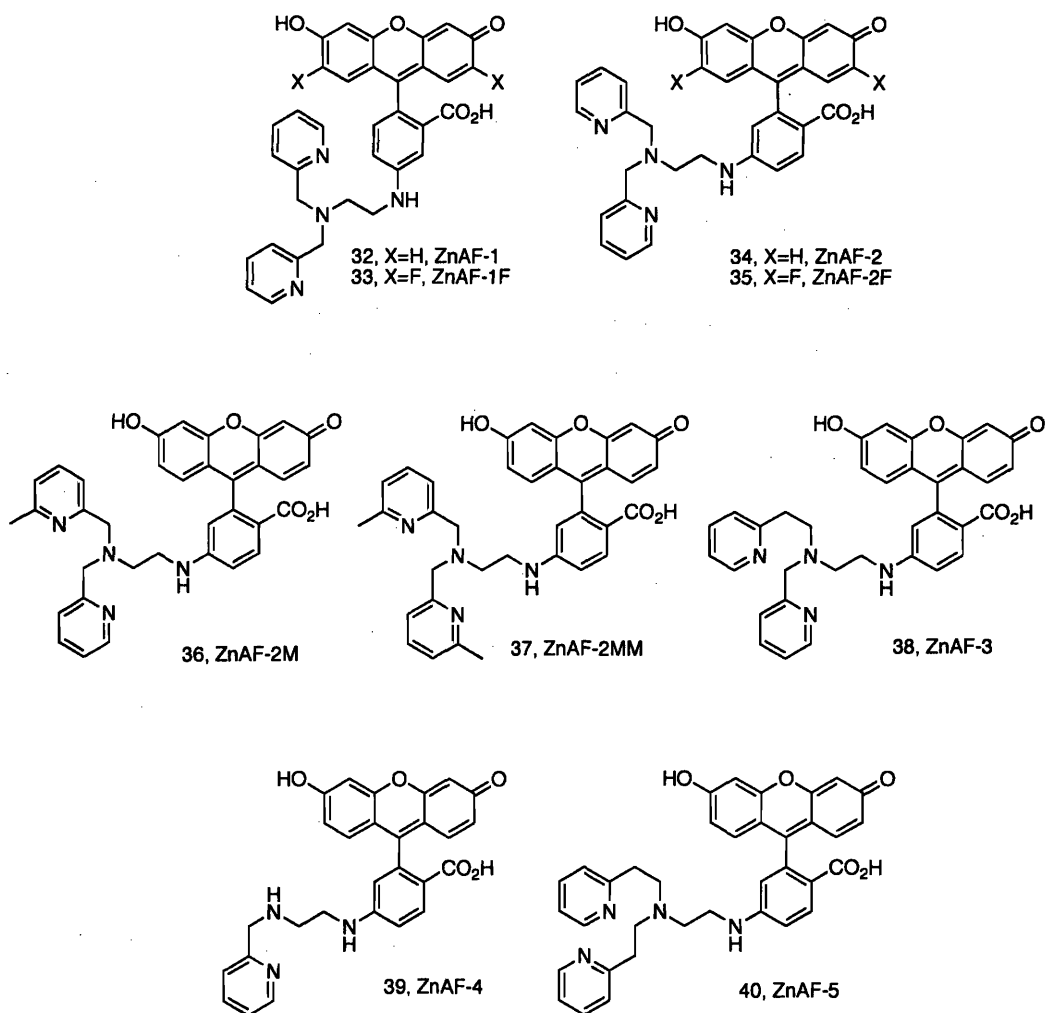
Figure 1.9. The ZnAF family of fluorescent Zn(II) sensors by Nagano and co-workers.

41, ZP1: X=Cl
42, ZP2: X=H

47, ZP4

45, ZP1(6-CO₂H), R=H
43, ZP1(6-CO₂Et), R=Et

46, ZP1(5-CO₂H), R=H
44, ZP1(5-CO₂Et), R=Et
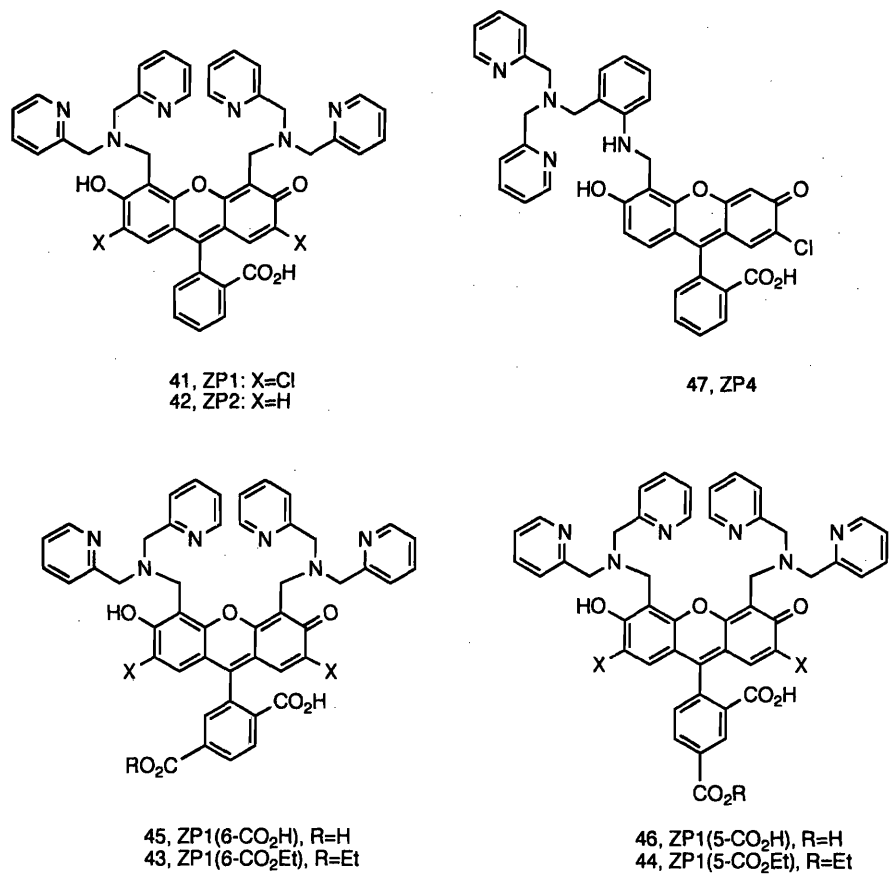
Figure 1.10. Fluorescent Zn(II) sensors of the Zinpyr family.
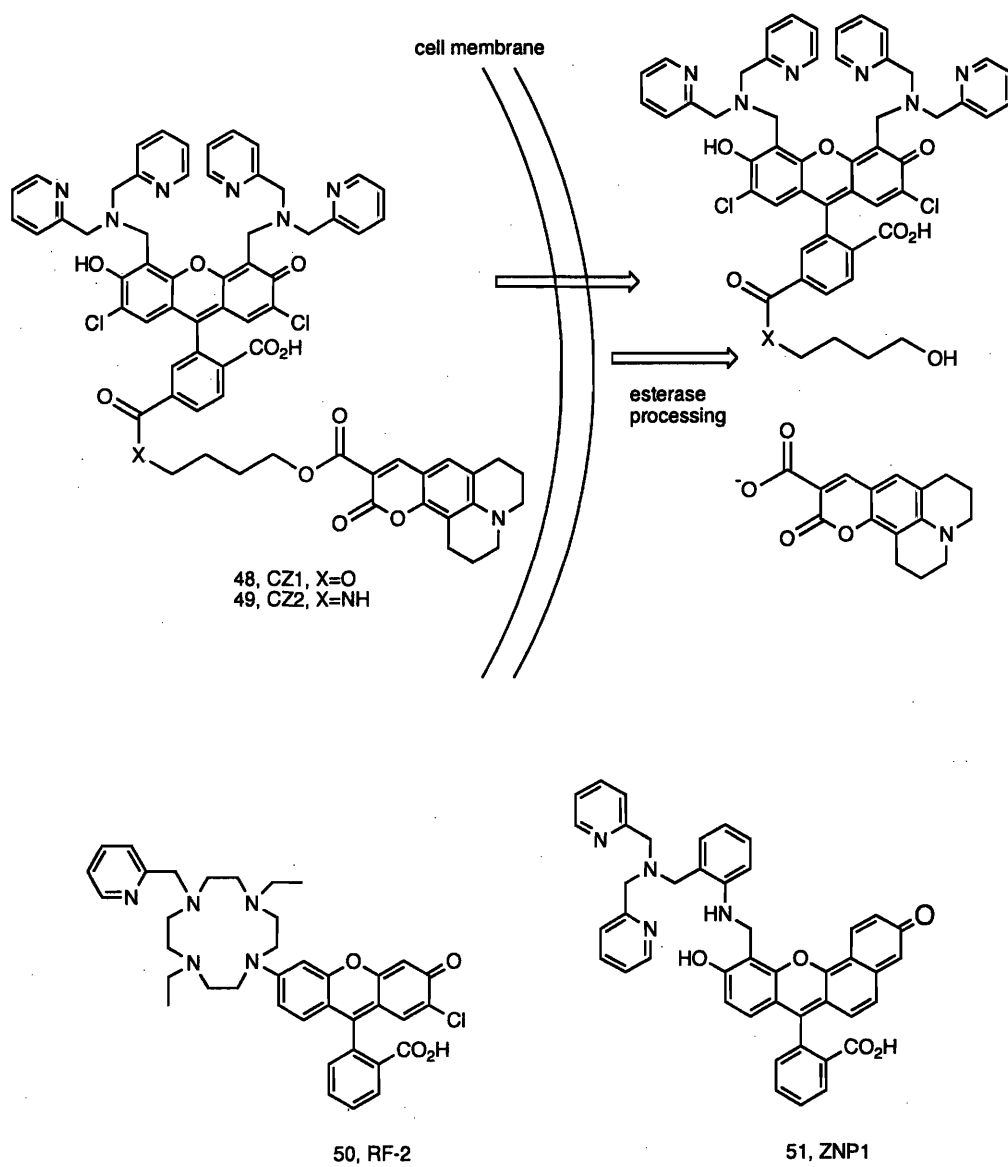
Figure 1.11. Dual- and single-fluorophore approaches to ratiometric Zn(II) detection.
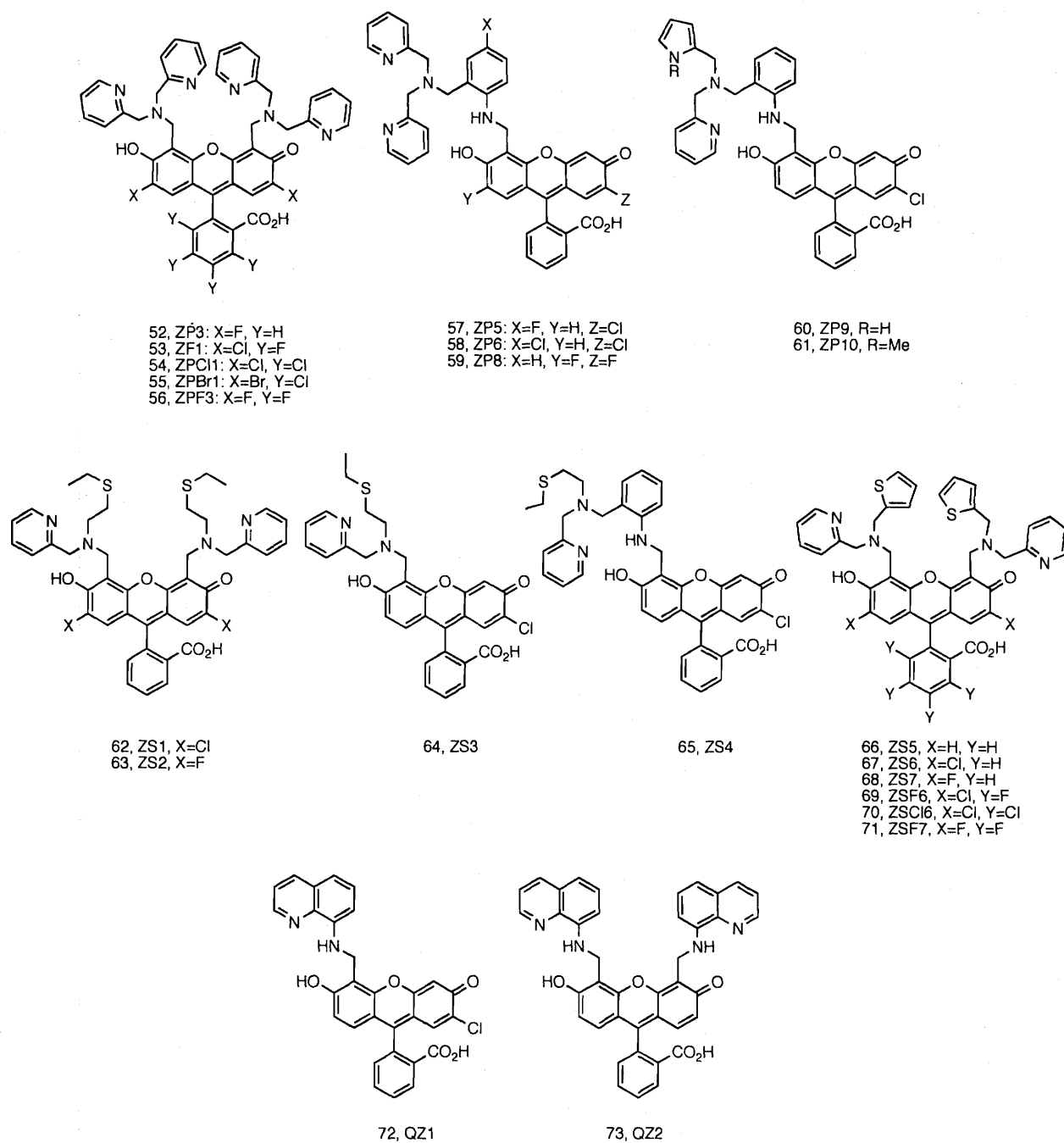
Figure 1.12. Zinc sensors presented in this thesis.

52, ZP3: X=F, Y=H
53, ZF1: X=Cl, Y=F
54, ZPCl1: X=Cl, Y=Cl
55, ZPBr1: X=Br, Y=Cl
56, ZPF3: X=F, Y=F

57, ZP5: X=F, Y=H, Z=Cl
58, ZP6: X=Cl, Y=H, Z=Cl
59, ZP8: X=H, Y=F, Z=F

60, ZP9, R=H
61, ZP10, R=Me

62, ZS1, X=Cl
63, ZS2, X=F

64, ZS3

65, ZS4

66, ZS5, X=H, Y=H
67, ZS6, X=Cl, Y=H
68, ZS7, X=F, Y=H
69, ZSF6, X=Cl, Y=F
70, ZSCl6, X=Cl, Y=Cl
71, ZSF7, X=F, Y=F

72, QZ1

73, QZ2

Chapter 2

Zinc Sensors Based on Monosubstituted Fluorescein Platforms I:

Routes to Electronic Variation, Syntheses and

Spectroscopic Characterization

Introduction

The role of zinc in neurobiology is a topic of substantial current interest.[1-5] High concentrations of loosely bound and mobile zinc are found in the mossy fiber terminals of the hippocampus, a region of the mammalian brain associated with learning and memory.[6,7] This zinc is colocalized with glutamate in synaptic vesicles, and its release has been implicated in neurological processes including long-term potentiation[8] and neurotransmission,[9-11] in addition to several neuropathologies.[12-14] Despite these implications, the functional significance of Zn(II) in neurobiology remains unclear.[15-19] In order to elucidate the role of Zn(II) in neurological processes, detection methods that exhibit selectivity and sensitivity for Zn(II) and are also suitable for use in biological fluids and tissues are required[20-22] and a substantial portion of the work described herein addresses this basic need.

As described in the proceeding chapter, our laboratory devised the Zinpyr (ZP) family of Zn(II) probes[23-25] and Figure 2.1 shows the ZP probes that were prepared prior to this work. Solutions of the first-generation ZP probes, ZP1, **1**, and ZP2, **2**, exhibit ~3 and ~6-fold fluorescence enhancement with addition of 1 equiv of Zn(II).[23,24] Compared to other Zn(II) sensors in the literature,[26-29] these probes have relatively high background fluorescence (ZP1, $\Phi = 0.32$; ZP3, $\Phi = 0.25$) and can form dinuclear Zn(II) complexes owing to the two di(2-picolyl)amine (DPA) moieties installed on the 4′ and 5′ positions of the xanthenone ring. In an effort to lower the brightness ($\Phi \times \varepsilon$) of the free ZP dyes and to obtain mononuclear Zn(II) complexes, ZP4, **3**, was designed (Figure 2.1).[25] This sensor contains an aniline-based DPA-derivatized ligand framework linked to an asymmetrical functionalized fluorescein platform. ZP4 exhibits lower background fluorescence ($\Phi = 0.06$) than the first-generation ZP probes, which was initially attributed to a decrease of the pK_a values of the nitrogen atom presumed to be responsible for photoinduced electron transfer (PET) quenching of the metal-free fluorophore (ZP1, $pK_a = 8.4$; ZP4, $pK_a = 7.2$). Since protonation can disrupt the PET

quenching pathway, a lower pK_a value for the PET switching nitrogen atom should correspond to lower background fluorescence.[30] Although we currently understand the details of the quenching mechanism to be more complex, this notion inspired the work presented in this chapter.

In particular, we explore the effect of varying the electronic properties of substituents on the fluorescence of asymmetrical ZP4-like sensors. The overall goal was to use these substituent effects to improve the fluorescence properties of parent sensor ZP4. This chapter can be roughly divided into two parts that address variation of substituents on the zinc-binding and fluorophore moieties, respectively. We first reasoned that, by altering the electronic properties of the zinc-binding unit, we might further tune the pK_a of the aniline nitrogen atom and thereby control the fluorescence properties of the sensor. Accordingly, we varied the electron-donating properties of the substituent para to the aniline nitrogen atom of parent sensor ZP4 (X = H, F, Cl, OMe), shown in Figure 2.1. We anticipated that installation of an electron-withdrawing substituent would lower the value of the aniline nitrogen atom pK_a and thereby afford reduced background fluorescence as compared to ZP4. Photophysical characterization of the new compounds in this series revealed both expected and unanticipated properties. This investigation also introduced a convergent synthetic strategy to assemble the sensors that requires an asymmetrical fluorescein carboxaldehyde, as detailed below. In the second thrust, we probed the effect of fluorescein halogenation on the sensor photophysical properties by preparing a modified ZP4 sensor with fluorine atoms in the 2′ and 7′ positions of the fluorescein. This initiative required the preparation of a fluorinated fluorescein precursor and utilized the sensor assembly pathway devised for ZP5 and ZP6.[31] Based on work in our laboratory[32] and elsewhere,[33] we anticipated that fluorination of the xanthenone moiety would yield lower background fluorescence and the results met this expectation.

Experimental Section

Reagents. Ethyl acetate, dimethylformamide, and pyridine were dried over 3 Å molecular sieves. Chlorobenzene and 1,2-dichloroethane (DCE) were distilled from CaH_2 under nitrogen and stored over 3 Å molecular sieves. Acetonitrile was either distilled over CaH_2 under nitrogen or was saturated with Ar and dried by passing through an activated Al_2O_3 column. DMSO was vacuum distilled from CaH_2 immediately before use or purchased from Aldrich in its anhydrous form. The preparation of the asymmetrical 7'-chloro-4'-fluoresceincarboxaldehyde, **4**, was conducted as described elsewhere[31,34] and as depicted in Scheme 2.1 with several modifications, the most important being that the reaction to form benzophenone **5** was not heated.[25] Aniline ligand **6** was synthesized according to the published protocol,[25] but with a shorter (~1 h) hydrogenation time to avoid decomposition of the desired product.

Materials and Methods. Silica gel-60 (230-400 mesh), Brockman I activated basic aluminum oxide (150 mesh), and octadecyl-functionalized silica gel (reverse phase, RP, RP18) were used as the solid phases for column chromatography. Merck F254 silica gel-60 plates, Merck F254 aluminum oxide-60 plates, or octadecyl-functionalized silica gel (RP18) plates were used for analytical thin layer chromatography (TLC). TLC plates were viewed with UV light or after developing with ninhydrin stain. NMR spectra were collected using either a Varian 300 MHz, a Varian 500 MHz, or a Bruker 400 MHz spectrometer operating at ambient probe temperature, 283 K, with internal standards for ^{1}H and ^{13}C NMR. External $CFCl_3$ was used to reference ^{19}F NMR spectra. IR spectra were obtained with an Avatar 360 FTIR instrument. Electron impact (EI) and electrospray ionization (ESI) spectrometry were performed by staff in the MIT Department of Chemistry Instrumentation Facility.

2-Nitro-5-fluorobenzylbromide (7). 2-Nitro-5-fluorotoluene (**8**, 9.3 g, 60 mmol), 1,2-dibromo-5,5-dimethylhydantoin (20 g, 70 mmol), and 1,1'-azobis(cyclohexane-

carbonitrile) (VAZO 88, 600 mg, 2.5 mmol) were combined in chlorobenzene (600 mL) with stirring. Glacial acetic acid (300 µL) was added and the solution was stirred at 40 °C for 96 h. The reaction was washed with 3 x 200 mL portions of warm saturated NaHCO$_3$, dried over MgSO$_4$, filtered and the solvent was removed under reduced pressure. The crude product is a red-orange solid and consists of approximately 1:1 starting material and product. This material was carried forward to the next step without further purification. Pure **7** can be obtained by column chromatography on silica (6:1 hexanes/EtOAc) as a brown solid (3.8 g, 37%). TLC R$_f$ = 0.70 (silica, 4:1 hexanes/EtOAc); mp = 33-34 °C. ^{1}H NMR (CDCl$_3$, 300 MHz) δ 4.83 (2H, s), 7.17 (1H, t,), 7.31 (1H, d), 8.16 (1H, m). ^{13}C NMR (CDCl$_3$, 125 MHz) δ 33.65, 74.27, 116.60, 119.34, 128.33, 136.17, 166.18. ^{19}F NMR (300 MHz) δ 69.91. FTIR (KBr, cm^{-1}) 3081, 2952, 2865, 1617, 1590, 1529, 1484, 1442, 1414, 1345, 1276, 1251, 1224, 1161, 1139, 1074, 969, 946, 906, 873, 837, 761, 732, 691, 610, 569. HRMS (EI): Calcd [M + H]$^+$, 232.9482; Found, 232.9497.

1-Fluoro-4-nitro-3-[bis(2-pyridylmethyl)aminomethyl]benzene (9). A portion (~7 g, ~30 mmol, obtained from a 13.9 g mixture containing ~50% **8**) of **7**, di(2-picolyl)amine (DPA, 7.4 g, 36 mmol), K$_2$CO$_3$ (49 g, 355 mmol), and activated 3 Å molecular sieves were combined in 250 mL of CH$_3$CN and stirred for 12 h at room temperature. The reaction was filtered through Celite and the solvent was removed in vacuo to yield a brown oil. Column chromatography on basic Al$_2$O$_3$ with a solvent gradient (9:1 to 4:1 to 7:3 CH$_2$Cl$_2$/EtOAc) yielded the product as a brown solid (4.8 g, 40%). TLC R$_f$ = 0.63 (Al$_2$O$_3$, 3:1 CH$_2$Cl$_2$/EtOAc); mp = 72-74 °C. ^{1}H NMR (CDCl$_3$, 300 MHz) δ 3.81 (4H, s), 4.08 (2H, s), 6.99 (1H, m), 7.13 (2H, t), 7.38 (2H, d), 7.63 (3H, m), 7.86 (1H, m), 8.61 (2H, d). ^{13}C NMR (CDCl$_3$, 125 MHz) δ 55.66, 60.25, 114.75, 118.20, 122.61, 123.53, 127.36, 137.17, 138.95, 148.81, 158.13, 163.05, 166.44. ^{19}F NMR (300 MHz) δ 71.88. FTIR (KBr, cm^{-1}) 3109, 3056, 2934, 2852, 1620, 1589, 1519, 1474, 1434, 1364, 1337, 1304, 1262, 1209, 1146, 1065, 958, 904, 845, 824, 773, 761, 684, 620, 581. HRMS (ESI) Calcd [M + H]$^+$, 353,1308; Found, 353.1414.

4-Amino-1-fluoro-3[bis(2-pyridylmethyl)aminomethyl]benzene (10). A flask containing Pd/C (10% activated, 2g) was purged with Ar and 100 mL of MeOH was added. A portion (1.0 g, 3.0 mmol) of **9** was dissolved in 100 mL of MeOH and added to the reaction flask with a syringe. The reaction was stirred vigorously under H_2 (1 atm) for 2 h, purged with Ar, filtered through Celite and the solvent was removed in vacuo. Column chromatography on basic Al_2O_3 using a solvent gradient (4:1 CH_2Cl_2/EtOAc to 7:2:1 CH_2Cl_2/EtOAc/MeOH) afforded the product as a yellow oil (340 mg, 37%). TLC R_f = 0.58 (Al_2O_3, 3:1 CH_2Cl_2/EtOAc). ^{1}H NMR ($CDCl_3$, 300 MHz) δ 3.63 (2H, s), 3.80 (4H, s), 6.54 (1H, m), 6.79 (2H, m), 7.15 (2H, m), 7.36 (2H, d,), 7.61 (2H, t), 8.55 (2H, d). ^{13}C NMR ($CDCl_3$, 125 Hz) δ 50.50, 57.21, 58.64, 122.94, 113.23, 116.75, 122.87, 123.70, 125.55, 137.74, 148.92, 149.51, 157.37. ^{19}F NMR (300 MHz) δ 44.84. FTIR (NaCl disk, cm^{-1}) 3320, 3214, 2054, 3010, 2923, 2824, 1617, 1590, 1434, 1368, 1287, 1246, 1148, 1093, 1034, 864, 814, 762, 619, 511. HRMS (ESI) Calcd [M + Na]$^+$, 345.1486; Found, 345.1497.

2-[5-({2-[(Bis(pyridin-2-ylmethyl)amino)methyl]-4-fluorophenylimino}methyl)-2-chloro-6-hydroxy-3-oxo-9,9a-dihydro-3H-xanthen-9-yl]benzoic acid (11, Zinpyr-5 Imine). A portion (100 mg, 0.312 mmol) of **4** was combined with **10** (125 mg, 0.317 mmol) in 6 mL of EtOAc to yield a pink solution, which was stirred at room temperature for 20 h. A light pink precipitate formed. The mixture was cooled on ice and filtered, and the precipitate was washed with cold EtOAc. The product was used without further purification (135 mg, 62%). ^{1}H NMR (CD_3OD, 400 MHz) δ 3.88 (4H, s), 3.96 (2H, d), 6.66 (1H, s), 6.69 (1H, d), 6.80 (1H, d), 6.99 (1H, s), 7.15 (1H, t), 7.20 (2H, t), 7.34 (4H, m), 7.56 (2H, d), 7.68 (2H, td), 7.77 (1H, t), 7.83 (1H, t), 7.91 (1H, s), 8.08 (1H, d), 8.36 (2H, d), 9.25 (1H, s). ^{19}F NMR (300 MHz) δ 56.30. FTIR (KBr, cm^{-1}) 3420, 2920, 2849, 1763, 1634, 1594, 1481, 1359, 1271, 1224, 1178, 1151, 1106, 1037, 998, 871, 800, 761, 732, 613, 546, 487. HRMS (ESI) Calcd [M + H]$^+$, 699.1811 (major), 700.1844, 701.1781, 702.1815; Found, 699.1807 (major), 700.1888, 701.1851, 702.1911.

2-[5-({2-[(Bis(pyridin-2-ylmethyl)amino)methyl]-4-fluorophenylamino}methyl)-2-chloro-6-hydroxy-3-oxo-9,9a-dihydro-3*H*-xanthen-9-yl]benzoic acid (12, Zinpyr-5, ZP5). A portion (85 mg, 0.123 mmol) of **11** was dissolved in 10 mL of DCE and NaB(OAc)₃H (39 mg, 0.184 mmol) was added. The reaction was stirred for 2.5 h and changed from cloudy yellow-orange to clear red-orange. The reaction was quenched with 10 mL of brine and the brine was extracted (3 x 10 mL) with chloroform. The combined organic layers were dried over $MgSO_4$, and the solvent was removed in vacuo to yield a pink solid. A ¹H NMR spectrum of the crude material showed >90% purity. Reverse phase column chromatography (65:35 MeOH/0.1 N HCl) followed by solvent removal generated the HCl salt of ZP5, **12**. To obtain the free dye, the HCl salt was loaded onto a second reverse phase column (100% H_2O) and thoroughly washed with H_2O. The product was flushed off the column (100% MeOH) and a portion of solvent was removed. The remaining solution was taken up in H_2O, washed with hexanes and dried to yield ZP5 as a red-pink solid (26 mg, 30%). TLC R_f = 0.71 (RP18 silica, MeOH); mp = 99-103 °C. ¹H NMR (DMF-d_7, 300 MHz) δ 3.80 (6H, m), 4.60 (2H, s), 6.86 (2H, s), 6.93 (1H, d), 6.96 (3H, m), 7.17 (3H, m), 7.45 (3H, t), 7.54 (2H, t), 7.83 (1H, t), 7.89 (1H, t), 8.02 (1H, s), 8.09 (1H, d), 8.38 (2H, d). ¹⁹F NMR (300 MHz) δ 45.43. FTIR (KBr, cm⁻¹) 3422, 1664, 1574, 1508, 1460, 1375, 1342, 1307, 1222, 1153, 1009, 939, 886, 835, 765, 716, 630, 598, 549, 468. HRMS (ESI) Calcd [M + H]⁺, 701.1967 (major), 702.2001, 703.1938, 704.1971; Found, 701.1963 (major), 702.2001, 703.1967, 704.1952.

2-Nitro-5-chlorobenzylbromide (13). 2-Nitro-5-chlorotoluene (**14**, 6.0 g, 35.0 mmol), 1,3-dibromo-5,5-dimethylhydantoin (10.6 g, 37.1 mmol), and VAZO 88 (400 mg, 1.6 mmol) were combined in 275 mL of chlorobenzene and stirred. Glacial acetic acid (200 μL) was added and the reaction was heated to 40 °C for 120 h. The reaction was washed (5 x 150 mL) with warm saturated $NaHCO_3$ and once with water (150 mL). The organic layer was dried over $MgSO_4$ and the solvent was removed in vacuo to yield a pink-red oily solid that consists of 2-nitro-5-chlorotoluene (~40%) and the desired product

(~60%), which was carried on to the next reaction without further purification. Column chromatography on silica gel (25:1 hexanes/EtOAc) yields pure **13** as a brown solid (38%). TLC R_f = 0.51 (silica, 7:1 hexanes/EtOAc); mp = 60-61 °C. ^{1}H NMR (CDCl$_3$, 300 MHz) δ 4.79 (2H, s), 7.45 (1H, dd), 7.56 (1H, d), 8.0 (1H, d). ^{13}C NMR (CDCl$_3$, 125 MHz) δ 28.43, 127.02, 129.61, 132.37, 134.64, 139.91, 145.96. FTIR (KBr, cm^{-1}) 1604, 1569, 1522, 1474, 1443, 1338, 1306, 1227, 1202, 1109, 1064, 908, 827, 757, 707, 685, 524. HRMS (EI) Calcd [M]$^+$, 248.9192, 250.9172 (major); Found, 248.9186, 250.9152 (major).

2-Nitro-5-chloro-1-[bis(2-pyridylmethyl)aminomethyl]benzene (8). A portion (~3.5 g, ~14.0 mmol, obtained from a 9.3 g mixture containing ~40% **14**) of **13**, DPA (3.32 g, 16.0 mmol), K$_2$CO$_3$ (2.6 g, 19 mmol), and 3 Å molecular sieves (3.5 g) were combined in 100 mL of CH$_3$CN and stirred at room temperature for 24 h. The brown reaction was filtered through Celite and the solvent was removed in vacuo to yield a brown oil. Column chromatography on basic Al$_2$O$_3$ using gradient elution (9:1 to 4:1 to 1:1 CH$_2$Cl$_2$/EtOAc) yields the product as a brown solid (5.8 g, 64% based on the assumed composition of the starting mixture). TLC R_f = 0.60 (Al$_2$O$_3$, 2:1 CH$_2$Cl$_2$/EtOAc); mp = 60-63 °C. ^{1}H NMR (CDCl$_3$, 300 MHz) δ 3.65 (4H, s), 3.92 (2H, s), 6.94 (2H, m), 7.07 (1H, dd), 7.20 (2H, d), 7.44 (2H, td), 7.56 (2H, m), 8.28 (2H, d). ^{13}C NMR (CDCl$_3$, 125 MHz) δ 55.22, 60.27, 121.89, 122.91, 125.48, 127.47, 130.76, 136.06, 136.67, 138.37, 147.49, 148.59, 157.83. FTIR (KBr, cm^{-1}) 1604, 1589, 1565, 1515, 1474, 1448, 1429, 1363, 1333, 1299, 773, 761, 747. HRMS (ESI) Calcd [M + H]$^+$, 369.1118 (major), 370.1152, 371.1089, 372.1123; Found, 369.1115 (major), 370.1142, 371.1076, 372.1114.

2-Amino-5-chloro-1-[bis(2-pyridylmethyl)aminomethyl]benzene (16). To a flask purged with Ar were added Pd/C (10% activated, 1.0 g), 40 mL of MeOH, and a portion (569 mg, 1.55 mmol) of **15** dissolved in 10 mL of MeOH. The reaction was vigorously stirred under H$_2$ (1 atm) for 1 h at room temperature, purged with Ar, filtered through Celite and dried in vacuo to yield a brown oil that was used without further purification (380 mg, 72%). The product can be purified by column chromatography on

basic Al_2O_3 (20:4:2.5 CH_2Cl_2/EtOAc/^{i}PrNH$_2$) to give a brown oil (65%). TLC R_f = 0.47 (Al_2O_3, 100:1 CH_2Cl_2/MeOH). ^{1}H NMR (CDCl$_3$, 300 MHz) δ 3.59 (2H, s), 3.80 (4H, s), 6.52 (1H, d), 7.00 (2H, m), 7.11 (2H, m), 7.38 (2H, m), 7.60 (2H, td), 8.55 (2H, d). ^{13}C NMR (CDCl$_3$, 125 MHz) δ 57.18, 58.71, 116.62, 121.28, 121.98, 123.20, 123.67, 127.91, 130.29, 136.39, 144.94, 148.64, 158.22. FTIR (NaCl disk, cm^{-1}) 3323, 3211, 3051, 2926, 2820, 1591, 1570, 1493, 1434, 1369, 1298, 1265, 1205, 1150, 1121, 1093, 1049, 997, 975, 895, 868, 820, 758, 731, 701, 643, 552, 487. HRMS (ESI) Calcd [M + H]$^+$, 339.1377 (major), 340.1410, 341.1347, 342.1381; Found, 339.1383 (major), 340.1417, 341.1335, 342.1364.

2-[5-({2-[(Bis(pyridin-2-ylmethyl)amino)methyl]-4-chlorophenylamino}methyl)-2-chloro-6-hydroxy-3-oxo-9,9a-dihydro-3H-xanthen-9-yl]benzoic acid (Zinpyr-6 Imine, 17). A portion (66 mg, 0.20 mmol) of **16** was combined with **4** (77 mg, 0.20 mmol) in 7 mL of EtOAc and stirred at room temperature to yield a cloudy orange-pink solution. A yellow precipitate formed over the course of 12 h. The reaction was cooled on ice, filtered, and the precipitate was washed with cold EtOAc, dissolved in 1:1 CH_2Cl_2/MeOH, washed off the frit, and the solvent was evaporated to afford a pink solid that was used without further purification (67 mg, 48%). ^{1}H NMR (DMF-d_7, 400 MHz) δ 3.10 (4H, s), 3.98 (2H, s), 6.80 (1H, m), 6.92 (3H, m), 7.24 (2H, m), 7.29 (1H, s), 7.50 (5H, m), 7.74 (2H, td), 7.86 (2H, m), 8.10 (1H, d), 8.50 (2H, dq), 9.48 (1H, s). FTIR (KBr, cm^{-1}) 3432, 3055, 2920, 2849, 1764, 1632, 1613, 1590, 1478, 1433, 1359, 1264, 1225, 1177, 1150, 1090, 1105, 1036, 1013, 871, 799, 762. HRMS (ESI) Calcd [M + H]$^+$, 715.1515 (major), 716.1549, 717.1486, 718.1520; Found, 715.1532 (major), 716.1567, 717.1522, 718.1557.

2-[5-({2-[(Bis(pyridin-2-ylmethyl)amino)methyl]-4-chlorophenylamino}methyl)-2-chloro-6-hydroxy-3-oxo-9,9a-dihydro-3H-xanthen-9-yl]benzoic acid (18, Zinpyr-6, ZP6). A portion (67 mg, 95 μmol) of **18** was dissolved in 10 mL of DCE and stirred. NaB(OAc)$_3$H (25 mg, 118 μmol) was added and the reaction was left to stir at room temperature. The cloudy orange solution became clear over the course of 5 h. The

reaction was washed with 10 mL of saturated brine and the brine was extracted (3 x 10 mL) with chloroform. The combined organic layers were dried over $MgSO_4$ and the solvent was removed to give **18** as an orange solid (61 mg, 90%). The crude material is ~90% pure. An analytically pure sample was obtained by dissolving ~7 mg of the crude product in 300 μL of DMF and adding 1:1 MeOH/0.1% aq TFA (3 mL), which resulted in the immediate precipitation of **18** as an orange solid. TLC R_f = 0.72 (RP18 silica, MeOH); mp = 124-128 °C. ^1H NMR (DMF-d_7, 300 MHz) δ 3.75 (6H, m), 4.61 (2H, s), 6.72 (1H, d), 6.85 (1H, s), 6.92 (1H, d), 7.04 (1H, d), 7.20 (4H, m), 7.43 (2H, t), 7.56 (2H, t), 7.81-7.94 (2H, dt), 8.10 (1H, d), 8.38 (2H, d). ^{13}C NMR (DMF-d_7, 125 MHz) δ 57.29, 60.23, 83.47, 104.67, 110.45, 111.60, 111.71, 112.95, 113.10, 116.85, 119.46, 122.41, 122.56, 123.45, 124.35, 124.60, 125.17, 127.23, 128.04, 128.47, 128.61, 130.69, 136.00, 136.88, 147.72, 149.22, 149.40, 151.17, 151.45, 152.67, 156.06, 158.97, 159.16, 169.04. FTIR (KBr, cm^{-1}) 3423, 3059, 2805, 1761, 1682, 1471, 1429, 1284, 1255, 1205, 1133, 1072, 1025, 836, 800, 762, 723, 702. HRMS (ESI) Calcd [M − H]⁻, 715.1515 (major), 716.1549, 717.1486, 718.1520; Found, 715.1526 (major), 716.1526, 717.1503, 718.1541.

4-Fluororesorcinol (20). The synthesis and purification of 4-fluororesorcinol was adapted from two previously published procedures[35,36] for improved yield and purity. A portion (6.1 g, 39 mmol) of 1,3-dimethyoxy-4-fluorobenzene,[35] **21**, was dissolved in 20 mL of glacial acetic acid and 20 mL of HBr was added. The solution was refluxed for 7 h, cooled and poured into 200 mL of H_2O. The solution was extracted with Et_2O (6 x 250 mL), the combined organic layers were dried over $MgSO_4$, and the solvent was removed in vacuo to yield the crude product as an oily brown-orange solid. Pure **19** was obtained by sublimation as an off-white solid (4.0 g, 79%). ^1H NMR (CDCl$_3$, 300 MHz) δ 6.30 (1H, m), 6.50 (1H, m), 6.92 (1H, m). Additional characterization is available in the literature.[35,36]

4-Fluoro-2-methylresorcinol (22). Selectfluor™ (15.0 g, 42.3 mmol) was dissolved in 250 mL of MeCN and placed in an addition funnel. A portion (5.02 g, 40.4 mmol) of 2-

methylresorcinol was placed in a 500 mL round-bottom flask, dissolved in 25 mL of MeCN, and cooled to 0 °C. The Selectfluor™ solution was added to the 2-methylresorcinol solution drop-wise with stirring over the course of ~1 h. The reaction was stirred at 0 °C for an additional 15 h and warmed to room temperature. The reaction was poured into Et$_2$O (200 mL) and was extracted with saturated NaCl (3 x 300 mL). The combined organic portions were dried over MgSO$_4$ and the solvent was removed under reduced pressure to give the crude product as a brown oil. This material was purified by chromatography on silica gel (4:1 hexanes/EtOAc) to give a light brown solid (4.0 g , 77%). TLC R$_f$ = 0.27 (4:1 hexanes/EtOAc); mp = 46 – 47 °C. ^{1}H NMR (CDCl$_3$, 300 MHz) δ 5.05 (1H, s), 5.43 (1H, d), 6.30 (1H, m), 6.79 (1H, m). FTIR (KBr, cm^{-1}) 3386, 1627, 1486, 1371, 1304, 1242, 1208, 1148, 1068, 995, 949, 893, 795, 746, 676, 614, 586, 496, 467. HRMS (ESI) Calcd M$^+$, 142.0425; Found, 142.0426. *Warning:* reactions requiring multi-gram quantities of Selectfluor™ are exothermic and must be run at low temperature with slow addition.

2′-Carboxy-5-fluoro-3-methyl-2,4-dihydroxybenzophenone (23). Phthalic anhydride (4.8 g, 32 mmol) and **22** (4.6 g, 32 mmol) were combined in 175 mL of nitrobenzene and the solution was cooled to 0 °C. Aluminum chloride (11.4 g, 85 mmol) was added in three ~4 g portions over the course of 30 min. The reaction was warmed to room temperature and stirred overnight. The reaction was poured into a solution of 1 M HCl (1L) and hexanes (400 mL), and the mixture was stirred vigorously for ~1.5 h. An off-white precipitate formed and was filtered. Recrystallization from boiling 1:1 MeOH/H$_2$O gave the pure fluorinated benzophenone as a white crystalline solid (2.7 g, 29%); mp = 225-227 °C. ^{1}H NMR (CD$_3$OD, 300 MHz) δ 2.13 (3H, s), 6.57 (1H, d), 7.35 (1H, d), 7.55-7.68 (2H, m), 8.08 (1H, d). ^{13}C NMR (CD$_3$OD, 125 MHz) δ 8.15, 112.46, 112.54, 115.35, 115.56, 115.83, 129.59, 130.48, 130.93, 131.64, 133.62, 141.63, 160.45, 168.77, 202.78. ^{19}F NMR (300 MHz) δ 27.43. FTIR (KBr, cm^{-1}) 3325, 2640, 1698, 1630, 1590, 1575, 1490, 1449, 1424, 1347, 1298, 1252, 1220, 1170, 1152, 1133, 1084, 1050, 1036, 995, 907, 865, 827,

800, 784, 764, 739, 723, 707, 683, 650, 639, 617, 529, 500. HRMS (ESI) Calcd [M – H]⁻, 289.0518; Found, 289.0506.

2′,7′-Difluoro-4′-methylfluorescein (24). A portion (3.50 g, 12.1 mmol) of **23** and **20** (1.55 g, 12.1 mmol) were ground together with a mortar and pestle to give an off-white powder. The powder was placed in a 50 mL flask and heated. Zinc chloride (2.0 g, 14.6 mmol) was added in three ~700 mg increments as the temperature increased from 127-156 °C. The reaction was heated to 250 °C, which gave a dark red viscous oil, which solidified upon cooling. The solid was placed in 300 mL of boiling 1 M HCl. The solution turned red and a black-red intractable material formed. The aqueous portion was removed, cooled to 0 °C and a red precipitate formed. The mixture was filtered and the precipitate dried. Analytical TLC on silica (9:1 CHCl₃/MeOH) showed that the red precipiate and the intractable material to be identical and that both contained a mixture of three fluorescent species with similar R_f values. The materials were combined and dried in vacuo to give a red-orange solid (5.1 g), which was carried on to the next step without further purification or full characterization. ¹H NMR analysis showed the presence of the desired difluoromonomethyl species and the difluorodimethyl byproduct in a ratio of ~2:1.

2′,7′-Difluoro-4′-methylfluorescein dibenzoate (25). Mixture **24** (5.1 g), obtained from the fusion reaction described above, and benzoic anhydride (12.0 g, 53.0 mmol) were combined in 80 mL of pyridine. The orange solution was refluxed for 3.5 h, cooled to 50 °C and poured into 400 mL of water. An off-white sticky substance formed and the mixture was stirred vigorously. The water was changed periodically and over the course of ~15 h, an off-white powder formed. The powder was filtered and dried in vacuo (4.82 g). ¹H NMR analysis indicated an ~2:1 ratio for the desired difluoromonomethyl species and the difluorodimethyl byproduct. Exhaustive attempts at separation by column chromatography failed owing to essentially identical R_f values and the crude mixture was carried on to the following step without further purification

attempts or characterization. HRMS (ESI) Calcd [M +H]$^+$, 591.1250; Found, 591.1227 (difluoromonomethyl) and Calcd [M + H]$^+$, 605.1398; Found, 605.1406 (difluorodimethyl).

2′,7′Difluoro-4′-bromomethylfluorescein dibenzoate (26). A portion (2.6 g) of **25**, 1,1-azobis(cyclohexanecarbonitrile) (VAZO 88, 60 mg, 0.245 mmol) and 1,3-dibromo-5,5-dimethylhydantoin (1.3 g, 4.41 mmol) were combined in 100 mL of chlorobenzene and glacial acetic acid (65 μL) was added. The reaction was heated to 40 °C for 192 h, at which time ^{1}H NMR analysis indicated it reached completion. The reaction cooled, extracted with warm NaHCO$_3$ (4 x 200 mL) and washed with H$_2$O (2 x 200 mL). The organic portion was dried over MgSO$_4$ and the solvent was removed in vacuo to give a viscous orange-brown oil. The oil was dissolved in a minimal volume of toluene (~30 mL) and EtOH (~80 mL) was added, which caused precipitation of a peach-colored powder. The mixture was cooled to 4 °C and filtered (2.2 g). This mixture contains an ~2:1 ratio of the monobromo and dibromo species and was carried on without attempts at purification or characterization. The methylene protons of the mono- and dibromo species can be observed at 4.73 and 4.80 ppm by ^{1}H NMR (CDCl$_3$, 300 MHz).

2′,7′-Difluorofluorescein-4′-carboxaldehyde (27). Mixture **26** (200 mg, 0.30 mmol) and NaHCO$_3$ (200 mg, 2.38 mmol) were combined in 10 mL of anhydrous DMSO and heated to 150 °C for 3 h. The reaction was cooled to 80 °C and poured into 50 mL of 4 N HCl. An orange precipitate formed and the mixture was stirred and filtered. The precipitate, which contained both the desired product and the dialdehyde, was washed with water (3 x 25 mL) and dried. Flash chromatography on silica gel afforded pure **27** as an orange powder (38 mg); TLC R$_f$ = 0.44 (silica, 9:1 CHCl$_3$/MeOH). ^{1}H NMR (CD$_3$OD, 500 MHz) δ 6.64-6.75 (2H, m), 6.78 (1H, d), 7.19 (1H, d), 7.57-7.62 (2H, m), 7.93 (1H, s), 8.06 (1H, d), 10.49 (1H, s). FTIR (KBr, cm^{-1}) 3428, 3000, 2964, 2928, 2855, 1577, 1423, 1379, 1337, 1159, 1122, 1088, 1044, 1012, 972, 924, 842, 712, 701, 675, 649, 620. HRMS (ESI) Calcd [M − H]$^-$, 395.0362; Found, 395.0355.

4'-[2-Bis(2-pyridylmethyl)aminomethyl]-*N*-methylaniline]-2',7'-difluorofluor-escein (28, Zinpyr-8, ZP8). Portions of **27** (20 mg, 0.05 mmol) and aniline **6** (16 mg, 0.05 mmol) were combined in 4 mL of 1:1 $CHCl_3$/MeOH and the wine-colored solution was stirred at room temperature for 24 h. The reaction was diluted with 3 mL of DCE and a portion of $NaB(OAc)_3H$ (22 mg, 0.10 mmol) was added. The mixture was stirred for 24 h at room temperature, during which time it became light orange. The solvent was removed under reduced pressure and preparative TLC on reverse phase silica gel (100% MeOH) gave the product as an orange powder (24 mg, 70%). ^{1}H NMR (CD_3OD, 500 MHz) δ 3.55-3.72 (6H, m), 4.53 (2H, br s), 6.52 (1H, d), 6.57-6.65 (1H, m), 6.78 (1H, d), 6.91 (1H, d,), 7.02 (1H, d), 7.10-7.14 (3H, m), 7.25 (1H, d), 7.33 (2H, d,), 7.44-7.50 (2H, m), 7.70-7.77 (3H, m), 8.10 (1H, d), 8.28 (2H, d). HRMS (ESI) Calcd [M − H]⁻, 683.2101; Found, 683.2114.

General Spectroscopic Methods. Ultrol grade PIPES, piperazine-*N,N'*-bis(2-ethanesulfonic acid) and KCl (99.997%) from Calbiochem, and $ZnCl_2$ (99.999%) from Aldrich were used as received. Millipore water (18.2 MΩ·cm at 25 °C) obtained from a Mili-Q Biocel purifier outfitted with a Quantum VX cartridge was used for all aqueous solutions. With the exception of the experiment to determine pK_a values, all spectroscopic measurements were conducted under simulated physiological conditions using 50 mM PIPES, 100 mM KCl adjusted to pH 7. Solutions (10 and 100 mM) of $ZnCl_2$ in water were prepared and diluted accordingly. Solutions for the dual-metal buffering system, which affords solutions with free zinc concentrations ranging from 0 to 25 nM, were prepared as previously described.[23] Stock solutions of ZP5 (0.76 mM), ZP6 (0.41 mM) and ZP8 (1 mM) in DMSO were prepared, stored frozen at −25 °C, and thawed in the dark immediately prior to use. An Orion glass electrode, calibrated prior to each use, was used to record solution pH. The KaleidaGraph software package was used to manipulate all data. Measurements were performed at least in triplicate and resulting averages are reported.

Optical Absorption Spectroscopy. UV-visible spectra were obtained with a Cary IE scanning spectrophotometer. A circulating water bath was used to maintain the temperature at 25 °C ± 1 °C. Samples were contained in 1-cm path length quartz cuvettes (3.5 mL volume).

Fluorescence Spectroscopy. Emission spectra were recorded on a Hitachi F-3010 spectrofluorimeter. A rhodamine quantum counter was used to normalize the spectra for excitation intensity, and manufacturer-supplied correction curves were utilized to normalize the emission spectra. Manufacturer-supplied photomultiplier curves were used to correct for emission intensity. The temperature was regulated at 25 °C ± 1 °C during all experiments with a circulating water bath. Samples were contained in 1 cm x 1 cm quartz cuvettes (3.5 mL volume, Starna).

Quantum Yield Measurements. The quantum yields of free and Zn(II)-bound ZP5 and ZP6 were referenced to fluorescein in 0.1 N NaOH ($\Phi = 0.95$)[37] as previously described.[24] In a typical experiment, a solution of ZP with A_{max} in the range of 0.04 – 0.08 was prepared in 50 mM PIPES, 100 mM KCl, pH 7. For metal-free studies, excess EDTA from a 100 mM K_4EDTA stock solution in water was added to the buffer solution. To obtain quantum yield values for the Zn(II)-bound sensors, excess Zn(II) from a 100 mM $ZnCl_2$ stock solution in water was added to the buffered ZP solution. The concentration of the fluorescein reference solution was adjusted such that the A_{max} value ($A_{max} = 490$ nm) matched that of the ZP solution of interest. The intersection point of the two spectra was taken as the excitation wavelength. For repetitive measurements, the concentrations were varied (A_{max} ~0.04 to ~0.08). Excitation was provided at 497 nm (ZP5 and ZP6, metal-free), 491 nm (ZP5, metal-bound), or 493 (ZP6, metal-bound). Emission spectra were integrated from 450-650 nm and the quantum yields were calculated by the standard equation.[24]

Determination of Protonation Constants that Affect Fluorescence. In a typical experiment, a 30 mL solution of 1 μM ZP in 100 mM KCl, 10 mM KOH was adjusted to

pH ~12.5 by drop-wise addition of KOH. Aliquots of 6, 2, 1, 0.5 and 0.01 N HCl were added to achieve pH changes of approximately 0.25, and the emission spectrum was recorded after each addition. The overall volume change for each experiment did not exceed ~2%. Excitation was provided at 498 nm for ZP5 and at 500 nm for ZP6. Data were integrated from 505 nm to 650 nm, normalized and plotted against pH. The normalized data were fit according to eq. 2.1 where ΔF_n is the fluorescence change associated with an individual protonation event.[24]

$$\Delta F = \frac{\Delta F_1}{1 + 10^{(pH - pK_{a1})}} + \cdots \frac{\Delta F_n}{1 + 10^{(pH - pK_{an})}} \qquad (2.1)$$

Selectivity of ZP for Zn(II) in the Presence of Other Metal Ions. The selectivity of ZP5 and ZP6 for Zn(II) over a number of divalent first-row transition metals, in addition to Ca(II), Mg(II) and Cd(II), was investigated by using fluorescence spectroscopy. Aqueous solutions for Ca(II), Mg(II), Mn(II), Co(II), Ni(II) and Cd(II) were prepared from the chloride salts. The Cu(II) solution was prepared from copper sulfate and Fe(II) solutions were prepared immediately before use with ferrous ammonium sulfate and water that was thoroughly purged with Ar. In a typical experiment, the emission spectrum of a 1 μM solution of free dye was recorded. A 15 μL aliquot of a 10 mM metal ion solution was added and the emission spectrum measured. Subsequently, 15 μL of 10 mM $ZnCl_2$ was added to the solution and the emission spectrum obtained. Excitation was provided at 498 nm (ZP5) or 500 nm (ZP6) and the spectra were integrated from 505-650 nm (ZP5) or 450-650 nm (ZP6) and normalized with respect to the emission of the free probe (F_o).

Zn(II) Binding Studies by Fluorescence Spectroscopy. The dissociation constants, K_d, for Zn(II) binding were determined with a dual-metal buffering system,[23] which affords concentrations of free Zn(II) in the nM range. Excitation was provided at 498 nm for ZP5 and at 500 nm for ZP6. The response was quantified by integrating the emission

intensity from 505-650 nm, subtracting the emission resulting from the free ligand and normalizing with respect to the maximum response. The plot of response versus [Zn(II)] was fit to the equation $r = B[Zn(II)]_{free}/(K_d + [Zn(II)]_{free})$, where r is the fluorescence response and B is 1 for normalized data.

Zn(II) Binding Studies by Absorption Spectroscopy. Metal-binding titrations and Job plots were obtained for ZP5 and ZP6 to determine the stoichiometry of the metal-bound complexes in solution. In a typical titration, 0.5 μL aliquots of a 10 mM $ZnCl_2$ solution were added to a 3 mL solution of ZP (concentration range 10 to 20 μM). The absorbance changes at 512 (ZP5, ZP6), 491 (ZP5), 492 (ZP5) and 462 (ZP5) nm were recorded and plotted against the equivalents of Zn(II) in solution. For the Job plot analyses, starting solutions of 10 μM Zn(II) and ZP were used. A* was calculated for three different wavelengths according to the equation $A^* = A_{obs} - \varepsilon_{ZP} \times [ZP]$, where ZP refers to the metal-free probe and ε_{ZP} is the extinction coefficient for the free sensor at the wavelength of interest, and plotted against the mol fraction of Zn(II) in solution.

Results and Discussion

Synthesis of Ligand Components. The syntheses of the metal-binding units for ZP5 and ZP6, starting from commercially available materials, are outlined in Scheme 2.2. Free radical bromination of the 5-subtituted-2-nitrotoluenes **8** and **14** under mild conditions affords multigram quantities of the corresponding brominated species **7** and **13**. These bromination reactions are sluggish, and were allowed to progress over the course of several days until no additional product formation occurred (monitored by TLC). The final starting material-to-product ratios were modest with ~50% or ~60% product formation observed for the fluorinated and chlorinated reagents, respectively. These mixtures can be separated by flash chromatography using silica gel and hexanes/EtOAc solvent mixtures; however, this separation was not required since the starting substituted toluenes do not interfere with the next step. The reaction of **7** and **13**

with DPA in CH_3CN followed by purification and hydrogen reduction of the nitro groups to amino groups using Pd/C (10% activated) gave the aniline-based ligand fragments **10** and **16** in modest yields and high purity. It should be noted that the hydrogenation reactions to form **10** and **16**, in addition to analogous reactions described throughout this work, must be monitored regularly by TLC since multiple byproducts may form, in part due to loss of the DPA or other amine-based ligand fragments, and complicate purification.

Synthetic Assembly of ZP5 and ZP6 From a Fluorescein Carboxaldehyde. Previously described syntheses of ZP probes followed one of three main routes. Mannich reactions between a fluorescein with halogen substitution at the 2′ and 7′ positions and the imminum ion condensation product of DPA and paraformaldehyde offer a simple and high yielding approach to symmetrical ZP sensors (ZP1, Figure 2.1) when recrystallization is employed for purification.[23,32] This method, however, is limited to ligands that incorporate a secondary amine. In an alternative preparation of symmetrical ZP sensors, a disubstituted fluorescein was created in four steps starting from 2-methylresorcinol and phthalic anhydride.[24] The carboxylate groups in the 4′ and 5′ positions of the fluorescein offer more flexibility for subsequent ligand attachment strategies than the Mannich reaction. Asymmetrical fluorescein platforms are required to assemble ZP sensors that contain only one metal-binding appendage and form mononuclear Zn(II) complexes in solution. To achieve this goal, a four-step synthesis for 2′-chloro-5′-bromomethylfluorescein-di-*tert*-butyldimethylsilyl ether was designed.[25] This fluorescein platform was used in the synthesis of ZP4 via its nitroxyl derivative, which was formed in situ, and deprotection of the fluorescein is required after installation of the aniline-based ligand fragment.

In related work, an asymmetrical fluorescein with an aldehyde functional group was prepared as an intermediate for the synthesis of aminotropoiminate complexes designed for nitric oxide sensing,[34] and the synthesis of this compound is depicted in

Scheme 2.1. The utility of platform **4** for the assembly of sensors with aniline-based ligands was investigated in the syntheses of ZP5 and ZP6 and proved extremely useful. Schiff base condensation of **4** with the aniline-based ligands **10** and **16** and subsequent reduction of the intermediate imine gave crude ZP5, **12**, and ZP6, **18**, in relatively high purity (~90% judging by NMR). Furthermore, since the benzoate protecting groups are lost during the DMSO oxidation reaction, deprotection of the fluroescein is not required after installation of the ligand moiety, as was necessary for the preparation of ZP4. This feature is important since fluorescein-based compounds, and especially the asymmetrical sensors with multiple pendant groups, are often difficult to handle and purify. Consequently, monoaldehyde **4** served as an invaluable building block for the preparation of most asymmetrical sensors described throughout this work. Although the synthesis of **4** has a low overall yield, resulting from the final DMSO oxidation, it is reproducible and aldehyde **4** has a shelf life of years when stored at room temperature. With time, several small modifications were made to the reported synthesis of **4**, the most important concerning benzophenone **5**. The acid-catalyzed condensation of 4-chlororesorcinol and phthalic anhydride or analogs thereof should be conducted only at room temperature. Heating this reaction mixture causes formation of a dark brown polymeric material that complicates the isolation and purification of **5** and related compounds.

Fluorescence Properties of ZP5 and ZP6. The fluorescence properties of asymmetrical ZP sensors are summarized in Table 2.1. Under simulated physiological conditions (50 mM PIPES, 100 mM KCl, pH 7) and in the presence of EDTA to scavenge any adventitious metal ions, ZP5 and ZP6 have quantum efficiencies of 0.29 (λ_{max} = 520 nm) and 0.10 (λ_{max} = 519 nm), respectively. Upon addition of excess Zn(II), the emission spectra blue-shift slightly and the quantum yields of ZP5 and ZP6 increase, affording values of 0.48 (λ_{max} = 517 nm) and 0.34 (λ_{max} = 515 nm), respectively. ZP5 gives an ~1.6-fold and ZP6 an ~3-fold increase in integrated emission with Zn(II) complexation

(Figure 2.2). Blue shifts are also observed in the optical absorption spectra of ZP5 and ZP6 following Zn(II) addition. For ZP5, the absorption maximum shifts by 9 nm from 504 (ε = 83,000 $M^{-1}cm^{-1}$) to 495 nm (ε = 91,000 $M^{-1}cm^{-1}$). ZP6 shows a shift from 506 (ε = 89,000 $M^{-1}cm^{-1}$) to 495 nm (ε = 98,000 $M^{-1}cm^{-1}$). These hypsochromic shifts reflect a perturbation of the fluorescein π-system and suggest that the phenol donor group of the fluorescein coordinates to Zn(II), as observed for ZP1, ZP2 and ZP4.

Our previous work on symmetrical ZP sensors and ZP4 revealed a correlation between the quantum yields of the apo ZP probes and the pK_a values of the nitrogen atom thought to be responsible for PET quenching.[24,25] One objective in the present work was to test this correlation through comparison of the quantum yields and aniline nitrogen atom pK_a values for ZP5 and ZP6. Figure 2.3 illustrates the pH-dependent fluorescence changes for ZP5 and ZP6. The fluorescence of both probes is ~50% quenched at high pH and increases in the physiological range. ZP6 displays maximum fluorescence at pH ~5 and its fluorescence is affected by three protonation events with apparent pK_a values of 11.2, 6.3 and 4.7. The first two values correspond to fluorescence enhancement when moving from high to low pH and are assigned to the tertiary amine and aniline nitrogen, respectively. The latter pK_a is attributed to fluorescein protonation, which results in fluorescence quenching.[38] Although the electron-withdrawing chloro substituent in ZP6 lowers the aniline nitrogen atom pK_a value relative to that in ZP4 (X=H, pK_a = 7.2), the quantum yield of ZP6 is slightly higher than that of ZP4 (ZP4, Φ = 0.06; ZP6, Φ = 0.10). The emission of ZP5 reaches a maximum around pH 8 and is maintained throughout the physiological range. Three protonation events affect the fluorescence of ZP5 and have apparent pK_a values of 10.9, 9.6 and 4.7. The pK_a of 10.9 is assigned to the aliphatic amine, and the pK_a of 9.6 to the aniline nitrogen atom. This pK_a value indicates that the aniline nitrogen atom is protonated at physiological pH and the quantum yield of free ZP5 is relatively high (Φ = 0.29). Variations in X have little effect on the pK_a values for the aliphatic amines and for formation of the non-fluorescent

isomers of fluorescein, as expected. In contrast, the pK_a of the aniline nitrogen atom is sensitive to changes in X and some correlation between the pK_a values and the quantum yield of the apo probes exists, especially when comparing ZP4 (X=H) to ZP5 (X=F).

Zinc Binding Studies of ZP5 and ZP6. Titrations of ZP5 and ZP6 with Zn(II) and Job plot analyses were performed to characterize Zn(II) complexation. Figure 2.4 shows the difference spectra obtained from titration of ZP5 with Zn(II). An absorption decrease at 512 nm and increases at 491 and 462 nm occur upon Zn(II) addition, and the metal-binding titrations reveal that ZP5 forms a 1:1 complex with Zn(II) in solution. Data for ZP6 are analogous. Job plots for Zn(II) binding to ZP5 and ZP6 yield maxima or minima at a mol fraction of 0.5, which further supports this notion (Figure 2.5).

The binding affinities of ZP5 and ZP6 for Zn(II) were determined by using a dual-metal buffering system previously described.[23] In this system, the concentrations of Ca(II) and EDTA remain constant at 2 and 1 mM, respectively, while the total Zn(II) concentration varies from 0 to 1 mM, which affords solutions that contain 0 to 25 nM free Zn(II). Figure 2.2 shows the emission responses from titrations of ZP5 and ZP6 with the dual-metal buffering system. The Zn(II) complexes of ZP5 and ZP6 both have apparent K_d values of 0.50 ± 0.10 nM. Such high affinity binding was expected given the choice of DPA as the chelate, which alone has an apparent K_{d1} of 70 nM for Zn(II) at pH 7,[39] and previous studies of ZP family members that show dissociation constants in this range. Given the conserved metal binding unit, we anticipate that ZP5 and ZP6 bind Zn(II) in an identical manner to ZP4. Previously conducted X-ray crystallographic model studies employed a salicylaldehyde-based ZP4 analog and revealed a distorted octahedral geometry. Scheme 2.3 gives our proposal for Zn(II) binding to asymmetrical ZP at neutral pH, which is based on the crystallographic modeling and pH studies.

Lastly, time-dependent density function theory (TDDFT) was employed to assign the absorption spectra of free and Zn(II)-bound ZP4 following geometry optimizations. The details of this approach are given in Chapter 7 and Appendix 2, and a rigorous

TDDFT calibration and fluorescein analysis preceded this work. The crystal structure of the salicyaldehyde-based ZP4 model complex $[Zn(BPAMP)(H_2O)](ClO_4)$[25] was used as a starting point for generating the ZP4:Zn(II) optimized geometry and good correlation between the experimentally determined and calculated M-L bond lengths was obtained. As mentioned above, Zn(II) coordination to asymmetrical ZP results in an ~10 nm blue shift of A_{max}, which we have previously assigned to perturbation of the fluorescein π system. Figure 2.6 illustrates the donor and acceptor molecular orbitals primarily responsible for absorption from ZP4 dianion, the species present at pH 7 where the fluorescein platform is completely deprotonated. TDDFT generates two excited states, A and B, of similar oscillator strength (A, oscillator strength = 0.164; B, oscillator strength = 0.120) that contribute to its absorption with A_{max} values of 496 and 498 nm (experimental, 506 nm). Both excited states have a dominant component transition between the HOMO and LUMO+3 molecular orbitals (A_1, weight = 0.319; B_1, weight= 0.262). This donor/acceptor orbital pair is analogous to that assigned to fluorescein dianion absorption (Appendix 2).

Figure 2.7 includes molecular orbital diagrams for the ZP4:Zn(II) complex and neutral ZP4. TDDFT on the ZP4:Zn(II) complex simulated the experimentally observed blue-shift and suggested that one excited state (C, oscillator strength = 0.364) is responsible for its absorption with A_{max} of 457 nm (experimental, 495 nm). The dominant molecular orbital transition is between the HOMO and the LUMO+3 (transition C_1, weight = 0.559). Some contribution also comes from the HOMO-2 to LUMO+3 transition (transition C_2, weight = 0.232). In both instances, the molecular orbitals are completely xanthenone based with no contribution from the Zn(II) center or ligand unit. Furthermore, the donor/acceptor orbital pairs are analogous to those assigned to fluorescein monoanion (Appendix 2) and neutral ZP4 absorption (transitions D_1 and D_2 for neutral ZP4, Figure 2.7). This comparison indicates that the perturbation caused by Zn(II) coordination to the phenol moiety is, to first

approximation, similar to that of protonation, which also causes a hypsochromic shift in fluorescein absorption. We note that TDDFT overestimated the magnitude of the blue shift, but the result is very acceptable.[40]

Selectivity of ZP5 and ZP6 for Zn(II). The fluorescence response of ZP5 and ZP6 to various divalent first-row transition metal ions, Zn(II) and Cd(II) is shown in Figure 2.8. Both compounds exhibit similar behavior. ZP5 and ZP6 fluorescence enhancement is specific for Zn(II) and Cd(II) and unaffected by the presence of excess Ca(II), Mg(II) and Mn(II). ZP5 and ZP6 form complexes with the divalent first-row transition metals considered. Metal binding titrations and Job plots indicate that ZP5 and ZP6 form 1:1 complexes with Mn(II) and Cu(II), and we anticipate the same stoichiometry for Co(II) and Ni(II). Complexation of ZP5 and ZP6 to these metal ions results in no appreciable fluorescence change. This behavior contrasts with the fluorescence quenching observed upon adding these metal ions to solutions of ZP1 and its symmetrical analogs. It presumably occurs because the aniline-based metal binding unit is a better quencher of fluorescein emission than the tertiary amine units employed in sensors such as ZP1. With the exception of Mn(II), addition of Zn(II) to solutions of ZP5 or ZP6 and a divalent first-row transition metal of interest results in no fluorescence change, indicating that Zn(II) cannot readily displace Fe(II), Co(II), Ni(II) or Cu(II) from the ZP probes. Analogous behavior was observed for ZP4.[25]

Additional Comparison of ZP5 and ZP6 to Other ZP Sensors. Characterization of ZP4[25] and ZP7,[31] **19**, are documented elsewhere and pertinent data are included in Table 2.1. ZP5 and ZP6 show changes in their optical absorption spectra that are similar to those of ZP4 upon Zn(II) binding. Both Job plot analyses and metal-binding titrations indicate formation of a 1:1 complex with Zn(II) for each sensor, which has been supported crystallographically through the study of several model complexes.[25] The apparent K_d values for the asymmetrical ZP probes are all in the sub-nanomolar range for Zn(II) and these probes exhibit comparable selectivity for Zn(II) in the presence of

other metals. Such similarities are not surprising because the sensors utilize the same fluorophore and metal-binding motif.

Unlike the properties described above, a comparison of the fluorescence enhancement upon Zn(II) binding, quantum efficiencies and protonation constants of the asymmetrical ZP sensors revealed some unexpected behavior. Since aniline nitrogen atoms have relatively low affinity for protons, it was anticipated that each of the asymmetrical probes would exhibit a low quantum yield relative to ZP1 and ZP2 at physiological pH in the metal-free form. Such behavior was observed for ZP4 and ZP7, as previously shown, and for ZP6. In contrast, the quantum yield of apo ZP5 is relatively high, 0.29, and comparable to that observed for ZP2 (0.25). These variations in quantum efficiencies can be roughly correlated to the pK_a values for the nitrogen atoms presumed to contribute to fluorescence quenching. For instance, the pK_a values for ZP4, ZP6 and ZP7 range from 6.3 (ZP6) to 7.2 (ZP4), indicating that the aniline nitrogen atoms of these probes are deprotonated at physiological pH. In contrast, the aniline nitrogen atom of ZP5 has a pK_a value of 9.6, a value similar to that observed for ZP2 (9.4), and relatively high background fluorescence is observed for this probe. The origin of the high pK_a value for ZP5 is unclear to us. It should also be noted that ZP7 (X=OMe) gives no fluorescence turn-on with Zn(II) coordination. In sum, this study suggests that variation of the substituent para to the aniline nitrogen atom is not a particularly valuable route for obtaining analogs with significantly reduced background emission and greater fluorescence enhancement with Zn(II) detection.

Design and Synthesis of ZP8. Modification of the fluorescein platform offers a second means by which to probe the effect of electronic variation on the fluorescence properties of ZP4 derivatives. In parallel work, we found that halogenation of the fluorescein platforms of symmetrical ZP sensors influences their photophysical properties.[24,32] The details of this particular investigation are discussed in Chapter 3. One noteworthy result was that substitution of the chlorine atoms in ZP1 with fluorine

atoms resulted in decreased background fluorescence (ZP1, Φ = 0.38; ZP3, Φ = 0.15), a lower tertiary amine pK_a value (ZP1, 8.4; ZP3, 6.8) and increased dynamic range. We therefore wondered whether the incorporation of fluorine atoms in the 2' and 7' positions of the fluorescein platform in asymmetrical ZP4 would be of benefit. We hypothesized that the addition of fluorine atoms to the xanthenone framework would lower the aniline nitrogen atom pK_a value and decrease the quantum yield of the free sensor relative to ZP4. We thus aimed to install an aldehyde functional group in the 4' position of 2',7'-difluorofluorescein and to use this platform to make a ZP4 analog.

Scheme 2.4 illustrates the synthetic route to the target aldehyde **27**. Although this synthesis is generally based on the preparation of monoaldehyde **4**, shown in Scheme 2.1, the synthesis of **27** presented its own set of challenges, which must be considered in terms of its long-term practicality and utility.

Fluorinated resorcinols are key starting materials for the synthesis of 4'-methyl-2',7'-difluorofluorescein and their preparation is a major bottleneck to multi-gram-scale syntheses of fluorinated fluoresceins. The synthesis of 4-fluororesorcinol, **20**, was conducted by modification of two existing literature procedures.[35,36] Although fluorination of resorcinol yields 4-fluororesorcinol in one step, a published report details extreme difficulties with purification of the resulting reaction mixture since resorcinol and the fluorinated products are inseparable by chromatography.[35] A clever alternative approach was conceived in which 1,3-dimethoxybenzene is fluorinated by the Selectfluor™ reagent in dry MeCN.[35] This reaction results in a mixture of starting material, 4-fluoro-1,3-dimethoxybenzene, **21**, and presumably 4,6-difluoro-1,3-dimethoxybenzene. Despite a difficult separation owing to the similar R_f values of the starting material and product, **21** can be isolated as a clear liquid in 45% yield following chromatography on silica gel (40:1 hexanes/EtOAc), assuming a very large column is employed. Deprotection of the phenol groups occurs readily in refluxing 1:1 HOAc/HBr and a light brown oily solid is obtained following work-up. Although a

literature preparation[35] states that the crude product can be purified by chromatography on silica gel (2:1 hexanes/EtOAc), the product sticks to the silica gel. Sublimation is a preferable purification route and yields **20** as a white solid in 81% yield. As described, small-scale syntheses of 4-fluororescorcinol are manageable and even easy; however, scaling up these reactions proves difficult, time-consuming and costly. The main problem are (i) the poor solubility of the Selectfluor™ reagent in acetonitrile and (ii) challenging and uneconomical column chromatography. In general, purification of 2 g of 4-fluoro-1,3-dimethoxybenzene requires ~4 L of solvent.

Direction fluorination of 2-methylresorcinol using Selectfluor™ in MeCN achieves 4-fluoro-2-methylresorcinol, **22**, in moderate to good yield depending on the chromatography. Analytical TLC on silica (4:1 hexanes/EtOAc) shows that the crude reaction consists of the starting material, product **22** and an impurity, presumably 4,5-difluoro-2-methylresorcinol. These three species have similar R_f values and, often for a reaction starting with ~5 g of 2-methylresorcinol, two 10 g-sized columns are required to obtain ~2.5 g (~40% yield) of pure **22**.

The fluorinated benzophenone, **23**, was obtained as an off-white crystalline powder in gram quantities by reaction of **22** and phthalic anhydride in nitrobenzene with $AlCl_3$ as the acid catalyst. Several conditions for the acid-catalyzed condensation of **23** with **20** to give 4'-methyl-2',7'-difluorofluorescein, **24**, were screened and included solvent-free fusion with $ZnCl_2$, reaction in either TFA or $MeSO_3H$ at 80 °C. Analytical TLC on silica gel (9:1 $CHCl_3$/MeOH) showed that each reaction gave the same mixture of three fluorescent products, which are 2',7'-difluorofluorescein, 4'-methyl-2',7'-difluorofluorescein and 4',5'-dimethyl-2',7'-difluorofluorescein, with similar R_f values. ^{1}H NMR analysis showed a disappointing ratio of ~2:1 for the monomethyl to dimethyl species, which contrasts to the ~9:1 ratio obtained for the 7'-chloro-4'-methylfluorescein case under similar conditions.[34] The fusion reaction with $ZnCl_2$ was chosen for large-scale reactions and the resulting mixture was carried on without further purification or

characterization. Protection of mixture **24** with benzoic anhydride in refluxing pyridine followed by precipitation in water afforded ~4.8 g of mixture **25** as an off-white solid after precipitation from toluene/EtOH. Exhaustive attempts to separate the benzoate protected mono- and dimethyl species by column chromatography failed owing to their nearly identical R_f values. Bromination of mixture **25** in chlorobenzene using 1,3-dibromo-5,5-dimethylhydantoin as the bromide source and VAZO 88 as the radical initiator is sluggish, and reaches completion after 8 days at 50 °C. As found in the synthesis of monoaldehyde **4**, DMSO/NaHCO$_3$ oxidation of the bromomethyl mixture yields deprotected mono- and dialdehydes, which can be separated by column chromatography on silica gel with a CHCl$_3$/MeOH solvent system. Sensor ZP8 was assembled from monoaldehyde **27** and aniline ligand **6**[25] according to the methodology developed for ZP5 and ZP6.

Spectroscopic Characterization of ZP8. Table 2.1 includes optical absorption and fluorescence spectroscopic characteristics for ZP8. As observed for the ZP1/ZP3 couple (see Chapter 3), incorporation of fluorine atoms in the 2' and 7' positions of the fluorescein unit decreases the background fluorescence (ZP4, Φ = 0.06; ZP8, Φ = 0.03). As a result, ZP8 shows an ~11-fold fluorescence enhancement with Zn(II) coordination (Φ_{Zn} = 0.35), which is an ~2-fold improvement over the dynamic range observed for ZP4. The pK_a values for ZP8 are 6.5 and 3.8 for aniline and fluorescein protonation, respectively. The metal-binding properties of ZP8 are analogous to ZP4-7 with an apparent K_d value of 0.60 ± 0.10 for Zn(II) at neutral pH.

Summary and Perspectives

This chapter focused on the preparation and characterization of halogenated ZP4 derivatives. The main thrust of this work was to determine whether electronic variation can be employed to alter the photophysical properties of the ZP4 platform, and modifications to both the metal binding unit and fluorophore were considered.

Variation of the substituent para to the aniline nitrogen atom is not a valuable route for tuning sensor emission. Although the electron-withdrawing chloride atom (ZP6) lowered the aniline pK_a to some degree, this change afforded no background fluorescence reduction. Some correlation between background fluorescence and pK_a is observed from comparison of ZP4, ZP6 and ZP7 with ZP5. Fluorination of the xanthenone platform dropped the background fluorescence by ~50% relative to parent compound ZP4 and also resulted in some lowering of the pK_a values relative to ZP4. This result is encouraging, but the synthesis of aldehyde **27** has significant pitfalls and an improved route must be sought to make this preparation economical and practical on a large scale. One possible alternative, which would circumvent the preparation of fluorinated resorcinols, is direct fluorination of a fluorescein or protected fluorescein platform. The convergent synthesis for the assembly of ZP5, ZP6 and ZP8 that employs the fluroescein carboxaldehyde detailed in this work proved valuable and, as will be shown in upcoming chapters, is useful for the assembly a variety of fluorescein-based sensors.

References

(1)   Vallee, B. L.; Falchuk, K. H. *Physiol. Rev.* **1993**, *73*, 79-118.

(2)   Frederickson, C. J.; Moncrieff, D. W. *Biol. Signals* **1994**, *3*, 127-139.

(3)   Takeda, A. *BioMetals* **2001**, *14*, 343-351.

(4)   Burdette, S. C.; Lippard, S. J. *Proc. Natl. Acad. Sci. USA* **2003**, *100*, 3605-3610.

(5)   Chang, C. J.; Lippard, S. J. *Metal Ions in Life Sciences* **2006**, *1*, 321-370.

(6)   Frederickson, C. J. *Int. Rev. Neurobiol.* **1989**, *31*, 145-238.

(7)   Budde, T.; Minta, A.; Whites, J. A.; Kay, A. R. *Neuroscience* **1997**, *79*, 347-358.

(8)   Li, Y.; Hough, X.; Frederickson, C. J.; Sarvey, J. M. *Neuroscience* **2001**, *21*, 8015-8025.

(9)   Huang, E. P. *Proc. Nat. Acad. Sci. USA* **1997**, *94*, 13386-13387.

(10)   Howell, G. A.; Welch, M. G.; Frederickson, C. J. *Nature* **1984**, *308*, 734-736.

(11)   Frederickson, C. J.; Bush, A. I. *BioMetals* **2001**, 353-366.

12)   Cuajungco, M. P.; Lees, G. J. *Neurobiology of Disease* **1997**, *4*, 137-169.

(13)   Suh, S. W.; Chen, J. W.; Motamedi, M.; Bell, B.; Listiak, K.; Pons, N. F.; Danscher, G.; Frederickson,

        C. J. *Brain Res.* **2000**, *852*, 268-273.

(14)   Choi, D. W.; Koh, J. Y. *Annu. Rev. Neurosci.* **1998**, *21*, 347-375.

(15)   Cole, T. B.; Wenzel, H. J.; Kafer, K. E.; Schwartzkroin, P. A.; Palmiter, R. D. *Proc. Nat. Acad. Sci.*

        USA **1999**, *96*, 1716-1721.

(16)   Lee, J.-Y.; Cole, T. B.; Palmiter, R. D.; Koh, J.-Y. *Neuroscience* **2000**, *20:RC79*, 1-5.

(17)   Kay, A. R. *J. Neurosci.* **2003**, *23*, 6847-6855.

(18)   Kay, A. R. *J. Neurophysiol.* **2006**, *95*, 1949-1956.

(19)   Kay, A. R. *Trends Neurosci.* **2006**, *29*, 200-206.

(20)   Kimura, E.; Koike, T. *Chem. Soc. Rev.* **1998**, *27*, 179-184.

(21)   Burdette, S. C.; Lippard, S. J. *Proc. Natl. Acad. Sci. USA* **2003**, *100*, 3605-3610.

(22)   Burdette, S. C.; Lippard, S. J. *Coord. Chem. Rev.* **2001**, *216-217*, 333-361.

(23)   Walkup, G. K.; Burdette, S. C.; Lippard, S. J.; Tsien, R. Y. *J. Am. Chem. Soc.* **2000**, *122*, 5644-5645.

(24)   Burdette, S. C.; Walkup, G. K.; Spingler, B.; Tsien, R. Y.; Lippard, S. J. *J. Am. Chem. Soc.* **2001**, *123*,

        7831-7841.

(25)   Burdette, S. C.; Frederickson, C. J.; Bu, W.; Lippard, S. J. *J. Am. Chem. Soc.* **2003**, *125*, 1778-1787.

(26)   Hirano, T.; Kikuchi, K.; Urano, Y.; Higuchi, T.; Nagano, T. *J. Am. Chem. Soc.* **2000**, *122*, 12399-

        12400.

(27)   Hirano, T.; Kazuya, K.; Urano, Y.; Higuchi, T.; Nagano, T. *Angew. Chem. Int. Ed.* **2000**, *39*, 1052-1053.

(28)   Fahrni, C. J.; O'Halloran, T. V. *J. Am. Chem. Soc.* **1999**, *121*, 11448-11458.

(29)   Gee, K. R.; Zhou, Z. L.; Qian, W.-J.; Kennedy, R. *J. Am. Chem. Soc.* **2002**, *124*, 776-777.

(30)   de Silva, A. P.; Gunaratne, Q. N.; Huxley, A. J.; McCoy, C. P.; Rademacher, J. T.; Rice, T. E. *Chem. Rev.* **1997**, *97*, 1515-1566.

(31)   Nolan, E. M.; Burdette, S. C.; Harvey, J. H.; Hilderbrand, S. A.; Lippard, S. J. *Inorg Chem.* **2004**, *43*, 2624-2635.

(32)   Chang, C. J.; Nolan, E. M.; Jaworski, J.; Burdette, S. C.; Sheng, M.; Lippard, S. J. *Chem. Biol.* **2004**, *11*, 203-210.

(33)   Hirano, T.; Kikuchi, K.; Urano, Y.; Nagano, T. *J. Am. Chem. Soc.* **2002**, *124*, 6555-6562.

(34)   Hilderbrand, S. A. *Fluorescence-Based Detection Methodologies for Nitric Oxide Using Transition Metal Scaffolds*, Doctoral Thesis, MIT, 2004.

(35)   Yang, J.-J.; Su, D.; Vij, A.; Hubler, T. L.; Kirchmeier, R. L.; Shreeve, J. M. *Heteroatom Chem.* **1998**, *9*, 299-239.

(36)   Gee, K. R.; Poot, H.; Klaubert, D. H.; Sun, W.-C.; Haligland, R. P.; Mao, F. *J. Org. Chem.* **1997**, *62*, 6469-6475.

(37)   Brannon, J. H.; Magde, D. *J. Phys. Chem.* **1978**, *82*, 705-709.

(38)   Sojback, R.; Nygren, J.; Kubista, M. *Spectrochimica Acta A* **1995**, *51*, L7-L21.

(39)   Wolf, H. U. *Experientia* **1973**, *29*, 241-249.

(40)   Baik, M.-H. *Personal communication.*

Table 2.1. Spectroscopic and Thermodynamic Properties of Asymmetrical ZP Sensors[a]

	Absorption λ (nm), $\varepsilon \times 10^4$ (M^{-1}cm^{-1})		Emission λ (nm), Φ [c]		$pK_a{}^d$	$pK_a{}^e$	$pK_a{}^f$	K_d (nM)
	Unbound	Zn(II)	Unbound	Zn(II)				
ZP4[b]	506, 6.1	495, 6.7	521, 0.06	515, 0.34	10.0	7.2	4.0	0.65±0.10
ZP5	504, 8.3	495, 9.1	520, 0.29	517, 0.48	10.9	9.6	4.7	0.50±0.10
ZP6	506, 8.9	495, 9.8	519, 0.10	517, 0.34	11.2	6.3	4.7	0.50±0.10
ZP7[b]	505, 6.8	495, 7.7	521, 0.04	517, 0.05	n.o.[g]	6.9	4.6	n.d.[g]
ZP8	500, 8.1	489, 7.8	516, 0.03	510, 0.35	n.o.[g]	6.5	3.8	0.60±0.10

[a]Measurements were performed at pH 7 in 50 mM PIPES, 100 mM KCl buffer. See Schemes 2.2 and 2.4 for nomenclature. [b] See refs. 25 and 31 for ZP4 and ZP7, respectively. [c]Quantum yields are based on fluorescein ($\Phi = 0.95$ in 0.1 N NaOH, ref 37). [d] The pK_a for the tertiary amine. [e]The pK_a for the aniline nitrogen atom. [f] The pK_a for fluorescein that results in formation of a non-fluorescent isomer. [g] n.o = not observed; n.d. = not determined.
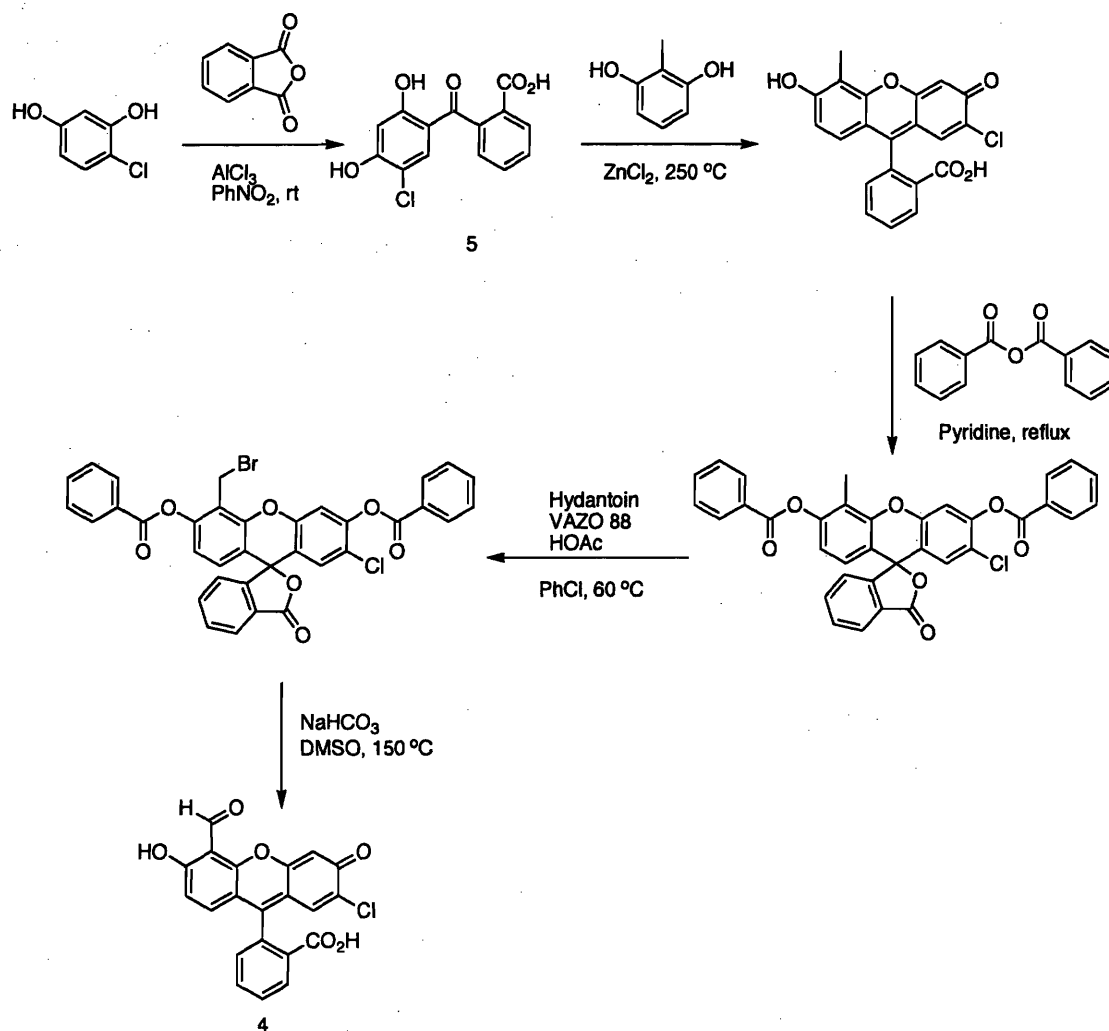
Scheme 2.1. Synthesis of 7'-chloro-4'-fluoresceincarboxaldehyde, **4**, a material used throughout this work. Details of this preparation are given in refs. 31 and 34.
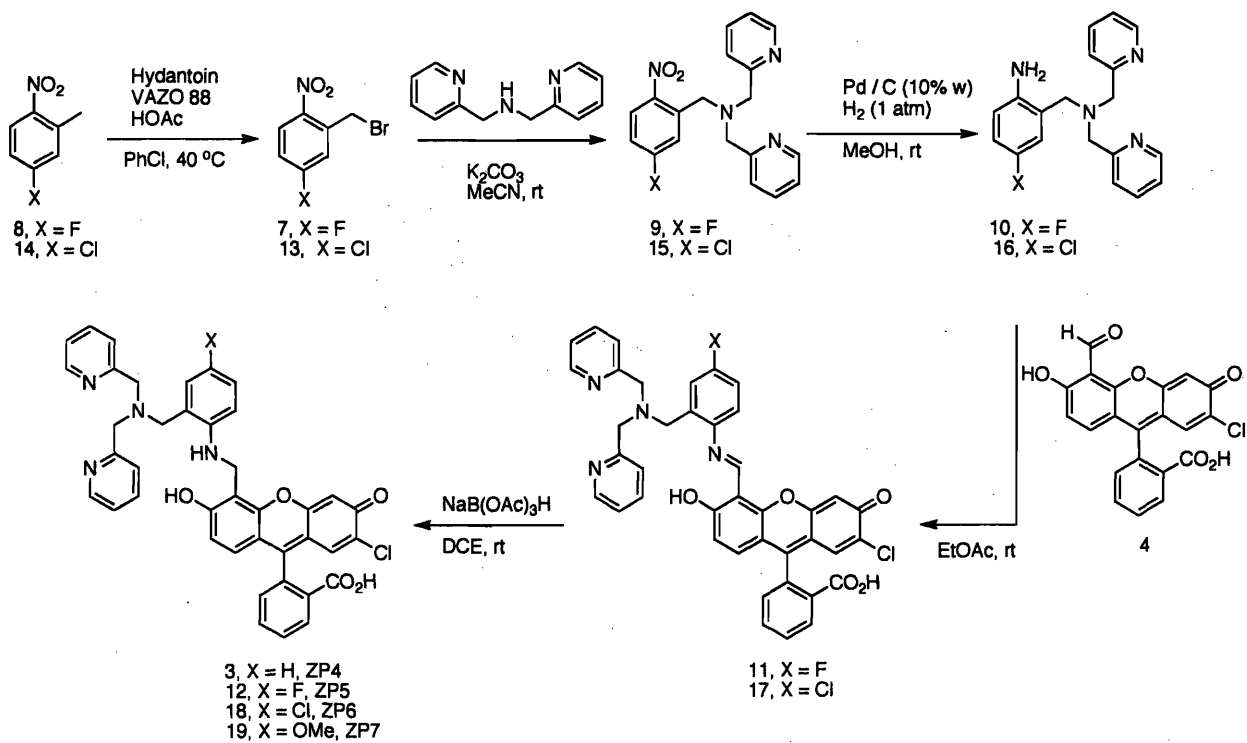
Scheme 2.2. Syntheses of sensors ZP5 and ZP6. See refs. 25 and 31 for ZP4 and ZP7.

X = H, Cl, OMe
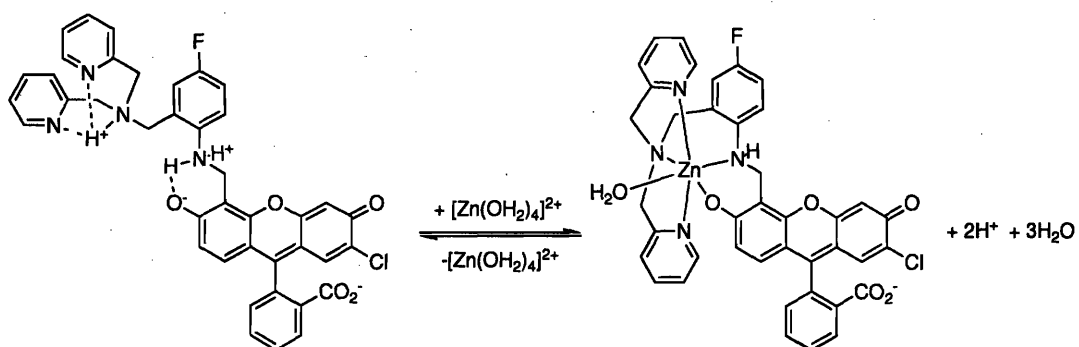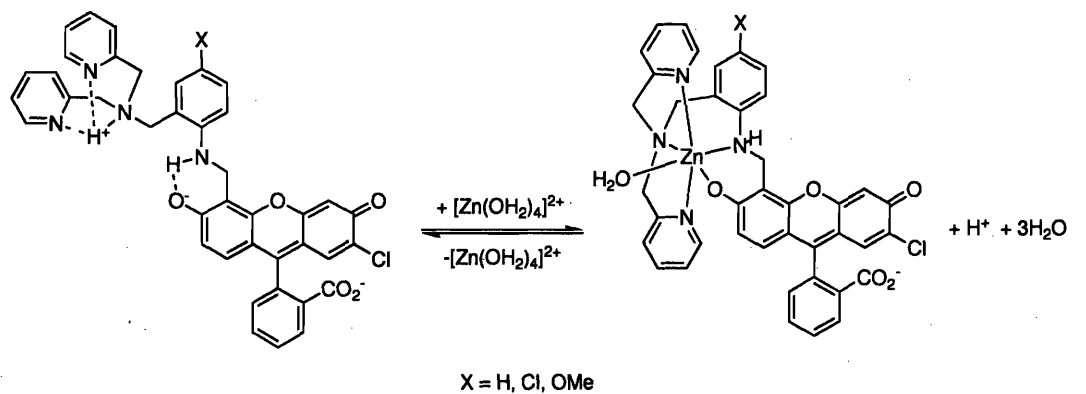
Scheme 2.3. Proposed mode of Zn(II) coordination to asymmetrical ZP.
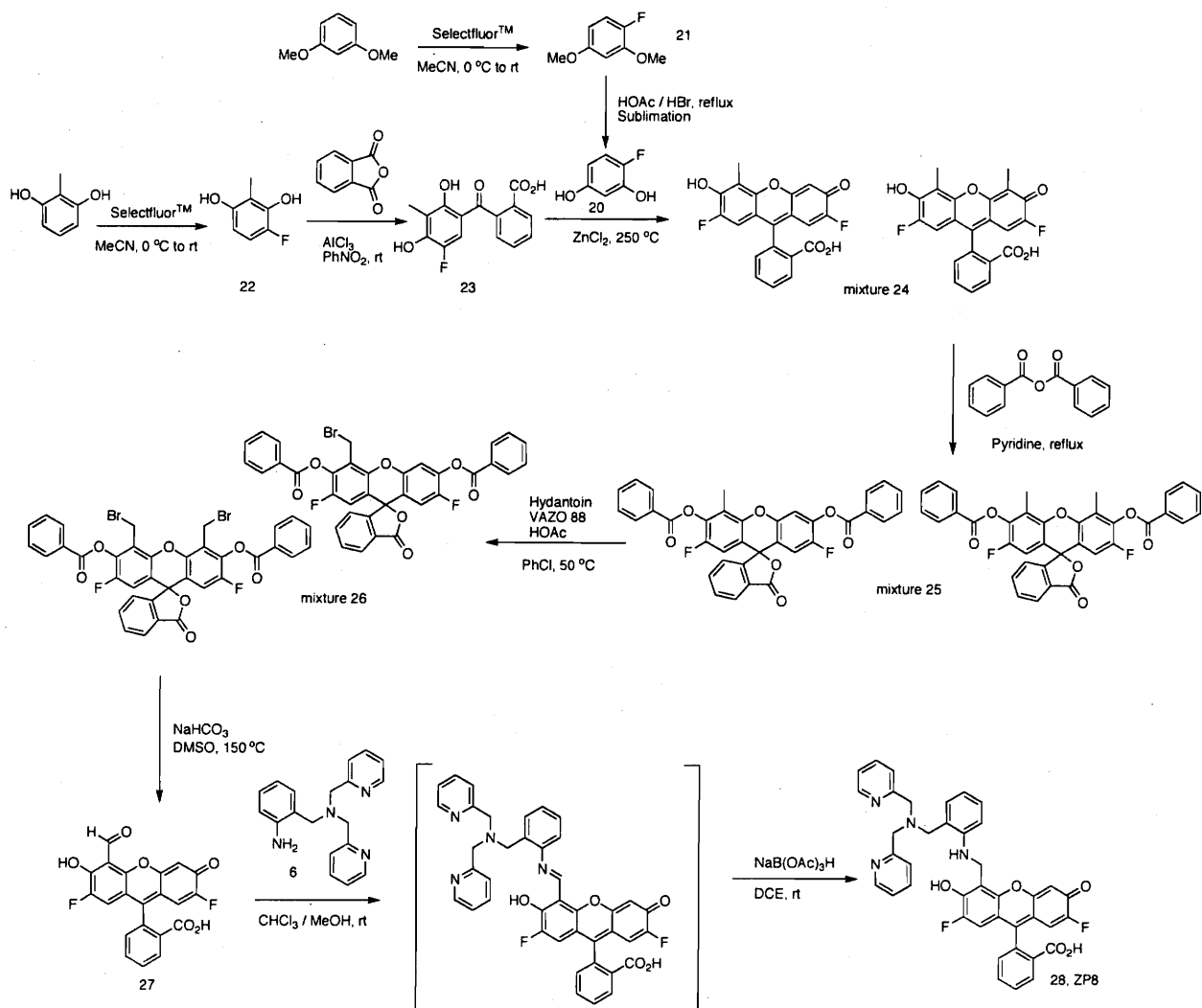
Scheme 2.4. Synthesis of a difluorofluorescein carboxaldehyde and sensor ZP8.

1, ZP1: X=Cl
2, ZP2: X=H

3, ZP4
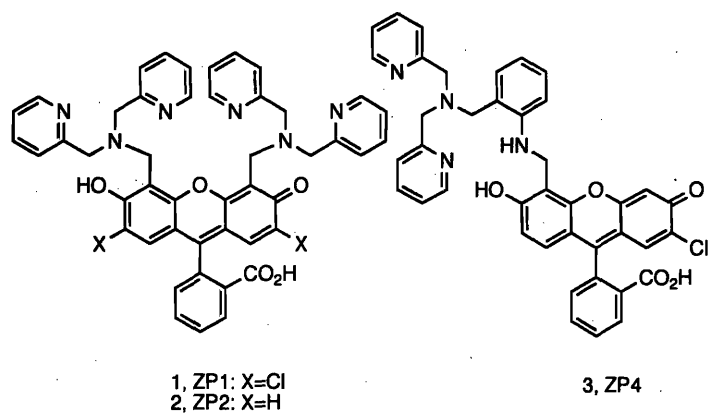
Figure 2.1. Original members of the ZP sensor family that inspired this work.
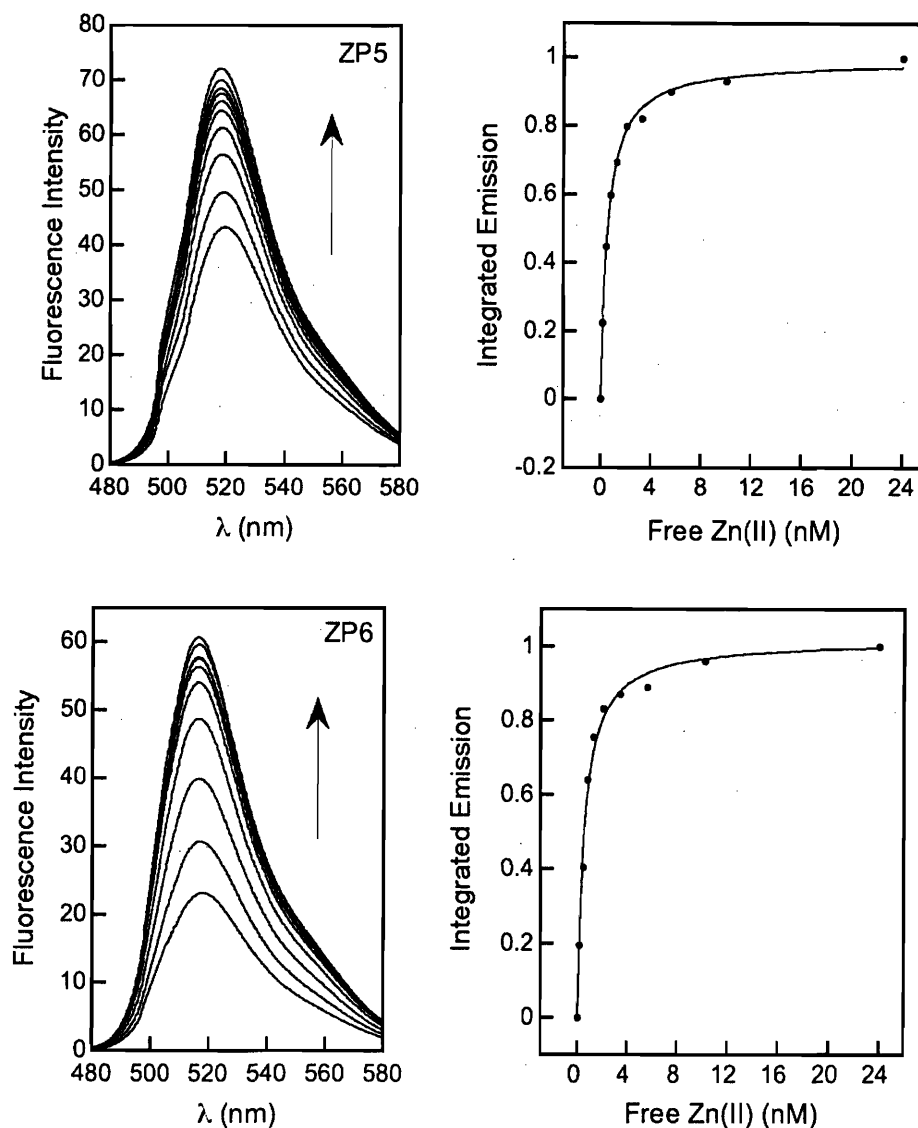
Figure 2.2. Fluorescence enhancement of ZP5 (top) and ZP6 (bottom) upon addition of buffered Zn(II) solutions at pH 7 in 50 mM PIPES, 100 mM KCl. The concentration of ZP is 500 nM, and the concentrations of free Zn(II) are 0.0, 0.17, 0.42, 0.79, 1.3, 2.1, 3.4, 5.6, 10.2 and 24 nM. Excitation was provided at 498 nm for ZP5 and at 500 nm for ZP6. The Zn(II) binding curves (right) were obtained by integrating the emission spectra, subtracting the emission of the free dye, and normalizing to the full response. Both sensors have apparent K_d values of 0.50 ± 0.10 nM for Zn(II).
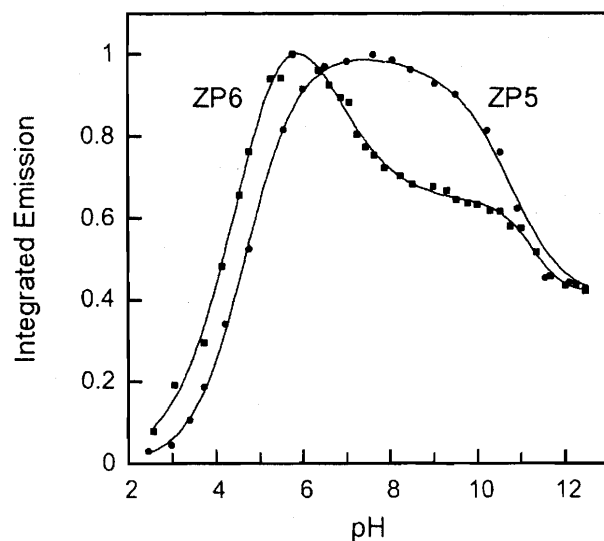
Figure 2.3. Normalized integrated emission versus pH for ZP5 (circles) and ZP6 (squares). A 1 μM solution of each dye was prepared in 10 mM KOH, 100 mM KCl and the emission recorded. The pH was decreased by addition of aqueous HCl. The data were integrated from 505 – 650 nm, normalized and plotted against pH. Excitation was provided at 498 nm for ZP5 and at 500 nm for ZP6. pK_a values are listed in Table 2.1.
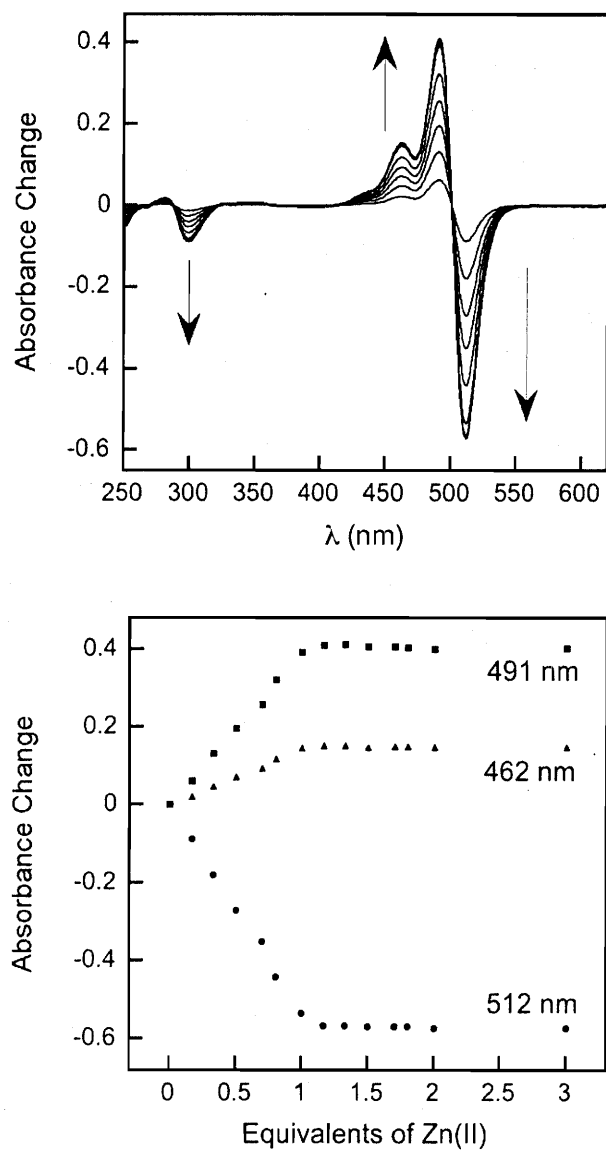
Figure 2.4. Optical absorption difference spectra (top) and corresponding metal-binding titration (bottom) for the addition of Zn(II) to 10 μM ZS5 at pH 7 (50 mM PIPES, 100 mM KCl). Absorption increases occur at 462 and 491 nm and decreases at 512 and 300 nm. The Zn(II) binding titration indicates formation of a 1:1 ZP5:Zn(II) complex.
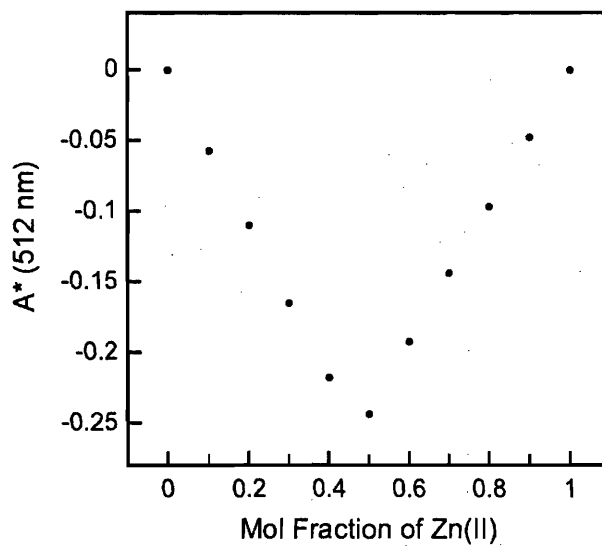
Figure 2.5. Representative Job plot for formation of the 1:1 ZP6:Zn(II) complex at neutral pH (50 mM PIPES, 100 mM KCl). Starting solutions of 10 µM ZP6 and Zn(II) were employed. The absorbance was monitored at 512 nm.

(-2.90)
(-2.99)

LUMO+3

(-3.38)

(-3.62)

(-3.99)

A_1 and B_1

(-4.68)
(-4.78)
(-4.91)

(-5.24)
(-5.36)
(-5.49)

HOMO
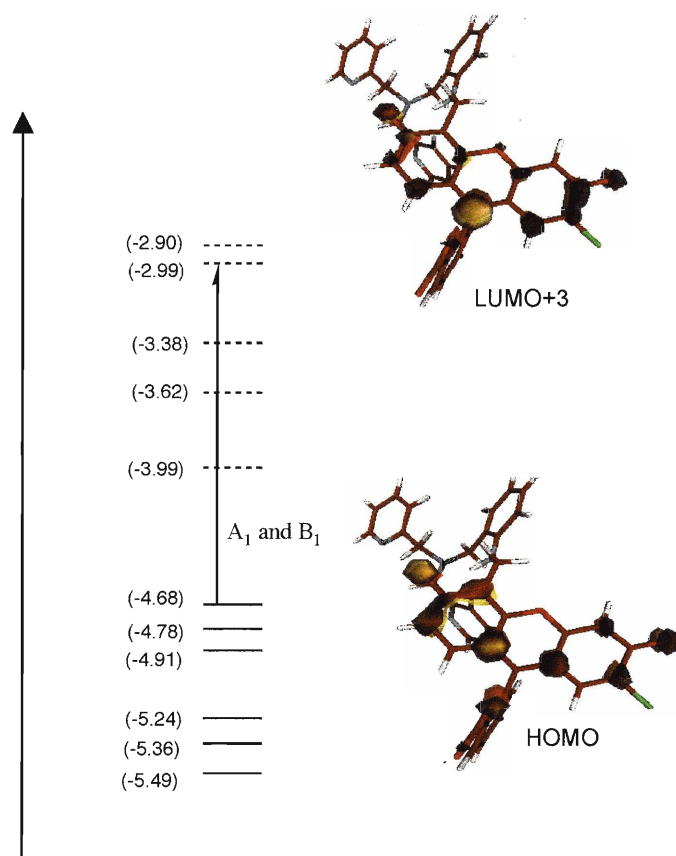
Figure 2.6. Partial molecular orbital diagram for ZP4 dianion generated by DFT analysis. The solid and dashed lines represent filled and empty molecular orbitals, respectively, and the listed energies are in eV. The arrow represents the major molecular orbital transition assigned to ZP4 dianion absorption as determined by TDDFT. The depicted molecular orbitals are those involved in the transition of interest. See text for transition labels.
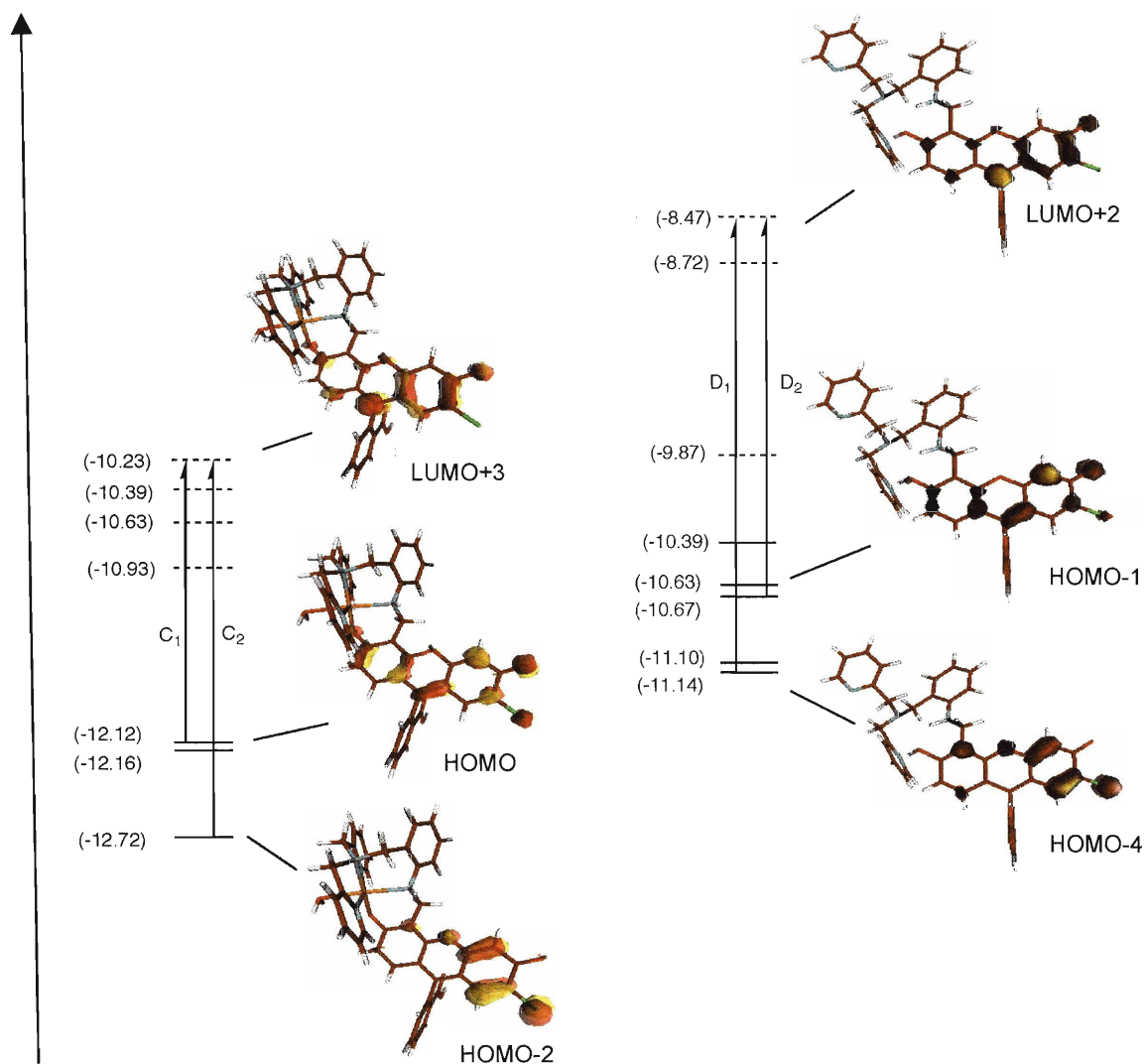
Figure 2.7. Partial molecular orbital diagrams for the ZP4:Zn(II) complex (left) and neutral ZP4 (right) generated by DFT analysis. The solid and dashed lines represent filled and empty molecular orbitals, respectively, and the listed energies are in eV. The arrows represent the major molecular orbital transitions assigned to the absorption profile of each species determined by TDDFT and the depicted molecular orbitals are those involved in the transitions of interest. See text for transition labels.
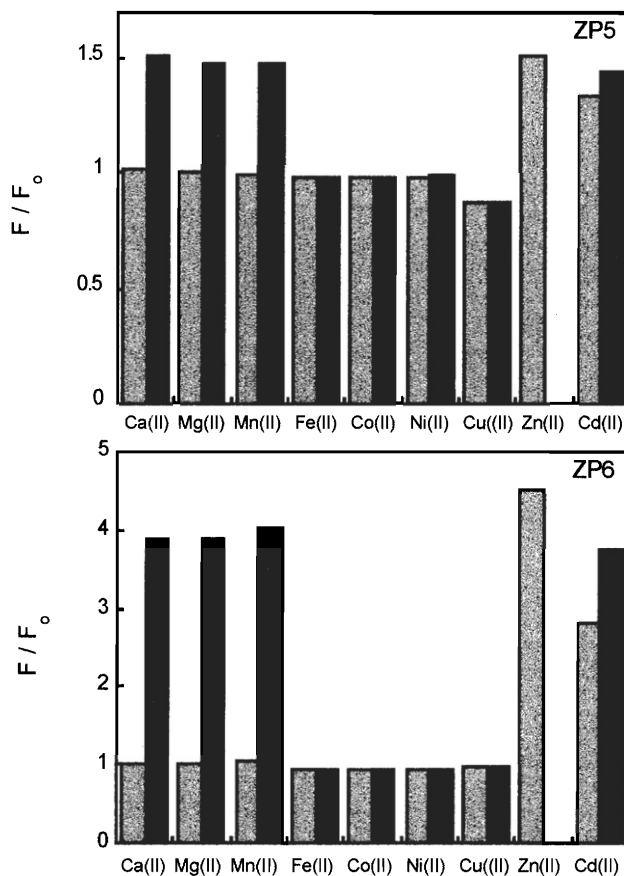
Figure 2.8. The selectivity of ZP5 (top) and ZP6 (bottom) for Zn(II) in the presence of other metal ions at pH 7 in 50 mM PIPES, 100 mM KCl. The response (F) is normalized with respect to the background fluorescence of the free dye (F_o). Grey bars: A 1 µM solution of ZP containing 50 equiv of M(II). Dark grey bars: Subsequent addition of 50 equiv of Zn(II) to the solution containing ZP and the cation of interest. No additional Zn(II) was added to the solution containing Zn(II) from the first addition. Excitation was provided at 498 nm for ZP5 and at 500 nm for ZP6. The fluorescence responses are also unaffected by millimolar concentrations of Na(I), K(I), Ca(II) and Mg(II) (data not shown).

Chapter 3

Characterization and Biological Applications of
Halogenated ZP Sensors

The syntheses and spectroscopic characterization of the probes discussed herein have
been published (*Chem. Biol.* **2004**, *11*, 203-210).

Introduction

Mobile zinc is implicated in many physiological[1-8] and pathological[8-12] phenomena, but the details of its function remain elusive and even controversial.[13-15] These questions, in part, stem from both a lack of Zn(II) probes suitable for specific biological applications and poor understanding of sensor behavior in the cell or tissue type of interest. From this perspective, the design and characterization of novel Zn(II) sensors and thorough investigations of their distribution, stability, cytotoxicity and Zn(II) sensitivity in biological samples are warranted.

Initial cell studies with ZP1, **1**, shown in Scheme 3.1, pointed to its potential utility for in vivo Zn(II) imaging in multiple contexts.[16,17] ZP1 readily enters cells and penetrates tissues, and responds to Zn(II) in these samples. Nevertheless, one major limitation of ZP1 is its high background fluorescence at physiological pH (Φ_{free} = 0.38), which results in a modest dynamic range and which can potentially complicate the interpretation of fluorescence images. As a result, reducing ZP1 background fluorescence was an important early goal. The investigations detailed herein focus on halogenated ZP1 analogs as a means to address this problem.

In this chapter, we first explore the effect of fluorescein halogenation on the spectroscopic and thermodynamic characteristics of symmetrical ZP sensors. Secondly, we consider ZP sensors in several biological contexts. We investigate the cytotoxic effects of selected ZP probes in HeLa cells. Control studies such as these are important because cytotoxicity is a potential side effect of sensor application that could influence the outcome of a biological experiment. We also present investigations of Zn(II) response and subcellular localization of ZP3, a 2′,7′-difluorofluorescein analog of ZP1, in several cell lines. Finally, we demonstrate that ZP3 detects endogenous pools of Zn(II) in both cultured cells and brain tissue. These investigations point to the general utility of ZP3, and potentially its analogs, for imaging endogenous Zn(II) stores and Zn(II) mobilization in vivo.

Experimental Section

Preparation of ZP Probes. The halogenated ZP sensors **2-6** discussed in this chapter were synthesized as described in the literature.[18,19] The general approach, which consists of a Mannich reaction between the imminium ion condensation product of DPA and formaldehyde and a halogenated fluorescein, is depicted in Scheme 3.1. This assembly route is facile and affords ZP sensors in high yield and excellent purity following recrystallization from boiling EtOH. Colorless block crystals of ZPCl1, **4**, suitable for X-ray analysis were obtained by slow evaporation of a MeOH/CHCl$_3$ solution of ZPCl1 at room temperature over two days.

X-ray Crystallographic Studies. Single crystals were mounted on the tips of glass fibers, coated with paratone-N oil, and cooled to −100 °C under a stream of N$_2$ maintained by a KRYO-FLEX low-temperature apparatus. Intensity data were collected on a Bruker APEX CCD diffractometer with graphite-monochromated Mo Kα radiation (λ = 0.71073 Å), controlled by a Pentium-based PC running the SMART software package.[20] Data collection and reduction protocols are described elsewhere.[21] The structures were solved by direct methods using the SAINTPLUS and SHELXTL software packages.[22,23] Empirical absorption corrections were applied by using the SADABS program,[24] and the structures were checked for higher symmetry by using the PLATON software.[25] All non-hydrogen atoms were located and their positions refined with anisotropic thermal parameters by least-squares cycles and Fourier syntheses. Hydrogen atoms were assigned to idealized positions and given thermal parameters equivalent to either 1.5 (methyl hydrogen atoms) or 1.2 (all other hydrogen atoms) times the thermal parameter of the carbon atom to which they were attached. The structure of ZPCl1 contains two ordered methanol molecules.

Spectroscopic Methods. All photophysical and metal-binding studies were conducted as described in Chapter 2.

Cell Culture. Cells were grown to 60 – 90% confluence in DMEM supplemented with 10% FCS, glutamine (2 mM), penicillin (100 units/mL) and streptomycin (100 µg/mL). HeLa and COS-7 cells were plated on untreated live imaging dishes. Human embryonic kidney (HEK293-T, HEK) cells were either plated on untreated live imaging dishes or on glass coverslips coated with 0.2% gelatin for at least 1 h at room temperature. Prior to treatment with ZP, the medium was removed and replaced with DMEM containing 1% serum. DMSO stock solutions of the sensors were diluted to 100 µM with either DMEM or PBS and applied to the cells bathed in DMEM with 1% serum for a final dye concentration of 10 µM for imaging experiments. Cells were generally incubated with ZP for 30 min (T = 37 °C, 5% CO_2), washed once with 2 mL of serum-free DMEM containing and bathed in serum-free DMEM (2 mL) before imaging.

Stock solutions of Zn(II)/pyrithione (1:2 or 1:1 ratio, 10 mM) were prepared from $ZnCl_2$ and sodium 2-mercaptopyridine-N-oxide (pyrithione) and DMSO and were diluted 10-fold with DMEM or PBS prior to cell treatment. Stock solutions of N',N',N'',N'-tetrakis(2-picolyl)ethylenediamine (TPEN, 10 mM) in DMSO were also diluted 10-fold with DMEM or PBS prior to imaging. In a typical experiment, a 100 µL aliquot of Zn(II)/pyrithione or TPEN was added to the live imaging dish by bath application and on the microscope stage to give a final Zn(II) or TPEN concentration of 50 µM. For Zn(II) release and mobilization experiments, S-nitrocysteine (SNOC, 10 mM) was prepared according to a literature procedure[26] and immediately added to the cells by bath application on the microscope stage.

Lysotracker Red (Invitrogen) and Mitotracker Red (Invitrogen) were employed for colocalization studies. In a typical experiment, a 1 mM stock solution of either marker in DMSO was diluted 100- to 200-fold with DMEM prior to cell treatment. The cells were co-treated with the organelle marker and ZP3 and were generally incubated with the reagents for 30 min (T = 37 °C, 5% CO_2) before imaging. The exact concentration of Lysotracker or Mitotracker used varied with cell type and lot number and was in the

range of 100 to 500 nM. Both probes photobleach readily, so appropriate care must be taken when handling the stock solutions in the light and during imaging experiments.

A pGolgi-DsRed construct was employed to label the Golgi apparatus. This plasmid expresses a fusion protein consisting of DsRed and a sequence encoding the N-terminal 81 amino acids of human beta 1,4-galactosyltransferase (Clontech). The latter sequence includes a membrane anchoring signal peptide, which directs the fusion protein to the trans-Golgi region. Overexpression of pGolgi-DsRed results in its presence in other compartments of the secretory pathway. A pMito-DsRed construct with a mitochondrial targeting sequence from subunit VIII of cytochrome c oxidase (Clontech) and the DsRed sequence was used for labeling mitochondria.[27] Cells were passed and plated on live imaging dishes 36 h before transfection. The cells were transiently transfected with either pGolgi-DsRed or pMito-DsRed using the Lipofectamine2000 reagent (manufacturer protocol) 24 – 36 h prior to imaging.

Cytotoxicity Studies I: Kill Curves and IC$_{50}$ Determination. IC$_{50}$ values for ZP1, ZP3 and ZPF1 were determined in HeLa cells by using the MTT assay. For a typical kill curve, HeLa cells were passed and plated into 96-well plates (500 cells per well, 100 μL of cell suspension) 12 – 16 h before treatment and cultured in DMEM containing 10% FCS, glutamine (2 mM), penicillin (100 units/mL) and streptomycin (100 μg/mL). Stock solutions of ZP (1 mM in DMSO) were diluted with DMEM containing 10% FCS, glutamine (2 mM), penicillin (100 units/mL) and streptomycin (100 μg/mL) and added to the HeLa cells (100 μL ZP solution per well) to yield final ZP concentrations ranging from 0 to 12 μM. The cells were incubated at 37 °C and under 5% CO$_2$ for five days and subsequently treated with 5 mg/mL MTT (20 μL/well) for 4 h (T = 37 °C, 5% CO$_2$). The medium was removed, the cells were dissolved in DMSO (100 μL/well), and the absorbance at 550 nm was recorded using a microplate reader. Each kill curve was repeated a minimum of four times with cells from different stocks and with at least two independently prepared ZP solutions. Two types of control studies were also

performed. To confirm that cell death resulted from the ZP probes and not DMSO, a DMSO-only kill curve was run parallel to each experiment. To show that ZP absorption did not influence the A_{550} reading, kill curves for each probe were run as described above, but the cells were not treated with MTT prior to analysis. These experiments confirmed that ZP accumulation in the cells does not influence the A_{550} reading.

To ascertain the cytotoxic effect of ZP treatment over a 24 h period, HeLa cells were passed and plated to ~60% confluence in 12-well plates 12 – 16 h before treatment and bathed in 1 mL of DMEM supplemented as described above. Prior to ZP treatment, the DMEM was removed and replaced with fresh DMEM, and aliquots of ZP stock solutions (1 mM DMSO) were added for final concentrations of 1, 5 and 10 µM. The treated cells were incubated for 24 h at 37 °C and under 5% CO_2, treated with 5 mg/mL MTT (100 µL/well) and incubated for an additional 2 – 4 h (T = 37 °C, 5% CO_2). The DMEM was removed and the cells were dissolved in DMSO (500 µL/well) and the absorbance at 550 nm was recorded.

Cytotoxicity Studies II: Nuclear Morphology Assays. Nuclear morphology assays were conducted to monitor HeLa cell viability qualitatively following a 24 h incubation with ZP. HeLa cells were passed and plated to ~60% confluence on 18 mm untreated glass coverslips 12 – 16 h before treatment. ZP solutions were added to the cells as described above for the 24 h MTT assay and the cells were incubated for 24 h (T = 37 °C, 5% CO_2). Subsequently, the medium was removed and the cells were washed (1 x 1 mL) with PBS and fixed for 5 min with paraformaldehyde (PBS containing 4% PFA, 4% sucrose, 1 mL). The cells were washed with PBS (2 x 1 mL) and bathed in PBS containing 800 nM Hoescht (Aldrich) for 5 min (1 mL). The Hoescht solution was removed and the cells were washed a final time with 1 mL of PBS, bathed in PBS and mounted onto glass slides using the Vectashield antifading reagent (Vector Labs).

Preparation of Cultures of Dentate Gyrus Neurons. Primary cultures of dentate gyrus (DG) cells were prepared by modification of a literature procedure.[28,29] Dentate

gyrus regions were dissected from the hippocampi of 4-day-old Sprague Dawley rat pups. The cells were plated on 24 mm glass coverslips (250 cells/mm^2) coated with poly-L-lysine (Sigma, 50 μg/mL). The cultures were maintained for the first 24 h in DMEM (Invitrogen) supplemented with 10% FCS (Invitrogen), glutamine (2 mM) and penicillin-streptomycin mix (50 μg/mL). Subsequently, the cells were kept in Neurobasal medium (Invitrogen) supplemented with B27 (Invitrogen), glutamine (2 mM), potassium chloride (20 mM) and penicillin-streptomycin mix (50 μg/mL). After 7 days in culture, the medium was removed and replaced with Neurobasal containing no B27 and the cells were treated with ZP for 20 – 30 min by bath application (T = 37 °C, 5% CO_2) and washed once with Neurobasal prior to imaging.

Acute Hippocampal Slice Preparation. The whole brains of 90-day old female Sprague-Dawley rats were removed. The hippocampi were dissected, cut into ~200 μm-thick slices and washed twice with Zn(II)-free Kreb's ringer buffer prepared according to a literature protocol.[30] Slices were incubated with 10 μM dye in Zn(II)-free Kreb's ringer buffer (T =37 °C, 5% CO_2) for 10 – 20 min, washed thoroughly with the Zn(II)-free buffer, and transferred to a glass-bottom imaging dish with a minimal volume of buffer for imaging.

Confocal Fluorescence Microscopy. A Zeiss LSM510 laser scanning microscopy system based on an Axiovert 200M inverted fluorescence microscope was used for confocal fluorescence imaging. The microscope was fashioned with an argon ion laser (λ_{ex}= 488 nm), 10x or 63x objective lens (0.7 to 3 x electronic zoom), and a 505 nm long pass emission filter. During imaging experiments, samples were kept on the microscope stage in a CTI-3700 incubator set at 37 °C under 5% CO_2. Additions of Zn/pyrithione and TPEN solutions to the biological samples were performed directly on the microscope stage by bath application.

DIC and Wide-Field Microscopy. A Zeiss Axiovert 200M inverted fluorescence microscope equipped with an EXFO illumination source, Hamamatsu C9100-12 camera

and 63x objective was used to obtain DIC and epifluorescence images of fixed cells. The microscope was controlled by the Volocity software package (Improvision).

Results and Discussion

Design Rationale and Syntheses. One potential disadvantage of PET-based sensors is proton sensitivity. Protonation of aliphatic amines, such as those in ZP1, 1, and ZP2, 7, disrupts the PET quenching pathway.[16,31] This phenomenon can cause several problems, including proton-induced background fluorescence and, in the biological context, uncertainy as to whether a visualized signal results from analyte detection or proton flux. At least in part due to the relatively high pK_a values of the tertiary amine nitrogen atoms of ZP1 (pK_a = 8.4) and ZP2 (pK_a = 9.4), these sensors suffer from high background fluorescence in the physiological pH range (Φ_{free} = 0.38, ZP1 and 0.25, ZP2), which results in a modest signal-to-noise ratio. At the start of this project, a paramount goal was to reduce background fluorescence and proton sensitivity, and several strategies were devised to address this issue. A first approach was the design of ZP4[32] and, subsequently, the derivatives described in Chapter 2. We also sought to reduce the background fluorescence of symmetrical ZP derivatives, which can be prepared in fewer synthetic steps than ZP4. Our approach of electronic variation parallels that described in Chapter 2 for the aniline-based ZP4-derivatives except that we solely focus on modification of the fluorescein platform. Given the decrease in pK_a observed with chlorination of the fluorescein (i.e. ZP2 to ZP1), we were particularly interested in the effect of fluorine introduction in the 2' and 7' positions of the xanthenone unit. Since halogenated fluoresceins are easily obtained by acid-catalyzed condensation of a 4'-substituted resorcinol and a substituted phthalic anhydride, we also explored how halogenation of the benzoate moiety influences the spectroscopic and thermodynamic properties of ZP sensors.

Scheme 3.1 depicts the syntheses of sensors **2-6**, which were all obtained in high yields from one-step Mannich reactions between DPA and a halogenated fluorescein. These reactions are facile on both the small (milligram) and large (multi-gram) scales and the ZP probes can be purified by recrystallization from boiling EtOH (X ≠ H). The latter feature is particularly important since fluroescein-based probes, and especially those appended with DPA or other nitrogen-containing ligands, often permanently stick to silica gel and aluminum oxide. X-ray quality colorless block crystals of ZPCl1 were obtained by evaporation of a concentrated solution of the probe in mixed $CHCl_3$/MeOH at room temperature. Table 3.1 includes the crystallographic parameters from the refinement and select bond lengths and angles are listed in Table 3.2. The ORTEP diagram of ZPCl1 is given in Figure 3.1. As evidenced by the colorless nature of the crystals, ZPCl1 crystallized in the non-emissive lactone form.[16]

Spectroscopic Characteristics. Table 3.3 summarizes data obtained from optical absorption and fluorescence spectroscopic examination of probes **2-6** in addition to parent compounds ZP1 and ZP2. In general, halogenation of the fluorescein platform induces red shifts in both excitation and emission maxima. Chlorination or fluorination of the benzoate ring causes ca. 20 nm red-shifts and chlorination of the 2′ and 7′ positions of the xanthenone framework also results in red-shifts relative to unsubstituted or fluorinated fluorescein. These substitutions afford an excitation and emission range of ~35 nm. Although modest, this feature could be useful for biological imaging experiments that require two Zn(II) sensors. Both in-house[33] and commercially available software, such as the Zeiss META detection system when operated in lamda mode, reportedly can identify and deconvolute excitation and emission wavelengths differing by only ca. 10 nm. Accordingly, one could image using ZPCl1 (λ_{ex} = 534 nm), which is cell-permeable, and an extracellular fluorescein-based sensor such as ZP1(6-CO_2H)[34] (λ_{ex} = 516 nm) or a difluorinated analog (λ_{ex} ~ 500 nm), to monitor zinc trafficking to and from cells. This sensor combination would be particularly useful since

both probes would have similar brightness resulting from the conserved fluorophore platform. Similarly, ZPCl1 could be used in conjunction with an extracellular fluorescein-based Ca(II) sensor for simultaneous monitoring of Zn(II) and Ca(II) signals.

Halogenation also significantly influences the quantum yields for apo and Zn(II)-bound ZP (Table 3.3). Benzoate ring substitution results in both decreased quantum efficiencies for the apo and Zn(II)-coordinated sensors relative to parent ZP1. This effect appears rather general since a similar diminution of quantum yield was observed with ZP1 derivatives containing carboxylate or ethyl ester moieties in the 5 or 6 position of the benzoate ring.[34] Incorporation of fluorine atoms into the xanthenone moiety lowers the free sensor quantum yield to 0.15 (ZP3) relative to 0.38 and 0.25 for ZP1 and ZP2, respectively. From the perspective of maintaining high dynamic range, achieving the brightest Zn(II)-bound species and requiring a relatively short synthesis, ZP3 is superior. Its dynamic range is ~6-fold and comparable to that of ZP2, which requires a multi-step synthesis and is less bright because of its relatively low extinction coefficient. Additionally, of the halogenated ZP sensors, the excitation wavelength of ZP3 is most compatible with the 488 nm line of the Ar laser, which may be of benefit for laser-scanning confocal microscopy.

The ZP probes have high extinction coefficients in the apo ($4.4 - 9.9 \times 10^4$ $M^{-1}cm^{-1}$) and Zn(II)-bound ($5.3 - 12.0 \times 10^4$ $M^{-1}cm^{-1}$) forms. Halogenation of fluorescein increases its molar absorptivity[35,36] and this trend is evident in the ZP sensor family (Table 3.3). Regardless of fluorescein substitution, addition of Zn(II) to solutions of ZP results in both a blue-shift and an increase in the wavelength of maximum absorption. Based on X-ray crystallographic studies of ZP1[23] and TDDFT analysis of related compounds (Chapters 2, 7), we attribute the latter feature to coordination of the 3'-oxo atom of the xanthenone ring to Zn(II).

Fluorescence Dependence on pH. Figures 3.2 and 3.3 display representative pH titrations for sensors **2-6** and Table 3.3 includes all derived pK_a values. We first consider

the effect of substitution only at the 2′ and 7′ positions of the fluorescein framework (Figure 3.2). Replacing fluorescein with 2′,7′-dichloro- or 2′,7′-difluorofluorescein results in a shift of the titration curve to lower pH. This trend is analogous to the known pH sensitivity of fluorescein[35] and its chlorinated[36] and fluorinated[37] analogs. As a result, the pK_a of the tertiary amine responsible for PET quenching of the unbound sensor is lowered upon halogenation. This effect is most dramatic for ZP3, which has a tertiary amine pK_a of 6.8. The reduction in pK_a for ZP3 relative to ZP1 can be correlated to a decrease in background fluorescence as measured by quantum yield (ZP3, Φ_{free} = 0.15; ZP1, Φ_{free}= 0.38 and pK_a = 8.4); however, the pK_a and quantum yield values for ZP2 do not fit this correlation (Φ_{free} = 0.25; pK_a = 9.4), and data presented in Chapters 5 and 6 suggest that the fluorination effect is not solely the result of a diminished pK_a value. Furthermore, although no explanation of the phenomenon was given, background fluorescence reduction was reported following fluorination of the xanthenone moiety in the ZnAF family of Zn(II) sensors,[38] which show no pH sensitivity in the physiological range. We conclude that the choice of 2′,7′-difluorofluorescein will afford sensors with lower Φ_{free} and that this effect is independent of amine pK_a. Future theoretical investigations will address this matter in more detail.

Fluorescence quenching occurs with further lowering of the pH and the pK_a values for this transition vary from 3.9 (ZP2) to 2.0 (ZP3). This trend follows that of the known phenol pK_a values for fluorescein (pK_a = 6.4)[35], 2′,7′-dichloro- (pK_a = 5.0)[36] and 2′,7′-difluorofluorescein (pK_a = 4.8)[37] and this transition is assigned to protonation of the phenol group. The effect of pH on ZP1 absorption further substantiates this assignment (Figure 3.2, bottom). Lowering of the pH from ~4 to ~1 causes a blue shift in the wavelength of maximum absorption and a significant decrease in molar absorptivity with an isosbestic point at 468 nm. The spectra obtained at pH > 2, which have two local peaks of maximum absorption ca. 467 and 507 nm are clear indicators of phenol protonation and formation of the dichlorofluorescein monoanion.[34] We note that the

phenolic pK_a values for ZP1 to ZP3 are lower than the reported values for fluorescein, DCF, and DFF, and we attribute this shift to hydrogen bonding of the tertiary amine proton to the phenol group (Scheme 3.2).

Figure 3.3 depicts pH titrations of ZP probes with halogenated benzoate rings, the corresponding pK_a values for which are given in Table 3.3. In contrast to the titration curves obtained for ZP1-3, which show that two protonation events influence emission, three pK_a transitions are observed. Two of these, with $pK_a \sim 7$ and $pK_a \sim 4$, correspond to fluorescence enhancement when moving from high to low pH and indicate sequential protonation of the two tertiary amine groups as depicted in Scheme 3.2, with the first tertiary amine protonation event responsible for more fluorescence enhancement than the second. Similar behavior was observed for ZP1(6-CO_2H) and related compounds.[34] As described above for ZP1-3, the $pK_a \sim 2$ transition is assigned to protonation of the 3'-oxo atom and formation of a non-fluorescent species at acidic pH. Based on these studies, we propose the protonation equilibria for symmetrical ZP depicted in Scheme 3.2. The quinoid isomer of fluorescein, rather than the zwitterionic form, is employed, the rationale for which is discussed in Chapter 4.

Metal-Binding Studies. ZP1 and ZP2 bind Zn(II) with sub-nM affinity[16] and, given the conserved metal binding framework, we expected that halogenated ZP **2-6** would also have K_{d1} values for Zn(II) in this range. Figures 3.3-7 exhibit representative fluorimetric titrations, which return K_{d1} values that vary from 0.7 (ZP3) to 1.1 (ZPBr1) nM (Table 3.3). Slight increases in the K_d values are observed with increasing fluorescein halogenation and may reflect weaker coordination by the phenol group. This notion is discussed in greater detail in Chapter 6. Based on previous studies,[16] we anticipate that the second Zn(II) binding event is of significantly lower affinity; K_{d2} values for **2-6** were not determined.

Figure 3.8 depicts the results of a metal ion selectivity study conducted for ZP3. Its behavior is analogous to that of parent compound ZP1 and other family members. The

ZP sensors are selective for Zn(II) over millimolar concentrations of Na(I), K(I), Ca(II) and Mg(II). With the exception of Mn(II), the divalent first-row transition metal ions considered cause fluorescence quenching and interfere with the Zn(II) response of the probe. These sensors give comparable fluorescence enhancement for both Zn(II) and Cd(II), and also respond to Hg(II); however, ZP bind Zn(II) with higher affinity than its Group 12 congeners. Mercury(II) coordination, in particular, induces a red-shift in both excitation and emission wavelengths, which is reversed by Zn(II) addition.

Cytotoxicity Studies. Cytotoxicity is a potential side effect of a probe that must be controlled when dealing with living cells or tissues. Although we saw no evidence for cytotoxic effects during the imaging experiments in cell lines or cultured neurons detailed below, most of our work required relatively short incubation periods up to several hours. We were therefore interested to study the possible consequences of a more extended sensor treatment on cell viability. To date we have only conducted cytotoxicity assays in HeLa cells, an immortalized cervical cancer cell line available in our laboratory, but this information should prove useful in the design of experiments requiring other cell lines. We anticipate that the cytotoxicity of the probes will be greater in HeLa or other dividing cells than in cultures of primary neurons, which do not divide and have a relatively slow metabolism.

We chose three probes for the analyses, ZP1, ZP3 and ZPF1. ZP1 and ZP3 are the most commonly used ZP probes to date for biological imaging and ZP1 is now commercially available. ZPF1 was arbitrarily selected to investigate whether bottom ring halogenation would affect cell viability. We began with a qualitative nuclear morphology assay, results for which are depicted in Figure 3.9. Following a 24 h treatment with 10 μM probe, the HeLa cells were fixed and treated with Hoescht, a nuclear stain that emits in the UV-region, mounted on glass coverslips and imaged by epifluorescence microscopy. Hoescht staining allows for visualization of chromatin condensation, a signal of cell death. Although we observed no evidence of chromatin

condensation and the nuclear morphology of treated cells looked similar to that of the untreated control (Figure 3.9), the cell density was greater on coverslips of control cells. This observation suggests that a population of the cells died as a result of ZP treatment and were presumably washed away during the fixation procedure.

We subsequently conducted colorimetric MTT assays,[39] both to quantify cell death over a 24 h treatment period and to determine an IC_{50} value for each probe. Oxidation of MTT, 3-(4,5-dimethylthiazol-2-yl)-2,5-diphenyltetrazolium bromide, by mitochondrial reductase enzymes produces formazan, which is purple and can be monitored by UV-visible spectroscopy, as an indicator of cell viability. In the former set of experiments, which were designed to mimic a typical imaging experiment, HeLa cells were plated (60 – 80% confluency) and treated with 1, 5 or 10 μM ZP for 24 h. The bar graphs depicted in Figures 3.10 depict the cytotoxicity data obtained from three independent trials and Table 3.4 details the quantification. These experiments indicate that the three ZP probes have similar cytotoxic effects. Greater than 90% cell survival occurs with 1 μM probe, but higher ZP concentrations result in substantially more cell death over a 24 h period, with less than 50% survival at 10 μM probe. Control studies show the amount of DMSO added to the cell culture dish (0.1 to 1% by volume), in order to deliver the sensor, is not cytotoxic to the HeLa cells over this time period.

The MTT assay was also used to determine IC_{50} values for ZP1, ZP3 and ZPF1. HeLa cells were treated with 0 –12 μM ZP for 5 days and representative kill curves are presented in Figure 3.11. Table 3.4 includes IC_{50} values, which range from ~2 to ~4 μM and show that the three probes have similar toxicity in HeLa cells. The kill curves in Figure 3.11 indicate that 1 μM ZP is essentially non-toxic over a period of five days.

In total, these cytotoxicity tests indicate that sub- and low-μM concentrations of ZP are essentially non-toxic and can safely be used for biological studies that require prolonged sensor treatment. Although we generally conduct our imaging experiments with 10 μM probe, the choice was an arbitrary one and significantly lower

concentrations can be used for imaging experiments. A recent study of synaptic activation in hippocampal slices employed 5 μM ZP4[15] and preliminary epifluorescence experiments in our laboratory indicate that intracellular fluorescence can be readily detected in HeLa cells treated with less than 500 nM ZP3.

Biological Imaging Studies I: Subcellular Localization. Preliminary cell studies with ZP1 indicated that it is readily cell permeable and localizes to the Golgi apparatus of COS-7 cells.[18] Given the improved fluorescence properties of ZP3, we sought to ascertain its behavior in cultured cells. The investigations detailed below point to the general applicability of ZP3 for biological imaging.

Figure 3.12 shows representative laser scanning confocal images of HeLa, COS-7 and HEK cells treated with 10 μM ZP3 (30 min, 37 °C) and after addition of 50 μM 1:1 or 1:2 Zn(II)/pyrithione. Pyrithione is a cell-permeable ionophore that is used to carry metal ions into cells. Our control studies in aqueous buffer showed that the presence of excess pyrithione, which has a $K_{a1} \sim 10^5$ M and a $K_{a2} \sim 10^{11}$ M for Zn(II),[40] did not hinder the fluorescence response of ZP3 to Zn(II). In each case, intracellular fluorescence enhancement is observed within 5 min of Zn(II) treatment. Addition of 50 μM TPEN, a cell-permeable heavy metal ion chelator, reverses the fluorescence rise to baseline generally within ~2 min of addition to the cell culture medium (HeLa, HEK, COS-7). These preliminary studies indicate that (i) ZP3 is permeable and zinc responsive in a number of cell lines and (ii) the fluorescence rise observed results from Zn(II) binding and not to some interfering phenomenon.

We next investigated the subcellular localization of ZP3 in HeLa and COS-7 cells. Representative images are given in Figures 3.13 and 3.14. The images in Figures 3.13 show no colocalization of ZP3 and the lysosomal or mitochondrial markers in HeLa cells, which indicates that ZP3 is trapped in some other subcellular compartment. Excellent colocalization of ZP3 and Golgi-DsRed occurs in HeLa cells (Figure 3.12) and imaging studies conducted with HeLa cells following 24 h incubation indicate that ZP3

is retained in the Golgi of viable cells. Figure 3.13 gives representative images for analogous experiments in COS-7 cells. Like the HeLa cells, ZP3 shows no colocalization with the mitochondrial and lysosomal markers. Although the punctate nature of ZP3 staining in COS-7 cells suggests Golgi localization, the overlay with the Golgi-DsRed signal is not as convincing as that obtained for ZP1 (Figure 3.14). Several possible explanations for this discrepancy exist and include (i) un-optimized expression of the Golgi-DsRed fusion protein; (ii) ZP3 localizes to the Golgi but is compartmentalized in a region where the fusion protein is not expressed; and (iii) some other organelle sequesters ZP3. Although further experiments are required to address this issue properly, we presume that options i and ii are most likely and that ZP3 resides in the Golgi or a Golgi associated compartment of COS-7 cells.

Biological Imaging Studies II: Detection of Endogenous Zn(II). Treating cultured cells with Zn(II)/pyrithione provides a means to test sensors in vivo, but has little physiological or pathological relevance. Once studies such as these are employed to ascertain the details of sensor distribution and Zn(II) response, the next step is to determine whether endogenous Zn(II) pools can be visualized. Several models for endogenous Zn(II) detection exist, two of which are considered here. First, cultured cells or neurons can be treated with a reagent that stimulates Zn(II) release from native stores. One way to accomplish this feat is to induce nitrosative stress by treatment with an NO donor. NO-induced Zn(II) release from proteins such as metallothionein and matrix metalloproteases is a well-documented phenomenon.[41-46] Following control studies in the solution phase, which showed that the NO donor S-nitrocysteine (SNOC) did not alter the emission of free ZP3 or interfere with the Zn(II)-induced fluorescence response, we treated both HEK (non-neuronal) and dentate gyrus (neuronal) cells with ZP3 and SNOC. Confocal fluorescence microscopy revealed intracellular fluorescence enhancement within 5 min of SNOC treatment in both cell types (Figure 3.15). The fluorescence rise was reversed with TPEN, which attributes it to Zn(II) detection.

The second model we consider is the hippocampal slice. Certain substructures of the mammalian hippocampus contain high concentrations of histochemically observable Zn(II). We therefore treated acute hippocampal slices from adult female Spraque-Dawley rats with 10 μM ZP3 (10 min, T = 37 °C, 5% CO_2). Confocal imaging revealed intense fluorescence in the dentate gyrus and CA3 regions (Figure 3.16) and optical z-sectioning confirmed that the sensor penetrated the slice under these conditions. Illumination of the DG and CA3 regions was eliminated following TPEN treatment, which confirms that the signal comes from endogenous Zn(II) and not a high local concentration of sensor.

Summary and Perspectives

This chapter details the characterization and biological application of halogenated ZP sensors and several important insights have been gained from these investigations. Photophysical studies indicate that fluorescein halogenation is a viable route for varying excitation and emission wavelengths over an ~35 nm range and to reduce ZP1 background fluorescence by ~2.5-fold at pH 7. The pH emission profiles of bottom ring halogenated ZP show that protonation of both tertiary amine ligands influence sensor emission in a step-wise manner. Metal binding studies revealed anticipated behavior in solution. More dramatic alterations to the ZP platform are required to achieve greater dynamic range, improved Zn(II) selectivity and varied Zn(II) affinity. The studies presented in forthcoming chapters address these needs.

From the perspective of biological applications, ZP3 and presumably its derivatives hold great promise. ZP3 can detect mobile zinc in a number of different cells types, including primary neuronal cultures, and in tissue samples. One immediate question to address is the generality of ZP3 subcellular compartmentalization and, in addition, the mechanism by which the probe is sequestered in the Golgi of certain cell types. As mentioned above, the range of excitation and emission wavelengths provided by the

halogenated probes, although modest, can be exploited for dual fluorophore imaging experiments. Lastly, the ZP probes described in this work all provide tight ($K_d < 1$ nM) and essentially irreversible (vide infra) Zn(II) binding. The former characteristic will be beneficial if very low concentrations of Zn(II) are released during a given signaling event, but may become a limitation in situations where Zn(II) flux is high. For this reason, it is necessary to conduct parallel experiments with intensity-based sensors of varying affinity to gauge relative Zn(II) concentrations. Further work in this arena is greatly needed.

References

(1)   Huang, E. P. *Proc. Nat. Acad. Sci. USA* **1997**, *94*, 13386-13387.

(2)   Li, Y.; Hough, C. J.; Suh, S. W.; Sarvey, J. M.; Frederickon *J. Neurophysiol.* **2001**, *86*, 2597-2604.

(3)   Li, Y. V.; Hough, C. J.; Sarvey, J. M. *Science STKE* **2003**, pe 19.

(4)   Maret, W. *BioMetals* **2001**, *14*, 187-190.

(5)   Takeda, A. *Biometals* **2001**, *14*, 343-351.

(6)   Redenti, S.; Chappell, R. L. *Vision Research* **2005**, *45*, 3520-3525.

(7)   Vogt, K.; Mellor, J.; Tong, G.; Nicoli, R. *Neuron* **2000**, *26*, 187-196.

(8)   Frederickson, C. J.; Bush, A. I. *Biometals* **2001**, *14*, 353-366.

(9)   Henshall, S. M.; et. al. *Oncogene* **2003**, *22*, 6005-6012.

(10) Suh, S. W.; Jensen, K. B.; Jensen, M. S.; Silva, D. S.; Kesslak, P. J.; Danscher, G.; Frederickson, C. J. *Brain Res.* **2000**, *852*, 274-278.

(11) Troung-Tran, A. Q.; Carter, J.; Ruffin, R. E.; Zalewski, P. D. *Biometals* **2001**, *14*, 315-330.

(12) Frederickson, C. J.; Maret, W.; Cuajungco, M. P. *The Neuroscientist* **2004**, *10*, 18-25.

(13) Kay, A. R. *J. Neurosci.* **2003**, *23*, 6847-6855.

(14) Kay, A. R. *Trends Neurosci.* **2006**, *29*, 200-206.

(15) Kay, A. R.; Toth, K. *J. Neurophysiol.* **2006**, *95*, 1949-1956.

(16) Burdette, S. C.; Walkup, G. K.; Springler, B.; Tsien, R. Y.; Lippard, S. J. *J. Am. Chem. Soc.* **2001**, *123*, 7831-7841.

(17) Frederickson, C. J.; Lippard, S. J. *Unpublished results.*

(18) Walkup, G. K.; Burdette, S. C.; Lippard, S. J.; Tsien, R. Y. *J. Am. Chem. Soc.* **2000**, *122*, 5644-5645.

(19) Chang, C. J.; Nolan, E. M.; Jaworski, J.; Burdette, S. C.; Sheng, M.; Lippard, S. J. *Chem. Biol.* **2004**, *11*, 203-210.

(20) · *SMART: Software for the CCD Detector System*, version 5.626; Bruker AXS: Madison, WI, 2000.

(21) Kuzelka, J.; Mukhopadhyay, S.; Spingler, B.; Lippard, S. J. *Inorg. Chem.* **2004**, *43*, 1751-1761.

(22) *SAINTPLUS: Software for the CCD Detector System*, version 5.01; Bruker AXS: Madison, WI, 1998.

(23) *SHELXTL: Program Library for Structure Solution and Molecular Graphics*, version 6.1; Bruker AXS: Madison, WI, 2001.

(24) Sheldrick, G. M. *SADABS: Area-Detector Absorption Correction;* University of Gottingen, Gottingen, Germany, 2001.

(25) Spek, A. L. *PLATON, A Multipurpose Crystallographic Tool*, Utrecht University: Utrecht, The Netherlands, 2000.

(26) Kroncke, K.-D.; Kolb-Bachofen, V. *Methods Enzymol.* **1999**, *301*, 126-135.

(27) Li, Z.; Okamoto, K.-I.; Hayashi, Y.; Sheng, M. *Cell* **2004**, *119*, 873-887.

(28) Brewer, G. J.; Toricelli, J. R.; Evege, E. K.; Price, P. J. *J. Neurosci. Res.* **1993**, *35*, 567.

(29) Figiel, J.; Kaczmarek, L. *Neurochem. Int.* **1997**, *31*, 299-240.

(30) Qian, W.-J.; Ge, K. R.; Kennedy, R. T. *Anal. Chem.* **2003**, *75*, 3468-3475.

(31)   de Silva, A. P.; Gunaratne, H. Q. N.; Gunnlaugsson, T.; Huxley, A. J. M.; McCoy, C. P.;

         Rademacher, J. T.; Rice, T. E. *Chem. Rev.* **1997**, *97*, 1515-1566.

(32)   Burdette, S. C.; Frederickson, C. J.; Bu, W.; Lippard, S. J. *J. Am. Chem. Soc.* **2003**, *125*, 1778-1787.

(33)   So, P. T. C. *Personal communication.*

(34)   Woodroofe, C. C.; Masalha, R.; Barnes, K. R.; Frederickson, C. J.; Lippard, S. J. *Chem. Biol.* **2004**, *11*,

         1659-1666.

(35)   Sjoback, R.; Nygren, J.; Kubista, M. *Spectrochim. Acta. Part A* **1995**, *51*, L7-L21.

(36)   Leonhardt, H.; Gordon, L.; Livingston, R. *J. Phys. Chem.* **1971**, *75*, 245-249.

(37)   Gee, K. R.; Poot, H.; Klaubert, D. H.; Sun, W.-C.; Haligland, R. P.; Mao, F. *J. Org. Chem.* **1997**, *62*,

         6469-6475.

(38)   Hirano, T.; Kikuchi, K.; Urano, Y.; Nagano, T. *J. Am. Chem. Soc.* **2002**, *124*, 6555-6562.

(39)   Mosmann, T. *J. Immunol. Meth.* **1983**, *65*, 55-63.

(40)   Doose, C. A.; Ranke, J.; Stock, F.; Bottin-Weber, U.; Jastorff, B. *Green Chem.* **2004**, *6*, 259-266.

(41)   Gu, Z.; Kaul, M.; Yan, B.; Kridel, S. J.; Jiankun, C.; Strongin, A.; Smith, J. W.; Liddington, R. C.;

         Lipton, S. A. *Science* **2002**, *297*, 1186-1190.

(42)   Spahl, D. U.; Berendji-Grun, D.; Suschek, C. V.; Kolb-Bachofen, V.; Kroncke, K.-D. *Proc. Natl.*

         Acad. Sci. USA **2003**, *100*, 13952-13957.

(43)   Pearce, L. L.; Gandley, R. E.; Han, W.; Wasserloos, K.; Stitt, M.; Kanai, A. J.; McLaughlin, M. K.;

         Pitt, B. R.; Levitan, E. S. *Proc. Natl. Acad. Sci. USA* **2000**, *97*, 477-482.

(44)   Cuajungco, M. P.; Lees, G. J. *Brain Res.* **1998**, *799*, 118-129.

(45)   Berendji, D.; Kolb-Bachofen, V.; Meyer, K. L.; Grapenthin, O.; Weber, H.; Wahn, V.; Kroncke, K.-

         D. *FEBS Lett.* **1997**, *405*, 37-41.

(46)   Chen, Y.; Ire, Y.; Keung, W. M.; Maret, W. *Biochemistry* **2002**, *41*, 8360-8367.

(47)   Brannon, J. H.; Madge, D. *J. Phys. Chem.* **1978**, *82*, 705-709.

Table 3.1. Summary of X-ray Crystallographic Data

	ZPCl1·2CH$_3$OH
Empirical Formula	C$_{48}$H$_{40}$Cl$_6$N$_6$O$_7$
Formula Weight	1025.56
Space Group	Pnma
a, Å	19.456(4)
b, Å	26.015(5)
c, Å	9.121(2)
V, Å^3	4616.8(16)
Z	4
ρ_{calc}, g/cm^3	1.475
T, °C	-100
μ(Mo Kα), mm^{-1}	0.432
Crystal size, (mm^3)	0.20 x 0.15 x 0.06
θ limits, deg	2.09 – 28.36
total no. of data	39487
no. of unique data	5721
no. of params	328
Goodness-of-fit on F^2	1.062
Final R incides [I>2σ(I)][a,b]	R = 0.0469; wR^2 = 0.1012
R indices (all data)[a,b]	R = 0.0636; wR^2 = 0.1076
max, min peaks, e/Å^3	0.551, -0.259

[a] $R = \Sigma \mid \mid F_o \mid - F_c \mid \mid / \Sigma \mid F_o \mid$

[b] wR$^2 = \{ \Sigma \ [w(F_o^2 - F_c^2)^2] / \Sigma \ [w(F_o^2)^2] \}^{1/2}$

Table 3.2. Selected Bond Lengths (Å) and Angles for ZPCl1

Bond Lengths	(Å)	Bond Angles	(Deg)
O(1)—C(16)	1.344(2)	C(14)—O(2)—C(14A)	119.21(19)
O(2)—C(14)	1.3795(19)	C(20)—O(3)—C(23)	112.76(17)
O(3)—C(20)	1.469(3)	O(4)—C(23)—O(3)	121.5(2)
O(3)—C(23)	1.3609(3)	N(3)—C(8)—C(7)	117.78(17)
O(4)—C(23)	1.194(3)	C(7)—N(2)—C(13)	110.26(14)
Cl(1)—C(24)	1.724(2)	N(2)—C(13)—C(15)	110.60(14)
Cl(2)—C(17)	1.7343(18)	O(1)—C(16)—C(17)	117.20(16)
N(2)—C(13)	1.467(2)	Cl(2)—C(17)—C(16)	119.03(14)
N(2)—C(6)	1.459(2)		
N(2)—C(7)	1.477(2)		
N(3)—C(8)	1.333(2)		

Table 3.3. Spectroscopic and Thermodynamic Data for Symmetrical ZP Sensors[a]

	Absorption λ (nm), ε x 10^4 ($M^{-1}cm^{-1}$)		Emission λ (nm), Φ [b]		pK_a[c]	pK_a[c]	pK_a[c]	K_d (nM)
	Unbound	Zn(II)	Unbound	Zn(II)				
ZP1[d]	515, 7.9	507, 8.4	531, 0.38	527, 0.87	8.4	n.o.	2.8	0.7±0.1
ZP2	498, 4.4	490, 5.3	522, 0.25	517, 0.92	9.4	n.o.	3.9	0.5±0.1
ZP3	502, 7.5	492, 8.5	521, 0.15	516, 0.92	6.8	n.o.	2.0	0.7±0.1
ZPF1	533, 9.9	525, 12.0	547, 0.11	544, 0.55	6.9	4.2	1.8	0.9±0.1
ZPCl1	534, 9.7	527, 12.0	550, 0.22	549, 0.50	7.0	4.3	1.9	0.9±0.1
ZPBr1	534, 4.5	528, 8.6	549, 0.25	547, 0.36	7.3	4.5	2.1	1.1±0.1
ZPF3	520, 8.7	510, 9.3	537, 0.14	533, 0.60	6.7	4.0	1.9	0.8±0.1

[a] Measurements were performed at pH 7 in 50 mM PIPES, 100 mM KCl buffer. Data for ZP1 and ZP2 were taken from ref. 17. [b] Fluorescein (Φ = 0.95 in 0.1 N NaOH, ref. 47) was used as the standard for quantum yield measurements. [c] The first column of pK_a values are those of the nitrogen atom responsible for PET switching in the probes. The pK_a values in the second column correspond to the second tertiary amine protonation event, which is not observed (n.o.) for ZP1, ZP2 and ZP3. The pK_a values in the third column correspond to protonation of the phenol group. [d] See Scheme 4.1 for nomenclature.

Table 3.4. Cytotoxicity Data for ZP Treated HeLa Cells

	% Cell Survival			$IC_{50}{}^{a}$ (μM)
	1 μM	5 μM	10 μM	
ZP1	96 ± 2	68 ± 5	40 ± 6	2.3 ± 0.5
ZP3	93 ± 4	73 ± 8	57 ± 13	4.3 ± 0.8
ZPF1	96 ± 8	70 ± 15	47 ± 18	3.0 ± 0.6

^{a} The concentration of sensor that gives 50% cell death.
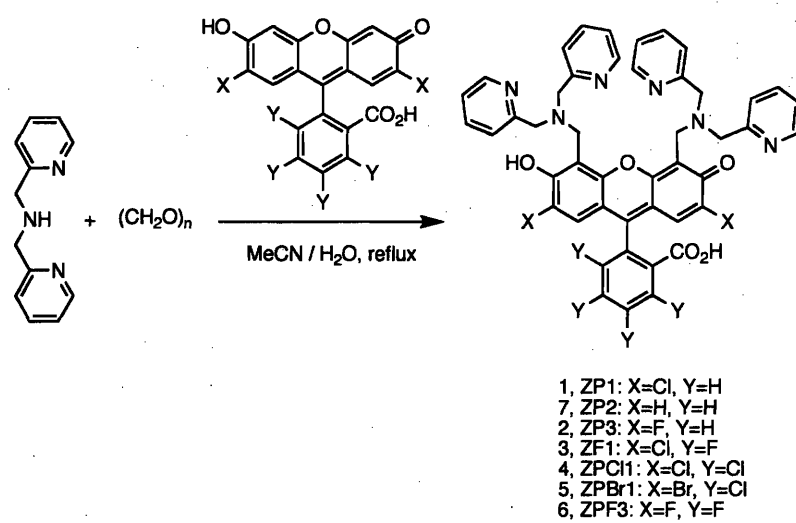
Scheme 3.1. Synthesis of halogenated ZP sensors **2-6**.
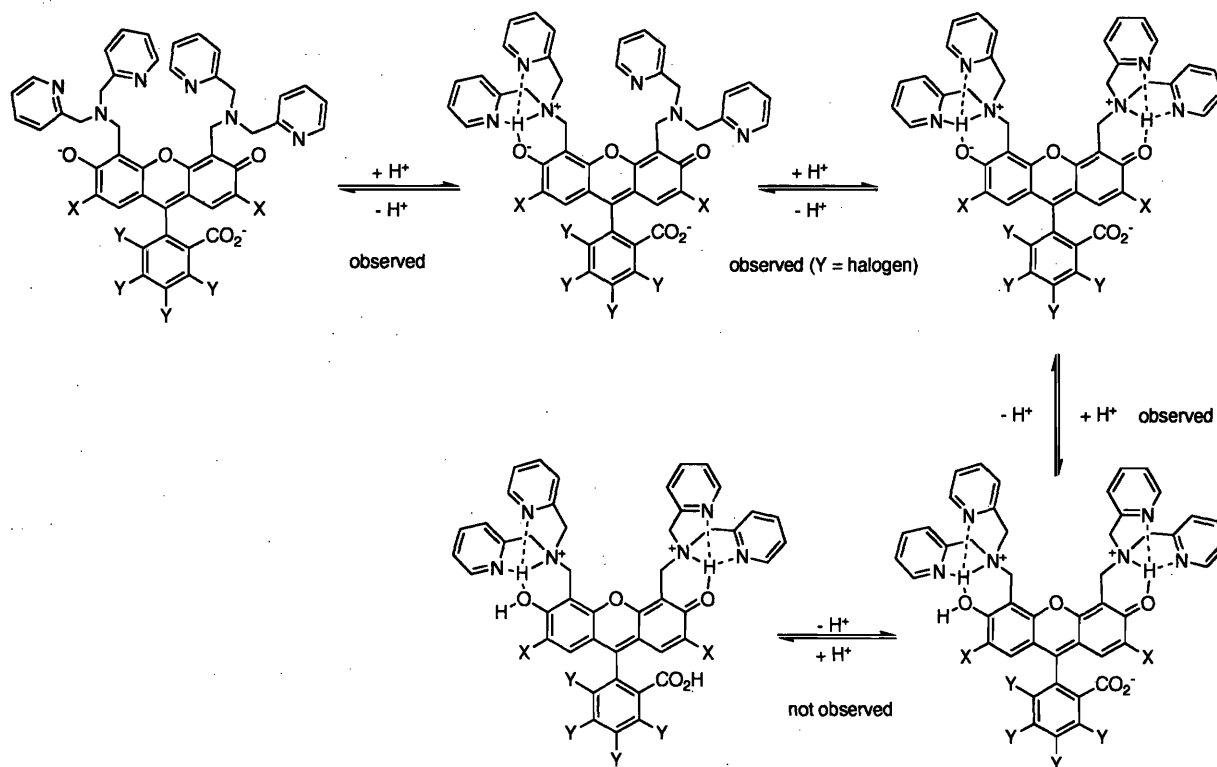
Scheme 3.2. Proposed protonation equilibria for symmetrical ZP probes based on fluorescence and UV-visible studies. Protonation of the carboxylate presumably occurs at pH < 2 and therefore was not observed in the experiments.
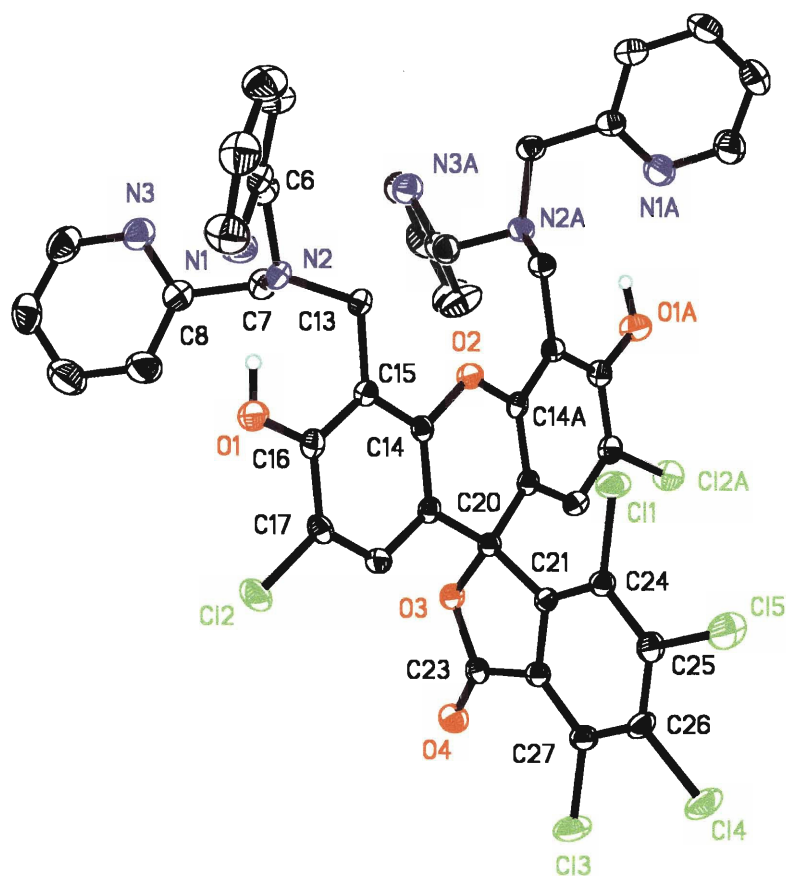
Figure 3.1. ORTEP diagram of ZPCl1 showing 50% probability thermal ellipsoids on all non-hydrogen atoms.
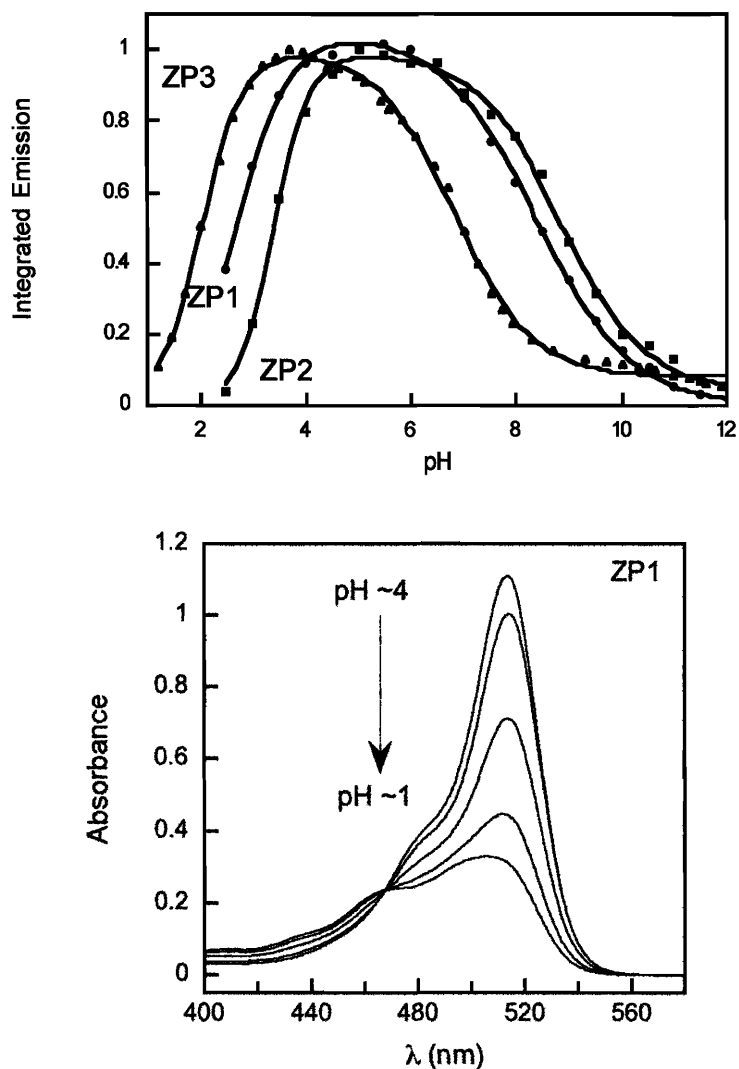
Figure 3.2. Top: Effect of pH on the fluorescence emission of ZP1 (circles), ZP2 (squares) and ZP3 (triangles). The concentration of ZP was 1 μM and the titrations were performed in 100 mM KCl (T = 25 °C). Protonation constants generated from the fits are given in Table 3.3. Bottom: Effect of pH on the optical absorption profile of ZP (100 mM KCl, T = 25 °C).
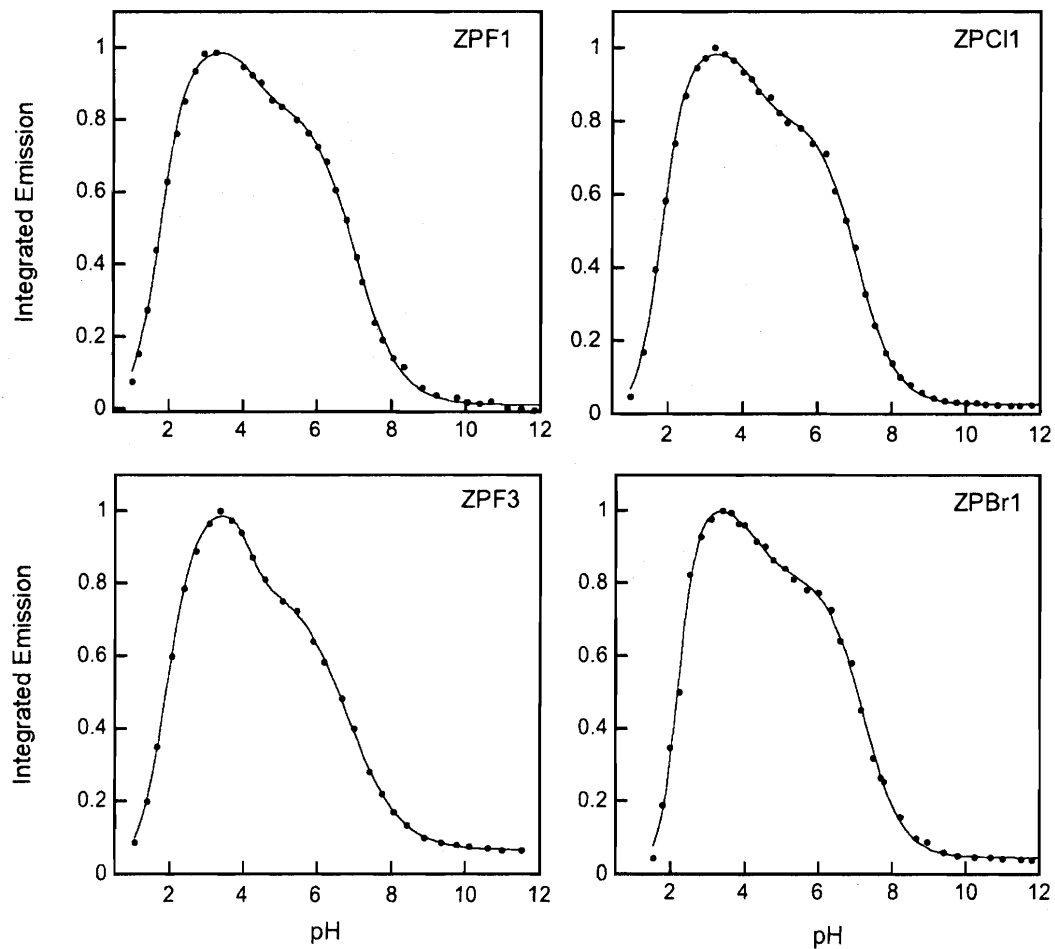
Figure 3.3. Representative plots of integrated emission vs. pH for benzoate halogenated ZPF1, ZPF3, ZPCl1 and ZPBr1. Titrations were conducted with 1 μM ZP (100 mM KCl, T = 25 °C). Derived protonation constants are given in Table 3.3.
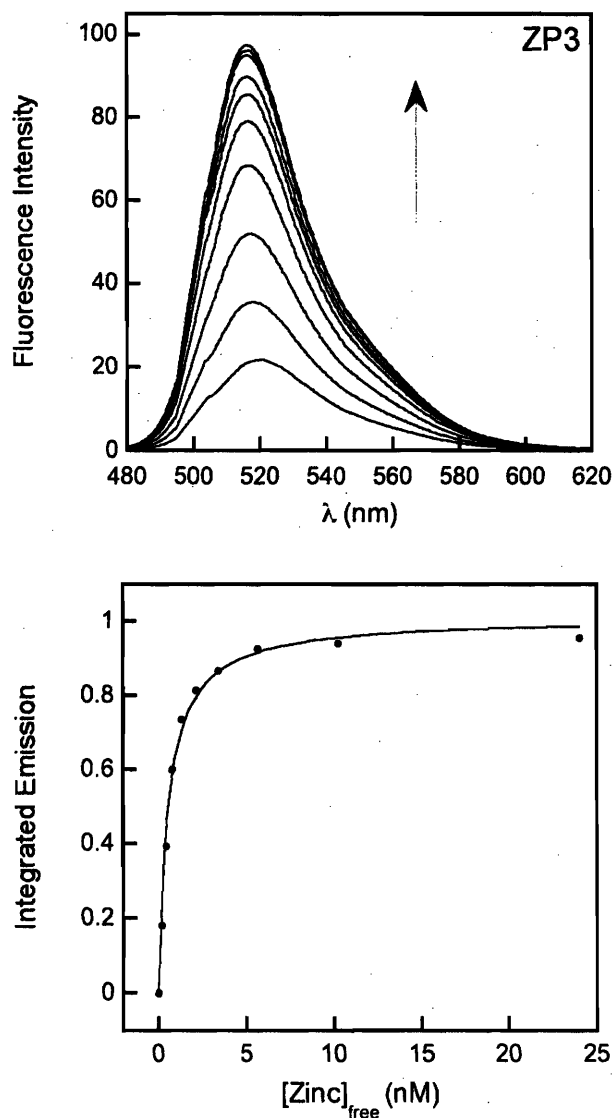
Figure 3.4. Fluorescence response of 500 nM ZP3 to solutions of Zn(II) buffered in the nM range (50 mM PIPES, 100 mM KCl, pH 7). Top: The emission spectra shown are for free Zn(II) concentrations buffered at 0.0, 0.17, 0.42, 0.79, 1.3, 2.1, 3.4, 5.6, 10.2 and 24 nM. Bottom: Integrated emission versus the free Zn(II) concentration corresponding to the emission spectra in the top panel. Excitation was provided at 490 nm and T = 25 °C. Calculated dissociation constants are given in Table 3.3.
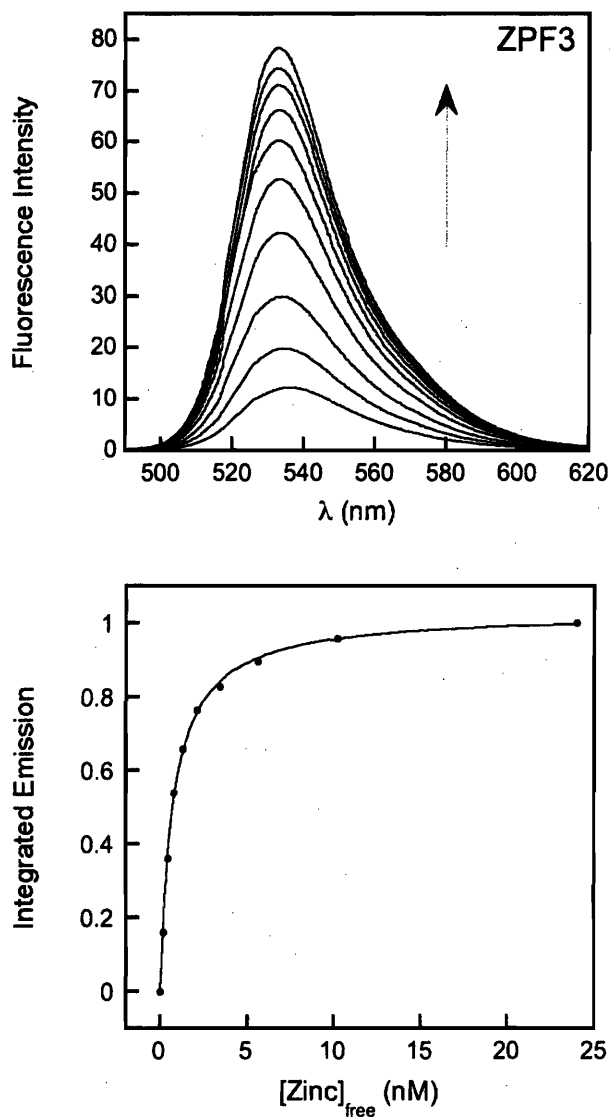
Figure 3.5. Fluorescence response of 500 nM ZPF3 to solutions of Zn(II) buffered in the nM range (50 mM PIPES, 100 mM KCl, pH 7). Top: The emission spectra shown are for free Zn(II) concentrations buffered at 0.0, 0.17, 0.42, 0.79, 1.3, 2.1, 3.4, 5.6, 10.2 and 24 nM. Bottom: Integrated emission versus the free Zn(II) concentration corresponding to the emission spectra in the top panel. Excitation was provided at 510 nm and T = 25 °C. Calculated dissociation constants are given in Table 3.3.
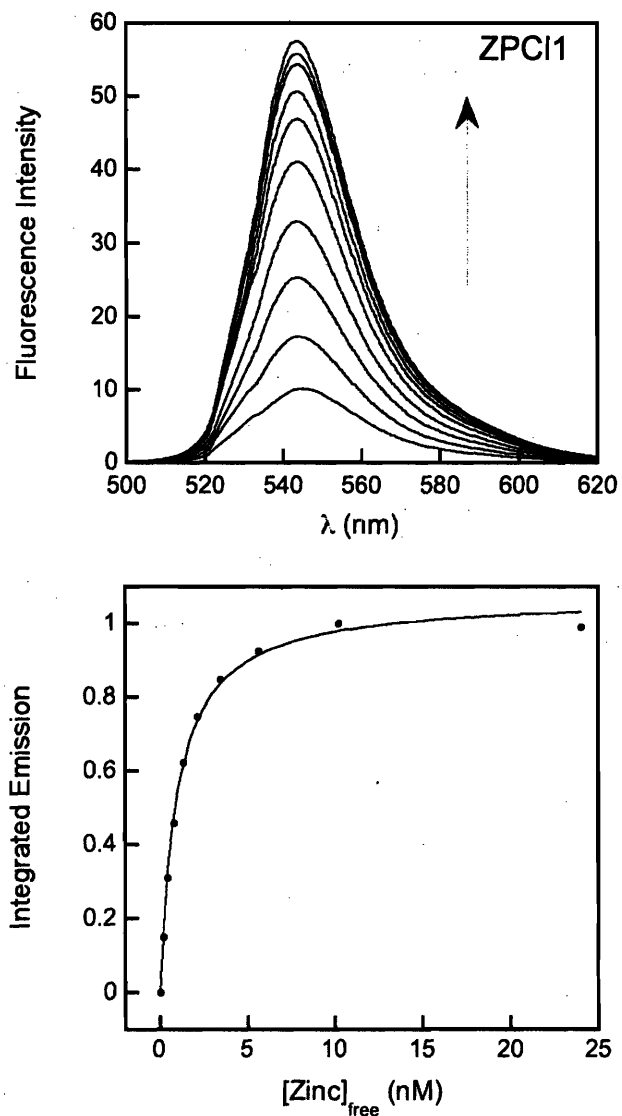
Figure 3.6. Fluorescence response of 500 nM ZPCl1 to solutions of Zn(II) buffered in the nM range (50 mM PIPES, 100 mM KCl, pH 7). Top: The emission spectra shown are for free Zn(II) concentrations buffered at 0.0, 0.17, 0.42, 0.79, 1.3, 2.1, 3.4, 5.6, 10.2 and 24 nM. Bottom: Integrated emission versus the free Zn(II) concentration corresponding to the emission spectra in the top panel. Excitation was provided at 527 nm and T = 25 °C. Calculated dissociation constants are given in Table 3.3.
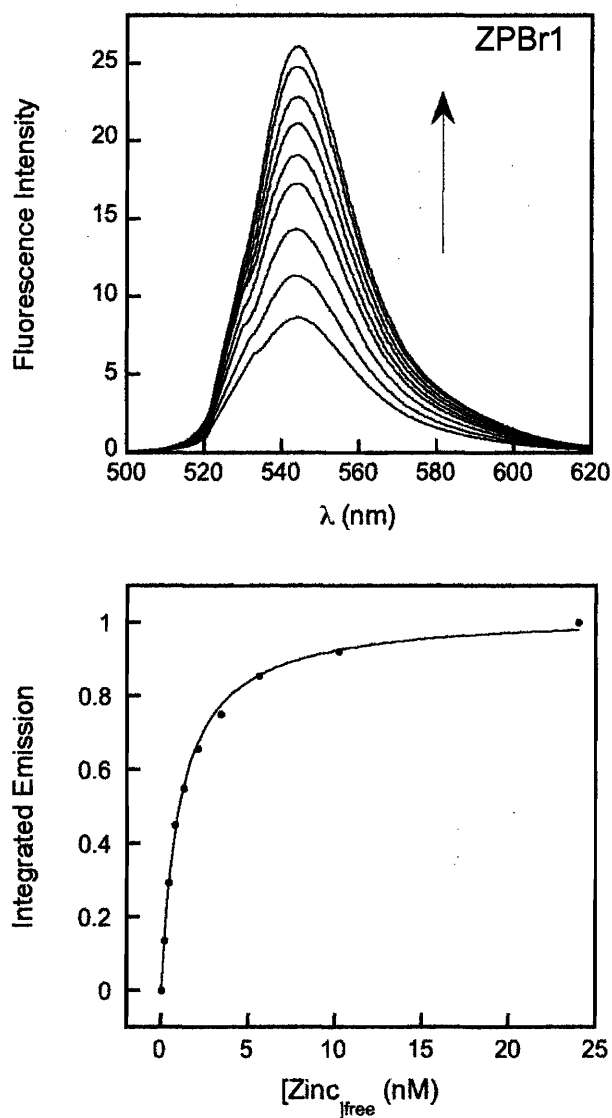
Figure 3.7. Fluorescence response of 500 nM ZPBr1 to solutions of Zn(II) buffered in the nM range (50 mM PIPES, 100 mM KCl, pH 7). Top: The emission spectra shown are for free Zn(II) concentrations buffered at 0.0, 0.17, 0.42, 0.79, 1.3, 2.1, 3.4, 5.6, 10.2 and 24 nM. Bottom: Integrated emission versus the free Zn(II) concentration corresponding to the emission spectra in the top panel. Excitation was provided at 527 nm and T = 25 °C. Calculated dissociation constants are given in Table 3.3.
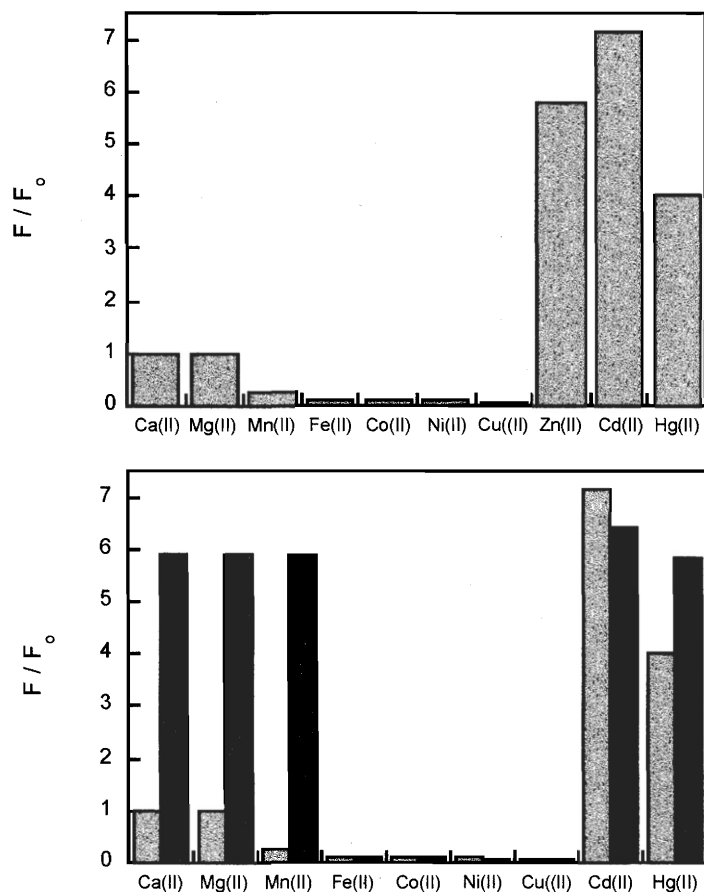
Figure 3.8. Selectivity of ZP3 for Zn(II) over other cations. Top plot: The bars indicate the fluorescence change that occurs upon addition of 50 equiv of each cation to a 1 μM solution of ZP3 (50 mM PIPES, 100 mM KCl, pH 7). Bottom plot: The light grey bars correspond to the bars in the top plot. The dark grey bars depict the fluorescence change that occurs after 50 equiv of Zn(II) is added to the solution of ZP3 and the cation of interest. Excitation was provided at 490 nm and T = 25 °C. All data is normalized with respect to the emission of the free dye (F_o).

ntr ZP1 ZP3 ZPF1
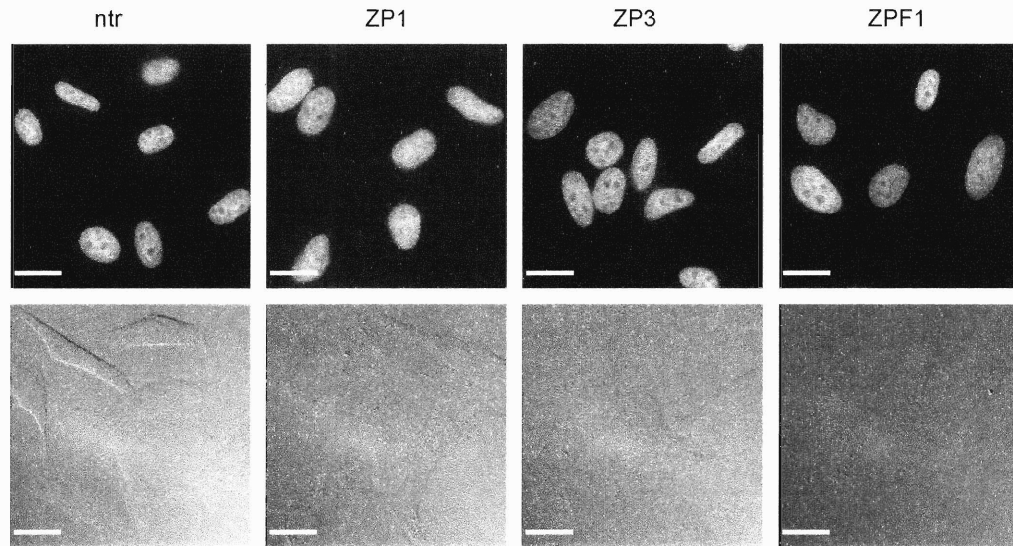
Figure 3.9. Representative epifluorescence (top panels) and DIC (bottom panels) images of HeLa cells treated with 10 μM ZP for 24 h, fixed and stained with Hoescht. The scale bars represent 25 μm.
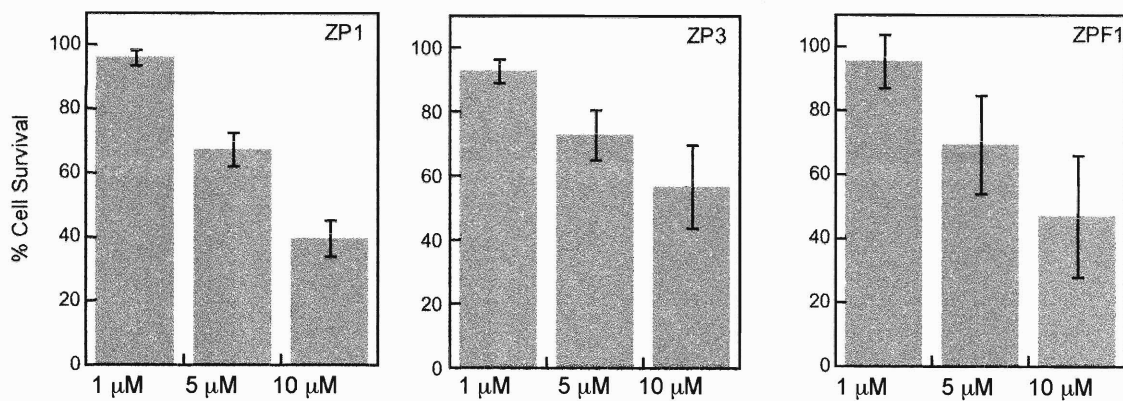
Figure 3.10. Cytotoxicity of selected ZP probes to HeLa cells following 24 h treatment as quantified by the MTT assay. These data represent the averages of three independent trials. Data are given in Table 3.4.
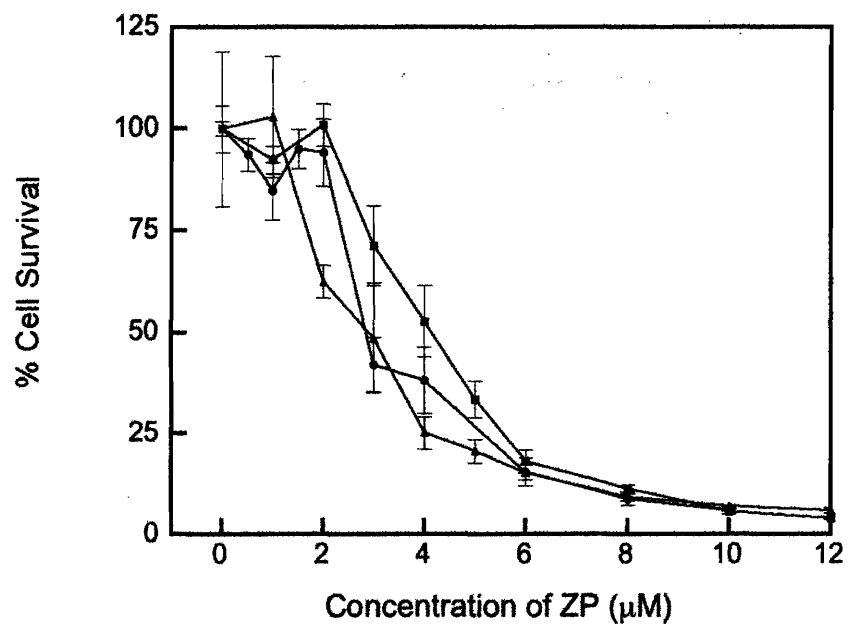
Figure 3.11. Representative kill curves for HeLa cells treated with ZP1 (circles), ZP3 (squares) and ZPF1 (triangles). Cell survival was quantified by the MTT assay and IC_{50} values are given in Table 3.4.
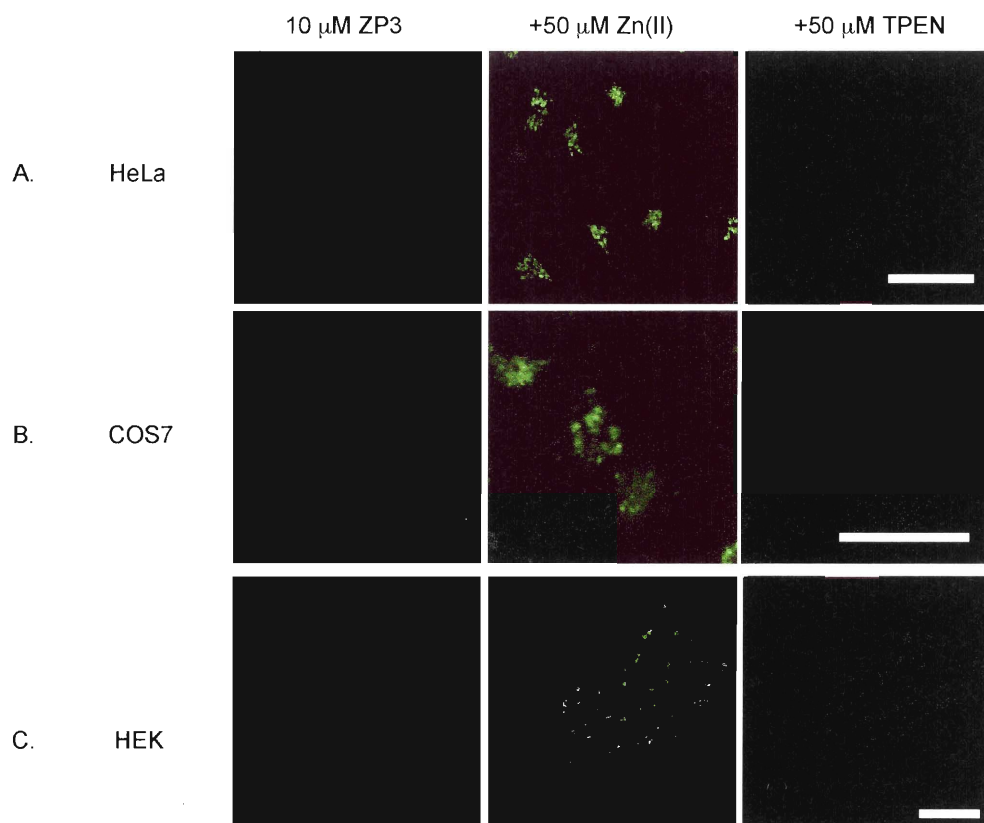
Figure 3.12. Response of ZP3 to exogenously added Zn(II) in cultured HeLa, COS-7 and HEK cells. The left panels are confocal images of cells treated with 10 μM ZP3 for 30 min (T = 37 °C, 5% CO_2) and washed with DMEM before imaging. The middle panels exhibit the fluorescence response 5 min after 50 μM Zn(II)/pyrithione (1:1 or 1:2 ratio) was added to the imaging dish. The right panels show the fluorescence decrease that occurs upon addition of the cell permeable metal ion chelator TPEN, which attributes the fluorescence rise to Zn(II) coordination. The COS-7 cells are substantially larger in the images than the HeLa and HEK cells because greater electronic zoom was employed during the imaging experiment. The scale bars represent 50 μm.
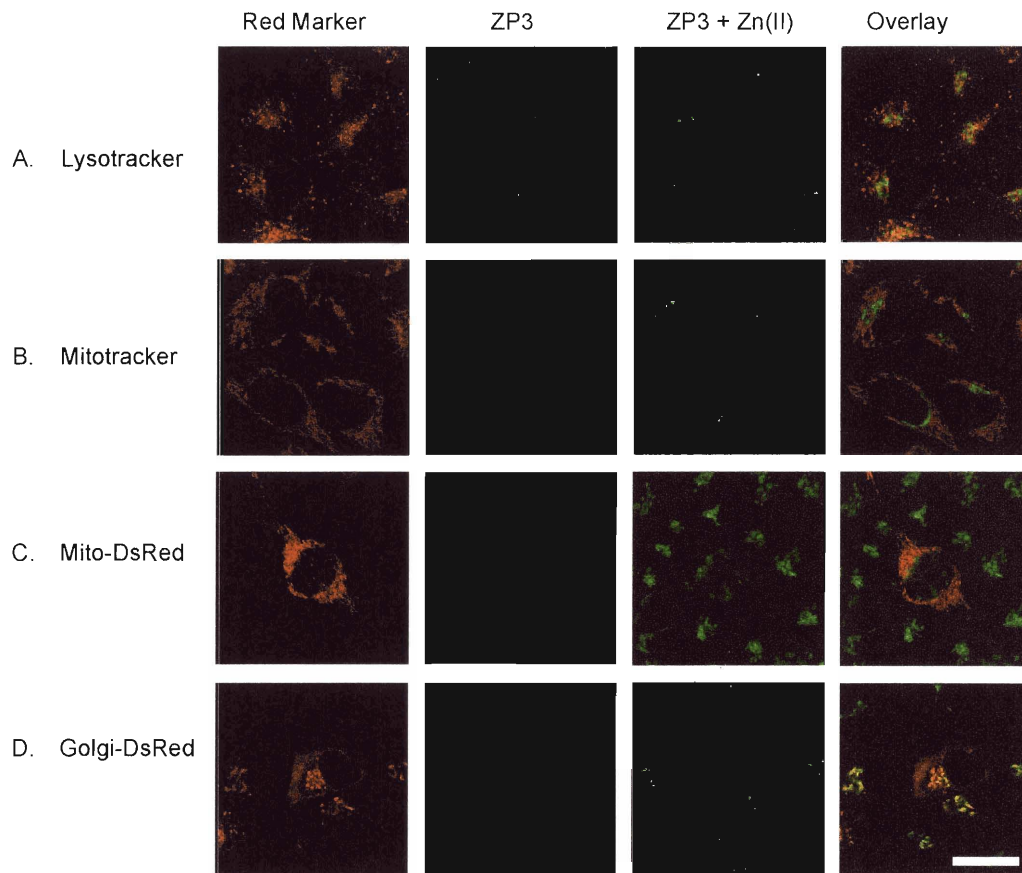
Figure 3.13. Colocalization studies in cultured HeLa cells. HeLa cells were treated or transfected with a red emitting organelle marker and with 10 μM ZP3. The images in the third column were obtained after the cells were treated with 50 μM Zn(II)/pyrithione (1:2 ratio) for 5 min. The images in the right-hand column show the overlay between the red organelle marker and the ZP3+Zn(II) signal. Addition of Zn(II)/pyrithione causes no alteration in dye localization over the period of this experiment. No colocalization is observed with the lysosomal and mitochondrial markers. Good colocalization is observed with ZP3 and the Golgi marker. The red circle in the Golgi image resulted form overexpression of Golgi-DsRed in that particular cell. The scale bar represents 25 μm for all images.
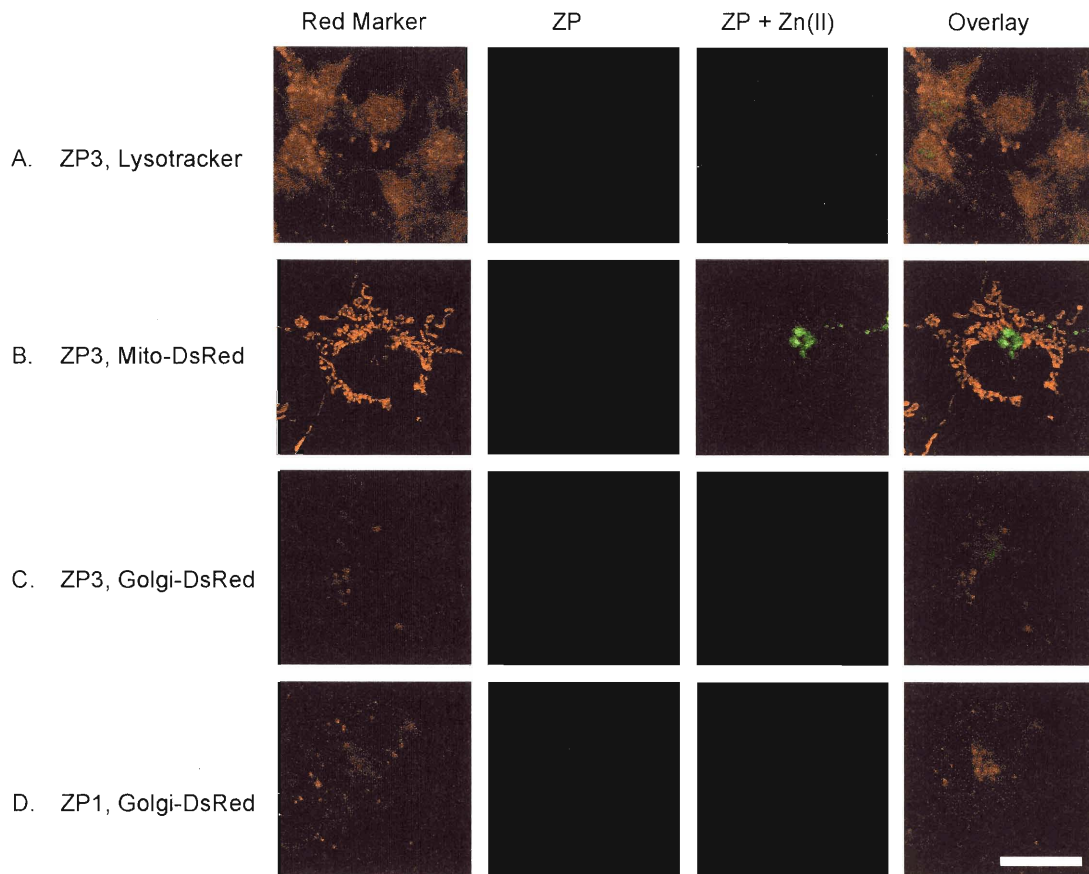
Figure 3.14. Colocalization studies in cultured COS-7 cells. COS-7 cells were treated or transfected with a red emitting organelle label and with 10 μM ZP3 or ZP1 (bottom panels) The images in the third column were obtained after the cells were treated with 50 μM Zn(II)/pyrithione (1:1 ratio) for 5 min. The images in the right-hand column show the overlay between the red organelle marker and the ZP3+Zn(II) signal. Addition of Zn(II)/pyrithione causes no alteration in dye localization over the period of this experiment. The scale bar represents 25 μm for all images.

| 10 μM ZP3 | +SNOC, 5 min | +TPEN, 5 min |

A. HEK Cells

B. Dentate Gyrus Neurons
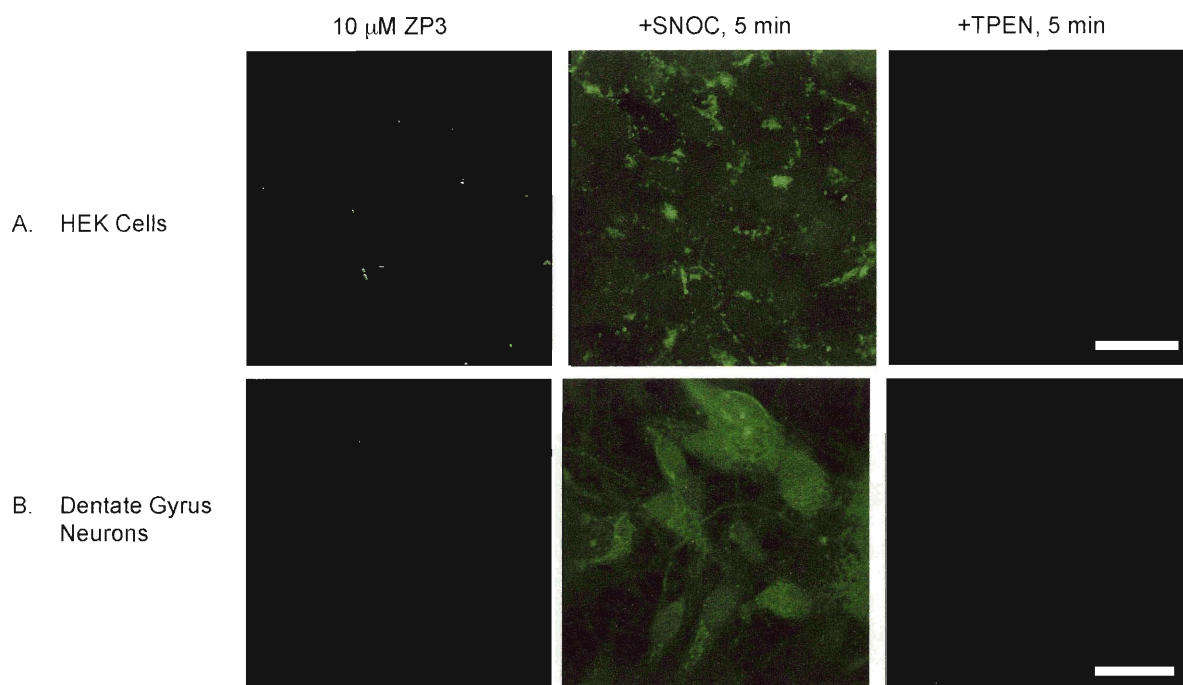
Figure 3.15. Imaging endogenous Zn(II) release in cultured HEK (top panels) cells and in primary dentate gyrus neuronal cultures with ZP3. Left panels: the cells were treated with 10 μM ZP3 and imaged. Middle panels: Fluorescence response 5 min after treatment with ~1 M SNOC. Right panels: Diminution of the fluorescence signal following TPEN addition.
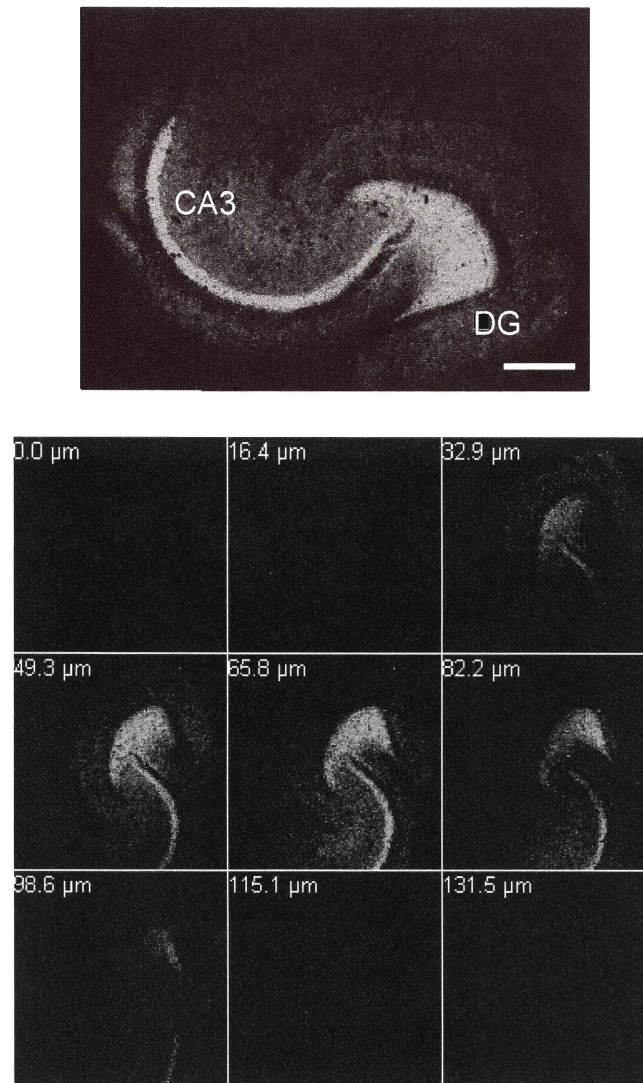
Figure 3.16. ZP3 staining of an acute hippocampal slice from an adult female Sprague-Dawley rat. The slice was prepared, washed with Zn(II)-free Kreb's ringer buffer, treated with 10 µM ZP3 for 10 min (T = 37 °C, 5% CO_2) and washed with Zn(II)-free Kreb's ringer buffer before imaging. ZP3 illuminates the DG to CA3 neuronal circuit. The bottom panels are the optical z-sections that correspond to the top image. These sections show that ZP3 penetrated the tissue. The CA3 region is not observed in the optical z-sections because the top image is comprised of two merged images, which is necessary since the entire hippocampus could not be imaged at 10x magnification. The scale bar indicates 0.5 mm.

Chapter 4

Zinc Sensors Based on Monosubstituted Fluorescein Platforms II:

Modulation of Zinc Affinity and Biological Applications

Introduction

Many factors determine the performance of small molecule sensors in vivo, including spectroscopic properties, sensitivity and selectivity for the analyte of interest, affinity for other species in the biological milieu, and behavior and localization within cells or tissues. Some of these features, such as emission profiles and binding affinity, are relatively easy to control, whereas those pertaining to performance in a given biological sample often cannot be readily anticipated prior to a first series of experiments. The work described in this chapter focuses on several of these issues in the context of Zn(II) sensor design and biological application.

In particular, we consider systematic alteration of the ZP4 sensor platform by exploring the effects of ligand variations on the spectroscopic and metal-binding properties of asymmetrical ZP sensors. We modified ZP4 by substituting one pyridyl moiety in the metal-binding unit with either pyrrole or N-methylpyrrole. The resulting sensors, ZP9, **1**, and ZP10, **2**, are shown in Scheme 4.1. Our specific aims here were three-fold. Firstly, we were interested to explore the effect of the pyridyl/pyrrole substitution on the fluorescence properties of the free and Zn(II)-bound sensors. This question was, in part, motivated by a study suggesting that groups apparently too distant from a fluorophore for electronic communication can contribute to photoinduced electron transfer (PET) quenching.[1] To address the contribution of the aniline moiety alone, we also prepared and characterized an asymmetrical fluorescein derivatized with aniline, **3**, depicted in Scheme 4.2. Secondly, we considered the Zn(II) binding properties and Zn(II) selectivity of sensors ZP9-10. As discussed in Chapter 1, sensors that span a range of dissociations constants and have high selectivity for Zn(II) are important objectives and, over the past few years, significant efforts have been made to devise Zn(II) sensors with nanomolar to micromolar affinities.[2-8] We anticipated that substitution of a pyridyl group with pyrrole or N-methylpyrrole, both of which are poor bases and weakly or non-coordinating heterocycles at neutral pH, would raise the

dissociation constant relative to sensors containing the di(2-picolyl)amine (DPA) chelate, which confers sub- to low-nanomolar affinity.[9-15] We emphasize that varying the K_d will have invaluable consequences for neurobiological imaging applications since estimated Zn(II) concentrations range from the picomolar to the sub-millimolar in the CNS.[16-18] Lastly, we consider further the utility of aniline-based ZP probes for select biological imaging applications. Based on previous work with ZP4, which revealed that it selectively stains dead or damaged neurons and thereby suggested cell impermeability,[11] we anticipated that ZP9 and ZP10 would also be cell impermeable without modification. Preliminary observations suggested otherwise and an account of our more detailed studies with ZP9 and ZP4 is provided.

Experimental Section

Reagents. Acetonitrile was purged with Ar and dried by passing through columns of Al_2O_3. Anhydrous EtOAc and 1,2-dichloroethane (DCE) were purchased from Aldrich and used as received. In preparation for the syntheses of amines **4** and **5**, ethanol and methanol were dried over $MgSO_4$ before use. N-(2-Pyridylmethyl)-N-(1H-2-pyrrolylmethyl)-amine[19], **4**, and 7'-chloro-4'-fluoresceincarboxaldehyde[14], **6**, were synthesized according to literature procedures. All other reagents were obtained from Aldrich and used as received.

General Methods. Analytical TLC was performed by using Merck F254 silica gel plates, Merck F254 aluminum oxide plates, or octadecyl-functionalized (reverse phase, RP18) plates (0.25 mm thickness). Preparative TLC was performed on reverse plate plates of 1 mm thickness manufactured by EM Science. NMR spectra were obtained on a Varian 300 MHz spectrophotometer operating at ambient probe temperature, 283 K. Both ^1H and ^{13}C NMR spectra were referenced to internal probe standards. An Avatar FTIR instrument was used to obtain IR spectra. High-resolution mass spectrometry was conducted by staff at the MIT Department of Chemistry Instrumentation Facility.

(2-Nitrobenzyl)pyridin-2-ylmethyl-(1*H*-pyrrol-2-ylmethyl)amine (7). Portions of 2-nitrobenzylbromide (533 mg, 2.47 mmol), **4** (502 mg, 2.47 mmol), K_2CO_3 (400 mg, 2.89 mmol) and activated 3 Å molecular sieves were combined in 20 mL of MeCN and stirred vigorously overnight at room temperature. The reaction was filtered through Celite and the solvent removed under reduced pressure to yield a brown-yellow oil. The crude product was flushed through a plug of Al_2CO_3 (5:1 CH_2Cl_2/EtOAc), which afforded a light-yellow solid (730 mg, 91%). TLC R_f = 0.58 (Al_2O_3, 2:1 hexanes/EtOAc); mp = 85-86 °C. ^{1}H NMR (CDCl$_3$, 300 MHz) δ 3.42 (2H, s), 3.68 (2H, s), 4.00 (2H, s) 6.04 (1H, d), 6.19 (1H, m), 6.88 (1H, m), 7.21 (1H, m), 7.33-7.43 (2H, m), 7.44-7.53 (2H, m), 7.54-7.77 (2H, m), 8.56 (1H, dq), 9.98 (1H, br s). ^{13}C NMR (CDCl$_3$, 125 MHz) δ 48.06, 55.69, 58.85, 107.64, 108.52, 117.88, 122.43, 124.50, 124.85, 126.87, 128.16, 131.38, 132.07, 134.25, 136.92, 148.35, 150.34, 158.51. FTIR (KBr, cm^{-1}) 3426 (m), 3198 (w), 3077 (w), 2970 (w), 2920 (m), 1595 (m), 1570 (m), 1528 (s), 1470 (m), 1442 (m), 1431 (m), 1413 (w), 1362 (s), 1300 (w), 1259 (w), 1243 (w), 1231 (w), 1151 (w), 1132 (w), 1114 (m), 1103 (m), 1079 (w), 1051 (w), 1029 (w), 1001 (w), 991 (m), 967 (w), 952 (w), 884 (m), 865 (w), 811 (m), 782 (m), 768 (m), 732 (s), 676 (s), 632 (w), 610 (w). HRMS (ESI): Calcd $[M + Na]^+$, 345.1322; Found, 345.1338.

2-{[Pyridin-2-ylmethyl-(1*H*-pyrrol-2-ylmethyl)amino]methyl}phenylamine (8). A flask containing Pd/C (10% activated, 180 mg) was purged with Ar and 10 mL of MeOH was added. A portion (101 mg, 0.313 mmol) of **7** dissolved in 15 mL MeOH was added and a balloon filled with H_2 attached. The reaction was stirred vigorously under H_2 for 2.5 h, purged with Ar, filtered through Celite and the solvent removed under reduced pressure. Flash chromatography on Al_2O_3 using a solvent gradient (10:1 to 4:1 CH_2Cl_2/EtOAc with 1% $^iPrNH_2$) yielded the purified product as a brown oil (48 mg, 52%). TLC R_f = 0.43 (Al_2O_3, 2:1 hexanes/EtOAc). ^{1}H NMR (CDCl$_3$, 300 MHz) δ 3.57 (2H, s), 3.69 (2H, s), 3.71 (2H, s), 4.95 (2H, br s), 6.07 (1H, m), 6.18 (1, m), 6.67 (2H, m), 6.85 (1H, m), 7.09 (2H, m), 7.32 (2H, m), 7.69 (1H, td), 8.62 (1H, dq). ^{13}C NMR (CDCl$_3$, 125

MHz) δ 47.92, 58.02, 50.10, 107.77, 108.33, 115.73, 117.48, 117.64, 122.41, 122.57, 124.61, 127.26, 128.47, 130.93, 136.86, 147.05, 148.75, 158.84. FTIR (NaCl disk, cm⁻¹) 3403 (m), 3298 (m), 2092 (w), 3011 (w), 2922 (w), 2832 (m), 1656 (w), 1614 (s), 1592 (s), 1569 (m), 1494 (s), 1475 (m), 1461 (m), 1435 (m), 1405 (w), 1366 (m), 1339 (w), 1315 (w), 1297 (w), 1284 (w), 1261 (w), 1236 (w), 1150 (m), 1091 (m), 1049 (w), 1027 (m), 997 (w), 980 (w), 970 (w), 956 (w), 926 (w), 884 (w), 841 (w), 801 (m), 751 (s), 720 (s), 640 (w), 615 (w), 560 (w), 540 (w), 500 (w). HRMS (ESI) Calcd [M + Na]⁺, 315.1580; Found, 315.1575.

2-{2-Chloro-6-hydroxy-3-oxo-5-[(2-{[pyridin-2-ylmethyl-(1*H*-pyrrol-2-ylmethyl)-amino]-methyl}phenylamino)methyl]-3*H*-xanthen-9-yl}benzoic acid (1, Zinpyr-9, ZP9). Portions of **8** (75 mg, 0.25 mmol) and **6** (72 mg, 0.26 mmol) were combined in 10 mL of EtOAc and stirred overnight at room temperature and the solution turned deep red. The solvent was removed under reduced pressure and the red residue, intermediate **9**, was suspended in 5 mL of DCE. A portion (160 mg, 0.754 mmol) of NaB(OAc)₃H was added and the reaction was stirred at room temperature. The reaction clarified and became light orange over the course of 3 h. Preparative TLC on reverse phase silica gel (6:1 MeOH/0.1 N HCl) yielded the pure product as a red solid (42 mg, 33%). This material can also be purified by preparative TLC on silica gel (20:1 CHCl₃/MeOH). TLC R$_f$ = 0.41 (RP silica, 6:1 MeOH/0.1 N HCl); mp > 325 °C, dec. ¹H NMR (CD₃OD, 300 MHz) δ 3.56-3.67 (6H, m), 4.57 (2H, s), 5.93 (1H, d), 6.63-6.73 (3H, m), 6.81 (1H, s), 6.99-7.24 (5H, m), 7.39 (1H, t), 7.71-7.83 (2H, m), 8.06 (1H, d), 8.26 (1H, d). FTIR (KBr, cm⁻¹) 3418 (s), 2050 (w), 2920 (m), 2850 (m), 1761 (s), 1632 (m), 1606 (s), 1582 (s), 1516 (m), 1490 (m), 1451 (s), 1368 (m), 1282 (s), 1252 (m), 1218 (m), 1149 (s), 1109 (m), 1091 (m), 1080 (m), 1025 (w), 1008 (m), 874 (w), 834 (w), 798 (w), 751 (m), 722 (m), 702 (m), 621 (w), 597 (w), 549 (w), 470 (m). HRMS (ESI): Calcd [M − H]⁻, 669.1910; Found, 669.1902.

(1-Methyl-1*H*-pyrrol-2-ylmethyl)pyridin-2-ylmethylamine (5). *N*-(Methyl)pyrrole-2-carboxaldehyde (2.0 g, 18.3 mmol) was dissolved in 25 mL of EtOH and stirred. A

portion (2.0 g, 18.5 mmol) of 2-(aminomethyl)pyridine was added dropwise with stirring and the reaction was refluxed for 30 min, during which time the solution turned yellow. The reaction was cooled and the solvent removed in vacuo to yield an orange oil. The oil was dissolved in 40 mL of MeOH and the solution was cooled to 0 °C. A portion (770 mg, 20.5 mmol) of $NaBH_4$ was added and the reaction was stirred at 0 °C for 30 min and warmed to room temperature. After stirring for an additional 30 min, the reaction was heated to reflux for 4 h and cooled. The solvent was removed under reduced pressure and the resulting yellow-white residue was dissolved in 20 mL of water, which was extracted with Et_2O (3 x 20 mL). The combined organics were dried over $MgSO_4$ and the solvent was removed in vacuo, which yielded the product as a yellow oil (3.1 g, 82%). TLC R_f = 0.44 (silica, 9:1 $CHCl_3$/MeOH). ^{1}H NMR ($CDCl_3$, 300 MHz) δ 2.15 (1H, br s), 3.65 (3H, s), 3.68 (2H, s), 3.78 (2H, s), 3.94 (2H, s), 6.04 (2H, d), 6.58 (1H, t), 7.16 (1H, m), 7.31 (1H, d), 7.64 (1H, td), 8.55 (1H, dq). ^{13}C NMR ($CDCl_3$, 125 MHz) δ 33.87, 45.05, 54.50, 108.56, 108.28, 122.04, 122.46, 130.95, 136.53, 149.37, 159.97. FTIR (NaCl disk, cm^{-1}) 3315 (m, br), 3090 (w), 3064 (w), 3007 (m), 2920 (m), 2828 (m), 1591 (s), 1569 (s), 1496 (s), 1473 (s), 1456 (m), 1433 (s), 1416 (m), 1356 (w), 1325 (w), 1300 (s), 1261 (w), 1215 (w), 1182 (w), 1170 (w), 1147 (w), 1113 (m), 1088 (s), 1049 (m), 1014 (w), 994 (m), 955 (w), 934 (w), 917 (w), 890 (w), 845 (m), 794 (m), 758 (s), 710 (s), 626 (m), 611 (m). HRMS (ESI): Calcd [M + Na]$^+$, 224.1158; Found, 224.1151.

(1-Methyl-1*H*-pyrrol-2-ylmethyl)-(2-nitrobenzyl)pyridin-2-ylmethylamine (10). 2-Nitrobenzylbromide (1.07 g, 4.95 mmol), K_2CO_3 (1.36 g, 9.84 mmol), 5 (1.00 g, 4.97 mmol) and activated 3 Å molecular sieves were combined in 50 mL of MeCN and the yellow solution was stirred vigorously at room temperature for 10 h. The mixture was filtered through Celite and the solvent removed under reduced pressure. Chromatography on silica gel (2:1 hexanes/EtOAc) afforded the purified product as light yellow solid after drying in vacuo (1.50 g, 89%). TLC R_f = 0.32 (silica, 1:1 hexanes/EtOAc); mp = 89 – 91 °C. ^{1}H NMR ($CDCl_3$, 300 MHz) δ 3.42 (3H, s), 3.56 (2H, s),

3.68 (2H, s), 3.99 (2H, s), 5.99 (1H, m), 6.07 (1H, m), 6.53 (1H, m), 7.12 (1H, td), 7.25 (1H, m), 7.34 (1H, td), 7.46 (1H, td), 7.50-7.63 (2H, m), 7.76 (1H, dd), 8.49 (1H, dq). ^{13}C NMR (CDCl$_3$, 125 MHz) δ 33.78, 51.15, 60.71, 106.53, 110.43, 122.13, 122.94, 123.43, 124.41, 128.00, 128.59, 131.81, 132.35, 134.58, 136.40, 148.88, 150.06, 159.16. FTIR (KBr, cm^{-1}) 3436 (w, br), 3103 (w), 3071 (w), 2006 (w), 2916 (w), 2878 (w), 2807 (m), 2792 (m), 2722 (w), 1608 (m), 1590 (m), 1568 (m), 1515 (s), 1489 (m), 1470 (m), 1434 (m), 1421 (m), 1375 (m), 1367 (m), 1356 (m), 1334 (s), 1298 (s), 1282 (m), 1261 (m), 1217 (m), 1146 (m), 1117 (s), 1094 (m), 1073 (w), 1047 (m), 1013 (w), 1000 (m), 983 (m), 968 (m), 954 (m), 895 (m), 886 (w), 871 (w), 856 (w), 847 (w), 795 (m), 764 (s), 739 (s), 725 (s), 689 (m), 676 (w), 652 (w), 632 (w), 617 (m), 600 (w), 511 (w), 481 (w), 436 (w). HRMS (ESI): Calcd [M + Na]$^+$, 337.1659; Found, 337.1666.

2-{[(1-Methyl-1H-pyrrol-2-ylmethyl)pyridin-2-ylmethylamino]methyl}phenyl-amine (11). Palladium on carbon (10% activated, 900 mg) was placed in a flask purged with Ar. A 20 mL solution of **10** (600 mg, 1.78 mmol) in 19:1 MeOH/CH$_2$Cl$_2$ was added with a syringe. The mixture was stirred vigorously and a balloon of H$_2$ was attached. After 1.5 h of stirring under H$_2$, the reaction was purged with Ar, filtered through Celite, and the solvents were removed in vacuo. Chromatography on Al$_2$O$_3$ (2:1 to 1:1 hexanes/EtOAc) yielded the purified product as an off-white solid (325 mg, 60%). TLC R$_f$ = 0.47 (silica, 2:1 hexanes/EtOAc); mp = 105 – 109 °C. ^{1}H NMR (CDCl$_3$, 300 MHz) δ 3.40 (3H, s), 2.57 (2H, s), 3.61 (2H, s), 2.73 (2H, s), 6.04 (1H, t), 6.12 (1H, m), 6.54 (1H, m), 6.11-6.73 (2H, m), 7.06-7.20 (4H, m), 7.60 (1H, td), 8.56 (1H, dq). ^{13}C NMR (CDCl$_3$, 125 MHz) δ 33.57, 50.11, 57.74, 59.80, 106.62, 110.33, 115.48, 117.46, 122.10, 122.70, 123.75, 128.60, 129.13, 131.42, 136.34, 146.80, 149.12, 159.57. FTIR (KBr, cm^{-1}) 3456 (s), 3311 (m), 3199 (w), 3022 (w), 2923 (m), 2886 (m), 2832 (m), 2809 (m), 1986 (w), 1956 (w), 1930 (w), 1896 (w), 1865 (w), 1713 (w), 1630 (s), 1605 (m), 1591 (m), 1578 (m), 1567 (m), 1493 (s), 1475 (m), 1461 (m), 1445 (m), 1431 (m), 1413 (m), 1370 (m), 1358 (m), 1326 (m), 1310 (m), 1298 (m), 1267 (m), 1250 (w), 1221 (w), 1207 (w), 1180 (w), 1146 (m), 1109 (m), 1099 (m),

1081 (m), 1048 (w), 1035 (w), 997 (m), 968 (m), 954 (m), 934 (m), 897 (w), 887 (w), 869 (m), 866 (m), 837 (w), 790 (m), 770 (m), 752 (s), 724 (s), 682 (w), 633 (w), 612 (m), 548 (w), 516 (m), 466 (w), 444 (w), 410 (w). HRMS (ESI): Calcd [M + H]$^+$, 307.1917; Found, 307.1915.

2-{2-Chloro-6-hydroxy-5-[(2-{[(1-methyl-1H-pyrrol-2-ylmethyl)pyridin-2-ylmethyl-amino]methyl}phenylamino)methyl]-3-oxo-3H-xanthen-9-yl}benzoic acid (2, Zinpyr-10, ZP10). Portions of 7'-chloro-4'-fluoresceincarboxaldehyde (**6**, 75 mg, 0.190 mmol) and **11** (58 mg, 0.190 mmol) were combined in 5 mL of EtOAc and stirred overnight at room temperature. The intermediate imine, **12**, precipitated as a peach-colored solid, and the mixture was cooled on ice and filtered. The precipitate was suspended in 5 mL of DCE and NaB(OAc)$_3$H (40 mg, 0.190 mmol) was added. Over the course of 3 h, the reaction became dark pink and clear, and then became light orange. Preparative TLC on reverse phase silica gel (10:1 MeOH/0.1 N HCl) yielded the product as an orange solid (38 mg, 29%); mp > 300 °C, dec. ^{1}H NMR (CD$_3$OD/CDCl$_3$, 300 MHz) δ 3.10 (3H, s), 3.31 (2H, m), 3.47-3.68 (4H, m), 4.50 (2H, s), 5.76 (1H, t), 5.92 (1H, m), 6.33 (1H, m), 6.67 (3H, m), 6.77 (1H, s), 6.96 (1H, d), 7.10 (1H, t), 7.20 (2H, m), 7.34 (1H, t), 7.71-7.82 (2H, m), 8.06 (1H, d), 8.25 (1H, d). FTIR (KBr, cm^{-1}) 3425 (s, br), 3062 (w), 2963 (m), 2921 (s), 2851 (m), 1763 (s), 1628 (m), 1605 (s), 1582 (s), 1519 (m), 1494 (m), 1367 (m), 1282 (s), 1260 (s), 1216 (m), 1149 (m), 1106 (m), 1089 (m), 1070 (m), 1011 (m), 872 (m), 797 (m), 756 (m), 702 (m), 613 (w), 597 (w), 546 (w), 509 (w), 470 (w), 409 (w). HRMS (ESI): Calcd [M–H]$^-$, 683.2056; Found, 683.2047.

2-(2-Chloro-6-hydroxy-3-oxo-5-phenylaminomethyl-3H-xanthen-9-yl)benzoic acid (3). To 3 mL of EtOAc were added fluorescein carboxaldehyde **6** (38 mg, 0.097 mmol) and aniline (12 mg, 0.13 mmol) and the resulting orange solution was stirred overnight at room temperature. The solvent was removed under reduced pressure, which gave a red-magenta residue. The residue was dissolved in 5 mL of DCE and NaB(OAc)$_3$H (24 mg, 0.11 mmol) was added. The cloudy orange solution was stirred overnight at room

temperature, diluted with 15 mL of CHCl$_3$, washed with water (3 x 15 mL) and dried in vacuo. Preparative TLC of the crude material on silica gel (10:1 CHCl$_3$/MeOH) gave pure **3** as a magenta solid (8.5 mg, 18%). TLC R$_f$= 0.53 (silica, 9:1 CHCl$_3$/MeOH); mp > 300 °C, dec. ^{1}H NMR (CD$_3$OD, 500 MHz) δ 4.48-4.59 (2H, q), 6.54 (1H, d), 6.61 (1H, t), 6.73 (1H, s), 6.86 (1H, d), 7.00 (1H, d), 7.08-7.13 (3H, m), 7.19 (1H, d), 7.56 (2H, q), 8.03 (1H, d). FTIR (KBr, cm^{-1}) 2960 (m), 2924 (s), 2854 (m), 1728 (w), 1638 (m), 1605 (m), 1575 (m), 1503 (m), 1461 (m), 1376 (m), 1301 (m), 1261 (s), 1222 (w), 1186 (w), 1147 (m), 1096 (m), 1014 (m), 963 (w), 936 (w), 881 (w), 823 (s), 802 (s), 749 (m), 715 (m), 690 (m), 662 (w), 623 (m), 598 (m), 547 (m), 499 (w). HRMS (ESI) Calcd [M + H]$^+$, 472.0946; Found, 472.0930.

ZP9-Piv (13). A portion (14.7 mg, 0.025 mmol) of ZP9 was dissolved in 3 mL of 5:1 CHCl$_3$/DMF, which gave a brown solution. Triethylamine (50 μL) and pivalic anhydride (15 μL, 74 μmol) were added and the reaction was stirred overnight at room temperature. The solvents were removed under reduced pressure, which gave a brown residue. Preparative TLC on silica gel (30:1 CHCl$_3$/MeOH) afforded the product as an off-white powder (8.5 mg, 40%). ^{1}H NMR (CDCl$_3$, 300 MHz) δ 1.28 (9H, s), 1.39 (9H, s), 3.38 (2H, q), 3.58 (2H, m), 4.40-4.52 (2H, m), 5.97 (1H, s), 6.08 (1H, d), 6.47 (1H, m), 6.75 (3H, m), 6.89 (3H, m), 7.09 (3H, m), 7.32 (3H, m), 7.69 (2H, m), 8.08 (1H, m), 8.42 (1H, d), 10.28 (1H, s, br). This material was used for preliminary biological tests without further characterization.

General Spectroscopic Procedures. Solution preparation and spectroscopic procedures were conducted as described in Chapter 2 unless otherwise noted. DMSO stock solutions (1 mM) of ZP9 and ZP10 were prepared, partitioned, stored at -25 °C and thawed in the dark before use. After dilution to the appropriate concentration, solutions for fluorescence measurements contained either 0.1% (1 μM dye solution) or 1% (10 μM dye solution) for fluorescence and absorption measurements, respectively. Rigorously treating the buffer (50 mM PIPES, 100 mM KCl, pH 7) with Chelex (BioRad) to remove

any potential metal ion contamination had negligible effect on the observed emission and Zn(II) response of ZP9 and ZP10. Quantum yields were measured relative to fluorescein in 0.1 N NaOH (Φ = 0.95).[20] Extinction coefficients were determined over a concentration range of 10 to 1 µM for apo ZP9 and ZP10. Limited solubility of the Zn(II) complexes restricted this analysis to the range of 5 to 1 µM. Stopped-flow kinetic studies, monitored by fluorescence detection, were conducted as detailed in Chapter 7. For metal ion selectivity experiments requiring Fe(II), controls with ZP1 were conducted since ZP1 preferentially binds Fe(II) over Zn(II). All reported data are the averages of at least three independent measurements.

Dissociation Constant Determination. The apparent zinc complex dissociation constants for ZP9 and ZP10 were determined by fluorimetric analysis. In a typical experiment, a 1 µM solution of the ZP compound was prepared (50 mM PIPES, 100 mM KCl, pH 7, Chelexed) and its emission spectrum recorded. Various aliquots of 1 or 10 mM aqueous $ZnCl_2$ solutions were added and the emission change noted. Excitation was provided at 496 nm and the data were integrated from 505 – 650 nm, normalized, and plotted against the concentration of Zn(II) in solution. The binding curves were fit to a 1:1 metal-ligand model.[21]

Cell Culture. Human embryonic kidney (HEK293-T, HEK) cells were plated on glass coverslips coated with 0.2% gelatin for at least 1 h at room temperature and grown to 90% confluence in DMEM supplemented with 10% FCS, glutamine (2 mM), penicillin (100 units/mL) and streptomycin (100 µg/mL). The medium was removed and replaced with DMEM containing 1% serum prior to ZP treatment. DMSO stock solutions (1 mM) of ZP were diluted to 100 µM with DMEM and added to the cells in DMEM containing 1% FCS by bath application for a final dye concentration of 10 µM. The cells were incubated with the probe for 2 h at 37 °C and under 5% CO_2, washed with serum-free DMEM (2 x 2 mL) and bathed in serum-free DMEM (2 mL) before imaging. Stock solutions of Zn/pyrithione (1:2 Zn(II)/pyrithione ratio, 10 mM) and

N',N',N'',N''-tetrakis(2-picolyl)ethylenediamine (TPEN, 40 mM) in DMSO were diluted 10- and 40-fold with DMEM prior to cell treatment.

Acute Hippocampal Slice Preparation. The whole brains of 90-day-old female Sprague-Dawley rats were removed. The hippocampi were dissected, cut into ~200 μm or ~400 μm thick slices and washed twice with Zn(II)-free Kreb's ringer buffer prepared according to a literature protocol.[22] Slices were incubated with 10 μM dye in Zn(II)-free Kreb's ringer buffer at 37 °C under 5% CO_2 for 10-20 min, washed thoroughly with the Zn(II)-free buffer, and transferred to a glass-bottom imaging dish with a minimum volume of buffer for imaging.

Confocal Fluorescence Microscopy. A Zeiss LSM510 laser scanning microscopy system based on an Axiovert 200M inverted fluorescence microscope was used for confocal fluorescence imaging. The microscope was equipped with an argon ion laser (λ_{ex}= 488 nm), 10x or 63x objective lens, and a 505 nm long pass emission filter. During imaging experiments, samples were kept on the microscope stage in a CTI-3700 incubator set at 37 °C under 5% CO_2. Additions of Zn/pyrithione and TPEN solutions to the biological samples were performed directly on the microscope stage by bath application. The Metamorph software package was used for quantification.

Results and Discussion

Syntheses. Sensors ZP9 and ZP10 were prepared by a convergent route that involves combination of an asymmetrical aldehyde-functionalized fluorescein and the aniline-based ligand moiety. Scheme 4.1 depicts the syntheses of ligand fragments **8** and **11** and assemblies of sensors ZP9 and ZP10. The pyridyl-amine-pyrrole ligand **4** was prepared from 2-(aminomethyl)pyridine and 2-pyrrolecarboxaldehyde according to a literature procedure.[19] The N-methyl analog, **5**, was obtained in 82% yield by an analogous route. Combination of secondary amines **4** and **5** with 2-nitrobenzylbromide and base afforded compounds **7** and **10** as yellow solids in high yields following

purification by column chromatography. Reduction of the nitro groups in **7** and **10** to amino groups by hydrogenation using Pd/C (10% activated) was efficient and yielded the aniline-derivatized ligand fragments **8** and **11** in 52% and 60% yields, respectively, following column chromatography.

The final assembly of sensors ZP9 and ZP10 followed previously described methods.[14] Schiff base condensation of aldehyde **6** and the aniline-derivatized ligands in EtOAc afforded the intermediate imines **9** and **12**. Reduction of the intermediate imines by NaB(OAc)$_3$H in DCE occurred readily and can be monitored by changes in solution clarity and color. Solutions of the fully reduced species were orange-yellow and clear. ZP9 and ZP10 were purified by preparative TLC on RP silica gel and obtained as orange solids in moderate yields. The solubility of these sensors in volatile organic solvents is modest with CHCl$_3$/MeOH mixtures being optimal.

Effect of pH on Sensor Emission. We investigated the effect of pH on the emission properties of ZP9 and ZP10; representative titrations are given in Figure 4.1. The pH profiles of these probes are essentially identical, as expected given their structural similarity. Both sensors show ~2-fold fluorescence enhancement as the pH is lowered from pH ~12 to ~6, and fluorescence quenching occurs in more acidic solutions. These titrations reveal two protonation events that alter sensor emission significantly and are assigned to aniline (pK_{a1} = 7.2, ZP9; 7.0, ZP10) and fluorescein (pK_{a2} = 5.0, ZP9; 4.8, ZP10) protonation (Table 4.1). The former assignment is in accord with the behavior of many PET sensors since nitrogen protonation often causes fluorescence enhancement.[10,23,24] Fluorescein itself is pH sensitive[25] and its emission is quenched at low pH, which forms the basis for the assignment of pK_{a2}. To understand this transition further, we employed optical absorption spectroscopy; representative spectra for ZP9 are given in Figure 4.1. Decreasing the solution pH causes a blue-shift and concomitant decrease in A$_{max}$. The absorption spectra at pH > 7 are indicative of the fluorescein dianion whereas those at pH ~2, with peaks at ca. 484 and 459 nm of similar and

significantly lower molar absorptivity, signal phenol protonation and formation of the fluorescein monoanion.[25] Based on these observations, we propose the protolytic equilibria for ZP9 and ZP10 shown in Scheme 4.3. We use the quinoid structure of fluorescein in this analysis (see Figure A2.1 for fluorescein structures). In previous work,[10,14] we suggested that the fluorescence quenching observed for ZP sensors in acidic solution corresponded to formation of a zwitterionic isomer, in part based on early literature studies of fluorescein protonation equilibria.[26] We recently employed density functional theory to compute the solution phase free energies for the quinoid and zwitterionic forms of fluorescein (Appendix 2). A comparison of these energies shows that the quinoid is significantly more stable than the zwitterion.[27]

The pK_a analysis above suggests that protonation of the tertiary amines in ZP9 and ZP10 has little influence on fluorophore emission. Analysis of the pH-dependent emission of **3** generally supports this notion and representative data are given in Figure 4.2. The proposed protonation equilibria are depicted in Scheme 4.4. The emission of **3** shows essentially no change as the pH is lowered from ~12 to ~7.5. A ~2-fold fluorescence rise occurs between pH ~7.5 and ~5.4, which returns a pK_{a1} value of 6.1 that is assigned to aniline nitrogen protonation. Further lowering of the pH causes quenching, with pK_{a2} of 4.7. Optical absorption spectroscopy reveals that phenol protonation is responsible for this transition (Figure 4.2, bottom). Some subtle differences in the pK_{a1} transition for **3** and ZP9 and ZP10 are worth noting. In contrast to the stable emission from **3** over the pH ~12 to ~7.5 range, ZP9 and ZP10 both show a slight rise, which may suggest that tertiary amine protonation has some contribution to the observed fluorescence enhancement in this pH regime. Given that a two-parameter model returns an excellent fit (r = 0.997 for both ZP9 and ZP10), we opted not to incorporate a third variable into our model, but acknowledge that some small contribution from tertiary amine protonation may influence emission in this range.

Spectroscopic Properties of ZP9 and ZP10. Table 4.1 details the spectroscopic and thermodynamic characterization of asymmetrical ZP sensors. ZP9 and ZP10 both have fluorescein-dominated emission spectra with $\lambda_{max} \sim 520$ nm and $\Phi_{free} < 0.1$ (50 mM PIPES, 100 mM KCl, pH 7). The quantum efficiencies are in the range of most asymmetrical ZP sensors that employ aniline-based DPA chelates.[11,14,28] This comparison suggests that the aniline-based ZP platform is relatively insensitive to variations in the tertiary amine fragment. Additional support for this notion comes from characterization of sensors with one or more thioether groups in this ligand framework (Chapters 5 and 9).[2,29] Photophysical characterization of compound **3**, which has $\Phi_{free} = 0.06$ (50 mM PIPES, 100 mM KCl, pH 7), further substantiates this claim. The fluorescence quenching observed in aniline-derivatized fluoresceins can be attributed to the aniline moiety with little, if any, contribution from the tertiary amine fragment. From the standpoint of achieving a sensor series with similar photophysical properties and varied affinity or Zn(II) selectivity (vide infra), such insensitivity to ligand variations is an advantage.[4]

The fluorescence responses of ZP9 and ZP10 to Zn(II) are shown in Figure 4.3. Solutions of ZP9 and ZP10 exhibit immediate fluorescence turn-on, visible by eye at low μM concentrations, following Zn(II) addition. These sensors give full emission enhancement in the presence of ~20 (ZP9) or ~30 (ZP10) equiv of Zn(II) with $\Phi_{zn} > 0.30$ (50 mM PIPES, 100 mM KCl, pH 7). Approximately 12- and 7-fold fluorescence turn-on occurs following Zn(II) coordination to ZP9 and ZP10, respectively. Blue shifts in both absorption and emission maxima occur as a result of Zn(II) binding, indicative of Zn(II) coordination to the phenol group, as previously discussed for ZP4-8 in Chapter 2. The absorption properties of ZP9 and ZP10, which are dominated by the fluorescein chromophore, are also listed in Table 3.1 and follow expected trends.

Thermodynamics and Kinetics of Zn(II) Binding to ZP9 and ZP10. We anticipated that substitution of a pyridyl moiety with a more weakly coordinating pyrrole group would achieve lower affinity Zn(II) binding compared to the parent asymmetrical ZP

sensors (K_d < 1 nM). Figure 4.4 depicts representative fluorimetric titrations for ZP9 and ZP10. The latter probe has an apparent zinc complex K_d value of 0.69 ± 0.04 μM. This value is three orders of magnitude higher than those for the parent ZP sensors, less than one order of magnitude higher than that of Fluo-3N (K_d = 15 nM),[30] a commercially available Zn(II) sensor that employs a modified BAPTA chelate, and similar to the K_d value of ZnAF-3 (K_d = 0.79 μM).[4] Substitution of the pyrrole with N-methylpyrrole further raises the K_d value to 1.9 ± 0.2 μM. Given the spectroscopic similarities between ZP4, ZP9 and ZP10, we anticipate that their parallel use for biological imaging will be of benefit and will allow for bracketing relative Zn(II) concentrations in the nM to low μM regime. ZP9 and ZP10 were designed to bind Zn(II) with 1:1 stoichiometry and Scheme 4.5 illustrates the anticipated coordination behavior in aqueous solution.

Stopped-flow kinetics investigations were conducted to determine the association rates, measured by fluorescence turn-on, of ZP9 and ZP10 for Zn(II). Full experimental details for analogous experiments, in addition to complete data for DPA-based ZP probes, are given in Chapter 7. Representative plots of k_{obs} vs. Zn(II) concentration (T = 4.3 °C) are shown in Figure 4.5 and yield second-order rate constants of 3.0 x 10^5 $M^{-1}s^{-1}$ (ZP9) and 2.0 x 10^5 $M^{-1}s^{-1}$ (ZP10). Temperature dependent studies reveal k_{on} values of >2 x 10^6 $M^{-1}s^{-1}$ at 25 °C. These association rates indicate rapid Zn(II) complexation on the sub-msec timescale and are of similar magnitude to the k_{on} values for di(2-picolyl)amine-based ZP^3 (3.3 – 5.2 x 10^6 $M^{-1}s^{-1}$, T = 25 °C, see Chapter 7) and ZnAF family members (1.3 – 3.1 x 10^6 $M^{-1}s^{-1}$, T = 25 °C).[4] The calculated k_{off} values for ZP9 and ZP10 are ~1.5 and ~3.8 s^{-1}, respectively, at T = 25 °C, which indicates significantly more rapid Zn(II) dissociation as compared to sensors with the DPA chelate (vide infra). As described in Chapter 7, this feature may be important for imaging Zn(II) flux during signaling events.

Variable temperature experiments were performed over the range of ~4 to ~40 °C and Eyring plots are given in Figure 4.5. Values for the activation enthalpies, $\Delta H^{\ddagger}$, are

14.4 ± 0.1 (ZP9) and 14.9 ± 0.6 (ZP10) kcal/mol and indicate a low activation barrier and fast association. The activation enthalpies, $\Delta S^{\ddagger}$, are 18.3 ± 0.9 (ZP9) and 20.3 ± 2.0 (ZP10) cal/mol-K. Positive values were previously observed for selected ZP and QZ sensors – see Chapter 7 for details – and may reflect the dissociation of water molecules or buffer components from the Zn(II) coordination sphere in the rate-determining step.

Metal Ion Selectivity of ZP9 and ZP10. Figure 4.6 details the Zn(II) selectivity of ZP9, and the data for ZP10 are similar. As anticipated, given the nitrogen-rich coordination sphere, ZP9 and ZP10 are selective for Zn(II) over mM concentrations of K(I), Na(I), Ca(II) and Mg(II). Of the divalent first-row transition metal ions considered, these sensors are selective for Zn(II) over both Mn(II) and Fe(II). The selectivity for Zn(II) over Fe(II) is a significant advantage relative to ZP1-8. The data presented in Figure 4.6 also show that the pyrrole-containing sensors are selective for Zn(II) over its Group 12 congeners Cd(II) and Hg(II).

Biological Imaging Applications. Given the fluorescence properties and Zn(II) affinities of ZP9 and ZP10, we initiated studies of their distribution and Zn(II) response in biological samples. Our initial expectations were based on previous biological imaging conducted with ZP4. Early studies with ZP4 showed that it selectively labels damaged neurons in brain tissue,[11] and subsequent work in our laboratory with a basic tissue culture room microscope suggested that ZP4-6 do not readily enter cultured HeLa cells.[14] From these observations, ZP4 and its derivatives were assumed to be cell impermeable and useful for extracellular imaging. Based on the structural similarities between ZP4 and the pyrrole derivatives described in this work, we reasoned that ZP9 and ZP10 would similarly be unable to penetrate the cell membrane without modification. We therefore prepared ZP9-Piv as shown in Scheme 4.5 by reaction of ZP9 with excess pivalic anhydride in the presence of base. This approach, which affords the lipophilic lactone isomer of fluorescein, is commonly used for delivering an otherwise impermeable probe into cells.[15]

Preliminary control studies suggested otherwise. Laser scanning confocal microscopy revealed that HEK cells treated with either ZP9 or ZP9-Piv exhibited intracellular staining (T = 37 °C, 5% CO_2). Further work definitively showed that ZP9 can respond to exogenously added Zn(II) in vivo, delivered by addition of the cell-permeable ionophore pyrithione. Representative images are given in Figure 4.7 (2 h incubation with ZP). Addition of the cell-permeable heavy metal ion chelator TPEN reversed the fluorescence increase to within 20% of the baseline, which confirms that the fluorescence rise results from Zn(II) coordination and not some other phenomena such as a proton flux or sensor photoactivation.

Based on our knowledge of ZP4, the behavior of ZP9 was a surprise and we concluded that relative incubation time is a key factor when defining the permeability of a probe, and that an "appropriate" incubation time will also depend on the type of cell or tissue under study. An incubation time of only ~1 min was employed during the first experiments conducted with ZP4 in samples of brain tissue, which was presumably too short for the probe to enter healthy cells. We therefore investigated ZP4 staining of cultured HEK cells in detail and observed a distribution and response comparable to that of ZP9 (Figure 4.7). Additional experiments conducted with other cells lines, including COS and HeLa, and primary neuronal cultures show that both ZP4 and ZP9 also enter these cell types. The details of the Zn(II) response in these cultures have not been investigated. These studies point to the need for caution when designating a given sensor as intra- or extracellular, and the necessity for rigorous control experiments.

Knowing that ZP4 and ZP9 can penetrate cell membranes and respond to Zn(II) in vivo, we sought to employ these probes to detect endogenous Zn(II) pools. We therefore treated acute hippocampal slices (~200 – 400 μm thickness) from adult rat brain with 10 μM ZP4 or ZP9 for 10 – 20 min (T = 37 °C, 5% CO_2). Figure 4.8 shows the confocal images obtained for a representative slice treated with ZP9 and subsequently with 50 μM TPEN. The DG is illuminated and the signal is reversed with TPEN

addition, which indicates that (i) ZP9 (K_d < 1 µM) can detect endogenous Zn(II) in this region and (ii) that the fluorescence is not due to a high local concentration of free sensor. Similarly, ZP4 (K_d < 1 nM) also stains the Zn(II)-rich regions of the mammalian hippocampus. Figure 4.9 shows the optical z-sectioning of a ZP4 treated hippocampal slice, which confirms that the sensor has indeed penetrated the tissue. We reiterate that this staining pattern differs significantly from those first obtained with a ~1 min incubation (room temperature, 3 h after slicing), which reflects one or more variations in the slice preparation and staining protocols. The slice study with ZP9 is particularly informative because it shows that the histochemically observable Zn(II) in the DG region can be visualized with a lower, sub-micromolar affinity probe and thus affords some indication of the relative Zn(II) concentration in this substructure of the hippocampus. This observation is in good agreement with a recent study employing low affinity ZnAF sensors.[4]

Summary and Perspectives

The investigations of ZP9 and ZP10 described in this chapter revealed several important facets of zinc sensor design and biological application. Incorporation of pyrrole groups afforded a new strategy for raising the Zn(II) dissociation constant and improving Zn(II) selectivity relative to sensors that use the DPA chelate. We determined that the fluorescence quenching of aniline-based sensors is primarily, if not completely, due to the aniline moiety itself. This observation is an important one and suggests that systematic modification of this sensor platform, via changes in the groups of the tertiary amine unit, will afford a series of Zn(II) sensors with comparable optical properties that span a range of dissociation constants and/or have varying metal ion selectivity. This type of series would be very useful for estimating Zn(II) concentrations in biological samples -- the preliminary images of ZP4 and ZP9 slice staining support this notion – or for determining what other free metal ions are present in a complicated mixture.

Finally, confocal imaging studies with ZP9 were particularly revealing and showed that aniline-based probes are cell permeable. As a result of this observation and subsequent studies, we revise our original claim[31] that ZP4 and its derivatives are exclusively extracellular Zn(II) sensors.

References

(1)   Sparano, B. A.; Shahi, S. P.; Koide, K. *Org. Lett.* **2004**, *6*, 1947-1949.

(2)   Nolan, E. M.; Lippard, S. J. *Inorg. Chem.* **2004**, *43*, 8310-8317.

(3)   Nolan, E. M.; Jaworski, J.; Okamoto, K.-I.; Hayashi, S. Y.; Sheng, M.; Lippard, S. J. *J. Am. Chem. Soc.* **2005**, *127*, 16812-16823.

(4)   Komatsu, K.; Kikuchi, K.; Kojima, H.; Urano, Y.; Nagano, T. *J. Am. Chem. Soc.* **2005**, *127*, 10197-10204.

(5)   Goldsmith, C. R.; Lippard, S. J. *Inorg. Chem.* **2006**, *45*, 555-561.

(6)   Henary, M. M.; Wu, Y.; Fahrni, C. J. *Chem. Eur. J.* **2004**, *10*, 3015-3025.

(7)   Shults, M. D.; Pearce, D. A.; Imperiali, B. *J. Am. Chem. Soc.* **2003**, *125*, 10591-10597.

(8)   Gee, K. R.; Zhou, Z. L.; Ton-That, D.; Sensi, S. L.; Weiss, J. H. *Cell Calcium* **2003**, *31*, 245-251.

(9)   Walkup, G. K.; Burdette, S. C.; Lippard, S. J.; Tsien, R. Y. *J. Am. Chem. Soc.* **2000**, *122*, 5644-5645.

(10)   Burdette, S. C.; Walkup, G. K.; Springler, B.; Tsien, R. Y.; Lippard, S. J. *J. Am. Chem. Soc.* **2001**, *123*, 7831-7841.

(11)   Burdette, S. C.; Frederickson, C. J.; Bu, W.; Lippard, S. J. *J. Am. Chem. Soc.* **2003**, *125*, 1778-1787.

(12)   Chang, C. J.; Nolan, E. M.; Jaworski, J.; Burdette, S. C.; Sheng, M.; Lippard, S. J. *Chem. Biol.* **2004**, *11*, 203-210.

(13)   Chang, C. J.; Jaworski, J.; Nolan, E. M.; Sheng, M.; Lippard, S. J. *Proc. Nat. Acad. Sci. USA* **2004**, *101*, 1129-1134.

(14)   Nolan, E. M.; Burdette, S. C.; Harvey, J. H.; Hilderbrand, S. A.; Lippard, S. J. *Inorg. Chem.* **2004**, *43*, 2624-2635.

(15)   Hirano, T.; Kikuchi, K.; Urano, Y.; Nagano, T. *J. Am. Chem. Soc.* **2002**, *124*, 6555-6562.

(16)   Bozym, R. A.; Thompson, R. B.; Stoddard, A. K.; Fierke, C. A. *ACS Chem. Biol* **2006**, *1*, 103-111.

(17)   Vogt, K.; Mellor, J.; Tong, G.; Nicoll, R. *Neuron* **2000**, *26*, 187-196.

(18)   Frederickson, C. J. *Int. Rev. Neurobiol.* **1989**, *31*, 145-238.

(19)   de Bruin, B.; Kicken, R. J. N.; Suos, N. F. A.; Donners, M. P. J.; den Reijer, C. J.; Sandee, A. J.; de Gelder, R.; Smits, J. M. M.; Gal, A. W.; Spek, A. L. *Eur. J. Inorg. Chem.* **1999**, 1581-1592.

(20)   Brannon, J. H.; Madge, D. *J. Phys. Chem.* **1978**, *82*, 705-709.

(21)   Lim, M. H.; Xu, D.; Lippard, S. J. *Nature Chem. Biol*, **2006**, *in press.*

(22)   Qian, W.-J.; Gee, K. R.; Kennedy, R. T. *Anal. Chem.* **2003**, *75*, 3468-3475.

(23)   de Silva, A. P.; Gunaratne, H. Q. N.; Gunnlaugsson, T.; Huxley, A. J. M.; McCoy, C. P.; Rademacher, J. T.; Rice, T. E. *Chem. Rev.* **1997**, *97*, 1515-1566.

(24)   de Silva, A. P.; Fox, D. B.; Huxley, A. J. M.; Moody, T. S. *Coord. Chem. Rev.* **2000**, *205*, 41-57.

(25)   Sjoback, R.; Nygren, J.; Kubista, M. *Spectrochim. Acta. Part A* **1995**, *51*, L7-L21.

(26)   Markuszewski, R.; Diehl, H. *Talanta* **1980**, *27*, 937-946.

(27)   Nolan, E. M.; Lippard, S. J.; Baik, M.-H. *Unpublished results.*

(28)   Chang, C. J.; Nolan, E. M.; Jaworski, J.; Okamoto, K.-I.; Hayashi, Y.; Sheng, M.; Lippard, S. J. *Inorg. Chem.* **2004**, *43*, 6774-6779.

(29)   Nolan, E. M.; Lippard, S. J. *J. Am. Chem. Soc.* **2003**, *125*, 14270-14271.

(30)   Gee, K. R.; Zhou, Z.-L.; Qian, W.-J.; Kennedy, R. *J. Am. Chem. Soc.* **2002**, *124*, 776-778.

(31)   Burdette, S. C.; Frederickson, C. J.; Bu, W.; Lippard, S. J. *J. Am. Chem. Soc.* **2003**, *125*, 1778-1787.

(32)   Burdette, S. C.; Walkup, G. K.; Spingler, B.; Tsien, R. Y.; Lippard, S. J. *J. Am. Chem. Soc.* **2001**, *123*, 7831-7841.

Table 4.1. Spectroscopic and Thermodynamic Data for Aniline-Based ZP Sensors[a]

	Absorption λ (nm), $\varepsilon \times 10^4$ (M^{-1}cm^{-1})		Emission λ (nm), Φ[b]		pK_a[c] (N)	pK_a[d]	K_d	DR[e]
	Unbound	Zn(II)	Unbound	Zn(II)				
ZP4[e]	506, 6.1	495, 6.7	521, 0.06	515, 0.34	7.2	4.0	0.65±0.10 nM	4.4
ZP5	504, 8.3	495, 9.1	520, 0.29	517, 0.48	9.6	4.7	0.50±0.10 nM	1.6
ZP6	506, 8.9	495, 9.8	519, 0.10	517, 0.34	6.3	4.7	0.50±0.10 nM	4
ZP7	505, 6.8	495, 7.7	521, 0.04	517, 0.05	6.9	4.6	n.d.	1
ZP8	500, 8.1	489, 7.8	516, 0.03	510, 0.35	6.5	3.8	0.60±0.10 nM	11
ZP9	505, 5.1	495, 4.4	526, 0.02	521, 0.41	7.2	5.0	0.69±0.04 µM	12
ZP10	506,5.5	497, 4.5	523, 0.08	516, 0.33	7.0	4.8	1.9±0.2 µM	7

[a] Measurements were performed at pH 7 in 50 mM PIPES, 100 mM KCl buffer. Data for ZP4 were taken from ref. 11. Data for ZP5-8 are included in Chapter 2 and in refs. 12 and 14. [b] Reported quantum yields are based on fluorescein (Φ = 0.95 in 0.1 N NaOH, ref 20). [c] The pK_a value assigned to protonation of the aniline nitrogen atom. [d] The pK_a value assigned to phenol protonation. [e] DR is the dynamic range, or the observed increase in integrated emission, that occurs with Zn(II) coordination. [e] See Schemes 2.1 and 4.1 for nomenclature.
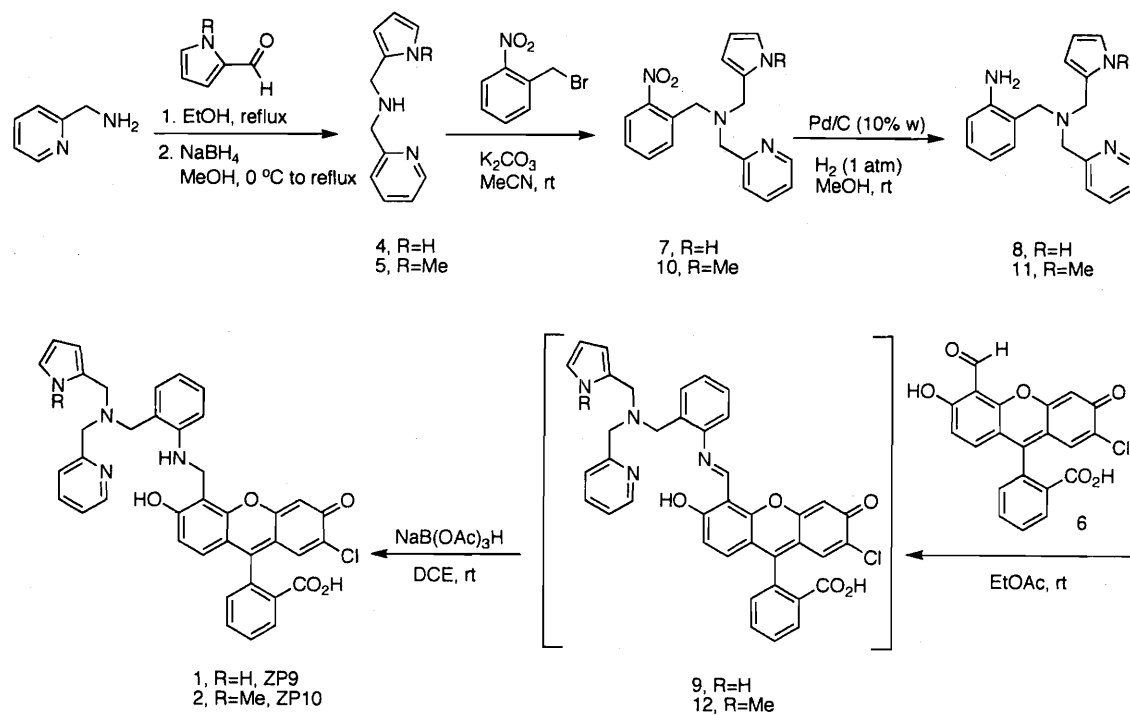
Scheme 4.1. Syntheses of ZP9 and ZP10.
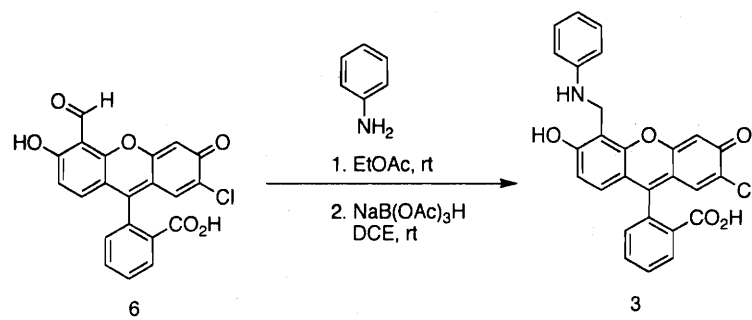
Scheme 4.2. Synthesis of an aniline-appended fluorescein.
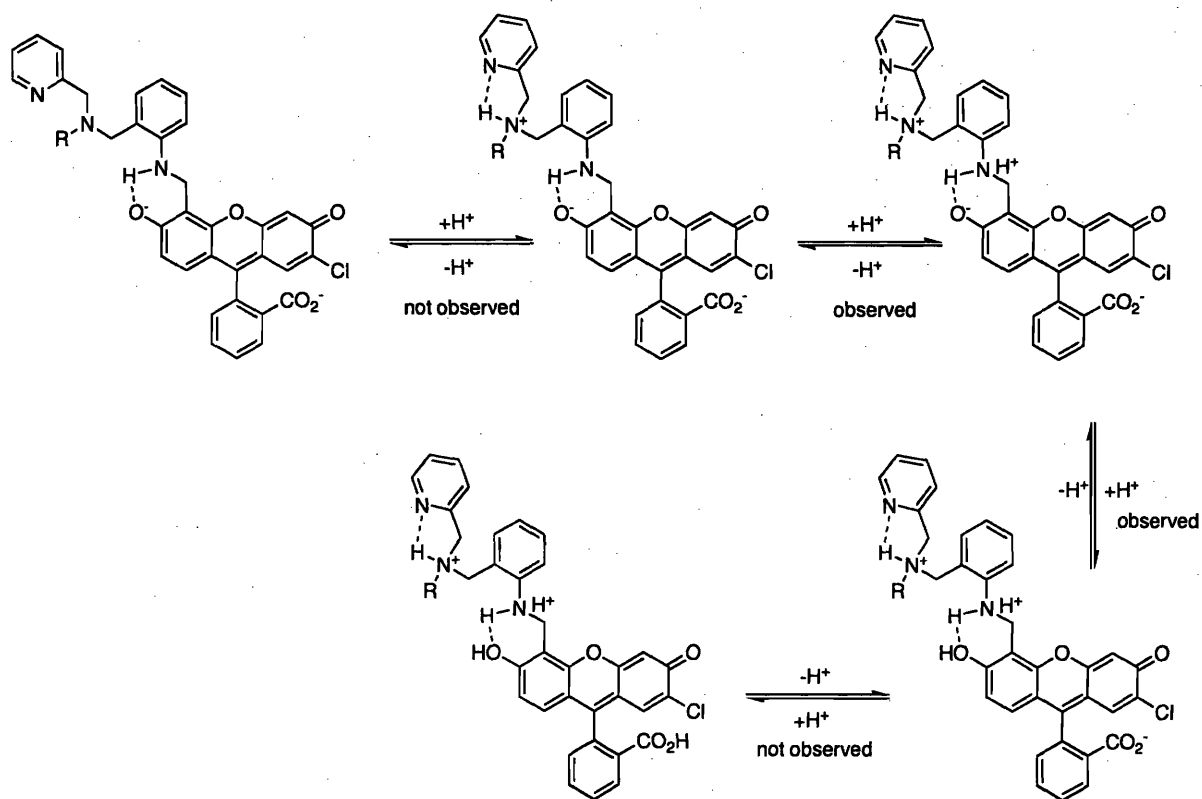
Scheme 4.3. Protonation equilibria for ZP9 and ZP10. "Observed" and "not observed" refer to the effect of these protonation events on sensor emission. Protonation of the carboxylate is presumed to occur at pH < 3 and is therefore not observed in the titrations (Figure 4.1). The R group indicates the pyrrole moiety.
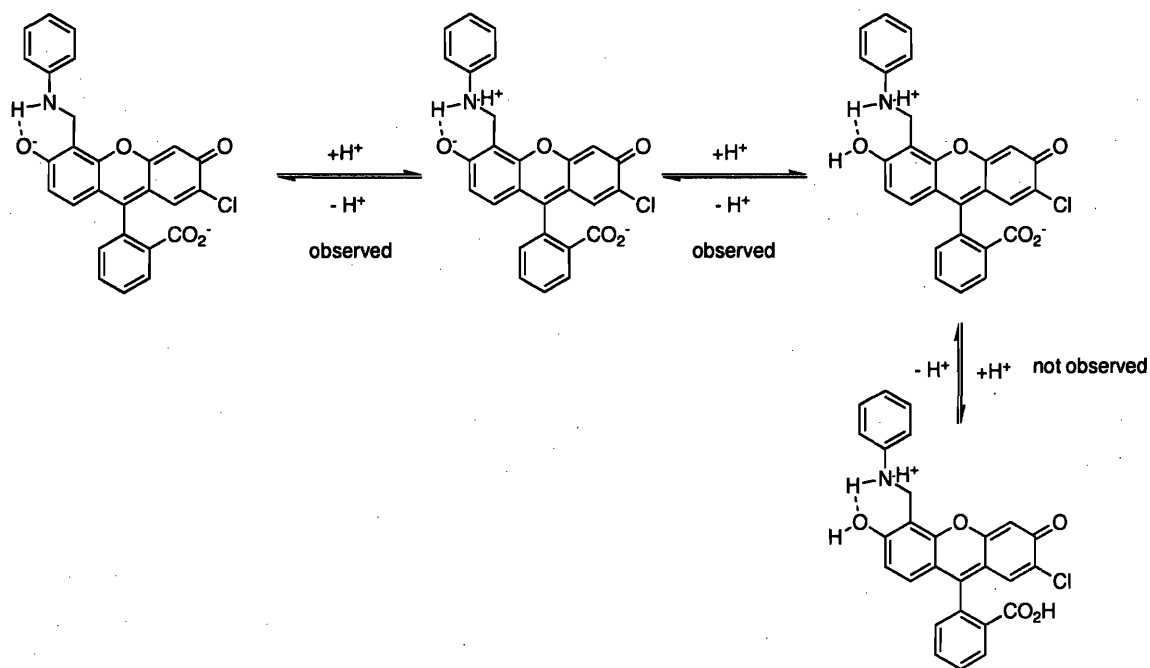
Scheme 4.4. Proposed protonation equilibria for compound **3**. Protonation of the aniline moiety and phenol group are observed by fluorimetric titration. Protonation of the carboxylate presumably occurs at pH < 3 and is thus not observed in the titration presented in Figure 4.2.

$$+ [Zn(OH_2)_4]^{2+}$$
$$-[Zn(OH_2)_4]^{2+}$$

$$+H^+ + 2H_2O$$
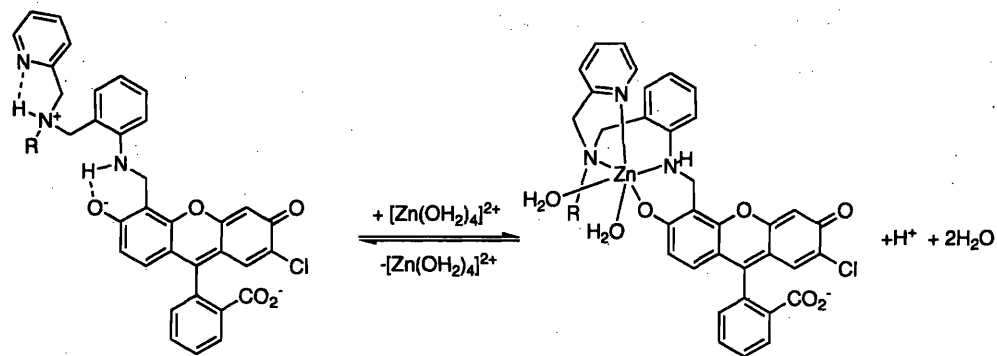
Scheme 4.5. Proposed mode of Zn(II) coordination for ZP9 and ZP10 in aqueous solution at neutral pH. The R groups indicates the pyrrole moieties of ZP9 and ZP10.
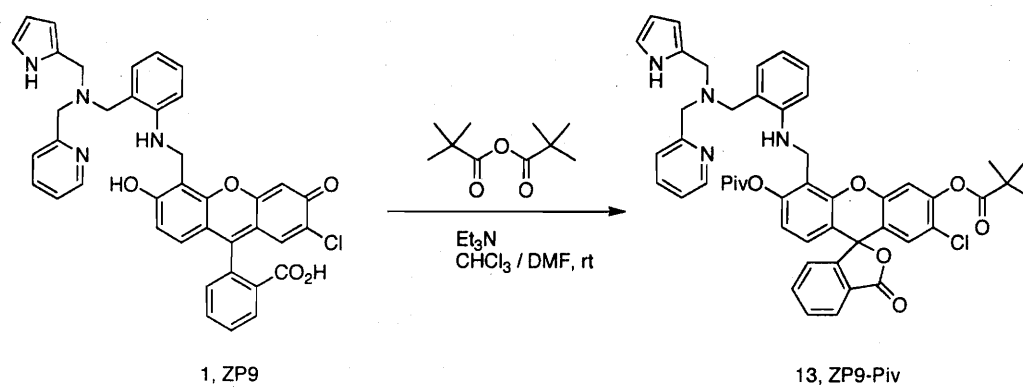
Scheme 4.6. Synthesis of ZP9-Piv.
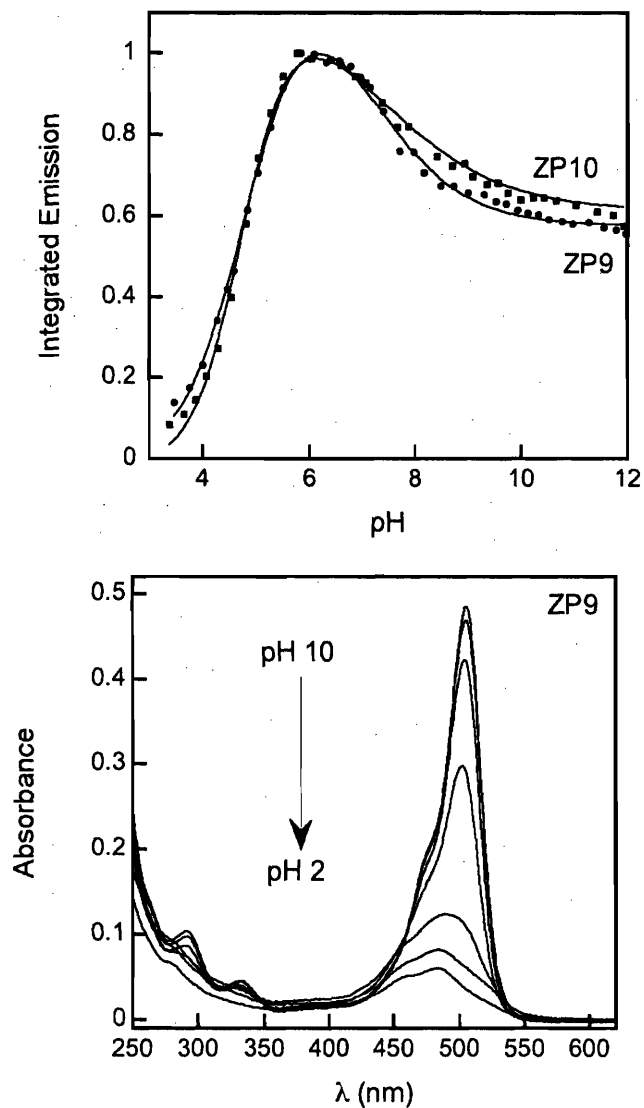
Figure 4.1. Top: Effect of pH on the emission of ZP9 (circles) and ZP10 (squares). Solutions of 1 μM ZP were prepared at pH ~12 (10 mM KOH, 100 mM KCl) and the pH was lowered in increments of ~0.25 by addition of aqueous HCl and the spectrum recorded at each point. The circles and squares represent the experimental data. The lines are the fit obtained using eq. 2.1 and calculated pK_a values are given in Table 4.1. Bottom: Effect of pH on the optical absorption properties of ZP9. A solution of 10 μM ZP9 at pH ~12 was prepared as described above and the pH was lowered by addition of aqueous HCl. See Scheme 4.3 for a description of the protonation equilibria.
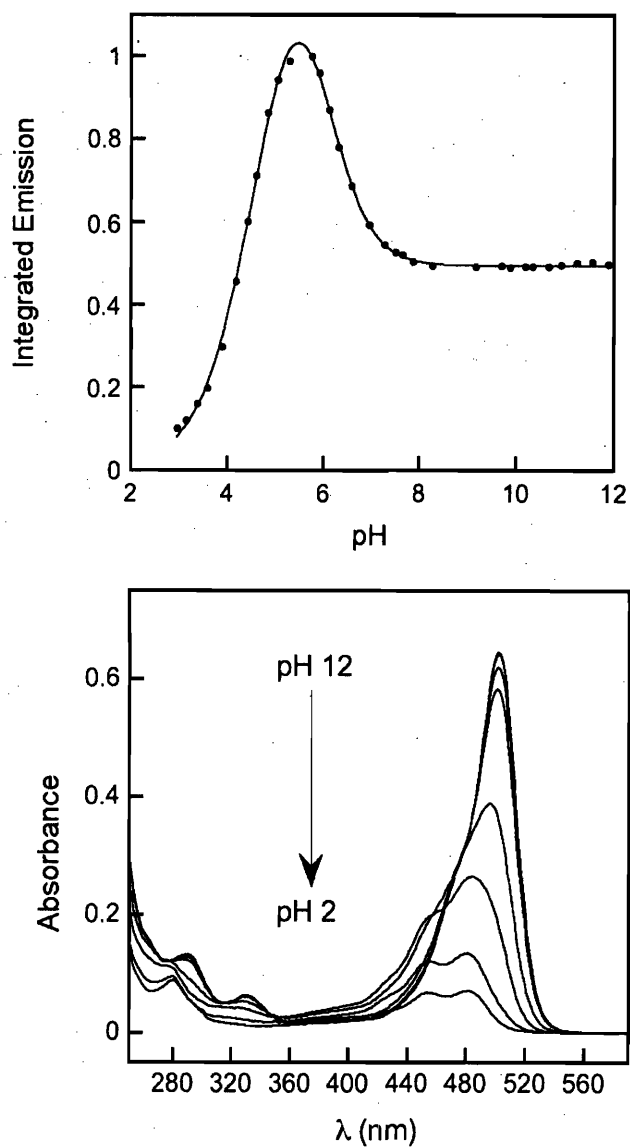
Figure 4.2. Effect of pH on the emission (top) and optical absorption (bottom) spectra of compound **3**. See the caption of Figure 4.1 for experimental details. The circles in the top plot are the experimental data and the line is the fit obtained by using eq. 2.1. Scheme 4.4 for a description of the protonation equilibria.
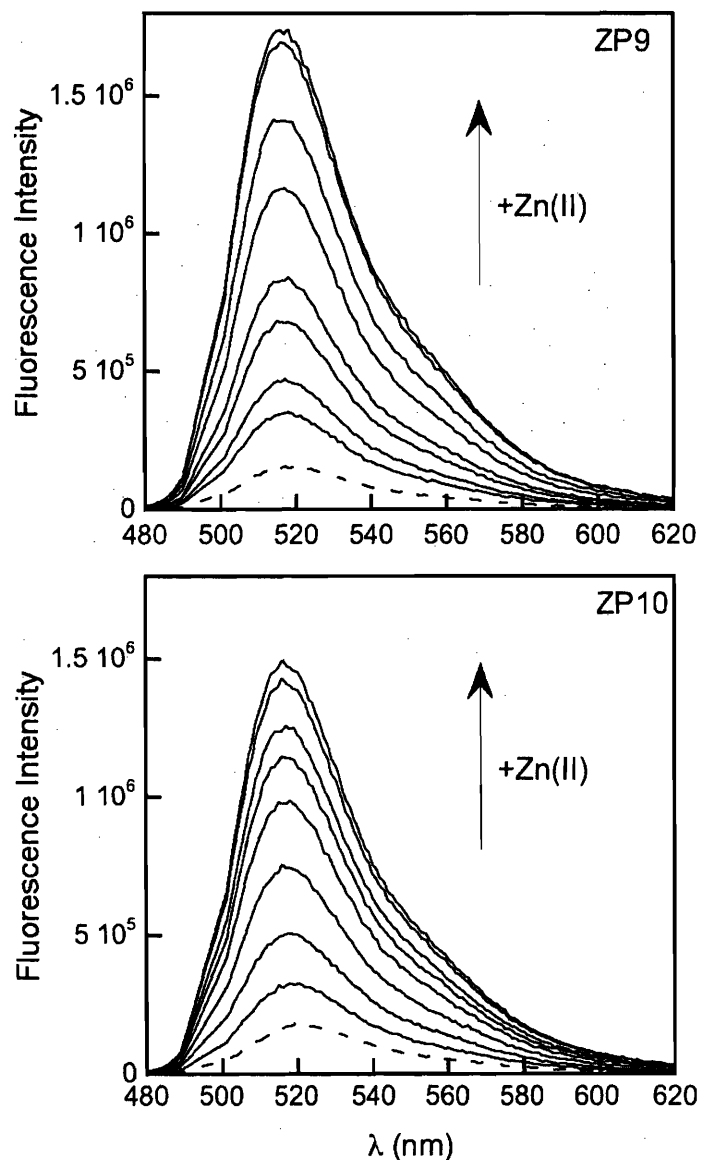
Figure 4.3. Fluorescence response of ZP9 and ZP10 to Zn(II) at pH 7 (50 mM PIPES, 100 mM KCl). Top: The dashed line indicates the emission from a 1 µM solution of ZP9. The solid lines represent the fluorescence enhancement that occurs in the presence of 0.17, 0.33, 0.66, 1, 2, 4, 7, and 30 µM Zn(II). Bottom: The dashed line indicates the emission from a 1 µM solution of ZP10. The solid lines represent the fluorescence enhancement that occurs in the presence of 0.33, 1, 2, 4, 6, 8, 20 and 30 µM Zn(II). Excitation was provided at 496 nm and T = 25 °C.
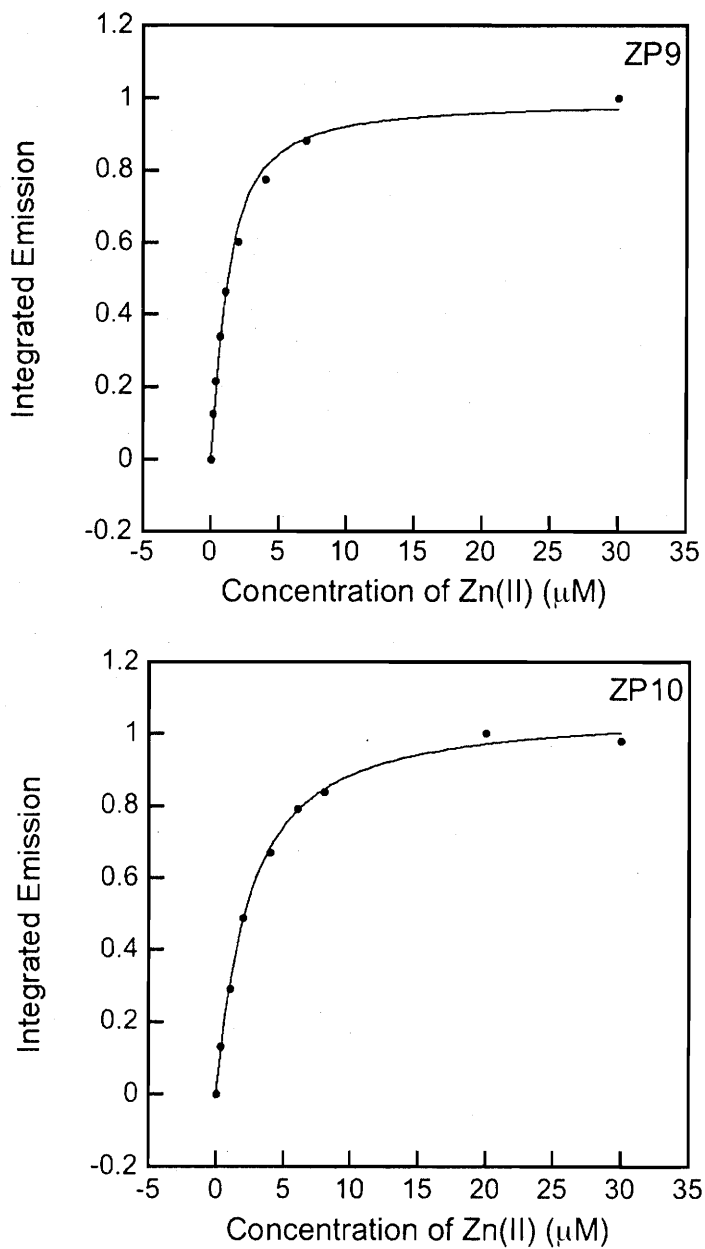
Figure 4.4. Normalized integrated emission vs. [Zn(II)] for ZP9 (top) and ZP10 (bottom) at pH 7 (50 mM PIPES, 100 mM KCl). The binding curves correspond to the titrations shown in Figure 4.3. Dissociation constants for ZP9 and ZP10 are listed in Table 4.1.
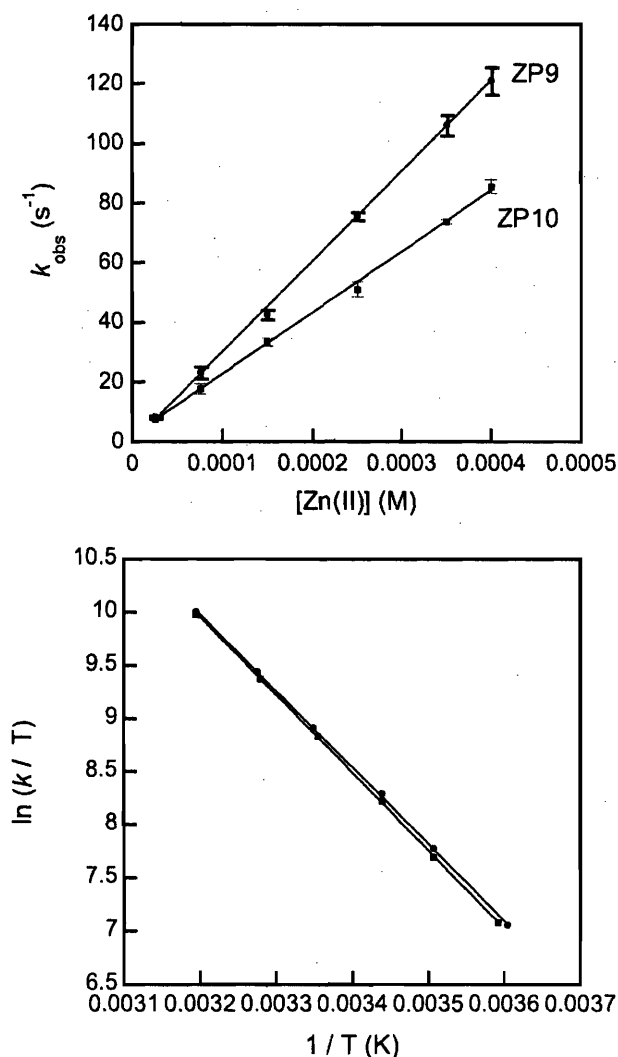
Figure 4.5. Top: Plot of k_{obs} vs. [Zn(II)] obtained from stopped-flow fluorescence studies of ZP9 (circles) and ZP10 (squares) at T=4.3 °C. The concentration of ZP was 0.5 µM after mixing and the Zn(II) concentration was varied from 0 to 400 µM. The data are from three independent trials and the error bars represent the standard deviation of the mean. Bottom: Eyring plots for Zn(II) coordination to ZP9 (circles) and ZP10 (squares). The concentrations of ZP and Zn(II) were 0.5 and 50 µM after mixing. The temperature was varied from ~4 to ~40 °C. Excitation was provided at 495 nm and all measurements were made at pH 7 (50 mM PIPES, 100 mM KCl).
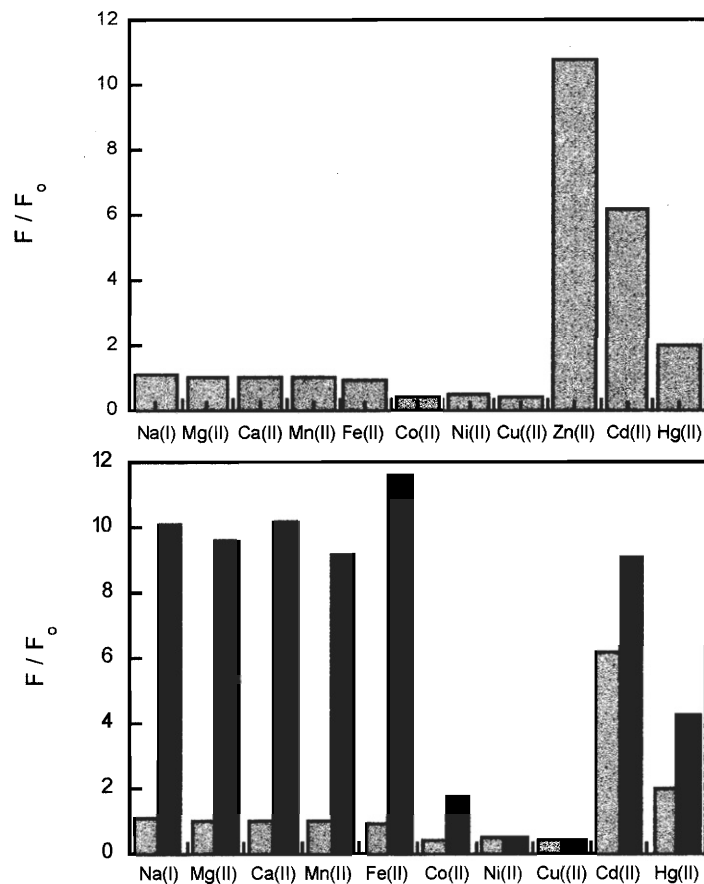
Figure 4.6. Selectivity of ZP9 for Zn(II) in the presence of other cations. Top plot: Fluorescence response of 1 μM ZP9 to 50 equiv of the cations of interest. The response (F) is normalized with respect to the emission of the free dye (F_o). Bottom plot: The fluorescence response of the solutions depicted in the top plot to Zn(II). The grey bars correspond to the bars in the top plot. The black bars indicate the fluorescence response of the solutions following introduction of 50 μM Zn(II). Excitation was provided at 495 nm. The Zn(II)-induced responses of ZP9 and ZP10 are also unaffected by mM concentrations of Na(I), K(I), Mg(II), and Ca(II) (data not shown).
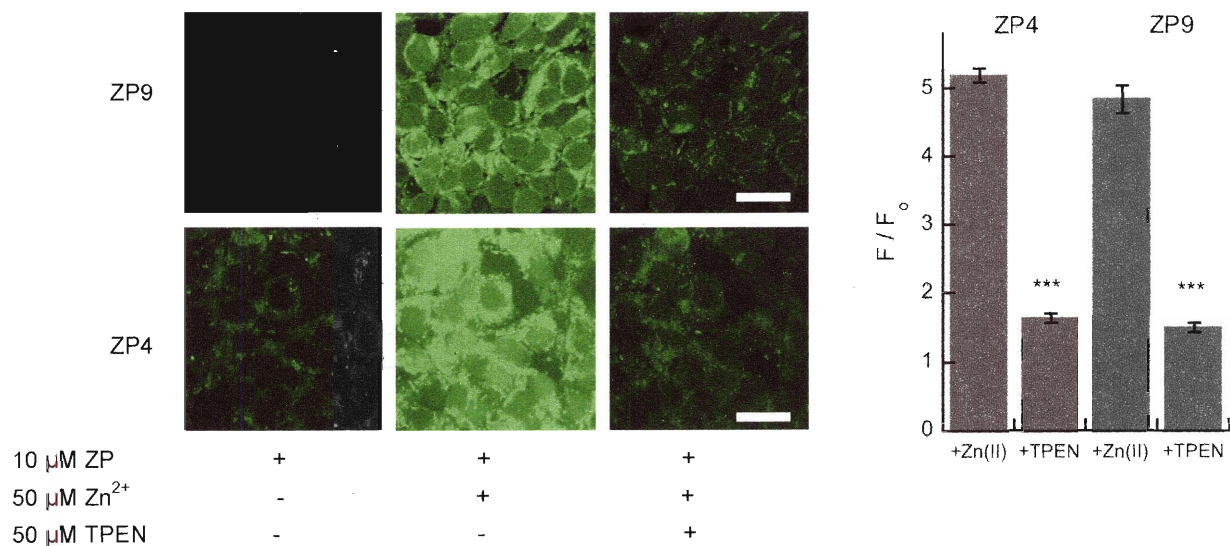
Figure 4.7. Confocal fluorescence imaging of HEK293-T cells treated with 10 μM ZP9 (top panels) or ZP4 (bottom panels). The cells were incubated with ZP in DMEM containing 1% serum (2 h, T = 37 °C, 5% CO_2), washed twice with serum-free DMEM and imaged in serum-free DMEM. Left: ZP-treated cells. Middle: Fluorescence increase observed following a 10 min incubation with 50 μM 1:2 $ZnCl_2$/pyrithione. Right: Fluorescence decrease observed following incubation with 50 μM TPEN for 10 min. The bar graph depicts quantification of the fluorescence rise and fall resulting from Zn(II) and TPEN treatments, respectively, and the data are normalized with respect to the non-treated cells. For ZP9, 32 cells were quantified and 20 cells were quantified for ZP4 (*** indicates $p < 0.001$, Mann-Whitney test). The error bars represent the standard error of the mean. The scale bar indicates 25 μm.

| 10 μM ZP9 | + | + |
| 50 μM TPEN | - | + |
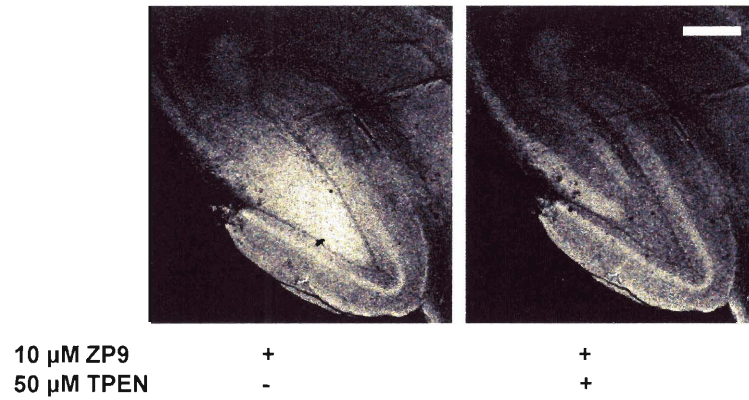
Figure 4.8. Confocal fluorescence images of an acute hippocampal slice from an adult female Sprague-Dawley rat. Left: the hippocampal slice was incubated with 10 μM ZP9 for 10 min (T = 37 °C, 5% CO_2) in Zn(II)-free Kreb's ringer buffer and washed thoroughly before imaging. Bright fluorescence is observed in the dentate gyrus region. Right: A fluroescence decrease is observed in the dentate gyrus following addition of 50 μM TPEN (5 min, T = 37 °C, 5% CO_2). The scale bar indicates 0.5 mm.
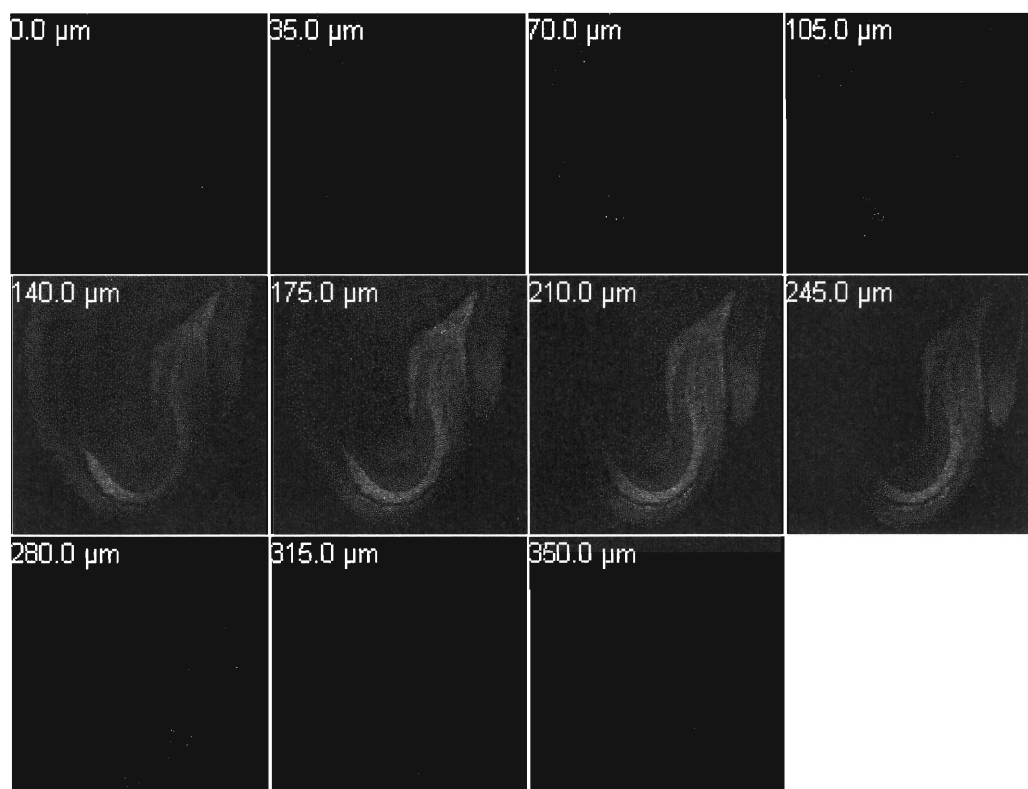
Figure 4.9. Optical z-sections obtained from confocal imaging of a hippocampal slice stainedwith 10 μM ZP4 for 20 min (T = 37 °C, 5% CO_2). The slice was treated as described in Figure 4.8. The optical sections indicate that the ZP dye has entered the tissue since no staining is observed at 0 and 350 μm.

Chapter 5

The Zinspy Family of Fluorescent Zinc Sensors:
Syntheses and Spectroscopic Investigations

Introduction

The creation of new tools and approaches for optical imaging in biology is an important goal, and investigations focused on these objectives will ultimately increase our understanding of many biological phenomena. Zinc is an essential nutrient required for normal growth and development,[1] and for key cellular processes such as DNA repair[2,3] and apoptosis.[4] Zinc concentrations are tightly regulated under normal physiological conditions.[1,5] Failure to maintain zinc homeostasis has been implicated in a number of pathologies including diabetes[6] and Alzheimer's disease.[7-9] Although most physiological zinc is tightly bound in metalloproteins,[1,10] histochemically observable and mobile zinc exists in several tissues including the brain.[11-15] In the glutamatergic neurons of the hippocampus, the center of learning and memory in the brain, calculations suggest that the concentrations of mobile or "free" zinc may reach near-millimolar values,[11] the physiological and pathological of which remains unclear.[12,16,17] Recent observations indicate that free zinc plays a number of beneficial and deleterious roles in neurobiology.[12,18-22] Our understanding of these phenomena has been hampered, in part, because of a lack of versatile imaging tools. The development and application of new zinc chemosensors for neurobiological investigations should ultimately help elucidate the significance of zinc in neurotransmission and memory formation, and in the pathogenesis of various neurological disorders.[23-33]

To address the need for fluorescent probes designed to detect zinc in biological samples, our laboratory has synthesized, characterized and utilized the Zinpyr (ZP) family of zinc sensors, many of which were described in Chapters 2-4 and are depicted in Figure 5.1.[34-39] ZP1-ZP8 contain either one or two di(2-picolyl)amine (DPA) derived ligands and generally give fluorescence enhancement with Zn(II) coordination. The high affinity of DPA for all divalent first-row transition metal ions, such as Fe(II) and Cu(II), is one disadvantage of the ZP family. With the aim of modulating binding affinity and increasing the selectivity of our sensors for zinc over other first-row

transition metals ions, we have investigated new ligand frameworks and a substantial portion of this work involved studies of ligands containing sulfur donors. Inspirations for assessing the utility of sulfur donors in zinc sensing come from the ubiquity of Zn—S linkages in biology,[10] the wealth of Zn—S coordination chemistry in the chemical literature and from our successful use of a thioether-derivatized fluroescein-based sensor, shown in Figure 5.1, for the detection of mercuric ion, a congener of Zn(II), in aqueous media.[40] Furthermore, we anticipated that sulfur donors should retain selectivity for Zn(II) over biologically relevant alkali and alkaline earth metals including Na(I), K(I), Ca(II) and Mg(II).

In this chapter, we introduce the Zinspy (ZS) family of zinc sensors. The members presented herein are based on halogenated fluorescein platforms and contain pyridyl-amine-thioether ligands. Since thioethers have relatively low affinity for Zn(II) and other borderline metal ions,[41] we reasoned that incorporation of this group into the Zn(II) binding chelate would confer lower affinity coordination and potentially improved selectivity relative to the parent ZP probes. Like the ZP family, the ZS sensors display water solubility and generally display fluorescence enhancement following Zn(II) complexation.

Experimental Section

Reagents. Solvents were prepared or purchased as described in Chapters 2 and 4. The asymmetrically derivatized fluoresceins, 7′-chloro-4′-fluoresceincarboxaldehyde,[37] **1**, and 7′-chloro-4′-bromomethylfluorescein di-*tert*-butyldimethylsilyl ether,[36] **2**, were synthesized as described elsewhere. 2′,7′-Difluorofluorescein (DFF) was purchased from Invitrogen, 2-(ethylthio)ethylamine was obtained from Alfa Aesar, and all other chemicals were purchased from Aldrich. With the exception of 2′,7′-dichlorofluorescein (DCF), which was recrystallized from boiling EtOH, all reagents were used as received.

Materials and Methods. Merck F254 silica gel-60 plates or octadecyl-functionalized silica gel (reverse phase, RP, RP18) plates were used for analytical thin layer chromatography (TLC). Preparative TLC was performed by using EM Science RP18 plates of 1 mm thickness. NMR spectra were obtained by using either a Varian 300 MHz or a Varian 500 MHz spectrometer operating at ambient probe temperature, 283 K. Internal probe standards were used for ^{1}H and ^{13}C NMR, and an external CFCl$_3$ reference was used for ^{19}F NMR. An Avatar 360 FTIR instrument was used to collect IR spectra. Low-resolution mass spectra were obtained by using an Agilent 1100 Series LC/MSD system. High-resolution mass spectrometry was performed by staff at the MIT Department of Chemistry Instrumentation Facility.

(2-Ethylsulfanylethyl)pyridin-2-ylmethylamine (3). Portions of 2-(ethylthio)ethyl-amine (1.0 g, 9.5 mmol) and 2-pyridinecarboxaldehyde (1.0 g, 9.4 mmol) were combined in 30 mL of dry MeOH to yield a light yellow solution that was stirred at room temperature. The solution turned brown and, after 18 h, NaB(OAc)$_3$H (2.4 g, 11 mmol) was added in two equal portions over 30 min. The mixture was stirred overnight at room temperature and the solvent was removed under reduced pressure to yield a brown oil. The oil was dissolved in CH$_2$Cl$_2$ (60 mL) and washed with saturated NaHCO$_3$ (3 x 60 mL) and water (1 x 60 mL). The organic portion was dried over MgSO$_4$ and the solvent was removed in vacuo to yield a brown oil. Flash chromatography on silica gel (10:1 CHCl$_3$/MeOH) afforded the purified product as a brown oil (1.0 g, 54%). TLC R$_f$ = 0.46 (silica, 10:1 CHCl$_3$/MeOH). ^{1}H NMR (CDCl$_3$, 300 MHz) δ 1.16 (3H, t), 2.44 (2H, q), 2.63 (2H, m), 2.78 (2H, t), 3.86 (2H, s), 7.07 (1H, m), 7.24 (1H, d), 7.55 (1H, t), 8.47 (1H, m). ^{13}C NMR (CDCl$_3$, 125 MHz) δ 14.75, 25.61, 31.72, 48.10, 54.72, 121.86, 122.09, 136.37, 149.19, 159.50. FTIR (NaCl disk, cm^{-1}) 3302 (m, br), 3050 (w), 3008 (w), 2963 (s), 2923 (s), 2870 (s), 2828 (s), 1711 (w), 1675 (w), 1590 (s), 1569 (s), 1473 (s), 1454 (s), 1433 (s), 1374 (m), 1356 (m), 1296 (w), 1264 (m), 1125 (w), 1048 (m), 994 (m), 973 (m), 844 (m), 756 (s), 628 (m), 609 (m). HRMS (ESI) Calcd [M + H]$^+$, 197.1107; Found, 197.1114.

(2-Ethylsulfanylethyl)(2-nitrobenzyl)pyridin-2-ylmethylamine (4). To 25 mL of MeCN were added **3** (500 mg, 3.06 mmol), 2-nitrobenzylbromide (662 mg, 3.06 mmol), K_2CO_3 (600 mg, 4.34 mmol), and activated 3 Å molecular sieves. The reaction was stirred vigorously at room temperature for 24 h and filtered through Celite, and the solvent was removed in vacuo to yield a brown oil. The crude material was flushed through a plug of silica gel (4:1 hexanes/EtOAc) to yield the pure product as a yellow oil (743 mg, 73%). TLC R_f = 0.35 (silica, 2:1 hexanes/EtOAc). ^{1}H NMR ($CDCl_3$, 300 MHz) δ 1.15 (3H, m), 2.39 (2H, q), 2.56-2.71 (4H, m), 3.75 (2H, s), 4.01 (2H, s), 7.11 (1H, m), 7.33-7.49 (2H, m), 7.51 (1H, td), 7.61 (1H, td), 7.72 (1H, d), 7.78 (1H, dd), 8.46 (1H, m). ^{13}C NMR ($CDCl_3$, 125 MHz) δ 14.86, 26.07, 28.80, 54.26, 56.08, 60.46, 122.24, 123.08, 124.52, 128.14, 131.25, 132.63, 134.64, 136.66, 148.92, 149.93, 150.10. FTIR (NaCl disk, cm^{-1}) 3064 (w), 3008 (w), 2963 (m), 2926 (m), 2828 (m), 2721 (w), 1608 (m), 1589 (s), 1570 (m), 1528 (s), 1474 (m), 1434 (m), 1362 (s), 1302 (m), 1265 (m), 1147 (m), 1114 (m), 1089 (m), 1047 (m), 994 (m), 973 (m), 857 (m), 819 (w), 783 (m), 760 (s), 730 (s), 705 (w), 668 (m), 638 (w), 617 (w). HRMS (ESI) Calcd [M + H]$^+$, 332.1427; Found, 332.1417.

2-{[(2-Ethylsulfanylethyl)pyridin-2-ylmethylamino]methyl}phenylamine (5). Pd black (606 mg) and 10 mL of MeOH were combined in a flask purged with Ar. A portion (308 mg, 0.929 mmol) of **4** was dissolved in 15 mL of MeOH and added to the reaction flask. The flask was purged with H_2 and the reaction was stirred vigorously under H_2 for 1.5 h. The mixture was filtered through Celite and the solvent was removed under reduced pressure. Chromatography on Al_2O_3 with a solvent gradient (5:1 to 1:1 hexanes/EtOAc) yielded the product as a yellow-orange oil (191 mg, 68%). TLC R_f = 0.45 (Al_2O_3, 3/1 hexanes:EtOAc). ^{1}H NMR ($CDCl_3$, 300 MHz) δ 1.14 (3H, m), 2.35 (2H, m), 2.64-2.75 (2H, m), 3.66 (2H, s), 3.73 (2H, s), 4.80 (2H, br s) 6.60-6.67 (2H, m), 7.00-7.14 (3H, m), 7.30 (1H, d), 7.60 (1H, td), 8.50 (1H, dq). ^{13}C NMR ($CDCl_3$, 125 MHz) δ 14.76, 25.78, 28.99, 53.26, 58.18, 60.09, 115.53, 117.50, 122.10, 122.33, 123.52, 128.60, 130.94, 136.36, 146.99, 149.00, 159.23. FTIR (NaCl disk, cm^{-1}) 3423 (s), 3314 (s), 3208 (m), 3009

(m), 2962 (s), 2924 (s), 2869 (m), 2813 (s), 2717 (w), 1616 (s), 1590 (s), 1569 (m), 1495 (s), 1474 (m), 1460 (s), 1433 (s), 1373 (m), 1315 (m), 1288 (m), 1265 (m), 1148 (m), 1125 (m), 1104 (m), 1048 (m), 995 (m), 969 (m), 932 (w), 869 (w), 847 (w), 752 (s), 723 (w), 637 (w), 614 (w), 541 (w). HRMS (ESI) Calcd [M + H]$^+$, 302.1685; Found, 302.1694.

2-{2-Chloro-5-[(2-{[(2-ethylsulfanylethyl)pyridin-2-ylmethylamino]methyl}phenyl-amino)methyl]-6-hydroxy-3-oxo-3*H*-xanthen-9-yl}benzoic acid (6, Zinspy-4, ZS4). Portions of **5** (53 mg, 0.192 mmol) and **1** (68 mg, 0.172 mmol) were combined in 3 mL of EtOAc and stirred overnight at room temperature. The intermediate Schiff base **7** precipitated as a bright yellow solid. The reaction was cooled on ice and filtered, and the precipitate was washed with ~3 mL of cold EtOAc and dried. The precipitate was dissolved in 5 mL of DCE and NaB(OAc)$_3$H (60 mg, 0.28 mmol) was added. The reaction was stirred at room temperature for 6 h, diluted with 5 mL of CH$_2$Cl$_2$ and washed with H$_2$O (3 x 10 mL). The organic layer was dried to yield a red-orange solid (71 mg, 60%, purity >90% by NMR). A portion (~32 mg) of the crude material was purified by preparative TLC on reverse phase silica gel (100% MeOH), which gave the product as a red-orange solid (18 mg, 56% recovered). TLC R$_f$ = 0.69 (RP18 silica, MeOH); mp = 89–91 °C. ^{1}H NMR (CDCl$_3$, 300 MHz) δ 1.10 (3H, t), 2.30 (2H, q), 2.63-2.71 (4H, m), 3.75 (4H, m), 4.78 (2H, s), 6.54 (2H, m), 6.76-6.95 (5H, m), 7.07-7.27 (5H, m), 7.58-7.72 (2H, m), 8.05 (1H, d), 8.49 (1H, d). FTIR (KBr, cm^{-1}) 3436 (s), 2963 (w), 2924 (w), 2853 (w), 1761 (m), 1674 (s), 1625 (m), 1613 (m), 1514 (w), 1455 (m), 1422 (m), 1375 (w), 1261 (s), 1201 (s), 1178 (s), 1092 (s), 1022 (s), 871 (w), 800 (s), 757 (w), 720 (w), 702 (w). HRMS (ESI) Calcd [M + H]$^+$, 680.1980; Found, 680.1962.

2-(2,7-Dichloro-4,5-bis-{[(2-ethylsulfanylethyl)pyridin-2-ylmethylamino]methyl}-6-hydroxy-3-oxo-3*H*-xanthen-9-yl)benzoic acid (8, Zinspy-1, ZS1). Paraformaldehyde (12 mg, 0.41 mmol) and **3** (79 mg, 0.31 mmol) were combined in MeCN (6 mL) and refluxed for 1 h. A slurry of 2′,7′-dichlorofluorescein (50 mg, 0.13 mmol) in 1:1 MeCN/H$_2$O (6 mL) was added to the reaction and the solution immediately turned

pink-red. The reaction was refluxed for 24 h and cooled, and the solvents were removed under reduced pressure. Preparative TLC on reverse phase silica gel (100% MeOH) yielded the purified product as an orange-pink solid (69 mg, 67%). TLC R_f = 0.44 (RP18 silica, MeOH); mp = 79-80 °C. ^{1}H NMR (CD$_3$OD, 300 MHz) δ 1.14 (6H, t), 2.41 (4H, q), 2.79 (4H, t), 2.97 (4H, t), 4.07 (4H, s), 4.24 (4H, s), 6.61 (2H, s), 7.24 (1H, d), 7.34 (2H, t), 7.46 (2H, d), 7.71-7.80 (4H, m), 8.06 (1H, d), 8.55 (2H, d). ^{13}C NMR (DMF-d_7, 125 MHz) δ 14.66, 25.45, 28.13, 49.90, 53.50, 58.22, 82.81, 110.72, 112.09, 116.96, 123.20, 124.21, 124.46, 125.42, 127.05, 127.15, 130.90, 136.11, 137.63, 148.77, 149.17, 152.14, 156.58, 157.43, 168.77. FTIR (KBr, cm^{-1}) 3121 (w), 2967 (w), 2923 (w), 2851 (w), 1760 (s), 1625 (m), 1597 (m), 1572 (m), 1466 (s), 1434 (s), 1399 (s), 1283 (s), 1262 (m), 1211 (m), 1152 (w), 1095 (s), 1013 (m), 889 (w), 867 (m), 801 (w), 758 (m), 727 (w), 699 (m), 676 (w), 619 (w), 560 (w), 482 (w). HRMS (ESI) Calcd [M − H]$^-$, 815.1901; Found, 815.1931.

2-(4,5-Bis-{[(2-ethylsulfanylethyl)pyridin-2-ylmethylamino]methyl}-2,7-difluoro-6-hydroxy-3-oxo-3H-xanthen-9-yl)benzoic acid (9, Zinspy-2, ZS2). Paraformaldehyde (13.1 mg, 0.452 mmol) and **3** (80.6 mg, 0.411 mmol) were combined in MeCN (6 mL) and refluxed for 1 h. A slurry of 2′,7′-difluorofluorescein (50.0 mg, 0.136 mmol) in 1:1 MeCN/H$_2$O (6 mL) was added to the reaction and the solution immediately turned pink-red. The reaction was refluxed for 24 h and cooled, and the solvents were removed under reduced pressure. Preparative TLC on reverse phase silica gel (100% MeOH) yielded the purified product as an orange-pink solid (42 mg, 39%). TLC R_f = 0.36 (RP18 silica, MeOH); mp = 65-67 °C. ^{1}H NMR (CD$_3$OD, 300 MHz) δ 1.15 (6H, t), 2.43 (4H, q), 2.87 (4H, t), 3.17 (4H, t), 4.24 (4H, s), 4.42 (4H, s), 6.54 (2H, d), 7.22 (1H, d), 7.33 (2H, t), 7.47 (2H, d), 7.68-7.81 (4H, m), 8.09 (1H, d), 8.52 (2H, d). ^{13}C NMR (DMF-d_7, 125 MHz) δ 14.67, 25.47, 28.30, 49.65, 53.74, 58.35, 108.61, 112.58, 112.75, 113.38, 123.11, 124.07, 124.47, 125.43, 127.15, 130.72, 135.88, 137.64, 146.32, 147.48, 149.03, 149.40, 157.80, 168.78. ^{19}F NMR (300 MHz) δ 27.62. FTIR (KBr, cm^{-1}) 3392 (m, br), 2962 (m), 2923 (m), 2851 (m), 1760 (m), 1701 (w), 1647 (m), 1606 (m), 1570 (w), 1559 (w), 1476 (s), 1438 (s), 1394 (m),

1373 (s), 1289 (s), 1262 (m), 1204 (m), 1163 (m), 1098 (m), 1043 (m), 864 (w), 802 (w), 761 (m), 717 (w), 635 (w), 577 (w), 520 (w). LRMS (ESI) Calcd [M − H]⁻, 783.3; Found, 783.3.

2-(2-Chloro-5-{[(2-ethylsulfanylethyl)pyridin-2-ylmethylamino]methyl}-6-hydroxy-3-oxo-3*H*-xanthen-9-yl)benzoic acid (9, Zinspy-3, ZS3). To 3 mL of MeCN were added 2′-chloro-5′-bromomethylfluorescein di-*tert*-butyldimethylsilyl ether (**2**, 100 mg, 0.146 mmol) and K_2CO_3 (100 mg, 0.724 mmol) and the solution was stirred. A portion (20 mg, 0.148 mmol) of **3** was dissolved in 2 mL of MeCN and added drop-wise to the reaction mixture. The color changed from yellow-orange to pink and the reaction was stirred overnight at room temperature. A pink precipitate formed and the solution was filtered. TLC analysis on RP18 silica (100% MeOH) showed that both the filtrate and precipitate contained the desired product. Preparative TLC of the combined materials on RP18 silica gel (100% MeOH) afforded pure ZS3 as an orange solid (70 mg, 83%). TLC R_f = 0.65 (RP18 silica, MeOH); mp = 97-100 °C. ^{1}H NMR (CD₃OD, 300 MHz) δ 1.15 (3H, t), 2.42 (2H, q), 2.85 (2H, t), 3.01 (2H, t), 4.08 (2H, s), 4.28 (2H, s), 6.56 (1H, d), 6.67 (1H, d), 6.77 (1H, s), 6.82 (1H, s), 7.23 (1H, d), 7.34 (1H, t), 7.50 (1H, d), 7.69-7.83 (3H, m), 8.06 (1H, d), 8.52 (1H, d). ^{13}C NMR (DMF-d_7, 125 MHz) δ 14.74, 25.45, 28.07, 48.27, 53.55, 58.83, 104.39, 110.03, 110.42, 110.57, 113.25, 117.72, 122.89, 123.91, 124.73, 125.24, 127.50, 128.01, 128.40, 130.53, 135.73, 137.29, 149.18, 150.59, 151.55, 152.31, 157.83, 158.27, 160.83, 169.08. FTIR (KBr, cm⁻¹) 3431 (m, br), 2954 (w), 2923 (w), 1760 (m), 1627 (m), 1578 (s), 1516 (m), 1489 (m), 1464 (s), 1384 (s), 1284 (m), 1259 (m), 1210 (m), 1151 (m), 1107 (m), 1091 (m), 1070 (w), 1009 (w), 871 (w), 801 (w), 759 (w), 702 (w), 622 (w), 597 (w), 551 (w), 471 (w). HRMS (ESI) Calcd [M + H]⁺, 575.1407; Found, 575.1428.

General Spectroscopic Procedures. All aqueous solutions were prepared with Millipore water (18.2 MΩ·cm at 25 °C) obtained from a Mill-Q Biocel purified outfitted with a Quantum VX cartridge. Buffer components were purchased from either Calbiochem or Sigma in the highest available purity. A 100 mM stock solution of Zn(II) was prepared from 99.999% anhydrous $ZnCl_2$ purchased from Alrdrich. DMSO stock

solutions of the ZS probes (1 mM ZS1 to ZS3, 0.77 mM ZS4) were prepared, aliquoted, stored at –25 °C and thawed in the dark immediately before use. A buffer containing 50 mM PIPES, piperazine-N,N'-bis(2-ethanesulfonic acid), 100 mM KCl was used for measurements at pH 7. Data collected at pH 11 were obtained by using 50 mM CABS, 4-cyclohexylamino-1-butanesulfonic acid, 100 mM KCl as the buffer. Fluorescence spectra were obtained on a Hitachi F-3010 spectrophotometer. UV-visible spectra were recorded on a Hewlett-Packard 8453A diode array or on a Cary 1E scanning spectrophotometer. All instruments were maintained at 25 °C ± 1 °C with a circulating water bath. Samples were contained in 1 cm x 1 cm quartz cuvettes (3.5 mL volume, Starna). Quantum yields were determined relative to fluorescein in 0.1 N NaOH (Φ = 0.95).[42] All spectroscopic measurements were conducted as described in Chapter 2.

Results and Discussion

Syntheses. Two general strategies for the assembly of fluorescein-based metal ion sensors have been employed in our laboratory.[35-37] These methodologies include the following: (i) Mannich reactions between a 2',7'-disubstituted fluorescein and the imminium ion condensation product of paraformaldehyde and a secondary amine, which yield symmetrical sensors with two metal ion coordination sites; and (ii) stepwise routes that afford asymmetrical sensors with one metal ion binding site. The general applicability of these synthetic approaches is further illustrated in the present work.

The synthesis of the pyridine-amine-thioether ligand, **3**, the fragment common to all sensors in this ZS group, is shown in Scheme 5.1. Combination of 2-(ethylthio)-ethylamine and 2-pyridinecarboxaldehyde in dry MeOH followed by reduction of the intermediate Schiff base with NaB(OAc)$_3$H afforded **3** in moderate yield (56%) following purification on silica gel (10:1 CHCl$_3$/MeOH) as a volatile yellow-brown oil with a faint odor. We note that this reaction is concentration-dependent and adequate solvent must be used for the reaction to proceed reproducibly. Without further

modification, **3** can be used in the construction of metal ion sensors that contain a tertiary amine as the PET quenching moiety (vide infra) analogous to the DPA-derived sensors ZP1 – ZP3. Scheme 5.1 also illustrates the route to the aniline-derivatized compound **5**, which serves as a ligand fragment for ZS4 and is analogous to the DPA-incorporated metal-binding unit found in sensors ZP4-ZP8. The synthesis of **5** was accomplished in two additional steps, each of good yield. Combination of **3** with 2-nitrobenzylbromide and excess K_2CO_3 in dry MeCN afforded **4** as a yellow-orange oil in 73% yield after purification on silica gel (3:1 hexanes/EtOAc). Hydrogenation of **4** in MeOH using Pd black followed by chromatography on Al_2O_3 with a solvent gradient (5:1 to 1:1 hexanes/EtOAc) gave pure **5** as a yellow-orange oil in 68% yield. Compounds **3** - **5** are stable for a minimum of two years when stored at 4 °C.

Sensors ZS1, **8**, and ZS2, **9**, were assembled via Mannich reactions between either 2',7'-dichlorofluorescein (ZS1) or 2',7'-difluorofluorescein (ZS2) and the imminium ion condensation product of **3** and paraformaldehyde, as indicated in Scheme 5.2. Unlike the ZP sensors, which precipitate from refluxing MeCN/H_2O mixtures, ZS1 and ZS2 remained in solution after cooling to 0 °C. After solvent removal, the sensors were purified by preparative TLC on RP silica gel (100% MeOH). ZS1 and ZS2 were both obtained as orange-red solids in moderate to good yields of 67% and 39%, respectively.

The syntheses of ZS3, **10**, and ZS4, **6**, are outlined in Schemes 5.1 and 5.2. In both cases, the chemosensors were assembled from an asymmetrical fluorescein derivatized in the 4' position with either a benzyl bromide (ZS3) or carboxaldehyde (ZS4). Combination of **3** and 1 equiv of **2** with excess K_2CO_3 in dry MeCN gave crude ZS3. The TBS protecting groups of **2** are unstable to these conditions, and deprotection occurs during the course of the reaction. Purification by preparative TLC on RP silica gel (100% MeOH) afforded ZS3 as an orange powder in 83% yield. Combination of **5** with 7'-chloro-4'-fluoresceincarboxaldehyde, **1**, in dry EtOAc resulted in precipitation of the intermediate Schiff base as a bright yellow solid. After filtration, the intermediate imine

was reduced with NaB(OAc)$_3$H in DCE to afford crude ZS4 in 60% yield (purity ~90%). Preparative TLC on RP silica gel (100% MeOH) yielded pure ZS4 as a red-orange solid (56% of material recovered).

Spectroscopic Characterization. Table 5.1 summarizes the fluorescence and optical absorption spectroscopic properties for the dyes investigated here, together with several other zinc sensors developed in our laboratory for comparison. Like the ZP probes, the ZS dyes are intensity-based sensors that utilize tertiary amine- (ZS1 – ZS3) or aniline-based groups as the photoinduced electron transfer (PET) quenching units.

Spectroscopic Properties of ZS1 and ZS2. The sensitivity of PET-based ZP probes to protonation is well documented.[34-39] To assess the effect of pH on the emission of free ZS1 and ZS2, fluorescence titrations were conducted. Representative data are given in Figure 5.2. ZS1 and ZS2 exhibit similar pH-dependent fluorescence spectral properties. Two protonation events alter the emission of apo ZS1 and ZS2, with the former exhibiting values for pK_{a1} of 7.7 and pK_{a2} of 2.0, and for the latter pK_{a1} is 7.7 and pK_{a2} is 2.7. In both instances, pK_{a1} is assigned to protonation of the tertiary amine responsible for PET quenching of the free probe. pK_{a2} is attributed to protonation of the fluorescein fragment and formation of a nonfluorescent isomer at low pH. Based on related studies presented in Chapters 2 and 3, we assign this transition to phenol protonation.

Under simulated physiological conditions (50 mM PIPES, 100 mM KCl, pH 7) and in the presence of excess EDTA to scavenge any adventitious metal ions, apo ZS1 and ZS2 exhibit quantum yields of 0.50 (λ_{max} = 531 nm) and 0.39 (λ_{max} = 523 nm), respectively. These data show that substitution of the chlorine atoms at the 2′ and 7′ positions of the fluorescein in ZS1 with fluorine to give ZS2 decreases the quantum yield of the unbound dye without influencing the pK_a of the tertiary amine nitrogen atom responsible for PET quenching in the apo form. These results were initially surprising to us, given our earlier study investigating the effect of fluroescein halogenation on the properties of ZP sensors (Chapters 2 and 3).[39] A comparison of ZP1 and ZP3 indicated

that substitution of chlorine atoms at the 2' and 7' positions of the fluorescein moiety with fluorine reduced the background fluorescence (ZP1, Φ = 0.38; ZP3, Φ = 0.15) and also lowered the tertiary amine pK_a significantly (ZP1, pK_a = 8.4; ZP3, pK_a = 6.8). A comparison of the ZS1/ZS2 to the ZP1/ZP3 results indicates that the relative magnitude of the quantum yield for an apo sensor is not solely a function of nitrogen pK_a. Although tertiary amine pK_a may be used as a rough indicator of anticipated relative background fluorescence, the correlation is not as clear as originally thought from studies of DPA-based ZP sensors.[39] Also, a background fluorescence reduction was previously documented in the ZnAF series of benzoate-ring substituted Zn(II) sensors, where substitution of fluorescein with 2',7'-difluorofluorescein lowered the quantum yield of from 0.022 (ZnAF-1) to 0.004 (ZnAF-1F).[28]

Modest fluorescence enhancement is observed upon addition of excess Zn(II) to aqueous solutions of ZS1 and ZS2. For both sensors, Φ_{Zn} is ~0.7 for the Zn(II) complexes, with ZS1 displaying an ~1.4-fold increase and ZS2 an ~2-fold increase in integrated emission (Figure 5.3). Both emission and optical absorption spectra for free ZS1 and ZS2 are dominated by the fluroescein chromophore and blue-shift slightly upon Zn(II) coordination (Table 5.1). For ZS1, the absorption maximum shifts from 510 nm (ε = 84,000 $M^{-1}cm^{-1}$) to 501 nm (ε = 75,000 $M^{-1}cm^{-1}$), and the difference spectrum shows an absorption decrease at 515 nm and increases at 462 and 493 nm. ZS2 exhibits a 10 nm shift from 499 nm (ε = 67,000 $M^{-1}cm^{-1}$) to 489 nm (ε = 68,000 $M^{-1}cm^{-1}$) and the difference spectrum shows an absorption decrease at 506 nm and increases at 454 nm and 484 nm. These blue shifts reflect a perturbation of the fluorescein π-system and indicate that the phenol oxygen atoms are involved in Zn(II) coordination. Like the ZP probes, ZS1 and ZS2 also display enhanced fluorescence upon the addition of Cd(II) (Table 5.1.).

Spectroscopic Properties of ZS3. Fluorescence spectroscopy was used to monitor the pH dependent properties of ZS3, revealing two protonation events that alter ZS3 fluorescence with pK_{a1} = 9.3 and pK_{a2} = 4.5 (Figure 5.2). The former value is assigned to

protonation of the tertiary amine atom responsible for PET quenching of the unbound dye and the latter to protonation of the fluorescein phenol moiety. The latter pK_a value is in agreement with those determined for other sensors based on the monochlorofluorescein platform.[37,40] ZS3 maintains its maximum fluorescence from pH ~6 to ~8 and exhibits a quantum yield of 0.71 (λ_{max} = 525 nm) at pH 7 and in the presence of EDTA. It is interesting to note that ZS3 has a similar pK_a value to the symmetrical sensor ZP2 (pK_a = 9.4; Φ_{free} = 0.25)[35] and significantly greater background fluorescence as measured by Φ_{free}. This behavior indicates that both tertiary amine-based ligands contibute to fluorophore quenching in the symmetrical ZP and ZS probes. The absorption spectrum of ZS3 has a maximum at 500 nm (ε = 87,000 $M^{-1}cm^{-1}$). As a result of the high quantum yield of apo ZS3, essentially no fluorescence increase occurs upon addition of excess Zn(II) at neutral pH. Addition of excess Cd(II) causes an ~10% fluorescence increase and excess Hg(II) causes an ~40% fluorescence decrease at pH 7.

The high background fluorescence of ZS3 renders it unsuitable for any sensing application at neutral pH. To investigate further PET and the effect of the pyridyl/thioether ligand substitution, we conducted several studies at pH 11, which should favor deprotonation of the tertiary amine atom and decrease background fluorescence. At pH 11 (50 mM CABS, 100 mM KCl), the fluorescence of ZS3 is effectively quenched with Φ_{free} = 0.07 (λ_{max} = 525 nm). An ~2.4-fold fluorescence enhancement occurs upon addition of excess Zn(II) with Φ_{Zn} = 0.17. Coordination of ZS3 to Cd(II) and Hg(II) yields greater fluorescence enhancement at pH 11 than observed for Zn(II). Upon addition of excess Cd(II) to ZS3 at pH 11, an ~15-fold increase in integrated emission is observed, resulting from changes in both quantum yield and molar absorptivity (λ_{max} = 527 nm, Φ_{Cd} = 0.69; ε_{500} = 84,000 $M^{-1}cm^{-1}$). Excess Hg(II) cases an ~5.7-fold fluorescence enhancement (λ_{max} = 530 nm, Φ_{Hg} = 0.40; ε_{505} = 84,000 $M^{-1}cm^{-1}$). Job plots and metal ion binding titrations conducted at pH 7 and 11 indicate that ZS3 forms a 1:1 complex with all three Group 12 metal ions (Figures 5.4 and 5.5).

Spectroscopic and Metal Binding Properties of ZS4. Sensor ZS4 contains an aniline-derivatized (2-ehtylsulfanylethyl)pyridin-2-ylmethylamine moiety (Scheme 5.1). On the basis of previous studies in our laboratory comparing ZP1 to ZP3 with ZP4 to ZP8, we anticipated that ZS4 would exhibit lower background fluorescence than ZS1 to ZS3. As expected, at pH 7 and 100 mM ionic strength, free ZS4 has a quantum yield of 0.12 (λ_{max} = 522 nm) compared to 0.71 for ZS3, 0.50 for ZS1 and 0.39 for ZS2. The fluorescence pH profile of ZS4, depicted in Figure 5.1, shows two changes deriving from pK_{a1} = 7.6 and pK_{a2} = 5.1. The former value is assigned to the aniline nitrogen atom and the latter to phenol protonation and formation of a non-fluroescent isomer. A comparison of the pH profiles included in Figure 5.1 shows that less fluorescence change occurs following protonation of the aniline nitrogen atom in ZS4 compared to tertiary amine protonation in other ZS sensors.

As indicated in Figure 5.3, sensor ZS4 exhibits ~4.5-fold fluorescence enhancement immediately after addition of excess Zn(II) and a quantum yield of 0.50 (λ_{max} = 520 nm) at neutral pH. Although this result was encouraging, an ~25% decrease in fluorescence intensity was observed several minutes after mixing of the ZS4/Zn(II) solution, which contrasts the stable fluorescence increase observed for ZS1-3 and ZP sensors upon Zn(II) addition. Unexpected changes were also observed in the optical absorption spectra (Figure 5.6). Upon introduction of Zn(II) to a solution of ZS4, the absorption spectrum initially undergoes a blue shift from 507 (ε = 81,000 $M^{-1}cm^{-1}$) to 495 nm (spectra a and b). Over the course of ~15 min, A_{max} decreases substantially, and a shoulder develops at ~530 nm (spectra b to c). Inspection of the sample revealed formation of a precipitate, supported by the rising baseline in the red region of the optical spectrum, arising from light scattering. Upon introduction of excess EDTA, the absorption spectrum undergoes a red shift back to 507 nm with no change in A_{max} immediately after mixing (spectra c to d). Over the course of several hours, the absorption spectrum for the EDTA-containing solution becomes comparable to the

initial spectra of free ZS4 (spectra d to e). These data indicate that ligand decomposition is not responsible for the spectral changes observed upon introduction of Zn(II) to a solution of ZS4.

Under identical conditions, stable fluorescence enhancement of ZS4 is observed upon addition of Cd(II) or Hg(II), although the increase upon Hg(II) addition is negligible (Figure 5.7). The presence of excess Cd(II) causes an ~4-fold fluorescence increase (λ_{max} = 521 nm, Φ_{Cd} = 0.50) and the absorption spectrum blue-shifts to 498 nm (ε = 90,000 $M^{-1}cm^{-1}$). Metal binding titrations and Job plots for the addition of Cd(II) and Hg(II) to solutions of ZS4 indicate formation of well-defined 1:1 complexes (Figures 5.8 and 5.9). Although Cu(II) binding results in slight fluorescence quenching, its coordination to ZS4 and the water solubility of the resulting complex were also investigated to gain further insight into the metal-binding properties of this ligand. In addition to bands associated with perturbation of the xanthene π system, the optical absorption difference spectrum of solutions containing ZS4 and Cu(II) exhibits an intense band ca. 450 nm, attributed to $\sigma(s) \rightarrow$ Cu(II) LMCT.[43] Like Cd(II) and Hg(II), metal binding titrations of ZS4 with Cu(II) reveal 1:1 stoichiometry in solution (Figures 5.8 and 5.10) and this complex exhibits good solubility at a concentration of 10 µM. Given the water solubility of these 1:1 complexes, the insolubility of the ZS4:Zn(II) complex, even at 1 µM concentration, is anomalous. Although we speculate that the ZS4:Zn(II) species may be some dimeric or polymeric species, its exact nature is currently unknown. We questioned if the high chloride concentration in the buffer might contribute to the precipitation problem since chloride can bridge between two Zn(II) centers, but ruled this possibility out since similar spectral changes were observed in buffer containing nitrate as the anion.

Zinc Coordination and Selectivity. The sensors described in this section have either N_2SO (ZS1-3) or N_3SO donor sets. Given the choice of a sulfur donor that has low affinity for borderline metals, one question that arises is whether the thioether moiety

might be involved in Zn(II) coordination. Multiple literature reports show that alkyl transfer to a Zn(II)-coordinated thiolates results in displacement of the resulting thioether from the Zn(II) coordination sphere,[44-46] which suggests that the thioether moieties of ZS1-4 may not bind. On the other hand, Zn(II)-bound thioethers were isolated from methylation of several Zn(II) heteroscorpinoate ligands[47] and other complexes with Zn(II)-bound thioethers have been characterized crystallographically, which include ligands with mixed nitrogen and sulfur donor sets.[48,49] Although dissociation constants were not determined for the ZS sensors, excess Zn(II) is required to achieve full fluorescence enhancement for ZS1 and ZS2, indicative of lower affinity binding relative to the parent ZP probes. Additionally, qualitative comparisons of Job plots and metal binding titrations of ZS3 and ZS4 with Zn(II) and its Group 12 congeners suggests an affinity ordering of Hg(II) > Cd(II) > Zn(II). This trend presumably reflects preferential coordination of the thioether to the soft Hg(II) center. We speculate that the thioether donor is either only weakly associated to or non-coordinating with the Zn(II) center.

Achieving Zn(II) selectivity is important. As stated above, we anticipated that replacement of one pyridyl arm of a ZP sensor with a soft sulfur donor, such as the thioether moiety utilized in this work, might improve selectivity for Zn(II). All ZS sensors exhibit analogous metal ion selectivity and Figure 5.11 illustrates the results of these studies for representative ZS2 and ZS4. Both molecules are selective for Zn(II) over Ca(II), Mg(II), Mn(II) and Fe(II). The selectivity for Zn(II) over Fe(II) is a significant advantage over the behavior observed for DPA-derived zinc sensors.

Summary and Perspectives

The Zinspy sensors presented in this chapter were the first fluorescein-based probes with ligands other than DPA prepared in our laboratory that achieved fluorescence enhancement following Zn(II) coordination. Although the fluorescence properties of

these sensors are at best modest, this systematic study afforded several key pieces of information. Firstly, we observed that the correlation between background fluorescence, measured by quantum yield, and pK_a observed for ZP1/ZP3 and ZP4/ZP8 does not always hold. Some other feature of the 2',7'-difluorofluorescein platform contributes to lowering of the quantum yield relative to fluorescein or 2',7'-dichlorofluorescein. Secondly, we found that significantly less fluorescence quenching occurs when a fluorescein is substituted with only one tertiary amine-based chelate (ZS3) instead of two (ZS1, ZS2), which suggests that both ligand groups contribute to quenching of the fluorescein excited state. This observation contributed to work on the QZ systems, which are discussed in Chapter 7. Thirdly, we found that replacement of a pyridyl group of DPA with a weak donor modulates Zn(II) affinity and selectivity. The selectivity for Zn(II) over Fe(II) may be significant for biological work since failure of Fe(II) homeostasis has been correlated with various pathologies. In the next chapter, we present modified ZS sensors designed to maintain selectivity for Zn(II) over Fe(II) and improve dynamic range.

References

(1)   Vallee, B. L.; Falchuk, K. H. *Physiol. Rev.* **1993**, *73*, 79-118.

(2)   Ho, E.; Ames, B. N. *Proc. Nat. Acad. Sci. USA* **2002**, *99*, 16770-16775.

(3)   Daiyasu, H.; Osaka, K.; Ishino, Y.; Toh, H. *FEBS Lett.* **2001**, *503*, 1-6.

(4)   Troung-Tran, A. Q.; Carter, J.; Ruffin, R. E.; Zalewski, P. D. *Biometals* **2001**, *14*, 315-330.

(5)   Takeda, A. *Biometals* **2001**, *14*, 343-351.

(6)   Chausmer, A. B. *J. Am. Coll. Nutr.* **1998**, *17*, 109-115.

(7)   Bush, A. I. *Alzheimer Dis. Assoc. Disord.* **2003**, *17*, 147-150.

(8)   Bush, A. I. *Trends Neurosci.* **2003**, *26*, 207-214.

(9)   Suh, S. W.; Jensen, K. B.; Jensen, M. S.; Silva, D. S.; Kesslak, P. J.; Danscher, G.; Frederickson, C. J. *Brain Res.* **2000**, *852*, 274-278.

(10)   Lippard, S. J.; Berg, J. M. *Principles of Bioinorganic Chemistry, First Edition;* University Science Books: Mill Valley, 1994.

(11)   Frederickson, C. J. *Int. Rev. Neurobiol.* **1989**, 31, 145-238.

(12)   Frederickson, C. J.; Bush, A. I. *Biometals* **2001**, *14*, 353-366.

(13)   Qian, W.-J.; Gee, K. R.; Kennedy, R. T. *Anal. Chem.* **2003**, *75*, 3468-3475.

(14)   Gee, K. R.; Zhou, Z.-L.; Qian, W.-J.; Kennedy, R. *J. Am. Chem. Soc.* **2002**, *124*, 776-778.

(15)   Zalewski, P. D.; Millard, S. H.; Forbes, I. J.; Kapaniris, O.; Slavotinek, A.; Betts, W. H.; Ward, A. D.; Lincoln, S. F.; Mahadevan, I. *J. Histochem. Cytochem.* **1994**, *42*, 877-884.

(16)   Kay, A. R. *J. Neurosci.* **2003**, *23*, 6847-6855.

(17)   Frederickson, C. J.; Maret, W.; Cuajungco, M. P. *The Neuroscientist* **2004**, *10*, 18-25.

(18)   Cuajungo, M. P.; Lees, G. J. *Neurobiol. Disease* **1997**, *4*, 137-169.

(19)   Choi, D. W.; Koh, J. Y. *Annu. Rev. Neurosci.* **1998**, *21*, 347-375.

(20)   Bush, A. I. *Curr. Opin. Chem. Biol.* **2000**, *4*, 184-191.

(21)   Li, Y. V.; Hough, C. J.; Sarvey, J. M. *Science STKE* **2003**, pe 19.

(22)   Frederickson, C. J. *Science STKE* **2003**, pe 18.

(23)   Frederickson, C. J.; Kasarskis, E. J.; Ringo, D.; Frederickson, R. E. *J. Neurosci. Methods* **1987**, *20*, 91-103.

(24)   Henary, M. M.; Wu, Y.; Fahrni, C. J. *J. Phys. Chem. A* **2002**, *106*, 5210-5220.

(25)   Henary, M. M.; Wu, Y.; Fahrni, C. J. *Chem. Eur. J.* **2004**, *10*, 3015-3025.

(26)   Taki, M.; Wolford, J. L.; O'Halloran, T. V. *J. Am. Chem. Soc.* **2004**, *126*, 712-713.

(27)   Maruyama, S.; Kikuchi, K.; Hirano, T.; Urano, Y.; Nagano, T. *J. Am. Chem. Soc.* **2002**, *124*, 10650-10651.

(28)   Hirano, T.; Kikuchi, K.; Urano, Y.; Nagano, T. *J. Am. Chem. Soc.* **2002**, *124*, 6555-6562.

(29)   Woodroofe, C. C.; Lippard, S. J. *J. Am. Chem. Soc.* **2003**, *125*, 11458-11459.

(30)   Chang, C. J.; Jaworski, J.; Nolan, E. M.; Sheng, M.; Lippard, S. J. *Proc. Natl. Acad. Sci. USA* **2004,** *101,* 1129-1134.

(31)   Sensi, S. L.; Ton-That, D.; Weiss, J. H.; Rothe, A.; Gee, K. R. *Cell Calcium* **2003,** *34,* 281-284.

(32)   Jiang, P.; Guo, Z. *Coord. Chem. Rev.* **2004,** *248,* 205-229.

(33)   Kikuchi, K.; Komatsu, K.; Nagano, T. *Curr. Opin. Chem. Biol.* **2004,** *8,* 182-191.

(34)   Walkup, G. K.; Burdette, S. C.; Lippard, S. J.; Tsien, R. Y. *J. Am. Chem. Soc.* **2000,** *122,* 5644-5645.

(35)   Burdette, S. C.; Walkup, G. K.; Springler, B.; Tsien, R. Y.; Lippard, S. J. *J. Am. Chem. Soc.* **2001,** *123,* 7831-7841.

(36)   Burdette, S. C.; Frederickson, C. J.; Bu, W.; Lippard, S. J. *J. Am. Chem. Soc.* **2003,** *125,* 1778-1787.

(37)   Nolan, E. M.; Burdette, S. C.; Harvey, J. H.; Hilderbrand, S. A.; Lippard, S. J. *Inorg. Chem.* **2004,** *43,* 2624-2635.

(38)   Chang, C. J.; Nolan, E. M.; Jaworski, J.; Okamoto, K.-I.; Hayashi, Y.; Sheng, M.; Lippard, S. J. *Inorg. Chem.* **2004,** *43,* 6774-6779.

(39)   Chang, C. J.; Nolan, E. M.; Jaworski, J.; Burdette, S. C.; Sheng, M.; Lippard, S. J. *Chem. Biol.* **2004,** *11,* 203-210.

(40)   Nolan, E. M.; Lippard, S. J. *J. Am. Chem. Soc.* **2003,** *125,* 14270-14271.

(41)   Sigel, H.; Rheinberger, V. M.; Fischer, B. E. *Inorg. Chem.* **1979,** *18,* 3334-3339.

(42)   Brannon, J. H.; Madge, D. *J. Phys. Chem.* **1978,** *82,* 705-709.

(43)   Miskowski, V. M.; Thich, J. A.; Solomon, R.; Schugar, H. J. *J. Am. Chem. Soc.* **1976,** *98,* 8344-8350.

(44)   Wilker, J. J.; Lippard, S. J. *J. Am. Chem. Soc.* **1995,** *117,* 8682-8683.

(45)   Wilker, J. J.; Lippard, S. J. *Inorg. Chem.* **1997,** *36,* 969-978.

(46)   Grapperhaus, C. A.; Tuntulani, T.; Reibenspies, J. H.; Darensbourg, M. Y. *Inorg. Chem.* **1998,** *37,* 4052-4058.

(47)   Hammes, B. S.; Carrano, C. J. *Inorg. Chem.* **2001,** *40,* 919-927.

(48)   Berreau, L. M.; Makowska-Grzyska, M. M.; Arif, A. M. *Inorg. Chem.* **2000,** *39,* 4390-4391.

(49)   Berreau, L. M.; Makowska-Grzyska, M. M.; Arif, A. M. *Inorg. Chem.* **2001,** *40,* 2212-2213.

Table 5.1. Spectroscopic Data for ZS and Selected ZP Sensors

	M(II)	Absorption λ (nm), $\varepsilon \times 10^4$ ($M^{-1}cm^{-1}$)		Emission λ (nm), Φ^a		$pK_a{}^b$	$pK_a{}^c$
		Unbound	Bound	Unbound	Bound[+]		
ZS1[d]	Zn	510, 8.4	501, 7.5	531, 0.50	526, 0.70	7.7	2.0
	Cd		511, 7.5		534, 0.70		
ZS2[d]	Zn	499, 6.7	489, 6.8	523, 0.39	516, 0.69	7.7	2.7
	Cd		498, 6.8		525, 0.71		
ZS3[d]	Zn	500, 8.7	n.d.[i]	525, 0.71	525, n.d[i]	9.3	4.5
ZS3[e]	Zn	500, 7.6	503, 7.6	525, 0.07	522, 0.17		
	Cd		500, 8.4		527, 0.69		
ZS4[d]	Zn	507, 8.1	495, n.d.[i]	522, 0.12	520, 0.50	7.6	5.1
	Cd		498, 9.0		521, 0.50		
ZP1[d,f]	Zn	515, 7.9	507, 8.4	531, 0.38	527, 0.87	8.4	2.8
ZP2[d,f]	Zn	498, 4.4	490, 5.3	522, 0.25	517, 0.92	9.4	3.9
ZP3[d,f]	Zn	502, 7.5	492, 8.5	521, 0.15	516, 0.92	6.8	2.0
ZP4[d,g]	Zn	506, 6.1	495, 6.7	521, 0.06	515, 0.34	7.2	4.0
ZP8[d,h]	Zn	500, 8.1	489, 7.8	516, 0.03	510, 0.35	6.5	4.1

[a] Quantum yields relative to fluorescein in 0.1 N NaOH ($\Phi = 0.95$, ref 42). [b] pK_a of the nitrogen atom responsible for quenching of the unbound dye. [c] pK_a for formation of a non-fluorescent isomer. [d] Data obtained at pH 7 in 50 mM PIPES, 100 mM KCl. [e] Data obtained at pH 11 in 50 mM CABS, 100 mM KCl. [f] See refs 35 and 39. [g] See ref 36. [h] See ref 38. [i] n.d. = not determined.
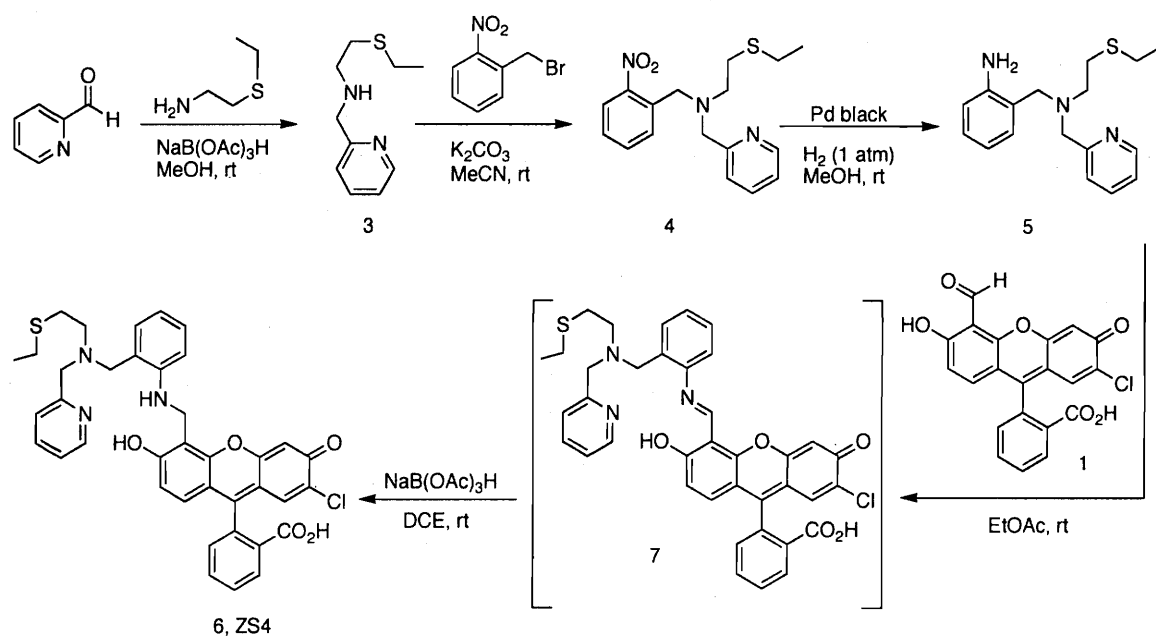
Scheme 5.1. Synthesis of the thioether-containing ligands and sensor ZS4.
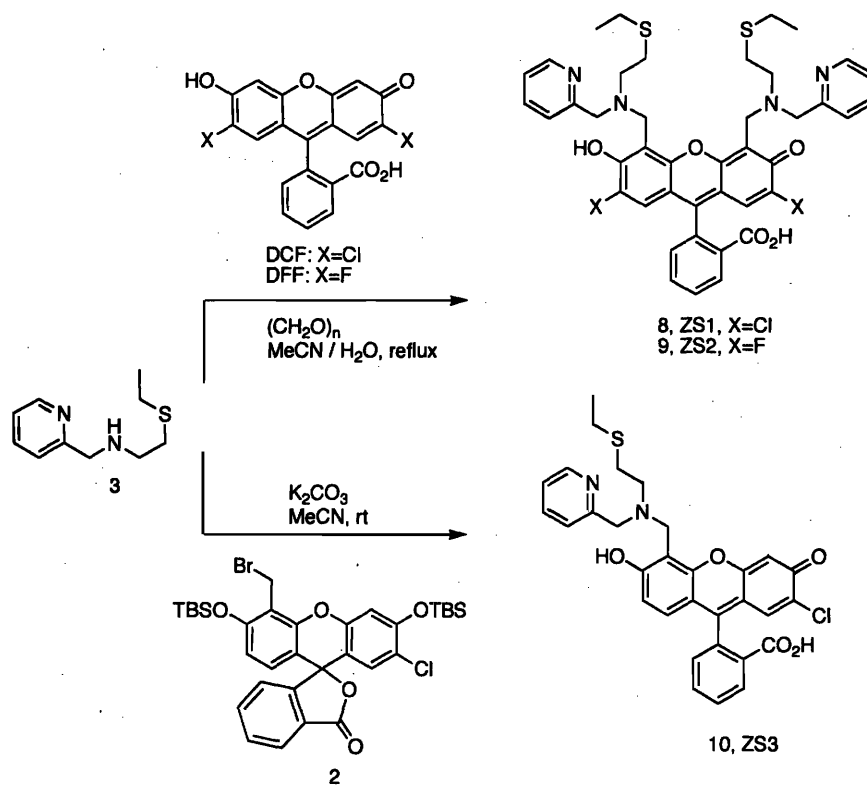
Scheme 5.2 Syntheses of sensors ZS1, ZS2 and ZS3.

ZP1: X=Cl
ZP2: X=H
ZP3: X=F

ZP4: X=H, Y=Cl
ZP8: X=F, Y=F

MS1
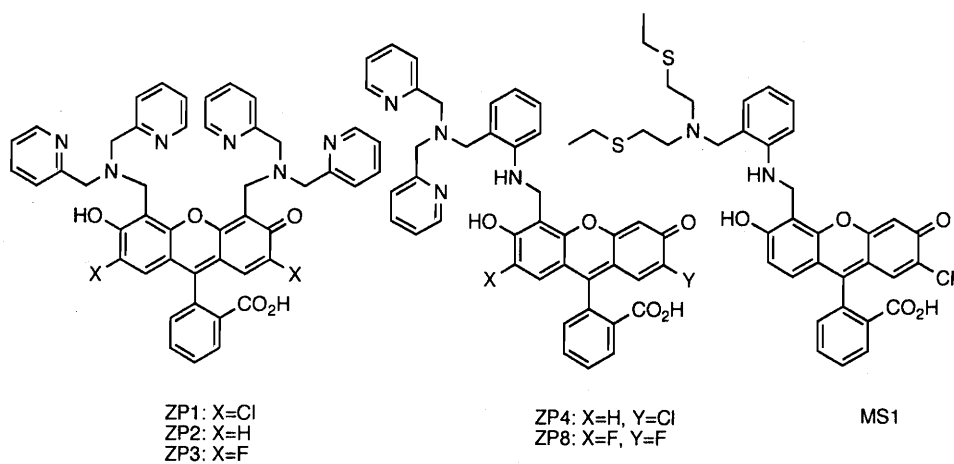
Figure 5.1. Representative symmetrical and asymmetrical ZP sensors, which use the DPA chelate, and mercury sensor MS1.
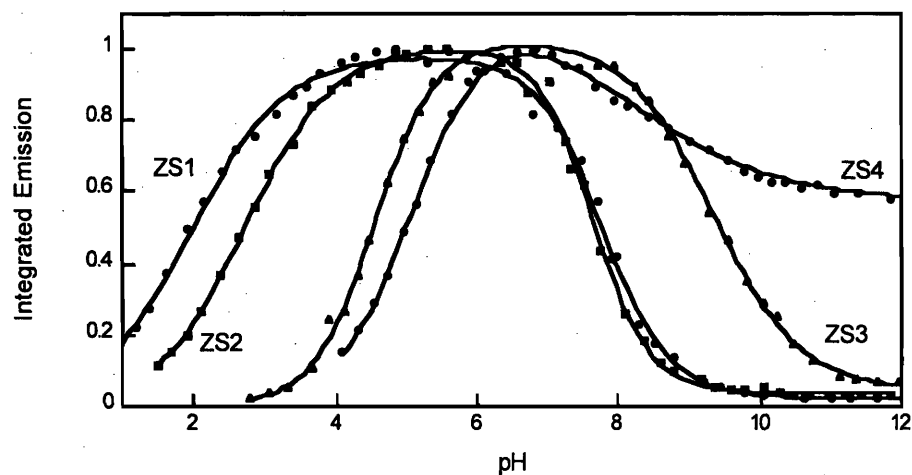
Figure 5.2. Fluorescence dependence on pH for ZS1 – ZS4. A 1 µM solution of each dye was prepared in 10 mM KOH, 100 mM KCl, pH ~12 and the emission spectrum collected. The pH was decreased in increments of ~0.25 by addition of 6, 2, 1, 0.5 and 0.1 N HCl, and the emission spectrum was recorded at each point. The data were integrated from 450 to 650 nm and fit according to eq. 2.1. pK_a values are given in Table 5.1. Circles: ZS1; squares, ZS2; triangles, ZS3; diamonds, ZS4.
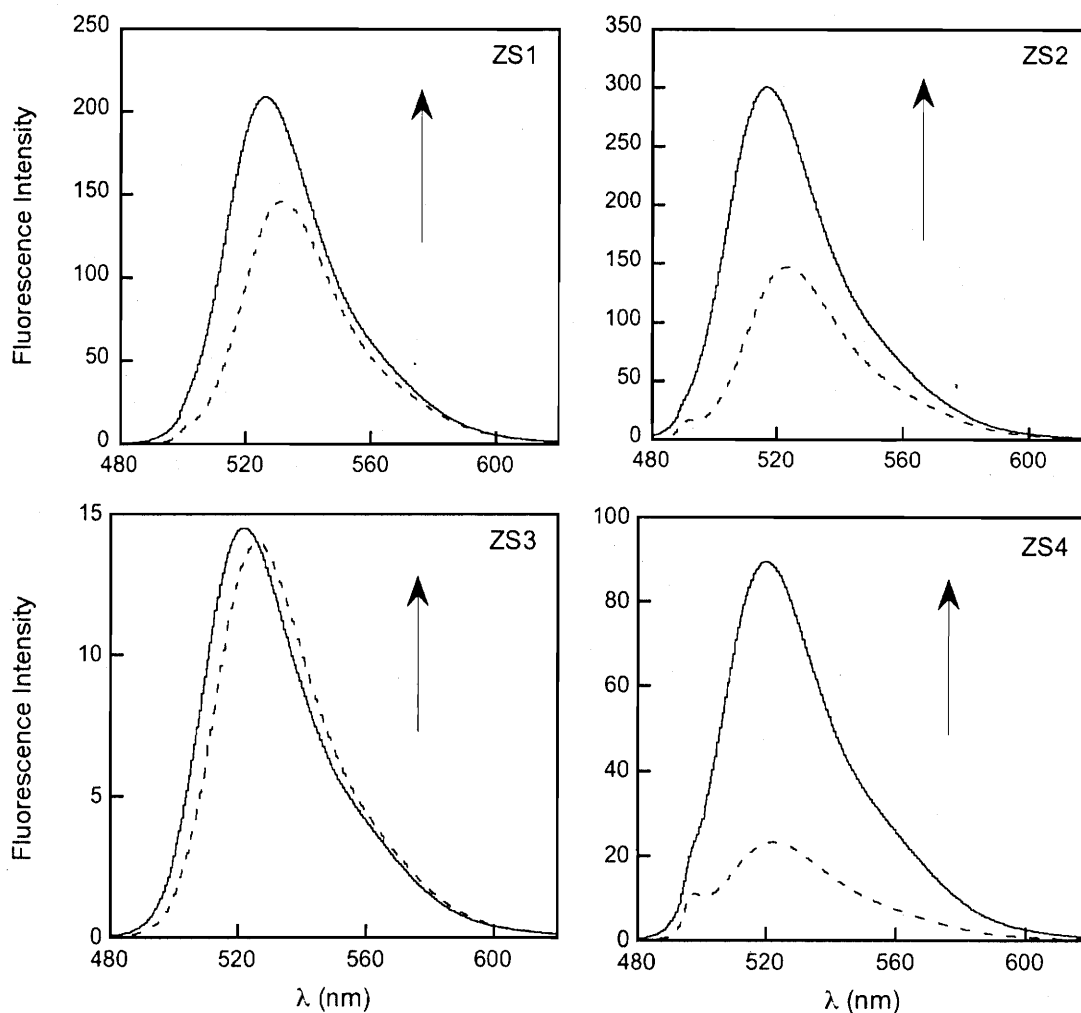
Figure 5.3. Fluorescence spectra of ZS probes before (dashed lines) and after (solid lines) addition of 67 equiv of Zn(II) at pH 7 (50 mM PIPES, 100 mM KCl). All probe concentrations are 1 μM. Excitation and emission slits were set at 3 nm with the exception of the ZS3 measurements, were 1.5 nm slits were used. Excitation was provided at 500 (ZS1, ZS3), 489 (ZS2) or 495 (ZS4) nm.
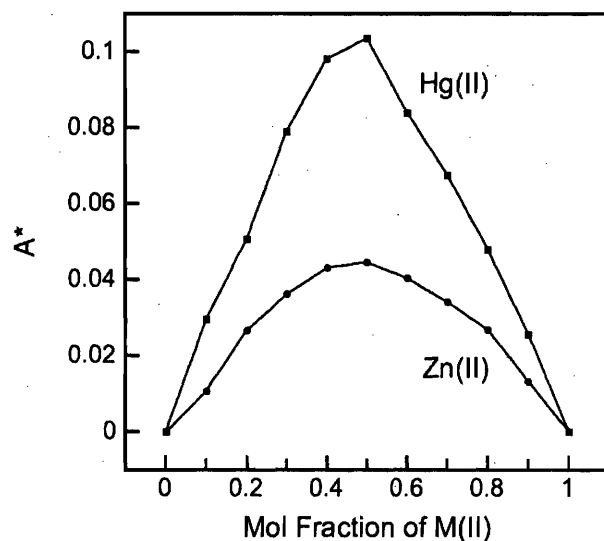
Figure 5.4. Job plots for formation of the Zn(II) (circle) and Hg(II) (squares) complexes of ZS3 at pH 7 (50 mM PIPES, 100 mM KCl). Solutions of 10 μM were used. The absorption change was monitored at 487 and 514 nm for the addition of Zn(II) and Hg(II), respectively, and A* was calculated from the equation $A^* = A_{observed} \times \varepsilon_{ZS3}[ZS3]$ at the wavelength of interest, where ZS3 refers to the unbound dye. The maxima at 0.5 indicate 1:1 ZS3:M(II) complexes in solution. Comparison of the curvature qualitatively suggests that ZS3 binds Hg(II) with higher affinity than Zn(II).
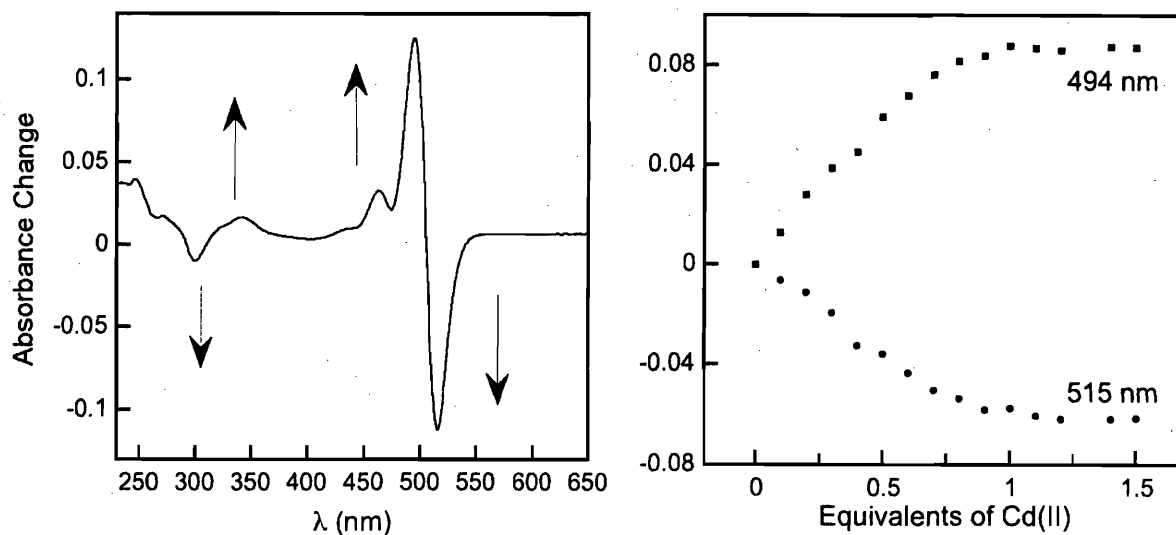
Figure 5.5. Left: Optical absorption difference spectra for addition of Cd(II) to ZS3 at pH 11 (50 mM CABS, 100 mM KCl). A decrease in absorption at 514 nm and increases at 462 and 494 nm occur with Cd(II) binding. Right: Metal binding titration for addition of 0, 0.1, 0.2, 0.3, 0.4, 0.5, 0.6, 0.7, 0.8, 0.9, 1, 1.1, 1.2, 1.4 and 1.5 equiv of Cd(II) to 10 μM ZS3 at pH 11. The absorbance change was monitored at 494 and 514 nm. The break at 1 equiv of Cd(II) indicates formation of a 1:1 ZS3:Cd(II) complex.
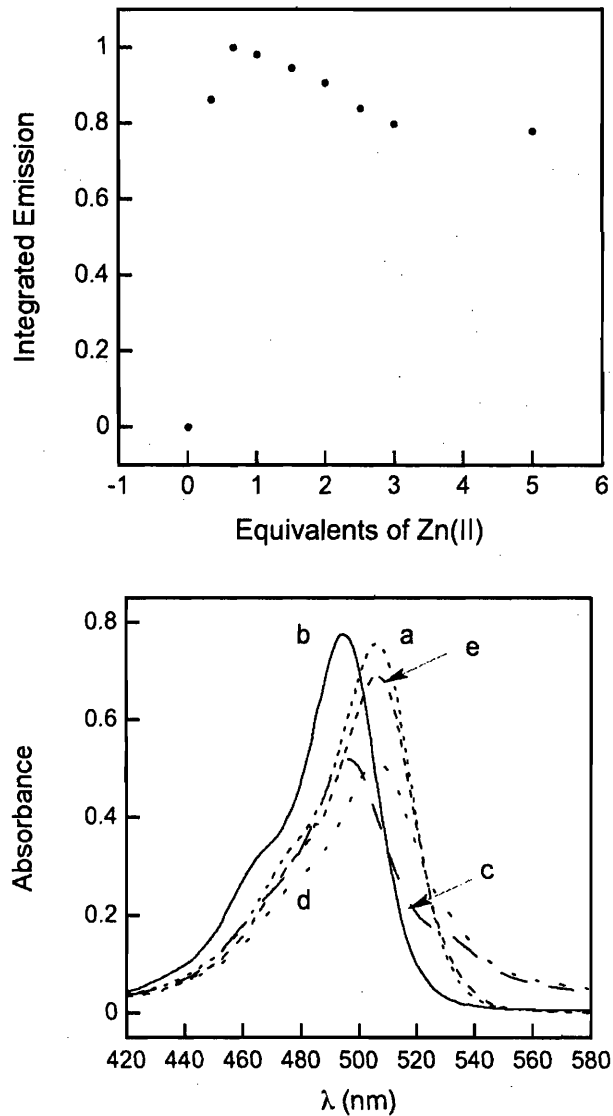
Figure 5.6. Top: Fluorescence response of 1 μM ZS4 to added Zn(II) at pH 7 (50 mM

PIPES, 100 mM KCl). Bottom: Optical absorption spectra for ZS4 in 50 mM PIPES, 100

mM KCl, pH 7. Dotted line a: ZS4, 10 μM. Solid line b: spectrum immediately after

addition of 10 equiv of Zn(II) to a. Dashed line c: solution b after ~15 min. Dashed line

d: addition of 100 equiv of EDTA to c. Dotted line e: the change in spectrum d after

several hours. Precipitation was observed several minutes after addition of Zn(II), and

the precipitate was no longer apparent after addition of EDTA.
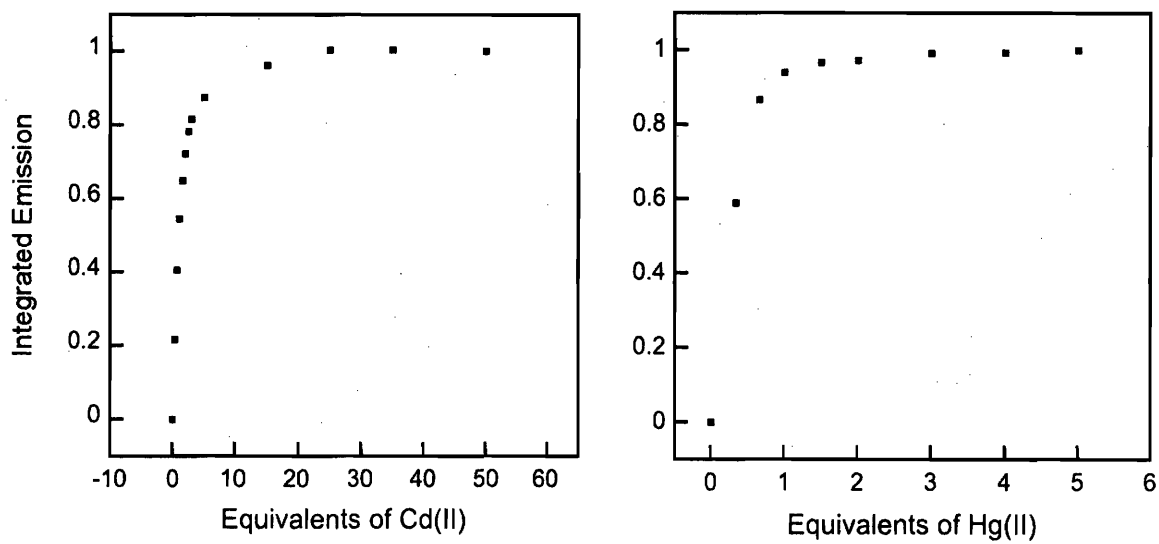
Figure 5.7. Normalized fluorescence response of 1 μM ZS4 to Cd(II) (left) and Hg(II) (right) at pH 7 (50 mM PIPES, 100 mM KCl).
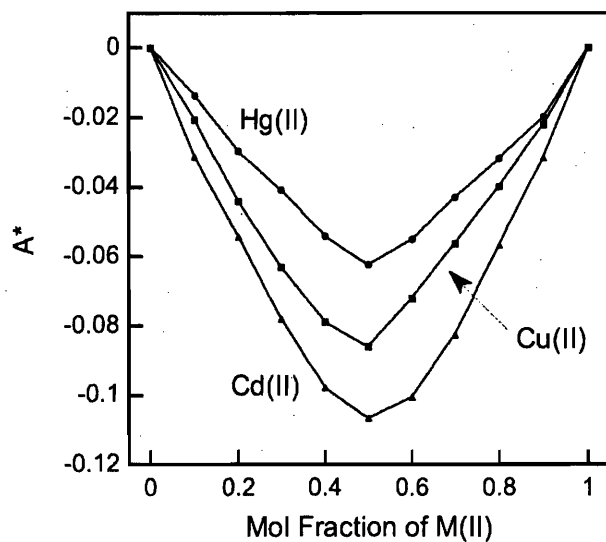
Figure 5.8. Job plots for the formation of the Cu(II) (squares), Cd(II) (triangles) and Hg(II) (circles) complexes of ZS4 at pH 7 (50 mM PIPES, 100 mM KCl). The absorption change was monitored at 512, 514 and 518 nm for Cu(II), Cd(II) and Hg(II), respectively. Starting ZS4 and M(II) solutions of 10 μM were used. A* was calculated as described in the caption of Figure 5.4. These data show that ZS4 forms 1:1 complexes with Cu(II), Hg(II) and Cd(II) at neutral pH.
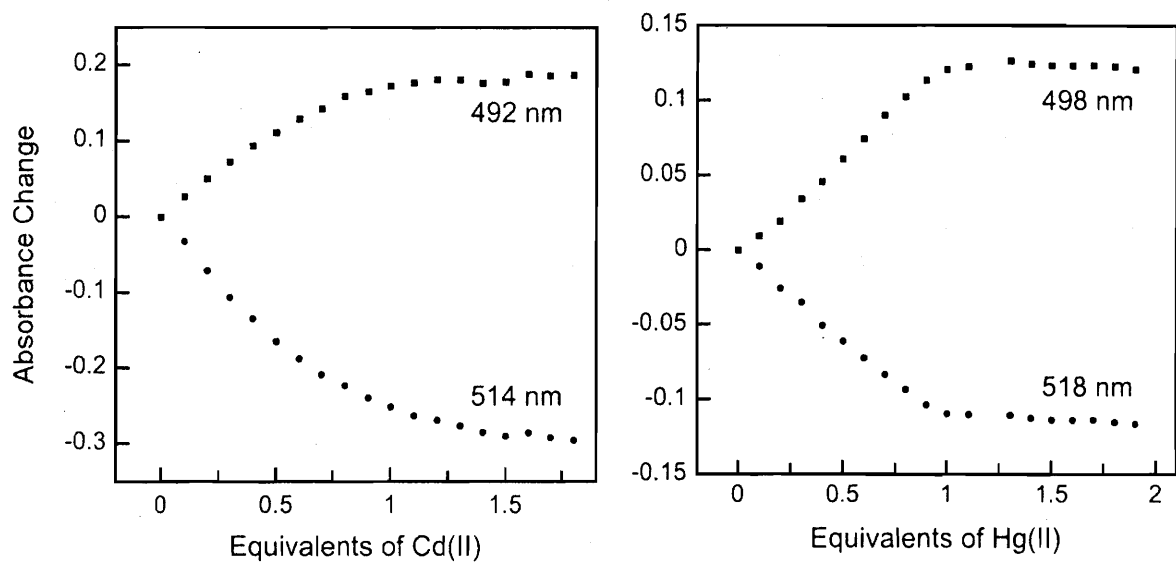
Figure 5.9. Metal binding titrations for 10 µM ZS4 with Cd(II) (left) and Hg(II) (right) at pH 7 (50 mM PIPES, 100 mM KCl). Both titrations are indicative of 1:1 ZS4:M(II) coordination and a comparison of the titrations suggests that ZS4 binds Hg(II) with greater affinity than Cd(II).
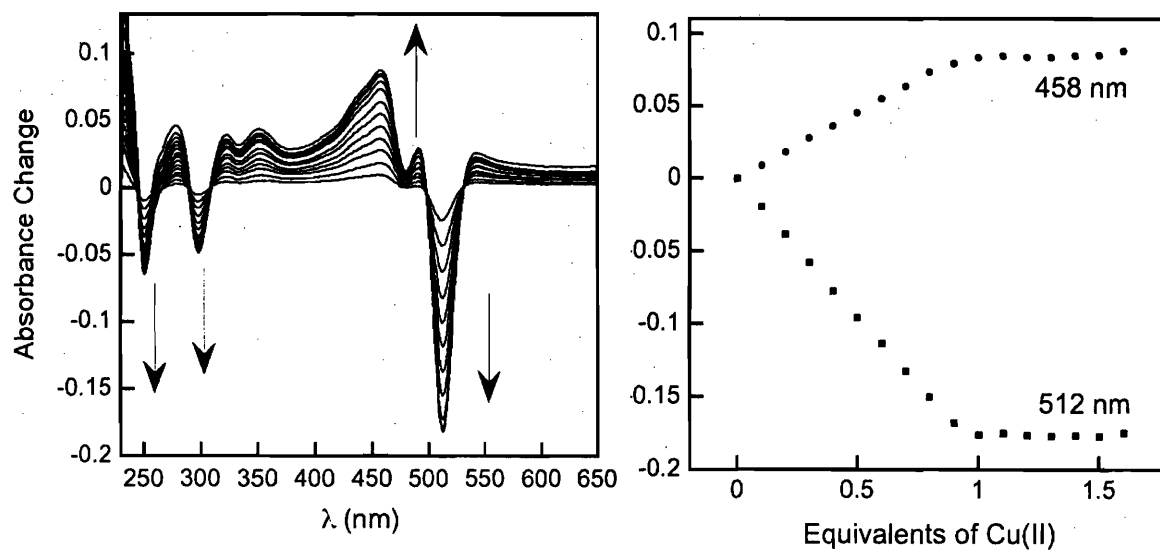
Figure 5.10. Titration of 10 µM ZS4 with Cu(II) at pH 7 (50 mM PIPES, 100 mM KCl). Aliquots of 1 mM Cu(II) in water were added to give 0, 0.1, 0.2, 0.3, 0.4, 0.5, 0.6, 0.7, 0.8, 0.9, 1.0, 1.1, 1.2, 1.3, 1.4, 1.5 and 1.6 equiv of Cu(II). Left: Optical absorption difference spectrum. Right: Metal binding titration. The break at 1 equiv of Cu(II) indicates formation of a 1:1 ZS4:Cu(II) complex.
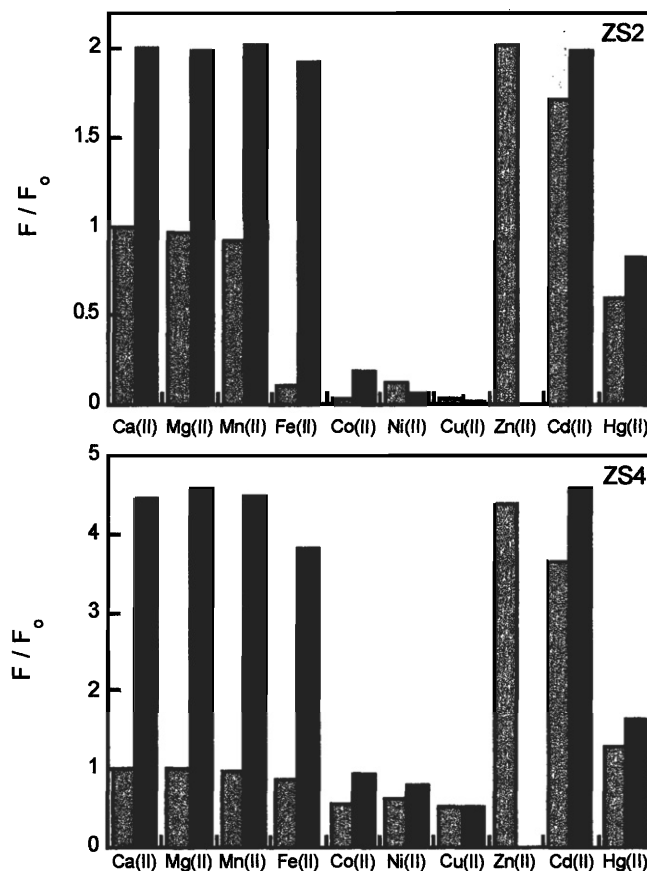
Figure 5.11. Selectivity of ZS2 (top) and ZS4 (bottom) for Zn(II) over other metal ions (50 mM PIPES, 100 mM KCl, pH 7). The light grey bars represent the emission of the ZS probe in the presence of 67 equiv of the cation of interest. The dark grey bars represent the fluorescence change that occurs when 67 equiv of Zn(II) is added to each solution. There is no dark grey bar in the column labeled Zn(II) because no additional Zn(II) was added to the solution. The response (F) is normalized with respect to free ZS (F_o). Excitation was provided at 500 nm for ZS2 and the data were integrated from 450 – 650 nm. Excitation was provided at 495 nm for ZS4 and the spectra integrated from 510 to 650 nm.

Chapter 6

Zinspy Sensors with Enhanced Dynamic Range:
Imaging Zinc Uptake and Mobilization with a Low Affinity Probe

Introduction

Mobile Zn(II) exists in certain substructures of the mammalian hippocampus, a region of the forebrain associated with learning and memory[1-13] and questions regarding the concentrations of Zn(II) in this tissue, both under normal homeostatic conditions and during periods of stress, remain unanswered. The dearth of quantitative information regarding the amount of Zn(II) released during signaling events makes it difficult to draw conclusions about the roles of this ion. Motivated by these considerations, efforts have been made recently to procure sensors that respond rapidly to Zn(II) and with varied affinity for neurobiological imaging.[14-16] The Zinspy molecules described in Chapter 5 were a first step in our quest to design sensors with lower affinity for Zn(II) compared to parent compound ZP1 and its analogs by incorporation of sulfur donors.

In this chapter, we present Zinspy sensors with enhanced dynamic range. Based on several observations from our laboratory and a recent literature report that claims groups distant from a fluorophore can contribute to PET quenching,[17] we reasoned that incorporating multiple aromatic heterocycles, including those with heteroatoms, in the tertiary amine-based ligand is important for achieving relatively low background fluorescence and good dynamic range, at least for symmetrical probes. Substitution of the thioether moiety in ZS1 or ZS2 with a thiophene group is one way to accomplish this task. Thiophenes are less basic than thioethers and thus we assumed that the thiophene moiety would be non-coordinating to yield a N_2O donor set for Zn(II) binding. Confocal imaging studies show that these probes are compatible with the biological milieu and Zn(II)-responsive in a number of cell types.

Experimental Section

Reagents. Acetonitrile was dried using columns of aluminum oxide, and anhydrous 1,2-dichloroethane (DCE) was purchased from Aldrich. Methanol was filtered through

an aluminum oxide plug before use. Ligand **1**[18] and 4′,5′-fluorescein dicarboxaldehyde, **2**,[19] were prepared as previously described. 2′,7′-Difluorofluorescein was purchased from Invitrogen and 2′,7′-dichlorofluorescein from Aldrich. The latter was recrystallized from boiling EtOH before use. All other halogenated fluorescein derivatives were prepared by acid catalyzed condensation of the appropriate resorcinol and substituted phthalic anhydride.[20] Other reagents were obtained from Aldrich and used as received.

Materials and Methods. Merck F254 silica gel plates were used for analytical TLC and were visualized with UV light. Preparative TLC was performed on Whatman silica gel-60 plates of 1 mm thickness manufactured by EM Science. NMR spectra were acquired on a Varian 300 or 500 MHz spectrophotometer operating at ambient probe temperature, 283 K. The spectra were referenced to internal standards. An Avatar FTIR instrument was used to obtain IR spectra. High-resolution mass spectra were collected by staff at the MIT Department of Chemistry Instrumentation Facility.

2-{6-Hydroxy-3-oxo-4,5-bis[(pyridin-2-ylmethylthiophen-2-ylmethylamino)-methyl]-3H-xanthen-9-yl}benzoic acid (3, Zinspy 5, ZS5). A portion of fluorescein **2** (50 mg, 0.13 mmol) was dissolved in 5 mL of DCE and 30 μL of HOAc were added. Compound **1** (77 mg, 0.38 mmol) was dissolved in 5 mL of DCE and added to the fluorescein solution in a dropwise manner. The cloudy and orange reaction mixture was stirred for 1 h at room temperature. A portion (70 mg, 0.33 mmol) of NaB(OAc)$_3$H was added and the solution clarified. The reaction was stirred overnight at room temperature and became orange-brown. The solution was diluted with 15 mL of CHCl$_3$ and washed with water (3 x 15 mL). The organic portion was dried over MgSO$_4$ and the solvent was removed in vacuo, which gave an orange solid. Preparative TLC on silica gel (20:1 CHCl$_3$/MeOH) gave the product as an orange-red powder (37 mg, 38%). TLC R$_f$ = 0.59 (silica, 9:1 CHCl$_3$/MeOH); mp > 280 °C, dec. ^{1}H NMR (CD$_3$OD, 300 MHz) δ 3.90 (4H, q), 4.06 (4H, m), 4.15 (4H, m), 6.59 (2H, d), 6.88-7.01 (6H, m), 6.90 (3H, m), 7.25 (2H, d), 7.56 (4H, m), 7.65 (2H, t), 8.00 (1H, d), 8.35 (2H, d). FTIR (KBr, cm^{-1}) 3432 (s, br),

3064 (w), 2921 (w), 2851 (w), 1754 (m), 1635 (s), 1587 (s), 1522 (m), 1506 (m), 1463 (s), 1436 (s), 1395 (m), 1371 (m), 1284 (m), 1251 (m), 1214 (m), 1151 (m), 1081 (m), 1040 (w), 1003 (w), 975 (w), 851 (w), 832 (w), 789 (w), 759 (m), 708 (w), 697 (w), 670 (w), 627 (w), 609 (w), 592 (w), 583 (w), 566 (w), 559 (w), 546 (w), 541 (w), 518 (w), 508 (w), 484 (w), 478 (w), 463 (w), 455 (w), 452 (w), 444 (w), 437 (w), 419 (w), 406 (w). HRMS (ESI) Calcd [M + Na]$^+$, 787.2019; Found, 787.2024.

2-{2,7-Dichloro-6-hydroxy-3-oxo-4,5-bis-[(pyridin-2-ylmethylthiophen-2-ylmethyl-amino)methyl]-3H-xanthen-9-yl}benzoic acid (4, Zinspy-6, ZS6). Portions of 1 (200 mg, 0.979 mmol) and (CH$_2$O)$_n$ (50 mg, 1.72 mmol) were combined in 5 mL of MeCN and heated to reflux for 45 min. A slurry of 2′,7′-dichlorofluorescein (131 mg, 0.327 mmol) in 7 mL of 1:1 MeCN/H$_2$O was added to the reaction and the solution turned pink. The reaction was heated to reflux for 22 h, during which time a pink precipitate formed, and cooled. The mixture was filtered and the precipitate was washed with 15 mL of Et$_2$O. The pure product was obtained as a light pink powder after recrystallization twice from boiling EtOH (223 mg, 85%); mp = 200 – 201 °C. ^{1}H NMR (DMSO-d_6, 300 MHz) δ 3.96 (8H, m), 4.08 (2H, s), 6.54 (2H, s), 6.96 (4H, m), 7.33-7.43 (8H, m), 7.74-7.84 (5H, m), 7.99 (1H, d), 8.59 (2H, d). FTIR (KBr, cm^{-1}) 3112 (w), 3075 (w), 2061 (w), 2013 (w), 2957 (w), 2932 (w), 2917 (w), 2859 (w), 2808 (w), 2791 (w), 1758 (vs), 1624 (m), 1603 (m), 1590 (m), 1577 (m), 1569 (m), 1488 (m), 1477 (m), 1464 (m), 1433 (s), 1394 (m), 1378 (m), 1369 (m), 1357 (m), 1340 (m), 1309 (w), 1295 (m), 1281 (s), 1241 (m), 1215 (s), 1184 (w), 1155 (w), 1099 (s), 1086 (m), 1055 (w), 1038 (m), 1015 (m), 983 (w), 971 (w), 953 (w), 934 (w), 893 (m), 877 (m), 866 (m), 854 (m), 828 (w), 815 (w), 759 (m), 741 (m), 712 (m), 700 (m), 675 (w), 638 (w), 611 (w), 569 (w), 560 (w), 532 (w), 505 (w), 487 (w), 475 (w). HRMS (ESI): Calcd [M – H]$^-$, 831.1264; Found, 831.1265.

2-{2,7-Difluoro-6-hydroxy-3-oxo-4,5-bis-[(pyridin-2-ylmethylthiophen-2-ylmethyl-amino)methyl]-3H-xanthen-9-yl}benzoic acid (5, Zinspy-7, ZS7). Portions of 1 (83 mg, 0.41 mmol) and (CH$_2$O)$_n$ (13 mg, 0.45 mmol) were combined in 5 mL of MeCN and

heated to reflux for 1 h. A slurry of 2',7'-difluorofluorescein (50 mg, 0.14 mmol) in 10 mL of 1:1 MeCN/H_2O was added to the reaction and the solution turned orange. The reaction was heated to reflux for 22 h and a light pink precipitate formed. The reaction was cooled to room temperature and filtered, and the precipitate was recrystallized from boiling EtOH twice (71 mg, 60%); mp = 182 – 183 °C. ^1H NMR (DMSO-d_6 with NaOD, 300 MHz) δ 3.74 (4H, s), 3.91 (8H, m), 6.265 (2H, d), 6.88-7.00 (5H, d), 7.13 (2H, m), 7.31 (2H, d), 7.44 (2H, qd), 7.64 (4H, m), 7.98 (1H, dd), 8.36 (2H, d). FTIR (KBr, cm^{-1}) 3671 (w), 3570 (w), 3448 (m, br), 3106 (w), 3063 (w), 2949 (w), 2918 (w), 2857 (w), 2792 (w), 1759 (s), 1641 (w), 1606 (m), 1591 (m), 1571 (w), 1491 (s), 1464 (m), 1435 (s), 1399 (m), 1370 (m), 1356 (m), 1338 (m), 1300 (m), 1282 (m), 1246 (s), 1202 (m), 1182 (w), 1157 (w), 1101 (s), 1085 (m), 1041 (s), 1031 (w), 1014 (w), 995 (w), 983 (w), 977 (w), 972 (w), 955 (m), 900 (m), 888 (m), 855 (m), 829 (w), 820 (w), 759 (m), 751 (m), 743 (m), 713 (m), 699 (w). HRMS (ESI): Calcd [M – H]$^-$, 799.1855; Found, 799.1866.

2-{2,7-Dichloro-6-hydroxy-3-oxo-4,5-bis-{(pyridin-2-ylmethylthiophen-2-ylmethyl-amino)methyl]-3H-xanthen-9-yl}-3,4,5,6-tetrafluorobenzoic acid (6, Zinspy-F6, ZSF6). Portions of 1 (200 mg, 0.971 mmol) and $(CH_2O)_n$ (48 mg, 1.7 mmol) were combined in 5 mL of MeCN and heated to reflux for 1 h. A slurry of 3,4,5,6-tetrafluoro-2',7'-dichlorofluorescein in 10 mL of 1:1 MeCN/H_2O was added to the reaction and solution turned dark pink. The reaction was refluxed for 22 h and a pink precipitate formed. The mixture was filtered and the pink precipitate washed with 10 mL of H_2O and recrystallized twice from boiling EtOH (208 mg, 68%); mp > 250 °C, dec. ^1H NMR (DMSO-d_6, 300 MHz) δ 3.96 (8H, s), 4.06 (4H, s), 6.96 (4H, m), 7.26 (2H, s), 7.39 (6H, m), 7.85 (2H, t), 8.61 (2H, d). FTIR (KBr, cm^{-1}) 3445 (s, br), 2926 (w), 2854 (w), 2792 (w), 1775 (s), 1624 (m), 1603 (m), 1578 (m), 1572 (m), 1515 (s), 1475 (m), 1433 (m), 1397 (m), 1366 (m), 1342 (m), 1300 (m), 1285 (m), 1194 (m), 1155 (w), 1113 (w), 1095 (w), 1090 (w), 1064 (w), 1039 (w), 1025 (w), 1018 (w), 996 (w), 983 (w), 972 (w), 949 (w), 926 (m), 909 (w), 881 (w), 853 (m), 830 (m), 797 (w), 754 (m), 715 (m), 706 (m), 696 (m), 636 (w), 611 (w), 600

(w), 581 (w), 562 (w), 547 (w), 532 (w), 525 (w), 518 (w), 504 (w), 489 (w), 473 (w), 454 (w), 446 (w), 436 (w), 428 (w), 417 (w). HRMS (ESI): Calcd [M − H]⁻, 903.0887; Found, 903.0893. Colorless block crystals suitable for X-ray crystallography were grown at room temperature by vapor diffusion of Et_2O into a solution of ZSF6 in CH_2Cl_2.

2-{2,7-Dichloro-6-hydroxy-3-oxo-4,5-bis-{(pyridin-2-ylmethylthiophen-2-ylmethyl-amino)methyl]-3H-xanthen-9-yl}-3,4,5,6-tetrachlorobenzoic acid (7, Zinspy-Cl6, ZSCl6). Portions of **1** (200 mg, 0.979 mmol) and $(CH_2O)_n$ (48 mg, 1.7 mmol) were combined in 5 mL of MeCN and heated to reflux for 1 h. A slurry of 2′,3,4,5,6,7′-hexachlorofluorescein in 10 mL of 1:1 MeCN/H_2O was added to the reaction and the solution turned deep magenta. The reaction was heated to reflux for 22 h, during which time a pink precipitate formed, cooled and filtered. The precipitate was washed with 10 mL of MeCN and recrystallized twice from boiling EtOH, which afforded a light pink powder (255 mg, 80%); mp = 216 − 217 °C. ¹H NMR (DMSO-d_6, 300 MHz) δ 3.95 (8H, s), 4.05 (4H, s), 6.98 (4H, s), 7.26 (2H, s), 7.42 (6H, m), 7.86 (2H, m), 8.63 (2H, m). FTIR (KBr, cm⁻¹) 3105 (w), 3088 (w), 30589 (w), 3014 (w), 2920 (w), 2850 (w), 2790 (w), 1771 (vs), 1623 (m), 1602 (m), 1588 (m), 1569 (m), 1476 (m), 1447 (m), 1433 (s), 1399 (m), 1380 (s), 1358 (m), 1344 (m), 1298 (m), 1233 (m), 1217 (s), 1189 (m), 1147 (m), 1114 (w), 1084 (w), 1048 (w), 1039 (w), 1013 (w), 995 (w), 984 (w), 973 (w), 951 (w), 929 (m), 870 (m), 860 (m) 851 (w), 841 (w), 820 (m), 762 (m), 751 (m), 734 (m), 725 (m), 698 (s), 685 (m), 660 (w), 634 (w), 611 (w), 570 (w), 543 (w), 524 (w), 506 (w), 488 (w), 479 (m), 468 (w). HRMS (ESI): Calcd [M −H]⁻, 966.9705; Found, 966.9705.

2-{2,7-Difluoro-6-hydroxy-3-oxo-4,5-bis-{(pyridin-2-ylmethylthiophen-2-ylmethyl-amino)methyl]-3H-xanthen-9-yl}-3,4,5,6-tetrafluorobenzoic acid (8, Zinspy-F7, ZSF7). Portions of **1** (207 mg, 1.01 mmol) and $(CH_2O)_n$ (50 mg, 1.72 mmol) were combined in 6 mL of MeCN and heated to reflux for 30 min. A slurry of 2′,3,4,5,6,7′-hexafluorofluorescein (148 mg, 0.336 mmol) in 10 mL of 1:1 MeCN/H_2O was added to the reaction and the reaction turned deep pink-red. The reaction was heated to reflux

for 24 h, during which time a pink precipitate formed, cooled and filtered. The precipitate was recrystallized twice from boiling EtOH, which gave the product as a pink-orange powder (185 mg, 63%); mp > 250 °C, dec. ^{1}H NMR (DMSO-d_6 with NaOD, 300 MHz) δ 3.78 (4H, s), 3.93 (8H, s), 6.66 (2H, m), 6.89 (4H, m), 7.14 (2H, m), 7.33 (2H, d), 7.51 (2H, m), 7.61 (2H, m), 8.37 (2H, s, br). FTIR (KBr, cm^{-1}) 3449 (w, br), 3069 (w), 3017 (w), 2916 (w), 2852 (w), 2806 (w), 1778 (s), 1641 (m), 1603 (m), 1591 (m), 1573 (m), 1515 (s), 1502 (s), 1491 (s), 1435 (s), 1397 (s), 1389 (s), 1377 (s), 1358 (s), 1344 (m), 1304 (s), 1277 (m), 1240 (w), 1205 (s), 1194 (s), 1153 (w), 1134 (w), 1116 (m), 1134 (w), 1116 (m), 1097 (w), 1088 (w), 1073 (w), 1043 (s), 1036 (s), 1012 (m), 996 (w), 981 (m), 957 (m), 926 (m), 901 (w), 880 (m), 854 (m), 840 (m), 828 (m), 798 (w), 790 (w), 773 (m), 760 (m), 750 (m), 737 (w), 729 (w), 714 (m), 700 (m), 664 (w), 640 (w), 613 (w), 599 (w), 570 (w), 560 (w), 548 (w), 512 (w), 501 (w), 485 (w), 477 (w), 469 (w), 436 (w). HRMS (ESI): Calcd [M – H]$^-$, 871.1478; Found, 871.1492.

2-[(Pyridin-2-ylmethyl]thiophen-2ylmethylamino)methyl]phenol (9, LH). Salicyl-aldehyde (310 mg, 2.54 mmol) was dissolved in 20 mL of 1,2-dichloroethane and glacial HOAc (500 μL) was added. A solution of 1 (512 mg, 2.51 mmol) in 1,2-dichloroethane (10 mL) was added dropwise to the aldehyde with stirring. The reaction was stirred at room temperature for 1 h and became yellow. A portion (600 mg, 2.83 mmol) of NaB(OAc)$_3$H was added and the reaction was stirred overnight at room temperature, during which time it became clear. Water (30 mL) was added to the reaction and the layers were partitioned. The aqueous phase was washed with CHCl$_3$ (2 x 30 mL) and the combined organic layers were dried over MgSO$_4$ and concentrated, which gave a yellow-brown oil. Flash chromatography on silica gel (3:1 hexanes/EtOAc) afforded the pure product as a white solid (474 mg, 61%). TLC R$_f$ = 0.40 (silica, 1:1 hexanes/EtOAc); mp = 85 – 87 °C. ^{1}H NMR (CDCl$_3$, 300 MHz) δ 4.10 (2H, s), 4.17 (2H, s), 4.22 (2H, s), 7.09 (1H, td), 7.20 (1H, dd), 7.25 (2H, m), 7.35 (1H, d), 7.45-7.61 (4H, m), 7.97 (1H, td), 8.92 (1H, dt). ^{13}C NMR (CDCl$_3$, 125 MHz) δ 51.45, 56.31, 58.70, 116.62, 119.28, 122.19, 123.51,

125.74, 126.97, 127.66, 129.20, 129.85, 137.04, 139.45, 149.39, 157.66, 157.81. FTIR (KBr, cm^{-1}) 3080 (w), 3001 (w), 2962 (w), 2922 (w), 2877 (w), 2816 (m), 2706 (w), 1613 (m), 1583 (s), 1569 (s), 1486 (s), 1467 (m), 1434 (m), 1381 (m), 1368 (m), 1340 (w), 1311 (w), 1293 (w), 1262 (m), 1237 (m), 1172 (w), 1148 (w), 1094 (m), 1036 (m), 1036 (m), 1000 (m), 986 (m), 967 (m), 954 (m), 938 (w), 884 (m), 869 (w), 851 (m), 826 (m), 801 (m), 760 (s), 707 (s), 668 (m), 642 (w), 625 (w), 609 (w), 559 (w), 500 (w), 487 (w), 455 (w). HRMS (ESI): Calcd [M + H]$^{+}$, 311.1213; Found, 311.1212.

[Zn$_2$(L$_2$)](OTf)$_2$ (10). A portion (51 mg, 0.16 mmol) of **LH** was dissolved in 5 mL of CH$_2$Cl$_2$ and added to Zn(OTf)$_2$ (59 mg, 0.16 mmol). The mixture was sonicated for 5 min and filtered. Colorless block crystals suitable for X-ray crystallographic analysis formed following vapor diffusion of Et$_2$O into the reaction mixture at room temperature. After 2 days, the solvent was removed and the crystals washed with Et$_2$O (3 x 5 mL) and dried in vacuo (13.5 mg, 13%). ^{1}H NMR (DMSO-d_6, 500 MHz) δ 3.45 (1H, d), 3.69 (2H, t), 3.95 (2H, q), 4.16 (1H, d), 6.42 (1H, m), 6.57 (2H, d), 6.97-7.11 (3H, t), 7.10 (1H, t), 7.610 (3H, m), 6.10 (1H, t), 8.69 (1H, d). FTIR (KBr, cm^{-1}) 3436 (w, br), 3112 (w), 3090 (w), 3063 (w), 3035 (w), 3009 (w), 2971 (w), 2941 (w), 2912 (w), 2870 (w), 2844 (w), 1609 (m), 1598 (m), 1572 (m), 1483 (s), 1455 (m), 1435 (m), 1392 (w), 1344 (m), 1315 (s, br), 1288 (m), 1272 (s), 1256 (m), 1236 (s), 1211 (s), 1170 (m), 1115 (w), 1083 (w), 1063 (w), 1054 (w), 1040 (m), 1018 (s), 995 (w), 970 (w), 959 (w), 934 (w), 919 (w), 885 (m), 851 (w), 842 (w), 832 (m), 818 (m), 785 (m), 758 (m), 741 (w), 719 (m), 634 (s), 588 (m), 569 (m), 558 (m), 516 (m).

[Cu$_2$(L$_2$)(CH$_3$OH)$_2$](BF$_4$)$_2$ (11). A solution of Cu(BF$_4$)$_2$ (38 mg, 0.16 mmol, 2 mL) in MeOH was added dropwise to **LH** (50 mg, 0.16 mmol) in 2 mL of MeOH with stirring. The reaction turned dark green immediately and was filtered. Vapor diffusion of Et$_2$O into the reaction mixture at room temperature for ~24 h afforded dark green block single crystals. The solvent was decanted after 2 days and the crystals washed with Et$_2$O (4 x 10 mL) and dried in vacuo (38 mg, 24%). FTIR (KBr, cm^{-1}) 3400 (m, br), 3104 (w), 3065 (m), 3030 (w), 2945 (w), 2913 (m), 2957 (w), 1612 (m), 1598 (m), 1571 (m), 1528 (w),

1481 (s), 1455 (s), 1432 (m), 1388 (m), 1371 (m), 1359 (m), 1349 (m), 1317 (w), 1291 (m), 1266 (s), 1247 (m), 1236 (m), 1197 (m), 1156 (m), 1114 (s), 1093 (s), 1074 (s), 1032 (s), 994 (s), 963 (m), 944 (m), 907 (m), 884 (m), 868 (w), 855 (m), 835 (m), 815 (m), 786 (m), 770 (s), 751 (m), 723 (m, br), 660 (w), 637 (w), 609 (w), 591 (m), 567 (w), 547 (w), 519 (w), 497 (w), 480 (m), 455 (w), 427 (m). Anal: Calcd for $C_{38}H_{30}Cu_2N_4O_4S_2B_2F_8$: C, 46.98; H, 3.11; N, 5.77. Found: C, 46.00; H, 3.38; N, 6.00.

X-ray Crystallographic Studies. Single crystals were mounted on the tips of glass fibers coated with paratone-N oil, and cooled to −100 °C under a stream of N_2 maintained by a KRYO-FLEX low-temperature apparatus. Intensity data were collected on a Bruker APEX CCD diffractometer with graphite-monochromated Mo Kα radiation (λ = 0.71073 Å), controlled by a Pentium-based PC running the SMART software package.[21] Data collection and reduction protocols are described elsewhere.[22] The structures were solved by direct methods using the SAINTPLUS and SHELXTL software packages.[23,24] Empirical absorption corrections were applied by using the SADABS program,[25] and the structures were checked for higher symmetry by using the PLATON software.[26] All non-hydrogen atoms were located and their positions refined with anisotropic thermal parameters by least-squares cycles and Fourier syntheses. In general, hydrogen atoms were assigned to idealized positions and given thermal parameters equivalent to either 1.5 (methyl hydrogen atoms) or 1.2 (all other hydrogen atoms) times the thermal parameter of the carbon atom to which they were attached. The structure of sensor ZSF6 contains a dichloromethane molecule that was modeled as disordered over four positions (10:60:15:30). In the structure of **10**, the triflate groups were modeled as disordered over two positions (77:23) and a site in the lattice is occupied by disordered dichloromethane or ether (50:50). The thiophene moiety in **11** was modeled as disordered over 2 positions (59:41) and the tetrafluoroborate anion as disordered over three positions (34:23:46).

General Spectroscopic Methods. Aqueous solutions were prepared with Millipore water. Puratonic grade KCl was purchased from Calbiochem and molecular biology grade PIPES, piperazine-N,N'-bis(2-ethanesulfonic acid), from Sigma. With the exception of the pK_a titrations, measurements were made at pH 7 in 50 mM PIPES, 100 mM KCl buffer. Parallel experiments in buffer rigorously treated or not treated with Chelex resin (Bio-Rad) returned identical dynamic range and K_d values for ZS5. Excess EDTA (1 mM final concentration) was added to solutions of apo ZS prior to quantum yield and extinction coefficient determinations. Zinc stock solutions (100 mM, 500 mM) were prepared from anhydrous 99.999% $ZnCl_2$ (Aldrich) and water. DMSO stock solutions (1 mM) of ZS sensors were prepared, partitioned into ~300 μL aliquots and stored at 4 or –25 °C and thawed in the dark before use. Decomposition of the ZS5 solutions occurs after ~2-3 months for samples stored at 4 °C. A starting solution of 10 mM KOH, 100 mM KCl, pH ~12 was used for pK_a titrations and the pH of the solution was raised by addition of 6, 2, 1, 0.5 or 0.1 N HCl. Quantum yields were measured by using fluorescein in 0.1 N NaOH (Φ = 0.95) as the standard.[27] Extinction coefficients were generally measured over a concentration range of 1 to 10 μM. Apo ZS5 and ZS6 were exceptions, which appear to aggregate at concentrations greater than 3 μM under these experimental conditions. Experimental details for all spectroscopic measurements performed in this study are available in Chapter 2. All spectroscopic measurements were repeated a minimum of three times using material from at least two separate synthetic preparations and the resulting averages are reported.

Stopped-Flow Kinetic Studies. Single-mixing stopped-flow kinetics studies were performed with a Hi-Tech SF-61 DX2 double-mixing stopped-flow apparatus equipped with a fluorescence detector. Excitation was provided at 490 (ZS5, ZS7), 505 (ZS6), 510 (ZSF7) or 520 nm (ZSF6). A GG495 glass cutoff filter (<455 nm) was placed over the exit of to the photomultiplier tube and the emission was monitored from 455 to 700 nm. All solutions were prepared in 50 mM PIPES, 100 mM KCl, pH 7 buffer. Conditions for

pseudo first-order kinetics were maintained by using at least a 10-fold excess of Zn(II) in all experiments. Except for temperature dependent studies, all experiments were conducted at 4.3 ± 0.1 °C. Further experimental details are given in Chapter 7.

Cell Culture. HeLa cells were cultured in Dulbecco's Modified Eagle Medium (DMEM, Invitrogen) supplemented with 10% fetal calf serum (FCS, Invitrogen), glutamine (2 mM), Penicillin (100 units/mL) and Streptomycin (100 μg/mL). Two days before imaging, the cells were passed and plated on 10 mm glass coverslips. For labeling, cells were transferred to DMEM containing 1% FCS and incubated with 10 μM sensor at 37 °C under 5% CO_2. The cells were washed once with DMEM containing no FCS prior to imaging and/or zinc addition. Zinc was introduced to the cultured cells as the pyrithione salt using a Zn(II)/pyrithione ratio of 1:1 or 1:2. Stock solutions of $ZnCl_2$ (10 mM) and sodium pyrithione (20 mM) in DMSO were diluted 10-fold with DMEM prior to addition. In a typical experiment, a 100-μL aliquot of this solution was added to the cells bathed in 2 mL of DMEM. A stock solution of TPEN (10 or 20 mM) was also diluted 10-fold with DMEM containing no FCS prior to cell treatment. S-Nitrosocysteine (SNOC) was prepared immediately before use according to a literature procedure.[28] Colocalization experiments were conducted as described in Chapter 2.

Preparation of Neuronal Cultures. Hippocampal primary cultures were prepared from day 19 (E19) Sprague-Dawley rat embryos according to a previously reported protocol.[29] Medium density cultures (150 cells / mm^2) were plated on glass coverslips coated with poly-D-lysine (30 μg/ml) and laminin (2.5 μg/ml). Hippocampal cultures were grown in Neurobasal media (Invitrogen) supplemented with B27 (Invitrogen), glutamine (0.5 mM) and glutamate (12.5 μM). After 16-20 days in culture, the medium was removed and replaced with fresh Neurobasal containing no B27. The cells were stained by bath application of the appropriate dye to the media and incubated at T = 37 °C under 5% CO_2. The ZS5 DMSO stock solution was diluted 10-fold with either Neurobasal or PBS before addition. The Zinc/pyrithione mix has poor solubility in

Neurobasal, so these DMSO stock solutions were diluted with either PBS or serum-free DMEM before addition. Cultures of dentate gyrus neurons were prepared from the hippocampi of 4-day-old Sprague-Dawley rat pups as described in Chapter 3.

Laser Scanning Confocal Microscopy. A Zeiss LSM510 microscope equipped with a 63x or 100x oil-immersion objective was used to obtain confocal images. Electronic zoom (1.5x) was used in combination with the 100x objective in some colocalization experiments. The samples were excited at 488 nm with an Ar laser. The microscope stage was outfitted with CTI-3700 incubator, which maintained samples at 37 °C and under 5% CO_2 All additions of reagents were performed on the microscope stage.

DIC and Epifluorescence Microscopy. A Zeiss Axiovert 200M inverted fluorescence microscope equipped with an EXFO illumination source, Hamamatsu C9100-12 camera and either a 63x or 100x oil-immersion objective was used to obtain DIC and epifluorescence images of fixed cells. The microscope was controlled by the Volocity software package (Improvision).

Results and Discussion

Design and Syntheses of Probes. Two main considerations influenced the design of the sensors described in this chapter. Our primary goal was to improve the dynamic range and maintain both the Zn(II) selectivity and relatively low Zn(II) affinity of thioether-containing ZS sensors. Based on observations from work in our laboratory and a study that suggested groups apparently too distant from a fluorophore can contribute to PET quenching,[17] we decided to substitute the thioether moiety of our first-generation ZS sensors with a thiophene group. We anticipated that replacement of an alkyl chain with an aromatic heterocycle would result in lower background emission and, in turn, greater fluorescence enhancement following Zn(II) coordination. A second objective was to prepare sensors in relatively few steps and in high yield. For this reason, we focus on symmetrical species with tertiary-amine based ligands.

Scheme 6.1 illustrates the syntheses of symmetrical ZS sensors **3-8**. The probes based on halogenated fluoresceins were prepared by Mannich reactions of the fluorescein and the imminium ion condensation product of paraformaldehyde and **1**. In each case, the desired product precipitated from the reaction solution either during reflux or after cooling to room temperature. Multiple (2 or 3) recrystallizations of the precipitate from boiling EtOH yielded sensors **4-8** as light pink to bright pink powders in moderate to high yields and high purity. Fluorescein-based ZS5, **3**, was prepared from **1** and dialdehyde **2** (Scheme 6.1.) using $NaB(OAc)_3H$ as the reducing agent and obtained in moderate yield after work-up and preparative TLC on silica gel.

Colorless block single crystals of ZSF6 were obtained by vapor diffusion of Et_2O into a solution of the sensor in CH_2Cl_2 at room temperature. Figure 6.1 displays the ORTEP diagram of ZSF6. Tables 6.1 and 6.2 provide crystallographic parameters and selected bond lengths and angles, respectively. Like ZPCl1 (Chapter 4), ZSF6 crystallized in the lactone form.

Photophysical Properties of Thiophene-Containing ZS Sensors. Table 6.3 includes photophysical characterization and thermodynamic parameters for ZS sensors, in addition to data for the symmetrical ZP probes for comparison. We have not conducted full analyses for $ZSCl_4$ and exclude it from Table 6.3. Like the halogenated ZP family members (Chapter 3), the wavelengths of maximum excitation and emission for the ZS sensors fall within a ca. 35 nm range, which may be beneficial for imaging experiments requiring more than one Zn(II)-specific probe.

The data in Table 6.3 reveal that introduction of a thiophene group into the metal-binding unit results in lower background emission and greater fluorescence enhancement than observed for thioether-containing ZS. This trend is particularly evident for the ZS2/ZS7 pair where Φ_{free} decreases from 0.39 to 0.25 (50 mM PIPES, 100 mM KCl, pH 7). As a result, the quantum yields and dynamic ranges of thiophene-containing ZS more closely resemble those of the ZP family, although Φ_{free} is

consistently higher and indicates that DPA quenches the fluoescein excited state more effectively. Depending on the substitution pattern on the fluorescein rings, compounds **3-8** offer ~2.2 to ~4-fold fluorescence turn-on following Zn(II) coordination. Representative emission spectra for select probes are given in Figures 6.2 and 6.3. The optical absorption spectra of both Zn(II)-free and –bound forms of the ZS sensors are characterized by high molar extinction coefficients, and Zn(II) coordination results in a slight (ca. 10 nm) blue shift and increase in the wavelength of maximum absorption. This behavior parallels that of many previously characterized ZS and ZP sensors, and indicates that the phenol moiety is involved in Zn(II) coordination.

Effect of pH on ZS Emission. The ZS sensors presented in this work operate via a PET mechanism.[30,31] Sensors of this type are often pH sensitive. Figure 6.4 displays representative pH titrations for **3-8** and pK_a values are given in Table 6.3. These data show some similarities and some differences to those of analogous ZP compounds. We first consider ZS5-7, which lack benzoate halogenation (Figure 6.4, top). Like ZP1-3, the 2′,7′-dichloro (ZS6) and 2′,7′-difluoro platforms (ZS7) shift the pH titration curve toward lower pH relative to unsubstituted fluroescein (ZS5). This trend parallels the known pH-dependent emission profiles and pK_a values of the parent fluorophore, with fluorescein having a phenolic pK_a value of 6.4[32] compared to 5.0[33] for 2′,7′-dichloro- and 4.8[34] for 2′,7′-difluorofluorescein. As a result, the pK_a transition assigned to tertiary amine protonation decreases from 8.0 (ZS5, X=H) to 7.0 (ZS7, X=F). We note that this range is smaller than that observed for ZP1-3 (ZP2, X=H, pK_a = 9.4; ZP3, X=F, pK_a = 6.8). Fluorescence quenching occurs at pH < ~6 which is attributed to phenol protonation. These pK_a values range from 4.6 to 2.7 with X = H > Cl > F.

Titrations of bottom-ring halogenated ZSF6 and ZSF7 are given in the bottom panel of Figure 6.4. These profiles are both characterized by two pK_a transitions, with pK_{a1} ~ 7 assigned to tertiary amine protonation and pK_a < 3 assigned to protonation of the phenol. The pK_{a2} values are slightly higher than those observed for ZPF1 (pK_a = 6.9) and

ZPF3 (pK_a = 6.7), but follow the same trend of further diminution upon fluorination of the 2′ and 7′ positions. Interestingly, only one tertiary amine protonation event is observed with ZSF6 and ZSF7 as compared to sequential protonation with ZPF1 and ZPF3. The reason for this difference is not clear. Scheme 6.3 depicts the protonation equibria for the thiophene-containing ZS sensors proposed based on these experiments and on the low basicity of thiophene moieties.

The titrations in Figure 6.4 illustrate that emission of the ZS sensors is effectively quenched at high pH. The quantum yield of apo ZS5 drops from 0.36 at pH 7 to 0.04 at pH 9. As a result, ZS5 shows greater than 20-fold fluorescence enhancement following Zn(II) coordination at pH 9 with Φ_{Zn} = 0.73 (50 mM CHES, 100 mM KCl) as compared to ~4-fold at pH 7 (50 mM PIPES, 100 mM KCl). This behavior is consistent with the PET mechanism.[30]

Metal Binding Properties I: Zinc Affinity and Coordination. Fluorescence spectroscopy was used to determine apparent Zn(II)-complex K_d values for ZS5, ZS7 and ZSF7, which are listed in Table 6.3. Representative binding curves are given in Figure 6.4. ZS5 exhibits maximum fluorescence in the presence of ~10 equiv of Zn(II) and has a K_d value of 1.5 ± 0.2 μM. This value is ~3 orders of magnitude greater than the K_{d1} value of ZP2 (K_{d1} = 0.5 ± 0.1 nM), and about twice that of ZP9 (K_d = 0.69 ± 0.04 μM).

Fluorination of the xanthenone and benzoate moieties raises the K_d value significantly, with ZS7 and ZSF7 having K_{d1} values of 3.7 ± 0.4 μM and 5.0 ± 0.3 μM, respectively (Figure 6.4). We attribute this behavior to variation in the donor ability of the deprotonated phenol group. Incorporation of fluorine atoms reduces the electron density on the oxygen atom, making it a poor donor relative to X = H. As a result, the Zn—O bond is weaker in fluorinated ZS relative to ZS5. This trend is in accord with the pH studies described above, where the pK_a of the phenol decreases with fluorination of the fluorescein platform.

To further elucidate the nature of metal ion coordination to ZS sensors containing pyridyl-amine-thiophene ligands, a salicylaldehyde-based model complex, **9**, was prepared by reductive amination of salicylaldehyde with ligand **1** as shown in Scheme 6.4. X-ray quality crystals of several metal complexes, including those with Zn(II), Cu(II), Ni(II) and Co(II) centers, were obtained from small-scale crystallization trials. X-ray structural determination of these complexes confirmed that, regardless of the metal ion, the thiophene moiety does not coordinate. To illustrate this feature, the refined Zn(II), **10**, and Cu(II), **11**, structures are shown in Figure 6.6. Crystallographic data and selected bond lengths and angles are included in Tables 6.1 and 6.2, respectively. Both **10** and **11** are dinuclear with deprotonated phenol oxygen atoms bridging between the two metal ions. The Zn(II) centers in **10** are five-coordinate and bound by the tertiary amine and pyridyl nitrogen atoms, the two bridging phenol moieties and a triflate molecule. The thiophene moieties are directed away from the Zn(II) ions, which confirms that no Zn(II)—S(thiophene) interaction occurs. The dinuclear Cu(II) complex, **11**, exhibits some similar features. Each Cu(II) center is five-coordinate with square pyramidal geometry. The phenol, tertiary amine and pyridyl nitrogen atoms are in the square plane and a protonated methanol molecule in the apical position. Like **10**, the thiophene moieties point away from the Cu(II) centers.

Bridging of two metal ion centers by the 3′-oxo atoms in fluorescein-based ZS sensors is considered unlikely. This oxygen atom in fluorescein is less electron-rich than that of salicylaldehyde because of delocalization of charge on the xanthenone ring. Also, as discussed in Chapter 7, computational work indicates that salicylaldehyde-based model complexes have significant shortcomings.[35] As a result, we conclude that the utility of the model ligand **9** does not extend beyond confirmation that the thiophene moiety does not bind to the metal ions under study.

The thiophene-containing ZS sensors have two possible metal-binding sites. By analogy to the ZP systems and chemical intuition, we propose step-wise binding with

formation of the 1:1 complex at relatively low Zn(II) concentrations and formation of 1:2 complexes at significantly higher concentrations of Zn(II) (Scheme 6.4). Fluorimetric titrations show that the fluorescence response of 1 μM ZS to Zn(II) maximizes at 10 – 50 μM Zn(II) depending on the fluorophore platform, which indicates that the second binding event has little influence on the fluorescence response. For this reason values for K_{d2} were not determined.

Metal Binding Properties II: Zinc Selectivity. One objective of this investigation was to maintain the Zn(II) selectivity observed for thioether-containing ZS. Figure 6.5 illustrates the selectivity of ZS5 for Zn(II) in the presence of biologically relevant cations, divalent first-row transition metal ions, Cd(II) and Hg(II). The data for the halogenated sensors are generally analogous, although the degree of quenching observed following Hg(II) addition varies with fluorescein substitution. As anticipated, the behavior of ZS5 follows that of ZS1-4 with selectivity for Zn(II) over Fe(II) maintained. The greater affinity of ZS5 for Zn(II) vs. Hg(II) is an improvement over the thioether-containing ZS sensors, which irreversibly coordinate to Hg(II) (Chapter 5). This difference results from loss of a strong Hg—S bond between the metal ion center and the thioether donor.

Metal Binding Properties III: Kinetics of Zn(II) Association. The fluorescence response of the ZS probes is rapid and observable immediately after Zn(II) addition. We therefore conducted stopped-flow kinetic studies to determine the rate constants for Zn(II) association, measured by fluorescence turn-on, for selected ZS sensors. Table 6.4 lists the experimentally determined second-order rate constants for Zn(II) association (k_{on}) and, in some instances, calculated rate constants for Zn(II) dissociation (k_{off}). These experiments were conducted as described in Chapter 7; relevant equations and additional discussion are included therein. Plots of k_{obs} versus Zn(II) concentration are given in Figure 6.8 (T = 4.3 °C), which return k_{on} values ranging range from 3.3 to 5.9 x 10^5 M^{-1}s^{-1} at this temperature. Data from temperature variation experiments indicate k_{on}

values of 1.8 to 3.0 x 10^6 at 25 °C, which are comparable to those of DPA-based probes such as ZP (Chapter 7) and $ZnAF^{14,36}$ family members. The dissociation rate constants, k_{off}, were calculated from the experimentally determined k_{on} and K_d values and range from 3.3 to 13.5 s^{-1} at 25 °C, which yields $t_{1/2}$ values of 50 to 210 msec. These kinetic parameters demonstrate that the ZS sensors bind Zn(II) both rapidly and reversibly.

Temperature variation experiments were conducted to determine the activation enthalpies and entropies for Zn(II) coordination to the ZS sensors and these data are also included in Table 6.4. Figure 6.9 displays representative Eyring plots for each probe, from which we compute $\Delta H^{\ddagger}$ to be 12.6 to 13.3 kcal/mol and $\Delta S^{\ddagger}$ to range from 12.5 to 15.2 cal/mol-K. The former values are indicative of a low activation barrier and fast association rate, and are comparable to those determined for ZP family members (Chapter 7). The positive $\Delta S^{\ddagger}$ values are also typical and may reflect loss of water molecules or buffer components from the Zn(II) center or loss of protons from ZS in the transition state.

Cytotoxicity of ZS5. During preliminary biological imaging experiments, ZS5 showed great promise. As a result, investigations of its cytotoxicity in cell lines and neurons were initiated. Figure 6.10 shows images of HeLa cells and hippocampal neurons that were treated with 10 μM ZS5 for 24 h, fixed and treated with the nuclear stain Hoescht. This assay indicated no significant difference between untreated controls and cells incubated with ZS5. To obtain more quantitative information, MTT assays were conducted on HeLa cells and primary hippocampal neurons following 24 treatment with 1 – 10 μM ZS5. The data presented in Figure 6.11 indicate that HeLa cells show ~100% viability following treatment with 1 μM ZS5 and 78% ± 4% cell survival following incubation with 10 μM probe. The latter value compares to 40% ± 6% for ZP1 and 57% ± 13% for ZP3 (Chapter 3). Although an IC_{50} value for ZS5 has not been rigorously determined, preliminary kill curves show slightly more gradual cell death than for ZP1 and suggest an IC_{50} value of ca. 5 μM (HeLa, 5 days).

The MTT assay was also employed to determine the viability of primary cultures of hippocampal neurons treated with 5 or 10 μM ZS5 over a 24 h period. This analysis, however, was limited by a small sample size because these cultures come from live animals. Furthermore, primary cultures contain many cell types, so the results of this assay do not necessarily reflect the effect of ZS5 on the neurons of interest. With these shortcomings in mind, we present the data for ZS5-treated cultures of hippocampal neurons in Figure 6.11. These results suggest that 5 μM ZS5 is essentially non-toxic over a 24 h period, with greater cell death occurring at 10 μM probe. Whether this increase in cell death results from dying neurons or non-neuronal cells present in the cultures is unclear, although purple-stained neurons were observed by-eye following MTT treatment, indicating viability.

In summary, these preliminary cytotoxicity assays suggest that low μM concentrations of ZS5 are relatively non-toxic to both HeLa cells and primary cultures of hippocampal neurons, and should be employed in any experiments requiring a relatively long incubation time. The majority of the imaging work described below was conducted with 10 μM sensor and no evidence for toxic effects was noted during the courses of the experiments.

Biological Imaging Studies I. Response of ZS5 to Zinc in Cultured Cells and Subcellular Localization. Several features of the ZS probes, including improved dynamic range relative to the thioether-containing parent compounds and low μM affinity for Zn(II), motivated us to consider their utility for in vivo work. We began these investigations with ZS5, the first compound in this series that was prepared, and quickly learned that it is photostable and versatile. We therefore focused our attention on this probe for biological imaging.

Initial cell studies indicated that ZS5 permeates a number of cell types and is Zn(II)-responsive in vivo. Figure 6.12 exhibits representative images of ZS5 treated HeLa, COS-7 and HEK cells. In preliminary work, the cells were treated with ZS5 for varying

incubation times, which showed that 30 min (T = 37 °C, 5% CO_2) is optimal in terms of economical time use. Longer incubation periods are also acceptable and shorter (ca. 20 min or less) ones are generally insufficient. Addition of Zn(II) to the cells as the 1:1 or 1:2 Zn(II)/pyrithione complex affords intracellular fluorescence enhancement, which is reversed with TPEN treatment.

An important observation from these preliminary experiments concerned the subcellular localization of ZS5. Figure 6.13 shows a side-by-side comparison of HeLa cells treated with ZS5 or ZP3. Whereas ZP3 exhibits punctate Golgi-associated staining, the ZS5 pattern is much more diffuse. Cololocalization studies were conducted in HeLa cells to determine where ZS5 resides, and representative images are shown in Figure 6.14. Treatment of HeLa cells with ZS5 (free or zinc-bound) and either Lysotracker or pGolgi-DsRed showed that ZS5 does not localize to either the lysosomes or the Golgi. Excellent co-localization of ZS5 and Mitotracker Red was observed, however, which establishes that ZS5 is sequestered in the mitochondria of healthy HeLa cells.

The observation that Zn(II) sensors can be directed to different subcellular organelles as a result of structural modification is intriguing and potentially advantageous. Although subcellular compartmentalization of sensors has been described as problematic,[37] we believe that a clear understanding of sensor localization in the cell type under study will be beneficial for studying Zn(II) entry into and trafficking between certain organelles. Mitochondrial localization is relevant from the standpoint of Zn(II) toxicity, because rapid influx of Zn(II) into the mitochondria has been implicated in neuronal death.[38-40]

Biological Imaging Studies II: Response of ZS5 to Zinc in Primary Neuronal Cultures. We next focused our efforts on studying the behavior of ZS5 in primary neuronal cultures. Figure 6.15 exhibits representative images of both hippocampal and dentate gyrus neurons treated with ZS5 and exogenous Zn(II). ZS5 is stable and Zn(II) responsive in both cell types. Additionally, ZS5 appears to detect endogenous Zn(II) in

some cultures. A comparison of the panels in Figure 6.14A illustrates this notion because green fluorescent dots are observed in the ZS5-treated cells and disappear following TPEN treatment. ZP3 staining of hippocampal and dentate gyrus neurons has also revealed green dots in certain cases,[41] and a dot-like staining pattern was observed in cortical neurons treated with TSQ.[42] At present, we do not know the physiological significance of these green dots, let alone if they are the same thing in different neuron types, and their proper identification is needed to determine their relevance.

Preliminary colocalization studies of ZS5 in hippocampal neurons give some support for mitochondrial localization, although these studies are not definitive and have been hampered by several technical problems, including extremely poor photostability of Mitotracker and Lysotracker in the neuronal cultures. Figure 6.16 presents some example images of hippocampal neurons that are cotreated with ZS5 and Mitotracker. Although good colocalization of the Mitotracker and ZS5 signals is seen in certain regions of the cell body, essentially no overlap is observed in the projections. Treating cells with mitochondrial-specific probes at 4 °C for 5 – 10 min prior to incubation at 37 °C is apparently one method employed to enhance mitochondrial uptake.[43] We considered this approach, but found that the neurons did not tolerate this treatment very well, judging by their morphology.

Biological Imaging Studies III: Fast Imaging of Exogenous Zinc Uptake with ZS5. A series of time-course experiments where cells were treated with ZS5 and Zn(II)/prythione and imaged over the course of 1 to 5 min revealed that ZS5 responds to exogenously added Zn(II) more quickly in neurons than in other cell types, such as HeLa and COS-7. Figure 6.17 includes images of both HeLa cells (panels labeled A) and neurons (panels labeled B) treated with ZS5 and 50 μM 1:1 Zn(II)/pyrithione. Essentially no fluorescence change is observed 1 min after addition of Zn(II) to the HeLa cells and full turn-on is observed at 5 min. In contrast, the full response of ZS5 is observed within 1 min of Zn(II) addition to neurons. We believe this variation stems

from the relative ability of HeLa cells and neurons to internalize the Zn(II)/pyrithione complex. The kinetics of the Zn(II)-induced response also depends on the concentration of added Zn(II); panels in Figure 6.17C illustrate this fact. When only 1 equiv of Zn(II)/pyrithione is added to ZS5-treated neurons, some fluorescence rise is observed 1 min following Zn(II) addition and the full effect is seen after 5 min.

Our next aim was to image ZS5 responding to Zn(II) on a faster timescale. Figure 6.18 shows time-series images of a neuron cell body treated with 10 μM ZS5 before and after treatment with 50 μM 1:1 Zn(II)/pyrithione and 50 μM TPEN. The images were captured at ~2.4 sec intervals and show that ZS5 responds to Zn(II) on this timescale. Some fluorescence rise occurs during the first few seconds after TPEN addition. This behavior is reproducible and we have observed the same phenomenon in other cell types such as HeLa. Parallel control studies show that pre-treament of the neurons with TPEN blocks any response of ZS5 to Zn(II)/pyrithione (data not shown). The value of these experiments lies in the proof that ZS5 can respond to Zn(II) rapidly and reversibly in a biological system and points towards its utility for monitoring Zn(II) flux.

We note that the images in Figure 6.18 show more robust fluorescence from the neurons as compared to the HeLa cells (same microscope settings employed for all images). This behavior is quite general for ZS5; we typically see more vibrant staining in neuronal cultures than in HeLa, HEK or COS-7 cells. We do not currently understand the origin of this difference, but it may reflect greater uptake of ZS5 in neurons than in other cell types.

Biological Imaging Studies IV: Effect of Glutamate on Exogenous Zinc Uptake. Treating cells with Zn(II)/pyrithione is essentially a brute force approach to generating a robust intracellular signal. Pyrithione appears to deliver Zn(II) indiscriminately throughout the cell. As a result, experiments that use Zn(II)/pyrithione have little physiological or pathophysiological significance. We were thus motivated to investigate other routes of Zn(II) entry that might be relevant for neurobiological signaling.

The Zn(II)-containing synaptic vesicles in the mammalian hippocampus also house glutamate (E), an excitatory neurotransmitter, and both species are released into the synaptic cleft following exocytosis of vesicles at the pre-synaptic membrane. Given this association, it is reasonable to think that glutamate may modulate Zn(II) uptake into the post-synaptic neuron or other nearby cells. Several reports indicate that glutamate or kainite, a glutamate mimic, can trigger excessive intracellular accumulation of Zn(II) in neurons.[44-46] These studies, however, were directed at Zn(II) toxicity, and the neurons were pre-treated with high concentration (0.3 to 1 mM) of zinc prior to glutamate treatment. In this work, we co-treated ZS5-loaded hippocampal neurons with $ZnCl_2$ and glutamate (1:1 or 1:2 ratio, 50 μM zinc) and monitored the response by confocal imaging. Figure 6.19 includes representative images, which show significantly different staining than that observed for neurons treated with Zn(II)/pyrithione. Fluorescence enhancement occurs in several dendritic projections 1 min after addition of the Zn(II)/E mix and this rise persists for at least 5 min. The staining pattern consists of green dots that may be associated with dendritic spines, although detailed colocalization studies must be conducted to address this possibility. Control studies where hippocampal neurons were treated with only $ZnCl_2$ showed no fluorescence change, indicating that Zn(II) does not permeate the neuronal cell membrane over this time period. Control studies where the ZS5-loaded neurons were treated with glutamate only also showed no fluorescence change over a 10 min time period. This experiment clearly shows that glutamate modulates the uptake of extracellular Zn(II) into hippocampal neurons rapidly and at specific locales.

Biological Imaging Studies V: Imaging Endogenous Zinc Mobilization with ZS5. In Chapter 3, we demonstrated that ZP3 can detect endogenous Zn(II) moblization that results from nitrosative stress.[47,48] Nevertheless, this proof of principle experiment provided us with little information regarding the concentration of Zn(II) released from native protein stores following SNOC treatment. Since ZP3 binds Zn(II) with sub-nM

affinity, it is possible that only nM concentrations of Zn(II) were released or that the concentration of Zn(II) is higher and the ZP3 signal saturated. Thus, we determined whether ZS5 (K_d = 1.5 ± 0.2 μM) could detect Zn(II) in primary neuronal cultures following SNOC treatment. Figure 6.20 shows a representative time course experiment where dentate gyrus neurons were loaded with 10 μM ZS5 and subsequently treated with SNOC. Significant fluorescence enhancement occurs in the neuron cell bodies and projections at ca. 3 min following SNOC addition and the response maximizes at ca. 6 min. Dentate gyrus neurons clearly release Zn(II) concentrations observable with a low-μM affinity probe following nitrosative stress.

Summary and Perspectives

In this chapter, we presented the synthesis, characterization and imaging applications of ZS sensors appended with pyridyl-amine-thiophene ligands. These sensors exhibit improved dynamic range and Zn(II) selectivity as compared to their counterparts with thioether groups in the metal binding unit. Additionally, these sensors have dissociation constants for Zn(II) in the low micromolar range, which makes them an important addition to our Zn(II) sensor toolkit, and fast association rates. The biological imaging work presented above shows that ZS5 is a versatile Zn(II) imaging tool with great potential. ZS5 readily enters and responds to Zn(II) in multiple cell types, including primary neuronal cultures. Colocalization studies in HeLa cells indicate mitochondrial localization, and more detailed experiments in other cell types will help elucidate the generality of this feature. Experiments in hippocampal neurons show that Zn(II)/glutamate co-treatment results in Zn(II) uptake into neuronal projections. Finally, ZS5 detects Zn(II) released following nitrosative stress in dentate gyrus neurons, which complements previous work conducted with ZP3. It also indicates that the concentration of Zn(II) released is well within the detection limit of a low micromolar affinity probe. Future work directed at using ZP3 and ZS5 in parallel to

both estimate relative Zn(II) concentrations following release and to ascertain what subcellular compartments are targeted will prove invaluable to our understanding of Zn(II) mobilization in both physiological and pathological contexts. Lastly, although the natural proclivity of sensors to compartmentalize to particular subcellular locales can be used, this type of behavior is not readily predictable and may vary with cell type. Our investigations of the ZP and ZS sensors, in addition to reports in the calcium sensor literature,[37] point to the necessity of designing Zn(II) sensors capable of programmable site-specific localization.

References

(1)   Frederickson, C. J. *Int. Rev. Neurobiol.* **1989**, *31*, 145-238.

(2)   Frederickson, C. J.; Bush, A. I. *Biometals* **2001**, *14*, 353-366.

(3)   Huang, E. P. *Proc. Nat. Acad. Sci. USA* **1997**, *94*, 13386-13387.

(4)   Li, Y.; Hough, C. J.; Suh, S. W.; Sarvey, J. M.; Frederickon *J. Neurophysiol.* **2001**, *86*, 2597-2604.

(5)   Manzerra, P.; Behrens, M. M.; Canzoniero, M. T.; Wang, X. Q.; Heidinger, V.; Ichinose, T.; Yu, S. P.; Choi, D. W. *Proc. Nat. Acad. Sci. USA* **2001**, *98*, 11055-11061.

(6)   Maret, W. *BioMetals* **2001**, *14*, 187-190.

(7)   Takeda, A. *Brain Res. Rev.* **2000**, *34*, 137-148.

(8)   Takeda, A. *Biometals* **2001**, *14*, 343-351.

(9)   Vogt, K.; Mellor, J.; Tong, G.; Nicoli, R. *Neuron* **2000**, *26*, 187-196.

(10)   Suh, S. W.; Jensen, K. B.; Jensen, M. S.; Silva, D. S.; Kesslak, P. J.; Danscher, G.; Frederickson, C. J. *Brain Res.* **2000**, *852*, 274-278.

(11)   Cuajungo, M. P.; Lees, G. J. *Neurobiol. Disease* **1997**, *4*, 137-169.

(12)   Choi, D. W.; Koh, J. Y. *Annu. Rev. Neurosci.* **1998**, *21*, 347-375.

(13)   Kay, A. R. *J. Neurosci.* **2003**, *23*, 6847-6855.

(14)   Komatsu, K.; Kikuchi, K.; Kojima, H.; Urano, Y.; Nagano, T. *J. Am. Chem. Soc.* **2005**, *127*, 10197-10204.

(15)   Nolan, E. M.; Lippard, S. J. *Inorg. Chem.* **2004**, *43*, 8310-8317.

(16)   Nolan, E. M.; Jaworski, J.; Okamoto, K.-I.; Hayashi, S. Y.; Sheng, M.; Lippard, S. J. *J. Am. Chem. Soc.* **2005**, *127*, 16812-16823.

(17)   Sparano, B. A.; Shahi, S. P.; Koide, K. *Org. Lett.* **2004**, *6*, 1947-1949.

(18)   Banerjee, S. R.; Levadala, M. K.; Lazarova, N.; Wei, L.; Valliant, J. F.; Stephenson, K. A.; Babich, J. W.; Maresca, K. P.; Zubieta, J. *Inorg. Chem.* **2002**, *41*, 6417-6425.

(19)   Burdette, S. C.; Walkup, G. K.; Springler, B.; Tsien, R. Y.; Lippard, S. J. *J. Am. Chem. Soc.* **2001**, *123*, 7831-7841.

(20)   Chang, C. J.; Nolan, E. M.; Jaworski, J.; Burdette, S. C.; Sheng, M.; Lippard, S. J. *Chem. Biol.* **2004**, *11*, 203-210.

(21)   *SMART: Software for the CCD Detector System*, version 5.626; Bruker AXS: Madison, WI, 2000.

(22)   Kuzelka, J.; Mukhopadhyay, S.; Spingler, B.; Lippard, S. J. *Inorg. Chem.* **2004**, *43*, 1751-1761.

(23)   *SAINTPLUS: Software for the CCD Detector System*, version 5.01; Bruker AXS: Madison, WI, 1998.

(24)   *SHELXTL: Program Library for Structure Solution and Molecular Graphics*, version 6.1; Bruker AXS: Madison, WI, 2001.

(25)   Sheldrick, G. M. *SADABS: Area-Detector Absorption Correction;* University of Gottingen, Gottingen, Germany, 2001.

(26)   Spek, A. L. *PLATON, A Multipurpose Crystallographic Tool*, Utrecht University: Utrecht, The Netherlands, 2000.

(27)   Brannon, J. H.; Madge, D. *J. Phys. Chem.* **1978**, *82*, 705-709.

(28)   Kroncke, K.-D.; Kolb-Bachofen, V. *Methods Enzymol.* **1999**, *301*, 126-135.

(29)   Brewer, G. J.; Toricelli, J. R.; Evege, E. K.; Price, P. J. *J. Neurosci. Res.* **1993**, *35*, 567.

(30) de Silva, A. P.; Gunaratne, H. Q. N.; Gunnlaugsson, T.; Huxley, A. J. M.; McCoy, C. P.; Rademacher, J. T.; Rice, T. E. *Chem. Rev.* **1997**, *97*, 1515-1566.

(31) de Silva, A. P.; Fox, D. B.; Huxley, A. J. M.; Moody, T. S. *Coord. Chem. Rev.* **2000**, *205*, 41-57.

(32) Sjoback, R.; Nygren, J.; Kubista, M. *Spectrochim. Acta. Part A* **1995**, *51*, L7-L21.

(33) Leonhardt, H.; Gordon, L.; Livingston, R. *J. Phys. Chem.* **1971**, *75*, 245-249.

(34) Gee, K. R.; Poot, H.; Klaubert, D. H.; Sun, W.-C.; Haligland, R. P.; Mao, F. *J. Org. Chem.* **1997**, *62*, 6469-6475.

(35) Nolan, E. M.; Lippard, S. J.; Baik, M.-H. *Unpublished results.*

(36) Hirano, T.; Kikuchi, K.; Urano, Y.; Nagano, T. *J. Am. Chem. Soc.* **2002**, *124*, 6555-6562.

(37) Takahashi, A.; Camacho, P.; Lechileiter, J. D.; Herman, B. *Physiol. Rev.* **1999**, *79*, 1089-1125.

(38) Manev, H.; Kharlamov, E.; Uz, T.; Mason, R. P.; Cagnoli, C. M. *Exp. Neurol.* **1999**, *146*, 171-178.

(39) Sensi, S. L.; Yin, H. Z.; Carriedo, S. G.; Rao, S. S.; Weiss, J. H. *Proc. Natl. Acad. Sci. USA* **1999**, *96*, 2414-2419.

(40) Sensi, S. L.; Yin, H. Z.; Weiss, J. H. *Eur. J. Neurosci.* **2000**, *12*, 3813-3818.

(41) Chang, C. J.; Nolan, E. M.; Jaworski, J.; Sheng, M.; Lippard, S. J. *unpublished results.*

(42) Colvin, R. *ZincSignals Conference*, **2005**, Galveston, TX, November 2005.

(43) Sensi, S. L. *Personal communication.*

(44) Sensi, S. L.; Ton-That, D.; Weiss, J. H. *Neurobiol. Disease* **2002**, *10*, 100-108.

(45) Sensi, S. L.; Canzoniero, L. M. T.; Yu, S. P.; Ying, S. P.; Ying, H. S.; Koh, J.-Y.; Kerchner, G. A.; Choi, D. W. *J. Neurosci.* **1997**, *17*, 9554-9564.

(46) Colvin, R. A.; Davis, N.; Nipper, D. R. W.; Carter, P. A. *J. Nutrition* **2000**, *130*, 1484S-1487S.

(47) Chen, Y.; Ire, Y.; Keung, W. M.; Maret, W. *Biochemistry* **2002**, *41*, 8360-8367.

(48) Spahl, D. U.; Berendji-Grun, D.; Suschek, C. V.; Kolb-Bachofen, V.; Kroncke, K.-D. *Proc. Natl. Acad. Sci. USA* **2003**, *100*, 13952-13957.

Table 6.1. Summary of X-ray Crystallographic Data

	ZSF6·CH$_2$Cl$_2$	10·0.5CH$_2$Cl$_2$·0.5Et$_2$O	11
Empirical Formula	C$_{45}$H$_{32}$Cl$_2$F$_4$N$_4$O$_5$S$_2$	C$_{40.5}$H$_{34}$ClF$_6$N$_4$O$_{8.50}$S$_4$Zn$_2$	C$_{38}$H$_{42}$B$_2$Cu$_2$F$_8$N$_4$O$_4$S$_2$
Formula Weight	990.695	1121.15	983.596
Space Group	P$\bar{1}$	P$\bar{1}$	P2$_1$/n
a, Å	13.0106(9)	10.8605(8)	10.1101(7)
b, Å	13.7993(10)	13.0832(10)	15.7610(11)
c, Å	14.1006(1)	17.4505(13)	13.0036(9)
α, deg	73.9770(10)	79.5640(10)	
β, deg	78.8810(10)	72.5750(10)	100.800(10)
γ, deg	63.8530(10)	79.7160(10)	
V, Å^3	2176.8(3)	2306.1(1)	2305.4(2)
Z	2	2	2
ρ$_{calc}$, g/cm^3	1.508	1.615	1.611
T, °C	-100	-100	-100
μ(Mo Kα), mm^{-1}	0.437	1.360	1.231
θ limits, deg	1.75 – 25.00	2.30 – 25.00	2.42 – 28.33
total no. of data	15511	32161	35042
No. of unique data	7576	8115	5061
No. of params	715	650	298
Goodness-of-fit on F^2	1.037	1.019	1.051
Final R indices [I>2σ(I)]^{a,b}	R=0.0614; wR^2=0.1685	R=0.0546; wR^2=0.1505	R=0.0494; wR^2=0.1395
R indices (all data)^{a,b}	R=0.0657; wR^2=0.1734	R1=0.0679; wR^2=0.1615	R1=0.0533; wR^2=0.1434
max, min peaks, e/Å^3	0.798, -0.553	1.627, -0.499	1.424, -1.344

^{a} $R = \Sigma \mid \mid F_o \mid - F_c \mid \mid / \Sigma \mid F_o \mid$

^{b} $wR^2 = \{ \Sigma [w(F_o^2 - F_c^2)^2] / \Sigma [w(F_o^2)^2] \}^{1/2}$

Table 6.2. Selected Bond Lengths (Å) and Angles

ZSF6 (6)

Bond Lengths	(Å)	Bond Angles	(Deg)
O(1)—C(27)	1.335(3)	C(25)—O(2)—C(37)	118.9(2)
O(3)—C(35)	1.344(3)	O(1)—C(27)—C(28)	117.6(2)
O(2)—C37)	1.380(3)	O(1)—C(27)—C(26)	123.3(2)
O(2)—C(25)	1.382(3)	C(44)—O(5)—C(31)	111.6(2)
O(5)—C(31)	1.507(3)	C(11)—N(1)—C(6)	111.8(2)
O(4))—C(44)	1.203(4)	C(11)—N(1)—C(12)	110.1(2)
F(1)—C(39)	1.333(3)	C(1)—N(2)—C(5)	118.6(2)
Cl(1)—C(28)	1.733(3)	C(7)—S(1)—C(10)	92.17(15)
N(1)—C(12)	1.470(3)		
N(1)—C(6)	1.463(3)		
N(1)—C(11)	1.462(3)		

[Zn₂(L)(OTf)₂] (10)

Bond Lengths	(Å)	Bond Angles	(Deg)
Zn(1)—N(1)	2.164(4)	O(1)—Zn(1)—N(2)	165.28(14)
Zn(1)—N(2)	2.069(4)	O(1)—Zn(1)—N(1)	89.47(13)
Zn(1)—O(1)	1.997(3)	O(1)—Zn(1)—O(2)	96.30(13)
Zn(1)—O(2)	2.068(3)	N(1)—Zn(1)—N(2)	80.04(14)
Zn(1)—Zn(1A)	3.0206(10)	O(2)—Zn(1)—N(1)	104.87(14)
		O(2)—Zn(1)—N(2)	96.35(14)

[Cu₂(L)(CH₃OH)₂](BF₄)₂ (11)

Bond Lengths	(Å)	Bond Angles	(Deg)
Cu(1)—N(1)	2.032(2)	O(1)—Cu(1)—O(2)	93.07(8)
Cu(1)—N(2)	1.961(2)	O(1)—Cu(1)—N(1)	106.28(8)
Cu(1)—O(1)	2.245(2)	O(1)—Cu(1)—N(2)	91.34(8)
Cu(1)—O(2)	1.9199(18)	O(2)—Cu(1)—N(1)	94.34(8)
Cu(1)—Cu(1A)	3.0549(6)	O(2)—Cu(1)—N(2)	175.53(8)
		N(1)—Cu(1)—N(2)	83.66(9)

Table 6.3. Spectroscopic and Thermodynamic Data for Symmetrical ZP and ZS Sensors[a]

	Absorption λ (nm), $\varepsilon \times 10^4$ ($M^{-1}cm^{-1}$)		Emission λ (nm), Φ[b]		pK_{a1}[c] (N)	pK_{a2}[d]	~DR[e]
	Unbound	Zn(II)	Unbound	Zn(II)			
ZP1	515, 7.9	507, 8.4	531, 0.38	527, 0.87	8.4	2.8	2.5
ZP2	498, 4.4	490, 5.3	522, 0.25	517, 0.92	9.4	3.9	6
ZP3	502, 7.5	492, 8.5	521, 0.15	516, 0.92	6.8	2.0	6
ZPF1	533, 9.9	525, 12.0	547, 0.11	544, 0.55	6.9	1.8	6
ZPCl1	534, 9.7	527, 12.0	550, 0.22	549, 0.50	7.0	1.9	2.5
ZPBr1	534, 4.5	528, 8.6	549, 0.25	547, 0.36	7.3	2.1	2.2
ZPF3	520, 8.7	510, 9.3	537, 0.14	533, 0.60	6.7	1.9	5
ZS1	510, 8.4	501, 7.5	531, 0.50	526, 0.70	7.7	2.0	1.4
ZS2	499, 6.7	489, 6.8	523, 0.39	516, 0.69	7.7	2.7	2
ZS5	497, 3.3	490, 4.2	522, 0.36	517, 0.80	8.0	4.6	4
ZS6	515, 4.5	505, 6.0	533, 0.44	527, 0.64	7.8	3.3	2.2
ZSF6	532, 6.3	522, 7.0	549, 0.19	545, 0.63	7.1	2.0	3
ZS7	500, 6.2	490, 6.6	524, 0.25	518, 0.79	7.0	2.7	4
ZSF7	521, 6.2	511, 7.0	535, 0.24	527, 0.68	6.9	2.5	4

[a]All measurements were conducted at pH 7 (50 mM PIPES, 100 mM KCl). ZP1 and ZP2 data were taken from ref. 19. Data for the remaining ZP are in Chapter 2. [b]Quantum yields were measured using fluorescein in 0.1 N NaOH as a standard ($\Phi = 0.95$, ref 27). [c]The pK_a value associated with fluorescence enhancement as the pH is lowered. This corresponds to the first pK_a value for benzoate halogenated ZP sensors. [d]The pK_a value associated with fluorescence quenching as the pH is lowered. [e]DR is the dynamic range or observed change in emission resulting from Zn(II) coordination.

Table 6.4. Kinetic and Thermodynamic Parameters for Zn(II) Binding to ZS Sensors[a]

| | k_{on} $(M^{-1}s^{-1})$[b] | k_{on} $(M^{-1}s^{-1})$[c] | K_{d1}[d] (μM) | k_{off} (s^{-1})[e] | $\Delta H^{\ddagger}$ [f] | $\Delta S^{\ddagger}$ [f] |
	4.3 °C	25 °C	25 °C	25 °C	(kcal/mol)	(cal/mol-K)
ZS5	$3.6\pm0.2 \times 10^5$	$2.2\pm0.1 \times 10^6$	1.5 ± 0.2	3.3	13.3 ± 0.1	15.2 ± 0.2
ZS6	$3.7\pm0.1 \times 10^5$	$2.1\pm0.1 \times 10^6$	n.d.	n.d.	12.9 ± 0.4	14.0 ± 0.7
ZS7	$5.9\pm0.1 \times 10^5$	$3.0\pm0.1 \times 10^6$	3.7 ± 0.2	11	12.5 ± 0.3	12.9 ± 1.3
ZSF6	$3.3\pm0.1 \times 10^5$	$1.8\pm0.1 \times 10^6$	n.d.	n.d.	12.6 ± 0.2	12.4 ± 0.9
ZSF7	$5.0\pm0.1 \times 10^5$	$2.7\pm0.1 \times 10^6$	5.0 ± 0.3	13.5	12.6 ± 0.2	13.0 ± 0.7

[a]All measurements were made at pH 7 (50 mM PIPES, 100 mM KCl). [b]Experimentally determined values for k_{on} at 4.3 ± 0.1 °C. [c]Experimentally determined k_{on} at 25 ± 0.1 °C. [d]Dissociation constants obtained experimentally by fluorimetric titration at 25 ± 1 °C.. [e]Calculated k_{off} for ZS at 25 °C. [f] Activation parameters were determined over a temperature range of ~4 to ~40 °C.
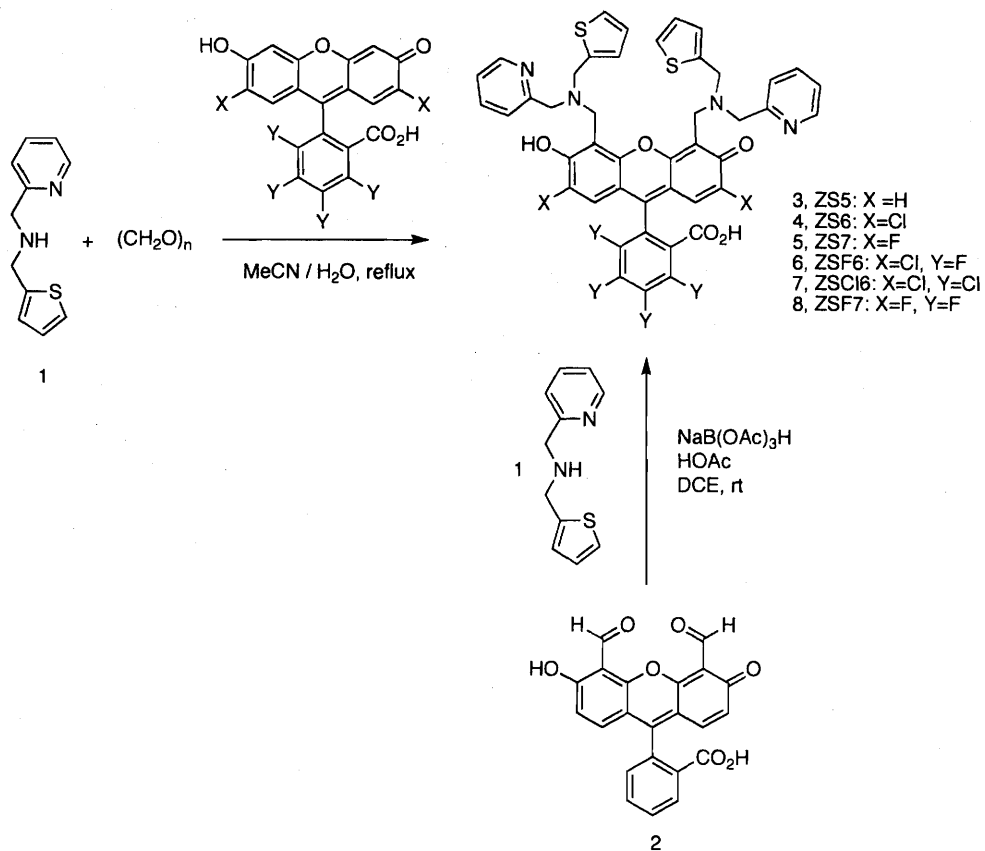
Scheme 6.1. Syntheses of ZS sensors **3-8**.
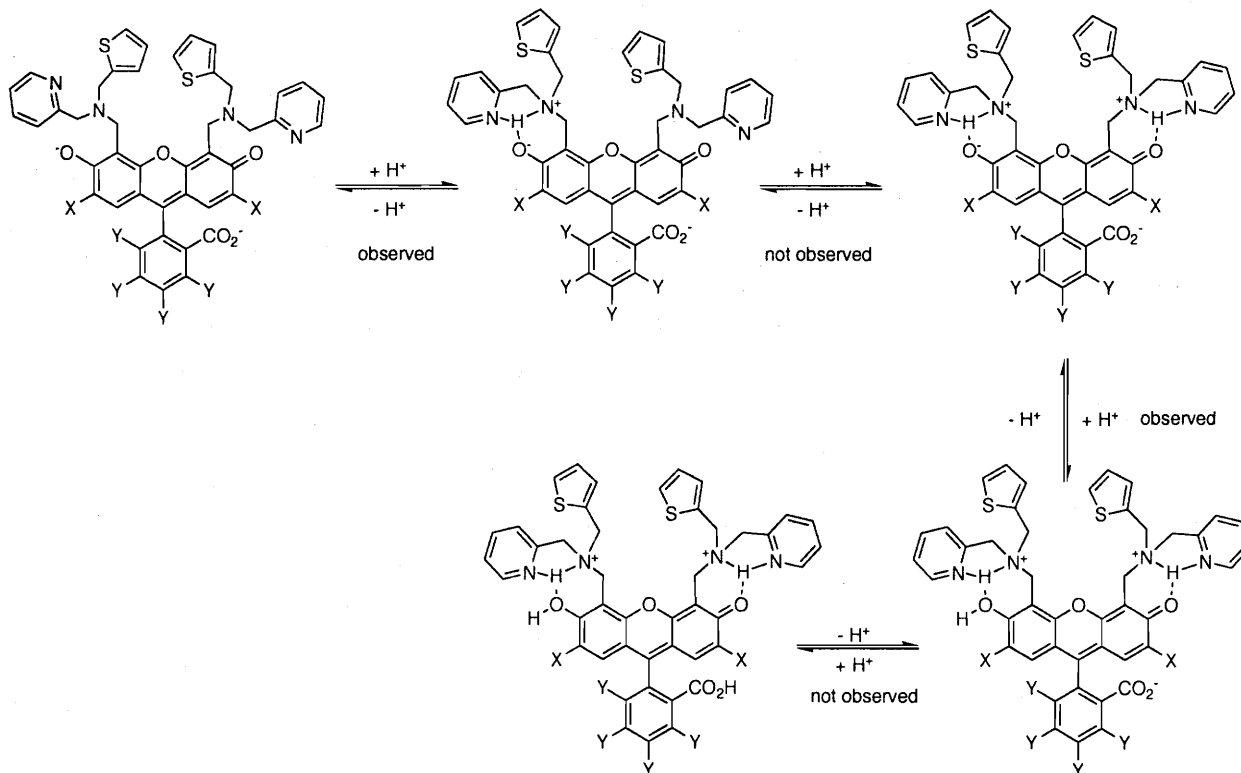
Scheme 6.2. Protonation equilibria for compounds **3-8**. "Observed" and "not observed" refer to the effect of these protonation events on sensor emission. Protonation of the carboxylate occurs at pH < 2 and is not observed during the experiment.
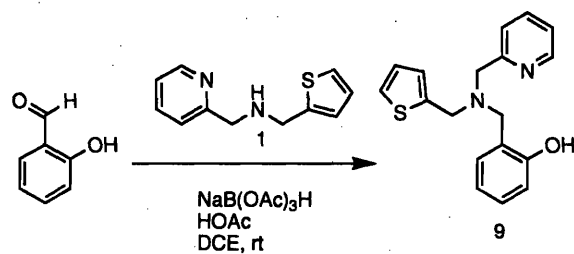
Scheme 6.3. Synthesis of the salicylaldehyde-based model ligand **9**.
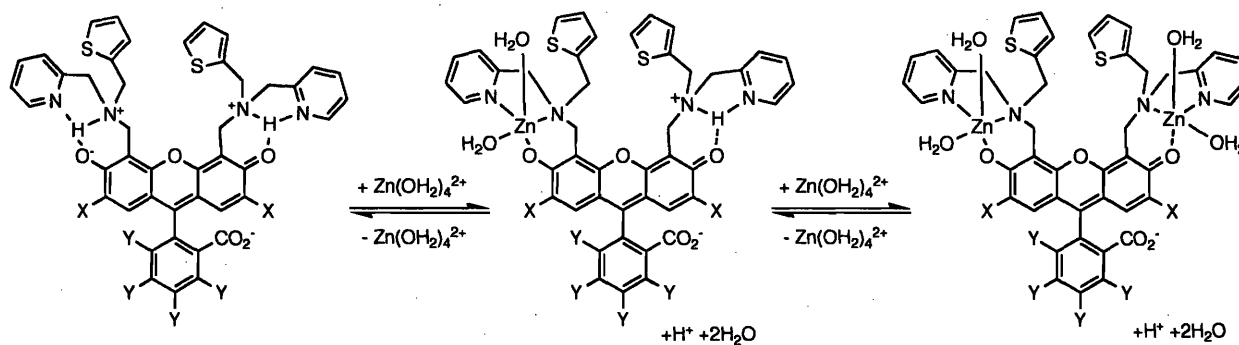
Scheme 6.4. Proposed Zn(II) coordination for thiophene-containing ZS sensors.
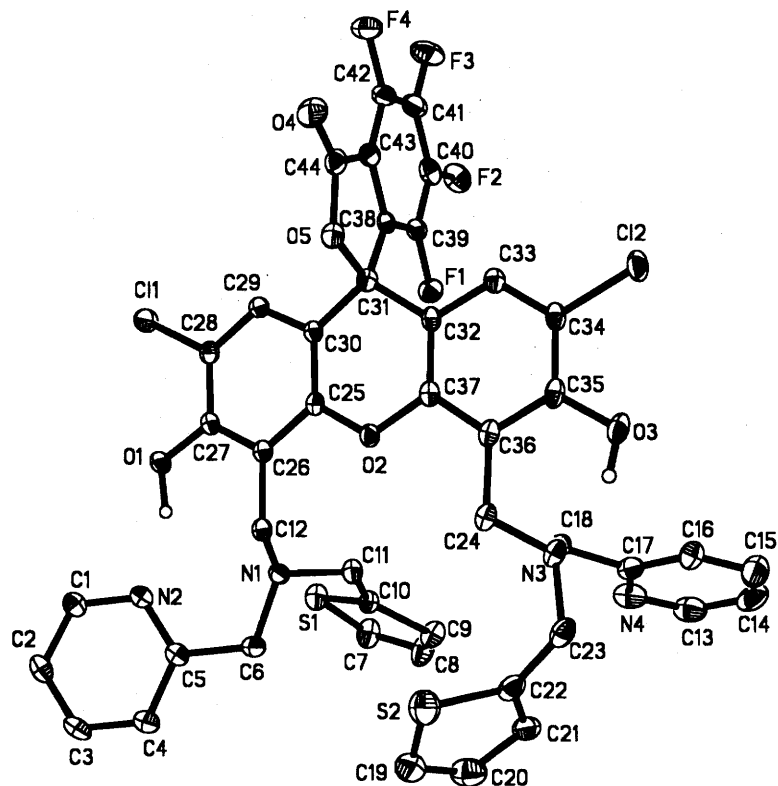
Figure 6.1. ORTEP diagram for the structure of ZSF6 showing 40% probability ellipsoids on all non-hydrogen atoms.
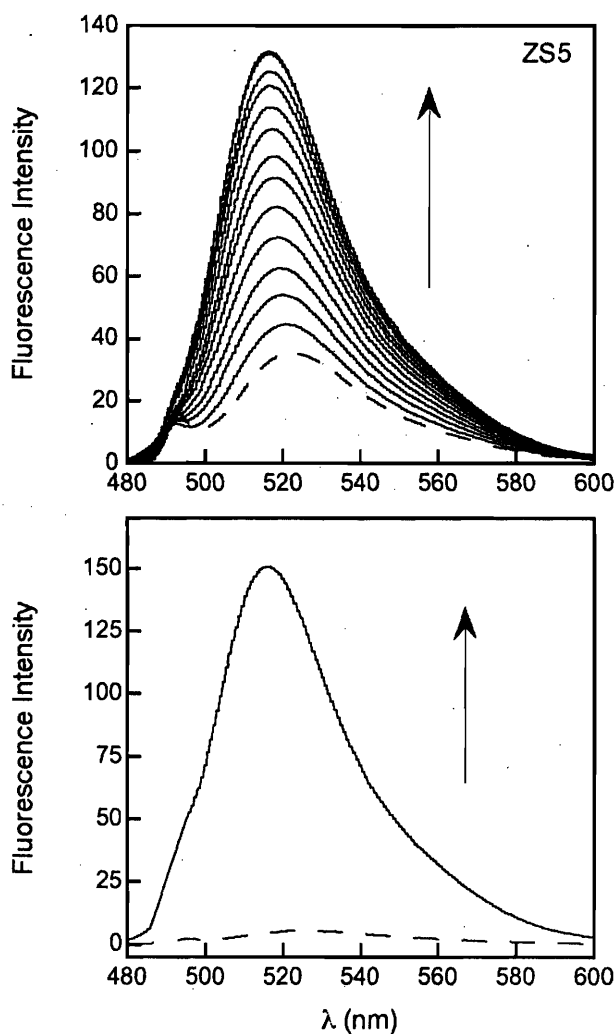
Figure 6.2. Fluorescence response of ZS5 to Zn(II). Top: Response of ZS5 to Zn(II) at pH 7 (50 mM PIPES, 100 mM KCl). Aliquots of 1 and 10 mM $ZnCl_2$ in water were added to afford 0, 0.33, 0.66, 1.0, 1.5, 2.0, 3.0, 4.0, 6.0, 8.0, 10, 15, 20, 50 μM Zn(II). Bottom: response of ZS5 to 50 equiv of Zn(II) at pH 9 (50 mM CHES, 100 mM KCl). For all experiments, [ZS5] = 1 μM, λ_{ex} = 490 nm and T = 25 °C.
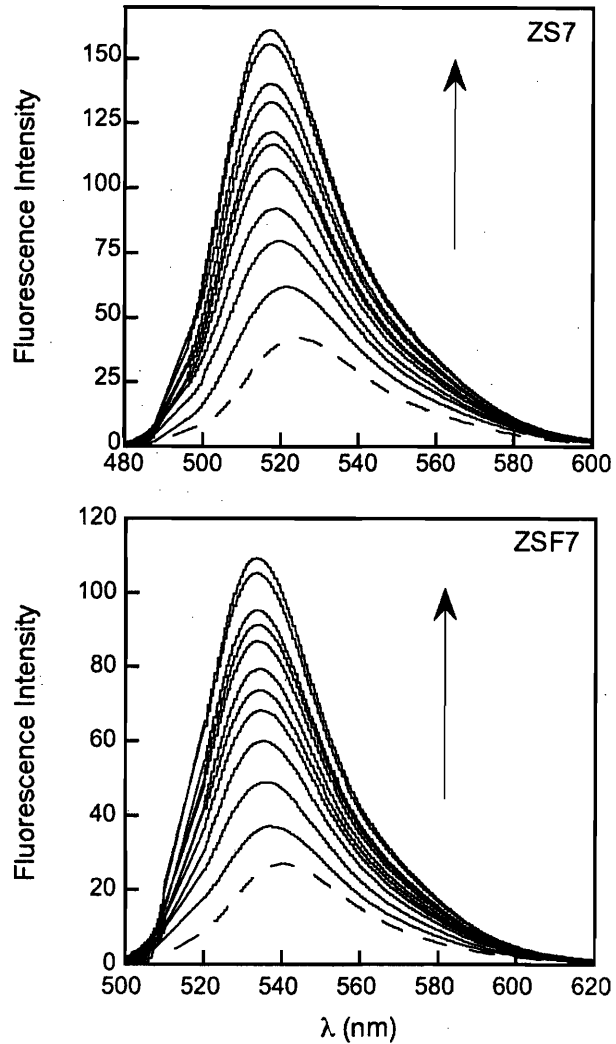
Figure 6.3. Fluorescence response of fluorinated ZS to Zn(II) at pH 7 (50 mM PIPES, 100 mM KCl). Top: The dotted line indicates the emission from 1 μM ZS7 and the solid lines show the fluorescence change that occurs upon introduction of 1, 2, 3, 4, 6, 8, 10, 15, 20, 30 and 50 equiv of Zn(II). Excitation was provided at 490 nm and T = 25 °C. Bottom: Response of 1 μM ZSF7 to Zn(II). See description for the top plot. Excitation was provided at 510 nm and T = 25 °C.
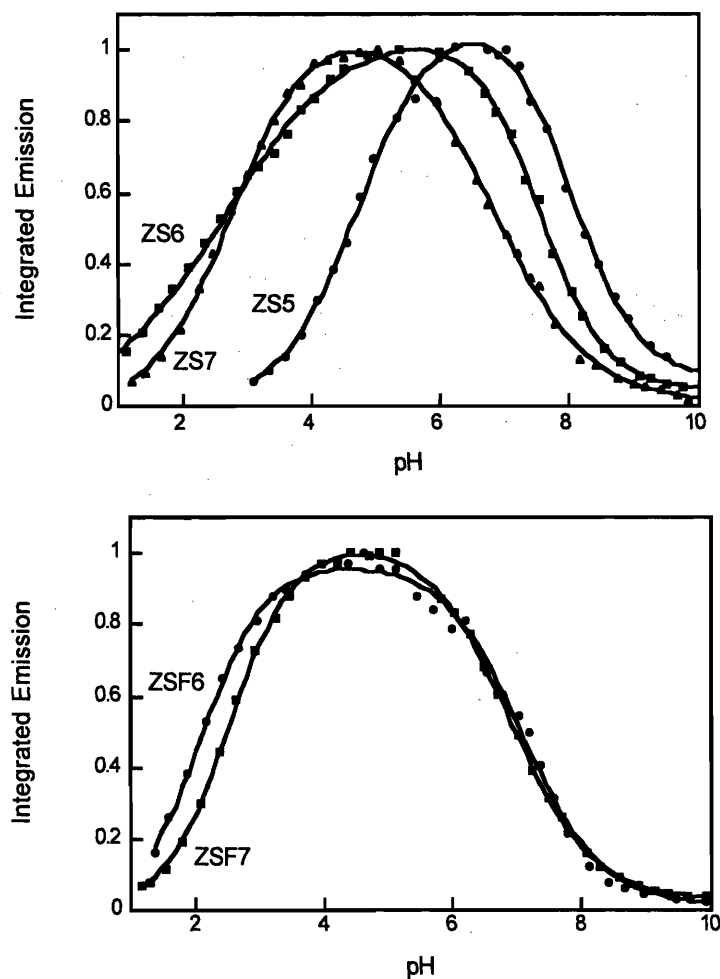
Figure 6.4. Effect of pH on integrated emission (100 mM KCl, T = 25 °C). Top plot: Representative pH titrations for ZS5 (circles), ZS6 (squares) and ZS7 (diamonds). Bottom plot: Representative pH titrations for ZSF6 (cicles) and ZSF7 (squares). For each titration, [ZS] = 1 μM and the pH was lowered by incremental addition of aqueous HCl. The pK_a values are listed in Table 6.3.
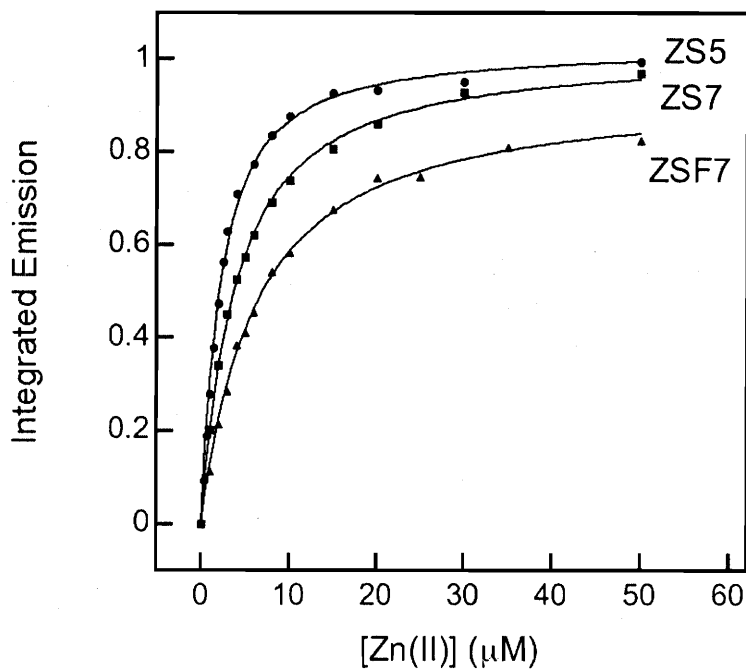
Figure 6.5. Representative plots of integrated emission vs. Zn(II) concentration for ZS5

(circles), ZS7 (squares) and ZSF7 (triangles) at pH 7 (50 mM PIPES, 100 mM KCl). These

binding curves correspond to the fluorimetric titrations presented in Figures 6.2 and 6.3.

Dissociation constants are included in Table 6.3.
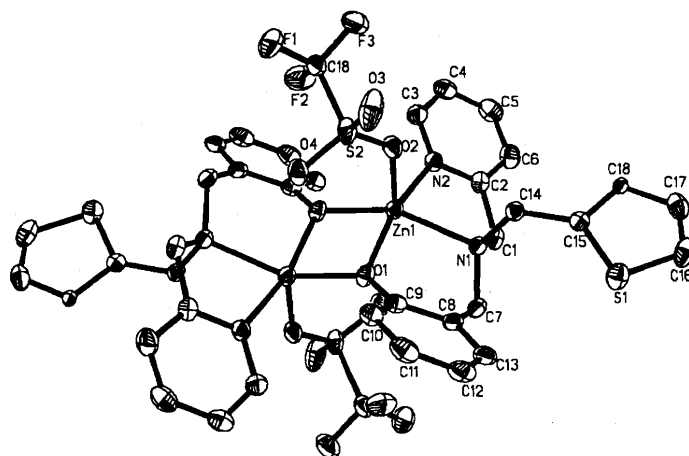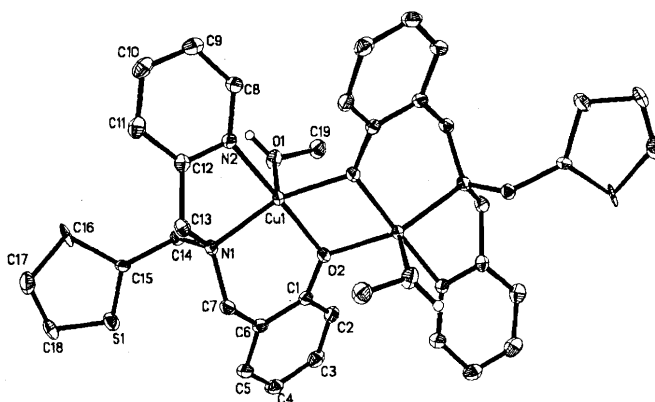
Figure 6.6. ORTEP diagrams showing 40% probability thermal ellipsoids on all non-hydrogen atoms for compounds **10** and **11**.
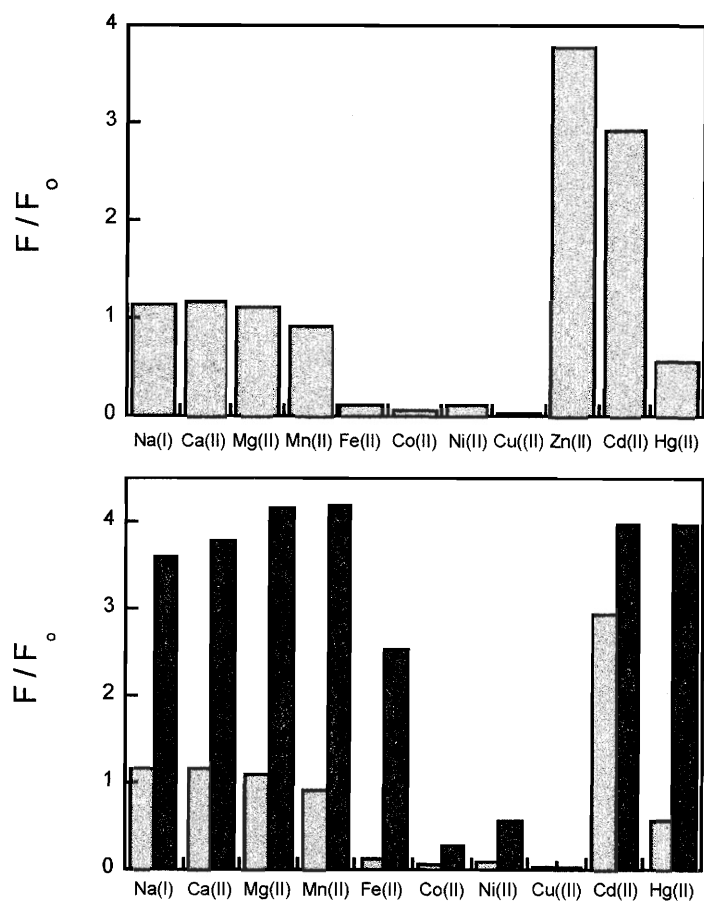
Figure 6.7. Selectivity of ZS5 for Zn(II) at pH 7 (50 mM PIPES, 100 mM KCl). Top plot: The fluorescence response of 1 μM ZS5 to 50 equiv of the cation of interest. Bottom plot: The light grey bars are equivalent to the bars in the top plot. The dark grey bars illustrate the fluorescence change that occurs after 50 equiv of Zn(II) is added to the solution containing 1 μM ZS5 and 50 equiv of the cation of interest. All data (F) is normalized with respect to emission from the free sensor (F_o). Excitation was provided at 490 nm and T = 25 °C.
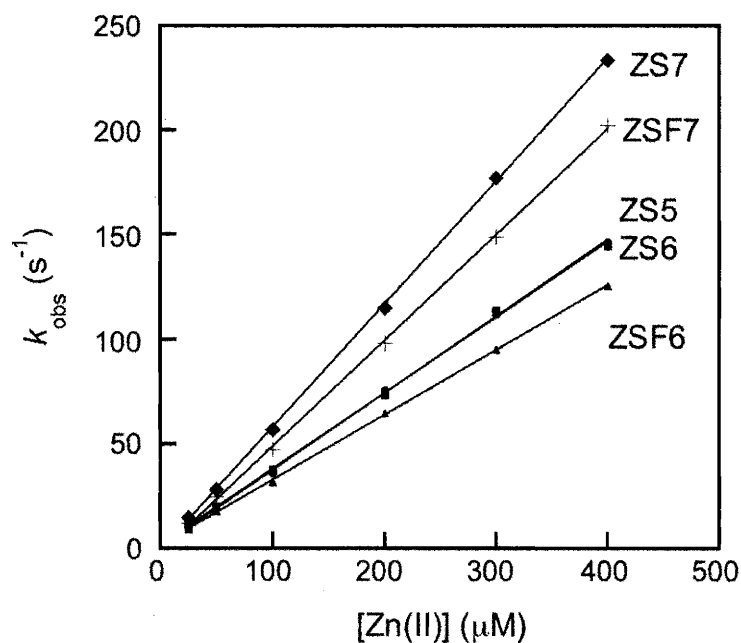
Figure 6.8. Plots of k_{obs} vs. concentration of Zn(II) for ZS family members obtained from stopped-flow fluorescence studies at pH 7 (50 mM PIPES, 100 mM KCl). The concetration of ZS was 0.5 μM after mixing and the concentration of Zn(II) was varied from 0 to 400 μM after mixing. The temperature was 4.3 ± 0.1 °C. Kinetic parameters are given in Table 6.4.
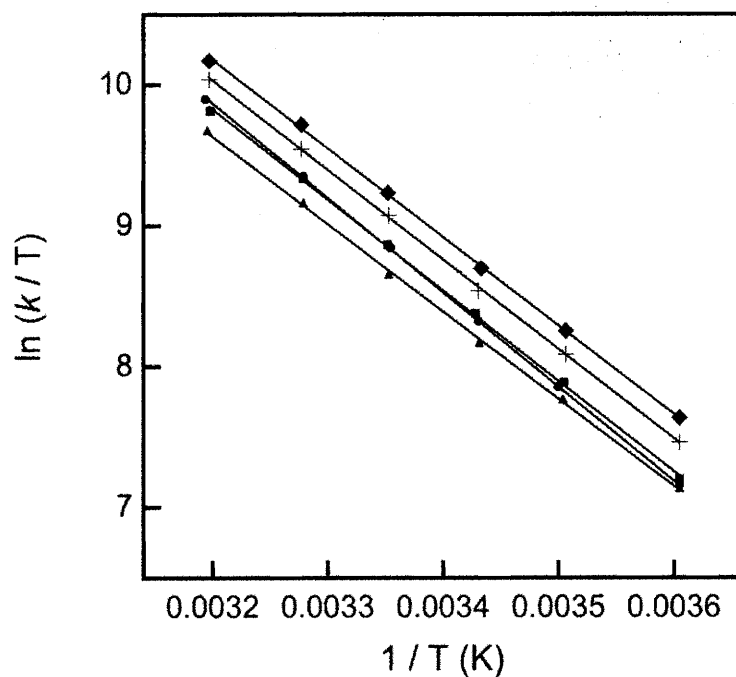
Figure 6.9. Representative Eyring plots for ZS5 (circles), ZS6 (squares), ZS7 (triangles), ZSF6 (diamonds) and ZSF7 (crosses). The concentration of ZS and Zn(II) were 0.5 and 75 µM after mixing, respectively, and the temperature was varied from ~4 to ~40 °C. Activation parameters are given in Table 6.4.
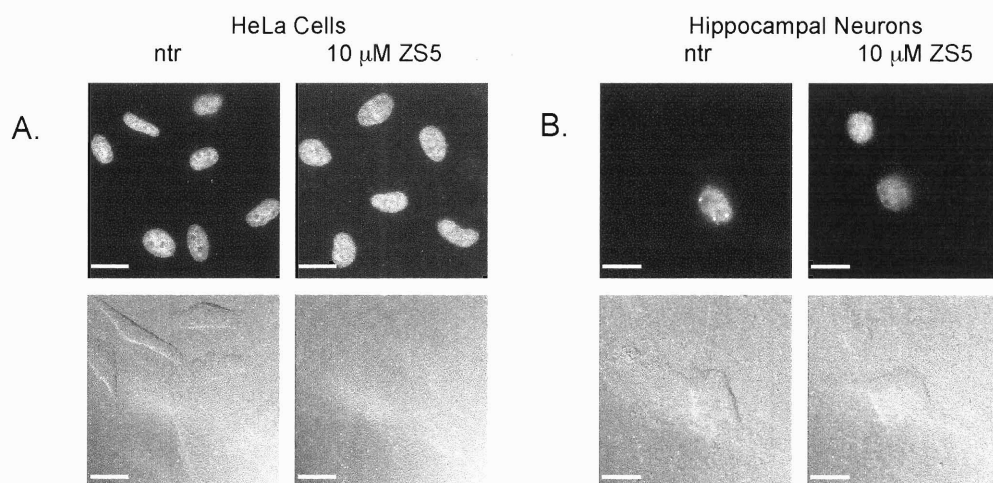
Figure 6.10. Nuclear morphology assays of cells treated with ZS5. A. Representative epifluorescence (top panels) and DIC (bottom panels) images of HeLa cells treated with 10 μM ZS5 for 24 h, fixed and stained with 800 nM Hoescht. The cells were imaged with a 63x objective and the scale bar represents 25 μm. B. Representative epifluorescence (top panels) and DIC (bottom panels) images of primary hippocampal neurons (DIV 20) treated with 10 μM ZS5 for 24 h, fixed and stained with 800 nM Hoescht. The cells were imaged with a 100x objective and the scale bar represents 16 μm.
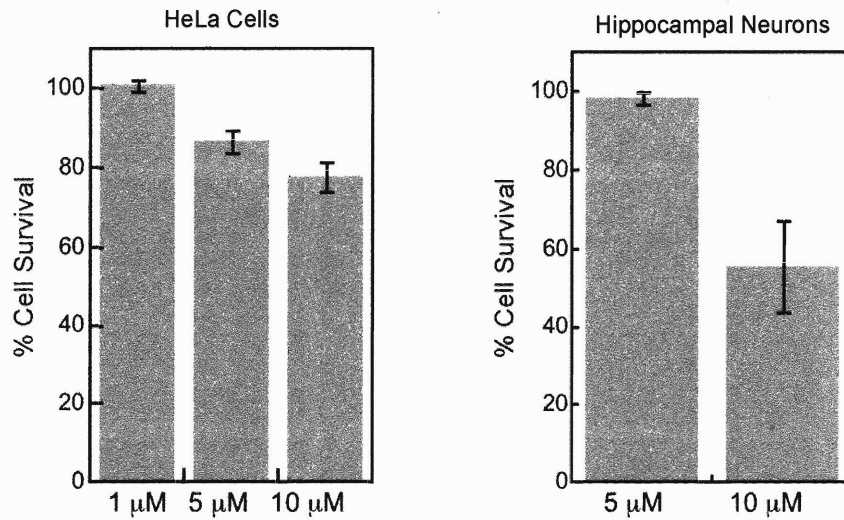
Figure 6.11. Cytotoxicity of ZS5 to HeLa cells and primary cultures of hippocampal neurons (DIV 20) following 24 h treatment as quantified by the MTT assay. These data represent the average of three independent trials for the HeLa cells and one trial for the hippocampal neurons.
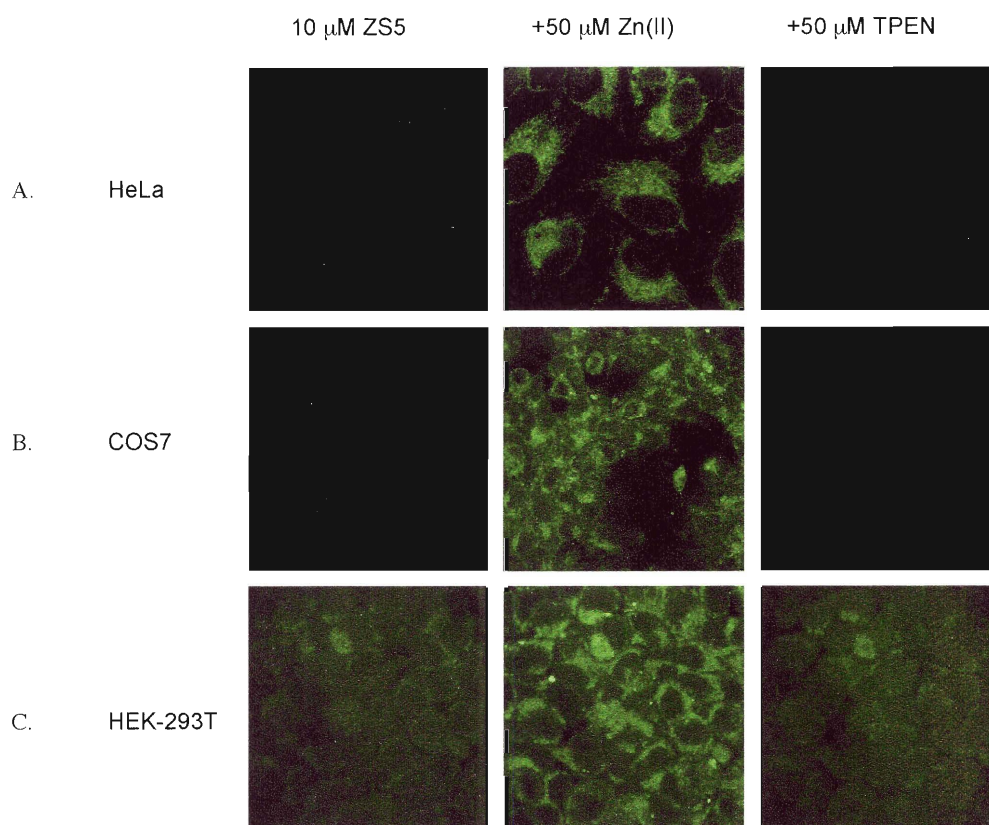
Figure 6.12. Response of ZS5 to exogenously added Zn(II) in HeLa, COS-7 and HEK cells. Left panels: the cells were treated with 10 μM ZS5 for 30 min (T = 37 °C, 5% CO_2), washed and imaged. Middle panel: 50 μM of Zn(II)/pyrithione (1:2 ratio) was added to the dish and the cells were imaged after 5 min (T = 37 °C, 5% CO_2). Right panels: Fluorescence decrease observed 5 min after addition of 50 μM TPEN.
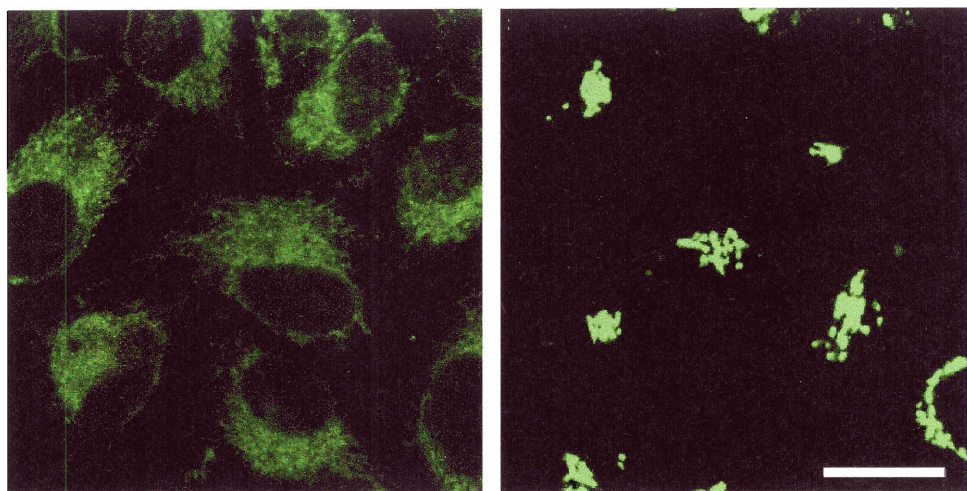
Figure 6.13. Comparsion of subcellular compartmentalization of ZS5 (left) and ZP3 (right). Both images were obtained 5 min after addition of 50 µM 1:2 Zn(II)/pyrithione to cells treated with 10 µM ZS5 or ZP3 (T = 37 °C, 5% CO_2). The scale bar is 25 µm.

| Red Marker | ZS5 | ZS5 + Zn(II) | Overlay |

A. Lysotracker

B. Golgi-DsRed

C. Mitotracker
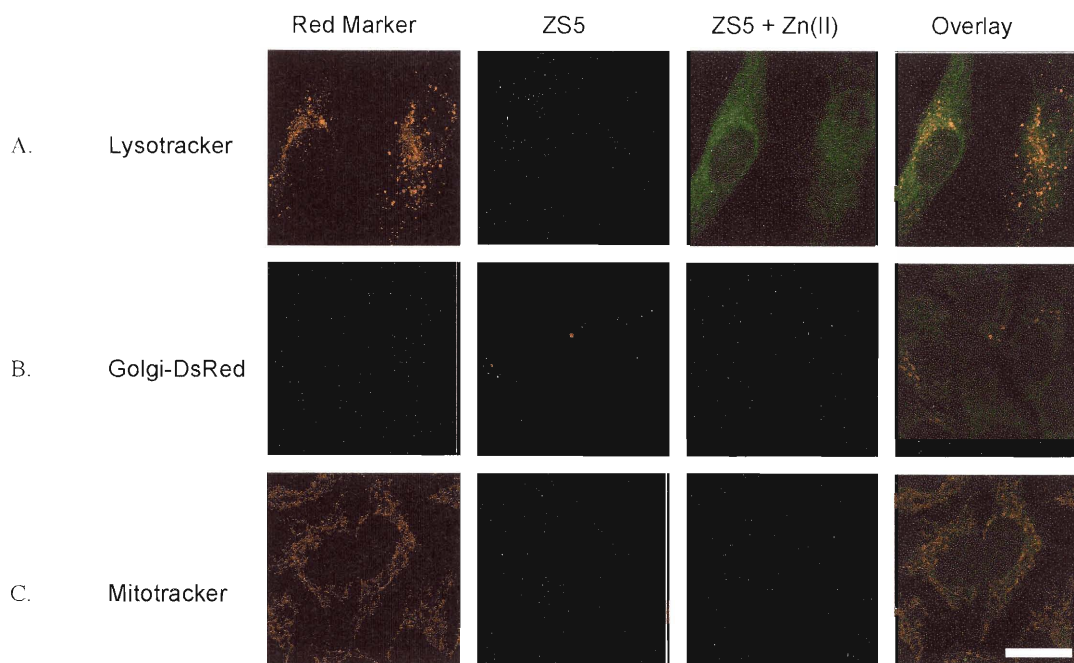
Figure 6.14. Colocalization studies with ZS5 in live HeLa cells. HeLa cells were treated or transfected with a red emitting organelle label and with 10 µM ZS5. The images in the third column were obtained after the cells were treated with 50 µM Zn(II)/pyrithione (1:2 ratio) for 5 min. The images in the right-hand column show the overlay between the red organelle marker and the ZS5+Zn(II) signal. Addition of Zn(II)/pyrithione causes no alteration in dye localization over the period of this experiment. No colocalization is observed with the lysosomal and Golgi markers. Good colocalziation is observed with ZS5 and the mitochondrial marker. The scale bar represents 25 µm for all images.
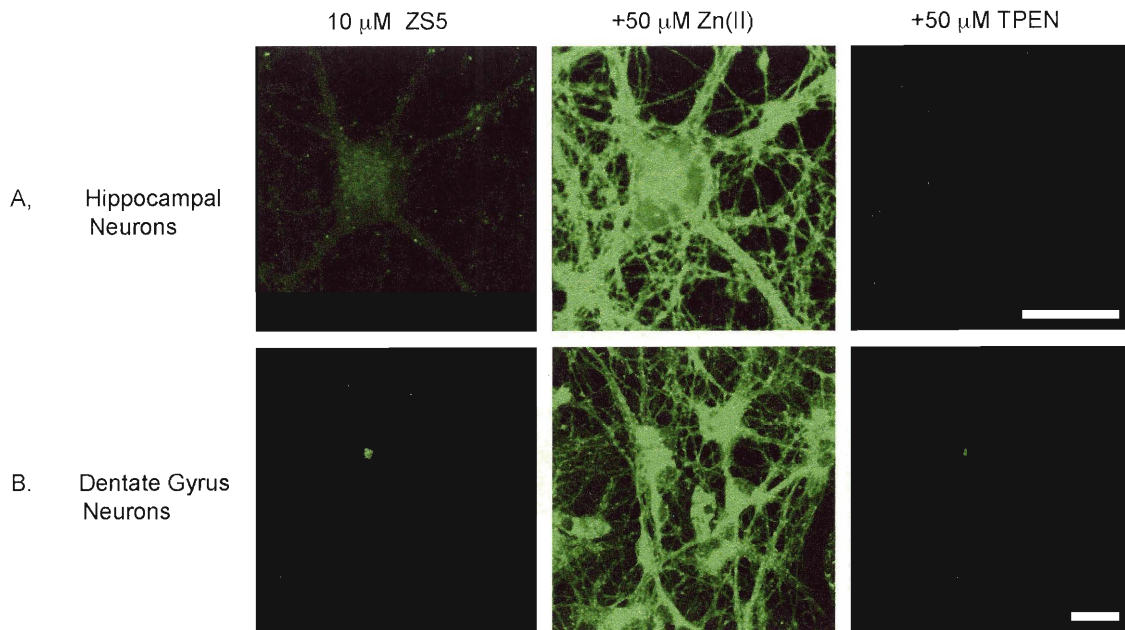
Figure 6.15. Response of ZS5 to exogenously added Zn(II) in primary cultures of hippocampal (top) and dentate gyrus (bottom) neurons. Left panels: The neurons were treated with 10 μM ZS5 for 30 min (T = 37 °C, 5% CO_2), washed and imaged. Middle panels: The fluorescence change observed 5 min after addition of 50 μM Zn(II)/pyrithione (1:2 ratio). Right panels: The fluorescence decrease observed 5 min after addition of 50 μM TPEN. The scale bars represent 25 μm.

Mitotracker   ZS5 + Zn(II)   Overlay
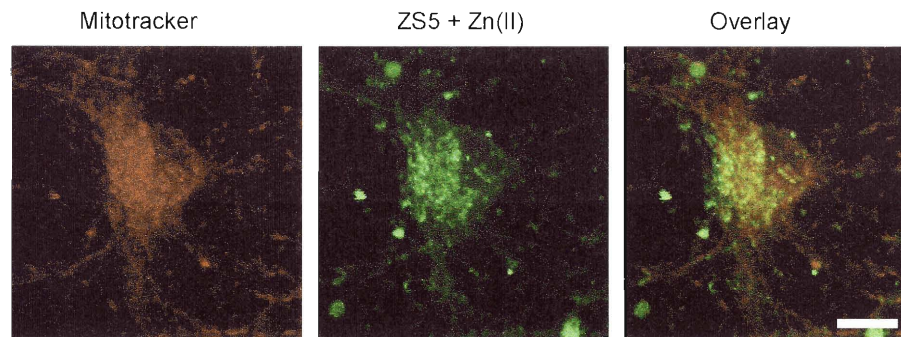
Figure 6.16. Representative images from preliminary colocalization studies of ZS5 and Mitotracker Red in primary cultures of hippocampal neurons from rat. The cells were treated with 10 μM ZS5 and 200 nM Mitotracker for 30 min (T = 37 °C, 5% CO_2), washed and then treated with 50 μM 1:1 Zn(II)/pyrithione for 5 min and imaged. The scale bar represents 10 μm.
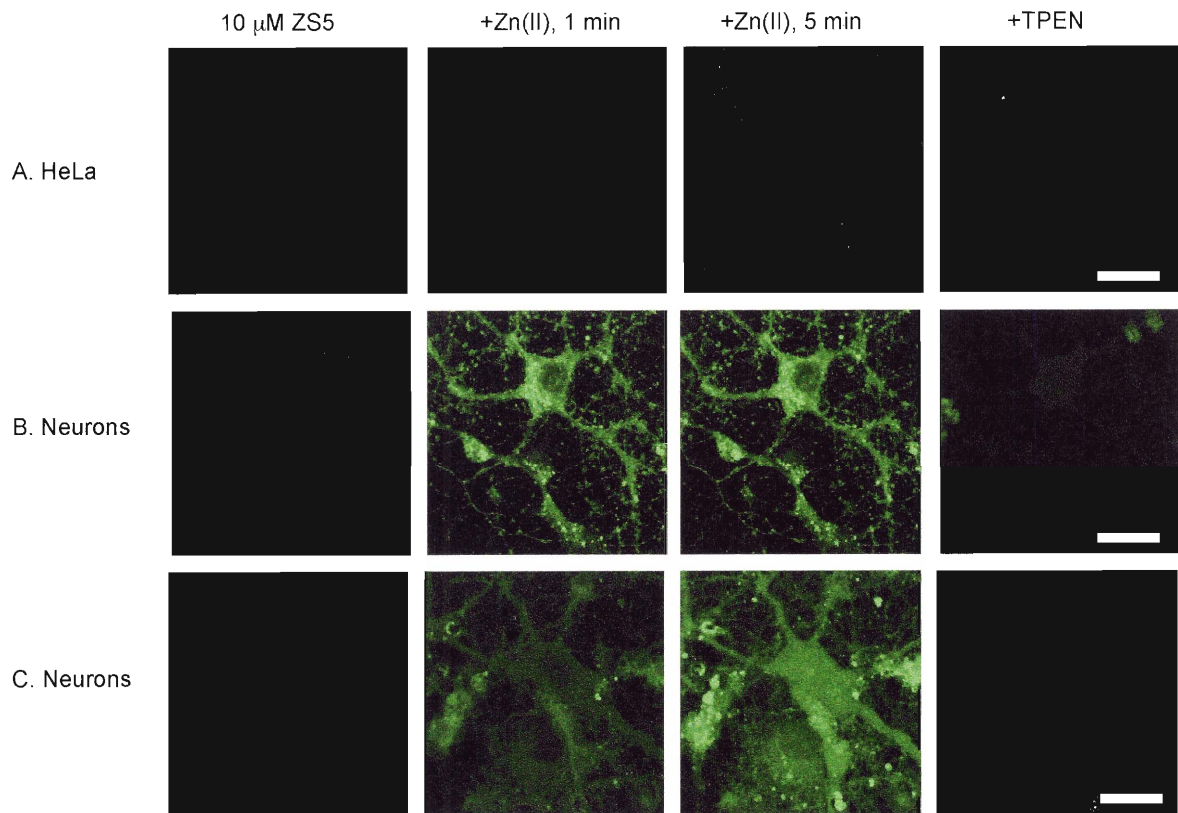
Figure 6.17. Time course experiments for Zn(II) addition to ZS5-treated HeLa cells and hippocampal neurons. A. Left panel: HeLa cells were treated with 10 μM ZS5 for 30 min (T = 37 °C, 5% CO_2), washed and imaged. 2nd and 3rd panels: Zn(II)/pyrithione (50 μM, 1:1 ratio) was added and the cells were imaged at 1 and 5 min after treatment. 4th panel: Fluorescence decrease 5 min after addition of 50 μM TPEN. B. Hippocampal neurons (DIV 18) treated with ZS5, Zn(II)/pyrithione and TPEN as described for part A. C. Hippocampal neurons treated as described in part A except that the concentration of added Zn(II)/pyrithione was 10 μM. The scale bars represent 25 μm.
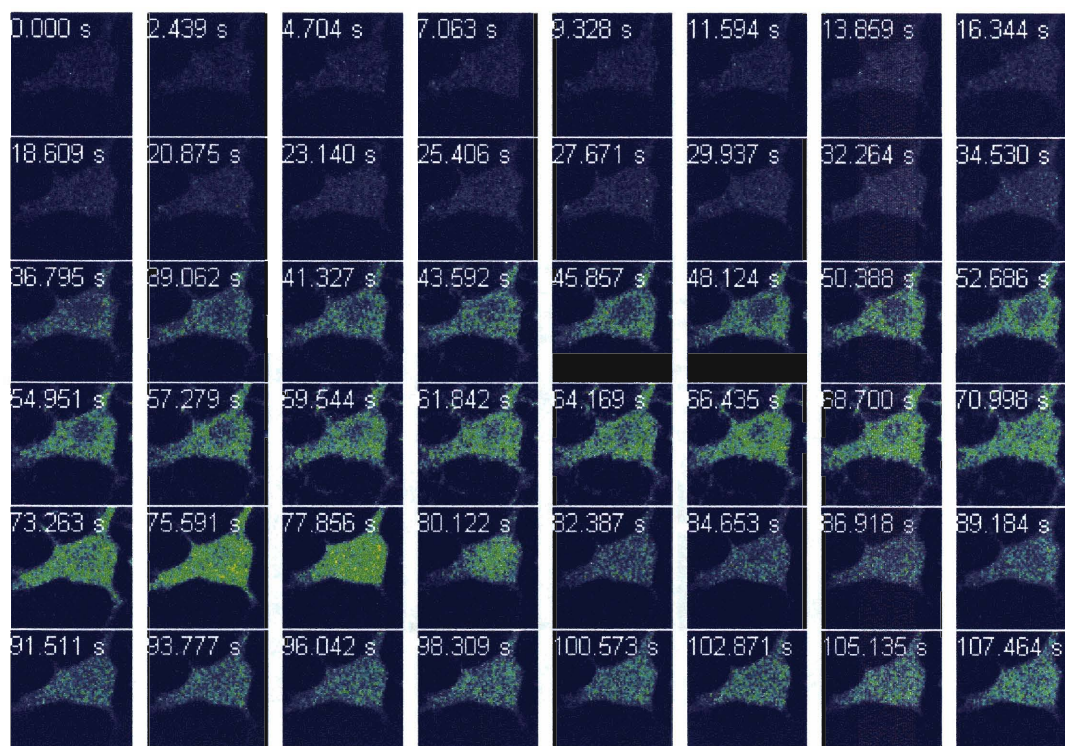
Figure 6.18. Fast confocal imaging of Zn(II) addition to primary cultures of hippocampal neurons (DIV 18) pre-treated with 10 µM ZS5. The ZS5-treated cells were imaged (0 – 27.671 sec). Zinc/pyrithione (50 µM, 1:1 ratio) was added during the image acquisition (29.937 – 34.530 sec) and a fluorescence rise is observed. An aliquot of TPEN (50 µM) was subsequently added during the data collection (66.435 – 70.998 sec) and a fluorescence decrease occurred at ca. 80 sec.
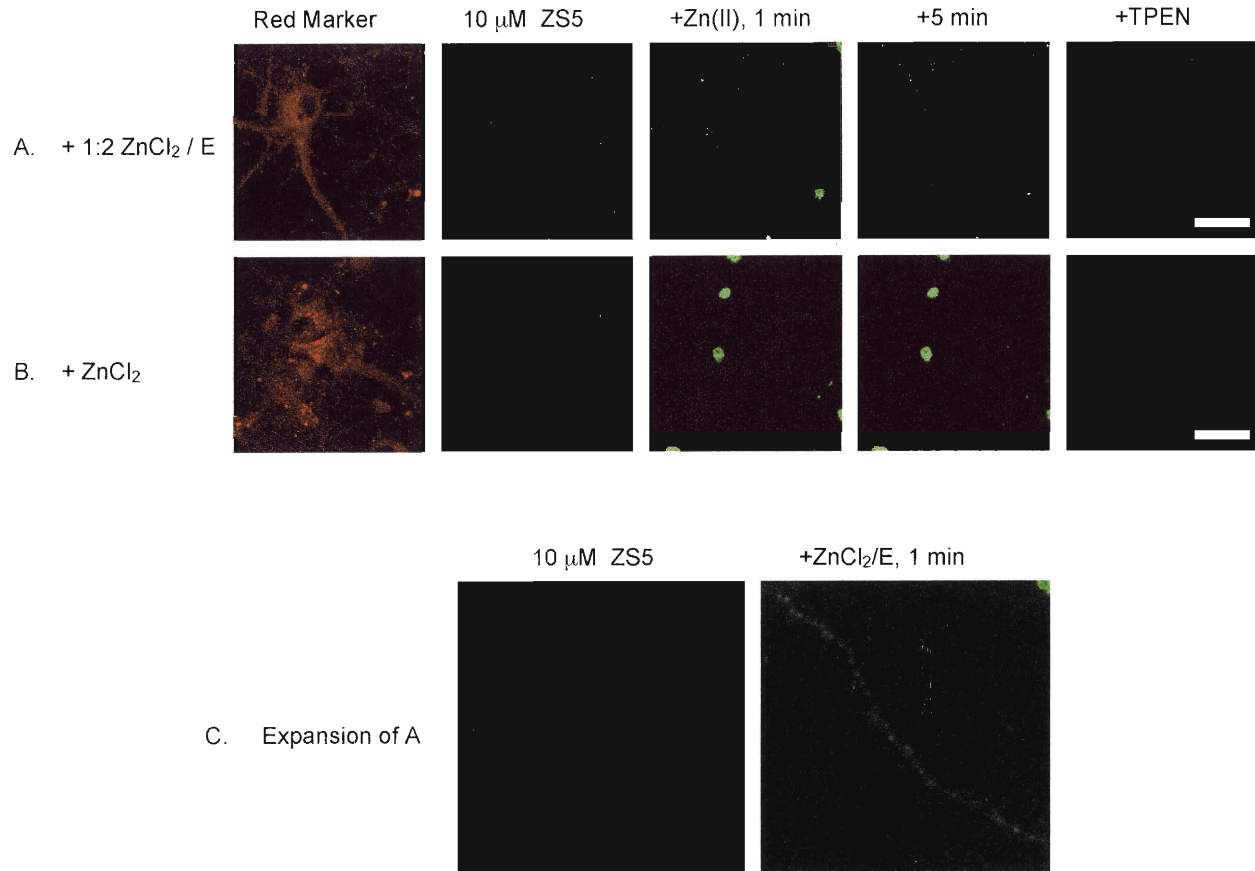
Figure 6.19. Uptake of exogenous Zn(II) by hippocampal neurons as a result of glutamate (E) treatment. A. Hippocamal neurons were treated with 10 μM ZS5 for 30 min (T = 37 °C, 5% CO_2), washed and imaged. The neurons were treated with 50 μM 1:2 $ZnCl_2$/E and imaged at 1 and 5 min. A fluorescence rise occurs in select dendrites after 1 min. B. Control study. Hippocampal neurons were treated with ZS5 as described for A, imaged and then treated with 50 μM $ZnCl_2$ and imaged at 1 and 5 min. No intracellular fluorescence change is observed. The big green dots are debris. C. Blown up image of a projection in A that light up following co-treatment with $ZnCl_2$ and E. The scale bars indicate 25 μm.
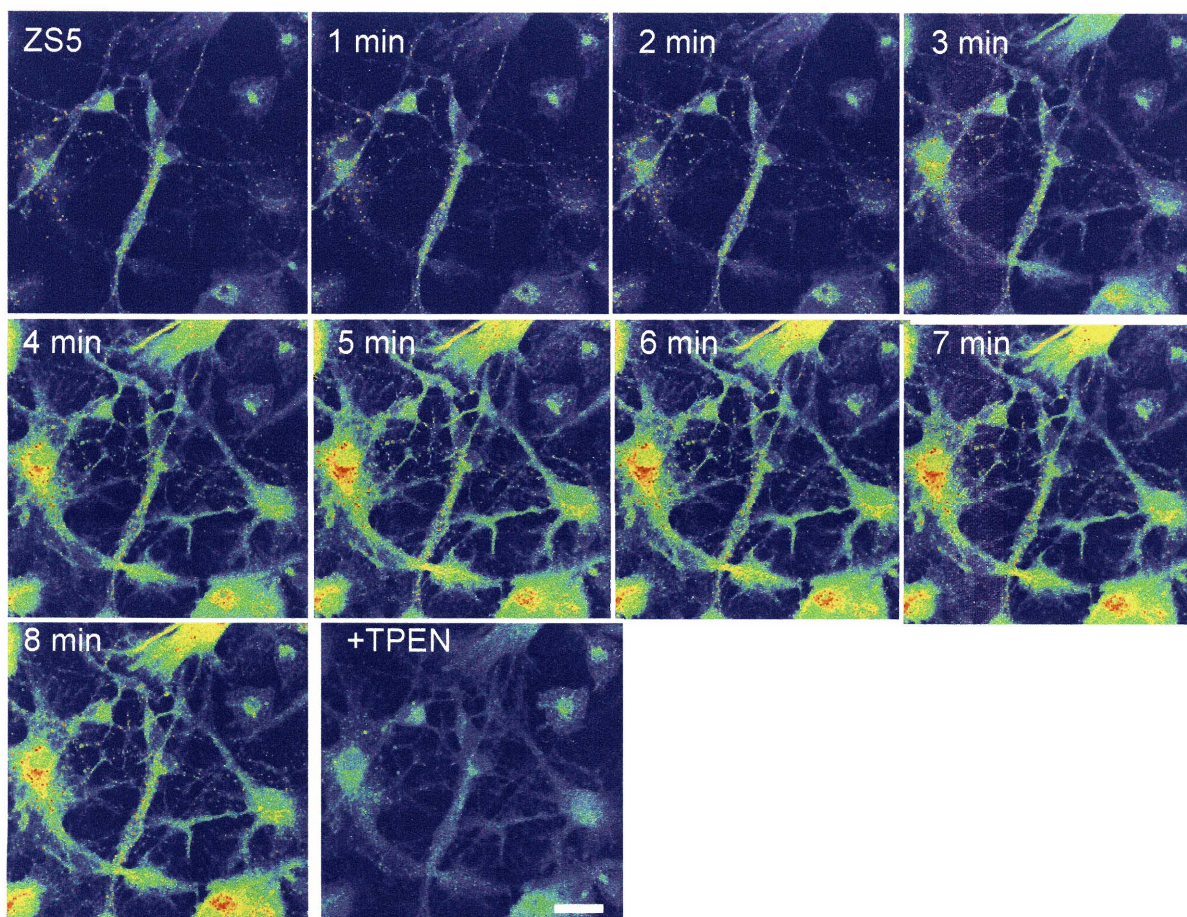
Figure 6.20. Imaging endogenous Zn(II) release in primary dentate gyrus neuronal cultures following nitrosative stress with ZS5. The cells were treated with 10 μM ZS5 (30 min, T=37 °C, 5% CO_2), washed and imaged. An aliquot of SNOC was added (final concentration = 1.5 mM) and the fluorescence change was recorded at 1 min intervals. The bottom right panel shows the fluorescence decrease that occurred 2 min after addition of 200 μM TPEN. The scale bar indicates 25 μm.

Chapter 7

QZ1 and QZ2: Rapid, Reversible Quinoline-Derivatized

Fluoresceins for Sensing Biological Zinc

Introduction

Zinc is an essential structural or catalytic component in over 300 metalloproteins,[1] is required for proper immune function,[2] is involved in DNA repair,[3,4] regulates caspase activity and apoptosis,[5,6] and is a proposed modulator of neurotransmission.[7-11] Most zinc is tightly bound in proteins and its concentrations are strictly regulated by specific transporters[12-15] and metallothionein;[16-19] however, pools of loosely bound and histochemically observable zinc exist in several tissues, including the pancreas[20,21] and brain.[7,9] In the synaptic clefts of the mossy fiber region of the hippocampus, the center of learning and memory in the brain, concentrations of Zn(II) are reported to reach micromolar to sub-millimolar levels under normal physiological conditions,[7,22] the functional significance of which remains a mystery.[23-25] Pathologically, disruptions in zinc homeostasis have been associated with susceptibility to infectious diseases[2], brain trauma and seizure,[26,27] and a variety of disorders that include depression,[28] diabetes,[29] prostrate cancer[30] and Alzheimer's disease.[31-35]

To explore the trafficking of physiological and pathological zinc, much effort has been devoted to devising new tools and tactics for zinc detection.[36-41] Fluorescence imaging in particular is well-suited for live imaging of biological Zn(II), which has no facile spectroscopic or magnetic signature due to its closed shell configuration. Successful application of this methodology requires the development of robust Zn(II) imaging agents with high sensitivity, selectivity and temporal fidelity. A variety of fluorescence-based approaches to Zn(II) detection have been documented recently, including small-molecule intensity based[42-54] and ratiometric sensors,[55-62] in addition to several methods based on proteins,[63-67] and peptides.[68-72] Although many of these systems are well-suited for investigating biological samples, arguably all suffer from one or more limitations, which continues to inspire the search for improved Zn(II) imaging tools.

The most widely used histological Zn(II) stains, TSQ (*N*-(6-methoxy-8-quinolyl)-*p*-toluenesulfonamide) and its congeners, shown in Figure 7.1, are quinoline derivatives bearing sulfonamide groups that give substantial fluorescence enhancement upon Zn(II) coordination.[73-79] These dyes, however, require high-energy UV-excitation (TSQ, λ_{ex} = 334 nm; Zinquin, λ_{ex} = 370 nm), which is potentially damaging to biological tissues. Despite a large dynamic range, these sensors have dim emission in the Zn(II)-bound forms owing to a weakly fluorescent reporting group (Φ_{Zn} ~ 0.1). For biological imaging applications, fluorescein is a superior chromophore because of its high brightness (Φ ~ 1, high ε), water solubility, desirable excitation and emission wavelengths and the availability of suitable microscope equipment. Fluorescent Zn(II) sensors with one or two di(2-picolyl)amine (DPA) moieties as the receptor are valuable because they bind Zn(II) selectively over intracellular concentrations of Ca(II) and Mg(II). DPA-derivatized fluorescein-based Zn(II) sensors include the ZnAF[52] and ZP[80-86] families of dyes (Figure 7.1). Because the DPA fragment binds Zn(II) with a K_d of 70 nM at pH 7,[87] DPA appended dyes saturate at low Zn(II) concentrations. Moreover, Zn(II) coordination to DPA-derivatized dyes is irreversible on the millisecond time scale (vide infra) of many biological processes, making them poorly suited for imaging time-dependent fluctuations in zinc levels. Since DPA has a high affinity for other first-row transition metals, including Co(II), Fe(II), Ni(II) and Cu(II), Zn(II)-induced fluorescence can be compromised. Because of these shortcomings, the design of fluorescent Zn(II) chemosensors with alternative metal-coordinating moieties remains an important goal. In particular, it is of interest to install a more weakly coordinating Zn(II)-binding unit, which conveys reversibility on the biological (millisecond) time-scale, while retaining or improving selectivity for Zn(II) and affording a large fluorescence response. The ZS senors, described in Chapters 5 and 6, were developed in our laboratory as a first step towards some of these goals.[88] More recently, a series of ZnAF probes having modified

pyridyl-based metal ion chelates that span a range of dissociation constants were reported.[89]

In this work, we describe new fluorescent Zn(II) chemosensors QZ1 and QZ2, fluorescein-based dyes containing one or two 8-aminoquinoline units on the xanthenone moiety, that meet these criteria. QZ1 and QZ2 exhibit a number of advantageous photophysical, thermodynamic, and kinetic properties compared to TSQ and sensors that use DPA for Zn(II) binding. These features include (i) Zn(II)-specific fluorescence enhancement, (ii) improved selectivity for Zn(II) over other metal ions as compared to DPA-containing sensors, (iii) micromolar dissociation constants, (iv) reversible Zn(II) binding, and (v) up to ~150-fold fluorescence enhancement upon Zn(II) coordination resulting from both low background fluorescence and highly emissive Zn(II) complexes.

Experimental Section

Reagents. Ethyl acetate was dried over 3 Å molecular sieves. Anhydrous 1,2-dichloroethane (DCE) was purchased from Aldrich and used as received. The xanthenone-functionalized fluorescein platforms, 7'-chloro-4'-fluoresceincarbox-aldehyde,[83] **1**, and 4',5'-fluoresceindicarboxaldehyde,[81] **2**, were synthesized as previously described. Sodium triacetoxyborohydride was purchased from Aldrich and 8-aminoquinoline from either Aldrich or Avocado.

Materials and Methods. Analytical TLC was performed on Merck F254 silica gel plates (0.25 mm thickness) with UV-light visualization. Whatman F254 silica gel-60 plates of 1 mm thickness were used for preparative TLC. NMR spectra were obtained on a Varian 300 or 500 MHz spectrophotometer operating at ambient probe temperature, 283 K, and both ^{1}H and ^{13}C NMR spectra were referenced to internal probe standards. IR spectra were obtained on an Avatar 360 FTIR instrument and samples

were prepared as KBr pellets. High-resolution mass spectrometry was conducted by staff at the MIT Department of Chemistry Instrumentation Facility.

2-[2-Chloro-6-hydroxy-3-oxo-5-(quinolin-8-ylaminomethyl)-3H-xanthen-9-yl]-benzoic acid (3, QZ1). To 5 mL of EtOAc were added 7'-chloro-4'-fluorescein-carboxaldehyde (1, 108 mg, 0.274 mmol) and 8-aminoquinoline (39 mg, 0.26 mmol). The reaction was stirred overnight at room temperature and an orange precipitate formed. The mixture was filtered and the precipitate was suspended in 10 mL of DCE. A portion (67 mg, 0.32 mmol) of NaB(OAc)$_3$H was added and the reaction was stirred overnight at room temperature, during which time the solution became clear. The solvent was removed under reduced pressure and the crude material was purified by preparative TLC on silica gel (9:1 CHCl$_3$/MeOH), which afforded pure QZ1 as a magenta solid (53 mg, 38%). TLC R_f = 0.48 (silica, 9:1 CHCl$_3$/MeOH); mp > 325 °C, dec. ^{1}H NMR (CD$_3$OD, 300 MHz) δ 4.80 (2H, s), 6.65 (2H, m), 6.79 (1H, s), 6.92 (1H, s), 7.02 (1H, d), 7.13, (2H, m), 7.33 (2H, m), 7.62 (2H, m), 8.03 (2H, m), 8.61 (1H, m). ^{13}C NMR (DMF-d_7, 125 MHz) δ 49.10, 103.53, 105.07, 108.59, 110.01, 112.07, 112.94, 120.34, 121.74, 123.50, 126.49, 128.08, 128.15, 128.29, 128.58, 129.05, 129.73, 130.20, 130.94, 134.92, 136.08, 138.64, 141.07, 145.79, 146.98, 155.80, 156.96, 170.86, 173.43, 181.03. FTR (KBr, cm^{-1}) 3416 (s, br), 1635 (m), 1578 (s), 1516 (m), 1455 (s), 1383 (s), 1340 (m), 1303 (m), 1225 (w), 1182 (w), 1153 (m), 1117 (w), 1087 (w), 1014 (m), 932 (w), 880 (w), 824 (w), 790 (w), 715 (w), 685 (w), 628 (w), 599 (w), 548 (w), 469 (w). HRMS (ESI) Calcd [M + H]$^+$, 523.1055; Found, 523.1061.

2-[6-Hydroxy-3-oxo-4,5-bis-(quinolin-8-ylaminomethyl)-3H-xanthen-9-yl]benzoic acid (4, QZ2). Portions of 8-aminoquinoline (74 mg, 0.51 mmol) and dialdehyde 2 (100 mg, 0.250 mmol) were combined in 3 mL of EtOAc and stirred overnight at room temperature. A light orange precipitate formed and the mixture was filtered and the precipitate washed with 3 mL of cold EtOAc. The precipitate was suspended in 4 mL of DCE and NaB(OAc)$_3$H (120 mg, 0.56 mmol) was added. The reaction became dark red and clear over the course of ~2 h. The reaction was stirred for an additional 12 h and

became orange. Preparative TLC of the reaction on silica gel (20:1 $CHCl_3/MeOH$) yielded pure QZ2 as a red-orange solid (47 mg, 29%). TLC R_f = 0.47 (silica, 9:1 $CHCl_3/MeOH$); mp > 325 ^{0}C, dec. ^{1}H NMR (CD_3OD, 300 MHz) δ 4.67 (4H, s), 6.57 (2H, s), 6.73 (2H, d), 6.92 (2H, d), 7.02 (2H, d), 7.11-7.16 (3 H, m), 7.24-7.29 (2H, m), 7.51 (2H, m), 7.98 (2H, t), 8.52 (2H, d). ^{13}C NMR ($CDCl_3$, 125 MHz) δ 37.81, 107.12, 112.81, 113.75, 115.02, 122.33, 124.16, 129.16, 130.00, 130.15, 130.53, 131.16, 131.66, 134.93, 137.21, 139.83, 141.74, 146.48, 147.81, 158.16, 160.76, 174.66, 181.04. FTIR (KBr, cm^{-1}) 3046 (s, br), 3041 (w), 2950 (w), 2923 (w), 2846 (w), 1638 (m), 1579 (s), 1515 (s), 1442 (s), 1393 (s), 1378 (s), 1330 (s), 1231 (w), 1148 (m), 1095 (m), 1035 (w), 818 (m), 789 (m), 741 (w), 672 (w), 642 (w), 604 (w), 529 (w), 501 (w), 456 (m). HRMS (ESI) Calcd [M + H]$^+$, 645.2132; Found, 645.2132.

General Spectroscopic Methods. All aqueous solutions were prepared with Millipore water (18.2 MΩ·cm at 25 °C) obtained from a Mill-Q Biocel system outfitted with a Quantum VX cartridge. Puratonic grade KCl was purchased from Calbiochem and molecular biology grade PIPES, piperazine-N,N'-bis(2-ethanesulfonic acid), from Sigma. With the exception of the pK_a titrations, measurements were made at pH 7 in 50 mM PIPES, 100 mM KCl buffer. Excess EDTA was added to solutions of apo QZ for quantum yield and extinction coefficient determination. Zinc stock solutions (100 mM, 500 mM) were prepared from anhydrous 99.999% $ZnCl_2$ and water. DMSO stock solutions (1 mM) of QZ1 and QZ2 were prepared, partitioned into ~300 μL aliquots and stored at –25 °C and thawed in the dark before use. These aliquots can be frozen and thawed multiple times, and a rise in basal fluorescence indicates decomposition. QZ1 is less photostable than QZ2 and aqueous solutions of QZ1 should not be left in the light or at room temperature for prolonged periods of time. A starting solution of 10 mM KOH, 100 mM KCl, pH ~12 was used for pK_a titrations and the pH of the solution was lowered by addition of 6, 2, 1, 0.5 or 0.1 N HCl. Quantum yields were measured using fluorescein in 0.1 N NaOH (Φ = 0.95) as the standard.[90] Extinction coefficients were

measured over a concentration range of 1 to 10 μM, except for the QZ2:Zn(II) complex, which was studied from 1 to 5 μM due to its limited solubility. Experimental details for all spectroscopic measurements performed in this study are available in Chapter 2. Measurements were repeated a minimum of three times, and with sensors obtained from multiple syntheses, and the resulting averages are reported.

Stopped-Flow Fluorescence Studies. Single-mixing stopped-flow kinetics studies were performed with a Hi-Tech SF-61 DX2 double-mixing stopped-flow apparatus equipped with a fluorescence detector. Excitation was provided at 505 (ZP1), 492 (ZP3), 495 (ZP4, ZP9, ZP10, QZ1) or 490 nm (QZ2) and a GG495 glass cutoff filter (< 455 nm) was placed over the exit to the photomultiplier tube and emission was monitored from 455 to 700 nm. All solutions were prepared in 50 mM PIPES, 100 mM KCl, pH 7. Conditions for pseudo first-order kinetics were maintained by using at least a 10-fold excess of Zn(II) in all experiments. With the exception of the temperature-dependent studies, all measurements were conducted at 4.3 °C ± 0.1 °C maintained by means of a circulating water bath. The temperature inside the sample chamber was monitored with an internal thermocouple.

Two series of concentration-dependent studies were performed. To determine the rate constants for Zn(II) binding to the selected ZP and QZ dyes, k_{on}, the concentration of Zn(II) was varied and multiple shots were taken at each Zn(II) concentration. To ensure that changes in dye concentration did not affect the observed rate constants and that dye aggregation did not occur, a series of experiments where the dye concentration was varied in the presence of at least 10-fold excess Zn(II) were also performed. Temperature-dependence studies were conducted to determine the activation enthalpy, $\Delta H^{\ddagger}$, and activation entropy, $\Delta S^{\ddagger}$, associated with Zn(II) coordination to ZP and QZ dyes. Values for k_{on} were determined in the presence of excess Zn(II) at a minimum of five temperatures over a range of ~4 to ~16 °C (QZ) or ~4 to ~40 °C (ZP). Each experiment was conducted a minimum of three times on different days and with

different solutions and the averages are reported. The observed rate constants obtained from all sets of experiments were calculated by employing the Kinet-Assyst software package (HiTech) to fit individual traces to monoexponentials and averaging the results for individual fits.

Calculational Methods. All calculations were performed with either the Jaguar 5.5 (Schrödinger Inc.) or the Amsterdam Density Functional (ADF) 200.01 software package. Geometries were optimized in Jaguar using the B3LYP functional and the LACVP** basis set. This basis set uses a standard Pople double-zeta quality basis set, 6-31G**, for non-transition metal ions and treats all inner shell electrons of transition metal ions with a pseudopotential, which accounts for relativistic effects. This basis set reliably predicts ground state geometries, but does not consider electron correlation and often generates inaccurate SCF energies. As a result, single point calculations were conducted on each 6-31G** geometry at the cc-pVTZ(-f) level of theory, which is a triple-zeta quality basis set that accounts for electron correlation and generates reliable E(SCF). Vibrational frequency calculations were performed with Jaguar to obtain zero point energies (ZPE) and entropies (ΔS), and to verify that each converged geometry was a ground state structure. A solvation continuum model, which treats the solvent as a dielectric continuum, was used to calculate solvation energies with a dielectric constant of 78.4 for water. Reported free energies of solution ($\Delta G_{solution}$) are both entropy and zero point energy corrected and were calculationed according to eqs. 7.1 – 7.3.

$$\Delta H_{gas} = E(SCF) + ZPE \tag{7.1}$$

$$\Delta G_{gas} = \Delta H_{gas} + T\Delta S \tag{7.2}$$

$$\Delta G_{solution} = \Delta G_{gas} + \Delta G_{solvation} \tag{7.3}$$

Time-dependent density functional theory (TDDFT) was implemented with the ADF software package. The LB94 functional, which was devised for predicting excited states, and basis set IV, a triple-zeta quality basis set comprised of Slater-type orbitals comparable to the Pople basis set 6-311G*, were employed. Since TDDFT is a relatively

new technique and few protocols have been rigorously tested on a wide variety of compounds, a large-scale TDDFT calibration was performed to determine what method would be most appropriate for studies of organic chromophores and related metal complexes. The details of this study are given in Appendix 2.

Cell Culture. HeLa cells were cultured in Dulbecco's Modified Eagle Medium (DMEM, Invitrogen) supplemented with 10% fetal calf serum (FCS, Invitrogen), glutamine (2 mM), penicillin (100 units/mL) and streptomycin (100 mg/mL). Two days before imaging, the cells were passed and plated on 10 mm glass coverslips. For labeling, cells were transferred to DMEM containing 1% FCS and incubated with 10 μM sensor at 37 °C under 5% CO_2. The cells were washed once with DMEM containing no FCS prior to imaging and/or zinc addition. Zinc was introduced to the cultured cells as the pyrithione salt using a Zn(II)/pyrithione ratio of 10:2. Stock solutions of $ZnCl_2$ (10 – 40 mM) and sodium pyrithione (20 – 80 mM) in DMSO were combined and diluted 10-fold with DMEM prior to addition. In a typical experiment, a 100-μL aliquot of this solution was added to the cells bathed in 1 mL of DMEM. A stock solution of TPEN (10 or 20 mM) was also diluted 10-fold with DMEM containing no FCS prior to cell treatment. For experiments involving fixed cells, the cells were treated with 4% PFA (1 mL, PBS containing 4% PFA and 4% surcose) for 5 min, washed 3 x 1 mL with PBS and mounted onto glass microscope slides using the Vectashield reagent (Vector Labs).

Laser Scanning Confocal Microscopy. A Zeiss LSM510 microscope equipped with a 63x objective (with 1.5x electronic zoom) was used to obtain confocal images. The samples were excited at 488 nm with an Ar laser. A z-series of 7 slices taken at depth intervals of 0.75 nm was acquired for each image. The Metamorph software package was used for quantification.

Two-Photon Microscopy. Two-photon fluorescence imaging was conducted by using a custom-made two-photon laser-scanning microscope based on an Olympus Fluoview 300/BX50WI microscope, equipped with a 60x objective lens and a 570-nm

short-pass emission filter, and a Spectraphysics Tsunami Ti:sapphire laser pumped by Millennia Xs.

Results and Discussion

Design Considerations. Several factors were considered in the design of QZ1 and QZ2. Although a number of quinoline-containing fluorescent Zn(II) sensors exist,[78,91,92] none of these contain fluorescein as the reporting group. Given the superior photophysical properties of fluorescein and the successful application of quinoline derivatives in biological Zn(II) sensing, we expected a combination of quinoline and fluorescein to be advantageous. Since Zn(II) concentrations in the synaptic clefts of the hippocampus are presumed to reach near-mM concentrations, a Zn(II)-specific probe with a micromolar dissociation constant should be useful to monitor Zn(II) flux in this region.[39] Reducing the number of donor atoms in the coordination sphere is one way to raise the dissociation constant, which should be achieved by substitution of a N_3O or N_4O coordinating unit in a ZP sensor with a N_2O donor set. For controlling background fluorescence, a substantial body of work from our laboratory shows that aniline nitrogen atoms generally quench fluorescein emission more efficiently than tertiary amines.[82,83,85] The ligand 8-aminoquinoline satisfies these additional criteria. We therefore installed 8-aminoquinoline moieties in the 4'- and 5'-positions of fluorescein to give N_2O donor sets with aniline-type nitrogen atoms that can presumably act as photoinduced electron transfer (PET) switches.

Syntheses. Scheme 7.1 illustrates the syntheses of QZ1 and QZ2 from 8-aminoquinoline and fluorescein aldehyde precursors, the latter of which were prepared in 4 or 5 steps according to previously described methodology.[81,83] Condensation of 1 equiv of 8-aminoquinoline with monoaldehyde 1 in EtOAc resulted in precipitation of the intermediate imine as an orange solid. Reduction of the imine under mild conditions using $NaB(OAc)_3H$ in DCE gave QZ1 in moderate yield following

purification by preparative TLC on silica gel with $CHCl_3/MeOH$ mixtures. QZ2 was obtained by an analogous procedure starting from the symmetrical dialdehyde **2** and 2 equiv of 8-aminoquinoline. Pure QZ1 and QZ2 are both magenta to red-orange solids that are readily soluble in MeOH. Through incorporation of a commercially available ligand moiety, the QZ syntheses are more economical than those for asymmetric ZP and ZS sensors, where multiple steps are required to assemble the ligand fragments.

Spectroscopic Properties of QZ1. Table 7.1 summarizes the results of fluorescence and UV-visible spectroscopic experiments conducted at pH 7 (50 mM PIPES, 100 mM KCl) for QZ1 and QZ2. Selected results for the ZP and ZS sensors are included for comparison. Unbound QZ1, in the presence of excess EDTA to scavenge any potentially interfering metal ions, has a quantum yield of 0.024 (λ_{max} = 524 nm). Addition of excess Zn(II) causes the quantum yield to increase ~33-fold to 0.78 (λ_{max} = 524 nm). The absorption spectrum undergoes a blue-shift from 505 nm (ε = 68,900 $M^{-1}cm^{-1}$) to 498 nm (ε = 69,800 $M^{-1}cm^{-1}$) upon Zn(II) binding indicating a perturbation of the fluorescein π system by Zn(II) coordination to the phenol (vide infra). Taken together, there is a ~42-fold increase in integrated emission resulting from Zn(II) binding to QZ1 (Figure 7.2).

The pH dependence of the QZ1 fluorescence was investigated as shown in Figure 7.3. QZ1 fluorescence exhibits little change from pH ~12 to ~7 and reaches its maximum at pH ~5.5. Two protonation events affect QZ1 fluorescence, with pK_{a1} = 6.1 and pK_{a2} = 5.0. The former is assigned to the aniline nitrogen atom and the latter value corresponds to protonation of the fluorescein and formation of a non-fluorescent state. We assign this transition to phenol protonation. Less than 2-fold fluorescence change occurs upon protonation of the aniline nitrogen atom compared to ~42-fold fluorescence enhancement upon Zn(II) coordination, rendering QZ1 relatively insensitive to pH changes.

Spectroscopic Properties of QZ2. QZ2, depicted in Scheme 7.1, is a symmetrical analog of QZ1 and contains two 8-aminoquinoline moieties. We elected to prepare and

characterize QZ2 based on experience with several asymmetric and symmetric Zn(II) sensors previously synthesized in our laboratory. A comparison of the ZS1/ZS3 couple (Figure 7.1) shows that installation of a second tertiary amine-based ligand on the xanthene framework results in a substantial decrease in background fluorescence (symmetric ZS1 Φ_{free} = 0.50; asymmetric ZS3 Φ_{free} = 0.71).[88] A similar trend occurs for DPA-based ZP1 and its asymmetric analog.[93] This behavior makes intuitive sense when the simple PET quenching mechanism is considered.[94,95] According to this model, a free nitrogen lone pair quenches emission from the metal-free dyes by electron transfer into the hole produced during photoexcitation. Given that symmetrical sensors have two nitrogen lone pairs available to quench the fluorophore excited state compared to only one nitrogen lone pair in the asymmetrical analogs, relatively less background fluorescence is expected. We reasoned that a symmetric QZ dye would exhibit even further reduced background fluorescence than asymmetrical QZ1 while maintaining a high degree of Zn(II)-induced turn-on.

In accord with this notion, apo QZ2 has a very low quantum yield of 0.005 (λ_{max} ~ 520 nm) at pH 7 (50 mM PIPES, 100 mM KCl) and in the presence of EDTA to complex any potentially interfering metal ions (Table 7.1). An ~150-fold fluorescence increase occurs upon introduction of excess Zn(II) to a solution of QZ2 (Figure 7.2), and the quantum yield for the Zn(II)-bound complex is 0.70 (λ_{max} = 518 nm). This fluorescence enhancement is unprecedented for xanthenone-substituted fluorescent Zn(II) sensors. The absorption spectrum of QZ2 blue-shifts by 10 nm upon Zn(II) coordination, moving from 499 nm (ε = 37,200 $M^{-1}cm^{-1}$) to 489 nm (ε = 33,600 $M^{-}cm^{-1}$). The relatively low extinction coefficients of QZ2 are reminiscent of those determined for the fluorescein-based DPA-derivatized Zn(II) sensor ZP2 (Table 7.1) and can be rationalized on the basis of the nature of the fluorescein chromophore. Unsubstituted fluorescein has an extinction coefficient of ~77,000 $M^{-1}cm^{-1}$ (0.1 N NaOH)[96] and fluoresceins halogenated in the 2′ and 7′ positions exhibit more intense absorption. For instance, the reported

extinction coefficient for 2',7'-dichlorofluorescein is 101,000 $M^{-1}cm^{-1}$ (0.1 N NaOH).[97] Relative extinction coefficients for our dyes with and without chloro substitution in these positions (ZP1/ZP2, QZ1/QZ2) reflect this trend.

Figure 7.3 includes a representative pK_a titration of QZ2, which shows that two protonation events influence QZ2 emission. The pK_a values of 7.0 and 4.9 are assigned to aniline nitrogen and phenol protonation, respectively. Only ~2-fold fluorescence enhancement occurs upon protonation of the aniline nitrogen atom compared to the ~150-fold fluorescence increase associated with Zn(II) coordination, which indicates that QZ2 fluorescence is also virtually insensitive to protons. This feature is an improvement over symmetric sensors ZP1-3, which display greater degrees of proton-induced fluorescence turn-on. It is also relevant to biological imaging studies, where changes in proton concentration may occur and potentially interfere with the Zn(II) response of a proton-sensitive dye.

Metal-Binding Properties of QZ1 and QZ2 I: Solution Studies. The acquisition of molecules with varying dissociation constants (K_d) is an important goal in biological Zn(II) sensor development. Since near-mM concentrations of Zn(II) are presumed to exist in synaptic clefts located in substructures of the mammalian hippocampus, fluorescent Zn(II) sensors with K_d values in the mid- to high-micromolar range should be advantageous for imaging this pool. Investigations of Zn(II) pathology involving high influx levels of Zn(II) could also benefit from such low affinity chemosensors. QZ1 and QZ2 exhibit maximum fluorescence response in the presence of high micromolar to millimolar concentrations of Zn(II). Metal binding titrations monitored by fluorescence spectroscopy revealed that QZ1 gives maximum emission in the presence of ~300 μM Zn(II) with an apparent K_d value of 33 ± 2 μM at 25 °C (Figure 7.4). Titrations monitored by optical absorption spectroscopy returned a K_d value of 46 ± 6 μM (monitored at 513 nm) or 31 ± 1 μM (monitored at 492 nm) at 25 °C (Figure 7.5). A similar value, 48 ± 3 μM, was obtained from stopped-flow kinetic studies performed at 4.3 °C (see below). Sensor

QZ2 can coordinate two Zn(II) ions and responds to even higher concentrations of Zn(II). Fluorescence titrations reveal that ~50% of the total fluorescence increase occurs when QZ2 encounters ~770 μM Zn(II), and low millimolar concentrations are required to achieve full fluorescence enhancement (Figure 7.3). Stopped-flow kinetic experiments, see Figure 7.12 and discussion below, indicate a K_{d1} value of 41 ± 3 μM for Zn(II) binding to QZ2 at 4.3 °C, comparable to that of QZ1. Given the comparable K_{d1} values of QZ1 and QZ2 and the fact that low millimolar concentrations of Zn(II) are required to saturate the QZ2 response, we conclude that both binding events cause fluorescence enhancement. The second Zn(II)-binding event is of significantly lower affinity; its K_d value was not determined. As anticipated from the micromolar affinity of each QZ dye for Zn(II), the metal ion binding events are readily reversible. Addition of the heavy metal chelator N,N,N',N'-tetrakis-(2-pyridylmethyl)ethylenediamine (TPEN) to solutions of QZ and Zn(II) decreases the fluorescence to baseline immediately upon mixing as shown in Figure 7.6.

The coordination of QZ1 and QZ2 to Zn(II) was also explored by using UV-visible spectroscopy. The optical absorption difference spectra for the QZ dyes are comparable to those obtained for members of the ZP family and reflect a similar perturbation to the fluorescein π system resulting from Zn(II) coordination, attributed to phenol coordination.[81] For QZ1, Zn(II) binding results in an absorption increase at 492 nm and a decreases at 513 and 250 nm (Figure 7.5). Less prominent features are observed at 460, 317 and 283 nm. The difference spectrum for QZ2 has analogous features with an absorption increase at 482 and a decrease at 504 nm (data not shown).

QZ1 was designed to bind Zn(II) with 1:1 stoichiometry. Job plots, obtained by fluorescence spectroscopy, show a break at 0.5, indicating formation of a 1:1 species in solution (Figure 7.7). Since Zn(II) forms 4-, 5- and 6-coordinate complexes, we propose that one or more water molecules or buffer components complete the Zn(II) coordination sphere defined by the N_2O donor set of the QZ ligand system.

Metal-Binding Properties of QZ1 and QZ2 II: Theoretical Studies. Since crystallizing metal complexes of fluorescein-based ligands is notoriously difficult and because QZ syntheses are only practical on a small scale, we first attempted to isolate crystals of a Zn(II)-bound salicylaldehyde-based model complex of QZ1. Although we were able to prepare and crystallographically characterize mononuclear Ni(II) and dinuclear tosylate-bridged Cu(II) complexes of this model ligand (data not shown), attempts at isolating a Zn(II) complex were unsuccessful. As an alternative to synthetic modeling studies, we employed density functional theory (DFT) to investigate the mode of Zn(II) coordination to QZ1 and time-dependent DFT (TDDFT) to explore the excitation profiles of the free and Zn(II)-bound sensor.

Because of its closed-shell configuration, Zn(II) can accommodate a range of coordination geometries. The tetrahedral motif is generally preferred for small molecule ligands such as ammonia and water, and other geometries can be imposed on the Zn(II) center by multidentate ligands. The QZ1 ligand framework provides three donor atoms in a N_2O motif and we investigated tetrahedral, trigonal bipyramidal and octahedral coordination geometries for Zn(II)-bound QZ1 by occupying the additional coordination sites with water molecules. This choice was based on experiments which showed that (i) QZ1 gives fluorescence turn-on in water following Zn(II) coordination and (ii) excluding chloride ion from the buffer (50 mM PIPES, 100 mM KCl, pH 7) has negligible affect on its response to Zn(II). Geometry optimizations showed that the octahedral complex is unstable; one water molecule is expelled from the first coordination sphere, which yields the trigonal bipyramidal structure. Well-defined structures were obtained for both the tetrahedral and trigonal bipyramidal complexes, as shown in Figure 7.8. Comparison of the zero-point energy and entropy corrected free energies of solution for these species indicates that the trigonal bipyramidal structure is thermodynamically favored by 4.3 kcal/mol. Based on this information and the pH

studies described above, we propose a scheme for Zn(II) coordination to QZ1 at neutral pH as shown in Figure 7.8.

It should be noted that preliminary calculations relied on the salicylaldehyde-based model of QZ1 with the aim of reducing processing time. Unfortunately, a number of observations relating to this system and others suggested that using salicylaldehyde models for fluroescein-based compounds is insufficient. Calculated binding energies of models for ZP and QZ family members failed to reproduce experimentally determined dissociation constants and pK_a values whereas preliminary work with xanthenone- and fluorescein-based systems gave more energetically reasonable values. We propose that the nature of the phenolic donor is, at least in part, responsible for this discrepancy. The π system of the xanthenone framework allows for delocalization of negative charge, which makes the phenolic oxygen atom involved in Zn(II) coordination electron deficient in fluorescein relative to that in the salicylaldehyde-based model.

In addition to studying ground state geometries, some time-dependent processes can be interrogated with theoretical techniques.[98] We used TDDFT to study the excitation profiles of free and Zn(II)-bound QZ1. QZ1 and QZ1:Zn(II) absorption is dominated by the fluorescein chromophore and the TDDFT results show good agreement with experimental observation. Figure 7.9 illustrates the donor and acceptor molecular orbitals involved in the major transitions for QZ1 dianion and the trigonal bipyramidal Zn(II) complex. For apo QZ1 dianion, the species present at neutral pH, TDDFT generates an excited state (A, oscillator strength = 0.274) with an absorption maximum at 475 nm (experimental, 505 nm). The dominant molecular orbital transition (weight = 0.605) occurs between the HOMO (-4.57 eV) and the LUMO+2 (-2.73 eV), both of which are xanthenone-based molecular orbitals analogous to the donor/acceptor pair presumably responsible for fluorescein dianion absorption (Appendix 2). TDDFT analysis of the trigonal bipyramidal QZ1:Zn(II) complex affords an excited state (B, oscillator strength = 0.392) with an A_{max} value of 451 nm, in good agreement with the

experimentally observed hypsochromic shift resulting from Zn(II) binding. The main contributor to this excited state (weight = 0.652) is the molecular orbital transition between the HOMO (-12.38 eV) and the LUMO+2 (-10.50 eV). These molecular orbitals are also completely xanthenone based and have no contribution from the Zn(II) center. This transition is analogous to the transition responsible for absorption from protonated fluorescein (Appendix 2), QZ1 with a protonated phenol (data not shown) and the ZP4:Zn(II) complex (Chapter 2).

Zn(II) Selectivity of QZ1 and QZ2. One challenge in Zn(II) sensor development is to procure systems that are selective for Zn(II) over a wide range of potentially competing metal ions. DPA is a valuable ligand for biological Zn(II) sensing because of its high affinity for Zn(II) over Ca(II), but dyes containing this ligand moiety readily bind other divalent metal ions that block Zn(II) coordination. Fluorescence spectroscopy was employed to investigate the selectivity of QZ1 and QZ2 for Zn(II) over other cations and representative data are shown in Figures 7.10 and 7.11. QZ1 and QZ2 readily bind Zn(II) in the presence of mM concentrations of Na(I), K(I), Ca(II) and Mg(II), indicating that these physiologically relevant components will not interfere with QZ detection of Zn(II) in such samples. Of the first-row transition metals considered, only Ni(II) and Cu(II) compromise the Zn(II)-induced fluorescence enhancement of the QZ sensors. This selectivity is a substantial advantage over ZP1-8, which preferentially bind Fe(II) and Co(II) in addition to Ni(II) and Cu(II). The QZ chemosensors also differentiate Zn(II) from Cd(II). The essentially negligible fluorescence change upon Cd(II) binding to QZ1 contrasts with that of the ZP and thioether-containing ZS dyes, which show comparable turn-on for both Zn(II) and Cd(II). As observed for aniline-based ZP, coordination of QZ to the paramagnetic metal ions results in only negligible fluorescence change attributed to the high degree of quenching in the unbound form.

Kinetic Investigations of ZP and QZ Sensors. The fluorescence response of the ZP and QZ dyes to zinc can be observed by eye or with a hand-held UV-lamp to occur

immediately upon mixing. Stopped-flow fluorescence studies were therefore conducted to measure the rate constants for Zn(II) association, via fluorescence turn-on, for QZ1, QZ2 and several ZP dyes. Rate constants for Zn(II) dissociation were either measured (QZ) or calculated (ZP) from k_{on} and experimentally determined dissociation constants. Equations 7.4 and 7.5 illustrate the relationship between the dissociation constant, K_d, the rate constants for Zn(II) binding, k_{on}, and Zn(II) release, k_{off}, and the observed pseudo first-order rate constant k_{obs}. To verify that k_{obs} is independent of initial dye concentration, a series of experiments were conducted where the dye concentration (after mixing) was varied from 0.5 to 5 µM in the presence of at least 10-fold excess Zn(II) (data not known). For each dye, this experiment showed that k_{obs} is independent of initial dye concentration, which confirmed that dye aggregation, or other potentially interfering phenomena, was not occurring during the course of the experiment.

$$k_{obs} = k_{on}[\text{Zn(II)}] + k_{off} \qquad (7.4)$$

$$K_d = k_{off}/k_{on} \qquad (7.5)$$

Given the sub-nM dissociation constants of the ZP dyes, essentially no back-reaction is observed on the time-scale of the stopped-flow measurements and eq. 7.4 can be simplified to eq. 7.6. Plots of k_{obs} vs. Zn(II) concentration for Zn(II) binding to the selected ZP dyes illustrate this notion since the lines pass through the origin (Figure 7.12). The data in Table 7.2 show that the DPA-containing ZP dyes are characterized by

$$k_{obs} = k_{on}[\text{Zn(II)}] \qquad (7.6)$$

k_{on} values in the range of 6.3 – 8.5 x 10^5 $M^{-1}s^{-1}$ at 4.3 °C. Kinetic data from temperature-dependent studies, see Figure 7.13 and discussion below, afford k_{on} values of 3.3 – 5.2 x 10^6 $M^{-1}s^{-1}$ at 25 °C for the ZP sensors. These association constants indicate that the ZP dyes can respond to Zn(II) on the millisecond time scale and are similar to those obtained for the ZnAF dyes (3.1 – 4.3 x 10^6 $M^{-1}s^{-1}$ at 25 °C), which also utilize DPA as the Zn(II) chelate.[52] Association rates for fluorescent macrocycle-based Zn(II) sensors are notably slower, generally exhibiting k_{on} values of 10 – 10^2 $M^{-1}s^{-1}$,[49] due to the rigidity of

the ligand moiety.[46,49] As calculated from the K_d and k_{on} values, ZP family members have relatively slow Zn(II) dissociation, which will be prohibitive for many imaging applications. Equation 7.5 affords k_{off} values that range of 2.3 – 3.4 x 10^{-3} s^{-1} at 25 °C and yield $t_{1/2}$ of 200 – 300 s for Zn(II) dissociation from DPA-containing ZP. Data for select ZS (Chapter 6) sensors are also included in Table 7.2.

The QZ dyes display readily reversible Zn(II) coordination. The kinetic data for QZ1 and QZ2 depicted in Figure 7.12 yield k_{on} values of 3.1-3.9 x 10^6 $M^{-1}s^{-1}$ at 4.3 °C, indicating faster Zn(II) complexation as compared to ZP and ZS, and return k_{off} values of 150 and 160 s^{-1}, respectively, at this temperature. Given the fast association rates observed for QZ, we were unable to obtain reliable kinetic data above 16 °C. Extrapolation of the Eyring plots in Figure 7.13 yields estimated k_{on} values of 3.7 and 4.5 x 10^7 $M^{-1}s^{-1}$ and k_{off} values of >10^3 s^{-1} for QZ1 and QZ2 at 25 °C. These computed k_{off} values are over five orders of magnitude greater than those observed for the DPA-containing ZP and ZnAF probes and yield $t_{1/2}$ < 0.5 ms. The QZ dissociation rates are greater than those of Fura-2, Indo-1 and Quin-2, fluorescent Ca(II) sensors that have been successfully used to measure Ca(II) changes in biological specimens.[99-101] This feature makes the QZ dyes potentially useful for biological studies that involve monitoring Zn(II) flux, such as those proposed to occur at synapses.

A series of temperature variation experiments were conducted and Figure 7.13 shows Eyring plots for the ZP and QZ dyes. Values for the activation enthalpy, $\Delta H^{\ddagger}$, and activation entropy, $\Delta S^{\ddagger}$, associated with Zn(II) binding and are given in Table 7.2. These sensors have $\Delta H^{\ddagger}$ between 10.7 – 12.5 kcal/mol, which reflects a relatively low activation barrier and fast rate of association. Values for $\Delta S^{\ddagger}$ are positive and range from 10.7 – 13.2 cal/mol-K. The positive $\Delta S^{\ddagger}$ values may be due to dissociation of buffer components from the reacting species in the transition state.

Comparison of QZ to ZP and Other Fluorescent Zn(II) Sensors. A comparison of spectroscopic and photophysical features of the QZ vs. the ZP and ZS dyes reveals

some expected similarities and several striking differences (Table 7.1). With the exception of ZP5, the asymmetrical aniline-derivatized ZP dyes, ZP4-8, have $\Phi_{free} <$ ~0.1, the latter of which is attributed to PET quenching of the fluorescein excited state at physiological pH by the aniline unit.[82] The quantum efficiency of QZ1 is 2.5-fold less than that of asymmetrical ZP4 (Φ_{free} = 0.06)[82] and comparable to that of ZP8 (Φ_{free} = 0.03).[85] Because of the addition of a second quenching moiety, symmetric QZ2 shows an even more pronounced reduction in background fluorescence with Φ_{free} = 0.005. This value is comparable to the quantum yields for select benzoate-substituted ZnAF dyes[52] and represents a ~76-fold reduction in background fluorescence relative to our first Zn(II) responsive dye, ZP1 as shown in Figure 7.14.

In addition to significantly reduced background fluorescence, Zn(II) binding to QZ1 and QZ2 efficiently alleviates fluorescence quenching and restores ~75 to ~85% of fluorescein emission (QZ1 Φ_{Zn} = 0.78, QZ2 Φ_{Zn} = 0.70). This behavior greatly contrasts with the turn-on observed for the aniline-derivatized ZP4-type dyes, where fluorescein emission remains substantially quenched following Zn(II) coordination (ZP4, Φ_{Zn} ~ 0.3). Taken together, QZ1 and QZ2 offer significantly enhanced dynamic ranges, ~42- and ~150-fold respectively, as compared to the ZP and ZS sensors previously reported (Table 7.1), as well as a number of commercially available Zn(II) sensors such as Newport Green.[50] QZ2 also shows greater fluorescence enhancement than the benzoate functionalized ZnAF dyes which, like ZP4-8, suffer from partially quenched fluorescein emission in the Zn(II) bound forms.[52] Because the fluorescein platform of QZ2 is not halogenated, which lowers the molar absorptivity, the brightness ($\Phi \times \varepsilon$) of the Zn(II)-bound species is less than those of ZP1 and ZP3 and similar to that of ZP4 (Figure 5.14). Incorporation of chloro or fluoro substituents in the 2' and 7' positions of the QZ2 fluorophore platform would increase brightness and maintain QZ2-like dynamic range; however, this modification is unnecessary because QZ2 is readily detectable in vivo (vide infra).

Other beneficial features of the QZ dyes include Zn(II)-specific turn-on and improved selectivity for Zn(II) over other potentially competing metal ions. These features are significant improvements over the DPA-based sensors and members of the ZS family. Lastly, stopped-flow kinetic analyses show that the QZ dyes display rapid and reversible Zn(II) binding, which affords high temporal resolution and contrasts to the slow dissociation of Zn(II) observed for ZP and other DPA-containing sensors.

Confocal Imaging and Zn(II) Response In Vivo. Preliminary confocal imaging experiments established that QZ1 and QZ2 are membrane permeable. We chose to focus our biological efforts on applications of QZ2 given its superior photostability and dynamic range. Given the μM K_d value of QZ for Zn(II), we conducted solution studies (50 mM PIPES, 100 mM KCl, pH 7) to determine whether QZ and pyrithione, an ionophore that delivers Zn(II) into cells, compete for Zn(II). Addition of excess 1:2 Zn(II)/pyrithione to QZ resulted in negligible fluorescence change, in agreement with the reported K_d of ~10^{-11} M for formation of the 1:2 Zn/pyrithione complex.[102] In vivo experiments were subsequently conducted by treating HeLa cells with 10 μM QZ2 and 100 μM Zn(II) with varying concentrations (5 to 30 μM) of pyrithione. This study indicated that substoichiometric pyrithione delivers Zn(II) into HeLa cells (data not shown) and we therefore employed a 10:2 Zn(II)/pyrithione ratio for all subsequent imaging experiments. Similar results were obtained in a study where the fluorescence response of Zinquin-treated chronic lymphocytic leukemia cells was monitored as a function of varying Zn(II)/pyrithione ratios.[78] Further control experiments indicated that the Zn(II)-induced fluorescence enhancement of QZ2 is reversible by addition of TPEN to the cell culture medium as shown in Figure 7.15.

Of particular interest is the use of intracellular Zn(II) sensors with varying K_d values to report on a range of Zn(II) concentrations in cells. To illustrate the utility of a relatively low affinity Zn(II) sensor in vivo, we compared the responses of ZP3 and QZ2 to varying intracellular concentrations of Zn(II). Figure 7.16 displays HeLa cells treated

with 10 μM dye and 0, 50, 100 or 200 μM total Zn(II). ZP3, which has a K_{d1} of 0.7 ± 0.1 nM for Zn(II), shows saturation behavior when 50 μM Zn(II) is added to the cells. In contrast, the fluorescence intensity of cells treated with QZ2 increases upon addition of up to 200 μM Zn(II). We did not exceed this value to avoid Zn(II) toxicity. Although the intracellular concentration of Zn(II) is unclear because substoichiometric pyrithione was used, the results displayed in Figure 7.16 indicate that probe affinity is an important parameter for in vivo metal ion detection and that lower-affinity sensors can be employed to report on relatively high concentrations of the analyte in vivo. This observation is in good agreement with a report in which ZnAF sensors with modified DPA ligands showed K_d-dependent Zn(II) responses in vivo[89] and contrasts with a study concluding that dye affinity is unimportant for in vivo Zn(II) detection.[103] We note that ZP3 and QZ2 show different intracellular staining patterns, with ZP3 localizing to the Golgi apparatus of HeLa cells (Chapter 3) and QZ2 showing a more diffuse pattern.

We next investigated ZP3 and QZ2 staining of acute hippocampal slices from adult rat. Whereas ZP3 vividly stained the DG and CA3 regions of the hippcampus, no differential staining was observed following treatment with either QZ1 or QZ2 (Figure 7.17). This comparison suggests that the levels of endogenous and histochemically observable Zn(II) in the DG and CA3 regions of the rat hippocampus are between the detection limits of ZP3 (K_d < 1 nM) and QZ (K_d ~ 40 μM) and further illustrates the utility of Zn(II) sensors with varying dissociation constants for analyzing mobile Zn(II) concentrations in vivo. If we also consider the data presented in Figure 4.8 where an acute hippocampal slice was treated with ZP9 (K_d ~ 700 nM), we can state that the concentration of Zn(II) in the dentate gyrus region is between the detection limits of ZP9 and QZ. This trend is in remarkable agreement with a study of extracellular Zn(II) release following addition of K(I).[89]

Biological Imaging with Two Photon Microscopy. The development and implementation of new optical imaging techniques parallels advances in chemosensor

design. Of current interest is the application of two-photon microscopy (TPM) to biological Zn(II) imaging.[57,85] Optical imaging by TPM has some advantages over conventional one-photon techniques.[104-106] By employing two photons of lower energy, laser excitation typically causes less photodamage to dyes and biological samples, and allows for penetration of thicker specimens. To determine the ability of QZ1 and QZ2 to undergo two-photon excitation, the fluorescence intensity of buffered solutions of 10 μM QZ and excess Zn(II) (50 mM PIPES, 100 mM KCl, pH 7) was evaluated following two-photon excitation over the 740 – 880 nm range. Figure 7.18 displays the relative fluorescence intensity of these solutions and reveals that maximum emission occurs with excitation at 780 nm. Live HeLa cells treated with QZ2 and Zn(II) were imaged by TPM with excitation at 780 nm and are depicted in Figure 7.19, establishing that QZ2 responds to two-photon excitation in vivo.

Summary and Perspectives

The preparation and photophysical characterization of 8-aminoquinline-derivatized fluorescein-based Zn(II) sensors QZ1 and QZ2 are presented. These dyes have dissociation constants for Zn(II) in the micromolar range, can readily detect Zn(II) in the presence of biologically relevant concentrations of Na(I), K(I), Mg(II) and Ca(II), and display superior selectivity for Zn(II) as compared to other known fluorescent Zn(II) probes. Stopped-flow kinetic analyses show that the QZ dyes display rapid and reversible Zn(II) binding, which affords high temporal resolution and contrasts with the slow dissociation of Zn(II) observed for ZP and other DPA-containing sensors. The results suggest that QZ-type systems will be valuable for biological imaging of Zn(II) flux at elevated concentrations. QZ1 and QZ2 also afford excellent ~42- and ~150-fold fluorescence enhancement upon Zn(II) binding and comparison of the photophysical properties of QZ to ZP and ZS systems indicates that the nature of the PET switching nitrogen atom is not the only determining factor for fluorescence behavior. Rather,

properties of the entire ligand fragment modulate both the degree of fluorescein quenching and the amount of fluorescence turn-on that results from analyte recognition. Quantum calculations will be employed in future work to investigate this matter further. Finally, single- and multi-photon microscopy reveal that QZ are cell-permeable and Zn(II)-responsive in vivo. Comparison of the response of QZ2 (μM K_d) to ZP3 (sub-nM K_d) to intracellular zinc indicates that sensor binding affinity plays a significant role in metal ion detection in vivo. Investigations of endogenous Zn(II) distribution in hippocampal slices as detected by the ZP3, ZP9 (sub-μM K_d) and QZ probes provides additional evidence for the importance of relative Zn(II) affinity. The sensors presented in Chapters 2–7 provide dissociation constants than span six orders of magnitude, several of which have been successfully applied to imaging endogenous Zn(II) stores and Zn(II) mobilization in biological samples. Future biological studies will benefit from this type of sensor suite.

Overview of Zn(II) Sensor Work

Through investigations of the sensors presented in Chapters 2 – 7, we can make several generalizations about sensor behavior that may be applied to the design of future probes. We refer the reader to Figure 1.12, which is a compilation of the new Zn(II) sensors described in this work, and to Table 7.1 to help guide this discussion.

We first consider the fluorescence properties of the ZP, ZS and QZ probes. To do so, we divide these sensors into three general types defined by the nature of the metal-binding unit: tertiary amine-, aniline- and quinoline-based. Sensors that use a tertiary amine as the PET switch are generally more emissive than those with an aniline unit in both the free and Zn(II)-bound forms. This comparison indicates that the tertiary amine unit is a less efficient PET quencher than the aniline moiety. This difference most likely arises because the orbitals of the aniline π system, in addition to the aniline nitrogen lone pair, contribute to fluorescence quenching. Moreover, Zn(II) coordination fails to

restore full fluorescein-like emission ($\Phi_{Zn} \leq 0.4$ in most instances) and aniline protonation results in only modest fluorescence enhancement in these systems. Such observations further define a key role of the aniline π system in fluorescence quenching. The quinoline-based QZ sensors, which have analogous PET-switching nitrogen atoms and show similar proton sensitivity to ZP4 and its analogs, exhibit much higher quantum efficiencies in the Zn(II)-bound form. Zn(II) coordination to QZ results in direct perturbation of the quinoline π system through coordination to the quinoline N_1 atom, and we propose that the enhanced turn-on exhibited by QZ originates from this feature. A comparison of the tertiary amine and aniline-based systems also indicates that the emission properties of the former probes are more sensitive to variation in the donor arms. Based on our studies to date, obtaining a reasonable Φ_{free} value for systems employing a tertiary-amine-based switch generally requires two aromatic heterocycles in the metal-binding unit. The entire ligand, not only the tertiary amine switch, contributes to fluorescence quenching. In contrast, variation of the donor arms in aniline-based systems has little effect on sensor emission. One additional trend is the effect of one versus two metal binding units: sensors with two metal binding units consistently exhibit lower background fluorescence than their asymmetrical analogs. Installation of only one tertiary amine-based ligand onto a fluorescein should be avoided; it is insufficient for achieving low background fluorescence at neutral pH.

The ligand modifications presented in Chapters 4 – 7 were made to vary Zn(II) binding affinity, association and dissociation rates, and selectivity. Regarding the former, reducing the number of donor atoms raises the apparent K_d of the Zn(II) complexes to the sub-μM and mid-μM range. Fluorescein halogenation can also be employed to tune the Zn(II) affinity with both xanthenone and benzoate substitution raising the apparent K_d value relative to probes based on unsubstituted fluorescein. More subtle modifications to the Zn(II) binding units are required to obtained sensors with dissociation constants in the low- to mid-nM range. All of the sensors described in

this work bind Zn(II) rapidly and, in some cases, reversibly. Departure from the DPA binding motif by substitution of one pyridyl donor with an alterative group has little effect on the Zn(II) association rate and affords faster Zn(II) dissociation. The QZ ligand system affords the most rapid and reversible Zn(II) binding.

Metal ion selectivity experiments reveal the degree to which a give sensor is Zn(II)-selective, for such a fluorescence response is critical for biological work. It is important that a given sensor detects Zn(II) over the biologically relevant cations K(I), Na(I), Ca(II) and Mg(II). All of the Zn(II) probes discussed in this work bind for Zn(II) over millimolar concentrations of these species, demonstrating that this selectivity is easy to maintain by using metal-binding units comprised of multiple nitrogen and sulfur atoms. We also routinely study the effect of coordination to divalent first-row transition metal ions and the Group 12 congeners on both sensor emission and Zn(II) response. Coordination of tertiary-amine-based sensors to Fe(II), Co(II), Ni(II) and Cu(II) always results in immediate and substantial fluorescence quenching. When aniline- and quinoline-based sensors bind to these particular metal ions, there is little or no effect on emission. We attribute this behavior to the fact that these sensors are substantially quenched in their metal-free forms.

The selectivity of a given probe for any one of the Group 12 congeners can be rationalized with the hard/soft acid/base principle where sensors with nitrogen-rich chelates preferentially coordinate to Zn(II) and those with a thioether group bind Hg(II) more tightly. The selectivity of each sensor for various divalent first-row transition metal ions is somewhat less clear. Substitution of one pyridyl group from the DPA unit with another moiety routinely conveys selectivity for Zn(II) over Fe(II). The origin of the selectivity for Zn(II) over Co(II) in the QZ systems is unique. Explanations of such behavior will be aided by crystallographic characterization of the fluorescein-metal complexes.

References

(1)   Vallee, B. L.; Falchuk, K. H. *Physiol. Rev.* **1993**, *73*, 79-118.

(2)   Walker, C. F.; Black, R. E. *Annu. Rev. Nutr.* **2004**, *23*, 255-275.

(3)   Daiyasu, H.; Osaka, K.; Ishino, Y.; Toh, H. *FEBS Lett.* **2001**, *503*, 1-6.

(4)   Ho, E.; Ames, B. N. *Proc. Nat. Acad. Sci. USA* **2002**, *99*, 16770-16775.

(5)   Troung-Tran, A. Q.; Carter, J.; Ruffin, R. E.; Zalewski, P. D. *Biometals* **2001**, *14*, 315-330.

(6)   Kimura, E.; Aoki, S.; Kikuta, E.; Koike, T. *Proc. Nat. Acad. Sci. USA* **2003**, *100*, 3731-3736.

(7)   Frederickson, C. J. *Int. Rev. Neurobiol.* **1989**, *31*, 145-238.

(8)   Huang, E. P. *Proc. Nat. Acad. Sci. USA* **1997**, *94*, 13386-13387.

(9)   Frederickson, C. J.; Bush, A. I. *Biometals* **2001**, *14*, 353-366.

(10)   Takeda, A. *Biometals* **2001**, *14*, 343-351.

(11)   Manzerra, P.; Behrens, M. M.; Canzoniero, M. T.; Wang, X. Q.; Heidinger, V.; Ichinose, T.; Yu, S. P.; Choi, D. W. *Proc. Nat. Acad. Sci. USA* **2001**, *98*, 11055-11061.

(12)   Liuzzi, J. P.; Cousins, R. J. *Annu. Rev. Nutr.* **2004**, *24*, 151-172.

(13)   Valente, T.; Auladell, C. *Mol. Cell. Neurosci.* **2002**, *21*, 189-204.

(14)   Cole, T. B.; Wenzel, H. J.; Kafer, K. E.; Schwartzkroin, P. A.; Palmiter, R. D. *Proc. Nat. Acad. Sci. USA* **1999**, *96*, 1716-1721.

(15)   Lee, J.-Y.; Cole, T. B.; Palmiter, R. D.; Koh, J.-Y. *J. Neurosci.* **2000**, *20*, RC79 1-5.

(16)   Jacob, C.; Maret, W.; Vallee, B. L. *Proc. Nat. Acad. Sci. USA* **1998**, *95*, 3489-3494.

(17)   Ebadi, M.; Iversen, P. L.; Cerutis, D. R.; Rojas, C. P.; Happe, H. K.; Murrin, L. C.; Pfeiffer, R. F. *Neurochem. Int.* **1995**, *27*, 1-22.

(18)   Maret, W. *BioMetals* **2001**, *14*, 187-190.

(19)   Knipp, M.; Meloni, G.; Roschitzki, B.; Vasak, M. *Biochemistry* **2005**, *44*, 3159-3165.

(20)   Qian, W.-J.; Gee, K. R.; Kennedy, R. T. *Anal. Chem.* **2003**, *75*, 3468-3475.

(21)   Qian, W.-J.; Ge, K. R.; Kennedy, R. T. *Anal. Chem.* **2003**, *75*, 3468-3475.

(22)   Vogt, K.; Mellor, J.; Tong, G.; Nicoli, R. *Neuron* **2000**, *26*, 187-196.

(23)   Kay, A. R. *J. Neurosci.* **2003**, *23*, 6847-6855.

(24)   Kay, A. R. *Trends Neurosci.* **2006**, *29*, 20-26.

(25)   Kay, A. R.; Toth, K. *J. Neurophysiol.* **2006**, *95*, 1949-1956.

(26)   Choi, D. W.; Koh, J. Y. *Annu. Rev. Neurosci.* **1998**, *21*, 347-375.

(27)   Frederickson, C. J.; Maret, W.; Cuajungco, M. P. *The Neuroscientist* **2004**, *10*, 18-25.

(28)   Garcia-Colunga, J.; Vazquez-Gomez, E.; Miledi, R. *Pharmacogenomics Journal* **2004**, *4*, 388-393.

(29)   Chausmer, A. B. *J. Am. Coll. Nutr.* **1998**, *17*, 109-115.

(30)   Henshall, S. M.; et. al. *Oncogene* **2003**, *22*, 6005-6012.

(31)   Cuajungo, M. P.; Lees, G. J. *Neurobiol. Disease* **1997**, *4*, 137-169.

(32)   Bush, A. I. *Curr. Opin. Chem. Biol.* **2000**, *4*, 184-191.

(33)   Bush, A. I. *Trends Neurosci.* **2003**, *26*, 207-214.

(34)   Bush, A. I. *Alzheimer Dis. Assoc. Disord.* **2003**, *17*, 147-150.

(35)   Suh, S. W.; Jensen, K. B.; Jensen, M. S.; Silva, D. S.; Kesslak, P. J.; Danscher, G.; Frederickson, C. J. *Brain Res.* **2000**, *852*, 274-278.

(36)   Kimura, E.; Koike, T. *Chem. Soc. Rev.* **1998**, *27*, 179-184.

(37)   Lim, N. C.; Freake, H. C.; Bruckner, C. *Chem. Eur. J.* **2005**, *11*, 38-49.

(38)   Jiang, P.; Guo, Z. *Coord. Chem. Rev.* **2004**, *248*, 205-229.

(39)   Frederickson, C. J. *Science STKE* **2003**, pe 18.

(40)   Kikuchi, K.; Komatsu, K.; Nagano, T. *Curr. Opin. Chem. Biol.* **2004**, *8*, 182-191.

(41)   Burdette, S. C.; Lippard, S. J. *Proc. Nat. Acad. Sci. USA* **2003**, *100*, 3605-3610.

(42)   Canzoniero, M. T.; Sensi, S. L.; Choi, D. W. *Neurobiol. Disease* **1997**, *4*, 275-279.

(43)   Kim, T. W.; Park, J.; Hong, J.-I. *J. Chem. Soc. Perkin Trans. 2* **2002**, 923-927.

(44)   Gee, K. R.; Zhou, Z.-L.; Qian, W.-J.; Kennedy, R. *J. Am. Chem. Soc.* **2002**, *124*, 776-778.

(45)   Sensi, S. L.; Ton-That, D.; Weiss, J. H.; Rothe, A.; Gee, K. R. *Cell Calcium* **2003**, *34*, 281-284.

(46)   Lim, N. C.; Yao, L.; Freake, H. C.; Bruckner, C. *Bioorg. Med. Chem. Lett.* **2003**, *13*, 2251-2254.

(47)   Koike, T.; Watanabe, T.; Aoki, S.; Kimura, E.; Shiro, M. *J. Am. Chem. Soc.* **1996**, *118*, 12696-12703.

(48)   Kimura, E.; Ikeda, T.; Aoki, S.; Shionoya, M. *J.Biol. Inorg. Chem.* **1998**, *3*, 259-267.

(49)   Aoki, S.; Kaido, S.; Fujioka, H.; Kimura, E. *Inorg. Chem.* **2003**, *42*, 1023-1030.

(50)   Hirano, T.; Kikuchi, K.; Urano, Y.; Higuchi, T.; Nagano, T. *Angew. Chem. Int. Ed.* **2000**, *29*, 1052-1054.

(51)   Hirano, T.; Kikuchi, K.; Urano, Y.; Higuchi, T.; Nagano, T. *J. Am. Chem. Soc.* **2000**, *122*, 12399-12400.

(52)   Hirano, T.; Kikuchi, K.; Urano, Y.; Nagano, T. *J. Am. Chem. Soc.* **2002**, *124*, 6555-6562.

(53)   Czarnik, A. *Acc. Chem. Res.* **1994**, *27*, 302-308.

(54)   Wu, Y.; Peng, X.; Guo, B.; Fan, J.; Zhang, Z.; Wang, J.; Cui, A.; Gao, Y. *Org. Biomol. Chem.* **2005**, *5*, 1387-1392.

(55)   Maruyama, S.; Kikuchi, K.; Hirano, T.; Urano, Y.; Nagano, T. *J. Am. Chem. Soc.* **2002**, *124*, 10650-10651.

(56)   Henary, M. M.; Wu, Y.; Fahrni, C. *J. Chem. Eur. J.* **2004**, *10*, 3015-3025.

(57)   Taki, M.; Wolford, J. L.; O'Halloran, T. V. *J. Am. Chem. Soc.* **2004**, *126*, 712-713.

(58)   Lim, N. C.; Bruckner, C. *Chem. Commun.* **2004**, 1094-1095.

(59)   Chang, C. J.; Jaworski, J.; Nolan, E. M.; Sheng, M.; Lippard, S. J. *Proc. Nat. Acad. Sci. USA* **2004**, *101*, 1129-1134.

(60)   Woodroofe, C. C.; Lippard, S. J. *J. Am. Chem. Soc.* **2003**, *125*, 11458-11459.

(61)   Woodroofe, C. C.; Won, A.; Lippard, S. J. *Inorg. Chem.* **2005**, *44*, 3112-3120.

(62)   Gee, K. R.; Zhou, Z.-L.; Ton-That, D.; Sensi, S. L.; Weiss, J. H. *Cell Calcium* **2002**, *31*, 245-251.

(63)   Elbaum, D.; Nair, S. K.; Patchan, M. W.; Thompson, R. B.; Christianson, D. W. *J. Am. Chem. Soc.*
        1996, *118*, 8381-8387.

(64)   Thompson, R. B.; Maliwal, B. P. *Anal. Chem.* **1998**, *70*, 1749-1754.

(65)   Thompson, R. B.; Whetsell, W. O.; Maliwal, B. P.; Fierke, C. A.; Frederickson, C. J. *J. Neurosci.*
        Methods, **2000**, *96*, 35-45.

(66)   Thompson, R. B.; Cramer, M. L.; Bozym, R.; Fierke, C. A. *J. Biomed. Optics* **2002**, *7*, 555-560.

(67)   Fierke, C. A.; Thompson, R. B. *BioMetals* **2001**, *14*, 205-222.

(68)   Stewart, J. D.; Roberts, V. A.; Crowder, M. W.; Getzoff, E. D.; Benkovic, S. J. *J. Am. Chem. Soc.*
        1994, *116*, 415-416.

(69)   Godwin, H. A.; Berg, J. M. *J. Am. Chem. Soc.* **1996**, *118*, 6514-6515.

(70)   Walkup, G. K.; Imperiali, B. *J. Am. Chem. Soc.* **1996**, *118*, 3053-3054.

(71)   Walkup, G. K.; Imperiali, B. *J. Am. Chem. Soc.* **1997**, *119*, 3443-3450.

(72)   Shults, M. D.; Pearce, D. A.; Imperiali, B. *J. Am. Chem. Soc.* **2003**, *125*, 10591-10597.

(73)   Frederickson, C. J.; Kasarskis, E. J.; Ringo, D.; Frederickson, R. E. *J. Neurosci. Methods* **1987**, *20*, 91-
        103.

(74)   Zalewski, P. D.; Millard, S. H.; Forbes, I. J.; Kapaniris, O.; Slavotinek, A.; Betts, W. H.; Ward, A.
        D.; Lincoln, S. F.; Mahadevan, I. *J. Histochem. Cytochem.* **1994**, *42*, 877-884.

(75)   Kimber, M. C.; Mahadevan, I. B.; Lincoln, S. F.; Ward, A. D.; Tiekink, E. R. T. *J. Org. Chem.* **2000**,
        65, 8204-8209.

(76)   Nasir, M. S.; Fahrni, C. J.; Suhy, D. A.; Kolodsick, K. J.; Singer, C. P.; O'Halloran, T. V. *J. Biol.*
        Inorg. Chem. **1999**, *4*, 775-783.

(77)   Fahrni, C. J.; O'Halloran, T. V. *J. Am. Chem. Soc.* **1999**, *121*, 11448-11458.

(78)   Zalewski, P. D.; Forbes, I. J.; Betts, W. H. *Biochem. J.* **1993**, *296*, 403-408.

(79)   Coyle, P.; Zalewski, P. D.; Philcox, J. C.; Forbes, I. J.; Ward, A. D.; Lincoln, S. F.; Mahadevan, I.;
        Rofe, A. M. *Biochem. J.* **1994**, *303*, 781-786.

(80)   Walkup, G. K.; Burdette, S. C.; Lippard, S. J.; Tsien, R. Y. *J. Am. Chem. Soc.* **2000**, *122*, 5644-5645.

(81)   Burdette, S. C.; Walkup, G. K.; Springler, B.; Tsien, R. Y.; Lippard, S. J. *J. Am. Chem. Soc.* **2001**, *123*, 7831-7841.

(82)   Burdette, S. C.; Frederickson, C. J.; Bu, W.; Lippard, S. J. *J. Am. Chem. Soc.* **2003**, *125*, 1778-1787.

(83)   Nolan, E. M.; Burdette, S. C.; Harvey, J. H.; Hilderbrand, S. A.; Lippard, S. J. *Inorg. Chem.* **2004**, *43*, 2624-2635.

(84)   Chang, C. J.; Nolan, E. M.; Jaworski, J.; Burdette, S. C.; Sheng, M.; Lippard, S. J. *Chem. Biol.* **2004**, *11*, 203-210.

(85)   Chang, C. J.; Nolan, E. M.; Jaworski, J.; Okamoto, K.-I.; Hayashi, Y.; Sheng, M.; Lippard, S. J. *Inorg. Chem.* **2004**, *43*, 6774-6779.

(86)   Woodroofe, C. C.; Masalha, R.; Barnes, K. R.; Frederickson, C. J.; Lippard, S. J. *Chem. Biol.* **2004**, *11*, 1659-1666.

(87)   Anderegg, G.; Hubmann, E.; Podder, N. G.; Wenk, F. *Helv. Chim. Acta* **1977**, *60*, 123-140.

(88)   Nolan, E. M.; Lippard, S. J. *Inorg. Chem.* **2004**, *43*, 8310-8317.

(89)   Komatsu, K.; Kikuchi, K.; Kojima, H.; Urano, Y.; Nagano, T. *J. Am. Chem. Soc.* **2005**, *127*, 10197-10204.

(90)   Brannon, J. H.; Madge, D. *J. Phys. Chem.* **1978**, *82*, 705-709.

(91)   Pearce, D. A.; Jotterand, N.; Carrico, I. S.; Imperiali, B. *J. Am. Chem. Soc.* **2001**, *123*, 5160-5161.

(92)   Xue, G.; Bradshaw, J. S.; Dalley, N. K.; Savage, P. B.; Izatt, R. M.; Prodi, L.; Montalti, M.; Zaccheroni, N. *Tetrahedron* **2002**, 4809-4815.

(93)   Nolan, E. M.; Chang, C. J.; Lippard, S. J. *Unpublished results*.

(94)   de Silva, A. P.; Gunaratne, H. Q. N.; Gunnlaugsson, T.; Huxley, A. J. M.; McCoy, C. P.; Rademacher, J. T.; Rice, T. E. *Chem. Rev.* **1997**, *97*, 1515-1566.

(95)   de Silva, A. P.; Fox, D. B.; Huxley, A. J. M.; Moody, T. S. *Coord. Chem. Rev.* **2000**, *205*, 41-57.

(96)   Sjoback, R.; Nygren, J.; Kubista, M. *Spectrochim. Acta. Part A* **1995**, *51*, L7-L21.

(97)   Leonhardt, H.; Gordon, L.; Livingston, R. *J. Phys. Chem.* **1971**, *75*, 245-249.

(98)   Jackson, A. P.; Timmerman, M. P.; Bagshaw, C. R.; Ashley, C. C. *FEBS Lett.* **1987**, *216*, 35-39.

(99)   Kao, J. P.; Tsien, R. Y. *Biophys. J.* **1988**, *53*, 635-639.

(100)   Quast, U.; Labhardt, A. M.; Doyle, V. M. *Biochem. Biophys. Res. Comm.* **1984**, *123*, 604-611.

(101)   Doose, C. A.; Ranke, J.; Stock, F.; Bottin-Weber, U.; Jastorff, B. *Green Chem.* **2004**, *6*, 259-266.

(102)   Dineley, K. E.; Malaiyandi, L. M.; Reynolds, I. J. *J. Mol. Pharmacol.* **2002**, *62*, 618-627.

(103)   So, P. T. C.; Dong, C. Y.; Masters, B. R.; Berland, K. M. *Annu. Rev. Biomed. Eng.* **2000**, *2*, 399-429.

(104)   Mainen, Z. F.; Maletic-Savatic, M.; Hayashi, S. Y.; Milinow, R.; Svoboda, K. *Methods* **1999**, *18*, 231-239.

(105)   Williams, R. M.; Zipfel, W. R.; Webb, W. W. *Curr. Opin. Chem. Biol.* **2001**, *5*, 603-608.

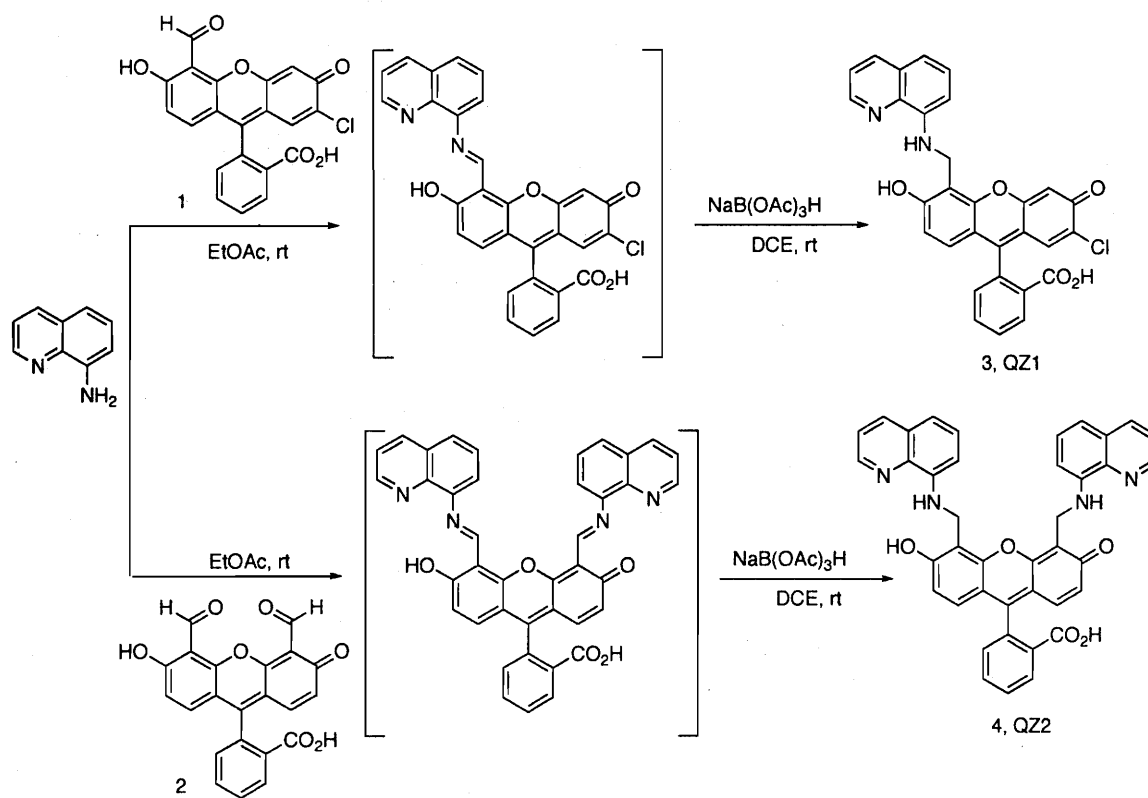**Table 7.1.** Spectroscopic and Thermodynamic Data for Fluorescent Zn(II) Sensors[a]

	Absorption λ (nm), $\varepsilon \times 10^4$ (M^{-1}cm^{-1})		Emission λ (nm), Φ^b		pK_a^c (N)	~DR^d	Ref.^{e}
	Unbound	Zn(II)	Unbound	Zn(II)			
ZP1^f	515, 7.9	507, 8.4	531, 0.38	527, 0.87	8.4	2.5	81
ZP1(6-CO$_2$H)	516, 7.6	506, 8.1	531, 0.21	528, 0.63	7.1	7	86
ZP2	498, 4.4	490, 5.3	522, 0.25	517, 0.92	9.4	4	81
ZP3	502, 7.5	492, 8.5	521, 0.15	516, 0.92	6.8	6	C3, 84
ZP4	506, 6.1	495, 6.7	521, 0.06	515, 0.34	7.2	4.4	82
ZP5	504, 8.3	495, 9.1	520, 0.29	517, 0.48	9.6	1.6	C2, 83
ZP6	506, 8.9	495, 9.8	519, 0.10	517, 0.34	6.3	4	C2, 83
ZP7	505, 6.8	495, 7.7	521, 0.04	517, 0.05	6.9	1	83
ZP8	500, 8.1	489, 7.8	516, 0.03	510, 0.35	6.5	11	C2, 83
ZP9	505, 5.1	495, 4.4	526, 0.02	521, 0.41	7.2	12	C4
ZP10	506, 5.4	497, 4.5	523, 0.08	516, 0.32	7.0	7	C4
ZPF1	533, 9.9	525, 12.0	547, 0.11	544, 0.55	6.9	6	C3, 84
ZPCl1	534, 9.7	527, 12.0	550, 0.22	549, 0.50	7.0	2.5	C3, 84
ZPBr1	534, 4.5	528, 8.6	549, 0.25	547, 0.36	7.3	2.2	C3, 84
ZPF3	520, 8.7	510, 9.3	537, 0.14	533, 0.60	6.7	5	C3, 84
ZS1	510, 8.39	501, 7.52	531, 0.50	526, 0.70	7.7	1.4	C5, 88
ZS2	499, 6.69	489 6.76	523, 0.39	516, 0.69	7.7	2	C5, 88
ZS3	500, 8.69	--	525, 0.71	--	9.3	1	C5, 88
ZS4	507, 8.11	495, ND	522, 0.12	520, 0.50	7.6	4.5	C5, 88
ZS5	497, 3.3	490, 4.2	522, 0.36	517, 0.80	8.0	4.6	C6
ZS6	515, 4.5	505, 6.0	533, 0.44	527, 0.64	7.8	3.3	C6
ZS7	500, 6.2	490, 6.6	524, 0.25	518, 0.79	7.0	2.7	C6
ZSF6	532, 6.3	522, 7.0	549, 0.19	545, 0.63	7.1	2.0	C6
ZSF7	521, 6.2	511, 7.0	535, 0.24	527, 0.68	6.9	2.5	C6
QZ1	505, 6.89	498, 6.98	524, 0.024	524, 0.78	6.1	42	C7
QZ2	499, 3.72	489 3.36	~520, 0.005	518, 0.70	7.0	150	C7

[a]Measurements were performed at pH 7 (50 mM PIPES, 100 mM KCl). [b] Fluorescein ($\Phi = 0.95$ in 0.1 N NaOH, ref. 90) was used as the standard. [c] The pK_a value of the nitrogen atom responsible for PET switching. [d] DR is the dynamic range, or the increase in brightness ($\Phi \times \varepsilon$) that results from Zn(II) coordination. [e] The C refers to the chapter number in this thesis. [f] See Figure 7.1 for nomenclature. ZP1(6-CO$_2$H) has a carboxylate at the 6-position of the benzoate moiety.

Table 7.2. Kinetic and Thermodynamic Parameters for Zn(II) Binding to ZP and QZ Sensors[a]

	k_{on} (M⁻¹s⁻¹)[b] 4.3 °C	k_{on} (M⁻¹s⁻¹)[c] 25 °C	K_{d1}[d] 4.3 °C	K_{d1}[e] 25 °C	k_{off} (s⁻¹)[f] 4.3 °C	~k_{off}(s⁻¹)[g] 25 °C	$\Delta H^{\ddagger}$[h] (kcal/mol)	$\Delta S^{\ddagger}$[h] (cal/mol-K)
ZP1	$6.3\pm0.1 \times 10^5$	$3.3\pm0.4 \times 10^6$		0.7 ± 0.1 nM		$2.3\pm0.4 \times 10^{-3}$	12.5 ± 0.1	13.2 ± 0.3
ZP3	$7.8\pm0.1 \times 10^5$	$4.3\pm0.3 \times 10^6$		0.7 ± 0.1nM		$2.9\pm0.4 \times 10^{-3}$	11.6 ± 0.2	10.7 ± 0.7
ZP4	$8.5\pm0.4 \times 10^5$	$5.2\pm0.1 \times 10^6$		0.65 ± 0.1 nM		$3.4\pm0.5 \times 10^{-3}$	12.2 ± 0.3	13.1 ± 0.1
ZS5	$3.2\pm0.2 \times 10^5$	$2.2\pm0.1 \times 10^6$		1.5 ± 0.2 µM		3.3	13.3 ± 0.1	15.2 ± 0.2
ZS6	$3.7\pm0.1 \times 10^5$	$2.1\pm0.1 \times 10^6$					12.9 ± 0.4	14.0 ± 0.7
ZS7	$5.9\pm0.1 \times 10^5$	$3.0\pm0.1 \times 10^6$		3.7 ± 0.2 µM		11	12.5 ± 0.3	12.9 ± 1.3
ZSF6	$3.3\pm0.1 \times 10^5$	$1.8\pm0.1 \times 10^6$					12.6 ± 0.2	12.4 ± 0.9
ZSF7	$5.0\pm0.1 \times 10^5$	$2.7\pm0.1 \times 10^6$		5.0 ± 0.3 µM		13.5	12.6 ± 0.2	13.0 ± 0.7
QZ1	$3.1\pm0.2 \times 10^6$	$3.7\pm0.2 \times 10^7$	48 ± 3 µM	33 ± 2 µM	$1.5\pm0.3 \times 10^2$	$1.2\pm0.1 \times 10^3$	10.7 ± 0.1	12.1 ± 0.1
QZ2	$3.9\pm0.3 \times 10^6$	$4.5\pm0.3 \times 10^7$	41 ± 3 µM		$1.6\pm0.2 \times 10^2$		10.7 ± 0.1	12.4 ± 0.1

[a]All measurements were made at pH 7 (50 mM PIPES, 100 mM KCl). [b]Experimentally determined values for k_{on} at 4.3 ± 0.1 °C. [c] Experimentally determined k_{on} for ZP and ZS sensors at 25 ± 1 °C. The k_{on} values for QZ were estimated by extrapolation of the Eyring plots (Figure 7.13). [d] Dissociation constants for QZ1 and QZ2 calculated from stopped-flow kinetic data obtained at 4.3 ± 0.1 °C. [e]Dissociation constants for ZP, ZS and QZ1 obtained experimentally by fluorimetric titration at 25 ± 0.1 °C. See Table 7.1 for references. [f]Experimentally determined k_{off} at 4.3 ± 0.1 °C. [g]Calculated k_{off} for ZP and at 25 ± 1 °C. [g]Activation parameters were determined over a temperature range of ~4 to ~20 °C for QZ and from ~4 to ~40 °C for ZP and ZS.
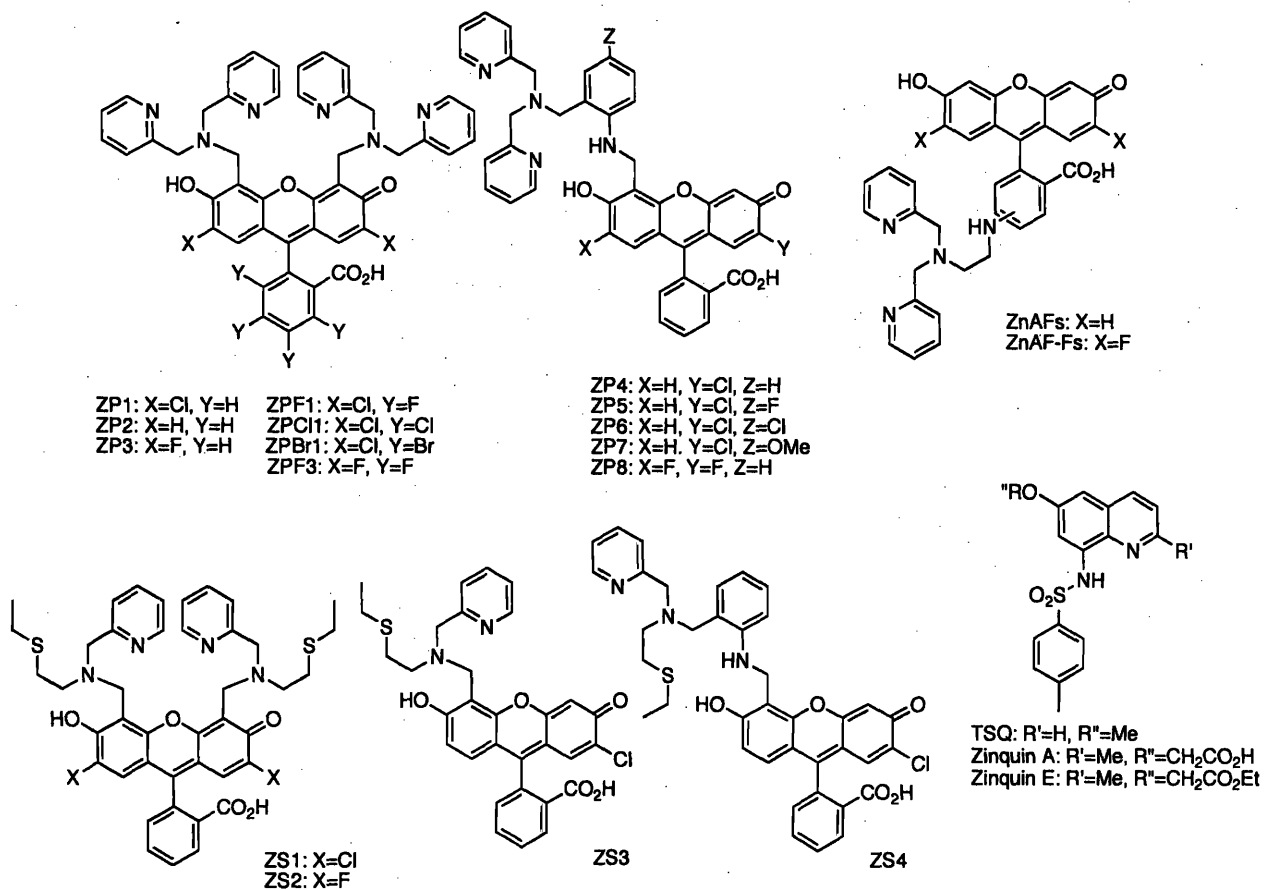
Scheme 7.1. Syntheses of QZ1 and QZ2.

ZP1: X=Cl, Y=H   ZPF1: X=Cl, Y=F
ZP2: X=H, Y=H   ZPCl1: X=Cl, Y=Cl
ZP3: X=F, Y=H   ZPBr1: X=Cl, Y=Br
            ZPF3: X=F, Y=F

ZP4: X=H, Y=Cl, Z=H
ZP5: X=H, Y=Cl, Z=F
ZP6: X=H, Y=Cl, Z=Cl
ZP7: X=H. Y=Cl, Z=OMe
ZP8: X=F, Y=F, Z=H

ZnAFs: X=H
ZnAF-Fs: X=F

ZS1: X=Cl
ZS2: X=F

ZS3

ZS4

TSQ: R'=H, R"=Me
Zinquin A: R'=Me, R"=CH$_2$CO$_2$H
Zinquin E: R'=Me, R"=CH$_2$CO$_2$Et

Figure 7.1. Selected fluorescent sensors for Zn(II). The ZP, ZS and ZnAF dyes are all fluorescein-based and give fluorescence enhancement upon Zn(II) coordination. The quinoline sulfonamides, which include TSQ and Zinquin, are the most commonly used biological Zn(II) stains and also give fluorescence turn-on following Zn(II) binding.
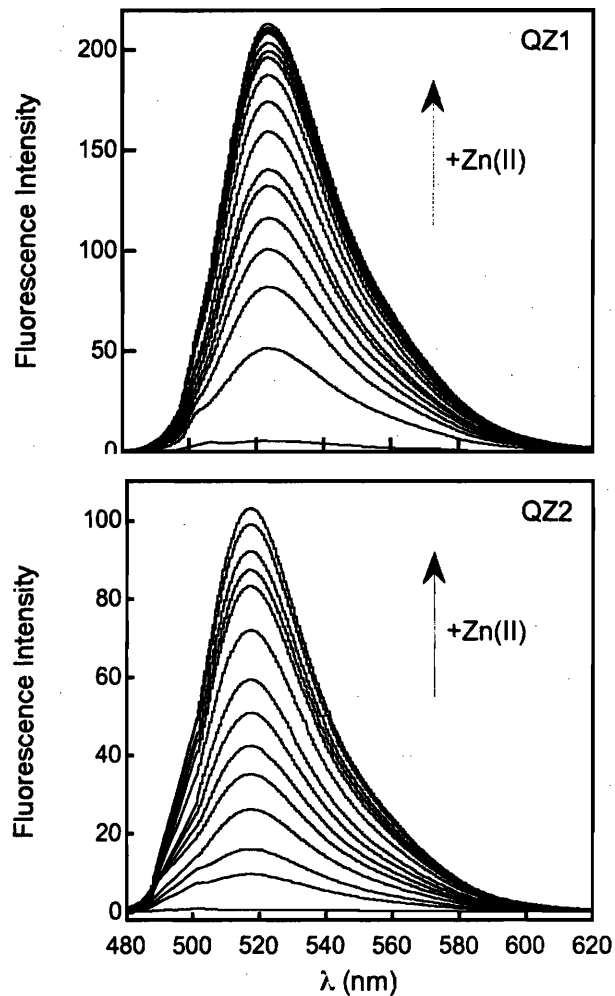
Figure 7.2. Fluorescence response of QZ1 (top) and QZ2 (bottom) to Zn(II) at pH 7 (50 mM PIPES, 100 mM KCl). Top: Emission of QZ1 before and after Zn(II) addition. Aliquots of 10 and 100 mM $ZnCl_2$ in water were added to yield Zn(II) concentrations of 0, 10, 20, 30, 40, 50, 60, 93, 127, 193, 260, 327, 392, 460, 593, 760 and 927 μM. [QZ1] = 1 μM; λ_{ex} = 500 nm. Bottom: Emission of QZ2 before and after Zn(II) addition. Aliquots of 100 and 500 mM $ZnCl_2$ were added to yield Zn(II) concentrations of 0, 0.05, 0.1, 0.2, 0.35, 0.5, 0.7, 1.0, 1.5, 2.0, 2.75, 3.75, 4.75 and 6.75 mM. [QZ2] = 1 μM; λ_{ex} = 490 nm.
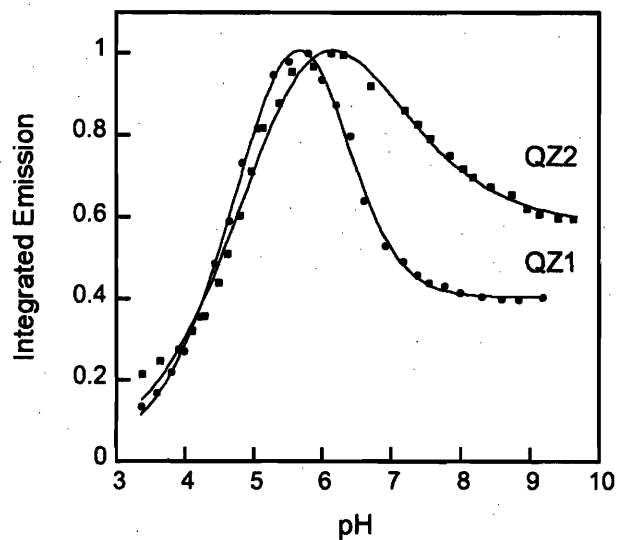
Figure 7.3. Fluorescence dependence on pH for QZ1 (circles) and QZ2 (squares). Solutions of 1 μM QZ were prepared in 10 mM KOH, 100 mM KCl, pH ~12 and the emission spectra recorded. The pH was decreased in increments of ~0.25 by addition of 6, 2, 1, 0.5 and 0.1 N HCl, and the emission spectra were recorded at each point. The emission was integrated, normalized, plotted against pH and fit according to eq. 2.1. Excitation was provided at 495 nm. Points above pH ~10 are omitted from the plot since no significant emission changes occurred in that regime.
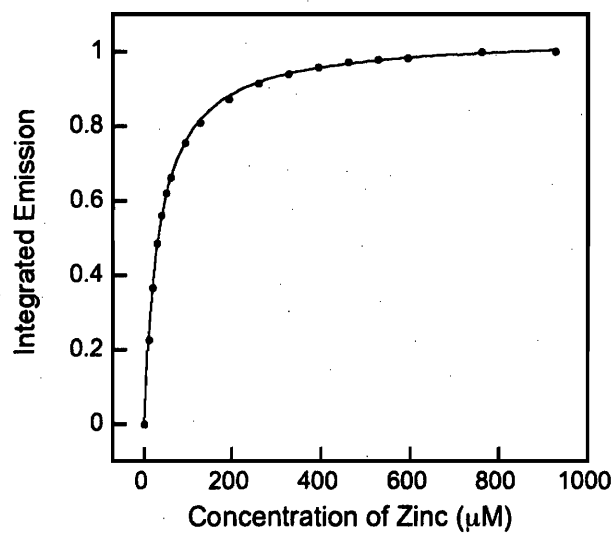
Figure 7.4. Normalized integrated emission versus [Zn(II)] for QZ1 at pH 7 (50 mM PIPES, 100 mM KCl, pH 7). This binding curve corresponds to the titration shown in Figure 7.2. A dissociation constant of 33 ± 2 μM was obtained for QZ1 by fluorimetric titration at 25 °C.
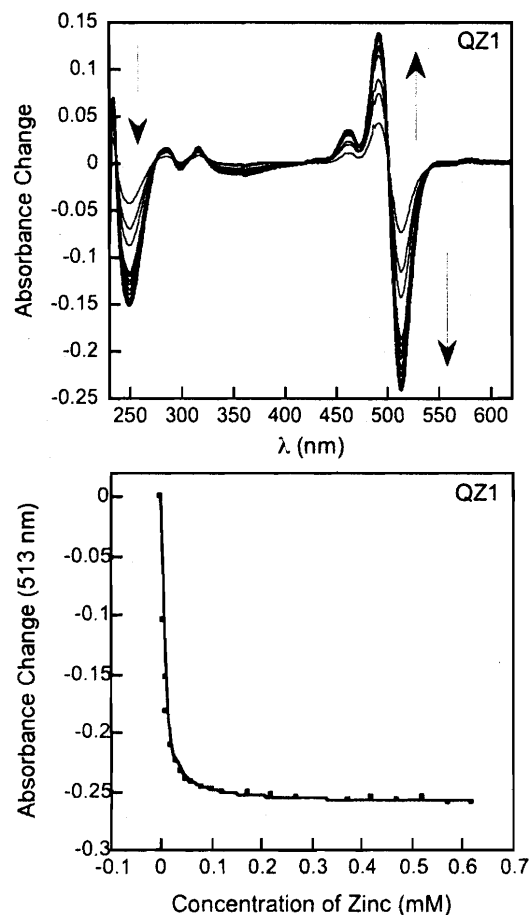
Figure 7.5. Top: Representative optical absorption difference spectra for the addition of Zn(II) to QZ1 at pH 7 (50 mM PIPES, 100 mM KCl). Decreases in absorption are observed at 513 and 250 nm where absorption increases occur at 492, 462, 317 and 283 nm. Bottom: The absorption change at 513 nm plotted against the concentration of Zn(II) in solution. The absorption due to the free dye was subtracted from all data. [QZ1] = 5 µM. Optical absorption titrations return a K_d value of 46 ± 6 µM or 31 ± 1 µM when the absorption change is monitored at 513 or 492 nm, respectively.
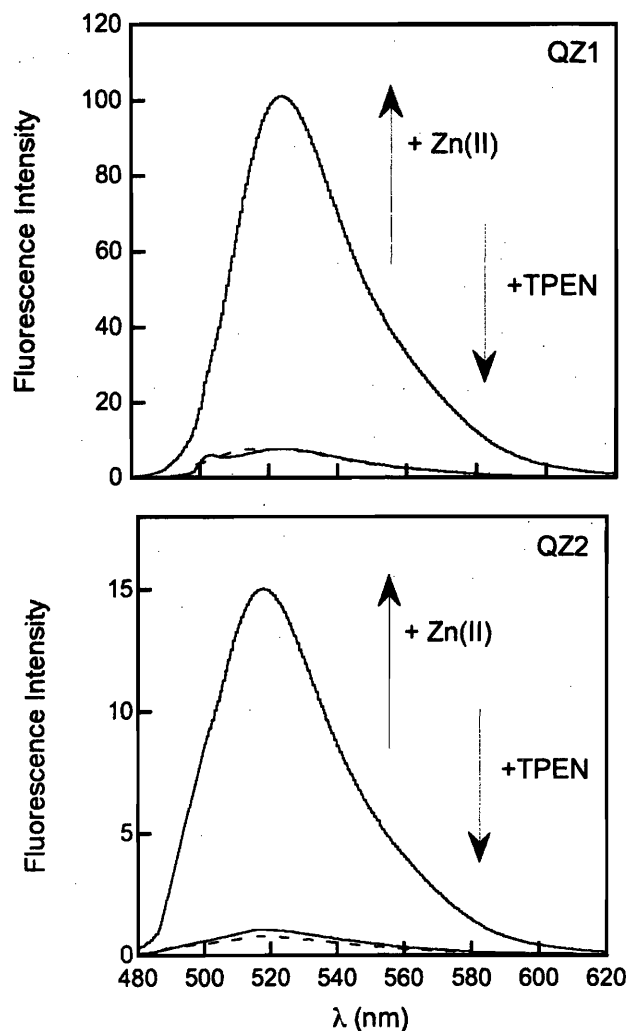
Figure 7.6. Reversibility of QZ1 (top) and QZ2 (bottom) binding to Zn(II) by addition of TPEN. A solution of 1 μM QZ was prepared in 50 mM PIPES, 100 mM KCl, pH 7 and the emission spectrum collected (dashed lines). Subsequently, 50 equiv of $ZnCl_2$ in water were added and the emission change recorded (top solid lines). Addition of 50 equiv of TPEN to the solution containing QZ and Zn(II) resulted in fluorescence decrease immediately upon mixing (bottom solid lines). The samples were excited at 495 (QZ1) and at 490 nm (QZ2).
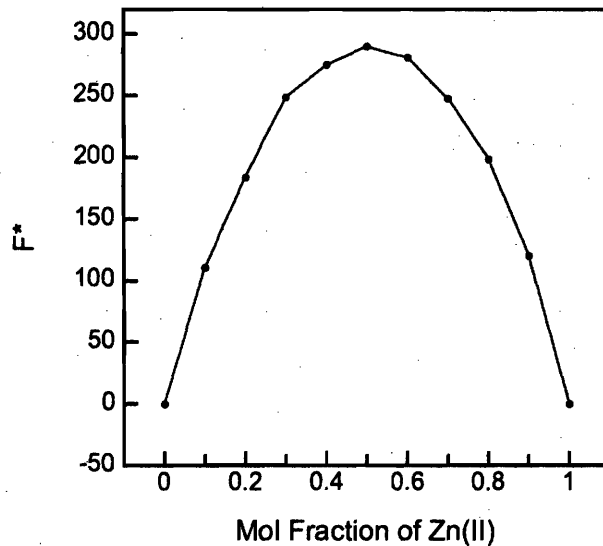
Figure 7.7. Job plot for the formation of the QZ1:Zn(II) complex determined by fluorescence spectroscopy (50 mM PIPES, 100 mM KCl, pH 7). F* is the fluorescence change associated with Zn(II) binding. The maximum at 0.5 equiv of Zn(II) indicates formation of a 1:1 QZ1:Zn(II) complex. The concentration of the initial QZ1 and Zn(II) solutions were 2 μM and samples were excited at 500 nm.
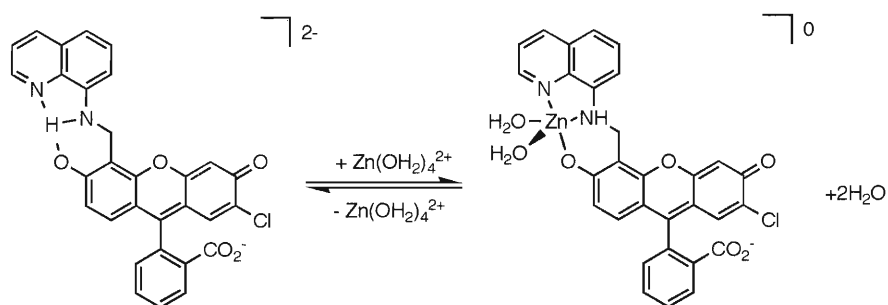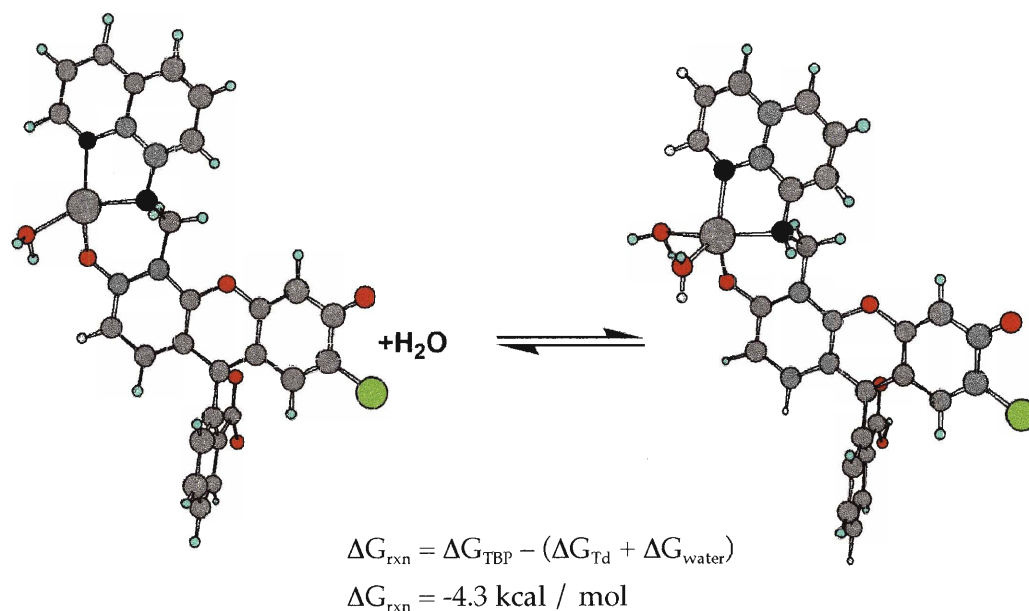
$$\Delta G_{rxn} = \Delta G_{TBP} - (\Delta G_{Td} + \Delta G_{water})$$

$$\Delta G_{rxn} = -4.3 \text{ kcal / mol}$$

Figure 7.8. Top: Optimized geometries for tetrahedral and trigonal bipyramidal coordination of Zn(II) to QZ1. The structures were optimized at the 6-31G**/LACVP** level of theory. The trigonal bipyramidal geometry is favored. Bottom: Proposed coordination of Zn(II) to QZ1 in aqueous solution at neutral pH.
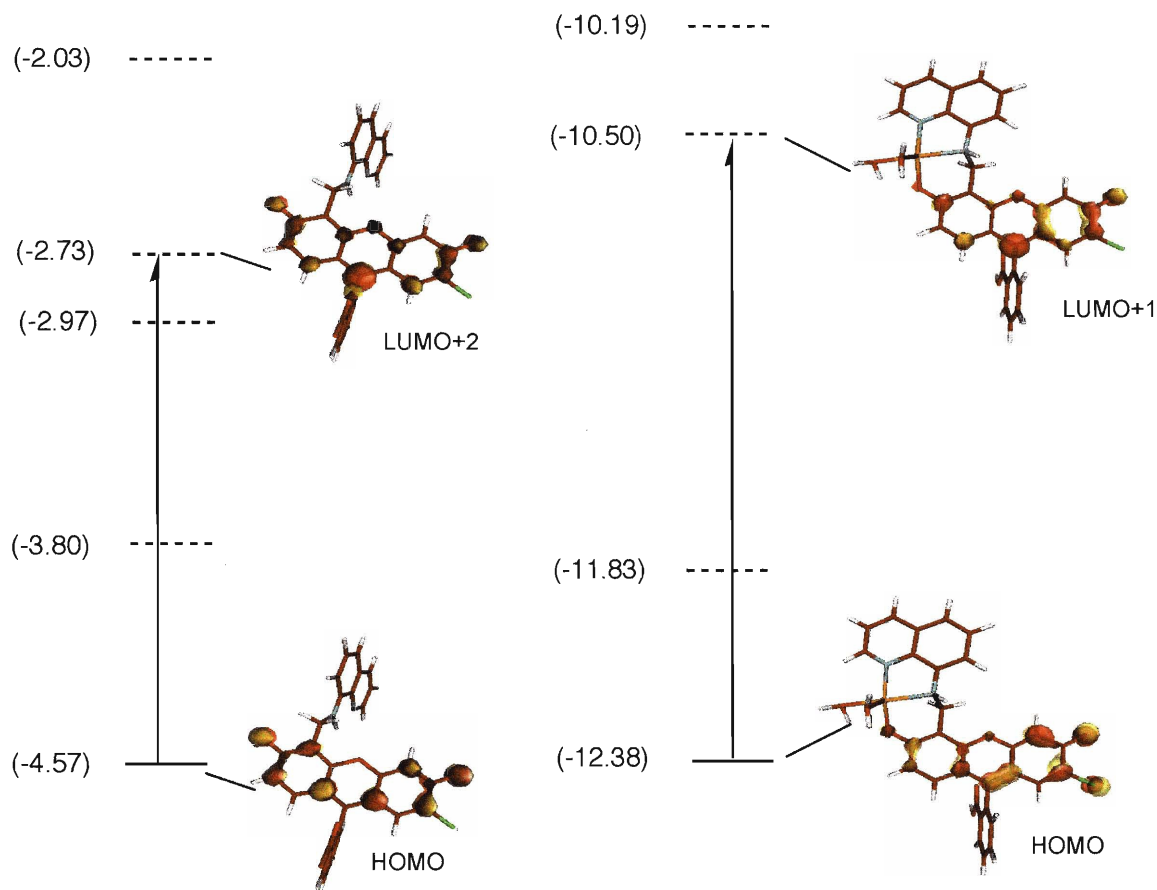
Figure 7.9. Partial molecular orbital diagrams for QZ1 dianion (left) and the trigonal bipyramidal QZ1:Zn(II) complex (right) obtained from DFT calculations. The solid and dashed lines represent filled and empty molecular orbitals, respectively. The arrows represent the dominant molecular orbital transitions responsible for QZ1 dianion and QZ1:Zn(II) absorption as determined by TDDFT. Energies are in eV.
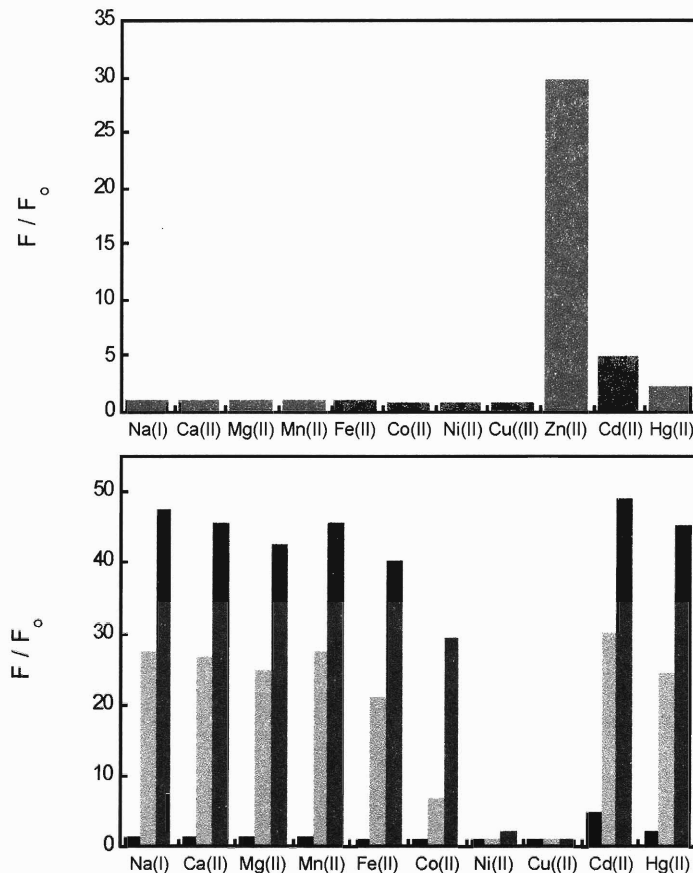
Figure 7.10. Selectivity of QZ1 for Zn(II) at pH 7 (50 mM PIPES, 100 mM KCl). Top: Fluorescence response of QZ1 following addition of 50 equiv of the metal ion of interest. Bottom: Selectivity of QZ1 for Zn(II) over the metal ions of interest. Black bars: QZ2 + 50 equiv of the cation, as shown in the top panel. Light grey bars: addition of 50 equiv of Zn(II) to the solution containing QZ1 and the cation of interest. Dark grey bars: introduction of an additional 500 equiv of Zn(II) to the solution containing QZ1 and the cation of interest. The emission spectra were integrated from 510 – 650 nm and all data (F) were normalized with respect to the emission of the free dye (F_o). [QZ1] = 1 μM; λ_{ex} = 495 nm. QZ1 is also selective for Zn(II) over mM concentrations of Na(I), K(I), Ca(II) and Mg(II) (data not shown).
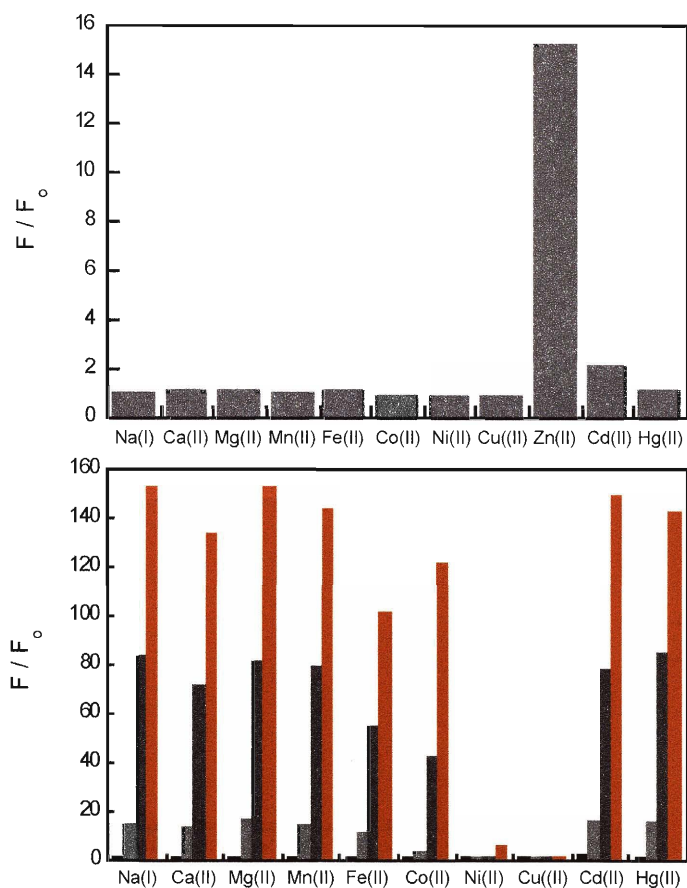
Figure 7.11. Selectivity of QZ2 for Zn(II) at pH 7 (50 mM PIPES, 100 mM KCl). Top: Fluorescence response of QZ2 following addition of 50 equiv of the metal ion of interest. Bottom: Selectivity of QZ2 for Zn(II) over the metal ions of interest. Black bars: QZ2 + 50 equiv cation, as shown in the top panel. Light grey bars: addition of 50 equiv of Zn(II) to the solution containing QZ2 and the cation of interest. Dark grey bars: introduction of an addition 450 equiv of Zn(II) to the solution containing QZ2 and the cation of interest. Red bars: introduction of an additional 2000 equiv of Zn(II). Samples were excited at 495 nm, and the emission spectra were integrated from 510 to 650 nm. All data (F) were normalized with respect to the emission of the free dye (F_o). [QZ2] = 1 μM. QZ2 is also selective for Zn(II) over mM concentrations of Na(I), K(I), Ca(II) and Mg(II) (data not shown).
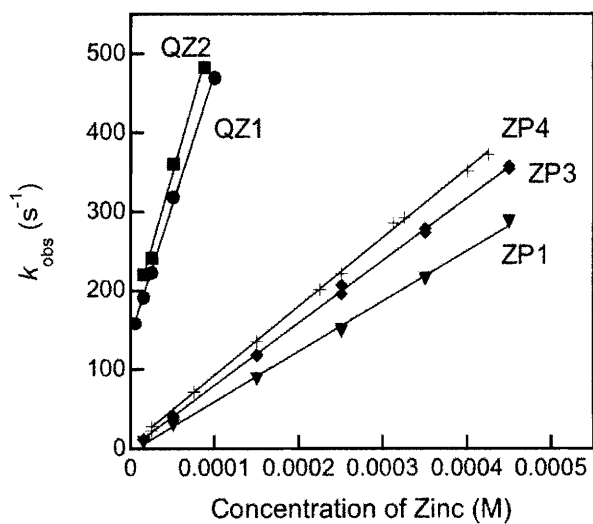
Figure 7.12. Results from stopped-flow fluorescence studies of Zn(II) binding to select ZP and QZ sensors. Plots of k_{obs} vs. concentration of Zn(II) for QZ1 (●), QZ2 (■), ZP1 (▼), ZP3 (◆) and ZP4 (+). All data were collected at 4.3 ± 0.1 °C. Table 7.2 includes the corresponding k_{on} values.
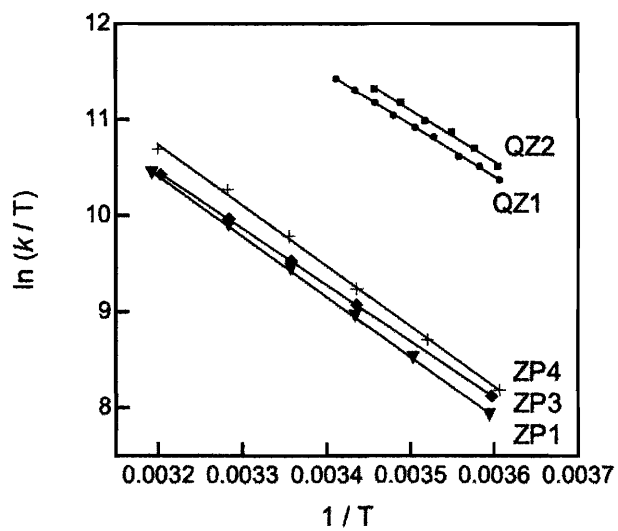
Figure 7.13. Eyring plots for QZ1 (●), QZ2 (■), ZP1 (▼), ZP3 (◆) and ZP4 (+). The temperature was varied from ~4 to ~16 °C (QZ) or from ~4 to ~40 °C (ZP). Values for $\Delta H^{\ddagger}$ and $\Delta S^{\ddagger}$ are given in Table 7.2.

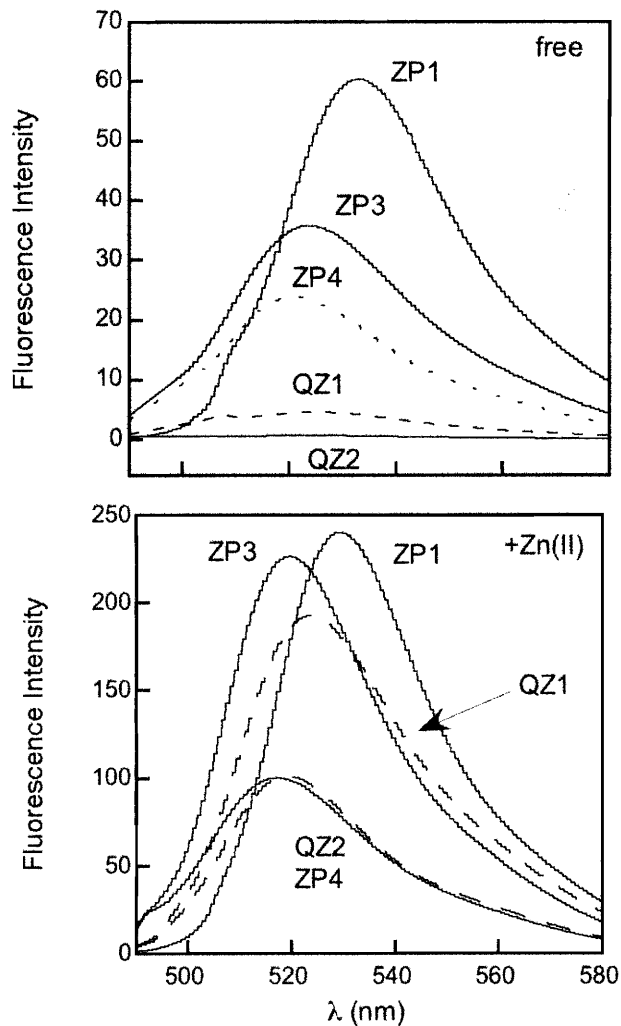**Figure 7.14.** Top: Relative fluorescence emission of 1 µM ZP1, ZP3, ZP4, QZ1 and QZ2. Solutions were prepared at pH 7 (50 mM PIPES, 100 mM KCl) with excess EDTA. Bottom: Relative fluorescence emission of the Zn(II)-saturated sensors ZP1, ZP3, ZP4, QZ1 and QZ2. Solution of 1 µM free sensor were prepared and excess Zn(II) was added to saturate the signals. Samples were excited at 490 (QZ2, ZP3), 495 (ZP1, QZ1) or 505 (ZP1) nm.
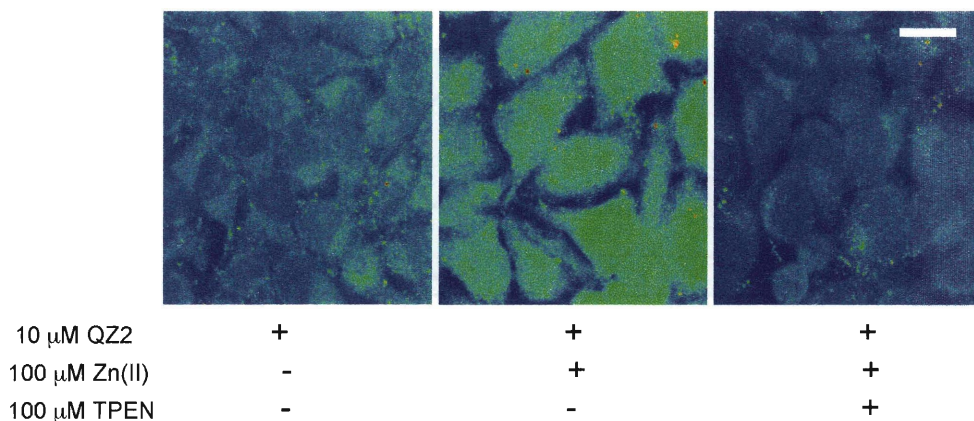
10 µM QZ2	+	+	+
100 µM Zn(II)	-	+	+
100 µM TPEN	-	-	+

Figure 7.15. Representative confocal fluorescence images of HeLa cells treated with QZ2. Left panel: HeLa cells incubated with 10 µM QZ2 for 4 h. Middle panel: Fluorescence change 10 min after introduction of 100 µM Zn(II) to the QZ2-treated HeLa cells. A 10:2 Zn(II)/pyrithione ratio was employed. Right panel: HeLa cells treated as described for the middle panel with subsequent addition of 100 µM TPEN for 10 min. The cells were kept at 37 °C and under 5% CO_2 during the course of the experiment. All cells were fixed (PBS with 4% PFA, 4% sucrose) and mounted onto microscope slides prior to imaging. The scale bar represents 40 µm.
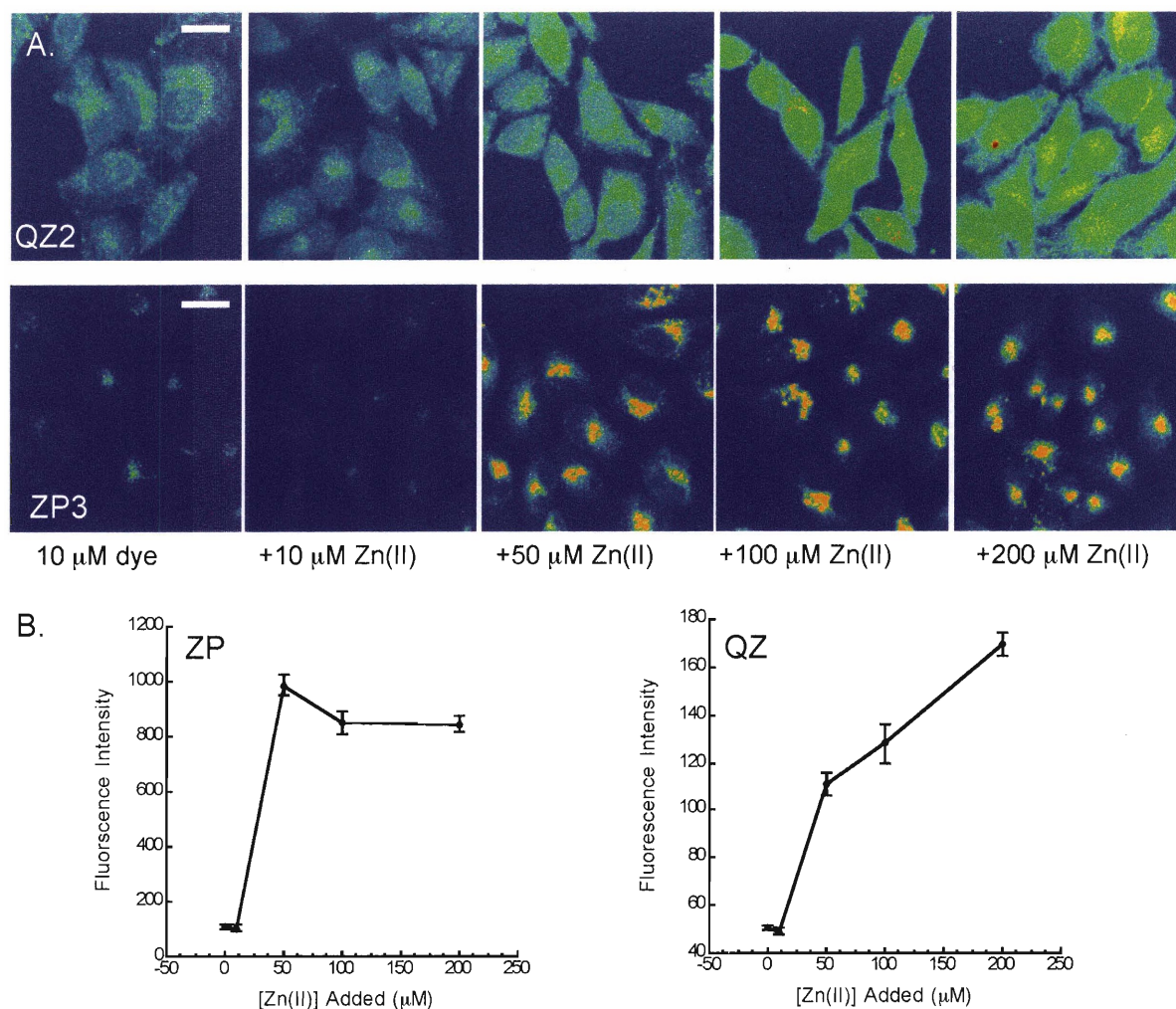
Figure 7.16. (A) Confocal imaging of fixed HeLa cels treated with QZ2 or QZ3. Top panels: HeLa cells treated with 10 μM QZ2 (4 h, 37 °C) and varying concentrations of Zn(II). Bottom panels: HeLa cells treated with 10 μM ZP3 (30 min, 37 °C) and varying concentrations of Zn(II). The cells were washed once with DMEM containing no FCS before Zn(II) addition and were incubated with Zn(II) for 10 min at 37 °C prior to fixing. A 10:2 Zn(II)/pyrithione ratio was employed. (B) Quantification of the fluorescence response. Left plot: Quantification of the ZP3 response. The fluorescence observed in the Golgi was monitored. Right plot: Quantification of QZ2 response. The error bars represent the standard error of the mean (sem) and $p < 0.001$ for the increase observed for QZ2 (Mann-Whitney test). A minimum of 29 cells were quantified at each Zn(II) concentration. The scale bar represents 40 μm.

10 µM ZP3   **10 µM QZ1**   **10 µM QZ2**
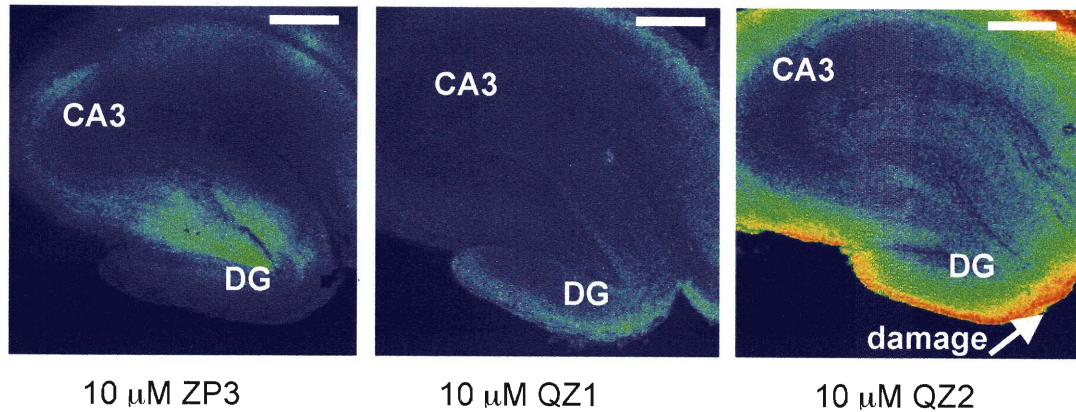
Figure 7.17. Confocal fluorescence microscopic images of hippocampal slices from adult rat stained with ZP3 (left), QZ1 (middle) or QZ2 (right). The slices were bathed in Zn(II)-free Krebs ringer buffer and incubated with 10 µM ZP3 or QZ prior to imaging. The slices treated with ZP3 shows intense fluorescence in the DG region and staining in the CA3 region. The slices treated with QZ show no differential staining in these substructures. The brighter ring around the QZ2 image is an artifact of the slice preparation and is visible because of the higher gain used to ensure that any Zn(II) staining in the DG region was not overlooked.

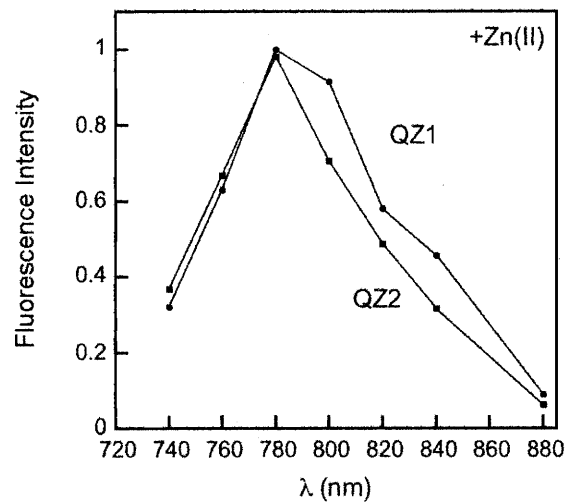**Figure 7.18.** Two-photon excitation profiles for QZ1 (circles) and QZ2 (squares) in the presence of 100 μM Zn(II). The solutions were prepared in 50 mM PIPES, 100 mM KCl, pH 7 and [QZ] = 10 μM. The emission was monitored from 0 to 570 nm.

10 μM QZ2	+	+	+
100 μM Zn(II)	-	+	+
100 μM TPEN	-	-	+
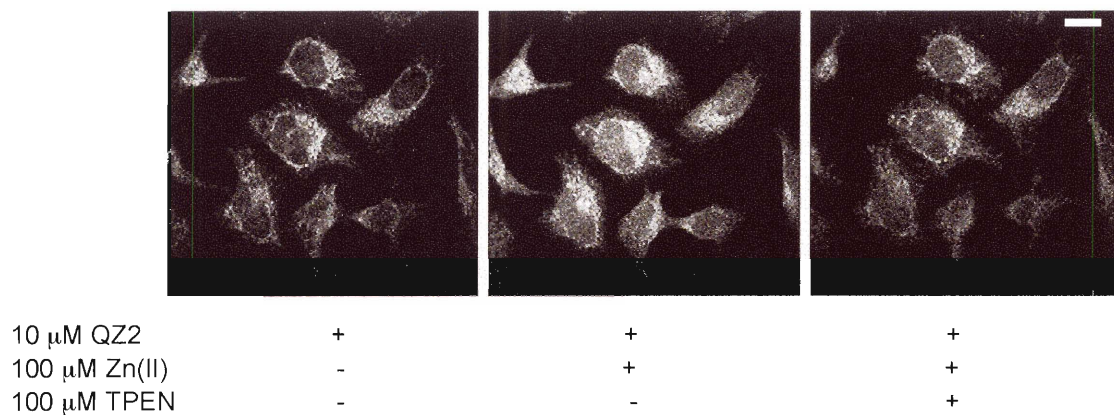
Figure 7.19. Images of live HeLa cells obtained by two-photon microscopy. Left panel: HeLa cells treated with 10 μM QZ2 (4 h, 37 °C). Middle panel: 5 min after addition of 100 μM Zn(II) as 10:2 Zn(II)/pyrithione (37 °C). Right panel: After treatment with 100 μM TPEN for 5 min at 37 °C. The fluorescence decreases to baseline. Samples were excited at 780 nm. Emission was monitored from 0 to 570 nm.

Chapter 8

A "Turn-On" Fluorescent Sensor for the Selective Detection of Mercuric Ion in Aqueous Media

Introduction

Heavy metal ion pollution poses severe risks for human health and the environment. Mercury contamination is widespread and occurs through a variety of natural and anthropogenic sources including oceanic and volcanic emissions,[1] gold mining,[2] solid waste incineration and the combustion of fossil fuels.[3] Once introduced into the marine environment, bacteria convert inorganic mercury to methylmercury, which enters the food chain and accumulated in higher organisms, especially in large edible fish.[1,3-7] Methyl mercury is neurotoxic and has been implicated as a cause of prenatal brain damage,[8-10] cognitive and motion disorders[11,12] and Minamata Disease.[13]

Our increased understanding of the deleterious effects of mercury exposure has sparked interest in the development of new tools for detecting Hg(II) in the environment. One major challenge involves creating Hg(II) sensors that function in water and are highly selective for Hg(II) against a background of competing analytes. Small synthetic molecules offer one approach to such probes. A number of small molecule Hg(II) detection methods have been examined and include colorimetric strategies,[14-17] fluoroionophores,[18-28] and a dithioamide functionalized lipid bilayer.[28] Most of these systems have limitations, which include interference from other metal ions, delayed response to Hg(II), and/or a lack of water solubility, requiring the use of organic or aqueous/organic solvent mixtures. Although a fluorescent probe based on the indoaniline chromophore exhibiting selectivity for Hg(II) in water was described,[26] Hg(II) binding caused a decrease of quantum yield (Φ) and brightness ($\Phi \times \varepsilon$).

In this chapter, we report the synthesis and metal-binding properties of mercury sensor 1 (MS1). This sensor is based on a fluorescein platform and elicits a positive fluorescence response following Hg(II) coordination in water or buffered solution at neutral pH. To the best of our knowledge, MS1 was the first reversible and water-soluble turn-on fluorescent sensor reported for Hg(II) and it subsequently inspired us to design additional Hg(II) detectors, which are presented in forthcoming chapters.

Experimental Section

Reagents. Solvents were dried as described in previous chapters. 3,9-Dithia-6-azaundecane,[29] **1**, and 7'-chloro-4'-fluoresceincarboxaldehyde,[30] **4**, were synthesized as previously described. Other reagents were obtained from Aldrich and used as received.

Materials and Methods. Silica gel-60 (230-400 mesh) was used as the solid phase for flash chromatography. Whatman silica gel-60 plates of 1 mm thickness were used for preparative thin layer chromatography (TLC) and Merck F254 silica gel-60 plates were used for analytical TLC. ^{1}H and ^{13}C NMR spectra were obtained either on a Varian 300 MHz or Varian 500 MHz spectrometer operating at 283 K and were referenced to internal probe standards. IR spectra were recorded on an Avatar 360 FTIR instrument. Mass spectrometry was performed by staff in the MIT DCIF.

N-(2-Nitrobenzyl)-3,9-dithia-6-azaundecane (3). 2-Nitrobenzylbromide (560 mg, 2.59 mmol), K_2CO_3 (400 mg, 2.89 mmol) and activated 3 Å molecular sieves were combined in 25 mL of CH_3CN and stirred. A 10 mL solution of 3,9-dithia-6-azaundecane (**1**, 501 mg, 2.59 mmol) in CH_3CN was added dropwise. The reaction was stirred at room temperature for 8 h, filtered through Celite and the solvent was evaporated to afford a yellow oil. The oil was flushed through a short silica plug (7:1 hexanes/EtOAc) and dried to yield the product, which is a viscous yellow oil (726 mg, 85%). TLC R_f = 0.38 (silica, 7:1 hexanes/EtOAc). ^{1}H NMR ($CDCl_3$, 300 MHz) δ 1.11 (6H, t), 2.35 (4H, q), 2.51 (4H, m), 2.71 (4H, m), 3.85 (2H, s), 7.28 (1H, t), 7.45 (1H, t), 7.70 (2H, m). ^{13}C NMR ($CDCl_3$, 125 MHz) δ 14.86, 26.03, 29.06, 54.03, 55.55, 124.10, 127.65, 130.68, 132.35, 134.68, 149.23. FTIR (NaCl disk, cm^{-1}) 3065 (w), 2963 (m), 2925 (m), 2864 (m), 2826 (m), 2727 (w), 1608 (m), 1576 (w), 1527 (s), 1483 (w), 1452 (m), 1360 (s), 1301 (m), 1268 (m), 1247 (w), 1227 (w), 1206 (w), 2289 (w), 1162 (w), 1124 (m), 1077 (w), 1059 (w), 1043 (w), 971 (m), 905 (w), 886 (w), 857 (m), 820 (w), 783 (m), 751 (w), 730 (s), 706 (w), 667 (w), 613 (w). HRMS (ESI) Calcd [M+H]$^+$, 329.1352; Found, 329.1359.

N-(2-Aminobenzyl)-3,9-dithia-6-azaundecane (4). A portion (2.5 g) of Pd black was placed in a flask purged with Ar after which 40 mL of MeOH was added. A portion (1.5 g, 4.6 mmol) of **3** was dissolved in 35 mL of MeOH and transferred to the reaction flask. Hydrogen was introduced to the reaction with vigorous stirring for 7 h. After purging wth Ar, the solution was filtered through Celite and the solvent was removed in vacuo to yield the pure product as a yellow-brown oil (921 mg, 67%). TLC R_f = 0.33 (silica, 7:1 hexanes/EtOAc). ^{1}H NMR (CDCl$_3$, 300 MHz) δ 1.21 (6H, t), 2.47 (4H, q), 2.71 (8H, m), 3.64 (2H, s), 4.75 (2H of NH$_2$, br s), 6.64 (2H, m), 6.97 (1H, d), 7.08 (1H, td). ^{13}C NMR (CDCl$_3$, 125 MHz) δ 14.63, 25.71, 28.86, 52.93, 58.00, 115.12, 117.09, 121.93, 128.09, 129.98, 146.59. FTIR (NaCl disk, cm^{-1}) 3423 (m), 3303 (m), 3205 (w), 3065 (w), 3022 (m), 2962 (s), 29234 (s), 2810 (s), 2725 (w), 2648 (w), 1616 (s), 1585 (m), 1495 (m), 1456 (m), 1374 (m), 1348 (w), 1315 (w), 1292 (m), 1267 (m), 1227 (w), 1187 (w), 1155 (w), 1118 (m), 1096 (m), 1058 (w), 1038 (w), 972 (m), 931 (w), 900 (w), 869 (w), 850 (w), 750 (s), 722 (w), 693 (w), 656 (w), 541 (w). HRMS (ESI) Calcd [M+Na]$^+$, 321.1430; Found, 321.1427. Several times the formation of byproducts was observed by analytical TLC. In these instances, the product was purified by flash chromatography on silica gel using 7:1 hexanes/EtOAc.

2-{5-[(2-{[Bis-(2-ethylsulfanylethyl)amino]methyl}phenolamino)methyl]-2-chloro-6-hydrozy-3-oxo-3H-xanthen-9-yl}benzoic acid (5, mercury sensor 1, MS1). A portion (73 mg, 0.245 mmol) of **4** was dissolved in 3 mL of EtOAc and 7'-chloro-4'-fluoresceincarboxaldehyde (**2**, 97 mg, 0.245 mmol) was added. The reaction became orange-pink and cloudy. An additional 1 mL of EtOAc was added and the mixture was stirred at room temperature for 18 h. During this time, the solution became clear and turned red. The EtOAc was removed under reduced pressure to yield a magenta foam, which was dissolved in 3 mL of 1,2-dichloroethane. A portion (65 mg, 0.307 mmol) of NaB(OAc)$_3$H was added and the reaction was stirred overnight at room temperature. The orange solution was diluted with 5 mL of CH$_2$Cl$_2$, washed with saturated NaHCO$_3$ (3 x 8 mL) and with deionized water (2 x 8 mL). The organic layer was dried over

$MgSO_4$ and the solvent was removed in vacuo to yield the crude product as a red solid. Chromatography on silica gel (50:1 $CHCl_3$/MeOH) followed by preparative TLC on silica gel using the same solvent system yielded the pure product as a deep magenta solid (88 mg, 52%). TLC R_f = 0.41 (silica, 9:1 $CHCl_3$/MeOH); mp = 58-61 °C. ^{1}H NMR (CD_3OD, 500 MHz) δ 1.02 (6H, t), 2.25 (4H, q), 2.37 (4H, q), 2.56 (4H, q), 3.59 (2H, s), 4.45-4.62 (2H, dd), 6.57 (2H, m), 6.68 (1H, s), 6.96 (1H, d), 7.00 (1H, d), 7.08 (1H, d), 7.12 (1H, s), 7.19 (1H, t), 7.29 (1H, d), 7.58 (2H, m), 8.04 (1H, d). ^{13}C NMR (CD_3OD, 125 MHz) δ 14.81, 25.53, 28.28, 40.63, 53.95, 58.03, 103.64, 108.83, 110.31, 112.69, 115.17, 122.69, 122.87, 126.48, 128.07, 128.40, 128.61, 128.69, 129.28, 129.68, 129.89, 130.08, 130.52, 130.75, 135.18, 140.88, 149.45, 155.64, 156.96, 170.66, 173.15, 179.68. FTIR (KBr, cm^{-1}) 3423 (m, br), 3049 (w), 2963 (w), 2919 (w), 1647 (m), 1607 (m), 1571 (s), 1509 (m), 1458 (s), 1374 (s), 1342 (s), 1302 (m), 1220 (m), 1149 (m), 1044 (w), 1007 (m), 937 (w), 883 (w), 828 (w), 746 (w), 714 (w), 689 (w), 621 (w), 598 (w), 547 (w), 469 (m). HRMS (ESI) Calcd $[M+Na]^+$, 699.1725; Found, 699.1720.

General Spectroscopic Procedures. All aqueous solutions were prepared with Millipore water (18.2 MΩ·cm at 25 °C) obtained from a Mill-Q Biocel system outfitted with a Quantum VX cartridge. An Orion glass electrode, calibrated prior to use, was employed to record solution pH. Ultrol grade PIPES (piperazine-N,N'-bis(2-ethanesulfonic acid), KCl (99.997%) and the heavy metal ion chelator N',N',N'',N''-tetra(2-picolyl)ethylenediamine (TPEN) were purchased from Calbiochem and used as received. Unless otherwise specified, all spectroscopic measurements were conducted at neutral pH with 50 mM PIPES, 100 mM KCl buffer adjusted to pH 7. Anhydrous $HgCl_2$ (99.998%) was obtained from Aldrich and used immediately upon opening to prepare mercury stock solutions (10 mM) in water. Stock solutions of MS1 (1 mM in DMSO) were prepared, divided into aliquots and stored at −20 °C. The MS1 solutions were thawed in the dark immediately before use. A given aliquot can be frozen and thawed multiple times and retain its spectroscopic integrity if it is protected from light. After

addition of the MS1 stock solution to aqueous buffers, the resulting solutions contained 0.1% or 1% DMSO for fluorescence or absorption measurements, respectively.

Optical Absorption Spectroscopy. UV-visible spectra were obtained by using either a Cary IE scanning spectrophotometer or a Hewlett Packard diode array spectrophotometer. Both instruments were controlled using the manufacturer supplied software packages. A circulating water bath was used to maintain the temperature at 25 ± 1 °C. Samples were contained in quartz cuvettes with a 1-cm path length (3.5 mL volume, Starna). All manipulations were performed at least in triplicate and the resulting averages are reported.

Fluorescence Spectroscopy. Emission spectra were obtained with a Hitachi F-3010 spectrofluorimeter linked to a PC running the SpectraCalc software package. A circulating water bath was used during all experiments to regulate the temperature at 25 ± 1 °C. Spectra were routinely obtained with 3 nm slit widths. All measurements were conducted at least in triplicate and the resulting averages are reported.

Mercury-Binding Studies by Absorption Spectroscopy. Metal-binding titrations and Job analyses were performed for MS1 to determine the stoichiometry of the metal-bound complex in solution. In a typical titration, 3 μL aliquots of a 1 mM $HgCl_2$ solution in water were added to a 10 μM solution of MS1 (50 mM PIPES, 100 mM KCl, pH 7) and the absorbance changes at 498 and 520 nm were plotted against equivalents of Hg(II) added. Starting solutions of 10 μM were used for the Job plot analyses.

Mercury-Binding Studies by Fluorescence Spectroscopy. The EC_{50} value, the concentration of Hg(II) required to obtain 50% of the total fluorescence change for 1 μM MS1, was determined by titration of 1 mM or 10 mM $HgCl_2$ into solutions of MS1 at pH 7 (50 mM PIPES, 100 mM KCl, pH 7). To illustrate the reversibility, a 3 μL aliquot of a 1 mM solution of TPEN in DMSO was added to a mixture of 1 μM MS1 and Hg(II).

Quantum Yield Measurements. The quantum yields of apo and Hg(II)-bound MS1 were determined by using fluorescein in 0.1 N NaOH ($\Phi = 0.95$)[31] as a standard. In a

typical experiment, a solution of MS1 ([MS1] ≤ 1 μM) and either excess K_4EDTA or excess Hg(II) was prepared. The solution A_{max} values were ~0.05 to ~0.08. The concentration of the fluorescein reference solution was adjusted such that A_{max} (490 nm) equaled A_{max} of MS1 (505 nm) or of the Hg(II) complex (501 nm). The excitation wavelength was chosen as the wavelength where the reference and probe excitation spectra intersect. Excitation was provided at 497 nm for MS1 and at 496 nm for the Hg(II) complex. Emission spectra were integrated from 510-650 nm and the quantum yields were calculated by standard methods.[32]

Determination of Protonation Constants. The pK_a values for MS1 that affect fluorescence were determined by plotting the integrated emission intensity versus pH from ~12 to ~4. In a typical experiment, a 30 mL solution of 1 μM MS1 in 10 mM KOH, 100 mM KCl (pH ~12) was prepared. Aliquots of 6, 2, 1, 0.5 and 0.1 N HCl were added to achieve pH changes of approximately 0.25 and the emission spectrum was recorded after each addition (λ_{ex} = 500 nm). The overall volume change for each titration did not exceed ~2%. The emission spectra were integrated from 500 to 650 nm, normalized and plotted against pH. The data were fit with eq. 2.1.

Selectivity of the Mercury-Induced Fluorescence Increase. The selectivity of MS1 for Hg(II) against a background of various alkali and alkaline earth metals, transition metal ions, Pb(II) and the Group 12 congeners Zn(II) and Hg(II) was investigated by fluorescence spectroscopy. Aqueous solutions of Li(I), Na(I), Rb(I), Mg(II), Ca(II), Sr(II), Ba(II), Mn(II), Co(II), Ni(II), Cd(II) and Hg(II) were prepared from the chloride salts. The Cu(II) solution was prepared from copper(II) sulfate and the Pb(II) solution from Pb(II) nitrate. A solution of Cr(III) was prepared from chromium acetate and stored at pH 1. Solutions of Fe(II) were prepared immediately before use with ferrous ammonium sulfate and water that was thoroughly purged with Ar. All metal ion stock solutions were 10 mM, with the exception of 100 mM NaCl. In a typical experiment, the emission spectrum of free MS1 (1 μM, 50 mM PIPES, 100 mM KCl, pH 7) was recorded.

A 20-μL aliquot of the 10 mM metal ion solution was then added and the emission spectrum obtained. Subsequently, a 20-μL portion of 10 mM HgCl$_2$ was added and the emission spectrum recorded. To determine the affect of chloride ion on the selectivity of MS1, analogous experiments were conducted in 50 mM PIPES, 100 mM KNO$_3$ buffered at pH 7. In order to ascertain the affect of mM concentrations of alkali and alkaline earth metals on the fluorescence of MS1, solutions of 100 mM Li(I), Na(I), Ca(II) and Mg(II), 10 mM Rb(II) and Sr(II) and 1 mM Ba(II) were prepared in 50 mM PIPES, 100 mM KCl buffered at pH 7. A solution of 1 μM MS1 in the buffer containing the cation of interest was prepared and the emission spectrum obtained. A 20-μL portion of 10 mM HgCl$_2$ was added and the emission change recorded. For all experiments, the samples were excited at 500 nm and the resulting spectra were integrated from 510-650 nm and normalized with respect to the free dye (F$_o$).

Results and Discussion

Design and Synthesis of MS1. MS1 is a water-soluble, turn-on fluorescein-based sensor that exhibits high selectivity and sensitivity for Hg(II). We selected fluorescein as the reporting group due to its superior brightness ($\Phi \sim 1$, high ε) and water solubility. Since Hg(II) has a high affinity for soft donors such as sulfur, we opted to incorporate a 3,9-dithia-6-azaundecane[29] moiety into an aniline-derivatized fluorescein-based ligand framework previously developed in our laboratory.[33] Scheme 8.1 illustrates the synthesis of MS1. N-(2-Aminobenzyl)-3,9-dithia-6-azaundecane, **4**, was prepared in 57% yield over two steps from 3,9-dithia-6-azaundecane an commercially available 2-nitrobenzylbromide. Condensation of 7'-chloro-4'-fluoresceincarboxaldehyde, **2**, prepared in five steps from commercially available materials,[30] with **4** in EtOAc followed by reduction of the resulting imine using NaB(OAc)$_3$H in 1,2-dichloroethane and purification on silica gel (50:1 CHCl$_3$/MeOH) afforded pure MS1 as a magenta powder in moderate (52%) yield.

Spectroscopic Properties of MS1. At pH 7 (50 mM PIPES, 100 mM KCl) and in the presence of excess EDTA to scavenge any adventitious metal ions, MS1 exhibits an emission maximum at 524 nm and a quantum yield of 0.04. The low quantum yield of the unbound sensor results from incorporation of aniline in the ligand moiety, which readily quenches fluorescein emission. Figure 8.1 shows the pH-dependent emission profile of MS1, which yields pK_a values of 7.1 and 4.8. These values are comparable to those of other aniline-derivatized fluorescein-based sensors. The transition with pK_a = 7.1 results in slight fluorescence enhancement when moving to more acidic pH and is assigned to the aniline nitrogen atom. The pK_a value of 4.8 is assigned to protonation of the fluorescein phenol group based on optical absorption spectroscopy (Figure 9.1). Lowering the pH in this regime results in a substantial decrease in absorption intensity with a concomitant blue shift and formation of two local maxima at ca. 482 and 456 nm; these changes reflect phenol protonation.[34]

Coordination of MS1 to Hg(II) results in a blue shift from 505 (ε = 61,00 $M^{-1}cm^{-1}$) to 501 nm (ε = 73,000 $M^{-1}cm^{-1}$) in the optical absorption spectrum. Hg(II) binding also disrupts the PET quenching pathway; the emission spectrum red-shifts to 528 nm and the quantum yield increases ~2.8-fold to 0.11. As shown in Figure 8.2, a ~5-fold increase in emission occurs following Hg(II) coordination to MS1 at pH 7 and with 100 mM KCl.

Variation of the anion contained in the buffer revealed that the fluorescence response of MS1 to Hg(II) depends on chloride ion. A weak, ~1.6-fold fluorescence enhancement occurs with Hg(II) coordination to MS1 in 50 mM PIPES, 100 mM KNO_3 buffer. Experiments performed in water or in buffer (50 mM PIPES, pH 7) showed that chloride ion addition to solutions of free MS1 caused essentially no change in its fluorescence spectrum. In contrast, addition of chloride ion to solutions of the MS1:Hg(II) complex caused an immediate emission enhancement (Figure 8.3). We concluded that the Hg(II) complex associates with one or more chloride ions in solution

and subsequently found that the emission of all MS sensors characterized to date shows chloride ion dependence (Chapters 9-11).

Mercury-Binding Properties of MS1. Both optical absorption and fluorescence spectroscopy were used to study the Hg(II)-binding properties of MS1. Metal-binding titrations and Job plots indicate that MS1 forms a 1:1 complex with Hg(II) in solution. Figure 8.4 shows representative UV-visible difference spectra and a titration for addition of Hg(II) to MS1. Essentially complete fluorescence enhancement occurs immediately after addition of 1 equiv of Hg(II) to a solution of MS1, which indicates that formation of the 1:1 complex is responsible for the fluorescence change. Titrations monitored by fluorescence spectroscopy, depicted in Figure 8.2, reveal an EC_{50} value of 410 nm for 1 μM MS1, corresponding to high affinity Hg(II) binding. Scheme 8.2 depicts the anticipated mode of Hg(II) coordination at neutral pH, where Hg(II) is bound to MS1 with distorted octahedral geometry through the thioether, nitrogen and phenol donors and the sixth coordination site is filled by a water molecule.

The fluorescence response of MS1 to various cations and its selectivity for Hg(II) are illustrated in Figure 8.5 (50 mM PIPES, 100 mM KCl, pH 7). The Hg(II) response of MS1 is unaffected by mM concentrations of alkali and alkaline earth metals found in natural waters,[35] including Li(I), Na(I), Rb(I), Mg(II), Ca(II), Sr(II) and Ba(II). A background of the Group 12 metals Zn(II) and Cd(II), in addition to Cr(III) and Pb(II), do not inhibit the fluorescence response of MS1 to Hg(II). Of the divalent first-row transition metals considered, only Cu(II) interferes with the Hg(II)-induced fluorescence increase. Analogous experiments using buffer containing 100 mM KNO_3 show that selectivity of MS1 does not depend on chloride ion (data not shown). The preference of MS1 for Cu(II) is strong – when an equimolar mixture of Cu(II) and Hg(II) is added to MS1, the solution turns light purple and no fluorescence enhancement occurs – and reminiscent of that encountered with several multidentate thioether-containing ligands that exhibit selectivity for metal ions in the "copper triangle" of the periodic table.[36] Attempts were

made to overcome this Cu(II) interference; however, these approaches were unsuccessful. Reduction of Cu(II) to Cu(I) by hydroxylamine hydrochloride indicated that MS1 binds Cu(I) over Hg(II). Subsequently, the addition of water-soluble copper chelators, such as cuprizone for Cu(II) and bathocuprinesulfonate for Cu(I) was considered, but the Cu(II) complexes of these chelators exhibit intense absorption that will cause inner filter effects and prevent emission from the MS1:Hg(II) complex..

MS1 binds Hg(II) reversibly. Addition of 1 equiv of N',N',N'',N''-tetra(2-picolyl)ethylenediamine (TPEN) to a stoichiometric mixture of MS1 and Hg(II) results in an immediate fluorescence decrease to within ~20% of the background value. As shown in Figure 8.6, this on/off behavior can be reversed by addition of another equivalent of Hg(II), restoring the fluorescence attributed to Hg(II) complexation.

The EPA standard for the maximum allowable level of inorganic mercury in drinking water is 2 ppb.[3] When 500 nM MS1 is added to an aqueous solution (50 mM PIPES, 100 mM KCl, pH 7) containing 2 ppb of Hg(II), a fluorescence increase of 11.3 ± 3.1% (average of 28 independent trials with a range of 9.1 – 15.9%), indicating that MS1 can detect environmentally relevant concentrations of Hg(II). A highly sensitive and selective fluorescein-based probe for Hg(II) that is water-soluble and gives a positive response upon analyte binding may be of some practical utility.

Summary and Perspectives

This chapter detailed the preparation and characterization of sensor MS1. This probe gives Hg(II)-selective fluorescence enhancement in aqueous solution at netural pH. To the best of our knowledge, MS1 was the first reversible and water-compatible fluorescence-based sensor for Hg(II) reported that gives turn-on detection. The only significant limitation of MS1 is its high affinity for copper. Whether this feature will be problematic for practical applications, such as environmental monitoring, has not been ascertained and will presumably depend on the amount of free copper in the sample.

Preliminary tests in water from the Charles River show that MS1 can detect added Hg(II) in this media, which points towards its potential utility. Avenues for future work include testing MS1 in water and fish samples, and fashioning MS1-derivatized devices (i.e. fiber optic) for work in the field.

References

(1)   Renzoni, A. Z., F.; Franchi, E. *Environ. Res.* **1998**, *77*, 68-72.

(2)   Malm, O. *Environ. Res.* **1998**, *77*, 73-78.

(3)   Mercury Update: Impact on Fish Advisories. EPA Fact Sheet EPA-823-F-01-011; EPA, Office of Water: Washington, DC, 2001.

(4)   Boening, D. *Chemosphere* **2000**, *40*, 1335-1351.

(5)   Nendza, M. H., T.; Kussatz, C.; Gies, A. *Chemosphere* **1997**, *35*, 1875-1885.

(6)   Hardy, S.; Jones, P. *J. of Chromatography A* **1997**, *791*, 333-338.

(7)   Harris, H. H.; Pickering, I. J. *Science* **2003**, *301*, 1203.

(8)   McKeown-Eyssen, G. E.; Ruedy, J.; Neims, A. *Am. J. Epidemol.* **1983**, *118*, 470-479.

(9)   Davidson, P. W. Myers, G.; Cox, C. et. al. *Neurotoxicol.* **1995**, *16*, 677-688.

(10)   Grandjean, P.; Weihe, P.; White, R. F.; Debes, F. *Environ. Res.* **1998**, *77*, 165-172.

(11)   Takeuchi, T.; Morikawa, N.; Matsumoto, H.; Shiraishi, Y. *Acta Neuropathol.* **1962**, *2*, 40-57.

(12)   Matsumoto, H.; Koya, G.; Takeuchi, T. et. al. *J. Neuropathol. Exp. Neurol.* **1965**, *24*, 563-574.

(13)   Harada, M. *Crit. Rev. Toxicol.* **1995**, *25*, 1-24.

(14)   Choi, M. J.; Kim, M.-Y.; Chang, S.-K. *Chem. Commun.* **2001**, 1664-1665.

(15)   Brümmer, O.; La Clair, J. J.; Janda, K. D. *Org. Lett.* **1999**, *1*, 415-418.

(16)   Sancenón, F.; Martínez-Máñez, R.; Soto, J. *Tetrahedron Lett.* **2001**, *42*, 4321-4323.

(17)   Sancenón, F.; Martínez-Máñez, R.; Soto, J. *Chem. Commun.* **2001**, 2262-2263.

(18) Prodi, L.; Bargossi, C.; Montalti, M.; Zaccheroni, N.; Su, N.; Bradshaw, J. S.; Izatt, R. M.; Savage, P. B. *J. Am. Chem. Soc.* **2000**, *122*, 6769-6770.

(19) Rurack, K.; Kollmannsberger, M.; Resch-Genger, U.; Daub, J. *J. Am. Chem. Soc.* **2000**, *122*, 968-969.

(20) Rurack, K.; Resch-Genger, U.; Bricks, J. L.; Spieles, M. *Chem. Commun.* **2000**, 2103-2104.

(21) Hennrich, G.; Sonnenschein, H.; Resch-Genger, U. *J. Am. Chem. Soc.* **1999**, *121*, 5073-5074.

(22) Chae, M.-Y.; Czarnik., A. W. *J. Am. Chem. Soc.* **1992**, *114*, 9704-9705.

(23) Yoon, J.; Ohler. N. E.; Vance, D. H.; Aumiller, W. D.; Czarnik, A. W. *Tetrahedron Lett.* **1997**, *28*, 3845-3848.

(24) Winkler, J. D.; Bowen, C. M.; Michelet, V. *J. Am. Chem. Soc.* **1998**, *120*, 3237-3242.

(25) Unterreitmaier, E.; Schuster, M. *Anal. Chim. Acta* **1995**, *309*, 339-344.

(26) Descalzo, A. B.; Martínez-Máñez, R.; Radeglia, R.; Rurack, K.; Soto, J. *J. Am. Chem. Soc.* **2003**, *125*, 3418-3419.

(27) Sakamoto, H.; Ishikawa, J.; Nakao, S.; Wada, H. *Chem. Commun.* **2000**, 2395-2396.

(28) Sasaki, D. Y.; Padilla, B. E. *Chem. Commun.* **1998**, 1581-1582.

(29) Tanaka, M.; Nakamura, M.; Ikeda, T.; Ikeda, K.; Ando, H.; Shibutani, Y.; Yajima, S.; Kimura, K. *J. Org. Chem.* **2001**, *66*, 7008-7012.

(30) Nolan, E. M.; Burdette, S. C.; Harvey, J. H.; Hilderbrand, S. A.; Lippard, S. J. *Inorg. Chem.* **2004**, *43*, 2624-2635.

(31) Brannon, J. H.; Madge, D. *J. Phys. Chem.* **1978**, *82*, 705-709.

(32) Burdette, S. C.; Walkup, G. K.; Spingler, B.; Tsien, R. Y.; Lippard, S. J. *J. Am. Chem. Soc.* **2001**, *123*, 7831-7841.

(33) Burdette, S. C.; Frederickson, C. J.; Bu, W.; Lippard, S. J. *J. Am. Chem. Soc.* **2003**, *125*, 1778-1787.

(34) Sjöback, R.; Nygren, J.; Kubista, M. *Spectrochimica Acta Part A* **1995**, *51*, L7-L21.

(35) Drever, J. I. *The Geochemistry of Natural Waters: Surface and Groundwater Environments*, 3rd ed.; Prentice Hall: Upper Saddle River, NJ, 1997.

(36) Cooper, T. H.; Mayer, M. J.; Leung, K.-H.; Ochrymowycz, L. A.; Rorabacher, D. B. *Inorg. Chem.* **1992**, *31*, 3796-3804.
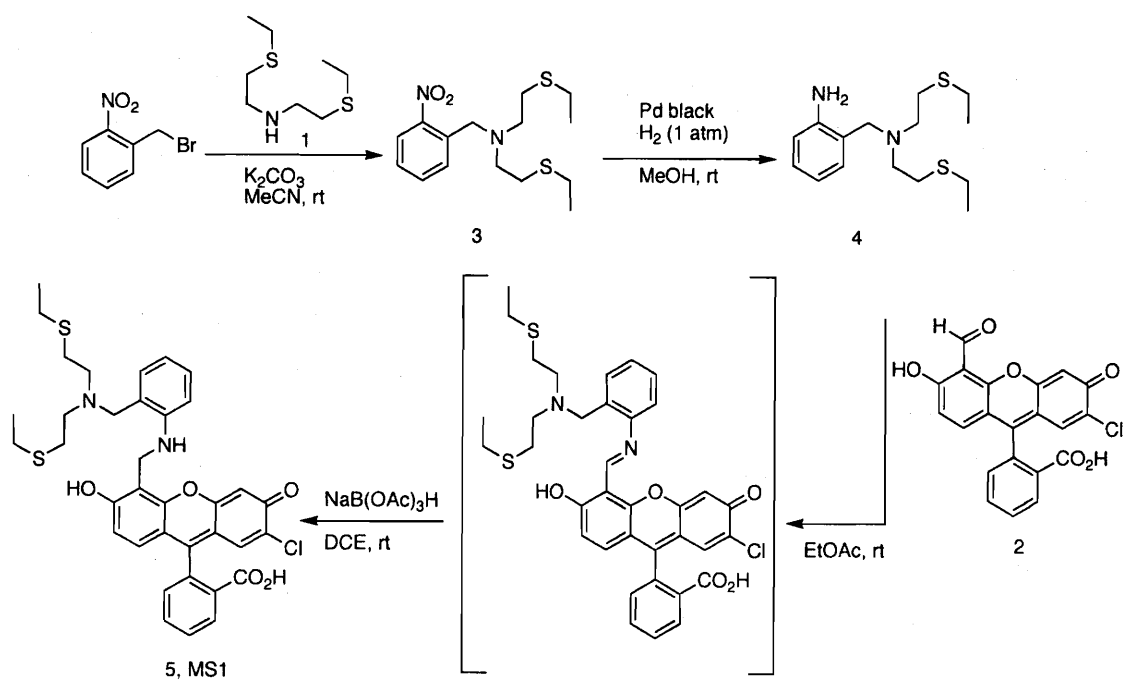
Scheme 8.1. Synthesis of MS1.
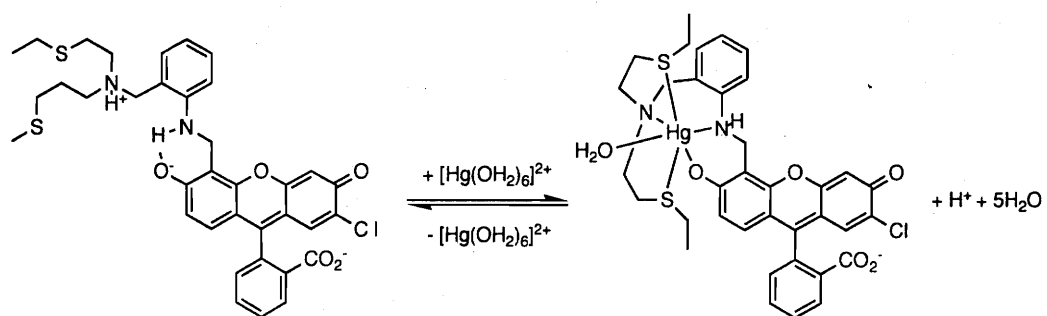
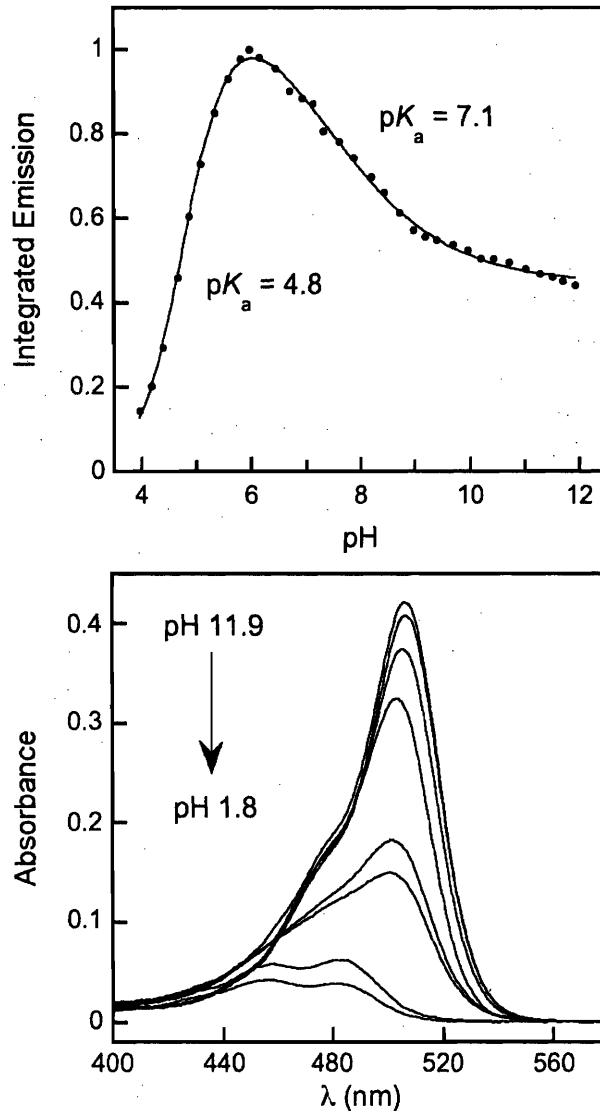**Scheme 8.2.** Proposed coordination of Hg(II) to MS1.

Figure 8.1. Top: fluorescence response of 1 μM MS1 to pH. A solution of MS1 in 10 mM KOH, 100 mM KCl was prepared (pH ~12) and the pH was lowered by addition of aqueous HCl. The fluorescence spectrum was obtained at each point (λ_{ex} = 500 nm). The spectra were integrated from 510 – 650 nm, normalized and plotted against pH. Bottom: Changes in MS1 (~8 μM in 10 mM KOH, 100 mM KCl) absorption as a function of pH. The pH was adjusted by addition of aqueous HCl or KOH. Spectra were obtained at pH values of approximately 11.9, 10.0, 7.5, 6.1, 5.4, 4.7, 2.4 and 1.8. The spectrum at pH > 6 indicate fluorescein dianion and those at pH > 5 fluorescein monoanion.
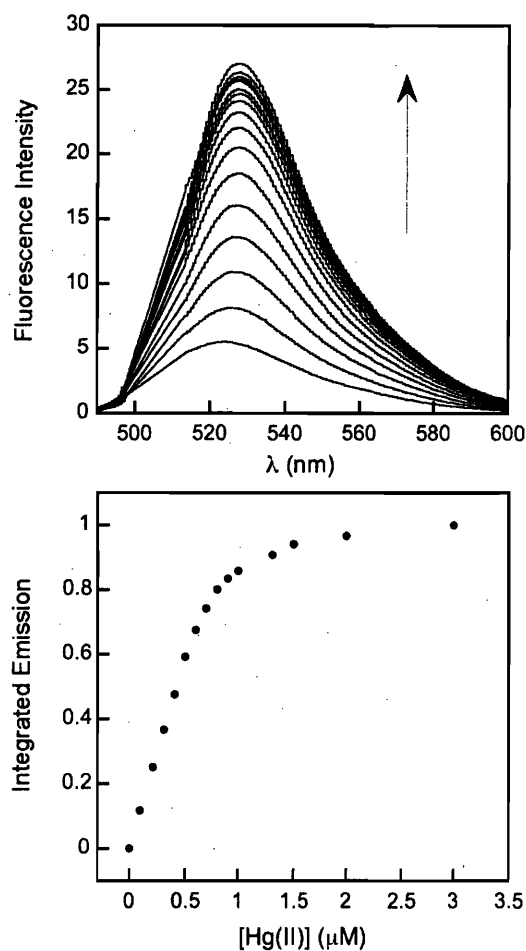
Figure 8.2. Fluorescence response of MS1 to addition of Hg(II) in water at pH 7 (50 mM PIPES, 100 mM KCl). [MS1] = 1 μM. Aliquots of 0.1 and 1 mM Hg(II) were added to yield final Hg(II) concentrations of 0, 0.1, 0.2, 0.3, 0.4, 0.5, 0.6, 0.7, 0.8, 0.9, 1.0, 1.3, 1.5 and 3 μM. Top plot: Emission spectra. Bottom plot: Normalized integrated emission versus concentration of Hg(II) corresponding to the emission spectra shown in the top plot. Excitation was at 500 nm and the emission was integrated from 510 – 650 nm. The EC_{50} value, the concentration of Hg(II) required to achieve 50% of the total fluorescence change for 1 μM probe, for MS1 is 410 nM.
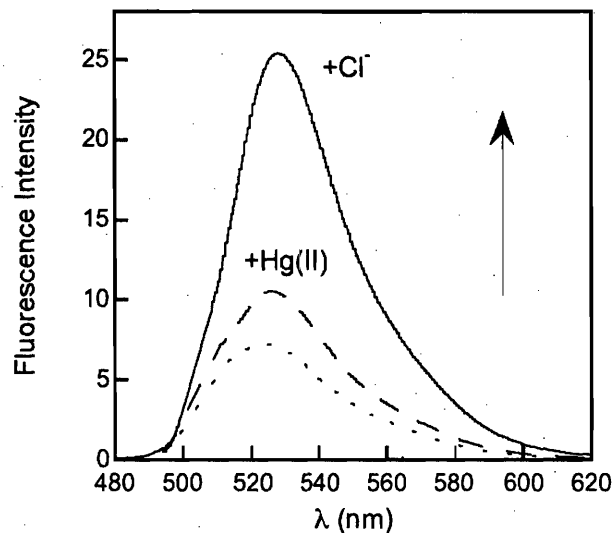
Figure 8.3. Effect of chloride ion on the emission of the MS1:Hg(II) complex. The dotted line represents the emission of 1 μM MS1 in the absence of chloride ion (50 mM PIPES, pH 7). The dashed line indicates the fluorescence change that occurs upon addition of 10 equiv of Hg(II) to the MS1 solution. Addition of excess chloride ion, either as KCl (shown) or NaCl, causes an immediate fluorescence enhancement, depicted by the solid line (final concentration of chloride ion is 100 mM). Addition of chloride ion has no affect on the emission properties of the free sensor (data not shown).
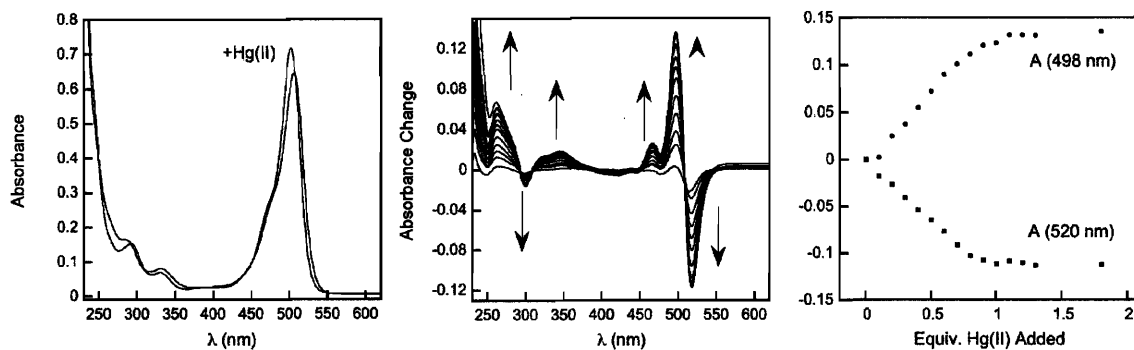
Figure 8.4. Left: Optical absorption spectra of 10 μM MS1 before and after addition of 1 equiv of Hg(II) at pH 7 (50 mM PIPES, 100 mM KCl). Middle: Optical absorption difference spectra corresponding to the addition of 0.1, 0.2, 0.3, 0.4, 0.5, 0.6, 0.7, 0.8, 0.9, 1.0, 1.1, 1.2, 1.3 and 1.8 equiv of Hg(II) to a 10 μM solution of MS1. Right: Absorbance change vs. added Hg(II) corresponding to the difference spectra. This titration indicates formation of a 1:1 MS1:Hg(II) complex.
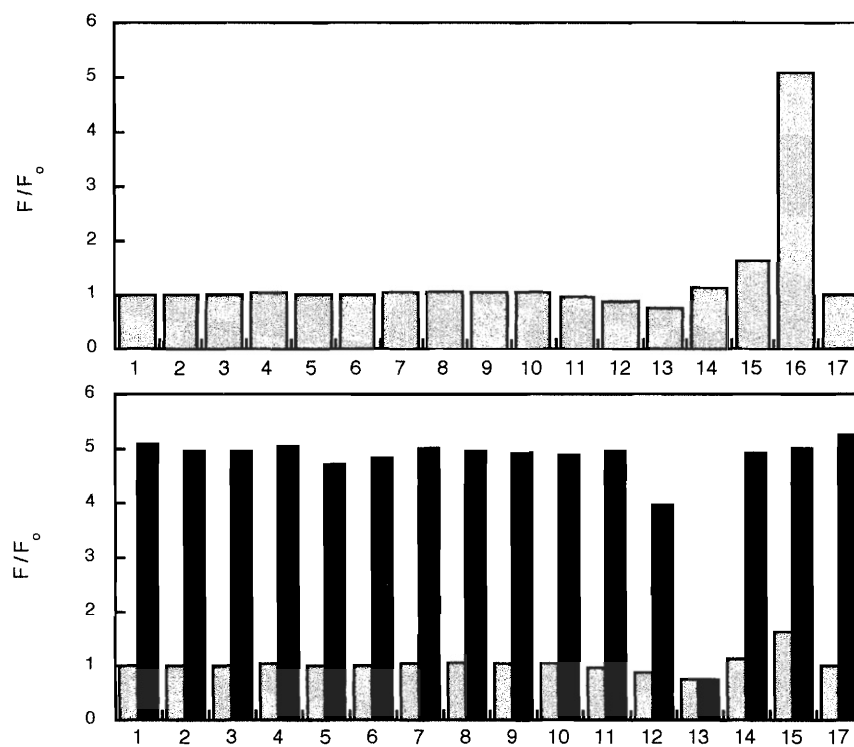
Figure 8.5. Top: Fluorescence response of MS1 to various cations in water at pH 7 (50 mM PIPES, 100 mM KCl). The response is normalized with respect to the free dye (F_o). The bars represent the emission of MS1 in the presence of 67 equiv of the cation of interest: 1, Li(I); 2, Na(I); 3, Rb(I); 4, Mg(II); 5, Ca(II); 6, Sr(II); 7, Ba(II); 8, Cr(III); 9, Mn(II); 10, Fe(II); 11, Co(II); 12, Ni(II); 13, Cu(II); 14, Zn(II); 15, Cd(II); 16, Hg(II); 17, Pb(II). Bottom: The selectivity of MS1 for Hg(II) in the presence of other cations. The light bars represent the emission of MS1 in the presence of 67 equiv of the cation of interest and correspond to the bars shown in the top panel. The dark bars represent the change in integrated emission that occurs upon subsequent addition of 67 equiv of Hg(II) to solutions containing MS1 and the cation of interest. The fluorescence of MS1 is also unaffected by millimolar concentrations of Li(I), Na(I), Rb(I), Mg(II), Ca(II), Sr(II), and Ba(II). [MS1] = 1 μM; λ_{ex}= 500 nm. The emission was integrated from 510 – 650 nm.
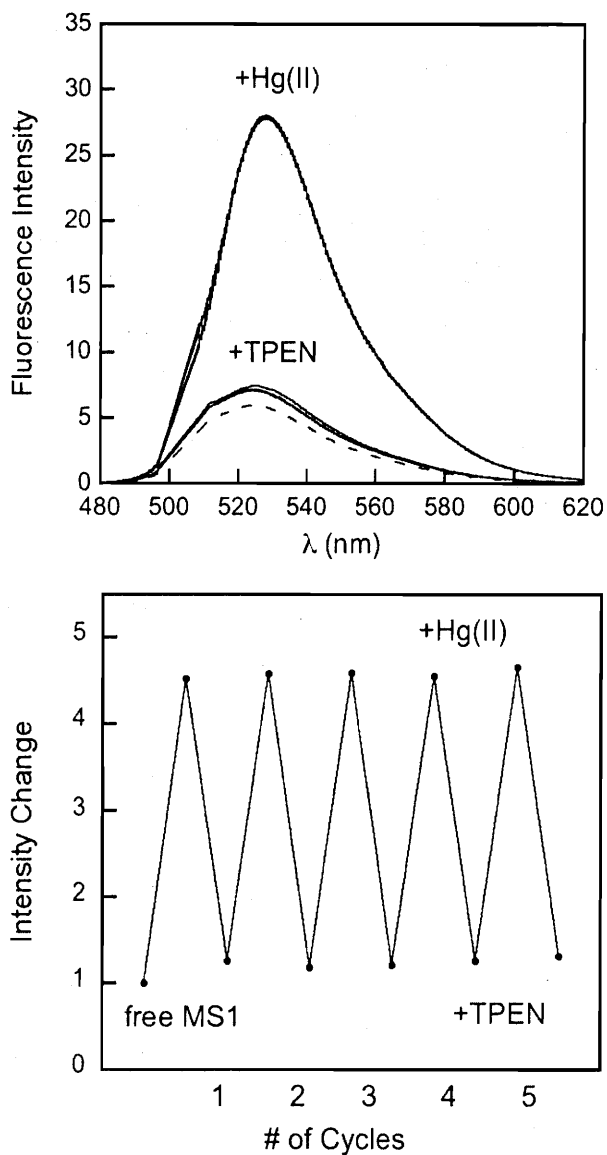
Figure 8.6. Reversibility of Hg(II) binding to MS1 upon addition of TPEN (50 mM PIPES, 100 mM KCl, pH 7). Top plot: Emission spectra corresponding to 1 μM free MS1 (dotted line), and the fluorescence changes upon addition of 1 equiv of Hg(II) or TPEN (solid lines). Bottom plot: Change in integrated emission following addition of Hg(II) and TPEN to the 1 μM MS1 solution over the course of five cycles. These data are normalized with respect to emission from free MS1.

Chapter 9

**Selective Hg(II) Detection in Aqueous Solution with
Thiol Derivatized Fluoresceins**

Introduction

Facile, sensitive and reliable methods for detecting heavy metal ions are important for research in environmental science and toxicology. Concern about human exposure to mercury through a variety of routes that include fish consumption,[1-5] vaccination,[6,7] dental amalgams,[8] and both the household[8,9] and workplace[10] environments suggests the need for new tools capable of detecting inorganic mercury in aqueous solution and in biological samples. Small-molecule fluorescent chemosensors that selectively bind to and report on the target analyte constitute one practical route towards this goal.[11-16]

The design of sensors that give fluorescence enhancement upon Hg(II) binding is an intriguing challenge since Hg(II), like many heavy elements, often causes fluorescence quenching.[17] Restricting such turn-on Hg(II) sensors to aqueous solution introduces additional complexity to this problem. A variety of small-molecule Hg(II) detection strategies that use fluorescence have been documented.[18-35] Nevertheless, many of these Hg(II) probes have one or more limitations, including irreversibility, slow response, incompatibility with aqueous solution, low selectivity, and fluorescence quenching upon Hg(II) coordination. Recently, several Hg(II) sensors that exhibit fluorescence turn-on and compatibility with the aqueous milieu have been described and include a biaryl species linked to an agrogel resin[36] and xanthenone-based MF1.[33] Other reported Hg(II) detection strategies relying on fluorescence output include nanoparticles,[37,38] polymers[39] and biomolecules.[25,40]

As part of an ongoing investigation focused on the preparation and utilization of small-molecule metal ion sensors, we reported mercury sensor 1 (MS1, Figure 9.1), which gives a positive fluorescence response to Hg(II) in aqueous solution at neutral pH.[41] In the design of MS1, we employed fluorescein as the reporting group because of its water solubility and excellent photophysical properties ($\Phi \sim 1$, high ε). The thioether moieties in the MS1 metal binding unit confer selectivity for Hg(II) over Zn(II) and Cd(II). Given the high affinity of Hg(II) for soft sulfur donors, including thiols, we have

expanded our MS sensor family to include thiol-derivatized fluoresceins. In this chapter, we describe the syntheses, photophysical characterization and Hg(II) binding properties of chemosensors containing pyridyl-amine-thiol ligands. Sensors MS2 and MS3, depicted in Scheme 9.1, are selective for Hg(II) over its Group 12 congeners, exhibit fluorescence turn-on immediately following Hg(II) coordination in aqueous solution, and are among the brightest fluorescent Hg(II) sensors described to date.

Experimental Section

Reagents. Solvents were dried as described in previous chapters. Isobutylene sulfide,[42] **1**, MEPAH,[43] **2**, MEPAHTr,[44] **3**, and 7'-chloro-4'-bromomethylfluorescein di-*tert*-butyldimethylsilyl ether,[45] **4**, were synthesized as previously described. Isobutylene oxide, used for the synthesis of **1**, was purchased from TCI America. All other reagents were obtained from Aldrich and used as received, with the exception of 2-(aminomethyl)pyridine, which was vacuum-distilled immediately before use.

Methods. Merck F254 silica gel-60 plates, Merck F254 aluminum oxide-60 plates and octadecyl-functionalized (reverse phase, RP, RP18) silica gel plates were used for analytical thin-layer chromatography (TLC). Whatman silica gel-60 plates and EM Science RP18 F254 plates of 1 mm thickness were used for preparative TLC. A Varian 300 MHz or 500 MHz spectrophotometer operating at 283 K was used to obtain ^{1}H and ^{13}C NMR spectra, which were referenced to the internal solvent peaks. IR spectra were obtained with an Avatar FTIR instrument. An Agilent 1100 Series LCMS was used for low-resolution electrospray ionization mass (ESI) spectrometry. High-resolution ESI spectrometry was performed by staff in the MIT DCIF.

2-Methyl-1-[(pyridin-2-ylmethyl)amino)propane-2-thiol (5). A portion (12.0 g, 111 mmol) of freshly distilled 2-aminomethylpyridine was dissolved in 40 mL of toluene and heated to reflux. Isobutylene sulfide (**1**, 5.0 g, 57 mmol) was dissolved in 60 mL of toluene and added dropwise to the refluxing solution over 4 h. The reaction was

refluxed for an additional 24 h, cooled and the solvent was removed in vacuo. Vacuum distillation yielded the purified product as a colorless oil (4.9 g, 21%). ^{1}H NMR (CDCl$_3$, 300 MHz) δ 1.35 (6H, s CH_3), 2.00 (2H, s, br, NH and SH), 2.60 (2H, s, CH_2CS), 3.93 (2H, s, NCH_2), 7.10 (1H, m, py-H), 7.30 (1H, d, py-H), 7.59 (1H, td, py-H), 8.49 (1H, dq, py-H). ^{13}C NMR (CDCl$_3$, 125 MHz) δ 30.73, 45.46, 55.78, 63.16, 121.85, 122.03, 136.35, 149.13, 159.97. An alternative preparation, which requires excess isobutylene sulfide, and further characterization are available elsewhere.[46]

(2-Methyl-2-triphenylsulfanylpropyl)pyridin-2-ylmethylamine (6). A portion (1.44 g, 5.54 mmol) of triphenylmethanol and **5** (1.08 g, 5.51 mmol) were combined in a dry flask and 9 mL of TFA was added. The reaction became brown-red and the triphenyl-methanol slowly dissolved. The reaction was stirred at room temperature for 2 h. The TFA was then removed under reduced pressure to yield an orange-red viscous oil. The oil was dissolved in 100 mL of ether and partitioned with 100 mL of 1 M NaOH and the layers were separated. The ether layer was concentrated under reduced pressure to afford the crude product as an off-white oily solid. Chromatography on Al$_2$O$_3$ with a solvent gradient (3:1 to 2:1 hexanes/EtOAc with 1% ^{i}PrNH$_2$) gave the purified product as an off-white solid (1.52 g, 63%). TLC R$_f$ = 0.43 (Al$_2$O$_3$, 3:1 hexanes/EtOAc); mp = 82-84 °C. ^{1}H NMR (CDCl$_3$, 300 MHz) δ 1.17 (6H, s, CH_3), 1.75 (2H, s, CH_2CS), 1.92 (1H, s, br, NH), 3.67 (2H, s, NCH_2), 7.06-7.33 (12H, m, Tr-H and py-H), 7.56 (1H, td, py-H), 7.66 (5H, m, Tr-H), 8.49 (1H, dd, py-H). ^{13}C NMR (CDCl$_3$, 125 MHz) δ 28.75, 52.58, 55.35, 59.23, 67.28, 121.58, 121.66, 126.33, 127.51, 129.81, 136.20, 145.20, 148.88, 160.46. FTIR (KBr, cm^{-1}) 3435 (s), 3348 (m), 3049(w), 3026 (w), 2993 (w), 2972 (w), 2959 (w), 2950 (w), 2905 (w), 2851 (w), 1642 (w), 1625 (w), 1589 (m), 1567 (m), 1486 (m), 1473 (m), 1444 (s), 1424 (m), 1380 (w), 1359 (m), 1319 (w), 1284 (w), 1242 (w), 1209 (w), 1130 (m), 1083 (w), 1031 (m), 1002 (w), 994 (w), 984 (w), 761 (m), 745 (s), 737 (s), 705 (s), 673 (w), 665 (w), 629 (m), 620 (m). HRMS (ESI) Calcd [M+H]$^+$, 439.2202; Found, 439.2209.

2-(2-Chloro-6-hydroxy-3-oxo-5-{[pyridin-2-ylmethyl-(2-triphenylsulfanyl-ethyl)-amino]methyl}-3*H*-xanthen-9-yl)benzoic acid (7, MS2Tr). To 8 mL of MeCN were combined 7'-chloro-4'-bromomethylfluorescein di-*tert*-butyldimethylsilyl ether (**4**, 150 mg, 0.22 mmol), MEPAHTr (**3**, 91 mg, 0.22 mmol) and K_2CO_3 (300 mg, 2.17 mmol), and the mixture was stirred overnight at room temperature. An orange precipitate formed and the reaction was filtered. TLC analysis showed the product to be present in both the precipitate and the filtrate. Preparative TLC of the combined material on RP silica gel (9:1 $CHCl_3$/MeOH) yielded the pure product as an orange solid (142 mg, 82%). ^{1}H NMR (CD_2Cl_2, 300 MHz) δ 2.48 (4H, m, C*H*$_2$C*H*$_2$S), 3.68 (2H, s, fl-C*H*$_2$N), 3.90 (2H, s, py-C*H*$_2$N), 6.50-6.58 (2H, m, fl-*H*), 6.78 (1H, s, fl-*H*), 6.88 (1H, s, fl-*H*), 7.15-7.37 (18H, m, Tr-*H*, py-*H* and fl-*H*), 7.63-7.72 (3H, m, fl-*H* and py-*H*), 8.02 (1H, d, fl-*H*), 8.51 (1H, d, py-*H*). FTIR (KBr, cm^{-1}) 3431 (s), 2922 (vs), 2852 (s), 1763 (m), 1581 (m), 1514 (w), 1489 (m), 1465 (m), 1444 (m), 1370 (w), 1259 (m), 1210 (m), 1150 (m), 1090 (m), 1012 (m), 873 (w), 743 (m), 700 (s), 617 (m), 473 (w), 444 (w). HRMS (ESI) Calcd [M+H]$^+$, 789.2184; Found, 789.2200.

2-(2-Chloro-6-hydroxy-5-{[(2-mercaptoethyl)pyridin-2-ylmethylamino]methyl}-3-oxo-3*H*-xanthen-9-yl)benzoic acid (8, MS2). A portion (142 mg, 0.180 mmol) of **7** was dissolved in 5 mL of TFA and a few drops of Et_3SiH were added. A white precipitate formed. The mixture was washed with hexanes (4 x 5 mL) and the TFA was removed under reduced pressure. Preparative TLC of the dark residue on RP silica gel (6:1 MeOH/0.1 N HCl) gave the product as an orange-red solid (55 mg, 56%). TLC R_f = 0.25 (RP silica, 6:1 MeOH\0.1 N HCl); mp = 194–196 °C, dec. ^{1}H NMR (CD_3OD, 300 MHz) δ 1.28 (1H, s, S*H*), 2.92 (2H, m, C*H*$_2$CS), 3.27 (2H, m, NC*H*$_2$), 4.27-4.46 (4H, m, NC*H*$_2$), 6.56 (2H, m, fl-*H*), 6.64 (1H, d, fl-*H*), 6.93 (1H, d, fl-*H*), 7.21 (1H, d, fl-*H*), 7.34 (1H, t, py-*H*), 7.43 (1H, d, py-*H*), 7.70-7.83 (3H, m, fl-*H* and py-*H*), 8.03 (1H, d, fl-*H*), 8.50 (1H, d, py-*H*). FTIR (KBr, cm^{-1}) 3434 (vs), 3055 (w), 2958 (w), 2918 (w), 2851 (w), 1762 (s), 1627 (s), 1600(s), 1581 (s), 1514 (w), 1489 (s), 1464 (s), 1452 (s), 1430 (s), 1370 (m), 1283 (s), 1260 (s),

1215 (s), 1149 (m), 1090 (m), 1106 (m), 1065 (w), 1012 (w), 874 (w), 822 (w), 801 (w), 760 (w), 702 (w), 621 (w), 596 (w). HRMS (ESI) Calcd [M-H]⁻, 545.0938; Found, 545.0963.

2-(2-Chloro-6-hydroxy-5-{[(2-mercapto-2-methylpropyl)pyridin-2-ylmethylamino]-methyl}-3-oxo-3H-xanthen-9-yl)benzoic acid (9, MS3). To 10 mL of MeCN and 1 mL of CH_2Cl_2 were added 7'-chloro-4'-bromomethylfluorescein di-*tert*-butyldimethylsilyl ether (**4**, 201 mg, 0.293 mmol), **6** (133 mg, 0.303 mmol), and K_2CO_3 (300 mg, 2.17 mmol). The reaction was stirred at room temperature for 24 h and filtered. The filtrate was evaporated to yield a dark orange residue, **10**, that was carried on without purification. Crude **10** was dissolved in 5 mL of TFA to yield a deep red solution and several drops of Et_3SiH were added. A white precipitate formed and the solution turned bright orange. The mixture was washed with hexanes (5 x 6 mL) and the TFA was removed in vacuo. Preparative TLC on silica gel (1:1:1:1 butanol/acetic acid/water/ethanol) followed by preparative TLC on RP silica gel (3:1 MeOH/0.1 N HCl) afforded MS3 as an orange solid (30 mg, 17%). TLC R_f = 0.23 (RP silica, 3:1 MeOH/0.1 N HCl); mp = 194-196 °C, dec. ¹H NMR (CD_3OD, 300 MHz) δ 1.28 (7H, m, CH_3 and SH), 3.30 (2H, m, CH_2CS) 4.31-4.45 (4H, m, NCH_2), 6.51 (2H, m, fl-H), 6.64 (1H, d, fl-H), 6.99 (1H, s, fl-H), 7.17 (1H, d, fl-H), 7.32-7.36 (2H, m, py-H), 7.70-7.79 (3H, m, fl-H and py-H), 8.02 (1H, d, fl-H), 8.40 (1H, d, py-H). FTIR (KBr, cm⁻¹) 3430 (vs), 2957 (w), 2918 (m), 2850 (w), 1764 (m), 1628 (s), 1611 (s), 1462 (m), 1452 (m), 1428 (m), 1370 (w), 1284 (m), 1255 (m), 1219 (w), 1151 (w), 1107 (w), 1090 (w), 1014 (w), 875 (w), 762 (w), 698 (w). HRMS (ESI) Calcd [M+H]⁺, 575.1402; Found, 575.1394.

General Spectroscopic Methods. All aqueous solutions were prepared with Millipore water (18.2 MΩ·cm at 25 °C) obtained from a Mili-Q Biocel purifier outfitted with a Quantum VX cartridge. PIPES, piperazine-N,N'-bis(2-ethanesulfonic acid), CHES, 2-(N-cyclohexylamino)ethanesulfonic acid, and CABS, 4-cyclohexylamino-1-butanesulfonic acid, buffers were purchased from Sigma or Calbiochem and used as received. Puratonic grade KCl was purchased from Calbiochem. Anhydrous $HgCl_2$

(99.998%) was purchased from Aldrich and used to prepare 10 mM Hg(II) stock solutions in water. Other stock solutions of metal ions were prepared as described in Chapter 9. With the exception of the pK_a titrations, measurements were made in buffered aqueous solution with 50 mM buffer and 100 mM KCl at pH 7 (PIPES), pH 9 (CHES) or pH 11 (CABS). A 10 mM KOH, 100 mM KCl (pH ~12) solution was used for the pK_a titrations. Solutions (1 mM) of MS2 and MS3 in DMSO were prepared, stored at –25 °C, and thawed in the dark before use. These stock solutions are stable for >12 months under these conditions judging by UV-vis and fluorescence spectroscopy, and can be frozen and thawed multiple times if kept in the dark while at room temperature. With the exception of the pK_a titrations, which were performed in duplicate, all manipulations were performed at least in triplicate and the averages are reported.

Optical Absorption Spectroscopy. UV-visible measurements were conducted as described in Chapters 2 and 8. In a typical Job analysis, starting solutions of 10 μM dye and 10 μM HgCl$_2$ were used. For a typical metal-binding titration, 3 μL aliquots of a 1 mM Hg(II) stock were added to a 10 μM solution of dye. The absorbance changes were plotted against equiv of Hg(II) in solution.

Fluorescence Spectroscopy. A Hitachi F-3010 spectrofluorimeter maintained at 25 °C ± 1 °C by a circulating water bath was employed. Quartz cuvettes (Starna) with a 1-cm path length and 3.5-mL volume were used for all fluorescence measurements. Quantum yields were measured relative to fluorescein in 0.1 N NaOH ($\Phi = 0.95$).[47] The pH-dependent pK_a values were determined as described in Chapter 2. Metal ion selectivity experiments were conducted as described for MS1 in Chapter 8.

Results and Discussion

Syntheses of Sensors MS2 and MS3. Several small-molecule Hg(II) detectors that employ sulfur donors have been reported by our laboratory[41,48] and others.[22,30,31,33-35] These probes have sulfur-containing macrocycles, thioether or thiourea groups in the

metal-binding units and generally exhibit good selectivity for Hg(II). Given the propensity of Hg(II) to bind thiols, we reasoned that incorporation of thiol donors into a sensor would elicit both high selectivity and sensitivity for Hg(II).

The syntheses for MS2 and MS3 are illustrated in Scheme 9.1. MEPAHTr, 3, was prepared according to a literature procedure.[44] Combination of 3 with the silyl-protected bromomethyl fluorescein,[45] 4, in the presence of excess K_2CO_3 and subsequent preparative TLC on RP silica gel (9:1 $CHCl_3$/MeOH) afforded MS2Tr, 7, in good yield (82%) as an orange solid. As observed in the reported synthesis of sensor ZS3,[49] the TBS protecting groups of 4 were unstable to these conditions, and deprotection occurred during the course of the reaction. The trityl protecting group was subsequently removed by dropwise addition of Et_3SiH to a solution of 7 in TFA followed by washing with hexanes. Preparative TLC of the crude product on RP silica gel (4.5:1 MeOH/0.1 N HCl) yielded pure MS2, 8, as an orange solid in moderate yield (56%).

MS3 differs from MS2 by having gem-dimethyl substituents incorporated into the pyridyl-amine-thiol ligand. Compound 5 was prepared from isobutylene sulfide, 1, and 2-aminomethylpyridine by analogy to the published procedure[43] for 2 and was obtained in moderate yield as a colorless oil following vacuum distillation. The thiol was protected with a trityl group, and 6 was isolated as a white solid in 63% yield following workup and chromatography on Al_2O_3 using a hexanes/EtOAc solvent gradient. The assembly of MS3 from 4 and 6 is analogous to that described above for MS2. During this procedure, however, intermediate 10 was not purified before deprotection of the thiol moiety. Pure MS3, 9, was isolated as an orange-red solid in relatively low (17%) yield after purification by preparative TLC. It should be noted that the purification of MS3 was significantly more difficult than that of MS2, which suggests that purification of intermediate 10 prior to deprotection may have been a preferable route. Both MS2 and MS3 have a faint sulfurous odor, and the purified sensors are stable for >12 months when stored in the dark at 4 °C as judged by absorption and fluorescence spectroscopy.

Spectroscopic Properties of MS2 and MS3. MS2 and MS3, shown in Scheme 9.1, were designed as turn-on photoinduced electron transfer (PET) sensors that utilize tertiary amines in the quenching unit. The generally accepted mechanism for fluorescence turn-on in amine-based PET sensors involves fluorescence quenching of the free dye by PET through back-electron transfer from a nitrogen lone pair electron into the fluorophore photoexcited state, followed by diminution of PET via coordination to a closed shell metal ion, which results in fluorescence enhancement.[13]

Table 9.1 summarizes the results from spectroscopic characterization of MS2 and MS3. These sensors have essentially identical pH-emission profiles, which are illustrated in Figure 9.2. The fluorescence of each probe is ~75% quenched at pH 12, and maximum fluorescence is reached at pH ~7. Two protonation events affect the fluorescence of MS2 (pK_a = 8.2, 4.6) and MS3 (pK_a = 8.0, 4.6). The pK_a ~ 8 transition is assigned to the tertiary nitrogen atom, protonation of which interferes with the PET quenching pathway and yields enhanced fluorescence at neutral pH. This assignment is based on a comparison of the pK_a profiles of tertiary amine-based ZP dyes[50] and related compounds,[49] although we note that the pK_a values for the thiols could also fall in this range. Fluorescein itself displays pH-dependent fluorescence with quenched emission at low pH, and the pK_a of 4.6 observed in Figure 9.2 corresponds to fluorescein protonation and formation of a non-fluorescent species at acidic pH. The pK_a values of 4.6 are similar to those observed for asymmetrical Zn(II) and Hg(II) sensors based on the monochlorofluorescein platform, including those with both tertiary amine- (ZS3) and aniline-based ligands (ZP4-11, ZS4, MS1), which indicates that this pK_a is relatively insensitive to the nature of the metal-binding unit.

MS2 and MS3 have quantum yields of 0.28 and 0.27 and emission maxima at 526 and 525 nm, respectively, at neutral pH (50 mM PIPES, 100 mM KCl, pH 7) and in the presence of the metal ion scavenger EDTA (Table 9.1). These quantum yield values are ~50% lower than that observed for the corresponding asymmetrical di(2-picolyl)amine-

based sensor ($\Phi \sim 0.6$),[51] which suggests that the thiol moiety also plays a role in quenching the fluorescein excited state. Addition of Hg(II) causes an ~1.5- (MS2) or ~2-fold (MS3) fluorescence enhancement, and the emission spectra for both species red-shift to 531 nm (Figure 9.3). The absorption spectra also undergo red-shifts upon Hg(II) complexation. For MS2, a 5 nm shift is observed from 500 ($\varepsilon = 62,000$ $M^{-1}cm^{-1}$) to 505 nm ($\varepsilon = 69,000$ $M^{-1}cm^{-1}$). The optical absorption spectrum for MS3 exhibits a similar shift from 501 ($\varepsilon = 51,000$ $M^{-1}cm^{-1}$) to 507 nm ($\varepsilon = 59,000$ $M^{-1}cm^{-1}$) following Hg(II) binding. Since introduction of Hg(II) to a solution of MS2 or MS3 results in essentially no change in quantum yield for either species (MS2, $\Phi_{Hg} = 0.27$; MS3, $\Phi_{Hg} = 0.28$) while causing an increase in molar absorptivity, the resulting fluorescence enhancement at pH 7 is due exclusively to the absorption increase since brightness is ($\Phi \times \varepsilon$).

Although modest, the fluorescence enhancement observed for these sensors upon addition of Hg(II) was intriguing. The pK_a of ~8 for MS2 and MS3 suggests that proton-induced background fluorescence compromises Hg(II)-induced emission turn-on at neutral pH. Raising the solution pH to deprotonate the tertiary amine nitrogen atom should enhance PET quenching, lower the quantum efficiency of each free dye, and result in greater fluorescence enhancement upon Hg(II) complexation. As anticipated, the quantum yield of free MS2 decreases substantially when the pH is rated to 9 (50 mM CHES, 100 mM KCl) or 11 (50 mM CABS, 100 mM KCl) with values of 0.10 and 0.07, respectively. An ~5-fold increase in integrated emission immediately results after addition of Hg(II) to MS2 in this pH regime (Figure 9.4) and the quantum yield of the Hg(II) complex is 0.28 (pH 9) or 0.24 (pH 11). MS3 exhibits analogous behavior, as summarized in Table 9.1. Despite the relatively modest degree of turn-on at pH 7, the choice of tertiary amine as a PET switch and fluorescein as the reporting group achieves greater brightness ($\Phi \times \varepsilon$) upon Hg(II) coordination than that observed for aniline-derivatized MS1 (Figure 9.1) and Hg(II) sensors reported by others.

Metal-Binding Studies of MS2 and MS3. Asymmetrical MS2 and MS3 were designed for 1:1 metal ion complexation, and the metal-binding properties of these probes were investigated by mass spectrometry, UV-visible and fluorescence spectroscopies. Low resolution mass spectrometry (negative ion mode) of a methanolic solution of equimolar MS2 and Hg(II) revealed a peak with m/z of 744.7, which corresponds to [MS2 +Hg – 3H] (calc. 745.1) and suggests 1:1 stoichiometry. Job plots for the addition of Hg(II) to solutions of MS2 and MS3 are shown in Figure 9.5 and the maxima at 0.5 indicate formation of 1:1 MS2:Hg(II) and MS3:Hg(II) complexes in aqueous solution. Metal-binding titrations reveal a break at 1 equiv of Hg(II) (Figure 9.6). At pH 7, the absorbance difference spectrum for the addition of Hg(II) to MS2 shows a decrease at 483 nm and increases ca. 300 and 512 nm. The difference spectrum for MS3 is similar (decrease at 482 nm; increases at ca. 300 and 510 nm). Comparable absorption changes are observed for Hg(II) binding at high pH. For instance, at pH 11 (50 mM CABS, 100 mM KCl), Hg(II) binding to MS2 results in an absorbance increase at ca. 300 and 510 nm and a decrease at 490 nm (Figure 9.6). The absorbance changes at ca. 500 nm are attributed to perturbation of the fluorescein π-π^* transition upon Hg(II) coordination and the increase at ca. 300 nm to RS⁻ $\rightarrow$ Hg(II) charge transfer bands.[52,53] Scheme 9.2 illustrates the proposed tetrahedral Hg(II) coordination to MS2&3 through the N_2SO donor set in aqueous solution at neutral pH.

Sensors MS2 and MS3 both show diminished fluorescence turn-on following Hg(II) binding at neutral pH in the absence of chloride ion, as previously observed for sensor MS1 (Chapter 8). For instance, at neutral pH (50 mM PIPES, 100 mM KX, X = OAc⁻, F⁻, NO_3^-), only negligible (KOAc, KF) or no (KNO₃) fluorescence enhancement occurs following Hg(II) binding to MS2. The presence of chloride ion has no effect on the emission profile of the free sensors, suggesting that an Hg—Cl bond or ion pairing causes the chloride-dependent fluorescence enhancement. Results obtained from low-resolution ESI mass spectrometric analysis support this notion. When a methanolic

solution of equimolar MS2 and Hg(II) is treated with aqueous KCl, two new intense peaks with m/z of 780.6 and 816.6 are observed in the negative ion mode mass spectrum (Figure 9.7). The former m/z ratio corresponds to the monochloro adduct [MS2 + Hg + Cl – 2H] (calcd 781.0) and the latter to the dichloro species [MS2 + Hg + 2Cl – H] (calcd 817.0). Although the precise nature of these chloride-containing complexes cannot be ascertained from this experiment, the data clearly reveal that the MS2:Hg(II) complex readily associates with one or more chloride ions in solution.

Fluorescence spectroscopy was used to determine the EC_{50} value, the concentration of Hg(II) required for 50% of the total fluorescence enhancement at [MS] = 1 μM, for Hg(II) binding to MS2 and MS3 (Figure 9.4). Essentially complete (~96%) turn-on results upon addition of 1 equiv of Hg(II) to a solution of MS2, and the EC_{50} of MS2 for Hg(II) is 384 nM. Addition of 1 equiv of Hg(II) to MS3 results in ~34% turn-on and maximum fluorescence is reached with ~6 equiv of Hg(II) in solution. The EC_{50} of MS3 for Hg(II) is 1.6 μM, indicating that the gem-dimethyl substituents adjacent to the thiol donor decrease the binding affinity.

Achieving high selectivity for the analyte of interest over a complex background of potentially competing species is a challenge in sensor development. Figure 9.8 illustrates the fluorescence response of MS3 to Hg(II) in the presence of alkali and alkaline earth metals found in natural waters, select divalent first-row transition metals, Cr(III), Pb(II), Zn(II) and Cd(II). A background of Group 1 and 2 metals does not interfere with Hg(II) coordination and subsequent fluorescence turn-on, even at mM concentrations. Neither Cr(III) nor Pb(II) prevent the Hg(II)-induced fluorescence enhancement. MS3 is selective for Hg(II) over Mn(II), Fe(II) and Co(II). MS3 preferentially binds Ni(II) and Cu(II) over Hg(II) at neutral pH. The selectivity of MS2 for Hg(II) is generally similar, although slightly less fluorescence enhancement occurs upon addition of Hg(II) to solutions of MS2 and Co(II) (Figure 9.9). The preference of these sensors for Cu(II) is not surprising given the N_2SO donor set and the fact that

sulfur-containing ligands exhibit high selectivity for metals in the "copper triangle" of the periodic table.[54] MS2 and MS3 both display greater affinity for Hg(II) than its Group 12 congeners. The positive fluorescence responses of these probes are Hg(II)-specific.

Reversibility is a criterion in sensor development since the ability to regenerate the free sensor is important for practical applications. During our investigations of anion effects, we observed that MS2 and MS3 do not coordinate Hg(II) in buffer containing 100 mM KI (50 mM PIPES, 100 mM KI, pH 7). Optical absorption spectroscopy showed that addition of Hg(II) to solutions of the sensors in this buffer resulted in no change in the chromophore absorption band centered at 500 nm and the formation of intense absorption bands centered at 265 and 321 nm attributed to $[HgI_4]^{2-}$ (Figure 9.10).[55,56] This finding and a recent report that Hg(II) complexation to a solid-state colorimetric Hg(II) sensor was reversed by washing with KI[57] motivated us to use KI to achieve reversible Hg(II) binding. Optical absorption spectroscopy shows that addition of excess KI to solutions of the MS2:Hg(II) complex causes an immediate blue shift in the fluorescein π—π^* transition from 505 to 500 nm with a concomitant intensity decrease, consistent with Hg(II) release. Formation of new bands in the 260-320 nm region signaled formation of $[HgI_4]^{2-}$ (Figure 9.10).

The EPA-mandated upper limit of allowable inorganic mercury in drinking water is 2 ppb.[3] A fluorescence change of 15.3 % ± 5% in MS2 (500 nM) emission occurs in the presence of 2 ppb Hg(II) (50 mM CABS, 100 mM KCl, pH 11), demonstrating that MS2 can detect environmentally relevant concentration of Hg(II).

Summary and Perspectives

This chapter included the syntheses and characterization of two water-compatible fluorescence sensors for Hg(II) detection that employ thiol donors in the metal binding unit, which confers selectivity for Hg(II) over its Group 12 congeners and several divalent first-row transition metal ions. Sensors MS2 and MS3 exhibit Hg(II)-induced

fluorescence turn-on and greater brightness than aniline-based MS1, but relatively small dynamic range at neutral pH and loss of selectivity for Hg(II) over Ni(II). The improved brightness results from the choice of a tertiary amine as the PET quenching unit. In an attempt to maintain high brightness and achieve MS1-like selectivity, several sensors with tertiary amine-based ligands containing multiple thioethers were subsequently prepared (Appendix 1). Unfortunately, these sensors all gave fluorescence turn-off with Hg(II) coordination at neutral pH, which suggests that aniline-based ligands are generally better suited for turn-on Hg(II) sensing than those relying on a tertiary amine as the PET switch. The MS2 and MS3 sensor may be useful for applications in toxicology and environmental monitoring.

References

(1)   Boening, D. W. *Chemosphere* **2000**, *40*, 1335-1351.

(2)   Renzoni, A.; Zino, F.; Franchi, E. *Environ. Res.* **1998**, *77*, 68-72.

(3)   Mercury Update: Impact on Fish Advisories. EPA Fact Sheet EPA-823-F-01-011; EPA, Office of Water: Washington, DC, 2001.

(4)   Nendza, M.; Herbst, T.; Kussatz, C.; Gies, A. *Chemosphere* **1997**, *35*, 1875-1885.

(5)   Harris, H. H.; Pickering, I. J.; George, G. N. *Science* **2003**, *301*, 1203.

(6)   Pichichero, M. E.; Cernichiari, E.; Lopreiato, J.; Treanor, J. *Lancet* **2002**, *360*, 1737-1741.

(7)   Magos, L. *J. Applied Toxicol.* **2001**, *21*, 1-5.

(8)   Clarkson, T. W.; Magos, L.; Myers, G. J. *New Eng. J. Med.* **2003**, *349*, 1731-1737.

(9)   Forman, J.; Moline, J.; Cernichiari, E.; Sayegh, S.; Torres, J. C.; Landrigan, M. M.; Hudson, J.; Adel, H. N.; Landrigan, P. J. *Environ. Heatlh Perspect.* **2000**, *108*, 575-577.

(10)   Malm, O. *Environ. Res.* **1998**, *77*, 73-78.

(11)   Czarnik, A. W. *Acc. Chem. Res.* **1994**, *27*, 302-308.

(12)   de Silva, A. P.; Fox, D. B.; Huxley, A. J. M.; Moody, T. S. *Coor. Chem. Rev.* **2000**, *205*, 41-57.

(13)   de Silva, A. P.; Guarante, H. Q. N.; Gunnlaugsson, T.; Huxley, A. J. M.; McCoy, C. P.; Rademacher, J. T.; Rice, T. E. *Chem. Rev.* **1997**, *97*, 1515-1566.

(14)   Prodi, L. *New. J. Chem.* **2005**, *29*, 20-31.

(15)   Prodi, L.; Bolletta, F.; Montalti, M.; Zaccheroni, N. *Coor. Chem. Rev.* **2000**, *205*, 59-83.

(16)   Callan, J. F.; de Silva, A. P.; Magri, D. C. *Tetrahedron* **2005**, *61*, 8551-8588.

(17)   Masuhara, H.; Shioyama, H.; Saito, T.; Hamada, K.; Yasoshima, S.; Mataga, N. *J. Phys. Chem.* **1984**, *88*, 5868-5873.

(18)   Chae, M.-Y.; Czarnik, A. W. *J. Am. Chem. Soc.* **1992**, *114*, 9704-9705.

(19)   Hennrich, G.; Sonnenschein, H.; Resch-Genger, U. *J. Am. Chem. Soc.* **1999**, *121*, 5073-5074.

(20)   Metivier, R.; Leray, I.; Valeur, B. *Chem. Eur. J.* **2004**, *10*, 4480-4490.

(21)   Ros-Lis, J. V.; Marcos, M. D.; Martínez - Máñez, R.; Rurack, K.; Soto, J. *Angew. Chem. Int. Ed* **2005**, *44*, 4405-4407.

(22)   Dickerson, T. J.; Reed, N. N.; La Clair, J. J.; Janda, K. D. *J. Am. Chem. Soc.* **2004**, *126*, 16582-16586.

(23)   Guo, X.; Qian, X.; Jia, L. *J. Am. Chem. Soc.* **2004**, *126*, 2272-2273.

(24)   Caballero, A.; Martinez, R.; Lloveras, V.; Ratera, I.; Vidal-Gancedo, J.; Wurst, K.; Tarraga, A.; Molina, P.; Veciana, J. *J. Am. Chem. Soc.* **2005**, *127*, 15666-15667.

(25)   Chen, P.; He, C. *J. Am. Chem. Soc.* **2004**, *126*, 728-729.

(26)   Moon, S.-Y.; Youn, N. J.; Park, S. M.; Chang, S.-K. *J. Org. Chem.* **2005**, *70*, 2394-2397.

(27)   Zhang, G.; Zhang, D.; Yin, S.; Yang, X.; Shuai, Z.; Zhu, D. *Chem. Commun.* **2005**, 2161-2163.

(28)   Liu, B.; Tian, H. *Chem. Commun.* **2005**, 3156-3158.

(29)   Yang, Y.-K.; Yook, K.-J.; Tae, J. *J. Am. Chem. Soc.* **2005**, *127*, ASAP.

(30)   Sakamoto, H.; Ishikawa, J.; Nakao, S.; Wada, H. *Chem. Commun.* **2001**, 2395-2396.

(31)   Descalzo, A. B.; Martínez - Máñez, R.; Radeglia, R.; Rurack, K.; Soto, J. *J. Am. Chem. Soc.* **2003**, *125*, 3418-3419.

(32)   Yoon, J.; Ohler, N. E.; Vance, D. H.; Aumiller, W. D.; Czarnik, A. W. *Tetrahedron Lett.* **1997**, *28*, 3845-3848.

(33)   Yoon, S.; Albers, A. E.; Wong, A. P.; Chang, C. J. *J. Am. Chem. Soc.* **2005**, *127*, 16030-16031.

(34)   Rurack, K.; Kollmannsberger, M.; Resch-Genger, U.; Daub, J. *J. Am. Chem. Soc.* **2000**, *122*, 968-969.

(35)   Rurack, K.; Resch-Genger, U.; Bricks, J. L.; Spieles, M. *Chem. Commun.* **2000**, 2103-2104.

(36)   Mello, J. V.; Finney, N. S. *J. Am. Chem. Soc.* **2005**, *127*, 10124-10125.

(37)   Chen, B.; Yu, Y.; Zhou, Z.; Zhong, P. *Chem. Lett.* **2004**, *33*, 1608-1609.

(38)   Zhu, C.; Li, L.; Fang, F.; Chen, J.; Wu, Y. *Chem. Lett.* **2005**, *34*, 898-899.

(39)   Fan, L.-J.; Zhang, Y.; Jones, W. E. *Macromolecules* **2005**, *38*, 2844-2849.

(40)   Ono, A.; Togashi, H. *Angew. Chem. Int. Ed* **2004**, *43*, 4300-4302.

(41)   Nolan, E. M.; Lippard, S. J. *J. Am. Chem. Soc.* **2003**, *125*, 14270-14271.

(42)   Snyder, H. R.; Stewart, J. M.; Ziegler, J. B. *J. Am. Chem. Soc.* **1947**, *69*, 2672-2674.

(43)   Brand, U.; Vahrenkamp, H. *Inorg. Chem.* **1995**, *34*, 3285-3293.

(44)   Kramer, D. J.; Davison, A.; Davis, W. M.; Jones, A. G. *Inorg. Chem.* **2002**, *41*, 6181-6183.

(45)   Burdette, S. C.; Frederickson, C. J.; Bu, W.; Lippard, S. J. *J. Am. Chem. Soc.* **2003**, *125*, 1778-1787.

(46)   Brand, U.; Vahrenkamp, H. *Inorg. Chim. Acta* **2000**, *308*, 97-102.

(47)   Brannon, J. H.; Magde, D. *J. Phys. Chem.* **1978**, *82*, 705-709.

(48)   Nolan, E. M.; Lippard, S. J. *J. Mat. Chem.* **2005**, *15*, 2778-2783.

(49)   Nolan, E. M.; Lippard, S. J. *Inorg. Chem.* **2004**, *43*, 8310-8317.

(50)   Burdette, S. C.; Walkup, G. K.; Spingler, B.; Tsien, R. Y.; Lippard, S. J. *J. Am. Chem. Soc.* **2001**, *123*, 7831-7841.

(51)   Nolan, E. M.; Lippard, S. J. *Unpublished Results.*

(52)   Watton, S. P.; Wright, J. G.; MacDonnell, F. M.; Bryson, J. W.; Sabat, M.; O'Halloran, T. V. *J. Am. Chem. Soc.* **1990**, *112*, 2824-2826.

(53) Fleissner, G.; Kozlowski, P. M.; Vargek, M.; Bryson, J. W.; O'Halloran, T. V.; Spiro, T. G. *Inorg. Chem.* **1999**, *38*, 3523-3528.

54) Cooper, T. H.; Mayer, M. J.; Leung, K.-H.; Ochrymowycz, L. A.; Rorabacher, D. B. *Inorg. Chem.* **1992**, *31*, 3796-3804.

(55) Griffiths, T. R.; Symons, M. C. R. *J. Chem. Soc. Trans. Farady Soc.* **1960**, *56*, 1752-1760.

(56) Griffiths, T. R.; Anderson, R. A. *Can. J. Chem.* **1991**, *69*, 451-457.

(57) Coronado, E.; Galan-Mascaros, J. R.; Marti-Gastaldo, C.; Palomares, E.; Durrant, J. R.; Vilar, R.; Gratzel, M.; Nazeeruddin, M. K. *J. Am. Chem. Soc.* **2005**, *127*, 12351-12356.

Table 9.1. Spectroscopic and Thermodynamic Data for Fluorescein-Based MS Sensors

	pH	Absorption λ (nm), $\varepsilon \times 10^4$ (M^{-1}cm^{-1})		Emission λ (nm), Φ^a		$pK_a{}^b$	$pK_a{}^c$	$EC_{50}{}^d$ (μM)
		Unbound	Hg(II)	Unbound	Hg(II)			
MS1^e	7	505, 6.1	501, 7.3	524, 0.04	528. 0.11	7.1	5.1	0.410
MS2	7	500, 6.2	505, 6.9	526, 0.28	531, 0.27	8.2	4.6	
	9	502, 6.3	505, 8.2	526, 0.10	531, 0.28			
	11	504, 6.1	507, 7.8	526, 0.07	531, 0.24			0.384
MS3	7	501, 5.1	507, 5.9	526, 0.27	531, 0.28	8.0	4.6	
	11	504, 5.5	507, 6.4	525, 0.10	531, 0.26			1.6

^{a}Fluorescein ($\Phi = 0.95$ in 0.1 N NaOH, ref. 47) was used as the standard for the quantum yield measurements. ^{b}The pK_a value of the aniline (MS1) or tertiary (MS2, MS3) nitrogen atom. This pK_a corresponds to a fluorescence increase when moving from high to low pH. ^{c}The pK_a value associated with formation of a non-fluorescent isomer. This pK_a values corresponds to a fluorescence decrease when moving from high to low pH. ^{d}The EC_{50} is the concentration of Hg(II) required to achieve 50% of the maximum fluorescence increase with 1 μM sensor. ^{e}Data for MS1 were taken from Chapter 8.
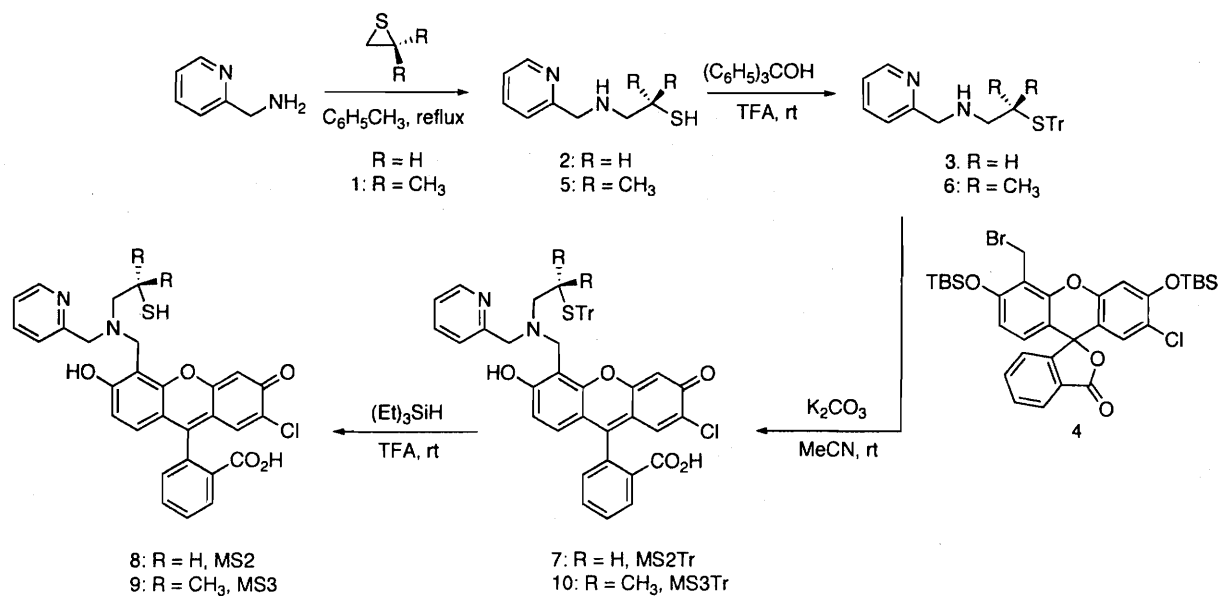
Scheme 9.1. Syntheses of MS2 and MS3.
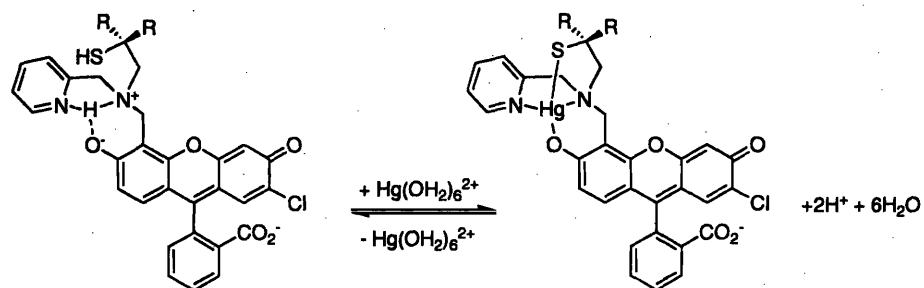
Scheme 9.2. Proposed mode of Hg(II) coordination in aqueous solution at neutral pH.

MS1
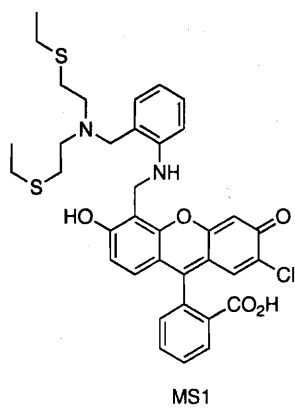
Figure 9.1. Structure of MS1. The preparation and characterization of this Hg(II) sensor are presented in Chapter 8.
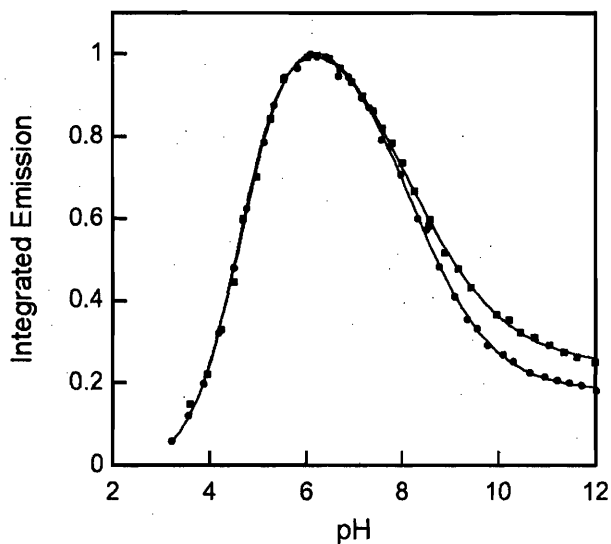
Figure 9.2. Fluorescence dependence on pH for free MS2 (circles) and MS3 (squares). A 1 μM solution of each dye was prepared and the emission spectrum was taken. Aliquots of 6, 2, 1, 0.5 and 0.1 N HCl were added to achieve pH changes of ~0.25 units and the emission spectrum was recorded at each interval. The emission was integrated from 500 to 650 nm (MS2) or from 450 to 650 nm (MS3), normalized and plotted against pH. Excitation was provided at 498 nm. Two protonation events affect the fluorescence of MS2 and MS3 with pK_{a1} = 8.2 (MS2) or 8.0 (MS3) and pK_{a2} = 4.6. The former transition results from tertiary amine protonation and the latter from protonation of the fluorescein platform.
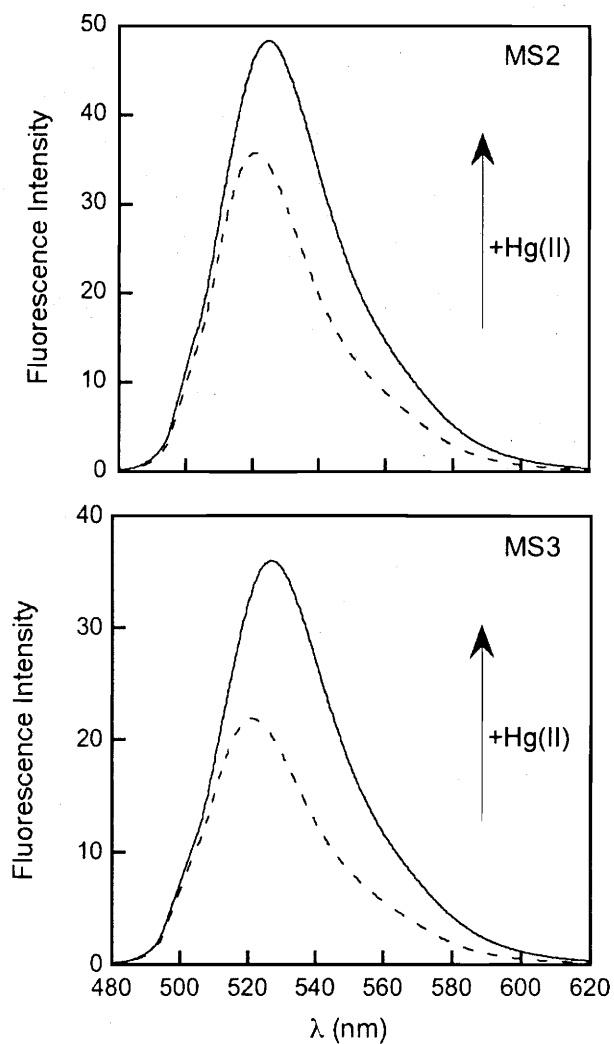
Figure 9.3. The fluorescence response of 1 μM MS2 (top) and MS3 (bottom) to 50 equiv

of Hg(II) at pH 7 (50 mM PIPES, 100 mM KCl). Dotted line: free MS2 or MS3; solid line:

+Hg(II). Excitation was provided at 500 nm for MS2 and at 504 nm for MS3.
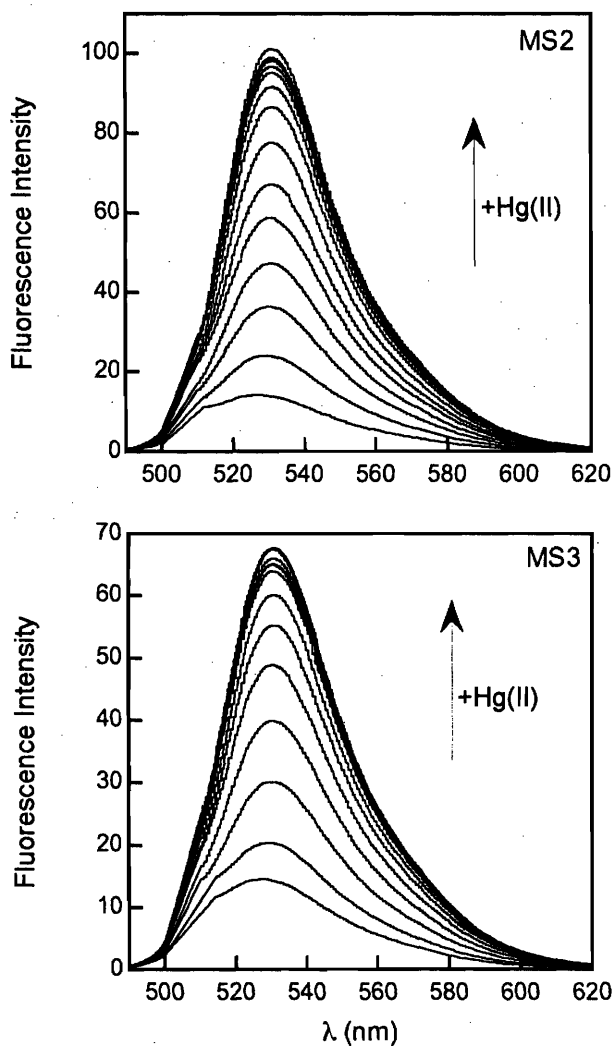
Figure 9.4. Fluorescence enhancement of MS2 and MS3 following addition of Hg(II) at pH 11 (50 mM CABS, 100 mM KCl, pH 11). Top: Fluorescence response of 1 μM MS2 to 0, 0.1, 0.2, 0.3, 0.4, 0.5, 0.6, 0.8, 1.0, 1.33, 1.66, 3.0 and 13 μM added Hg(II). Bottom: Fluorescence response of 1 μM MS3 to 0.5, 1, 1.5, 2, 2.5, 3, 3.5, 4, 5, 6, 7, 8, 9, 10 and 50 μM added Hg(II). The EC_{50} for MS2 is 384 nM and the EC_{50} for MS3 is 1.6 μM. Excitation was provided at 504 nm for both titrations.
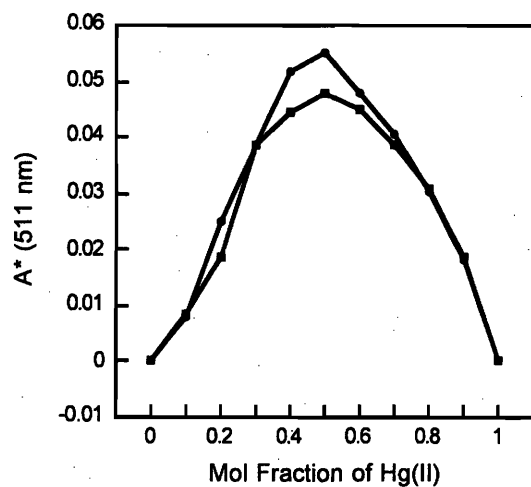
Figure 9.5. Representative Job plots for addition of Hg(II) to MS2 (circles) and MS3 (squares) at pH 7 (50 mM PIPES, 100 mM KCl) determined by optical absorption spectroscopy. The absorption change was monitored at 511 nm. The concentrations of the starting solutions were 10 μM. The maxima at 0.5 indicate that both MS2 and MS3 from 1:1 complexes with Hg(II).
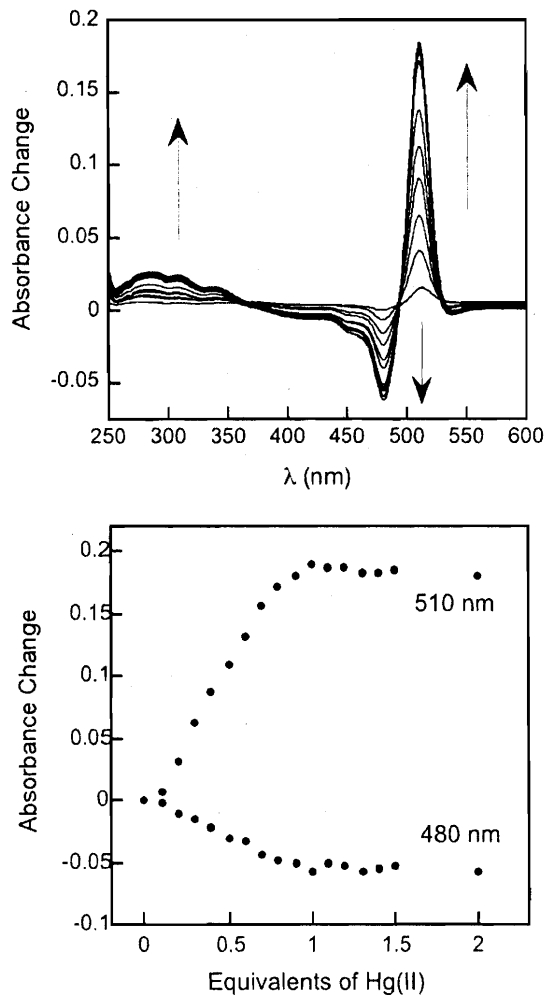
Figure 9.6. Top: Difference spectra obtained from the addition of Hg(II) to a solution of MS2 at pH 11 (50 mM CABS, 100 mM KCl). The concentration of MS2 was 10 μM. Aliquots of 1 mM $HgCl_2$ in water were added to yield Hg(II) concentrations of 0, 1, 2, 3, 4, 5, 6, 7, 8, 9, 10, 11, 12, 13, 14, 15 and 20 μM. Absoprtion increases occur at ca. 300 and 510 nm, and a decrease occurs at 480 nm upon Hg(II) coordination. Bottom: Absorption change versus equiv of Hg(II) in solution for MS2, which indicates formation of a 1:1 MS2:Hg(II) complex.
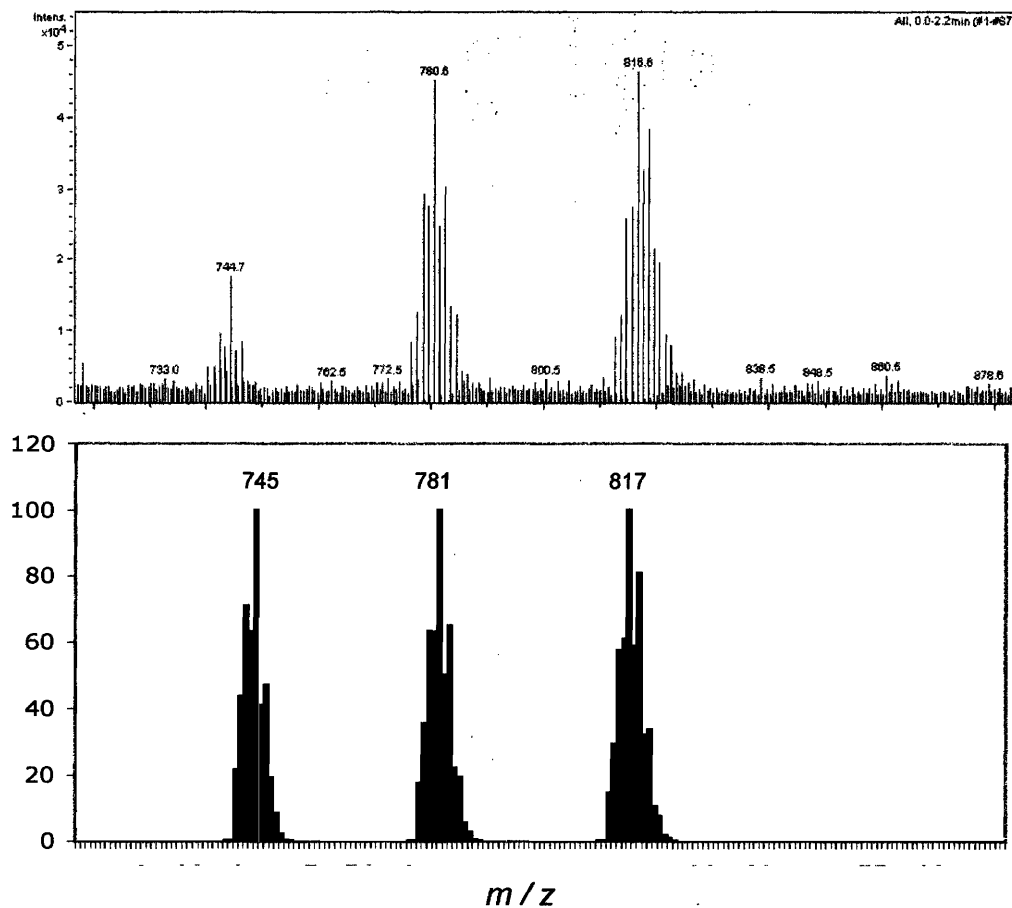
Figure 9.7. Top: Low resolution ESI spectrum (negative ion mode) of a methanolic solution of equimolar MS2 and Hg(II) containing aqueous KCl. The peaks with m/z of 744.7, 780.6 and 816.6 correspond to [MS2 + Hg(II) – 3H] (calcd 745.1), [MS2 + Hg(II) + Cl – 2H] (calcd 781.0) and [MS2 + Hg(II) + 2Cl – H] (calcd. 817.0), respectively. Bottom: Calculated mass spectrum for the species of interest.
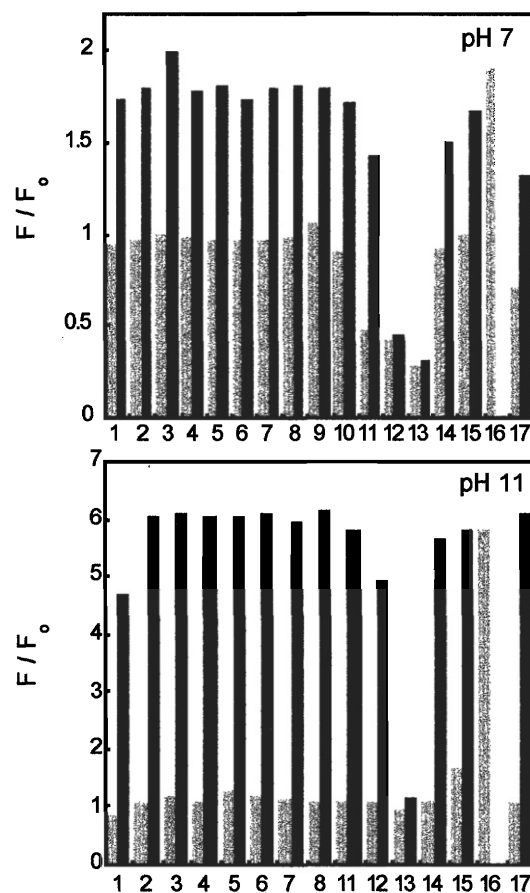
Figure 9.8. Selectivity of MS3 for Hg(II) at pH 7 (50 mM PIPES, 100 mM KCl) and pH 11 (50 mM CABS, 100 mM KCl). The light bars represent the fluorescence emission of a solution of MS3 and 67 equiv of the cation of interest: 1, Li(I); 2, Na(I); 3, Rb(I); 4, Mg(II); 5, Ca(II); 6, Sr(II); 7, Ba(II); 8, Cr(III); 9, Mn(II); 10, Fe(II); 11, Co(II); 12, Ni(II); 13, Cu(II); 14, Zn(II); 15, Cd(II); 16, Hg(II); 17, Pb(II). The dark bars show the fluorescence change that occurs upon addition of 67 equiv of Hg(II) to the solution containing MS3 and the cation. No additional Hg(II) was added to 16. The concentration of MS3 was 1 μM and excitation was provided at 500 nm. The response (F) is normalized with respect to the emission of the free dye (F_o).
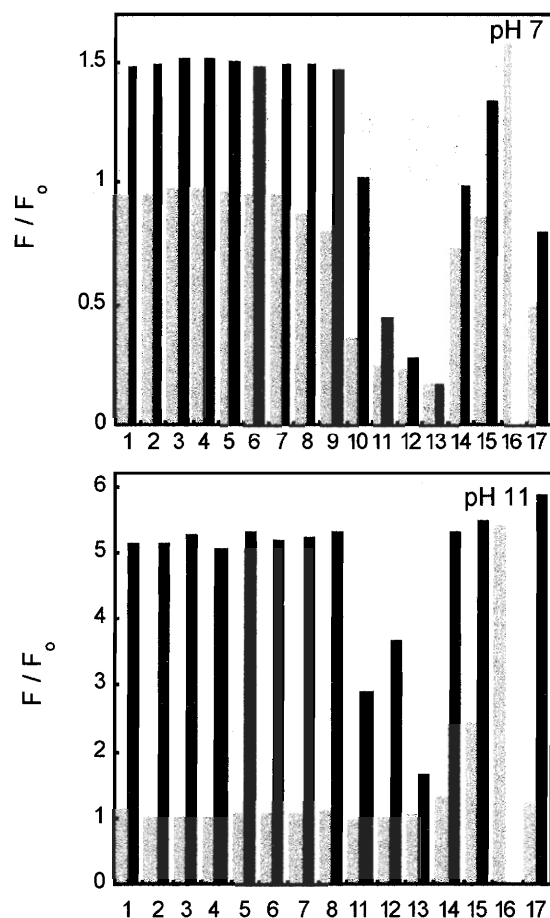
Figure 9.9. Selectivity of MS2 for Hg(II) at pH 7 (50 mM PIPES, 100 mM KCl) and pH 11 (50 mM CABS, 100 mM KCl). The light bars represent the fluorescence emission of a solution of MS3 and 67 equiv of the cation of interest: 1, Li(I); 2, Na(I); 3, Rb(I); 4, Mg(II); 5, Ca(II); 6, Sr(II); 7, Ba(II); 8, Cr(III); 9, Mn(II); 10, Fe(II); 11, Co(II); 12, Ni(II); 13, Cu(II); 14, Zn(II); 15, Cd(II); 16, Hg(II); 17, Pb(II). The dark bars represent show the fluorescence change that occurs upon addition of 67 equiv of Hg(II) to the solution containing MS2 and the cation. No additional Hg(II) was added to 16. The concentration of MS2 was 1 μM and excitation was provided at 500 nm. The response (F) is normalized with respect to the emission of the free dye (F_o).
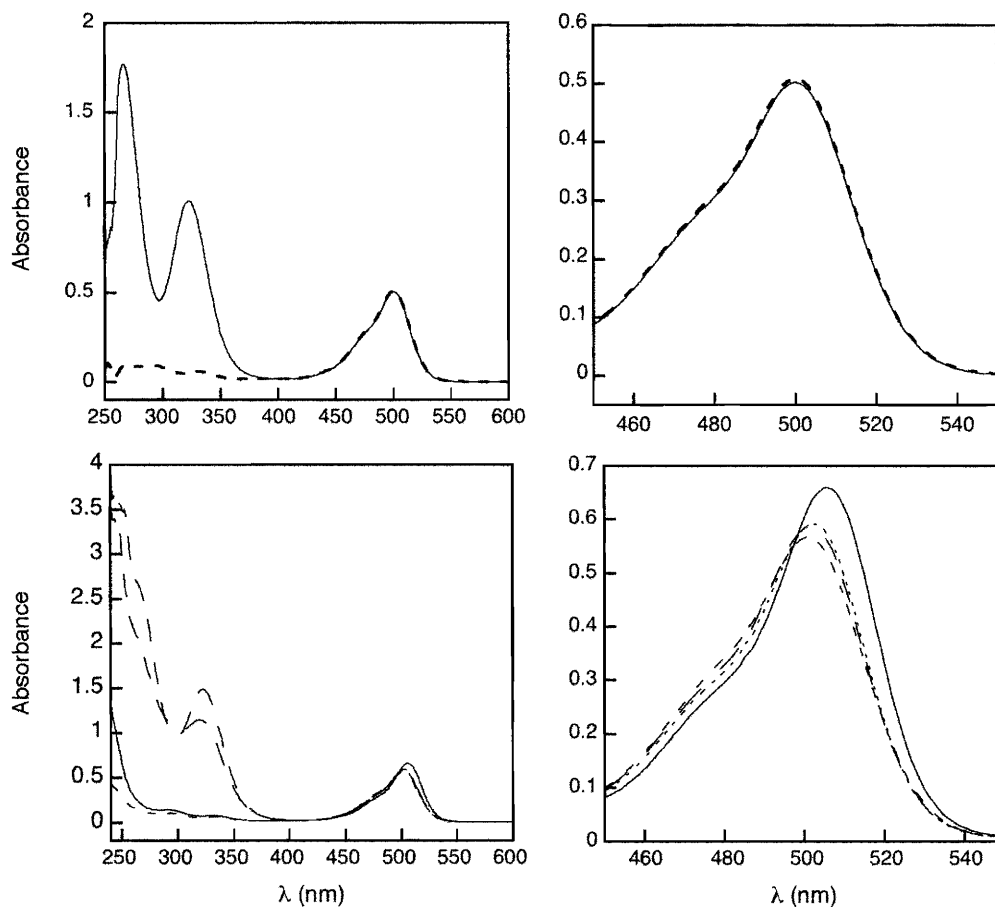
Figure 9.10. Reversibility of Hg(II) binding to MS2 following addition of KI. Top: Addition of Hg(II) to MS2 in 50 mM PIPES, 100 mM KI, pH 7. Dotted line: 10 μM MS2. Solid line: +10 equiv of Hg(II). The absorption bands centered at 265 and 321 nm indicate $[HgI_4]^{2-}$ formation. The right panel is an enlargement of the 550-450 nm range. No change in MS2 absorption occurs. Bottom: Reversibility of Hg(II) binding to MS2 by addition of KI (50 mM PIPES, 100 mM KCl, pH 7). Dotted line: 10 μM MS2. Solid line: +10 equiv of Hg(II). Dashed lines: +excess KI (~3.3 and ~10 mM). The bands at 265 and 321 nm indicate $[HgI_4]^{2-}$. The right panel is an enlargement of the 550 to 450 nm range, which illustrates the reversibility of Hg(II) binding with KI addition.

Chapter 10

MS4, A Seminaphthofluorescein-Based Chemosensor
for the Ratiometric Detection of Hg(II)

Introduction

Heavy metal ion pollution is a serious global problem that adversely affects human and environmental health. Inorganic mercury is one contaminant of particular concern.[1] Sources of mercury in the environment vary and stem from both natural and anthropogenic origins. The Mediterranean Sea, for example, has vast cinnabar deposits, which leach mercury into its water.[2] In the United States, ~87% of mercury emissions result from solid waste incineration and the combustion of fossil fuels.[3] Gold mining, cement production, forest fires and volcanic activity are additional sources of mercury pollution.[3,4] Upon entering freshwater and marine ecosystems, bacteria convert inorganic mercury to methylmercury, which reaches the top of the food chain and bioaccumulates in large predatory fish, such as tuna and swordfish, consumed by humans.[5-7] Methylmercury is lipophilic, readily absorbed through the GI tract, and a potent neurotoxin.[8,9] A number of neurological problems have been associated with mercury intoxication and are perhaps best exemplified by the various manifestations of Minamata Disease, the widespread poisioning of Japanese citizens that occurred during the 1950s following the release of methylmercury into the Agano River.[10,11]

Given these environmental and toxicological concerns, providing new mercury detection strategies for use in aqueous solution and in biological samples is an important goal. Fluorescence offers one convenient route to metal ion sensing since it only requires simple instrumentation and provides high temporal resolution.[12] Some desirable features of a fluorescent metal ion probe for use in environmental and/or biological monitoring include a positive and selective fluorescence response for the analyte of interest, high selectivity and sensitivity for the analyte, reversibility and water solubility. A significant body of research on fluorescence-based Hg(II) detection exists and this work includes a fiber optic,[13] a functionalized lipid bilayer,[14] and an array of fluoroionophores.[15-26] Some of these systems are incompatible with aqueous solution, have modest selectivity for Hg(II), are irreversible or given fluorescence turn-off upon

Hg(II) coordination. Recently, several systems that give fluorescence enhancement in aqueous solution have been reported. A mercury sensor based on the 3-aminonaphthalimide chromophore was described that gives substantial and selective fluorescence turn-on upon Hg(II) coordination in aqueous solution.[26] In Chapters 8 and 9, we presented fluorescein based sensors MS1-3, which afford positive and highly selective turn-on responses to Hg(II) at neutral pH.[27,28] Fluorescence-based Hg(II) sensing strategies that utilize biomolecules[29-31] have also been documented.

Most fluorescent Hg(II) ionophores are intensity-based and rely on either fluorescence turn-off or turn-on following Hg(II) coordination. Ratiometric fluorescence detection, which compares fluorescence intensity ratios at two different wavelengths before and following analyte recognition, offers another means of Hg(II) sensing. It is arguably more useful in quantification and in applications involving heterogeneous samples.[32] In what follows, we present the preparation and photophysical characterization of the ratiometric Hg(II) sensor MS4. This chemosensor is based on an asymmetrical seminaphthofluorescein platform,[33] gives a positive fluorescence response upon Hg(II) coordination and offers single-excitation dual-emission ratiometric detection of Hg(II) in aqueous solution. This work represents our entry into ratiometric Hg(II) sensing and design improvement, in addition to more detailed characterization of the seminaphthofluorescein platform itself, are included in Chapter 11. To the best of our knowledge, MS4 was the first ratiometric Hg(II) sensor documented that operates in aqueous solution. Shortly thereafter, a ratiometric chemodosimeter for Hg(II) was reported that operates in mixed aqueous/organic solution.[34]

Experimental Section

Reagents. Anhydrous methanol, chloroform, 1,2-dichloroethane (DCE) and NaB(OAc)$_3$H were purchased from Aldrich and used as received. The seminaphtho-

fluorescein carboxaldehyde,[33] 1, and aniline ligand,[35] 2, were synthesized according to literature procedures.

Methods. Analytical thin layer chromatography (TLC) was performed by using Merck F254 silica gel 60 plates (0.2 mm thickness). Whatman silica gel-60 plates (1 mm thickness) were used as the solid phase for preparative TLC. NMR spectra were collected on a Varian 300 MHz spectrophotometer operating at 283 K and the spectra were referenced to internal standards. IR spectra were collected on an Avatar FTIR instrument. High-resolution mass spectrometry was performed by staff in the MIT Department of Chemistry Instrumentation Facility.

2-{11-[(2-{[(Ethylsulfanylethyl)pyridin-2-ylmethylamino]methyl}phenylamino)-methyl]-10-hydroxy-3H-benzo[c]-xanthen-7-yl}benzoic acid (3, mercury sensor 4, MS4). To 4.5 mL of 7:2 $CHCl_3$/MeOH were added 1 (33 mg, 0.081 mmol) and 2 (24 mg, 0.081 mmol), and the resulting purple-brown solution was stirred at room temperature for 24 h. The reaction mixture was diluted with 1 mL of DCE and $NaB(OAc)_3H$ (27 mg, 0.13 mmol) was added. The reaction was stirred for an additional 24 h. The solvents were removed under reduced pressure and preparative TLC on silica gel (9:1 $CHCl_3$/MeOH) afforded pure MS4 as a deep purple solid (23 mg, 42%). TLC R_f = 0.55 (9:1 $CHCl_3$/MeOH); mp > 325 °C, dec. ^1H NMR (CD_3OD, 300 MHz) δ 0.84 (3H, t), 1.92 (2H, q), 2.22-2.46 (4H, m), 3.46-3.65 (4H, m), 4.70 (2H, q), 6.65 (1H, t), 6.73 (1H, d), 6.87 (1H, dd), 7.03-7.11 (3H, m), 7.17 (2H, t), 7.21-7.30 (5H, m), 7.38 (1H, t), 7.60-7.69 (2H, m), 8.15 (1H, dd), 8.21 (2H, m). FTIR (KBr, cm^{-1}) 3423 (s, br), 3050 (m), 2921 (m), 2849 (m), 1759 (w), 1639 (s), 1606 (m), 1587 (m), 1504 (w), 1469 (m), 1433 (m), 1374 (m), 1328 (w), 1297 (w), 1232 (w), 1148 (m), 1115 (m), 1071 (m), 1042 (m), 1000 (w), 878 (w), 846 (w), 830 (w), 791 (w), 748 (w), 697 (w), 672 (w), 607 (w), 523 (w). HRMS (ESI) Calcd [M + H]$^+$, 696.2527; Found, 696.2520.

Spectroscopic Reagents and Methods. All aqueous solutions were prepared as described in Chapters 8 and 9. DMSO stock solutions (1 mM) of MS4 were prepared,

stored as aliquots at −25 °C, and thawed in the dark immediately before use. These DMSO solutions are stable for ~60 min at room temperature and should be frozen and thawed only once. With the exception of the pH study, measurements were conducted in aqueous buffer and in the present of 100 mM KCl with the pH maintained at 7 (50 mM PIPES buffer), 8 (50 mM HEPES buffer), 9 (50 mM CHES buffer) or 11 (50 mM CAPS buffer). Fluorescence spectra were collected with a Photon Technology International (Lawrenceville, NJ) Quanta Master 4L-format scanning spectrofluorimeter equipped with a LPS-220B 75 W xenon lamp and power supply, A-1010B lamp housing with integrated igniter, switchable 814 photon-counting/analog PMT detector, and a MD-5020 motor driver. A Cary 1E double-beam scanning spectrophotometer was used for optical absorption spectroscopy. All samples were contained in quartz cuvettes (Starna) with a 1-cm path length. Circulating water baths were used to maintain the temperature at 25 ± 1 °C for all data acquisition.

Spectroscopic Measurements. With the exception of the pK_a titration, which was performed in duplicate, all measurements were repeated a minimum of three times. Quantum yields were determined relative to fluorescein in 0.1 N NaOH ($\Phi = 0.95$)[36] and the reported values are the averages of four independent measurements. Extinction coefficients were determined over a concentration range of 10 to 1 μM and are the averages of four independent titrations. Procedural details for other experiments are available in Chapters 2 and 8.

Results and Discussion

Synthesis of MS4. Seminaphthofluorescein dye MS4 was synthesized according to methodology previously developed in our laboratory for the assembly of asymmetrical fluorescein-based[37] sensors and for the seminaphthofluorescein-based[33] ratiometric Zn(II) sensor ZNP1 (Figure 10.1). These synthetic routes involve Schiff base condensation of an asymmetric fluorophore containing an aldehyde functional group

and an aniline-derivatized ligand moiety designed for metal ion complexation, followed by imine reduction under mild conditions. Scheme 10.1 illustrates the final reaction step that afforded sensor MS4 from previously reported compounds **1** and **2**, although the full synthesis of this sensor involves nine steps started from commercially available materials. Schiff base condensation of **1** and **2** followed by reduction of the intermediate imine using $NaB(OAc)_3H$ afforded pure MS4 as a deep purple solid in 42% yield after preparative TLC on silica gel using $CHCl_3/MeOH$.

Spectroscopic Properties of MS4. The optical absorption spectrum of MS4 exhibits a maximum centered at 548 nm ($\varepsilon = 9{,}000\ M^{-1}cm^{-1}$) at pH 8 (50 mM HEPES, 100 mM KCl). Introduction of excess Hg(II) to a solution of MS4 causes a slight 3 nm blue-shift and an increase in visible absorption with a maximum at 545 nm ($\varepsilon = 11{,}200\ M^{-1}cm^{-1}$). Upon excitation at 499 nm, the emission spectrum of apo MS4 shows two local maxima centered at 524 and 613 nm. Free MS4 has a quantum yield of 0.05 (50 mM HEPES, 100 mM KCl, pH 8, excess EDTA). Coordination of MS4 to Hg(II) causes the quantum yield to double to 0.10. Enhancement of the 613 nm emission band occurs upon Hg(II) coordination with no discernible intensity change at 524 nm as shown in Figure 10.2. This feature allows for single-excitation dual-emission ratiometric detection of Hg(II) by comparison of the intensity ratios at 624 and 524 nm ($\lambda_{624}/\lambda_{524}$) before and after Hg(II) binding. At pH 8 the ($\lambda_{624}/\lambda_{524}$) ratio increases ~4-fold upon Hg(II) coordination. The extent of the ratiometric enhancement shows pH dependence. An ~2-fold ratiometric change is observed at pH 7 (50 mM PIPES, 100 mM KCl) and, in more alkaline solution, an ~8-fold ratiometric change occurs (50 mM CAPS, 100 mM KCl, pH 11).

Effect of pH on Free MS4 Emission. Given the seminaphthofluorescein platform, which exhibits pH-dependent emission, and the presence of an aniline nitrogen atom that can function as a photoinduced electron transfer (PET) switch,[12] we anticipated that the emission of free MS4 would be pH dependent. The effect of pH on the integrated emission of apo MS4 is shown in Figure 10.3. A small change occurs between pH ~12

and ~6, the integrated emission rising by only ~10% across this range. This fluorescence increase is less than those observed for fluorescein based sensors such as MS1, which also include an aniline-derivatized ligand. One possible explanation for the relatively stable fluorescence of MS4 between pH 6-12 is that the protonation of both the aniline nitrogen atom, which would enhance fluorescence due to quenching of PET,[37,38] and the seminaphthofluorescein platform to form the monoanion, which quenches fluorescence, overlap in this regime. The fluorescence of MS4 is quenched at low pH, the fluorescence decrease having a pK_a value of 4.7 (Figure 10.3). This change is attributed to protonation of the seminaphthofluorescein platform and formation of a non-fluorescent species.

Figure 10.4 depicts the effect of pH on the emission profile of MS4. From pH ~12 to pH ~10, MS4 emission is essentially insensitive to pH and exhibits two local maxima centered at 524 and 613 nm. Upon further lowering of the pH to ~6.5, the emission decreases and increases at 620 and 558 nm, respectively. Below pH ~6.5, MS4 displays one emission maximum centered at 524 nm. Subsequent lowering of the pH causes fluorescence quenching with no shift in the wavelength of maximum emission.

MS4 Fluorescence Dependence on Chloride Ion. The fluorescence response of MS4 to Hg(II) depends on the presence of chloride ion. Figure 10.5 depicts the effect of chloride ion on the emission of the MS4:Hg(II) complex at pH 8. In the absence of chloride ion, a modest ~2-fold change in ($\lambda_{624}/\lambda_{524}$) occurs due to increased emission centered at 613 nm. Addition of aqueous KCl or NaCl to a solution of MS4 and Hg(II) causes the intensity of the 613 nm band to increase immediately following mixing (Figure 10.5). The presence of chloride ion has no effect on the emission of the free dye. As described in previous chapters, analogous behavior was observed for fluorescein-based MS1-3 and we tentatively propose that formation of a Hg—Cl bond or ion pairing may alter the coordination geometry around the Hg(II) center and thereby modulate the emission of the Hg(II)-fluorophore complex.

Selectivity of MS4 for Hg(II). The selectivity of MS4 for Hg(II) over a number of environmentally relevant alkali and alkaline earth metals, divalent transition metals and the Group 12 metals Zn(II) and Cd(II) was investigated at pH 8 in the presence of 100 mM KCl (50 mM HEPES, 100 mM KCl), and the results are depicted in Figure 10.6. The ratiometric fluorescence response of MS4 for Hg(II) is unaffected by millimolar concentrations of Na(I), Li(I), Rb(I), Mg(II), Ca(II), Sr(II), and Ba(II). Introduction of 50 equiv of the divalent first-row transition metals Mn(II), Fe(II), Co(II), Ni(II) and Cu(II) produces no significant change in the emission spectrum of MS4 and the chemosensor is selective for Hg(II) over the former three metal ions. MS4 preferably binds to Ni(II) and Cu(II), in agreement with our previous studies of the analogous ZS sensor,[35] which indicated that Zn(II) cannot displace Ni(II) or Cu(II) from the ZS coordination sphere, and in accord with previous work on thioether-based ligands.[39] Modest ratiometric enhancement occurs upon Zn(II) and Cd(II) coordination to MS4, but Hg(II) readily displaces Zn(II) and Cd(II) from the MS4 coordination sphere. The positive response of MS4 to Hg(II) also occurs in the presence of 20 equiv of Cr(III) and Pb(II). Scheme 10.2 illustrates the proposed mode of Hg(II) coordination to MS4 at neutral pH.

Binding of MS4 to Hg(II) is reversible by addition of N',N',N'',N''-tetra(2-picolyl)ethylenediamine (TPEN), as illustrated in Figure 10.7. Introduction of TPEN to a solution of the MS4:Hg(II) complex causes the fluorescence emission decreases to background levels immediately. Subsequent addition of Hg(II) resulted in fluorescence enhancement and this off/on behavior can be repeated at least three times.

Comparison of MS4 to Related Group 12 Metal Ion Sensors. As part of our research initiative to design and utilize water-soluble fluorescent Hg(II) sensors, we initially prepared and characterized mercsury sensor MS1, shown in Figure 10.1. Coordination of MS1 to Hg(II) alleviates PET quenching and results in ~5-fold fluorescence enhancement in aqueous chloride-containing solutions at neutral pH. Sensor MS4 differs from MS1 in both the nature of the aniline-derivatized ligand and

the fluorophore platform. Regarding the former, a comparison of the selectivity of MS1 and MS4 shows that substitution of a thioether moiety by a pyridyl group abrogates Hg(II) selectivity over Ni(II). As described in Chapter 9, MS2 and MS3, fluorescein-based Hg(II) sensors containing pyridyl-amine-thiol ligands, also prefer Ni(II) over Hg(II) in neutral buffered solution. These comparisons suggest that maintaining a soft, sulfur-rich coordination sphere is critical for achieving selectivity for Hg(II) over Ni(II).

The second difference between MS1 and MS4 is the fluorophore platform, the choice of which is important for obtaining desired photophysical properties. A potential advantage of this seminaphthofluorescein platform used in the assembly of MS4 is its ability to offer ratiometric metal ion detection, which is presumably useful for studies involving quantification and inhomogeneous samples. MS1 and MS4 have similar quantum yields. Because of the relatively high extinction coefficient of fluorescein, MS1 exhibits considerably greater brightness ($\Phi \times \varepsilon$) than MS4.

In a previous investigation of fluorescein-based dyes appended with pyridyl-amine-thioether ligands, one of which is shown in Figure 10.1, selectivity for Hg(II) over Zn(II) was observed.[35] Fluorescence enhancement, however, did not occur upon Hg(II) coordination to ZS1-3 and only a slight increase in emission was observed for ZS4 (50 mM PIPES, 100 mM KCl, pH 7). This behavior contrasts with that of sensor MS4, which gives a positive fluorescence response to Hg(II). These results indicate that proper matching of fluorophore and ligand moieties is necessary to achieve the desired fluorescence response.

Summary and Perspectives

Sensor MS4 gives single-excitation dual-emission ratiometric detection of Hg(II) in aqueous solution. This sensor exhibits Hg(II) selectivity analogous to that of MS2 and MS3, which suggests that maintaining a sulfur-rich coordination sphere is necessary to maintain selectivity for Hg(II) over Ni(II). The design of MS4 opened the door for

ratiometric Hg(II) detection in aqueous solution and, in the final chapter of this thesis, we look to improve upon this particular platform.

References

(1)   Boening, D. W. *Chemosphere* **2000**, *40*, 1335-1351.

(2)   Renzoni, A. Z., F.; Franchi, E. *Environ. Res.* **1998**, *77*, 68-72.

(3)   Mercury Update: Impact on Fish Advisories. EPA Fact Sheet (EPA-823-F-01-011); EPA, Office of Water: Washington, DC, 2001.

(4)   Malm, O. *Environ. Res.* **1998**, *77*, 73-78.

(5)   Nendza, M.; Herbst, T.; Kussatz, C.; Gies, A. *Chemosphere* **1997**, *35*, 1875-1885.

(6)   Harris, H. H.; Pickering, I. J.; George, G. N. *Science* **2003**, *301*, 1203.

(7)   Hardy, S.; Jones, P. *J. of Chromatography A* **1997**, *791*, 333-338.

(8)   Clarkson, T. W.; Magos, L.; Myers, G. J. *New Eng. J. Med.* **2003**, *249*, 1731-1737.

(9)   Bolger, P. M.; Schwetz, B. A. *New Eng. J. Med.* **2002**, *347*, 1735-1737.

(10)   Takeuchi, T.; Murikawa, N.; Matsumoto, H.; Shiraishi, Y. *Acta Neuropathol.* **1962**, *2*, 40-57.

(11)   Harada, M. *Crit. Rev. Toxicol.* **1995**, *25*, 1-24.

(12)   de Silva, A. P.; Guarante, H. Q. N.; Gunnlaugsson, T.; Huxley, A. J. M.; McCoy, C. P.; Rademacher, J. T.; Rice, T. E. *Chem. Rev.* **1997**, *97*, 1515-1566.

(13)   Zhang, X.-B.; Guo, C.-C.; Li, Z.-Z.; Shen, G.-L.; Yu, R.-Q. *Anal. Chem.* **2002**, *74*, 821-825.

(14)   Sasaki, D. Y.; Padilla, B. E. *Chem. Commun.* **1998**, 1581-1582.

(15)   Chae, M.-Y.; Czarnik, A. W. *J. Am. Chem. Soc.* **1992**, *114*, 9704-9705.

(16)   Czarnik, A. W. *Acc. Chem. Res.* **1994**, *27*, 302-308.

(17)   Yoon, J.; Ohler, N. E.; Vance, D. H.; Aumiller, W. D.; Czarnik, A. W. *Tetrahedron Lett.* **1997**, *28*, 3845-3848.

(18)   Winkler, J. D.; Bowen, C. M.; Michelet, V. *J. Am. Chem. Soc.* **1998**, *120*, 3237-3242.

(19)   Hennrich, G.; Sonnenschein, H.; Resch-Genger, U. *J. Am. Chem. Soc.* **1999**, *121*, 5073-5074.

(20)   Prodi, L.; Bargossi, C.; Montalti, M.; Zaccheroni, N.; Su, N.; Bradshaw, J. S.; Izatt, R. M.; Savage, P.
         B. *J. Am. Chem. Soc.* **2000**, *122*, 6769-6770.

(21)   Sakamoto, H.; Ishikawa, J.; Nakao, S.; Wada, H. *Chem. Commun.* **2001**, 2395-2396.

(22)   Rurack, K.; Kollmannsberger, M.; Resch-Genger, U.; Daub, J. *J. Am. Chem. Soc.* **2000**, *122*, 968-969.

(23)   Kim, J. H.; Hwang, A.-R.; Chang, S.-K. *Tetrahedron Lett.* **2004**, *45*, 7557-7561.

(24)   Metivier, R.; Leray, I.; Valeur, B. *Chem. Eur. J.* **2004**, *10*, 4480-4490.

(25)   Descalzo, A. B.; Martínez-Máñez, R.; Radeglia, R.; Rurack, K.; Soto, J. *J. Am. Chem. Soc.* **2003**, *125*,
         3418-3419.

(26)   Guo, X.; Qian, X.; Jia, L. *J. Am. Chem. Soc.* **2004**, *126*, 2272-2273.

(27)   Nolan, E. M.; Lippard, S. J. *J. Am. Chem. Soc.* **2003**, *125*, 14270-14271.

(28)   Nolan, E. M.; Racine, M. E.; Lippard, S. J. *Inorg. Chem.* **2006**, *45*, 2742-2749.

(29)   Chen, P.; He, C. *J. Am. Chem. Soc.* **2004**, *126*, 728-729.

(30)   Ono, A.; Togashi, H. *Angew. Chem. Int. Ed* **2004**, *43*, 4300-4302.

(31)   Thomas, J. M.; Ting, R.; Perrin, D. M. *Org. Biomol. Chem.* **2004**, *2*, 307-312.

(32)   Tsien, R. Y.; Peonies, M. *Trend Biochem. Sci.* **1986**, *11*, 450-455.

(33)   Chang, C. J.; Jaworski, J.; Nolan, E. M.; Sheng, M.; Lippard, S. J. *Proc. Nat. Acad. Sci. USA* **2004**,
         101, 1129-1134.

(34)   Liu, B.; Tian, H. *Chem Commun* **2005**, 3156-3158.

(35)   Nolan, E. M.; Lippard, S. J. *Inorg. Chem.* **2004**, *43*, 8310-8317.

(36)   Brannon, J. H.; Magde, D. *J. Phys. Chem.* **1978**, *82*, 705-709.

(37)   Nolan, E. M.; Burdette, S. C.; Harvey, J. H.; Hilderbrand, S. A.; Lippard, S. J. *Inorg. Chem.* **2004**, *43*,
         2624-2635.

(38)   Burdette, S. C.; Frederickson, C. J.; Bu, W.; Lippard, S. J. *J. Am. Chem. Soc.* **2003**, *125*, 1778-1787.

(39)   Cooper, T. H.; Mayer, M. J.; Leung, K.-H.; Ochrymowycz, L. A.; Rorabacher, D. B. *Inorg. Chem.*
         1992, *31*, 3796-3804.
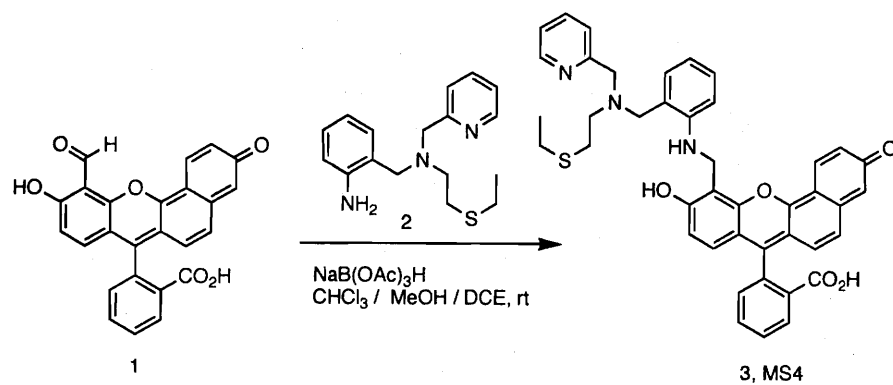
Scheme 10.1. Synthesis of MS4.
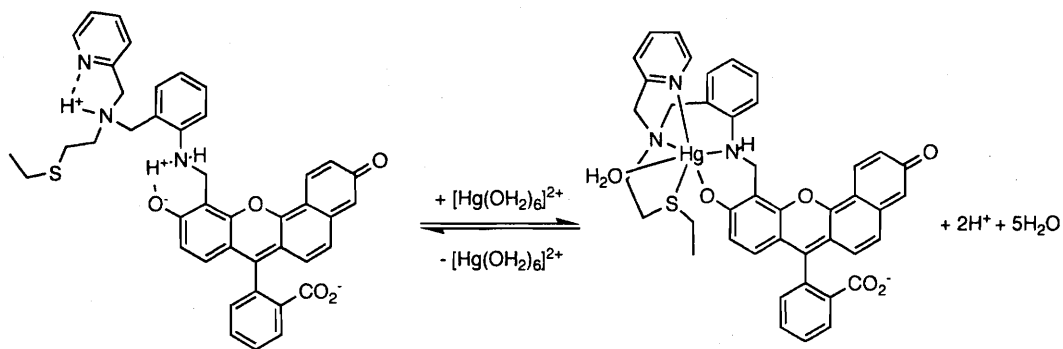
Scheme 10.2. Proposed Hg(II) coordination to MS4 in aqueous solution at pH 8.
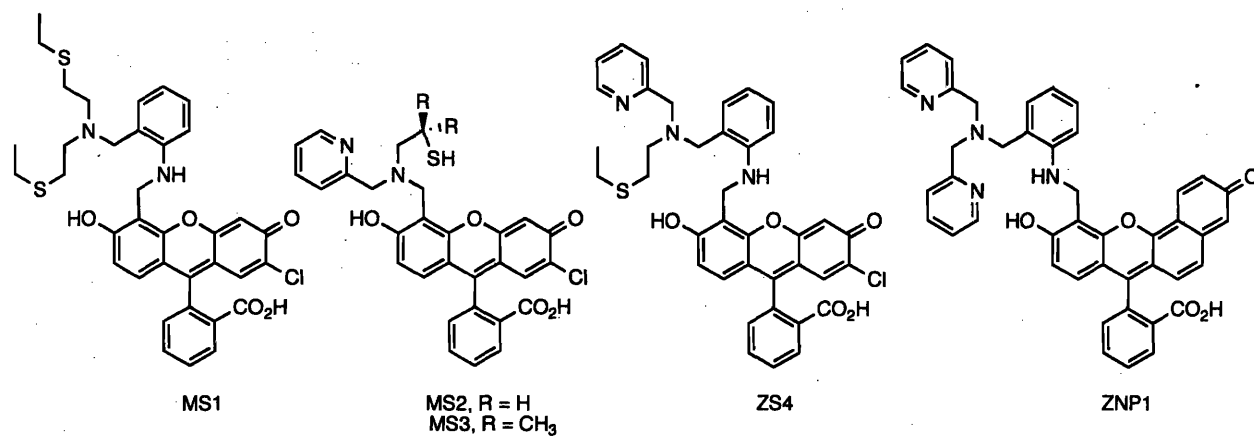
Figure 10.1. Sensors MS1, MS2, MS3, ZS4 and ZNP1. The fluorescein-based MS and ZS4 are turn-on chemosensors for Hg(II) and Zn(II), respectively, that operate in neutral buffered aqueous solution. Sensor ZNP1 utilizes a seminaphthofluorescein platform and affords single-excitation dual-emission ratiometric detection of Zn(II).
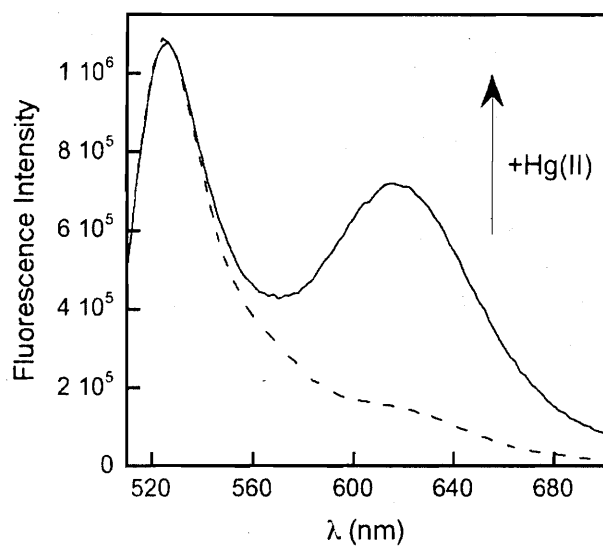
Figure 10.2. Fluorescence response of MS4 to Hg(II) at pH 8 (50 mM HEPES, 100 mM KCl). The dotted and solid lines represent free and Hg(II)-bound MS4, respectively.
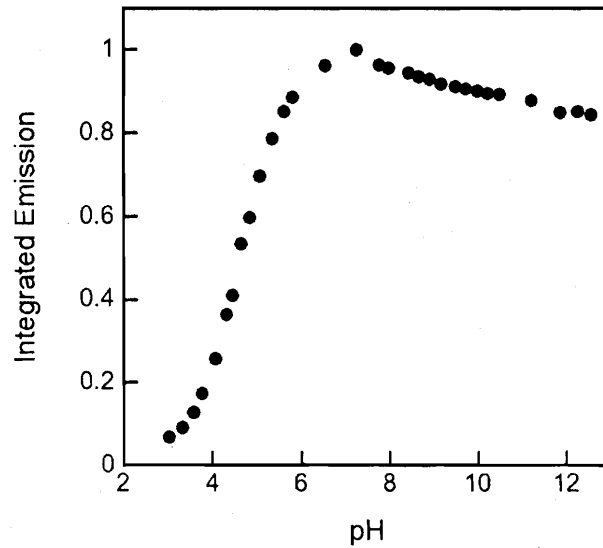
Figure 10.3. Effect of pH on the integrated emission of apo MS4. A 5 µM solution of MS4 was prepared in 10 mM KOH, 100 mM KCl (pH ~12) and the emission spectrum recorded. The pH was decreased in increments of ~0.25 by addition of 6, 2, 1 or 0.5 N HCl and the emission spectrum collected at each point. The spectra were integrated and the data normalized and plotted against pH. Excitation was provided at 499 nm.
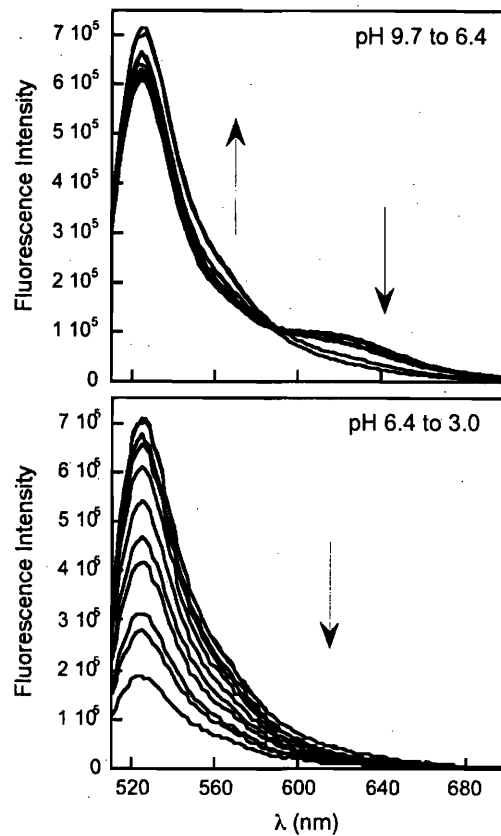
Figure 10.4. Effect of pH on the emission spectrum of apo MS4. These spectra correspond to the experiment described in the caption of Figure 10.3. Only negligible changes in the emission spectrum occur between pH 12.5 and 9.7 (data not shown).
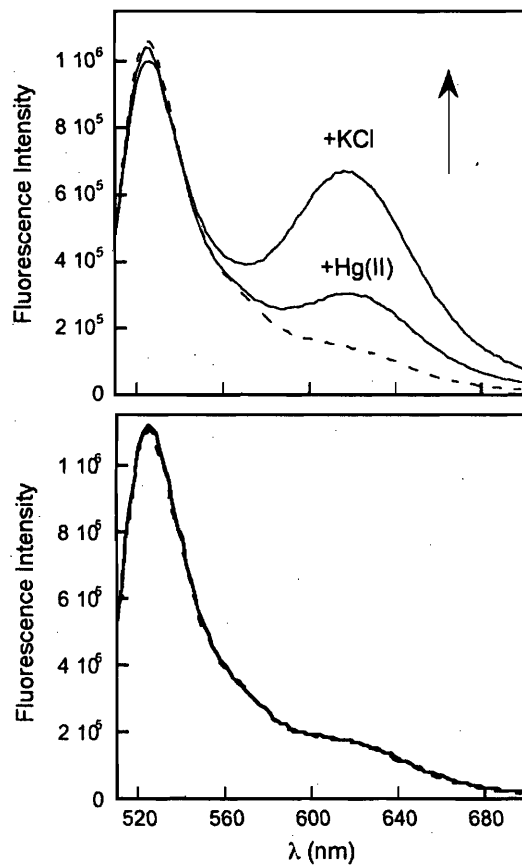
Figure 10.5. Effect of chloride ion on the emission of the MS4:Hg(II) complex. Top plot: The dotted line is the emission spectra of 10 μM MS4. The solid lines indicate the emission response of MS4 to 10 equiv of Hg(II) in the absence and presence of chloride ion (50 mM HEPES, pH 8). Substantial fluorescence increase is observed upon addition of an aliquot of 1 M KCl (final concentration = 100 mM). A similar change is observed following addition of 1 M NaCl, which indicates that the cation is not a factor. Bottom plot: Addition of KCl to free MS4 in 50 mM HEPES at pH 8. The presence of chloride ion has no effect on the emission of the free dye. Excitation was provided at 499 nm.
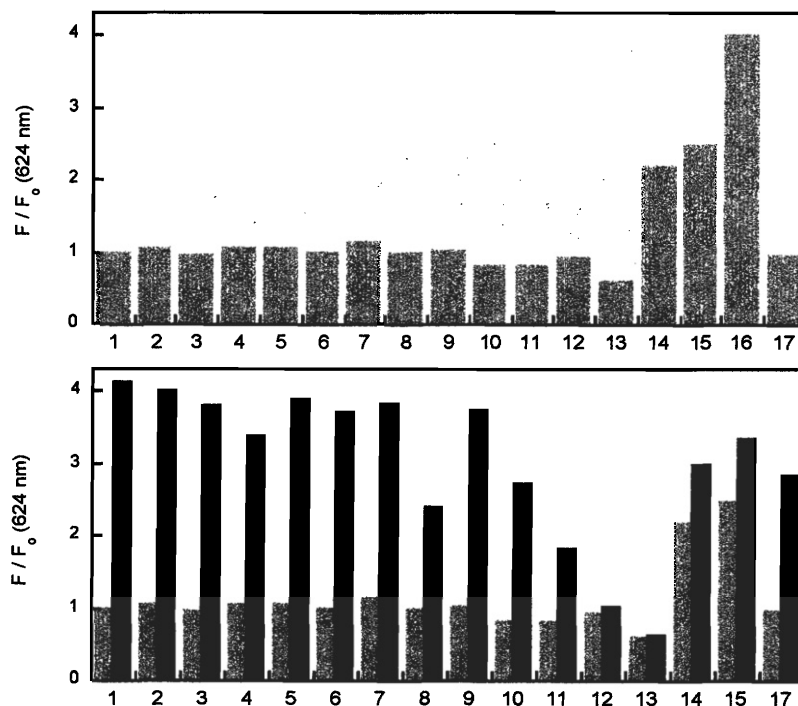
Figure 10.6. Fluorescence response of MS4 to selected cations in aqueous solutions at pH 8 (50 mM HEPES, 100 mM KCl). The response is normalized with respect to the emission of the free dye at 624 nm (F_o). Top plot: emission change at 624 nm upon addition of each cation: 1, Li(I); 2, Na(I); 3, Rb(I); 4, Mg(II); 5, Ca(II); 6, Sr(II); 7, Ba(II); 8, Cr(III); 9, Mn(II); 10, Fe(II); 11, Co(II); 12, Ni(II); 13, Cu(II); 14, Zn(II); 15, Cd(II); 16, Hg(II); 17, Pb(II). With the exception of Cr(III) and Pb(II), where 20 equiv of cation were added to minimize precipitation at pH 8, each solution contained 50 equiv of the cation of interest. Bottom plot: response of MS4 to 50 equiv Hg(II) in the presence of the selected cations. The grey bars are identical to those in the top plot and the black bars represent the change in emission at 624 nm that occurs upon introduction of Hg(II) to the solutions containing MS4 and the selected cation. No discernable change in emission at 524 nm was observed. The response of MS4 is also unaffected by 100 mM Li(I), Na(I), Mg(II), Ca(II), 10 mM Rb(II), Sr(II), and 1 mM Ba(I). Excitation was provided at 499 nm and [MS4] = 5 μM.
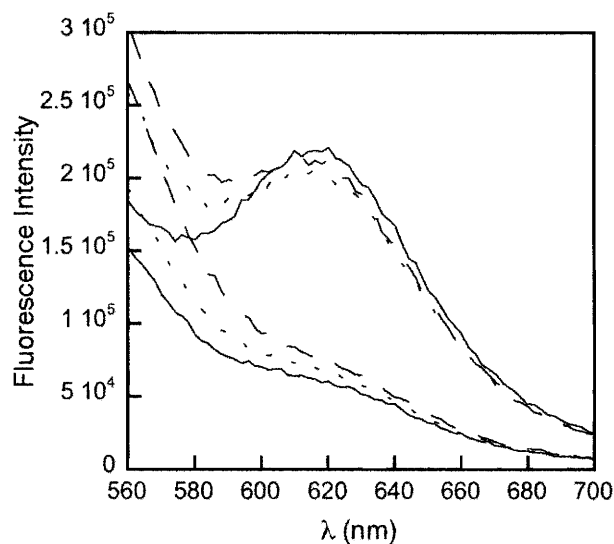
Figure 10.7. Reversibility of MS4 binding to Hg(II) by addition of TPEN. The top set of solid, dotted and dashed lines indicate the emission resulting from three additions of Hg(II) to a solution of MS4 at pH 8 (50 mM HEPES, 100 mM KCl) before and after the addition of TPEN. The bottom set of solid, dotted and dashed lines represent the emission of free MS4 before addition of Hg(II) and after successive additions of Hg(II) and TPEN. The concentration of MS4 was 5 μM and 10 equiv of Hg(II) or TPEN were added. The increasing emission ca. 560 nm is due to TPEN emission (control data not shown).

Chapter 11

Turn-On and Ratiometric Mercury Sensing in Water
with a Seminaphthofluorescein-Based Probe

Introduction

Mercury pollution is a serious environmental problem with harmful consequences for human health and ecology.[1] Natural and anthropogenic origins of mercury contamination include volcanic emissions and forest fires, fossil fuel combustion, solid waste incineration, chemical manufacturing and mining practices.[2,3] Once released into the atmosphere, Hg(0) is oxidized to Hg(II), which enters both fresh and marine water systems and accumulates in aquatic sediments. Bacteria that live in these sediments can methylate "inorganic" mercury to form methylmercury, which is very lipophilic and neurotoxic. Methylmercury works its way up the food chain and ultimately accumulates in predatory fish and whales, many of which are consumed by humans.[4,5] Mercury concentrations found in fish reach ppm levels, significantly higher than the 2 ppb upper limit for inorganic Hg(II) in drinking water mandated by the United States EPA.[2] Since methylmercury is readily absorbed by the GI tract and can cross the blood-brain barrier, consumption of contaminated fish is a serious concern.[6] Chronic exposure to low levels of mercury has been correlated with motion disorders, developmental and cognitive defects. The neurological problems caused by overt poisoning, although extremely rare, are best characterized by case studies of citizens of Minamata, Japan who ingested mercury-tainted water and fish in the early 1900s following its release into the Agano River by a chemical company.[7,8]

Research addressing the environmental and toxicological aspects of mercury pollution is warranted given our increased awareness of its deleterious effects. This work requires tools and tactics for detecting mercury in water and tissue samples. Techniques such as cold vapor atomic fluorescence spectroscopy and HPLC are commonly used in the analytical laboratory setting for determining mercury concentrations in water samples and fish. Although highly sensitive, these methods require sophisticated apparatus and, in some cases, complicated sample preparation. An alternative route involves using colorimetric[9-15] or fluorescent[16-28] sensors, which

often give an immediate response to the analyte that can be observed visually or with simple instrumentation. Furthermore, these sensing methods can easily be adapted for measurements in the field through the development of portable fiber optic devices or, as in the case of Pb^{2+} detection, commercial indicators for household use. Several such colorimetric- and fluorescence-based Hg(II) detectors have been reported and strategies addressing the latter method include dosimeters,[29-32] polymers,[33] nanoparticles,[34,35] biomolecules,[36-38] a lipid bilayer,[39] and many small-molecule fluorescent switches that either turn off or on following Hg(II) complexation. Despite this recent blossoming of new detection strategies, only a few of these fluorescent probes give a positive signal for Hg(II) in aqueous solution and only two reports of ratiometric Hg(II) detection exist.[25,32] Attempts to test the performance of small-molecule fluoresecent Hg(II) detectors in real-world situations are limited.[28]

In what follows, we present the synthesis and characterization of mercury sensor 5 (MS5), depicted in Scheme 11.1. This sensor is based on a seminaphthofluorescein chromophore, which affords red-shifted emission relative to fluorescein and other commonly used reporters and achieves both turn-on and ratiometric Hg(II) detection in aqueous solution. Because of the thioether-rich ligand moiety, MS5 binds Hg(II) rapidly and reversibly, and it affords selectivity for Hg(II) over many competing species, including those found in natural water samples.

Experimental Section

Reagents. Anhydrous methanol, chloroform and dichloromethane were purchased from Aldrich and used as received. Sodium triacetoxyborohydride, sodium borohydride and mercury(II) perchlorate hydrate were also obtained from Aldrich. N',N',N'',N''-tetra(2-picolyl)ethylenediamine (TPEN) was purchased from Invitrogen. The aniline derivatized ligand 1[24] and seminaphthofluorescein aldehyde 2[40] were synthesized according to previously published procedures. A portion of 2-(10-hydroxy-

3-phenylamino-methyl-3*H*-benzo[c]xanthen-7-yl)benzoic acid,[40] **3**, a precursor to **2**, was further purified by preparative TLC on silica gel (20:1 CHCl₃/MeOH) for use in spectroscopic studies. **CAUTION: The isolated Hg(II) complexes described below contain perchlorate ion, which can detonate explosively and without warning. Although we encountered no problems with the isolated compounds, all due precautions must be taken.**

Methods. All materials and methods employed are as detailed in Chapter 9.

2-{11-[(2-{[Bis-(2-ethylsulfanylethyl)amino]methyl}phenylamino)methyl]-3-hydroxy-10-oxo-10*H*-benzo[c]xanthen-7-yl}benzoic acid (4, MS5). To 9 mL of a 7:2 CHCl₃/MeOH mixture were added **1** (71 mg, 0.17 mmol) and **2** (52 mg, 0.17 mmol), which gave a red-brown solution that was stirred at room temperature. After 24 h, 3 mL of DCE and NaB(OAc)₃H (40 mg, 0.19 mmol) were added and the reaction was stirred for an additional 24 h, during which time it became wine-colored. The solvents were removed under reduced pressure and preparative TLC on silica gel (20:1 CHCl₃/MeOH) yielded pure MS5 as a purple solid (38 mg, 32%). TLC R_f = 0.64 (9:1 CHCl₃/MeOH); mp > 300 °C, dec. ¹H NMR (CD₃OD, 500 MHz) δ 0.84 (3H, t), 1.92 (2H, q), 2.22-2.46 (4H, m), 3.46-3.65 (4H, m), 4.70 (2H, q), 6.65 (1H, t), 6.73 (1H, d), 6.87 (1H, dd), 7.03-7.11 (3H, m), 7.17 (2H, t), 7.24-7.40 (5H, m), 7.38 (1H, t), 7.60-7.69 (2H, m), 8.15 (1H, d), 8.21 (2H, m). FTIR (KBr, cm⁻¹) 3428 (w, br), 3052 (w), 2957 (w), 2921 (w), 2857 (w), 2800 (w), 1752 (w), 1641 (m), 1600 (s), 1563 (m), 1504 (m), 1470 (s), 1443 (s), 1378 (m), 1339 (m), 1309 (m), 1251 (m), 1143 (m), 1091 (m), 1070 (w), 1047 (w), 1004 (w), 961 (w), 931 (w), 878 (w), 862 (w), 827 (w), 789 (w), 748 (w), 726 (w), 704 (w), 678 (w), 643 (w), 613 (w), 596 (w), 526 (w), 448 (w). HRMS (ESI) Calcd [M − H]⁻, 691.2306; Found, 691.2325.

2-[2-{[Bis-(2-ethylsulfanylethyl)amine]methyl}phenylamine)methyl]phenol (5, L). Salicylaldehyde (376 mg, 3.08 mmol) and *N*-(2-aminobenzyl)-3,9-dithia-6-azaundecane (**1**, 914 mg, 3.07 mmol) were combined in 40 mL of EtOAc and stirred for 10 h at room temperature. The solvent was removed in vacuo to yield an orange-yellow oil. The oil

was dissolved in 30 mL of DCE and NaB(OAc)$_3$H (700 mg, 3.33 mmol) was added. The reaction was stirred overnight at room temperature, diluted with 40 mL of dichloromethane, washed with saturated brine (3 x 80 mL) and then with water (1 x 80 mL). The organic portion was dried over MgSO$_4$ and the solvent was removed to yield an orange oil. Chromatography on Al$_2$O$_3$ with a solvent gradient (2:1 hexanes/EtOAc to 100% EtOAc) afforded the product as an orange oil (812 mg, 65%). TLC R$_f$ = 0.60 (Al$_2$O$_3$, 2:1 hexanes/EtOAc). ^{1}H NMR (CDCl$_3$, 300 MHz) δ 1.17 (6H, t), 2.37 (4H, q), 2.58 (4H, m), 3.70 (2H, s), 4.48 (2H, s), 6.78-6.91 (4H, m), 7.05 (1H, dd), 7.16-7.23 (3H, m). ^{13}C NMR (CDCl$_3$, 125 MHz) δ 14.79, 25.88, 29.34, 47.65, 53.02, 58.35, 113.18, 116.33, 119.25, 123.64, 124.71, 128.57, 128.90, 130.29, 147.42, 157.16. FTIR (NaCl disk, cm^{-1}) 3217 (s, br), 3043 (s), 2963 (s), 2924 (s), 2869 (s), 2845 (s), 2817 (s), 2717 (w), 1606 (s), 1588 (s), 1508 (s), 1490 (s), 1455 (s), 1375 (m), 1314 (m), 1294 (m), 1250 (m), 1149 (w), 1119 (m), 1102 (m), 1050 (m), 1036 (m), 983 (m), 932 (m), 855 (m), 839 (m), 753 (s), 723 (m), 629 (w), 565 (w), 531 (w). HRMS (ESI) Calcd [M + H]$^+$, 405.2029; Found, 405.2019.

2-(10-Hydroxy-3-oxo-11-phenylaminomethyl-3*H*-benzo[c]zanthen-7-yl)benzoic acid (6). Aniline (5.0 mg, 0.054 mmol) and aldehyde **2** (22 mg, 0.054 mmol) were combined in 5 mL of 3:2 CHCl$_3$/MeOH and the resulting brown-purple solution was stirred overnight at room temperature, during which time it turned brown-red. The reaction was cooled to 0 °C, diluted with 1 mL of DCE, and NaBH$_4$ (15 mg, 0.40 mmol) was added with stirring. The reaction immediately turned dark purple. The reaction was warmed to room temperature with stirring and, after 4 h, the solvent was removed under reduced pressure, which gave a dark purple residue. Preparative TLC of the crude material on silica gel (20:1 CHCl$_3$/MeOH) afforded pure **5** as a purple solid (18 mg, 69%). TLC R$_f$ = 0.45 (silica, 9:1 CHCl$_3$/MeOH); mp > 300 °C, dec. ^{1}H NMR (CD$_3$OD, 500 MHz) δ 4.70 (2H, q), 6.67 (2H, m), 6.84 (1h, d), 6.92 (3H, m), 7.00 (1H, dd), 7.12 (2H, t), 7.17 (2H, d), 7.60 (2H, qd), 8.09 (1H, dd), 8.33 (1H, d). FTIR (KBr, cm^{-1}) 3430 (m, br), 2952 (m), 2925 (m), 285 (m), 1632 (s), 1611 (s), 1601 (s), 1562 (m), 1470 (s), 1445 (s), 1428

(s), 1380 (s), 1316 (m), 1290 (w), 1250 (w), 1143 (m), 1101 (m), 1070 (w), 1045 (w), 992 (w), 934 (w), 919 (w), 880 (w), 824 (m), 790 (w), 763 (w), 728 (w), 693 (w), 676 (w), 641 (w), 618 (w), 599 (w), 523 (w). HRMS (ESI) Calcd [M + H]$^+$, 488.1492; Found, 488.1470.

[Hg(L)](ClO$_4$)$_2$·CH$_3$OH (7). A portion (9.7 mg, 0.024 mmol) of Hg(ClO$_4$)$_2$·H$_2$O was suspended in 0.5 mL of MeOH to which a solution of **L** (30 mg, 0.088 mmol) in 0.5 mL of MeOH was added dropwise as the solution turned yellow. The solution was sonicated for 5 min and filtered. Colorless thin needle crystals suitable for X-ray crystallographic analysis formed over the course of 48 h by vapor diffusion of Et$_2$O into the reaction at room temperature (11.5 mg, 48%). FTIR (KBr, cm^{-1}) 3546 (m, br), 3192 (m, br), 3069 (w), 2969 (w), 2932 (w), 2865 (w), 2700 (w), 2605 (w), 2552 (w), 2026 (w), 1969 (w), 1934 (w), 1609 (m), 1594 (m), 1496 (m), 1460 (s), 1421 (m), 1384 (m), 1368 (m), 1300 (w), 1258 (m), 1218 (w), 1188 (w), 1102 (s, br), 1084 (s), 1055 (s), 1047 (s), 1004 (m), 932 (m), 922 (m), 910 (m), 884 (m), 870 (m), 853 (m), 832 (w), 801 (w), 770 (s), 729 (w), 717 (w), 672 (w), 622 (s), 575 (w), 543 (w), 521 (w), 494 (w), 484 (w), 468 (w). HRMS (ESI) Calcd [M–2(ClO$_4$)–2H]$^+$, 605.1518; Found, 605.1578. Anal: Calcd for C$_{22}$H$_{32}$Cl$_2$HgN$_2$O$_8$S$_2$: C, 32.86; H, 4.01; N, 3.48. Found: C, 31.99; H, 3.80; N, 3.35.

[Hg(TPEN)](ClO$_4$)$_2$ (8). A portion (7.8 mg, 0.195 mmol) of Hg(ClO$_4$)$_2$·H$_2$O in 1 mL of MeOH was added dropwise to a solution of TPEN (7.9 mg, 0.184 mmol) in 1 mL of MeOH. The solution was mixed with a pipette and filtered. Colorless rod-like crystals suitable for X-ray crystallography formed over the course of 48 h from vapor diffusion of Et$_2$O into the reaction at room temperature, which were washed with Et$_2$O (4 x 3 mL) and dried (8.6 mg, 57%). ^{1}H NMR (DMSO-d_6, 500 MHz) δ 3.09 (4H, s), 3.89 (4H, q), 4.12 (4H, q), 7.52 (6H, q), 7.97 (3H, m), 8.60 (3H, d). FTIR (KBr, cm^{-1}) 3426 (w, br), 3108 (w), 3078 (w), 3033 (w), 2963 (w), 2936 (w), 2911 (w), 2985 (w), 2859 (w), 1600 (m), 1572 (w), 1486 (m), 1455 (m), 1441 (m), 1386 (w), 1335 (w), 1374 (w), 1318 (w), 1300 (w), 1294 (w), 1263 (m), 1221 (w), 1159 (w), 1130 (m), 1095 (vs), 1067 (s), 1051 (s), 1015 (m), 991 (m), 939 (w), 930 (w), 897 (w), 866 (w), 840 (w), 802 (m, br), 764 (m), 734 (w), 723 (w), 646 (w), 621

(m), 584 (w), 499 (w). HRMS (ESI) Calcd M^{2+}, 313.1040; Found, 313.1054. Anal: Calcd for $C_{26}H_{28}Cl_2HgN_2O_8$: C, 37.90; H, 3.42; N, 10.20. Found: C, 37.96; H, 3.23; N, 10.25.

X-ray Crystallographic Studies. Single crystals were mounted on the tips of glass fibers coated with paratone-N oil and cooled to −100 °C under a stream of N_2 maintained by a KRYO-FLEX low-temperature apparatus. Intensity data were collected on a Bruker APEX CCD diffractometer with graphite-monochromated Mo Kα radiation (λ = 0.71073 Å), controlled by a Pentium-based PC running the SMART software package.[41] Data collection and reduction protocols are described elsewhere.[42] The structures were solved by direct methods using the SAINTPLUS and SHELXTL software packages.[43,44] Empirical absorption corrections were applied by using the SADABS program,[45] and the structures were checked for higher symmetry by using the PLATON software.[46] All non-hydrogen atoms were located and their positions refined with anisotropic thermal parameters by least-squares cycles and Fourier syntheses. In general, hydrogen atoms were assigned to idealized positions and given thermal parameters equivalent to either 1.5 (methyl hydrogen atoms) or 1.2 (all other hydrogen atoms) times the thermal parameter of the carbon atom to which they were attached. One ordered methanol molecule was located in the structure of **7**.

Spectroscopic Materials and Methods. All aqueous solutions were prepared as detailed in Chapters 8 and 9. DMSO stock solutions of **3** (2 mM, deep red-purple), **6** (1 mM, deep purple) and MS5 (1 mM, deep purple) were prepared, partitioned into 40 μL aliquots, stored at -25 °C and thawed in the dark immediately before use. The DMSO stock solutions of MS5 are stable for ~1 h at room temperature in the dark and the occurrence of a brown color indicates decomposition. We note that the DMSO stock solutions of seminaphthofluorescein-based sensors are, in all cases studied thus far, less stable than those of the fluroescein-based analogs. All measurements, excluding the pH titrations and anion experiments, were conducted in buffered aqueous solution with a buffer concentration of 50 mM and 100 mM with KCl. Quantum yields were measured

relative to fluorescein in 0.1 N NaOH (Φ = 0.95).[47] Experimental details for the spectroscopic measurements are available in Chapters 2 and 9.

Fluorescence spectra were collected by using a Photon Technology International (Lawrenceville, NJ) Quanta Master 4L-format scanning spectrofluorimeter equipped with an LPS-220B 75-W xenon lamp and power supply, A-1010B lamp housing with integrated igniter, switchable 814 photon-counting/analog PMT detector, and a MD-5020 motor driver. Optical absorption spectra were collected on a Cary 1E double-beam scanning spectrophotometer. All samples were contained in 3 mL quartz cuvettes (Starna) and maintained at 25 °C by means of a circulating water bath.

Water Collection. Natural water samples from the Charles River (Cambridge, MA), Onondaga Lake (Upstate NY) and the harbor in Newburyport, MA were collected in August 2005 and stored in polypropylene bottles. The water samples were filtered through 0.2 μm filters to remove particulate and insoluble organic matter prior to use.

Results and Discussion

Design and Synthesis of MS5. Several considerations influenced the design of sensor MS5. The seminaphthofluorescein platform can afford single-excitation dual-emission ratiometric metal ion detection[25,40] and was therefore chosen to afford both a ratiometric response to Hg(II) and red-shifted emission relative to fluorescein-based MS sensors. Ligand 1 was previously employed in the synthesis of MS1[24] and confers better selectivity for Hg(II) than metal-coordinating groups with fewer sulfur donors (Figure 11.1). Scheme 11.1 shows the final reaction in the nine-step assembly of MS5. Combination of aniline 1 and aldehyde 2 in mixed $CHCl_3$/MeOH followed by imine reduction using NaB(OAc)$_3$H afforded sensor MS5 in 32% yield as a dark purple powder following preparative TLC on silica gel (20:1 $CHCl_3$/MeOH). The aniline-derivatized seminaphthofluorescein, 6, was prepared according to an analogous route

with $NaBH_4$ employed as the reducing agent as shown in Scheme 11.2 and obtained in 69% yield following purification by preparative TLC.

Because the MS5 synthesis is only practical on a small scale and crystal structures of fluorescein-containing compounds are difficult to obtain, we prepared a salicylaldehyde-based model for MS5, **L**, shown in Scheme 11.1, for use in X-ray crystallographic modeling studies. Ligand **L** was obtained in 65% yield as an off-white solid following Schiff base condensation of salicylaldehyde with aniline **1** and reduction in DCE using $NaB(OAc)_3H$ as the reducing agent.

Effect of pH on MS5 Absorption and Emission. Like fluorescein, semi-naphthofluorescein (SNAFL)[48] chromophores exhibit pH-sensitive absorption and emission. Understanding this behavior, at least qualitatively, is a prerequisite for studies of more complex systems such as MS5. Although these chromophores have been used in several applications, including pH measurements in vivo[49] and in the fabrication of fiber optic devices,[50] very few studies of their solution chemistry have been undertaken. A quick SciFinder search for "seminaphthofluorescein" yielded only 39 hits and "SNAFL" only 115, compared to over 58,000 hits generated by "fluorescein." We therefore investigated the effect of pH on the emission and absorption properties of the seminapthofluorescein platform itself (**3**, depicted in Figure 11.2), which was prepared during the synthesis of aldehyde **1**, under our experimental conditions. Figure 11.3 portrays a pH titration performed in the presence of 100 mM KCl and monitored by fluorescence spectroscopy for **3** (λ_{ex} = 525 nm). The emission of **3** is maximized at pH > 10 (λ_{max} = 595 nm) and lowering the pH to ~5 causes the emission intensity to decrease substantially with a blue shift in the wavelength of maximum emission to 564 nm. A plot of integrated emission vs. pH shows that this transition has a pK_a ~8. Figure 11.4 includes representative absorption and emission spectra for **3** obtained in solutions buffered in the pH range of 7 – 11. At pH 11 (50 mM CAPS, 100 mM KCl), the optical absorption spectrum of **3** exhibits one dominant band in the visible region centered at

549 nm. Lowering the pH into the neutral range results in a spectrum with two local maxima with relatively weak and approximately equal intensity entered at 499 and 528 nm (50 mM PIPES, 100 mM KCl, pH 7). This behavior is similar to that observed for fluorescein upon protonation of the phenol group. When excited at 499 nm, a solution of 3 at pH 11 exhibits two local emission maxima at 528 and 612 nm with the latter having significantly greater intensity. Lowering of the pH causes a decrease in emission at 612 nm and an isoemissive point at 564 nm.

The pH-dependent absorption and emission profiles of MS5 show some similarities and differences to those of 3. Figure 11.5 includes representative optical absorption spectra for free MS5 at pH > 7, which are generally analogous to those of 3 and indicate that the phenol group is protonated at pH 7. Wavelengths of maximum absorption and extinction coefficients are included in Table 11.1. In contrast, the pH-dependent emission profile of MS5 also reflects the presence of the proton-sensitive aniline unit, and is illustrated in Figure 11.6. At pH ~12, MS5 emission is characterized by two bands of similar intensity centered at ca. 524 and 624 nm (10 mM KOH, 100 mM KCl), and little variation occurs with lowering of the pH to ~9. As the pH is further reduced to ~6, the intensity of the 524 nm band increases dramatically whereas the 624 nm band decreases with an isoemissive point at 600 nm. Based on the data included in Figures 11.3 and 11.4, we propose the decrease in the 624 nm band results from protonation of the seminaphthofluorescein phenol group. This transition occurs at lower pH for MS5 relative to the seminaphthofluorescein platform itself, which could result from hydrogen bonding of the aniline proton to the phenol. Essentially no change in the emission of 3 occurs below 560 nm, which contrasts with the rise in the 524 nm band of MS5 as the pH is lowered to ~6. Based on our studies of fluorescein-based systems, protonation of the aniline moiety occurs in this pH range. We therefore attribute the increase in emission intensity at 524 nm to aniline protonation. Complete fluorescence quenching occurs upon further acidification.

Figure 11.6 includes a plot of integrated emission vs. pH for MS5. A ~1.6-fold increase in integrated emission occurs between pH ~10 and ~6, which can be fit to a pK_a value of 7.8 and is attributed to aniline protonation. The magnitude of this change is typical of aniline-based systems, although the pK_a is slightly higher (MS1, $pK_a = 7.1$). Quenching occurs at pH < 6 ($pK_a = 5.2$) because of seminaphthofluorescein protonation. This transition is tentatively assigned to protonation of the carboxylate.

The quantum yields for apo MS5 as a function of pH were determined and are listed in Table 11.1. At pH 7, the quantum yield is 0.018 and its magnitude decreases to ca. 0.01 at pH ≥ 8. This trend agrees with the pH titration curve shown in Figure 12.6. Compound 6 was prepared to investigate the effect of the aniline moiety itself on seminaphthofluorescein emission. We find that 6 and MS5 have similar quantum yields (6, $\Phi_{free} = 0.014$, pH 8; MS5, $\Phi_{free} = 0.010$, pH 8), which indicates that the aniline unit, not the tertiary amined-based ligand fragment as suggested by others,[51] is the chief contributor to fluorescence quenching. Analogous behavior was previously detailed for fluorescein-based systems (Chapter 2). Overall, the brightness ($\Phi \times \varepsilon$) of MS5 increases with pH and varies from ca. 50 (pH 7) to 310 (pH 11) $M^{-1}cm^{-1}$.

Response of MS5 to Hg(II) and pH Dependence. Preliminary investigations indicated that the response of MS5 to Hg(II) is pH-dependent; relevant spectroscopic data are listed in Table 11.1. Optical absorption spectra for the MS5:Hg(II) complex at pH ≥ 7 are shown in Figure 11.5 and are generally analogous to those of 3 and free MS5. A direct comparison of the UV-vis spectra for MS5 before and after Hg(II) addition at different pH values is given in Figure 11.7. The changes observed in the optical absorption spectra of MS5 resulting from Hg(II) coordination at pH ≥ 9 are similar to those observed for fluorescein-based MS1, where a blue-shift and increase in molar absorptivity occur and are attributed to Hg(II) coordination to MS5 dianion.

The fluorescence response of MS5 to Hg(II) is also pH dependent as illustrated in Figure 11.8 and quantum yield values are given in Table 11.1. At pH 7, an ~2.5-fold

fluorescence enhancement occurs following Hg(II) coordination (Φ_{Hg} = 0.032). Approximately 3.5-fold turn-on occurs at pH 7.5 and ~5.8-fold enhancement at pH 8 (Φ_{Hg} = 0.064). The integrated emission increases by more than 7-fold at pH 9 (Φ_{Hg} = 0.086). Significant increases in both the 524 and 624 nm emission bands contribute to the fluorescence enhancement at pH ≤ 8. At higher pH, Hg(II) coordination gives rise to only negligible changes in the 524 nm band with dramatic increases at 624 nm. This feature affords single-excitation dual-emission ratiometric detection of Hg(II) at pH > 8 by comparison of the ratio of the 524 and 624 nm ($\lambda_{624}/\lambda_{524}$) bands before and after Hg(II) addition (λ_{ex} = 499 nm). For instance, an ~6.2-fold ratio change occurs at pH 8.5 and an ~8-fold enhancement occurs at pH 11.

The extinction coefficient and quantum yield data (Table 11.1) indicate that the greater dynamic range observed at high pH results from a brighter Hg(II) complex rather than a reduction in background emission. We propose that the underlying cause of this behavior involves the protonation state of the seminaphthofluorescein platform. At pH 7, the seminaphthofluorescein platform is protonated and monanionic, hence less emissive. Coordination of Hg(II) to MS5 does not promote deprotonation of this moiety and seminaphthofluroescein anion emission is observed following Hg(II) coordination. At pH > 8, the seminaphthofluorescein is predominantly in its dianionic and most emissive form. The aniline unit effectively quenches emission and Hg(II) coordination restores bright emission from seminaphthofluorescein dianion.

Hg(II) Binding Studies. MS5 is a MS1 analog, which binds Hg(II) with 1:1 stoichiometry. These sensors each afford a N_2S_2O chelate and, in this work, we prepared a salicylaldehyde-based model complex, L, as shown in Scheme 11.1 with the aim of discovering the likely mode of Hg(II) coordination to these sensors. X-ray quality crystals were obtained by vapor diffusion of Et_2O into a methanolic solution containing a 1:1 L/Hg(ClO_4)$_2$ mixture at room temperature. Tables 11.2 and 11.3 contain crystallographic data from the refinement as well as selected bond lengths and angles,

respectively, for **7**. The ORTEP diagram of **7** in Figure 11.9 shows that the Hg(II) center is five-coordinate with a distorted trigonal bipyramidal geometry. The protonated phenol oxygen and tertiary amine nitrogen atoms are in the axial positions and the two thioether donors and protonated aniline nitrogen in the equatorial plane. The Hg—S(1) and Hg—S(2) bond lengths are 2.5075(10) and 2.4864(10) Å, respectively. These values are within in the general range of 2.47 – 2.73 Å for Hg(II)—S(thioether) bonds and indicate strong Hg—S interactions.[52] The Hg—O bond length is 2.569(3) Å, indicating a relatively weak interaction. The Hg—N(2) distance, 2.434(3) Å, is similar in to that of the Hg—N bond in [(beppa)Hg(ClO$_4$)]ClO$_4$ where beppa = {N,N-bis(2-ethylthio)ethyl-N-[(6-pivaloylamido-2-pyridyl)methyl]-amine[53] and the Hg—N bond of relevance is 2.412(6) Å. The structure of **7** is similar to that of [(beppa)Hg(ClO$_4$)]ClO$_4$, although the latter is described as six-coordinate because of a weak interaction between the Hg(II) center and one perchlorate ion (3.01 Å). The beppa ligand itself provides a distorted trigonal bipyramidal arrangement, where the tertiary amine and amide oxygen atoms are in the axial positions and two thioether donors and a pyridyl nitrogen in the equatorial plane. Scheme 11.3 illustrates our proposed mode of Hg(II) coordination to MS5 in aqueous solution at neutral and basic pH. Although our modeling study suggests a five-coordinate geometry, we presume that a water molecule or hydroxide ion will be at least weakly associated with, if not bound to, the Hg(II) center in aqueous solution.

Binding of MS5 to Hg(II) is readily reversible. Addition of TPEN to solutions of MS5 and Hg(II) causes an immediate fluorescence decrease to within ~20% of the baseline value (Figure 11.10). This behavior is expected given that TPEN has an apparent K_d of ~10^{-25} M for Hg(II) at 100 mM ionic strength.[54] Further addition of Hg(II) and TPEN shows that this on/off behavior can be cycled a number of times. To elucidate the structure of the Hg:TPEN complex, X-ray quality crystals were grown from vapor diffusion of Et$_2$O into a methanolic solution of 1:1 TPEN/Hg(ClO$_4$)$_2$. The ORTEP diagram of **8** is given in Figure 11.9; Tables 11.2 and 11.3 contain crystallographic data

and select geometric parameters. The Hg(II) center is six-coordinate and one perchlorate ion is associated with the Hg(II) center with a Hg—O(1) distance of ca. 2.72 Å. The tertiary amine Hg—N(1) and N(2) bond lengths are 2.470(5) Å and 2.434(5) Å and the bonds between the Hg(II) center and the pyridyl groups are generally shorter, ca. 2.35 Å, and similar in length to that of [(beppa)Hg(ClO$_4$)]ClO$_4$.[53] The Hg—N(5) bond is elongated by ca. 2 x 10^{-3} Å relative to the other Hg—N(pyridine) bonds and is thus relatively weakly associated with the Hg(II) center.

Selectivity of MS5 for Hg(II). Figure 11.11 depicts the results from metal ion selectivity studies of MS5. The selectivity of MS5 is analogous to that observed for MS1, with only Cu(II) interfering with the fluorescence response. Variations in pH from 7 – 9 have no effect of the observed selectivity, which is also independent of ionic strength and the choice of anion in the buffer (vide infra).

Chloride Ion Dependence. The fluorescence response of MS5 to Hg(II) depends on the presence of chloride ion. Figure 11.12 shows the fluorescence response of MS5 to Hg(II) in the presence and absence of chloride ion at pH 8. In 50 mM HEPES, an ~3-fold fluorescence enhancement occurs with Hg(II) coordination and subsequent introduction of 50 mM chloride ion immediately evokes full turn-on. Substitution of KCl with KX (X = F$^-$, Br$^-$, NO$_3^-$, OAc$^-$) shows that this effect is chloride ion specific, although acetate gives some emission enhancement.

In earlier work, we proposed that either formation of an Hg—Cl bond or ion pairing causes this fluorescence enhancement. Since we observe chloride ion dependence for Hg(II) sensors with a variety of ligand frameworks, it is somewhat difficult to rationalize how Hg—Cl bond formation would exert a conserved effect resulting in fluorescence enhancement. One hypothesis is that the Hg—Cl bond prevents formation of the Hg—O(xanthenone) bond. An electrostatic interaction between the chloride ion and the aniline proton has also been considered, which could strengthen the Hg—N

bond and further alleviate PET quenching. The specifics of this particular model would not apply to tertiary-amine-based MS2 and MS3.

We also note that the chloride ion dependence is not completely general. Several ZP sensors give fluorescence enhancement following Hg(II) coordination and the magnitude of change is independent of chloride ion in the buffer for ZP3 (tertiary amine-based switch) and ZP6 (aniline-based switch).[55] Fluo-5N, a sensor sold by Invitrogen gives fluorescence turn-on for a number of cations, including Hg(II). Its response to Hg(II) is enhanced ~2.5-fold by substituting chloride with nitrate ion (50 mM PIPES, 100 mM KX, pH 7). These experiments clearly show that buffer composition must considered when evaluating the response of fluorescent metal ion sensor.

MS5 Performance in Natural Water Samples. A long-term goal of this work is to employ fluorescent Hg(II) sensors for use in the field. This application presents a unique set of challenges, including method/device design and further studies of sensor performance in the environmental milieu. As a first step towards the latter objective, we tested the ability of MS5 to respond to Hg(II) in natural water. Samples were collected from three sources including the Charles River (Cambridge, MA) and representative data are given in Figure 11.13. In each case, MS5 shows ~5-fold or greater fluorescence turn-on after Hg(II) addition. This result indicates that MS5 is competent to detect Hg(II) in solutions with significantly more complex composition than laboratory buffer and points to potential utility in the field.

Summary and Perspectives

This chapter concludes our studies of fluorescent Hg(II) sensors that operate in aqueous solution. MS5 was designed to afford red-shifted emission, ratiometric Hg(II) detection and MS1-like selectivity. The results from our solution studies show that pH is a key factor for generating a ratiometric response to Hg(II), and we understand this behavior to reflect the requirement for the seminapthofluorescein dianion in significant

enhancement of the 624 nm emission band. It became evident during this investigation that the fundamental chemistry of seminaphthofluorescein is relatively unexplored. Detailed investigations of its protonation equilibria and fluorescence behavior in a number of different solvent systems will be especially helpful in guiding future sensor design. Lowering the value of the pK_a transitions responsible for fluorescence turn-on may be beneficial for obtaining sensors that give ratiometric response and brighter emission at neutral pH. Lastly, preliminary tests of MS5 in natural water samples indicate that its anion dependence will not be a limiting factor for practical applications.

References

(1)   Boening, D. W. *Chemosphere* **2000**, *40*, 1335-1351.

(2)   Mercury Update: Impact on Fish Advisories. EPA Fact Sheet (EPA-823-F-01-011); EPA, Office of Water: Washington, DC, 2001.

(3)   Malm, O. *Environ. Res.* **1998**, *77*, 73-78.

(4)   Nendza, M.; Herbst, T.; Kussatz, C.; Gies, A. *Chemosphere* **1997**, *35*, 1875-1885.

(5)   Renzoni, A.; Zino, F.; Franchi, E. *Environ. Res.* **1998**, *77*, 68-72.

(6)   Clarkson, T. W.; Magos, L.; Myers, G. J. *New Eng. J. Med.* **2003**, *349*, 1731-1737.

(7)   Harada, M. *Crit. Rev. Toxicol.* **1995**, *25*, 1-24.

(8)   Takeuchi, T. M., N.; Matsumoto, H.; Shiraishi, Y. *Acta Neuropathol.* **1962**, *2*, 40-57.

(9)   Brümmer, O.; La Clair, J. J.; Janda, K. D. *Org. Lett.* **1999**, *1*, 415-418.

(10)   Caballero, A.; Martinez, R.; Lloveras, V.; Ratera, I.; Vidal-Gancedo, J.; Wurst, K.; Tarraga, A.; Molina, P.; Veciana, J. *J. Am. Chem. Soc.* **2005**, *127*, 15666-15667.

(11)   Choi, M. J.; Kim, M. Y.; Chang, S.-K. *Chem. Commun.* **2001**, 1664-1665.

(12)   Coronado, E.; Galan-Mascaros, J. R.; Marti-Gastaldo, C.; Palomares, E.; Durrant, J. R.; Vilar, R.;

Gratzel, M.; Nazeeruddin, M. K. *J. Am. Chem. Soc.* **2005**, *127*, 12351-12356.

(13)   Palomares, E.; Vilar, R.; Durrant, J. R. *Chem. Commun.* **2004**, 362-363.

(14)   Sancenón, F.; Martínez - Máñez, R.; Soto, J. *Chem. Commun.* **2001**, 2262-2263.

(15)   Sancenón, F.; Martínez - Máñez, R.; Soto, J. *Tetrahedron Lett.* **2001**, *42*, 4321-4323.

(16)   Kim, J. H.; Hwang, A.-R.; Chang, S.-K. *Tetrahedron Lett.* **2004**, *45*, 7557-7561.

(17)   Chen, Q.-Y.; Chen, C.-F. *Tetrahedron Lett.* **2005**, *46*, 165-168.

(18)   Yoon, J. Ohler, N. E.; Vance, D. H.; Aumiller, W. D.; Czarnik, A. W. *Tetrahedron Lett.* **1997**, *28*,

3845-3848.

(19)   Descalzo, A. B.; Martínez-Máñez, R.; Radeglia, R.; Rurack, K.; Soto, J. *J. Am. Chem. Soc.* **2003**, *125*,

3418-3419.

(20)   Guo, X.; Qian, X.; Jia, L. *J. Am. Chem. Soc.* **2004**, *126*, 2272-2273.

(21)   Hennrich, G.; Walther, W.; Resch-Genger, U.; Sonnenschein, H. *Inorg. Chem.* **2001**, *40*, 641-644.

(22)   Hennrich, G. S., H.; Resch-Genger, U. *J. Am. Chem. Soc.* **1999**, *121*, 5073-5074.

(23)   Mello, J. V.; Finney, N. S. *J. Am. Chem. Soc.* **2005**, *127*, 10124-10125.

(24)   Nolan, E. M.; Lippard, S. J. *J. Am. Chem. Soc.* **2003**, *125*, 14270-14271.

(25)   Nolan, E. M.; Lippard, S. J. *J. Mater. Chem.* **2005**, *15*, 2778-2783.

(26)   Nolan, E. M.; Racine, M. R.; Lippard, S. J. *Inorg. Chem.* **2006**, *46*, 2742-2749.

(27)   Prodi, L. B., C.; Montalti, M.; Zaccheroni, N.; Su, N.; Bradshaw, J. S.; Izatt, R. M.; Savage, P. B. *J.*

Am. Chem. Soc. **2000**, *122*, 6769-6770.

(28)   Yoon, S.; Albers, A. E.; Wong, A. P.; Chang, C. J. *J. Am. Chem. Soc.* **2005**, *127*, 16030-16031.

(29)   Yang, Y.-K.; Yook, K.-J.; Tae, J. *J. Am. Chem. Soc.* **2005**, *127*, 16760-16761.

(30)   Zhang, G.; Zhang, D.; Yin, S.; Yang, X.; Shuai, Z.; Zhu, D. *Chem. Commun.* **2005**, 2161-2163.

(31)   Chae, M.-Y.; Czarnik, A. W. *J. Am. Chem. Soc.* **1992**, *114*, 9704-9705.

(32)   Liu, B.; Tian, H. *Chem. Commun.* **2005**, 3156-3158.

(33)   Fan, L.-J.; Zhang, Y.; Jones, W. E. *Macromolecules* **2005**, *38*, 2844-2849.

(34)   Zhu, C.; Li, L.; Fang, F.; Chen, J.; Wu, Y. *Chem. Lett.* **2005**, *34*, 898-899.

(35)   Chen, B.; Yu, Y.; Zhou, Z.; Zhong, P. *Chem. Lett.* **2004**, *33*, 1608-1609.

(36)   Thomas, J. M.; Ting, R.; Perrin, D. M. *Org. Biomol. Chem.* **2004**, *2*, 307-312.

(37)   Chen, P.; He, C. *J. Am. Chem. Soc.* **2004**, *126*, 728-729.

(38)   Ono, A.; Togashi, H. *Angew. Chem. Int. Ed* **2004**, *43*, 4300-4302.

(39)   Sasaki, D. Y. P., B. E. *Chem. Commun.* **1998**, 1581-1582.

(40)   Chang, C. J.; Jaworski, J.; Nolan, E. M.; Sheng, M.; Lippard, S. J. *Proc. Nat. Acad. Sci. USA* **2004**, *101*, 1129-1134.

(41)   *SMART: Software for the CCD Detector System*, version 5.626; Bruker AXS: Madison, WI, 2000.

(42)   Kuzelka, J.; Mukhopadhyay, S.; Spingler, B.; Lippard, S. J. *Inorg. Chem.* **3004**, *43*, 1751-1761.

(43)   *SAINTPLUS: Software for the CCD Detector System*, version 5.01; Bruker AXS: Madison, WI, 1998.

(44)   *SHELXTL: Program Library for Structure Solution and MOlecular Graphics*, version 6.1; Bruker AXS: Madison, WI, 2001.

(45)   Sheldrick, G. M. *SADABS: Area-Detector Absorption Correction;* University of Gottingern: Gottingen, Germany, 2001.

(46)   Spek, A. L. *PLATON, A Multipurpose Crystallographic Tool*, Utrecht University: Utrecht, The Netherlands, 2000.

(47)   Brannon, J. H.; Magde, D. *J. Phys. Chem.* **1978**, *82*, 705-709.

(48)   Whitaker, J. E.; Haugland, R. P.; Prendergast, F. G. *Anal. Biochem.* **1991**, *194*, 330-344.

(49)   Dansen, T. B.; Pap, E. H. W.; Wanders, R. J. A.; Wortz, K. W. A. *Histochem. J.* **2001**, *33*, 65-69.

(50)   Xu, Z.; Rollins, A.; Alcala, R.; Marchant, R. E. *J. Biomed. Mat. Res.* **1998**, *39*, 9-15.

(51)   Callan, J. F.; de Silva, A. P.; Magri, D. C. *Tetrahedron* **2005**, *61*, 8551-8588.

(52)   Wright, J. G.; Natan, F. M.; MacDonnell, D. M.; Ralston, D. M.; O'Halloran, T. V. *Prog. Inorg. Chem.* **1990**, *38*, 323.

(53)   Makowska-Gryska, M. M.; Doyle, K.; Allred, R. A.; Arif, A. M.; Bebout, D. C.; Berreau, L. M. *Eur. J. Inorg. Chem.* **2005**, 822-827.

(54)   von Giorgio, A.; Hubmann, E.; Podder, N. G.; Wenk, F. *Helv. Chim. Acta* **1977**, *60*, 123-140.

(55)   Nolan, E. M.; Lippard, S. J. *Unpublished Results.*

Table 11.1. Spectroscopic Characterization of MS5[a]

pH	Absorption λ (nm); $\varepsilon \times 10^3$ (M^{-1}cm^{-1})		Emission λ (nm); Φ^{b}	
	Unbound	Hg(II)	Unbound	Hg(II)
7	500 4.5; 528, 4.5	492, 7.0; 533, 7.8	536, 611; 0.018	524, 612; 0.032
8	531, 12.2	541, 16.0	532, 612; 0.009	546, 624; 0.064
9	552, 24.2	547, 27.2	522, 620; 0.010	534, 624; 0.086
11	552, 30.8	550, 30.0	524, 621; 0.009	526, 624; 0.027

[a]All measurements were made in the presence of 100 mM KCl and with 50 mM PIPES (pH 7), 50 mM HEPES (pH 8 and 9) or 50 mM CAPS (pH 11) buffer. [b]Fluorescein (Φ = 0.95 in 0.1 N NaOH, ref. 47) was used as the standard for the quantum yield measurements.

Table 11.2. Summary of X-ray Crystallographic Data

	[Hg(L)](ClO$_4$)$_2$ ·CH$_3$OH (7)	[Hg(TPEN)](ClO$_4$)$_2$ (8)
Empirical Formula	C$_{23}$H$_{36}$Cl$_2$HgN$_2$O$_{10}$S$_2$	C$_{26}$H$_{28}$Cl$_2$HgN$_6$O$_8$
Formula Weight	836.12	824.04
Space Group	P2$_1$/n	P2$_1$/n
a, Å	11.6923(6)	9.554(4)
b, Å	15.7382(8)	21.121(8)
c, Å	16.8933(9)	14.520(6)
β, deg	106.0550(10)	103.265(7)
V, Å^3	2987.4(3)	2852(2)
Z	4	4
ρ_{calc}, g/cm^3	1.859	1.919
T, °C	-100	-100
μ(Mo Kα), mm^{-1}	0.432	5.646
θ limits, deg	1.80 – 25.00	1.73 – 25.00
total no. of data	10602	20316
no. of unique data	5109	5032
no. of params	369	388
Goodness-of-fit on F^2	1.029	1.093
Final R indices [$I>2\sigma(I)$][a,b]	R1 = 0.0282; WR^2 = 0.0690	R1 = 0.0405; wR^2 = 0.0749
R indices (all data)[a,b]	R1 = 0.0319; wR^2 = 0.0713	R1 = 0.0562; wR^2 = 0.0799
max, min peaks, e/Å^3	1.815, -0.665	1.700, -1.204

[a] $R1 = \Sigma||F_o|-F_c||/\Sigma|F_o|$

[b] $wR^2 = \{\Sigma[w(F_o^2-F_c^2)^2]/\Sigma[w(F_o^2)^2]\}^{1/2}$

Table 11.3. Summary of Selected Bond Lengths (Å) and Angles (deg)

Distances (Å) & Angles (deg)	[Hg(L)](ClO$_4$)$_2$·CH$_3$OH (7)	[Hg(TPEN)](ClO$_4$)$_2$ (8)
Hg(1)—N(1)	2.333(3)	2.470(5)
Hg(1)—N(2)	2.434(3)	2.434(5)
Hg(1)—N(3)		2.337(5)
Hg(1)—N(4)		2.572(5)
Hg(1)—N(5)		2.360(5)
Hg(1)—N(6)		2.357(5)
Hg(1)—S(1)	2.5075(10)	
Hg(1)—S(2)	2.4864(10)	
Hg(1)—O(1)	2.569(3)	
N(1)—Hg(1)—N(2)	87.82(11)	74.55(17)
N(1)—Hg(1)—S(2)	121.01(8)	
N(2)—Hg(1)—S(2)	83.48(8)	
N(I)—Hg(1)—S(1)	114.52(8)	
N(2)—Hg(1)—S(1)	83.09(8)	
S(2)—Hg(1)—S(1)	121.99(3)	
N(1)—Hg(1)—O(1)	79.12(11)	
N(2)—Hg(1)—O(1)	166.47(11)	
S(2)—Hg(1)—O(1)	100.14(8)	
S(1)—Hg(1)—O(1)	105.47(8)	
N(3)—Hg(1)—N(6)		153.11(18)
N(3)—Hg(1)—N(5)		99.54(18)
N(6)—Hg(1)—N(5)		100.74(18)
N(3)—Hg(1)—N(2)		131.58(17)
N(6)—Hg(1)—N(2)		72.45(17)
N(5)—Hg(1)—N(2)		70.53(18)
N(3)—Hg(1)—N(1)		72.97(18)
N(6)—Hg(1)—N(1)		109.31(18)
N(5)—Hg(1)—N(1)		123.49(17)
N(3)—Hg(1)—N(4)		73.57(17)
N(6)—Hg(1)—N(4)		81.85(17)
N(5)—Hg(1)—N(4)		162.29(18)
N(2)—Hg(2)—N(4)		126.37(17)
N(1)—Hg(1)—N(4)		70.86(16)
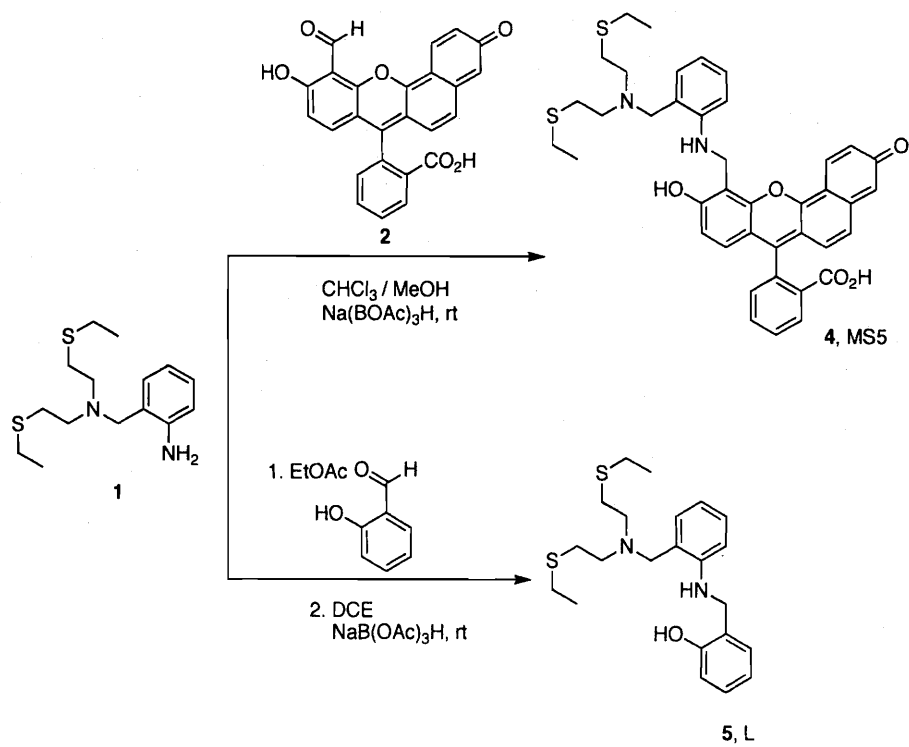
Scheme 11.1. Synthesis of MS5 and its salicylaldehyde model **L.**
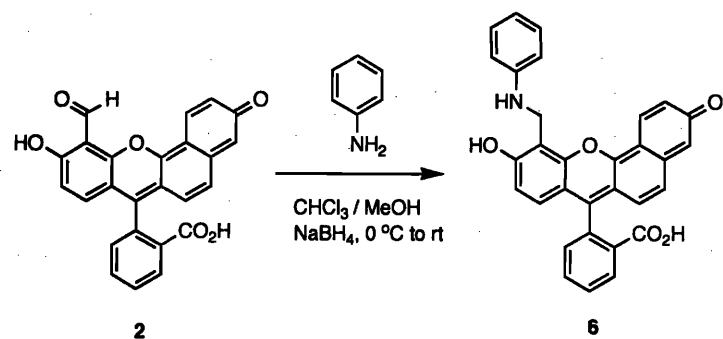
Scheme 11.2. Synthesis of aniline-derivatized seminaphthofluorescein **6**.
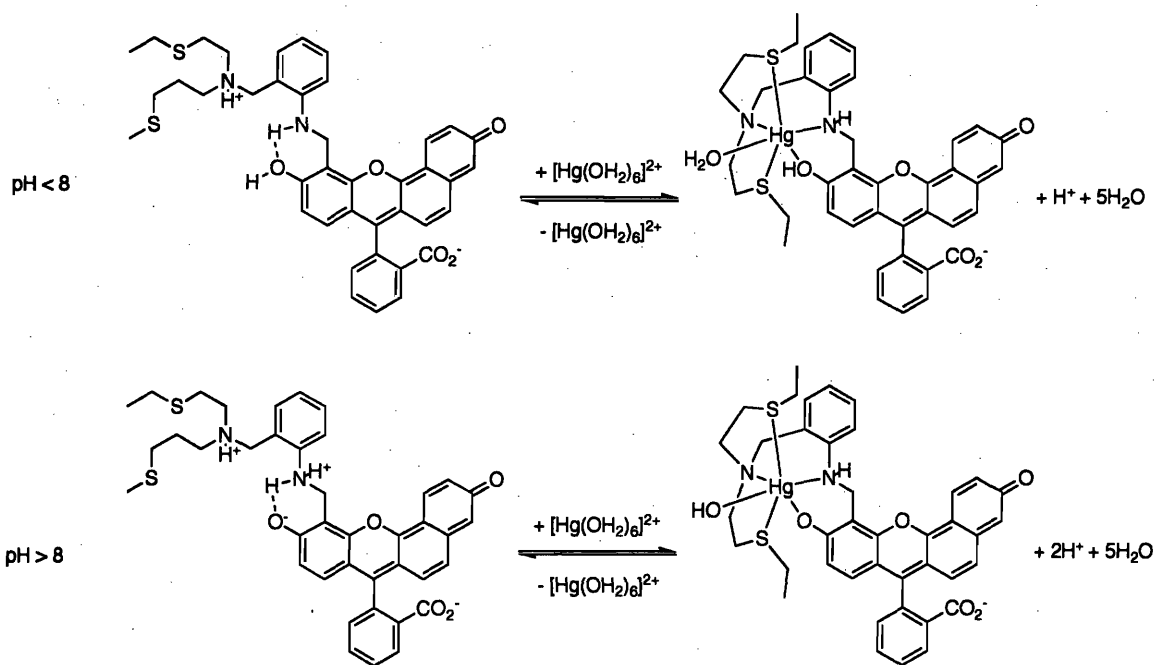
Scheme 11.3. Proposed mode of Hg(II) coordination to MS5 as a function of pH. We note that the seminaphthofluorescein can be drawn in multiple resonance forms.
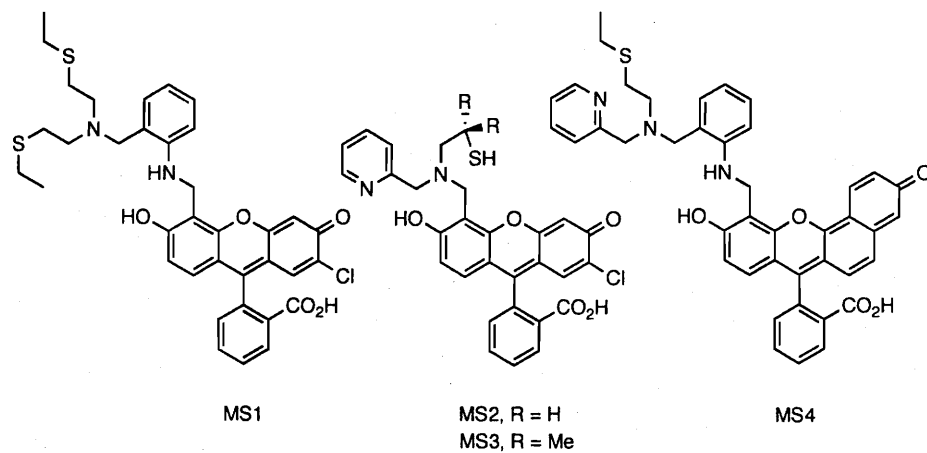
Figure 11.1. Fluorescein- and seminaphthofluorescein-based members of the MS family of Hg(II) sensors.
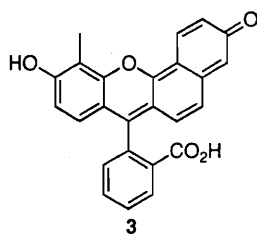
Figure 11.2. Seminaphthofluorescein 3.
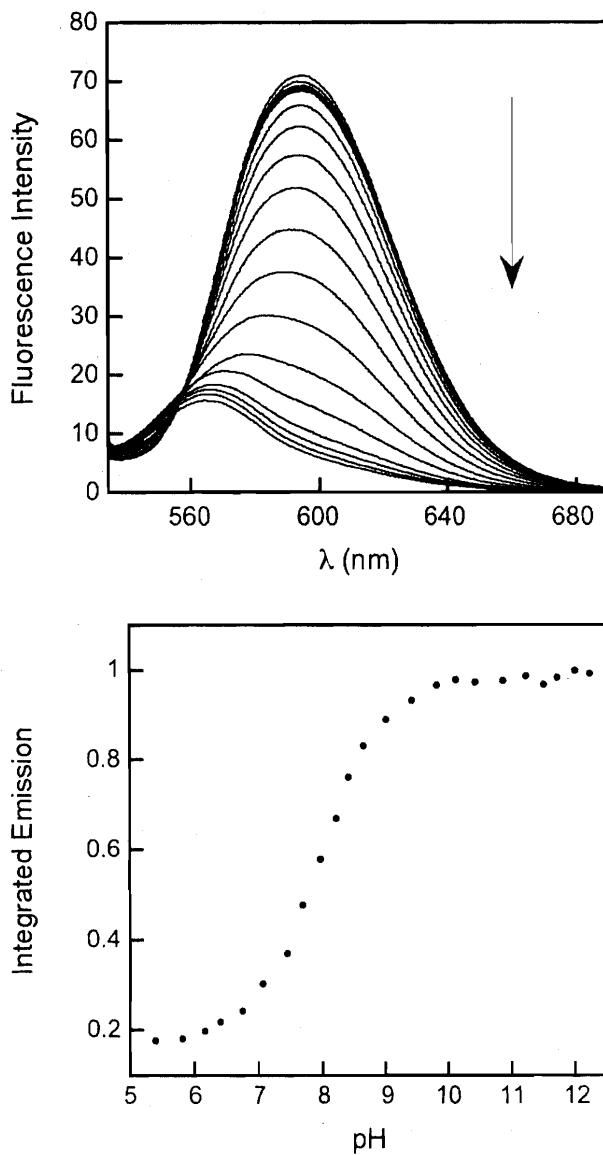
Figure 11.3. Effect of pH on the emission of **3** (λ_{ex} = 525 nm, 100 mM KCl, T = 25 °C). A solution of 2 μM **3** was prepared in 10 mM KOH, 100 mM KCl (pH ~12) and the pH was decreased in intervals of ~0.25 by addition of 6, 2, 1 and 0.5 N HCl. Top plot: Emission spectra, which shows a ca. 30 nm blue shift with a concomitant intensity decrease as the pH is lowered from ~12 to ~6. Bottom plot: Integrated emission vs. pH. The emission spectra were integrated from 540 – 700 nm and normalized.
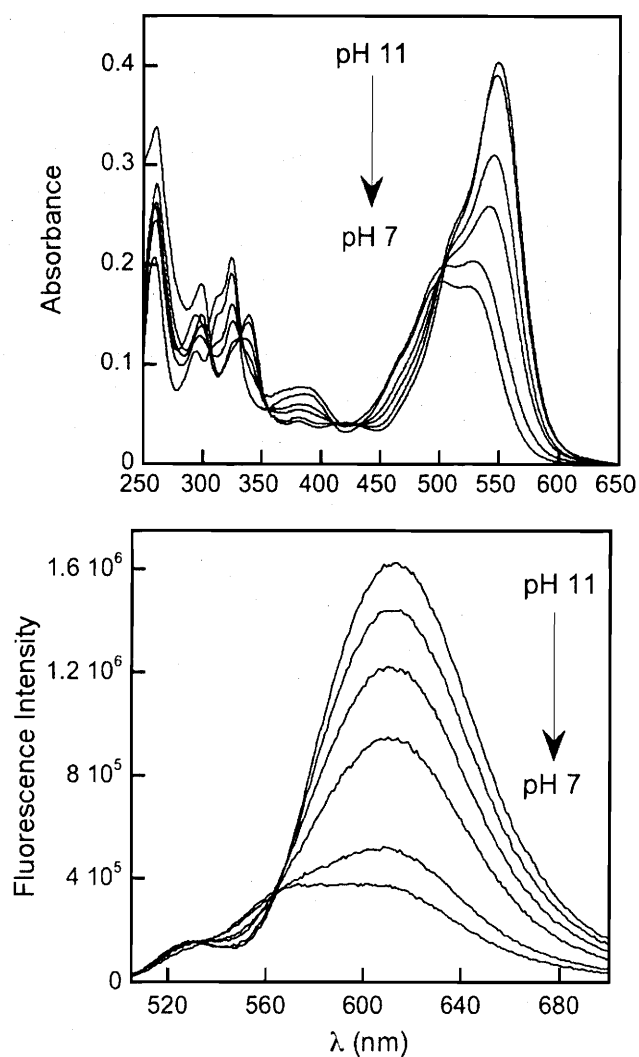
Figure 11.4. Effect of pH on the absorption (top) and emission (bottom) properties of **3**.

Solutions of 10 μM **3** were prepared at pH 7 (50 mM PIPES) 7.5 (50 mM HEPES), 8 (50

mM HEPES), 8.5 (50 mM HEPES), 9 (50 mM CHES), and 11 (50 mM CAPS) with 100

mM KCl and either the absorption or emission spectrum recorded. Excitation was

provided at 499 nm for fluorescence measurements. T = 25 °C.
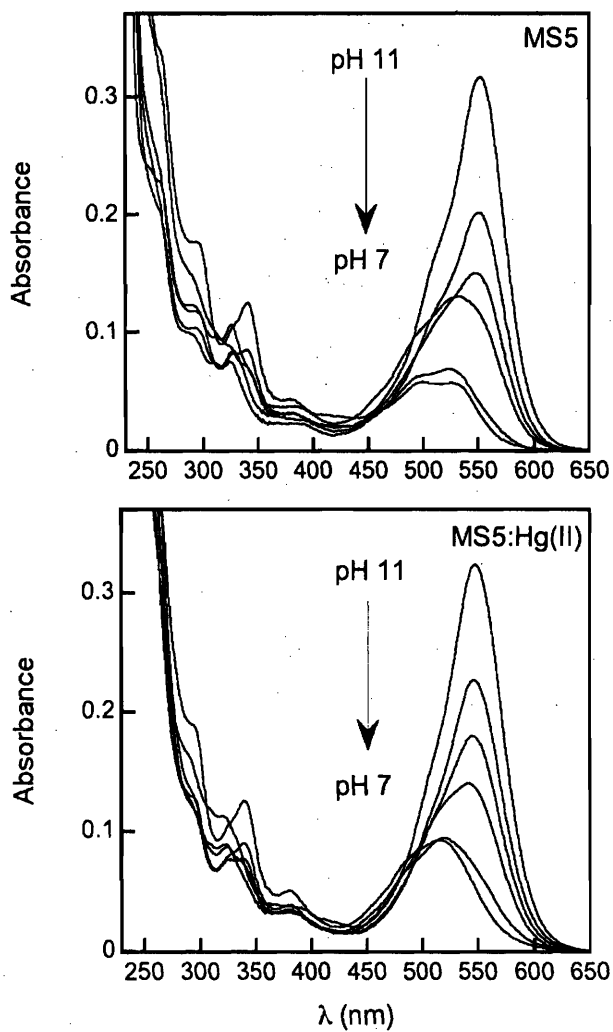
Figure 11.5. Effect of pH on the absorption properties of free (top) and Hg(II)-bound (bottom) MS5. Solutions of 10 μM MS5 and MS5:Hg(II) were prepared at pH 7 (50 mM PIPES, 100 mM KCl) 7.5 (50 mM HEPES, 100 mM KCl), 8 (50 mM HEPES, 100 mM KCl), 8.5 (50 mM HEPES, 100 mM KCl), 9 (50 mM CHES, 100 mM KCl), and 11 (50 mM CAPS, 100 mM KCl) and the absorption or emission spectrum recorded. T = 25 °C.
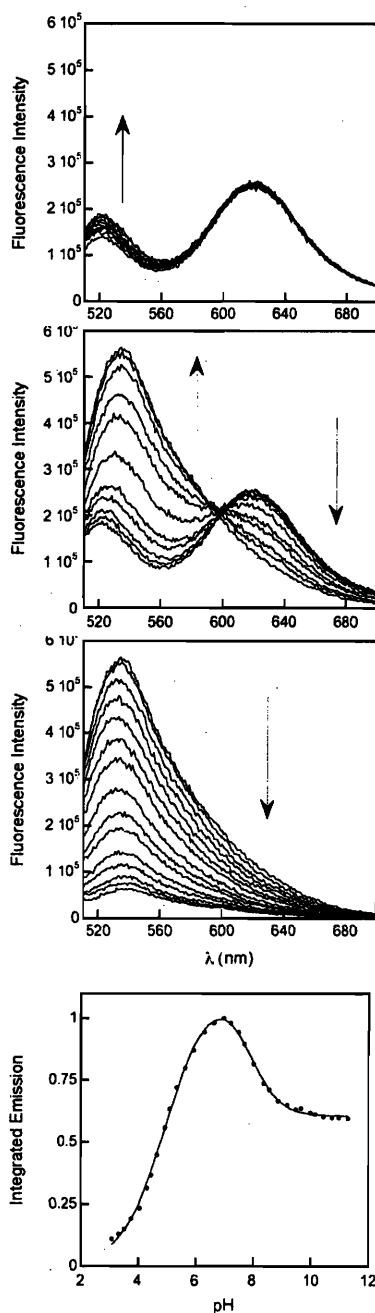
Figure 11.6. Effect of pH on the emission of MS5 (100 mM KCl). The top three panels illustrate the spectral changes that occur at pH > 9 (top panel), between pH 6 and 9 (2nd panel) and at pH < 6 (3rd panel). The bottom panel is a plot of integrated emission vs. pH. The circles represent the experimental data and the line is the calculated fit (eq. 2.1), which returns pK_{a1} = 7.8 (aniline) and pK_{a2} = 5.2 (seminaphthofluorescein).
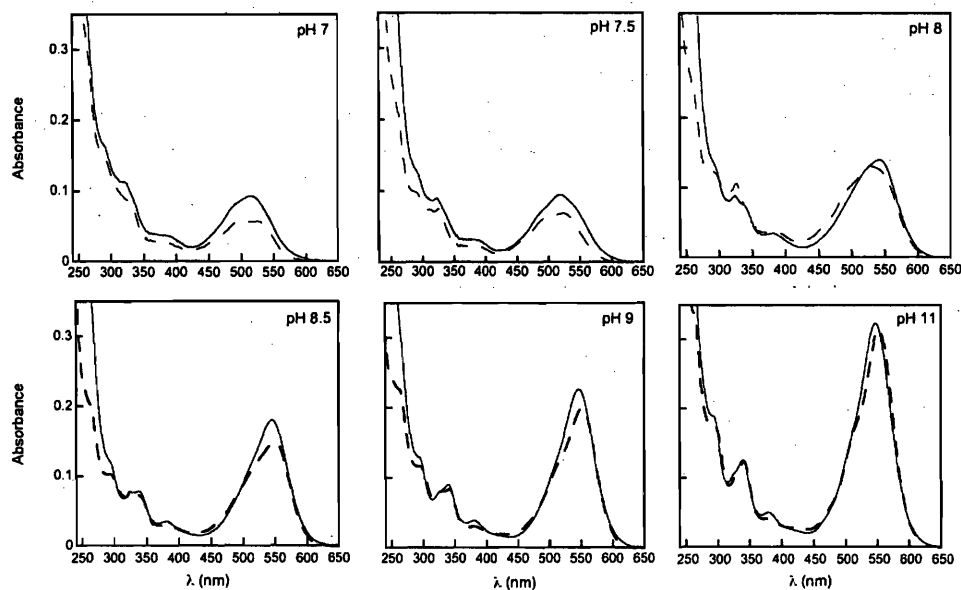
Figure 11.7. Optical absorption spectra showing the effect of Hg(II) addition to MS5 absorption at various pH values. The dashed and solid lines indicate absorption from MS5 and MS5:Hg(II), respectively. The concentration of MS5 was 10 μM and 10 equiv of Hg(II) were added. T = 25 °C.
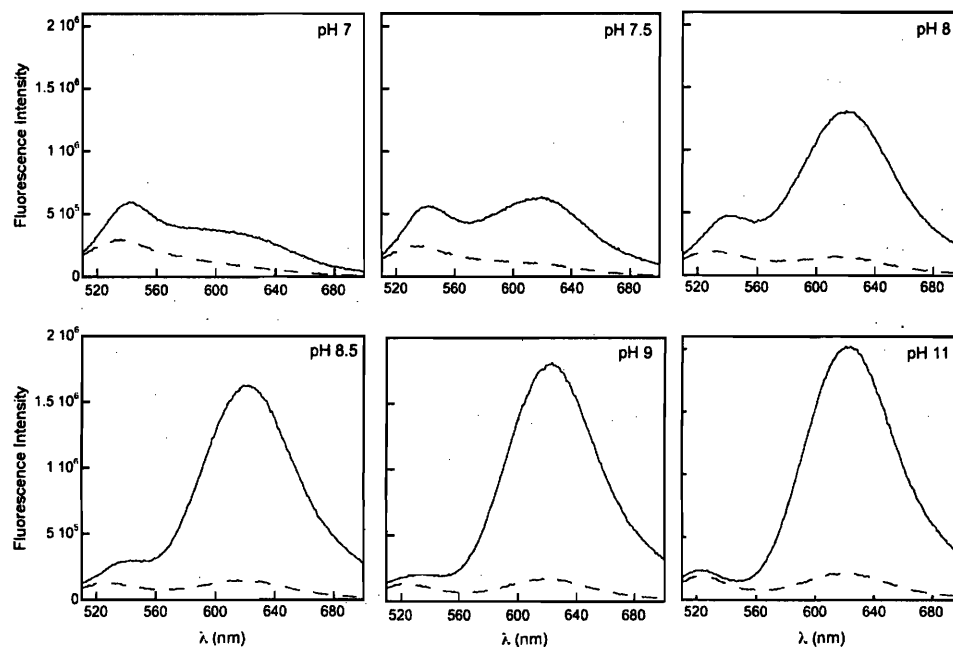
Figure 11.8. Fluorescence response of MS5 to Hg(II) as a function of pH. The concentration of MS5 was 5 μM and 10 equiv of Hg(II) were added. The dashed and solid lines indicate the emission before and after Hg(II) addition, respectively. Excitation was provided at 499 nm and T = 25 °C.

7

8

8
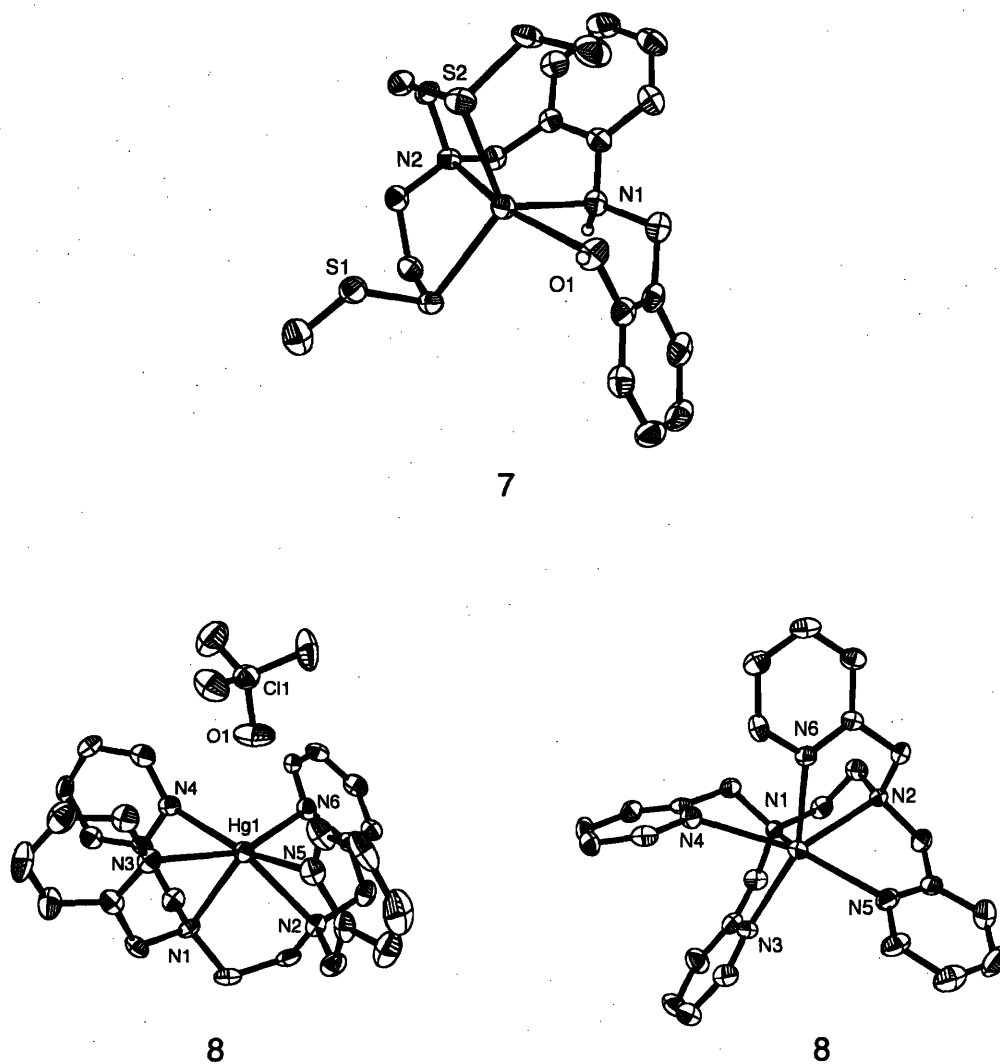
Figure 11.9. ORTEP diagrams showing 50% probability ellipsoids on all non-hydrogen atoms for Hg(II) complexes **7** and **8**. The aniline nitrogen and phenol moieties of **7** are protonated. The left ORTEP diagram of **8** illustrates the orientation of the associated perchlorate ion. The Hg—O(1) distance is ca. 2.72 Å.
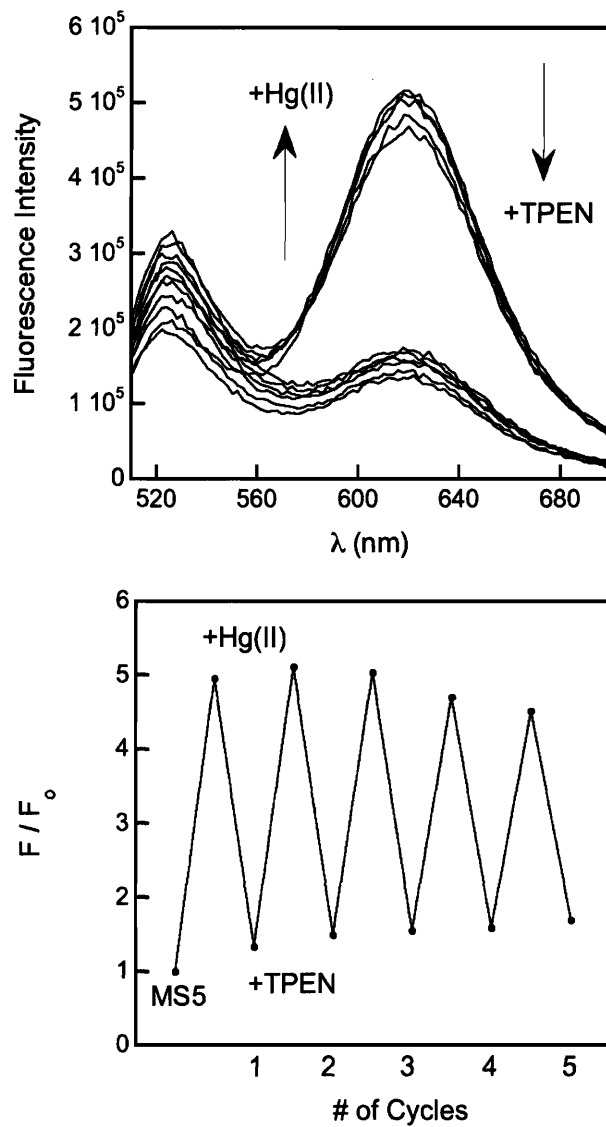
Figure 11.10. Reversibility of Hg(II) coordination to MS5 by TPEN addition (50 mM HEPES, 100 mM KCl, pH 8). The concentration of MS5 was 5 μM and 10 equiv of either Hg(II) or TPEN were added. Excitation was provided at 499 nm.
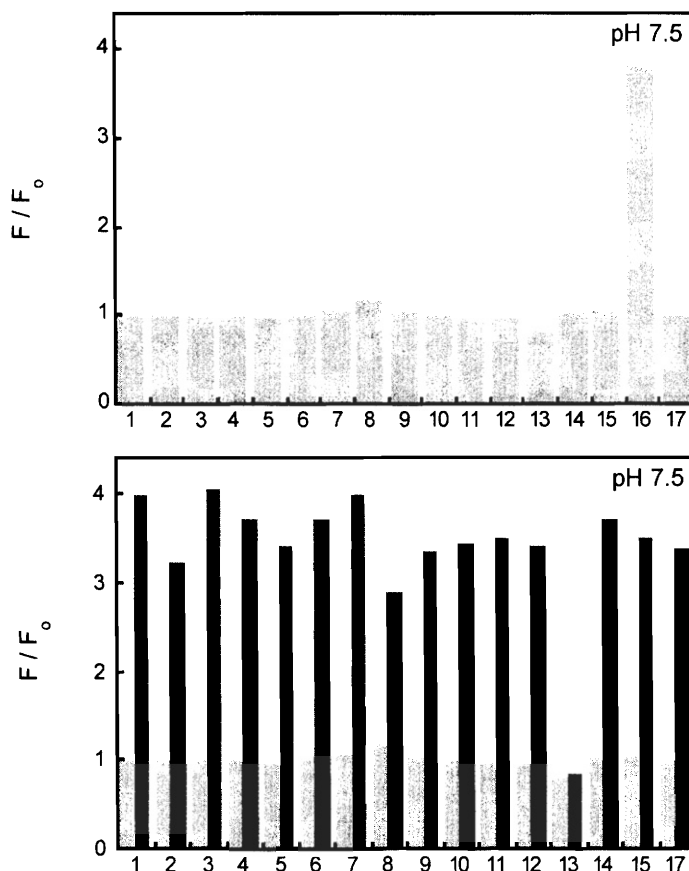
Figure 11.11. Selectivity of MS5 for Hg(II) over other cations (50 mM HEPES, 100 mM KCl, pH 7.5). Top plot: Fluorescence response of 5 μM MS5 following addition of 20 equiv of the cation of interest: 1, Li(I); 2, Na(I); 3, Rb(I); 4, Mg(II); 5, Ca(II); 6, Sr(II); 7, Ba(II); 8, Mn(II); 9, Cr(III); 10, Fe(II); 11, Co(II); 12, Ni(II); 13, Cu(II); 14, Zn(II); 15, Cd(II); 16, Hg(II); 17, Pb(II). Bottom plot: The light grey bars correspond to the bars in the top plot. The dark grey bars indicate the fluorescence change that occurs immediately following addition of 20 equiv of Hg(II) to the solutions containing MS5 and the cation of interest. All data (F) were normalized with respect to emission of the free sensor (F_o) and excitation was provided at 499 nm. T = 25 °C. MS5 is also selective for Hg(II) in the presence of mM concentrations of the alkali and alkaline earth metals considered (data not shown).
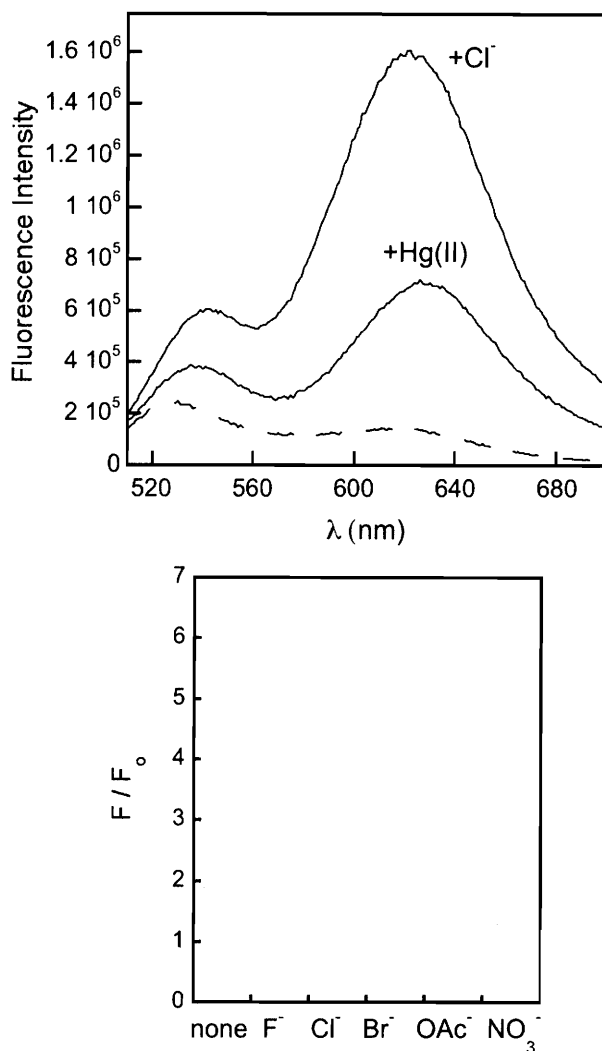
Figure 11.12. Effect of anions on the Hg(II) response of MS5. Top plot: Emission spectra for 5 μM MS5 before (dashed line) and after (solid line) the addition of 10 equiv of Hg(II) in the absence of chloride ion (50 mM HEPES, pH 8). Full turn-on occurs immediately after addition of 50 mM NaCl or KCl. Bottom plot: Fluorescence response of MS5 to Hg(II) in the presence of various anions at pH 8 (50 mM HEPES, 100 mM KX, X = anion of interest). The response (F) is normalized with respect to the emission of free MS5 (F_o).
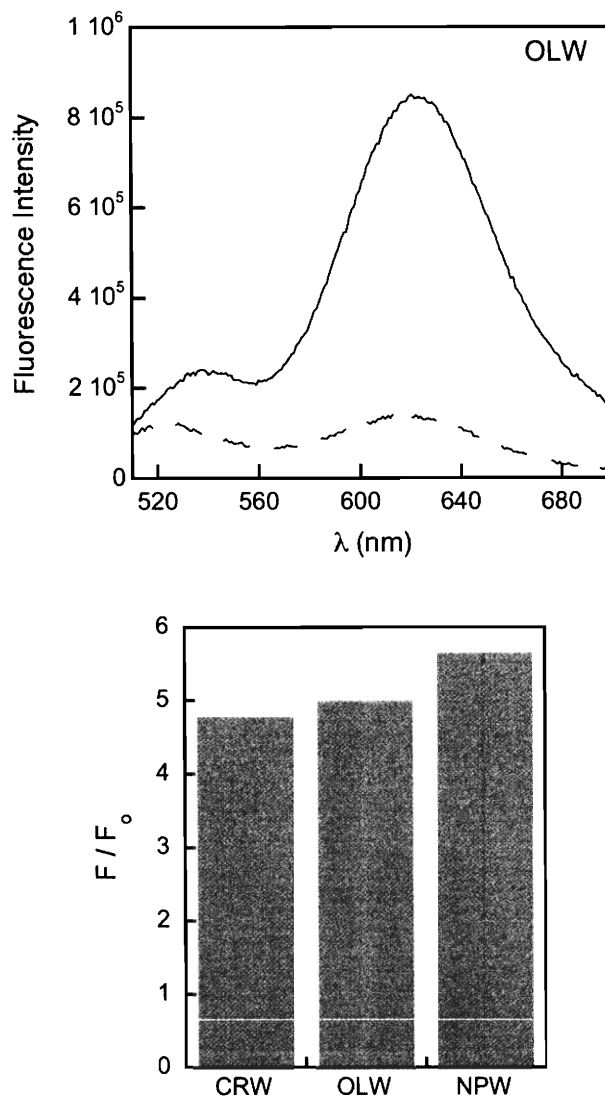
Figure 11.13. Response of MS5 to 10 equiv of Hg(II) added to natural water samples. Top plot: Fluorescence spectra for the MS5 response to Hg(II) in Onondaga Lake Water. The dotted and dashed lines represent the emission before and after Hg(II) addition, respectively Bottom plot: Fluorescence response of MS5 to Hg(II) in Charles River Water (CRW), Onondaga Lake Water (OLW) and Newburyport Water (NPW). The response (F) is normalized to the emission of the free sensor (F_o). [MS5] = 5 μM, T = 25 °C and excitation was provided at 499 nm.

Appendix I

Miscellaneous Fluorescein-Based Ligands

Introduction

In addition to compounds previously described in this work, other fluorescein-based compounds were prepared and, in some instances, characterized. These compounds were either not pursued in detail and/or suffer from some major limitation. In particular, fluorescence turn-on at neutral pH is an important criterion for our sensing projects. Many of the compounds included in this Appendix were designed for Hg(II) or Zn(II) detection and give fluorescence turn-off or no fluorescence change following metal ion coordination at pH 7. This Appendix details the design rationale, syntheses and, when applicable, spectroscopic characterization of such compounds.

Experimental Section

Reagents. All solvents were dried as described in previous chapters. Commercially available reagents were generally purchased from Aldrich in the highest available purity. Compounds 1[1], 2[2], 3[3], 4[4], 5[5], 6[4], 7[6] and 8[7] were prepared according to published methods.

Materials and Methods. These considerations are detailed in previous chapters.

N-(2-Nitrobenzyl)phthalimide (9). 2-Nitrobenzylbromide (5.03 g, 23.3 mmol) and potassium phthalimide (6.57 g, 35.4 mmol) were combined in 65 mL of DMF and heated to 90 °C for 4 h. A white precipitate formed. The reaction was cooled and $CHCl_3$ (65 mL) was added, and the solution was washed with 100 mL of H_2O. The aqueous layer was extracted with $CHCl_3$ (2 x 25 mL) and the combined organic layers were dried over $MgSO_4$ and the solution was concentrated under reduced pressure to yield an off-white oily residue. Upon addition of ether, the desired product precipitated as a white crystalline solid (5.55 g, 84%); mp = 216-218 °C. ^{1}H NMR ($CDCl_3$, 300 MHz) δ 5.32 (2H), 7.25 (1H, d), 7.46 (1H, td), 7.56 (1H, td), 7.79 (2H, m), 7.793 (2H, m), 8.13 (1H, dd). ^{13}C NMR ($CDCl_3$, 125 MHz) δ 39.14, 124.14, 125.80, 128.51, 128.89, 132.13, 132.26, 134.23,

134.85, 148.47, 168.33. FTIR (KBr, cm^{-1}) 1771, 1707, 1534, 1408, 1389, 1333, 1113, 949, 714. HRMS (ESI) Calcd [M + Na]$^+$, 305.0533; Found, 305.0530.

2-Nitrobenzylamine (10). 2-Nitrobenzyl phthalimide (**9**, 1.20 g, 4.24 mmol) was dissolved in 30 mL of EtOH and heated to 60 °C under Ar. Hydrazine monohydrate (485 mg, 9.69 mmol) was added dropwise and the resulting yellow solution was refluxed for 3 h. During the course of the reaction, a lumpy white precipitate formed. The reaction was cooled and the ethanol was evaporated to yield a yellow-white solid. The solid was dissolved in 30 mL of 1 M NaOH and extracted with CHCl$_3$ (3 x 30 mL). The combined organic layers were dried over MgSO$_4$ and the solvent removed under reduced pressure to yield an orange-yellow oil (623 mg, 97%). ^{1}H NMR (CDCl$_3$, 300 MHz) δ 4.09 (1H, s), 7.04 (1H, m), 7.60 (2H, m), 7.97 (1H, d). ^{13}C NMR (CDCl$_3$, 125 MHz) δ 44.34, 125.14, 128.13, 130.81, 133.99, 138.77, 148.63. FTIR (NaCl disk, cm^{-1}) 1521, 1345, 855, 788, 727. HRMS (ESI) Calcd [M + H]$^+$, 153.0659; Found, 153.0665.

N-(2-Nitrobenzyl)-1,2-dithia-5-azepane (11). 2-Nitrobenzylamine (**10**, 1.3 g, 8.5 mmol) was dissolved in 5 mL of C$_6$H$_5$CH$_3$ and placed in a thick-walled tube. The reaction was heated to ~40 °C and ethylene sulfide (720 mg, 12.0 mmol) was added dropwise. The tube was purged with Ar, sealed, and heated to ~100 °C for 96 h. After cooling, the reaction was filtered through Celite and concentrated to yield an odorous yellow-brown oil. Flash chromatography on silica gel (7:1 hexanes/EtOAc) gave the product as a yellow oil. (382 mg, 14%) ^{1}H NMR (CDCl$_3$, 300 MHz) δ 2.84 (4H, t), 3.16 (4H, t), 4.17 (2H, s), 7.40 (1H, td), 7.56 (2H, m), 7.78 (1H, dd). ^{13}C NMR (CDCl$_3$, 125 MHz) δ 40.06, 54.27, 55.62, 124.61, 128.16, 130.64, 132.49, 134.98, 149.74. FTIR (KBr, cm^{-1}) 3058 (w), 2948 (w), 2905 (w), 2834 (w), 1608 (w), 1577 (w), 1525 (s), 1452 (m), 1442 (m), 1420 (w), 1358 (m), 1301 (m), 1257 (w), 1196 (w), 1150 (m), 1136 (m), 1107 (w), 1020 (m), 982 (m), 895 (m), 857 (w), 813 (m), 782 (m), 726 (s), 700 (w), 665 (w). HRMS (ESI) Calcd [M + H]$^+$, 271.0569; Found, 271.0568.

N-(2-Aminobenzyl)-1,2-dithia-5-azepane (12). Pd black (500 mg) was placed in a flask purged with Ar and 10 mL of MeOH was added. N-(2-Nitrobenzyl)-1,2-dithia-5-azepane (**11**, 314 mg, 1.16 mmol) was dissolved in 7 mL of MeOH with a few drops of CH_2Cl_2 added to increase the solubility of the disulfide, and the solution was transferred to the reaction flask with a syringe. A balloon filled with H_2 was attached and the solution was left to stir vigorously under H_2 for 3 h. The reaction was purged with Ar, filtered though Celite and dried, which gave the dithiol product N-(2-aminobenzyl)-2-(2-mercaptoethylamino)ethanethiol. Flash chromatography on basic Al_2O_3 using gradient elution (7:1 to 1:1 hexanes/EtOAc) afforded the corresponding disulfide as a brown oil in low yield (46 mg, 17%). ^{1}H NMR (CDCl$_3$, 300 MHz) δ 2.80 (4H, t), 3.18 (4H, t), 3.85 (2H, s), 6.65 (2H, m), 7.00 (1H, dd), 7.15 (1H, t). HRMS (EI) Calcd, M$^+$, 240.0749; Found, 240.0756.

2-{2-Chloro-5-[(2-[1,2,5]dithiazepan-5-ylmethylphenylamino)methyl]-6-hydroxy-3-oxo-3H-xanthen-9-yl}benzoic acid (13). 7'-Chloro-4'-fluoresceincarboxaldehyde (**1**, 30 mg, 76 μmol) was dissolved in 3 mL of EtOAc and stirred to give an orange-pink solution. A portion (20 mg, 83 μmol) of **12** was dissolved in 1 mL of EtOAc and added and the solution immediately changed to bright red. The reaction was left to stir at room temperature for 21 h and became deep red. The solvent was removed to yield the product as a magenta residue. The residue was dissolved in 3.5 mL of DCE and NaB(OAc)$_3$H (55 mg, 260 μmol) was added. The reaction was stirred at room temperature for 6 h, during which time it changed from magenta to red-yellow, and was poured into 5 mL of brine and extracted with brine (2 x 5 mL). The brine was extracted with CH_2Cl_2 (2 x 5 mL) and the organic layers were dried over $MgSO_4$ and the solvent was evaporated to give a red solid. Preparative TLC on silica gel (20:1 CHCl$_3$/MeOH) yielded the pure product as a red solid (24 mg, 52%). ^{1}H NMR (CD$_3$OD, 300 MHz) δ 2.68 (4H, m), 3.00 (4H, m), 3.80 (2H, q), 4.58 (2H, q), 6.65 (3H, m), 6.97 (2H, m),

7.05 (2H, m), 7.20 (2H, m), 7.60 (2H, m), 8.05 (1H, m). HRMS (ES) Calcd [M + H]$^+$, 619.1123; Found, 619.1102.

[2-Methyl-2-(triphenyl-l4-sulfanyl)propyl](2-nitrobenzyl)pyridin-2-ylmethyl-amine (14). To 60 mL of MeCN were added o-nitrobenzylbromide (300 mg, 1.27 mmol), K_2CO_3 (300 mg, 2.17 mmol), **2** (520 mg, 1.27 mmol), and 3 Å molecular sieves The reaction was stirred vigorously at room temperature for 21 h, filtered through Celite and the solvent was removed in vacuo. Chromatography on silica gel (9:1 CH_2Cl_2/EtOAc with 1% ^{i}PrNH$_2$) yielded the purified product as a yellow foam (642 mg, 93%). ^{1}H NMR (CDCl$_3$, 300 MHz) δ 2.40 (2H, m), 2.50 (2H, m), 3.64 (2H, s), 3.84 (2H, s), 7.10-7.41 (16H, m), 7.51 (1H, td), 7.61 (1H, td), 7.72 (1H, d), 7.81 (1H, dd), 8.48 (1H, dq). ^{13}C NMR (CDCl$_3$, 125 MHz) δ 29.46, 53.56, 55.44, 60.27, 66.85, 122.02, 122.78, 124.34, 126.61, 127.75, 127.84, 129.55, 130.93, 132.59, 134.67, 136.43, 144.76, 148.78, 149.48, 150.83. HRMS (ESI) Calcd [M+H]$^+$, 546.2210; Found, 546.2221.

2-({[Pyridin-2-ylmethyl-[2-(triphenyl-l4-sulfanyl)ethyl]amino}methyl)phenylamine (15). Palladium black (612 mg) was placed in a flask purged with Ar and 10 mL of MeOH was added. A portion (356 mg, 0.653 mmol) of **14** was dissolved in 20 mL of 1:3 CH_2Cl_2/MeOH and added to the reaction flask. The reaction was purged with H$_2$ and allowed to stir vigorously under H$_2$ for 3 h at room temperature. The reaction was filtered through Celite and the solvent was removed under reduced pressure. Chromatography on Al_2O_3 with a solvent gradient (2:1 to 1:1 hexanes/EtOAc) yielded the pure product as an off-white solid (183 mg, 54%). ^{1}H NMR (CDCl$_3$, 300 MHz) δ 2.38 (2H, m), 2.53 (2H, m), 3.47 (2H, s), 3.57 (2H, s), 6.58-6.66 (2H, m), 6.92 (1H, d), 7.07-7.39 (21H, m), 7.60 (1H, t), 8.49 (1H, d). ^{13}C NMR (CDCl$_3$, 125 MHz) δ 29.55, 53.05, 57.99, 59.90, 66.68, 115.57, 117.55, 122.13, 123.55, 126.69, 126.75, 127.97, 128.59, 129.69, 131.05, 136.58, 144.91, 144.94, 146.98, 148.97, 149.12, 159.13. FTIR (KBr, cm^{-1}) 3433, 3054, 2961, 2925, 2811, 1734, 1591, 1488, 1443, 1370, 1316, 1291, 1261, 1183, 1148, 1082, 1033, 970,933, 887, 844, 804, 742, 698, 616, 505. HRMS (ESI) [M + Na]$^+$, 538.2287; Found, 538.2272.

[2-Methyl-2-(triphenyl-l4-sulfanyl)propyl]-(2-nitrobenzyl)pyridin-2-ylmethyl-amine (16). A portion (300 mg, 1.39 mmol) of o-nitrobenzylbromide, **3** (600 mg, 1.37 mmol), K_2CO_3 (300 mg, 2.17 mmol) and 3 Å molecular sieves were combined in 50 mL of MeCN and stirred vigorously at room temperature for 24 h. The reaction was filtered through Celite and the solvent was removed to give an orange oil. The crude material was purified by chromatography on silica gel (40:1 CH_2Cl_2/EtOAc) to afford a fluffy yellow solid (485 mg, 46%). ^{1}H NMR (CDCl$_3$, 300 MHz) δ 0.86 (6H, s), 2.06 (2H, s), 3.64 (2H, s), 3.92 (2H, s), 7.08-7.26 (11H, m), 7.31 (1H, t), 7.52-7.62 (8H, m), 7.85 (2H, t), 8.45 (1H, d). ^{13}C NMR (CDCl$_3$, 125 MHz) δ 27.65, 53.96, 57.36, 62.61, 66.51, 67.66, 122.09, 123.37, 124.54, 126.45, 127.50, 127.62, 130.12, 130.75, 132.83, 135.41, 136.19, 145.43, 149.14, 149.35, 158.71. FTIR (KBr, cm^{-1}) 3416, 3055, 2961, 2922, 1735, 1700, 1590, 1523, 1488, 1463, 1444, 1352, 1300, 1206, 1186, 1145, 1112, 1083, 1032, 995, 977, 851, 791, 763, 743, 703, 674, 643, 628, 620, 504. HRMS (ESI) Calcd [M + H]$^+$, 574.2523; Found, 574.2521.

[2-Methyl-2-(triphenyl-l4-sulfanyl)propyl]-(2-nitrobenzyl)pyridin-2-ylmethyl-amine (17). Palladium black (210 mg) and 5 mL of MeOH were combined in a flask purged with Ar. A portion (160 mg, 0.279 mmol) of **16** was dissolved in 15 mL MeOH with a few drops of CH_2Cl_2 and was added to the reaction flask. The reaction mixture was purged with H_2 and was left to stir vigorously under H_2 for 2 h. The reaction mixture was purged with Ar, filtered through Celite and the solvent was removed in vacuo. Chromatography on silica gel (2:1 hexanes/EtOAc with 1% Et$_3$N) gave the purified material as an off-white solid (41 mg, 27%). ^{1}H NMR (CDCl$_3$, 300 MHz) δ 0.84 (6H, s), 2.53 (2H, s), 3.53 (2H, s), 3.71 (2H, s), 6.55 (1H, d), 6.64 (1H, t), 6.93 (1H, d), 7.05 (1H, td), 7.13-7.28 (11H, m), 7.50-7.63 (7H, m), 8.55 (1H, dt). ^{13}C NMR (CDCl$_3$, 125 MHz) δ 28.09, 53.68, 60.26, 63.10, 66.65, 67.65, 115.34, 117.33, 122.12, 123.08, 123.86, 126.39, 127.56, 128.50, 130.22, 131.38, 136.12, 145.47, 147.14, 149.04, 159.40. FTIR (KBr, cm^{-1}) 3431, 3053, 2950, 2921, 2852, 1732, 1640, 1619, 1590, 1488, 1460, 1444, 1371, 1315, 1261, 1240,

1182, 1147, 1082, 1029, 803, 742, 701, 673, 615, 465. HRMS (ESI) Calcd [M + H]⁺, 544.2781; Found, 544.2775.

Syntheses of Sensors 18 and 19. Combination of equimolar fluorescein **1** and either **15** or **17** in dry EtOAc followed by imine reduction to afford the trityl protected sensors **20** and **21** occurs readily as described in analogous procedures. Dropwise addition of Et₃SiH into a solution of **20** or **21** in TFA results in immediate deprotection of the thiol moieties. Resulting sensors **18** and **19** have been identified by mass spectrometry and crude NMR, and mixed MeOH/buffer solutions of the crude compounds give fluorescence enhancement following introduction of Zn(II) or, if chloride ion is added, Hg(II). Despite exhaustive attempts at chromatography, we have been unable to isolate pure **18** or **19**. An alternative route where the thiol was deprotected prior to condensation of the aniline and fluorescein moieties was also pursued in detail but this approach did not facilitate purification of the final products.

2-(4-{[Bis-(2-ethylsulfanylethyl)amino]methyl}-2,7-dichloro-5-{[(2-ethylsulfanyl-ethyl)(3-ethylsulfanylpropyl)amino]methyl}-6-hydroxy-3-oxo-3H-xanthen-9-yl)-benzoic acid (22). To 8 mL of MeCN were added 3,9-dithia-6-azaundecane (**4**, 1.04 g, 5.38 mmol) and paraformaldehyde and the mixture was refluxed for 1 h. A portion (715 mg, 1.78 mmol) of 2′,7′-dichlorofluorescein dissolved in 10 mL of 1:1 MeCN:H₂O was added to the reaction dropwise and the reaction color changed from colorless to deep pink-red. The reaction was refluxed vigorously for 24 h and cooled. The solvent was removed under reduced pressure and boiling EtOH was added to the residue. Upon cooling to –25 °C the pure product precipitated as a pink-red solid (250 mg, 17%); mp = 98-101 °C, dec. ¹H NMR (CDCl₃, 300 MHz) δ 1.28 (12H, t), 2.27 (8H, q), 2.79 (8H, m), 2.91-2.96 (8H, m), 4.18 (2H, d), 6.64 (1H, s), 7.21 (1H, d), 7.27 (1H, s), 7.67-7.78 (2H, m), 8.06 (1H, d). ¹³C NMR (CDCl₃, 125 MHz) δ 14.91, 26.49, 28.54, 51.40, 53.50, 82.81, 109.33, 110.72, 117.55, 124.17, 125.69, 127.26, 127.95, 130.53, 135.57, 148.04, 151.48, 156.17, 168.91.

FTIR (KBr, cm⁻¹) 3432, 2957, 2923, 2852, 1760, 1627, 1576, 1466, 1375, 1284, 1212, 1099, 1019, 569. HRMS (ESI) Calcd [M + H]⁺, 811.1895; Found, 811.1896.

2-(5-{[Bis-(2-ethylsulfanylethyl)amino]methyl}-2-chloro-6-hydroxy-3-oxo-3H-xanthen-9-yl)benzoic acid (23). To 3 mL of MeCN were added fluroescein 7 (100 mg, 0.146 mmol), amine 4 (30.3 mg, 0.157 mmol) and K_2CO_3 (100 mg, 0.724 mmol) and the mixture was stirred vigorously overnight at room temperature. A red precipitate formed, and the mixture was cooled on ice, filtered and the precipitate washed with cold MeCN. TLC analysis showed that both the filtrate and precipitate contained the product. Preparative TLC of the combined material on silica gel (20:1 $CHCl_3$/MeOH) yielded the pure dye as a red, iridescent solid (56 mg, 67%). ¹H NMR (CD_3OD, 300 MHz) δ 1.24 (6H, q), 2.50-2.59 (4H, m), 2.82 (2H, t), 2.89-2.96 (4H, m), 3.23 (2H, t), 4.50 (2H, s), 6.62 (1H, d), 6.71 (1H, s), 7.07 (1H, d), 7.17 (1H, s), 7.22 (1H, s), 7.63 (2H, m), 8.08 (1H, dd). HRMS (ESI) Calcd [M + H]⁺, 572.1327; Found, 572.1352.

2-[5-({Bis-[2-(2-ethylsulfanylethylsulfanyl)ethyl]amino}methyl)-2-chloro-6-hydroxy-3-oxo-3H-xanthen-9-yl]benzoic acid (24). To 3 mL of MeCN were added amine 6 (40.6 mg, 0.059 mmol), fluorescein 4 (19 mg, 0.061 mmol) and K_2CO_3 (24 mg, 0.174 mmol). The yellow-orange reaction was stirred overnight at room temperature and filtered through Celite, and the Celite was washed with MeOH. Preparative TLC on silica gel (9:1 $CHCl_3$/MeOH) afforded the product as an orange solid (8 mg, 20%). ¹H NMR (CD_2Cl_2, 300 MHz) δ 1.21 (6H, t), 2.51 (6H, q), 2.70-2.87 (14H, m), 4.16 (2H, s), 6.53 (2H, d), 6.75 (1H, s, 6.96 (1H, s), 7.21 (1H, d), 7.63-7.75 (2H, m), 8.00 (1H, d). LRMS (ESI) Calcd [M − H]⁻, 690.1; Found, 690.2.

[2-(2-Ethylsulfanylethylsulfanyl)ethyl]-(2-ethylsulfanylethylsulfanylmethyl)-(2-nitrobenzyl)amine (25). 2-Nitrobenzylbromide (347 mg, 1.61 mmol), amine 6 (504 mg, 1.61 mmol), K_2CO_3 (314 mg, 2.27 mmol) and activated 3 Å molecular sieves were combined in 15 mL of MeCN. A balloon of Ar was attached to the reaction flask and the mixture was stirred vigorously at room temperature for 16 h. The reaction was filtered

through Celite and the solvent was removed in vacuo. Chromatography on silica gel (7:1 hexanes/EtOAc) followed by a second silica column (50:1 toluene/MeCN) gave the pure product as a yellow oil (259 mg, 36%). TLC R_f = 0.45 (silica, 5:1 hexanes/EtOAc). ^{1}H NMR (CDCl$_3$, 300 MHz) δ 1.80 (6H, t), 2.45-2.65 (20H, m), 3.90 (2H, s), 7.35 (1H, t), 7.52 (1H, t), 7.68 (1H, d), 7.77 (1H, d). ^{13}C NMR (CDCl$_3$, 125 MHz) δ 14.80, 25.93, 31.62, 32.27, 54.10, 55.65, 124.38, 127.99, 130.88, 132.63, 134.66, 149.49. FTIR (NaCl disk, cm^{-1}) 3065 (w), 2962 (s), 2924 (s), 2868 (s), 2825 (s), 2723 (w), 1700 (w), 1608 (m), 1576 (m), 1525 (s), 1451 (s), 1425 (s), 1360 (s), 1300 (m), 1261 (m), 1200 (m), 1112 (m), 1076 (w), 1042 (m), 971 (m), 857 (w), 784 (s), 730 (s), 660 (m), 609 (w). LRMS (ESI) Calcd [M + H]$^+$, 449.1; Found, 449.4

2-{[[2-(2-Ethylsulfanylethylsulfanyl)ethyl]-(2-ethylsulfanylethylsulfanylmethyl)-amino]-methyl}phenylamine (26). Pd black (500 mg) was placed in a flask under Ar. A portion of **25** (255 mg, 0.568 mmol) was dissolved in 10 mL of 9:1 MeOH/CH$_2$Cl$_2$ and added to the reaction flask with a syringe. A balloon of H$_2$ was attached and the reaction stirred vigorously under H$_2$ for 1 h. The reaction was purged with Ar and filtered through Celite and the solvents were removed under reduced pressure. Chromatography on silica gel (5:1 hexanes/EtOAc) yielded the purified product as a yellow oil (168 mg, 71%). TLC R_f = 0.29 (5:1 hexanes/EtOAc). ^{1}H NMR (CDCl$_3$, 300 MHz) δ 1.26 (6H, t), 2.41-2.72 (20H, m), 2.67 (2H, s), 6.86 (1H, m), 7.03 (1H, d), 7.28 (2H, m). ^{13}C NMR (CDCl$_3$, 125 MHz) δ 14.78, 25.91, 29.80, 31.57, 32.08, 53.33, 57.80, 113.64, 120.37, 122.35, 128.71, 129.56, 149.74. FTIR (NaCl disk, cm^{-1}) 3358 (s, br), 3211 (s, br), 2071 (m), 3043 (m), 2962 (s, br), 2924 (s, br), 2868 (s), 2919 (s, br), 2723 (m), 1607 (s), 1586 (m), 1486 (s), 1453 (s), 1424 (s), 1375 (s), 1298 (s), 1261 (s), 1201 (s), 1156 (w), 1127 (s), 1108 (s), 1094 (s), 1021 (s, br), 970 (m), 935 (m), 908 (s, br), 860 (w), 833 (m), 760 (s, br), 734 (s), 650 (w), 626 (w), 587 (w), 532 (w). HRMS (ESI) Calcd [M + H]$^+$, 419.1678; Found, 419.1679.

2-(5-{[2-({Bis-[2-(2-ethylsulfanylethylsulfanyl)ethyl]amino}methyl)phenylamino]-methyl}-2-chloro-6-hydroxy-3-oxo-3H-xanthen-9-yl)benzoic acid (27). Portions of 7′-

chloro-4'-fluoresceincarboxaldehyde (**1**, 89.5 mg, 0.227 mmol) and **26** (95 mg, 0.227 mmol) were combined in 6 mL of EtOAc to yield a cloudy lemon-colored solution. A balloon of Ar was attached and the reaction was stirred for 21 h, during which time the solution turned light-brown and a light tan precipitate formed. The solvent was removed under reduced pressure, which yielded a magenta solid. The solid was dissolved in 5 mL of DCE, a portion (63 mg, 0.297 mmol) of $NaB(OAc)_3H$ was added and the solution became cloudy and peach in color. Over the course of 7 h, the reaction turned red and became clear. The reaction was diluted with 10 mL of CH_2Cl_2 and washed with water (3 x 15 mL). The organics were dried over $MgSO_4$ and the solvent was evaporated to yield a red-orange residue. Preparative TLC on silica gel (15:1 $CHCl_3/MeOH$) yielded the pure dye as an orange-red solid (46 mg, 26%). ^1H NMR (CDCl$_3$, 300 MHz) δ 1.22 (6H, t), 2.50 (4H, q), 2.64-2.81 (16 H, m), 3.73 (1H, d), 3.96 (1H, d), 4.90 (2H, q), 6.61 (2H, s), 6.73 (1H, s), 6.99 (1H, s), 7.21 (1H, d), 7.28-7.34 (2H, m), 7.48 (1H, t), 7.64-7.73 (3H, m), 8.104 (1H, d). FTIR (KBr, cm^{-1}) 3427 (s, br), 3060 (w), 2959 (m), 2922 (s), 2853 (m), 1760 (s), 1632 (m), 1602 (s), 1580 (s), 1516 (m), 1490 (s), 1453 (s), 1369 (m), 1282 (s), 1259 (s), 1210 (m), 1149 (m), 1106 (m), 1089 (m), 1009 (m), 872 (w), 822 (w), 799 (w), 761 (m), 701 (m), 663 (w), 624 (w), 593 (w), 549 (w), 510 (w), 469 (m).

2-(Ethylthio)-*N*-(thiophen-2-yl)methyl)ethanamine (28). Portions of 2-(ethylthiol)-ethylamine (5.33 g, 47.5 mmol) and 2-thiophenecarboxaldehyde (5.00 g, 47.5 mmol) were combined in 200 mL of MeOH and stirred for 3 h at room temperature. The reaction was cooled to 0 °C and NaBH$_4$ (2.20 g, 58.2 mmol) was added. The reaction was stirred overnight at room temperature and the solvent removed under reduced pressure. The residue was partitioned with 200 mL of 1:1 H_2O/Et_2O. The aqueous phase was extracted with Et$_2$O (2 x 100 mL) and the combined organic layers were dried over MgSO$_4$ and concentrated to give the pure product as a colorless oil (8.75 g, 91%). TLC R$_f$ = 0.31 (silica, 20:1 $CH_2Cl_2/MeOH$). ^1H NMR (CDCl$_3$, 300 MHz) δ 1.29 (3H, t), 1.89 (1H, s, br), 2.58 (2H, q), 2.75 (2H, m), 2.91 (2H, m), 4.06 (2H, s), 6.98 (2H, m), 7.26 (1H, m). ^{13}C

NMR (CDCl$_3$, 125 MHz) δ 15.01, 25.86, 47.65, 48.18, 124.59, 125.07, 126.79, 144.12. FTIR (NaCl disk, cm^{-1}) 3300 (w), 3109 (w), 2068 (w), 2963 (s), 2923 (s), 2869 (s), 2825 (s), 2739 (w), 2687 (w), 2363 (w), 2325 (w), 2274 (w), 1792 (w), 1656 (w), 1588 (w), 1532 (w), 1452 (s), 1372 (m), 1330 (m), 1267 (m), 1226 (m), 1163 (m), 1110 (s), 1078 (w), 1038 (w), 973 (m), 852 (s), 826 (s), 757 (m), 699 (vs). HRMS (ESI): Calcd [M + H]$^+$, 202.0719; Found, 202.0717.

N-(2-Nitrobenzyl)-2-(ethylthio)-*N*-(thiophen-2-yl)methyl)ethanamine (29). 2-Nitrobenzylbromide (3.20 g, 14.8 mmol), amine 28 (3.00 g, 14.9 mmol), K$_2$CO$_3$ (4.00 g, 28.9 mmol) and activated 3 Å molecular sieves were combined in 50 mL of MeCN and stirred vigorously overnight at room temperature. The reaction was filtered through Celite and the solvent removed to yield a brown oil. Flash chromatography on silica gel (7:1 hexanes/EtOAc) gave the pure product as a yellow oil (4.1 g, 81%). TLC R$_f$ = 0.40 (silica, 7:1 hexanes/EtOAc). ^{1}H NMR (CDCl$_3$, 300 MHz) δ 1.20 (3H, t), 2.46 (2H, q), 2.62 (2H, m), 2.72 (2H, m), 3.84 (2H, s), 3.99 (2H, s), 6.93 (2H, m), 7.22 (1H, dd), 7.40 (1H, t), 7.59 (1H, td), 7.86 (2H, m). ^{13}C NMR (CDCl$_3$, 125 MHz) δ 14.91, 26.17, 29.22, 52.81, 53.47, 55.10, 124.56, 125.17, 126.19, 126.69, 128.01, 130.97, 132.88, 134.94, 141.73, 149.78. FTIR (NaCl disk, cm^{-1}) 3101 (w), 3069 (w), 2963 (s), 2925 (s), 2862 (s), 2824 (s), 1608 (m), 1576 (m), 1524 (s), 1486 (w), 1445 (m), 1360 (s), 1302 (m), 1266 (m), 1217 (w), 1157 (w), 1108 (m), 1072 (w), 1040 (m), 970 (m), 853 (m), 827 (m), 784 (s), 730 (s), 702 (s). HRMS (ESI): Calcd [M + H]$^+$, 337.1039; Found, 337.1044.

N-(2-Aminobenzyl)-2-(ethylthio)-*N*-(thiophen-2-yl)methyl)ethanamine (30). A portion (620 mg, 1.84 mmol) of 29 was dissolved in 20 mL of 19:1 MeOH/CHCl$_3$ and added to an argon-purged flask containing Pd/C (10% activated, 500 mg). A balloon of H$_2$ was attached and the reaction was stirred vigorously overnight. The reaction was purged with Ar, filtered through Celite and the solvent removed in vacuo. The resulting yellow oil was purified by flash chromatography on silica gel (4:1 hexanes/EtOAc with 1% Et$_3$N), which gave the pure product as an off-white oil (292 mg, 52%). TLC R$_f$ = 0.56

(silica, 4:1 hexanes/EtOAc). ^{1}H NMR (CDCl$_3$, 300 MHz) δ 1.21 (3H, t), 2.45 (2H, q), 2.72 (4H, m), 3.70 (2H, s), 3.83 (2H, s), 4.81 (2H, s, br), 6.66-6.72 (2H, m), 6.92-6.98 (2H, m), 7.05 (1H, d), 7.12 (1H, td), 7.25 (1H, dd). ^{13}C NMR (CDCl$_3$, 125 MHz) δ 14.87, 25.94, 29.21, 51.83, 52.57, 57.93, 115.74, 117.63, 122.20, 125.19, 126.61, 128.66, 130.90, 141.35, 147.20. FTIR (NaCl disk, cm^{-1}) 3433 (s, br), 3315 (s, br), 3203 (m), 3101 (m), 3067 (m), 3022 (m), 2975 (m), 2926 (m), 2810 (s), 2718 (m), 2645 (m), 1925 (w), 1892 (w), 1788 (w), 1723 (w), 1613 (s), 1493 (s), 1450 (s), 1362 (s), 1311 (s), 1286 (s), 1222 (s), 1155 (s), 1039 (m), 963 (s), 930 (s), 851 (s), 825 (s), 749 (s), 697 (s), 540 (m). HRMS (ESI) Calcd [M + H]$^+$, 207.1297; Found, 307.1295.

2-{2-Chloro-5-{[(2-ethylsulfanylethyl)thiophen-2-ylmethylamino]methyl}phenyl-amine)methyl]-6-hydroxy-3-oxo-3H-xanthen-9-yl}benzoic acid (31, mercury sensor 6, MS6). Portions of aniline **30** (35 mg, 0.11 mmol) and fluorescein **1** (41 mg, 0.10 mmol) were combined in 4 mL of dry EtOAc and the clear red-orange solution was stirred overnight at room temperature. The solvent was removed under reduced pressure to yield imine **32** as a magenta residue. The residue was dissolved in 4 mL of 1,2-dichloroethane and NaB(OAc)$_3$H (20 mg, 0.14 mmol) was added. The reaction was stirred for 4 h at room temperature and the solvent was removed in vacuo. Preparative TLC on silica gel (20:1 CHCl$_3$/MeOH) yielded pure MS6 as a red powder (49 mg, 69%). TLC R$_f$ = 0.33 (silica, 20:1 CHCl$_3$ /MeOH). ^{1}H NMR (CD$_3$OD, 300 MHz) δ 0.94 (3H, t), 2.12 (2H, q), 2.35 (2H, m), 2.48 (2H, m), 3.58 (2H, m), 3.73 (2H, s), 4.61 (2H, m), 6.60-6.71 (3H, m), 6.81 (2H, m), 7.00-7.11 (4H, m), 7.22 (2H, m), 7.63 (2H, m), 8.08 (1H, d). HRMS (ESI) Calcd [M + H]$^+$, 685.1892; Found, 685.1586.

N-(2-Nitrobenzyl)-N-methyl(pyridin-2-yl)methanamine (33). Portions of 2-nitro-benzylbromide (361 mg, 1.67 mmol), N-methyl(aminomethyl)pyridine (**8**, 204 mg, 1.67 mmol) and K$_2$CO$_3$ (360 mg, 2.60 mmol) were combined in 10 mL of MeCN and a scoop of Na$_2$SO$_4$ was added. The reaction was stirred at room temperature for 4 days, during which time it turned dark brown. The reaction was filtered and the solvent removed in

vacuo to yield a brown oil. Flash chromatography on silica gel (2:1 hexanes/EtOAc) afforded the pure product as a viscous brown oil (165 mg, 38%). TLC R_f = 0.30 (silica, 1:1 hexanes/EtOAc). ^{1}H NMR (CDCl$_3$, 300 MHz) δ 2.18 (2H, s), 3.69 (2H, s), 3.93 (2H, s), 7.15 (1H, t), 7.30 (2H, m), 7.54 (1H, td), 7.65 (2H, m), 7.81 (1H, dd), 8.50 (1H, dd). ^{13}C NMR (CDCl$_3$, 125 MHz) δ 42.39, 58.78, 63.59, 122.01, 122.79, 124.27, 127.98, 131.06, 132.36, 134.11, 136.52, 148.70, 149.79, 158.96. FTIR (NaCl disk, cm^{-1}) 3064 (m), 3009 (m), 2979 (m), 2948 (m), 2911 (m), 2877 (m), 2842 (s), 2798 (s), 1680 (w), 1609 (m), 1589 (s), 1570 (m), 1528 (vs), 1474 (s), 1455 (s), 1434 (s), 1363 (s), 1299 (m), 1263 (m), 1242 (m), 1195 (m), 1148 (m), 1126 (m), 1047 (m), 1031 (s), 995 (m), 980 (m), 954 (w), 883 (m), 860 (m), 818 (w), 783 (m), 762 (s), 733 (s), 705 (w), 679 (w), 670 (m), 639 (w), 617 (m), 518 (w). HRMS (ESI) Calcd [M + H]$^+$, 258.1237; Found, 258.1245. We note that TLC analysis showed this reaction was virtually complete after ~18 h.

N-(2-Aminobenzyl)-*N*-methyl(pyridin-2-yl)methanamine (34). Palladium black (50 mg) was placed in a flask and purged with Ar. A solution of 33 (150 mg, 0.660 mmol) in 6 mL of MeOH was added to the flask and a balloon with H$_2$ attached. The reaction was purged with H$_2$ and stirred vigorously under an H$_2$ atmosphere for 40 min. The reaction was purged with Ar and filtered through Celite. The solvent was removed under reduced pressure, which gave a brown oil. Flash chromatography on silica gel with a solvent gradient (CH$_2$Cl$_2$ to 9:1 CH$_2$Cl$_2$/MeOH) gave the product as a viscous brown oil (96 mg, 64%). TLC R_f = 0.20 (silica, 20:1 CH$_2$Cl$_2$/MeOH). ^{1}H NMR (CDCl$_3$, 300 MHz) δ 2.22 (3H, s), 3.58 (2H, s), 3.63 (2H, s), 3.68 (2H, s), 4.81 (2H, s, br), 6.64-6.70 (2H, m), 7.02 (1H, dd), 7.09 (1H, td), 7.17 (1H, td), 7.32 (1H, d), 7.65 (1H, td), 8.56 (1H, d). ^{13}C NMR (CDCl$_3$, 125 MHz) δ 42.39, 61.59, 63.57, 115.63, 117.65, 122.25, 122.92, 123.26, 128.62, 130.86, 147.10, 149.37, 159.26. FTIR (NaCl disk, cm^{-1}) 3353 (m), 3314 (m), 3202 (m), 3008 (w), 2992 (s), 2851 (m), 2792 (m), 1653 (m), 1616 (s), 1590 (s), 1569 (m), 1494 (s), 1460 (s), 1433 (m), 1364 (m), 1316 (m), 1286 (m), 1239 (w), 1192 (w), 1147 (w), 1124 (w), 1092 (w),

1021 (m), 995 (w), 971 (w), 930 (w), 867 (m), 842 (w), 749 (s), 725 (m), 638 (w), 613 (w), 540 (w). HRMS (ESI) Calcd [M + H]$^+$, 228.1495; Found, 228.1503.

Zinpyr-11 (34, ZP11). Portions of fluorescein **1** (50 mg, 0.13 mmol) and aniline **34** (27 mg, 0.13 mmol) were combined in 5 mL of EtOAc to yield a clear orange solution, which was stirred overnight at room temperature. Some yellow precipitate formed. The solvent was removed in vacuo, which gave a magenta foam. The foam was dissolved in 3 mL of DCE and NaB(OAc)$_3$H (30 mg, 0.14 mmol) was added and the solution was cloudy and orange. After stirring overnight at room temperature, the solvent was removed under reduced pressure and preparative TLC on silica gel (100% MeOH) gave the pure product as an orange powder (10 mg, 13%). ^{1}H NMR (CD$_3$OD/CDCl$_3$, 300 MHz) δ 2.10 (3H, s), 3.49 (4H, m), 4.54 (2H, m), 6.59 (3H, m), 6.95 (1H, d), 7.04-7.72 (6H, m), 7.28 (1H, d), 7.55 (2H, qd), 8.05 (1H, dd), 8.25 (1H, d). FTIR (KBr, cm^{-1}) 3436 (m, br), 2954 (w), 2922 (m), 2852 (m), 1764 (m), 1636 (s), 1608 (s), 1574 (s), 1524 (m), 1493 (m), 1493 (m), 1461 (m), 1371 (m), 1341 (m), 1262 (w), 1211 (w), 1341 (m), 1154 (m), 1092 (m), 1045 (w), 1008 (m), 939 (w), 863 (w), 824 (w), 754 (m), 714 (w), 629 (w), 597 (w), 552 (w). HRMS (ESI) Calcd [M – H]$^-$, 604.1645; Found, 604.1656.

2-((Quinolin-8-yl)methyl)isoindoline-1,3-dione (36). Potassium phthalamide (841 mg, 4.54 mmol) and 8-bromomethylquinoline (1.00 g, 4.54 mmol) were combined in 20 mL of DMF and heated to 90 °C. After 3 h, the reaction was poured into 100 mL of water and a white precipitate formed. The mixture was stirred for 30 min and filtered. The precipitate was washed with water and dried in vacuo (1.03 g, 78%). TLC R$_f$ = 0.35 (silica, 2:1 hexanes/EtOAc); mp = 218-220 °C. ^{1}H NMR (CDCl$_3$, 300 MHz) δ 5.66 (2H, s), 7.44 (2H, m), 7.76 (2H, m), 7.91 (1H, m), 8.16 (1H, dd), 8.98 (1H, m) ^{13}C NMR (CDCl$_3$, 125 MHz) δ 38.35, 121.48, 123.61, 126.34, 126.52, 127.58, 128.44, 132.44, 134.22, 136.44, 146.02, 149.77, 168.55. FTIR (KBr, cm^{-1}) 3464 (w), 3058 (w), 3041 (w), 3019 (w), 2941 (w), 1821 (w), 1805 (w), 1772 (w), 1705 (s), 1612 (m), 1596 (m), 1579 (m), 1498 (s), 1464 (m), 1421 (s), 1401 (s), 1388 (s), 1375 (s), 1337 (m), 1318 (m), 1250 (w), 1236 (w), 1192 (m), 1171 (w),

1133 (w), 1110 (s), 1088 (m), 1073 (m), 1047 (w), 1013 (w), 973 (m), 954 (s), 904 (m), 866 (m), 821 (s), 802 (m), 786 (s), 770 (m), 743 (s), 713 (s), 640 (m), 625 (w), 601 (m), 554 (m), 531 (m), 513 (m), 503 (m), 420, (m), 410 (m). HRMS (ESI) Calcd [M + H]$^+$, 289.0972; Found, 289.0967.

8-(Aminomethyl)quinoline (37). A portion (953 mg, 0.331 mmol) of **36** was suspended in 30 mL EtOH and heated to 60 °C. Hydrazine monohydrate (175 μL) was added and the reaction heated to reflux for 8 h, cooled and the solvent removed in vacuo. The resulting solid was dissolved in 50 mL of 1:1 1 M NaOH / CHCl$_3$ and the layers were partitioned. The aqueous phase was extracted with CHCl$_3$ (2 x 25 mL) and the combined organic layers were dried over MgSO$_4$ and concentrated under reduced pressure, which yielded the product as an orange-brown oil (433 mg, 83%) TLC R$_f$ = 0.35 (Al$_2$O$_3$, 9:1 CHCl$_3$/MeOH). ^{1}H NMR (CDCl$_3$, 300 MHz) δ 1.97 (2H, s), 4.38 (2H, s), 7.33-7.68 (2H, m), 7.59 (1H, d), 7.66 (1H, d), 8.09 (1H, dd), 8.88 (1H, dd). ^{13}C NMR (CDCl$_3$, 125 MHz) δ 44.21, 121.07, 126.47, 127.01, 127.73, 128.49, 136.41, 141.39, 146.69, 149.48. FTIR (KBr, cm^{-1}) 3073 (m, br), 2839 (w), 2712 (w), 2564 (w), 1782 (m), 1735 (m), 1675 (s), 1597 (m), 1506 (w), 1464 (w), 1443 (m), 1387 (m), 1308 (w), 1271 (w), 1199 (s), 1139 (s), 1045 (w), 998 (w), 912 (w), 835 (m), 798 (m), 760 (s), 721 (m), 706 (m), 596 (m), 518 (m). HRMS (ESI) Calcd [M + H]$^+$, 159.0917; Found, 1590923.

2-(5-(((Quinolin-8-yl)methylamino)methyl)-2-chloro-6-hydroxy-3-oxo-3H-xanthen-9-yl)benzoic acid (38, QZ3). Portions of amine **37** (31.0 mg, 0.195 mmol) and fluorescein **1** (75.5 mg, 0.191 mmol) were combined in 5 mL of EtOAc to yield a cloudy orange-pink solution that was stirred overnight at room temperature. A pink precipitate formed and the mixture was filtered and the precipitate washed with 15 mL of cold EtOAc. The precipitate was dissolved in 5 mL of 1,2-dichloroethane and NaB(OAc)$_3$H (41 mg, 0.193 mmol) was added. The reaction was stirred overnight at room temperature and the solvent removed under reduced pressure. Preparative TLC on silica gel (2:1 CHCl$_3$/MeOH) afforded the pure product as a deep red powder (9.7 mg, 10%). ^{1}H NMR

(CDCl$_3$, 300 MHz) δ 4.49 (2H, m), 4.80 (2H, m), 6.44 (1H, d), 6.55 (1H, s), 6.97 (1H, d), 7.16 (2H, m), 7.51-7.61 (5H, m), 7.82 (1H, d), 7.95 (1H, d), 8.03 (1H, m), 8.36 (1H, d), 8.96 (1H, m). HRMS (ESI) Calcd [M – H]$^-$, 535.1055; Found, 535.1042.

Results and Discussion

Design, Synthesis and Characterization of Compound 13. The Cys$_2$His$_2$ binding motif observed in the Zn(II) finger peptides inspired the design of **13** (Scheme A1.1). This fluorescein-based ligand incorporates an azepane ring into an aniline-derived ligand framework. We initially imagined that **6** could act as a pro-sensor and, upon entering cells, the disulfide bond would be reduced and afford an N$_2$S$_2$O chelate for Zn(II) detection. Scheme A1.1 illustrates the synthesis of compound **13**. The aniline-based ligand fragment **12** can be prepared in four steps starting from 2-nitrobenzylbromide. Conversion of the benzylbromide to the benzylamine **11** is achieved in two steps and in high yield (~80%) using the Gabriel synthesis. Cleavage of the phthalimide protecting group is most efficient using hydrazine monohydrate, and essentially quantitative yield is achieved when a basic workup is employed. The seven-member disulfide-containing ring is installed by reaction of amine **10** with excess ethylene sulfide at 100 °C in a small volume of C$_6$H$_5$CH$_3$ to give **11**. Although highly reproducible, this reaction is low-yielding (~14%) because of the large amounts of insoluble polymeric material that forms during the course of the reaction. Hydrogenation of **11** using 1 to 1.5 weight-equivalents of Pd black affords complete conversion to the hydrogenated product in 1-3 hours. Pd black was chosen because Pd/C was inactivated by reduction of the disulfide bond and thiol association. Pd black also reduces the disulfide to the corresponding dithiol, which is easily seen by TLC. Oxidation occurs on the column during chromatography, and disulfide **12** is eluted. Condensation of **12** with 2'-chloro-5'-fluoresceincarboxaldehyde, **1**, in EtOAc followed

by borohydride reduction in DCE and preparative TLC on silica (20:1 CHCl$_3$/MeOH) affords the final product in 52% yield.

Preliminary photophysical characterization of **13** revealed a quantum yield of 0.04 (50 mM PIPES, 100 mM KCl, pH 7). Like other aniline-derivatized fluorescein-based sensors, the emission of **13** is pH dependent, as depicted in Figure A1.1, with an aniline pK_a value of 6.4 and a pK_a of 5.0 for phenol protonation. All attempts to generate a fluorescence response to Zn(II) or Hg(II) failed. Addition of reducing agents, including glutathione and ascorbic acid, did not promote fluorescence enhancement. No further investigations of **6** were undertaken.

Attempted Syntheses of Compounds 18 and 19. As described in Chapter 9, Hg(II) sensors MS2 and MS3 both have pyridyl-amine-thiol ligands linked to the fluorescein platform through tertiary amines. During their preparation, we considered the design of an aniline-based analogs, compounds **18** and **19**, which we anticipated would have lower background fluorescence and be sensitive to Zn(II) and/or Hg(II). The routes to these dyes are illustrated in Scheme A1.2. Reaction of commercially available o-nitrobenzylbromide with either amine **2** or **3** in the presence of K$_2$CO$_3$ gives **14** and **16**, respectively, in high yields. Hydrogenation of **14** and **16** in MeOH using ~1.5 weight equiv of Pd black yields the aniline-derived ligand fragments **15** and **17** in 54% and 27% yield, respectively. Both of these aniline-derivatized ligands were coupled to the fluorescein carboxaldehyde, **1**, in EtOAc followed by reduction of the resulting imine using NaB(OAc)$_3$H as the reducing agent and both ^{1}H NMR and mass spectrometry indicated formation of the desired trityl protected sensors in good purity. Removal of the trityl groups can be accomplished by dropwise addition of Et$_3$SiH to a solution of **20** or **21** in TFA. Although the sensors **18** and **19** have been identified by mass spectrometry and although solutions of these sensors show fluorescence enhancement upon Zn(II) and Hg(II) addition, their purification remains a significant problem. Despite a number of syntheses and purification attempts, neither pure **18** nor pure **19**

have been isolated. Alternative synthetic routes, which allow for thiol deprotection before coupling of the aniline unit to fluorescein **1**, were pursued in detail; however, we were unable to purify the final products. In hindsight, this problem is not particularly surprising given the addition of a thiol group to a platform that already presents purification challenges.

Synthesis and Characterization of Compound 22. A thioether analog of our symmetric ZP sensors[8] was synthesized by a Mannich reaction between 2′,7′-dichlorofluorescein and the imminium ion condensation product of 3,9-dithia-6-azaundecane[4], **4**, and paraformaldehyde as shown in Scheme A1.3. Sensor **22** was isolated in 17% yield as an orange-pink solid following solvent evaporation and trituation with boiling EtOH. We anticipated that **22** would exhibit selectivity for Hg(II).

The pH profile of **22** is shown in Figure A1.2 and indicates that two protonation events affect its fluorescence with pK_{a1} = 8.2, assigned to the tertiary amine, and pK_{a2} = 1.9, which corresponds to protonation of the phenol oxygen atom and formation of a non-fluorescent isomer. The tertiary amine pK_a is similar to that of the di(2-picolyl)amine based Zn(II) sensor ZP1.[8] We find that apo **22** has a quantum yield of 0.39 (λ_{max} = 526 nm) at pH 7 (50 mM PIPES, 100 mM KCl, excess EDTA). Addition of Hg(II) to a solution of **22** causes immediate fluorescence quenching, depicted in Figure A1.3, with Φ_{Hg}= 0.25 (λ_{max} = 534 nm, pH 7). Coordination of Hg(II) to **22** also causes a red-shift in the UV-vis spectrum from 507 (ε = 79,000 $M^{-1}cm^{-1}$) to 516 (ε = 87,900 $M^{-1}cm^{-1}$) nm. The difference spectrum exhibits an absorption increase at 522 nm and a decrease at 503 nm, indicative of perturbation of the fluorescein π system by Hg(II) coordination. Introduction of Zn(II), Cd(II), Ni(II) and Cu(II) to solutions of **22** also resulted in fluorescence quenching at neutral pH. These preliminary metal binding studies also indicated that **22** has high selectivity for Cu(II), as previously observed for the thioether-containing Hg(II) sensor MS1.[9] When the pH is raised to pH 11, **22** shows ~5-fold turn-on with Hg(II) coordination (Figure A1.3).

Design, Synthesis and Characterization of Other Potential Hg(II) Sensors with Thioether Donors. Schemes A1.5 and A1.6 depict fluorescein-based sensors with multiple thioether donors that were prepared. Compounds **23** and **24** are thioether analogs of the tertiary amine-based Hg(II) sensors MS2 and MS3. We originally thought that substitution of the pyridyl-amine-thiol ligand moiety in MS2 with thioether-rich chelates would afford sensors with MS2-like brightness and MS1-like selectivity (see Chapters 8 and 9 for details). Compound **23** employs the 3,9-dithia-6-azaundecane[4] fragment that is common to previously described sensors MS1 and MS5. Motivated by a literature report where fluorescence turn-on was observed following Hg(II) coordination to nitrobenzyloxadiazolyl chromophores appended with multiple thioether groups,[10] we decided to assess the utility of ligand **6** (Scheme A1.4) for Hg(II) sensing and therefore prepared compound **24** (Scheme A1.5).

Given the latter objective, the preparation of bis-[2-(2-ethylsulfanylethylsulfanyl)-ethyl]amine, **6**, is necessary and proved challenging. Scheme A1.4 illustrates preparative routes to this species and a necessary intermediate, 2-ethylsulfanylethanethiol.[4,5] One literature synthesis of **5** involves reaction of excess 1,2-ethanedithiol with iodoethane in the presence of sodium.[4] This reaction generates considerable stench because of the ~25 g of 1,2-ethanedithiol required to theoretically obtain ~5 g of product. Despite multiple attempts and varied conditions, essentially no product was recovered following work-up and this general route was ultimately aborted. An alternative and intriguing literature preparation for alkylmercaptans involves reduction of 1,3-dithiolanes in liquid ammonia.[5] Selective cleavage of a single C—S bond in a substituted 1,3-dithiolane can be achieved when a stoichiometric quantity of Ca turnings is used. This route yielded **5** in good yield and high purity as a clear, colorless liquid from 2-methyl-13-dithiolane following work-up and vacuum distillation. The desired amine **6** was prepared from **5** and bis(2-chloroethyl)amine hydrochloride according to a literature procedure[4] and was isolated as a brown viscous oil with a faint stench. Approximately

two years after this synthetic work, alternative literature procedures for **5** and **6** were reported as part of the synthesis of a BODIPY-based sensor for Cu(I) ion.[11]

Compounds **23** and **24** were prepared by reaction of the appropriate thioether-derivatized secondary amine and bromomethyl fluorescein **7** in dry MeCN with base (Scheme A1.5). Both **23** and **24** were purified by preparative TLC on silica gel and were isolated as red (**23**) or orange (**24**) solids in moderate to good yields.

An asymmetrical MS1 analog employing ligand **6** was also prepared as shown in Scheme A1.6. The aniline-based ligand **26** was synthesized in two steps starting from commercially available 2-nitrobenzylbromide and **6**. Compound **25** was obtained in modest yield following chromatography on silica gel and reduction of the nitro group to an amino group occurred readily when Pd black was used. Schiff base condensation of **26** with fluorescein **1** followed by imine reduction gave **27** as an orange-red solid after preparative TLC on silica gel (15:1 $CHCl_3$/MeOH).

Some preliminary fluorescence investigations of **23, 24** and **27** were conducted. These studies revealed that all three sensors give fluorescence turn-off following Hg(II) coordination at neutral pH (50 mM PIPES, 100 mM KCl, pH 7). Figure A1.4 shows representative fluorescence spectra for **27** in the absence and presence of various metal ions. Coordination of **27** to Hg(II) causes ~2.7-fold fluorescence quenching and the quantum yield decreases from 0.19 ($\lambda_{max} = 530$ nm) to 0.13 ($\lambda_{max} = 531$ nm). Fluorescence turn-off is also occurs with addition of Ni(II), Cu(II), Zn(II), Cd(II) and Pb(II) to solutions of **27** (Figure A1.4); Cu(II) shows the most profound effect. The behavior of **27** was a surprise given the fluorescence enhancement previously observed for parent sensor MS1. No further spectroscopic characterization of **23, 24** or **27** was pursued.

Synthesis and Characterization of Hg(II) Sensor MS6. Our aim in this synthesis of mercury sensor 6 (MS6) was to learn whether substitution of one thioether moiety in MS1[9] with a thiophene group would yield a turn-on sensor with good Hg(II) selectivity and lower affinity than the parent compound ($EC_{50} = 410$ nM for 1 μM MS1).

Scheme A1.7 illustrates the preparation of MS6. Secondary amine **28** was obtained in high yield following Schiff base condensation and reductive amination of 2-thiophenecarboxaldehyde and 2-(ethylthiol)ethylamine. *N*-Alkylation of **28** with 2-nitrobenzylbromide gave **29** in 81% yield following purification by flash chromatography. Reduction of the nitro group using Pd/C (10% activated) afforded aniline **30** in moderate yield after purification. MS6 was assembled from 7'-chloro-4'-fluoresceincarboxaldehyde, **1**, by the established route and was isolated as a deep red solid in 69% yield following preparative TLC on silica gel.

Figure A1.5 depicts the fluorescence response of MS6 to excess Hg(II) at neutral pH and in the presence of chloride ion (50 mM PIPES, 100 mM KCl,). Modest ~1.9-fold fluorescence enhancement occurs following Hg(II) coordination. Whether this relatively smaller change is real or the result of a small fluorescent impurity that increases the baseline emission is currently unclear. Approximately ~250 equiv of Hg(II) are required to observe full turn-on, which indicates that the thiophene-for-thioether substitution decreases the Hg(II) affinity substantially. As shown in Figure A1.6, the selectivity of MS6 for Hg(II) is analogous to that of MS1 and only Cu(II) interferes with the Hg(II)-induced fluorescence response. No further characterization of MS6 was pursued.

Synthesis of ZP11. As described in Chapters 1 to 7 of this thesis, obtaining Zn(II) sensors with a range of dissociation constants can be achieved through modification of the Zn(II) binding unit. Reducing the number of the donor atoms is one powerful approach. In this section, we report the synthesis of Zn(II) sensor ZP11, which is a ZP4 derivative that lacks one pyridyl group. Scheme A1.8 illustrates the synthesis of the required aniline-based ligand **34**, which was obtained in modest yield over two steps, and the ZP11 assembly from fluorescein **1**. Although no careful spectroscopic characterization has been performed, ZP11 shows fluorescence enhancement following Zn(II) coordination. Based on our studies of ZP9 and ZP10 detailed in Chapter 2, we reason that ZP11 will have sub- or low-μM affinity for Zn(II).

Synthesis of QZ3. Given the success of QZ1 and QZ2, we are interested in preparing new QZ derivatives and QZ3, which contains an 8-(aminomethyl)quinoline moiety, is illustrated in Scheme A1.9. Several considerations motivated its preparation. From the perspective of Zn(II) coordination, the QZ3:Zn(II) complex will have two 6-membered chelate rings in contrast to one 5- and one 6-membered chelate in QZ1, which should result in stabilization of the Zn(II) complex relative to the parent compound (QZ1 K_d ~ 40 μM). We also questioned the effect of the inserted methylene unit on sensor emission and since this methylene spacer disrupts conjugation between the nitrogen atom considered the PET switch and the quinoline unit.

Scheme A1.9 illustrates the synthesis of QZ3. 8-(Aminomethyl)quinoline, **37**, was prepared from 8-(bromomethyl)quinoline by the Gabriel synthesis and obtained in good yield (65% over two steps) as an orange-brown oil. Schiff base condensation of **37** and fluorescein **1** followed by imine reduction afforded QZ3 in low yield (10%) as a deep red powder after preparative TLC on silica gel. The poor yield resulted from the purification procedure, which required multiple rounds of preparative TLC.

Preliminary fluorescence experiments with QZ3 indicated behavior in striking contrast to that of QZ1. At neutral pH (50 mM PIPES, 100 mM KCl, pH 7), QZ3 gives bright emission with Φ_{free} = 0.75 and essentially no fluorescenc echange with Zn(II) addition (Figure A1.7, top). Its background emission is similar to that of ZS3, an asymmetrical tertiary amine-based sensor. This structural variation also has a profound impact on pH sensitivity (Figure A1.7, bottom). Titrations monitored with fluorescence spectroscopy indicate that QZ3 fluorescence is affected by two protonation events with pK_{a1} = 10 (tertiary amine) and pK_{a2} = 4.8 (fluorescein phenol) and displays maximum and stable emission from ~5 to ~9. This pH profile is also reminiscent of asymmetrical tertiary-amine based ZS3. Solutions of cupric sulfate were added to QZ3 to determine the effect of a paramagnetic metal ion on its fluorescence (50 mM PIPES, 100 mM KCl, pH 7). An ~16-fold fluorescence decrease is observed upon addition of Cu(II) to QZ3,

which is similar to the behavior of tertiary-amine based ZP and ZS probes and contrasts the negligible fluorescence change observed following Cu(II) binding to QZ1 and other aniline-based sensors. No further experiments with QZ3 were conducted. Although this dye is useless from a Zn(II) sensing standpoint, its behavior in light of QZ1 is intriguing and further comparison of the two species is warranted and should help shed light on the details of the quenching mechanism in aniline-based probes.

References

(1)   Nolan, E. M.; Burdette, S. C.; Harvey, J. H.; Hilderbrand, S. A.; Lippard, S. J. *Inorg. Chem.* **2004**, *43*, 2624-2635.

(2)   Kramer, D. J.; Davison, A.; Davis, W. M.; Jones, A. G. *Inorg. Chem.* **2002**, *41*, 6181-6183.

(3)   Nolan, E. M.; Racine, M. E.; Lippard, S. J. *Inorg. Chem.* **2006**, *46*, 2742-2749.

(4)   Tanaka, M.; Nakamura, M.; Ikeda, T.; Ikeda, K.; Ando, H.; Shibutani, Y.; Yajima, S.; Kimura, K. *J. Org. Chem.* **2001**, *66*, 7008-7012.

(5)   Newman, B. C.; Eliel, E. L. *J. Org. Chem.* **1970**, *35*, 3641-3646.

(6)   Burdette, S. C.; Frederickson, C. J.; Bu, W.; Lippard, S. J. *J. Am. Chem. Soc.* **2003**, *125*, 1778-1787.

(7)   Fischer, A.; King, M. S.; Robinson, F. P. *Can. J. Chem.* **1978**, *56*, 3059-3067.

(8)   Burdette, S. C.; Walkup, G. K.; Spingler, B.; Tsien, R. Y.; Lippard, S. J. *J. Am. Chem. Soc.* **2001**, *123*, 7831-7841.

(9)   Nolan, E. M.; Lippard, S. J. *J. Am. Chem. Soc.* **2003**, *125*, 14270-14271.

(10)   Sakamoto, H.; Ishikawa, J.; Nakao, S.; Wada, H. *Chem. Commun.* **2001**, 2395-2396.

(11)   Zeng, L.; Miller, E. W..; Pralle, A.; Isacoff, E. Y.; Chang, C. J. *J. Am. Chem. Soc.* **2006**, *128*, 10-11.
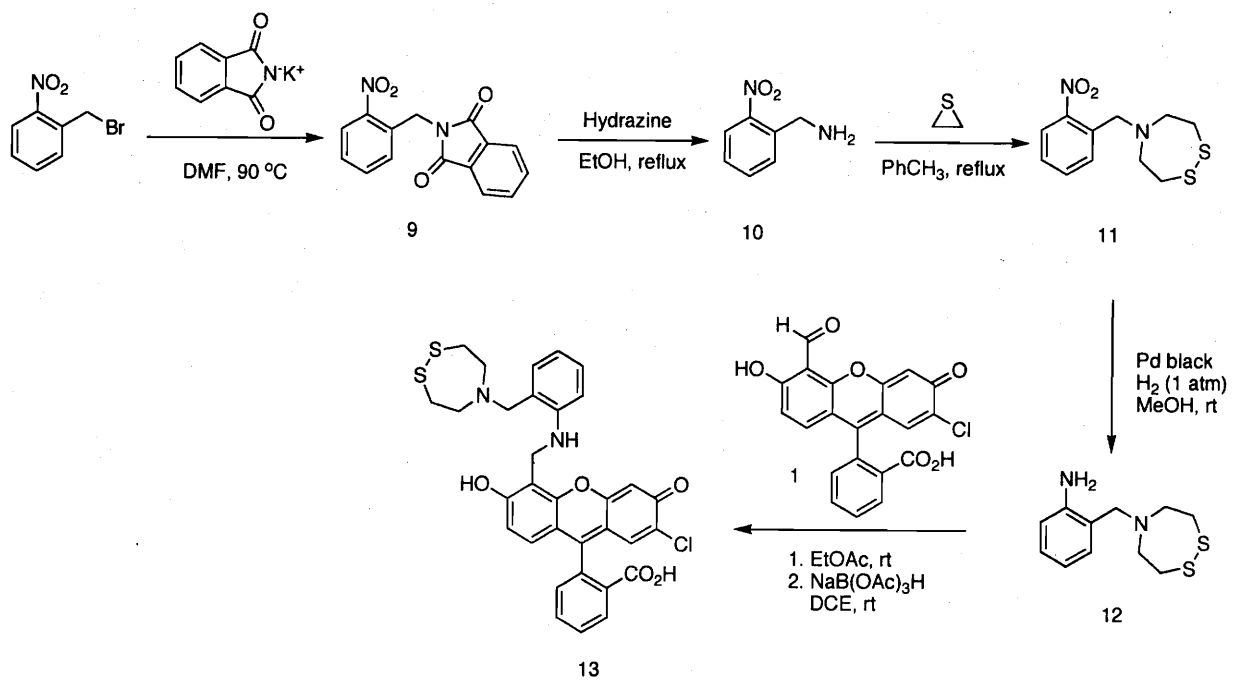
Scheme A1.1. Synthesis of compound **13**.
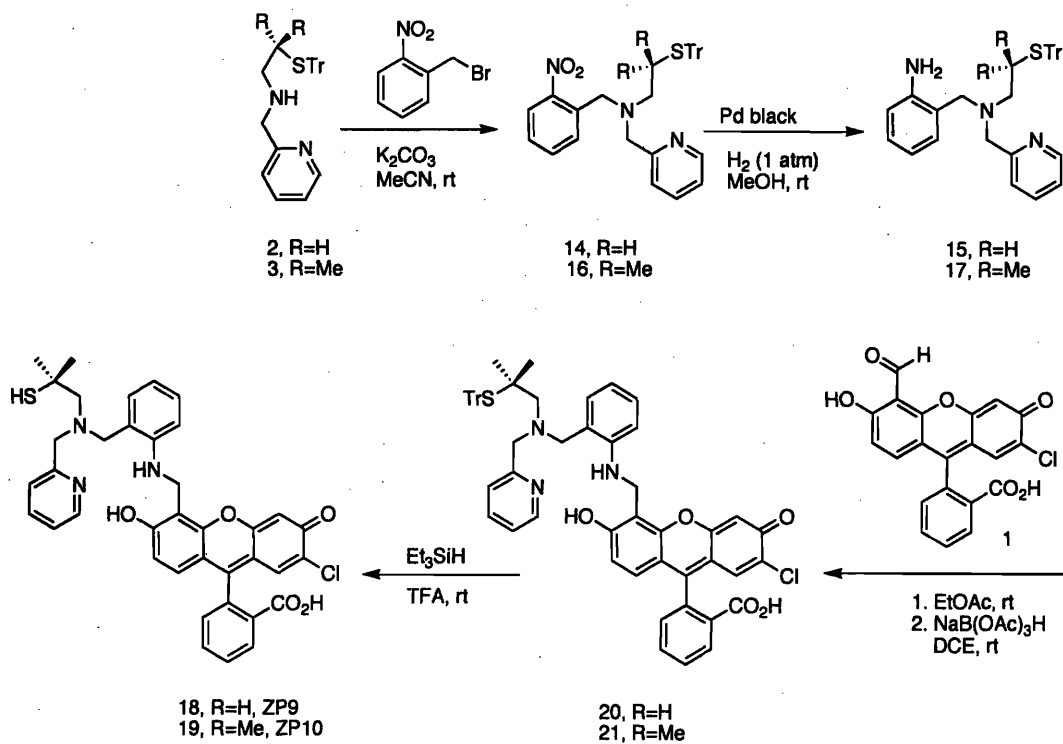
Scheme A1.2. Syntheses of compounds **18** and **19**.
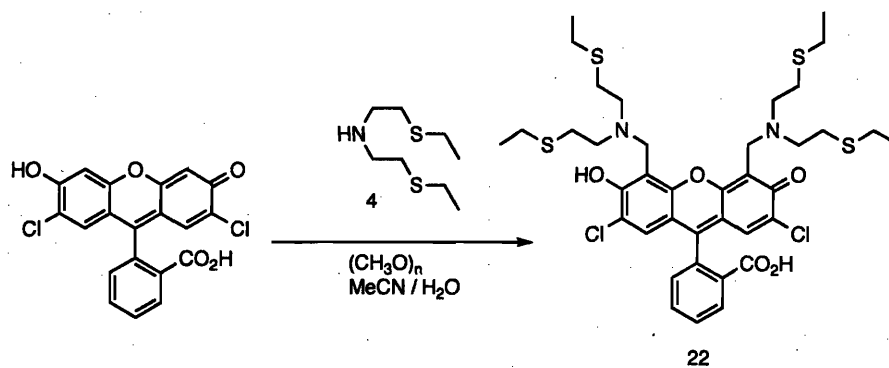
Scheme A1.3. Synthesis of compound **22.**
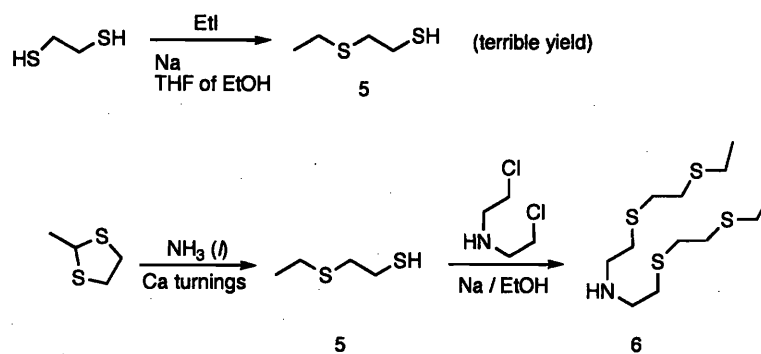
Scheme A1.4. Published synthetic routes to **5** and **6** (see refs. 4 and 5).
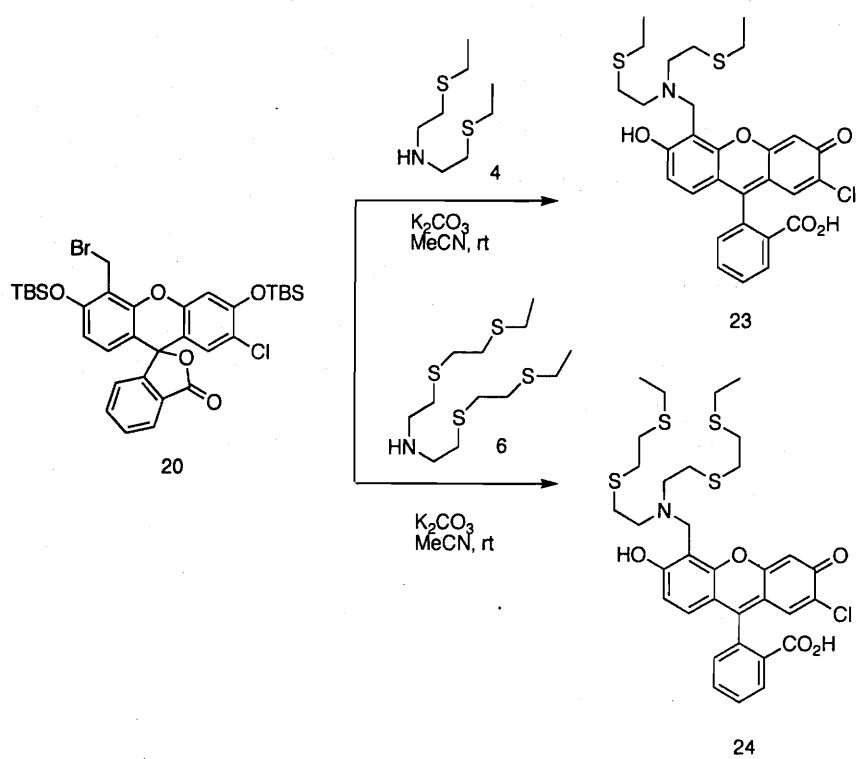
Scheme A1.5. Syntheses of compounds **23** and **24**.
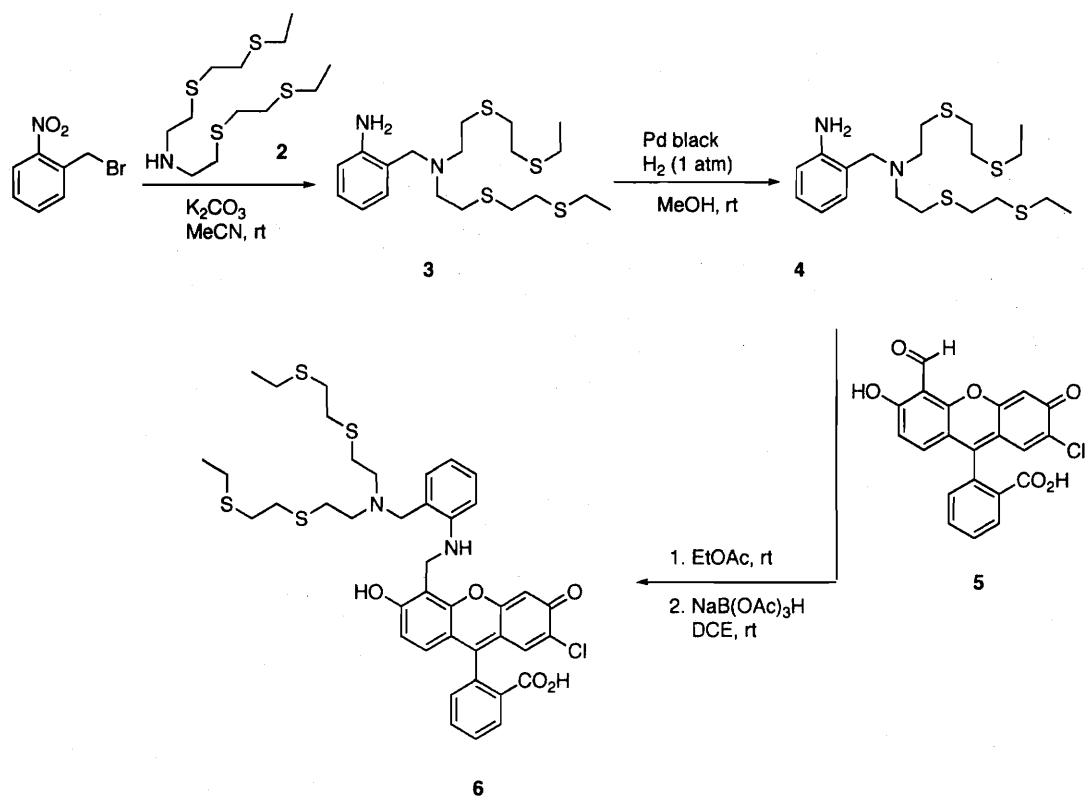
Scheme A1.6. Synthesis of compound **27**.
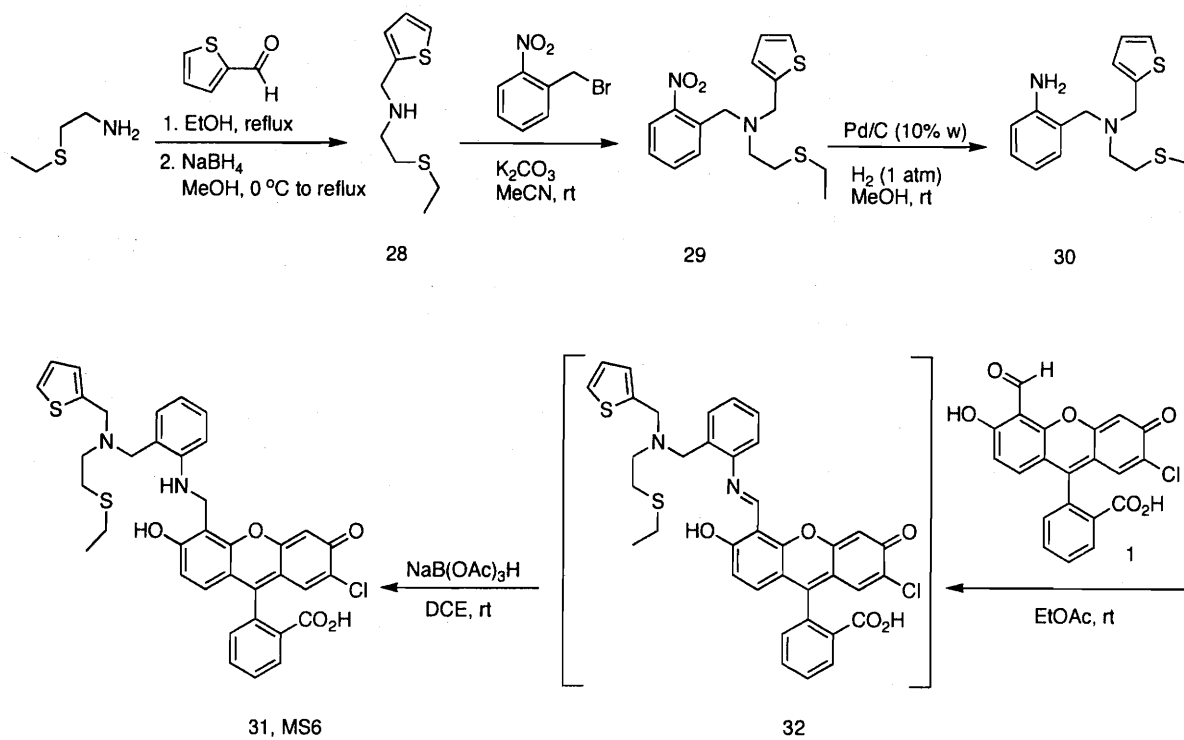
Scheme A1.7. Synthesis of MS6.
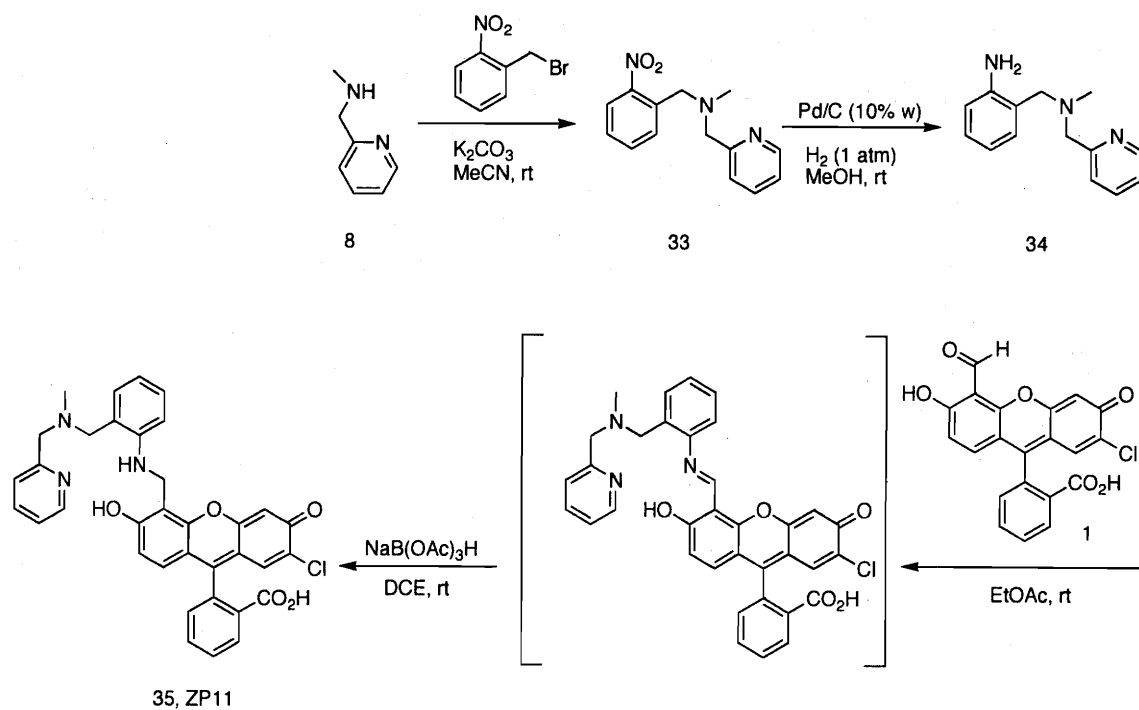
Scheme A1.8. Synthesis of Zn(II) sensor ZP11.
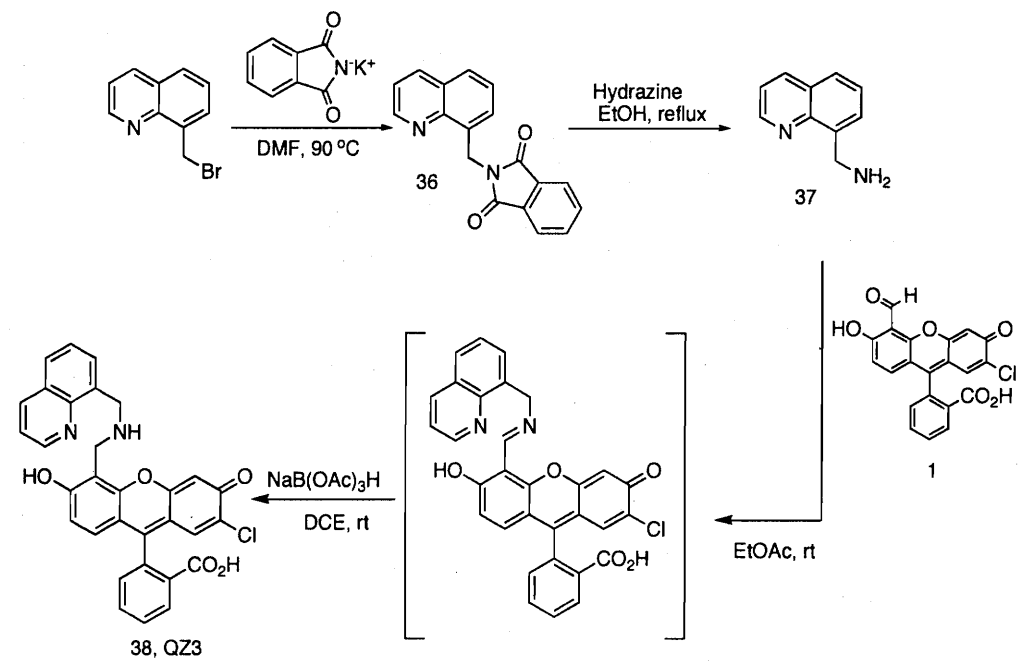
Scheme A1.9. Synthesis of QZ3.
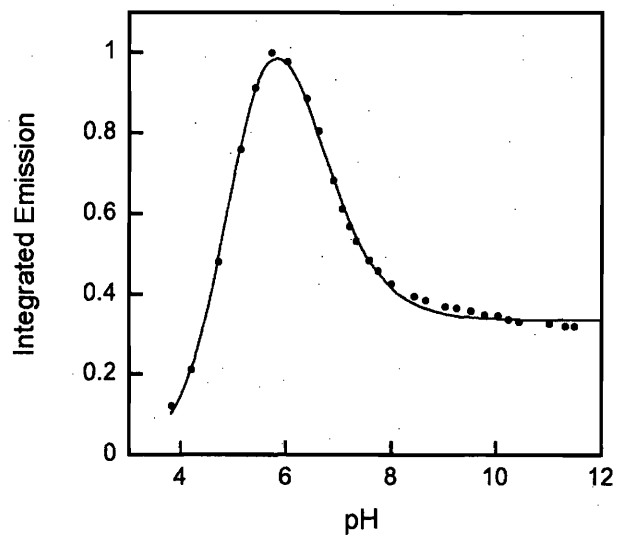
Figure A1.1. Representative pK_a titration for compound **13** that affords pK_{a1} = 6.4 (aniline nitrogen atom) and pK_{a2} = 5.0 (fluorescein phenol). [**13**] = 1 μM (100 mM KCl), λ_{ex} = 504 nm and T = 25 °C.
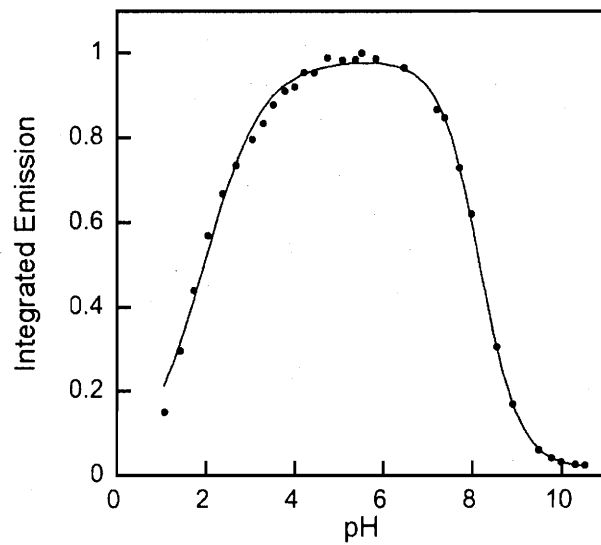
Figure A1.2. Representative pK_a titration for compound **22** that affords pK_{a1} = 8.2 (tertiary amine) and pK_{a2} = 1.9 (2′,7′-dichlorofluorescein phenol). [**22**] = 1 μM (100 mM KCl), λ_{ex} = 505 nm and T = 25 °C.
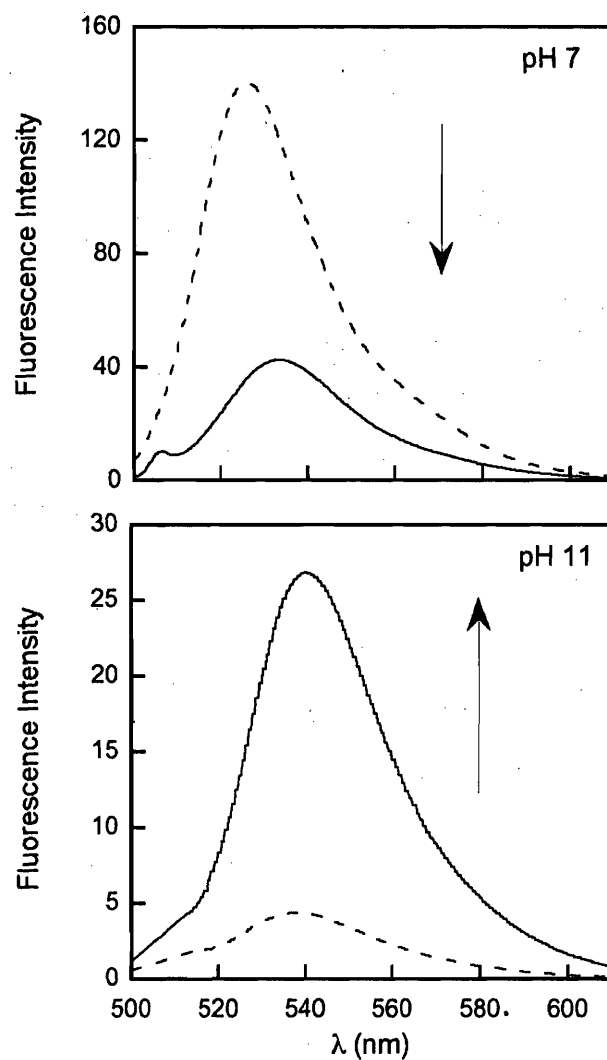
Figure A1.3. Fluorescence response of compound **22** to excess Hg(II) at pH 7 (top; 50 mM PIPES, 100 mM KCl, pH 7) and at pH 11 (bottom; 50 mM CABS, 100 mM KCl, pH 11). The dashed and solid lines represent the emission before and after Hg(II) addition, respectively. [**22**] = 1 µM, λ_{ex} = 505 nm and T = 25 °C.
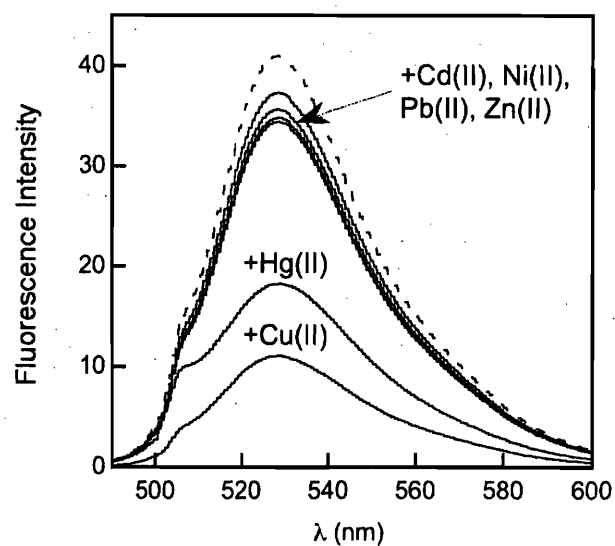
Figure A1.4. Fluorescence response of compound **27** to various divalent metal ions (50 mM PIPES, 100 mM KCl, pH 7). The dotted line represents emission from the free probe. [**27**] = 1 μM, λ_{ex} = 500 nm, T = 25 °C.
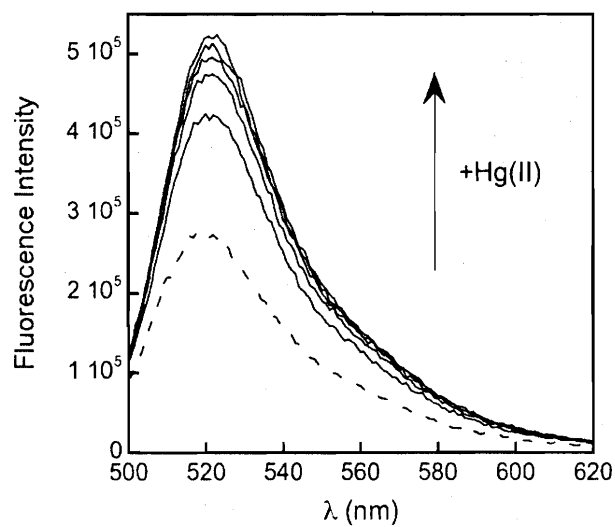
Figure A1.5. Fluorescence response of 1 µM MS6 (dotted line) to excess Hg(II) at pH 7

(50 mM PIPES, 100 mM KCl). Aliquots of 10 mM HgCl$_2$ in water were added to yield 0,

50, 100, 150, 200 and 250 µM Hg(II). An ~1.9-fold fluorescence enhancement is observed.

Excitation was provided at 495 nm and T = 25 °C.
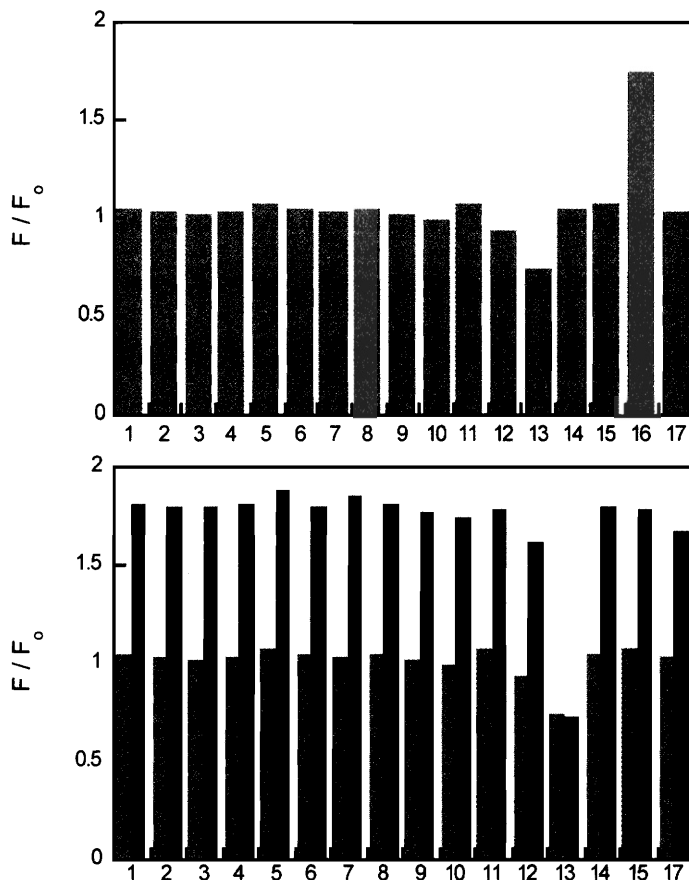
Figure A1.6. Selectivity of MS6 for Hg(II) over other metal ions at pH 7 (50 mM PIPES, 100 mM KCl, pH 7). Top plot: the light grey bars represent the fluorescence change upon introduction of 150 equiv of the cation of interest: 1, Li(I); 2, Na(I); 3, Rb(1); 4, Mg(II); 5, Ca(II); 6, Sr(II); 7, Ba(II); 8, Cr(III); 9, Mn(II); 10, Fe(II); 11, Co(II); 12, Ni(II); 13, Cu(II); 14, Zn(II); 15, Cd(II); 16, Hg(II); 17, Pb(II). Bottom plot: the light grey bars correspond to those in the top plot. The dark grey bars show the fluorescence change that occurs immediately upon introduction of 150 equiv of Hg(II) to the solution containing MS6 and the cation of interest. All data are normalized with respect to free dye emission (F_o). Excitation was provided at 495 nm, [MS6] = 1 μM and T = 25 °C.
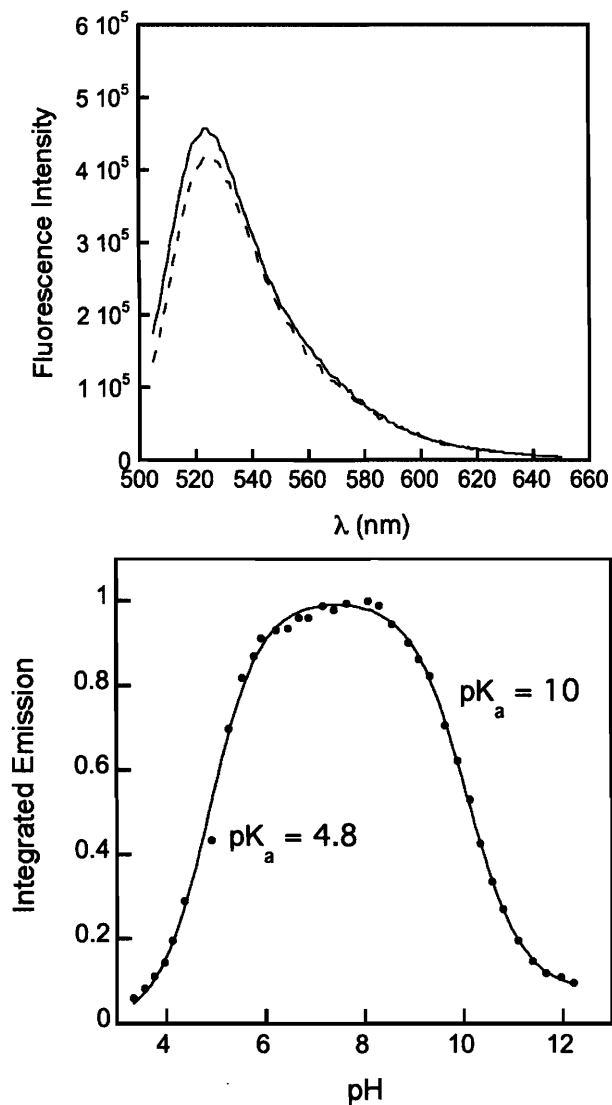
Figure A1.7. Top: Fluorescence response of 1 μM QZ3 to 500 equiv of Zn(II) at pH 7 (50 mM PIPES, 100 mM KCl). The dashed and solid lines represent emission before and after Zn(II) addition, respectively. Excitation was provided at 500 nm and T = 25 °C. Bottom: Effect of pH on the fluorescence emission of 1 μM QZ3 (100 mM KCl). Excitation was provided at 495 nm and T = 25 °C.

Appendix 2

Theoretical Investigations of Fluorescein Derivatives

Introduction

Despite the ubiquity of fluorescein in the biological and chemical literature and its rich ~150 year history, few theoretical investigations of the molecule and its derivatives have been undertaken.[1-3] The existing studies are generally limited in scope and only focus on the results of geometry optimizations of fluorescein in its various isomeric forms[1,2] or on other ground state phenomena.[3] The dearth of theoretical investigations on fluorescein and related chromophores may reflect the fact that calculating interactions of matter with light, including photoexcitation and fluorescence, is complicated. Standard density functional theory (DFT) only provides information pertaining to electronic ground states. Time-dependent DFT (TDDFT) must be used to study the photophysical behavior of molecules.[4]

With the ultimate goal of calculating intramolecular electron transfer (ET) rates for fluorescein-based metal ion sensors, which should correlate with fluorescence quenching, we have initiated theoretical investigations of fluorescein and related compounds. In this work, we use DFT to explore the energetics of fluorescein in its various forms and assign the protonation equilibria of 2′,7′-dichlorofluorescein. We also employ TDDFT to simulate and assign fluorescein absorption spectra. This work will provide a solid foundation for studies of more complex systems (ZP, Chapter 2; QZ, Chapter 7) in addition to future ET matrix element calculations. To the best of our knowledge, these studies include the first use of DFT and TDDFT to assign fluorescein pK_a values and absorption spectra, respectively.

Calculational Methods

All calculations were performed with either the Jaguar 5.5 (Schrödinger, Inc.) or the Amsterdam Density Function (ADF) 200.01 software package. In most circumstances, geometries were optimized in Jaguar using the B3LYP functional and the 6-31G** basis set. This basis set reliably predicts ground state geometries, but often generates

inaccurate SCF energies. As a result, single point calculations were conducted on each 6-31G** geometry with the cc-pVTZ(-f) basis set, a triple-zeta quality basis set that increases the computational cost substantially and generates reliable E(SCF). Geometries optimized with the cc-pVTZ(-f) basis set were used for determining pK_a values because results obtained from the 6-31G**/cc-pVTZ(-f) level of theory were energetically unreasonable. Vibrational frequency calculations were performed with Jaguar to obtain zero point energies (ZPE) and entropies (ΔS) and to verify that the converged geometries were ground state structures. Solvation energies were calculated with a model that treats the solvent as a dielectric continuum. A dielectric constant of 78.4 was used for water. Free energies of solution ($\Delta G_{solution}$) are both entropy and zero point energy corrected and were calculated according to the eq. A2.1 to A2.3. TDDFT was implemented with the ADF software package. Basis set IV was used for All TDDFT calculations. To determine the most appropriate method, the LB94, BLYP, PW91 and

$$\Delta H_{gas} = E(SCF) + ZPE \tag{A2.1}$$

$$\Delta G_{gas} = \Delta H_{gas} - (298.15 \text{ K})\Delta S \tag{A2.2}$$

$$\Delta G_{solution} = \Delta G_{gas} + \Delta G_{solvation} \tag{A2.3}$$

PBE functionals were tested for their ability to reproduce known absorption spectra of organic chromophores. The LB94 functional was employed for all subsequent calculations.

Results and Discussion

Energies of Fluorescein Isomers. Because of its propensity to exist in a variety of colors, the structure of solid fluorescein mystified researchers for over a century. In 1980, an IR study on carefully prepared yellow, red and colorless forms of fluorescein resulted in the correct structural assignments of these species.[5] This work showed that the yellow and red forms of fluorescein correspond to the zwitterionic and quinoid structures, respectively, and confirmed that the colorless powder is the lactone (Figure

A2.1). The structural assignments for the yellow and red forms were later verified by ^{13}C NMR spectroscopic analysis.[6] Although these investigations dispelled a significant amount of confusion regarding fluorescein color and structure in the solid state, several questions arguably remain concerning the nature of fluorescein in solution. The fact that the lactone isomer exists only in anhydrous, non-polar solvents is accepted. Introduction of the colorless lactone into polar or protic media immediately causes the solution to turn yellow, indicative of ring-opening. The nature of the ring-opened form – i.e. quinoid or zwitterion – in solution is somewhat less clear. In one study, solutions of fluorescein were prepared from either the red (quinoid) or yellow (zwitterion) solids, and the resulting solutions were both yellow in color.[7] Independent titrations of both species yielded essentially identical pK_a values. From these observations, the authors concluded that only one form of fluorescein exists and, because of the yellow color of the solution, the form must be the zwitterionic form.[7] This conclusion is not particularly satisfying since no other studies were reported that support this claim and there is no obvious reason why the quinoid structure should be a different color in solution. Approximately fifteen years later, an IR and Raman study of fluorescein in solution was reported, but there was absolutely no discussion of zwitterionic vs. quinoid structure.[8] Other publications state that the quinoid exists in solution, but give no proof for their assertion.[9] This state of affairs is particularly bothersome from a basic chemical standpoint and because fluorescein is widely encountered in the chemical and biological literature. One powerful approach to resolving this issue is to determine and compare the solution phase free energies of fluorescein in its various forms (Figure A2.1). Table A2.1 details the computational results from this investigation.

Well-defined structures for the quinoid and lactone forms of neutral fluorescein were obtained from geometry optimizations in both the gas and solution phase. The zwitterion, **2**, does not exist in the gas phase; lactone formation resulted from these geometry optimizations. Nevertheless, an optimized geometry for the zwitterion was

obtained by taking solvation into account (ADF software). A comparison of the free energies listed in Table A2.1 indicates that the quinoid structure is 1.4 kcal/mol more stable than the lactone and 35.9 kcal/mol more stable than the zwitterion ion in the gas phase at the 6-31G**/cc-pVTZ level of theory. The solution phase free energies for the quinoid and zwitterion differ by 20.3 kcal/mol with the quinoid structure being energetically favored. The smaller energy difference in the solution phase results from the higher solvation energy of the charge-separated zwitterion. These calculations indicate that the quinoid, not the zwitterion, is the predominant species present in aqueous solution. Calculations at the ccpTVZ(-f)++ level of theory also predict this trend, although the energy difference between the quinoid and zwitterion is smaller (10.7 kcal/mol).

Protonation Constants for 2',7'-Dichlorofluroescein. The effect of pH on fluorescein absorption and emission has been the topic of many experimental investigations.[7,9-12] The general consensus from these studies is that, upon moving from high to low pH, the phenol oxygen atom of the xanthene system protonates first, followed by protonation of the carboxylate group of the benzoate ring and subsequently protonation of the keto group to form the fluorescein cation,[9] although some studies suggest that the carboxylate protonates first.[11] The absolute pK_a values for these protonation events vary with substitution on the xanthenone ring. For instance, the pK_a values for 2',7'-dichlorofluorescein (pK_a = 4.95, 3.50, 0.47)[10] are all lower than those of unsubstituted fluorescein (pK_a = 6.4, 4.3, 2.2),[9] which results from the electron-withdrawing nature of the Cl substituents.

Accurately calculating the pK_a values of fluorescein and related species will offer credibility to our theoretical framework and will provide a basis for pK_a calculations for more complicated systems, including the sensors described in earlier chapters. Absolute pK_a values can be obtained by calculating ΔG_{deprot}, the solution phase free energy change associated with deprotonation, as shown below.[13]

$$FH \rightarrow F^- + H^+$$

$$\Delta G_{deprot} = \Delta G(F^-) + \Delta G(H^+) - \Delta G(FH) \qquad (A2.4)$$

where $\Delta G(F^-)$ and $\Delta G(FH)$ are the zero-point energy and entropy-corrected solution phase free energies for the deprotonated (F⁻) and protonated (FH) fluorescein, respectively. The value for $\Delta G(H^+)$, the free energy of a proton, was calculated as shown below in eq. A2.5 where ΔS is the translational entropy of a proton (26.014 cal/mol-K).[13]

$$\Delta G(H^+) = E_{solv} + 5/2RT - T\Delta S \qquad (A2.5)$$

Equation A2.6 illustrates the relationship between ΔG_{deprot} and the equilibrium constant, K_{deprot}, for the deprotonation reaction under consideration. The pK_a value can be calculated according to eq. A2.7 where the constant 1.3658 applies to T = 298.15 K and units of kcal/mol.

$$\Delta G_{deprot} = -RT \ln K_{deprot} \qquad (A2.6)$$

$$pK_a = \Delta G_{deprot} / 1.3658 \qquad (A2.7)$$

Since we commonly use 2',7'-dichlorofluorescein (DCF) to prepare Zn(II) sensors by the Mannich reaction, we first examined the protonation equilbria for this species. Figure A2.2 shows the possible deprotonation routes starting from DCF cation and gives both the experimentally and theoretically determined pK_a values. We find good agreement between the experimental and calculated values and a plot of calculated vs. experimental pK_a has a slope of 0.9995 (r = 0.946). Two possible paths exist for deprotonation of neutral DCF. In accord with experimental evidence,[10] the analysis indicates that the carboxylate moiety deprotonates first. Loss of a proton from the phenol of neutral DCF followed by deprotonation of the carboxylate is energetically unreasonable.

TDDFT Calibration and Method Determination. Our aim is to achieve a detailed, molecular orbital-based understanding of fluorescein absorption and our tool of choice is TDDFT. In order to establish a working theoretical framework for this investigation, we used TDDFT to simulate the absorption spectra of several known organic dyes and

structurally related compounds that span a wide range of excitation wavelengths. The performance of four different functionals (LB94, BLYP, PW91, PBE) was evaluated to determine the most appropriate method for reproducing the absorption spectra of organic chromophores. Table A2.2 summarizes the results from this comparative study, in addition to experimentally obtained data. We anticipated that the LB94 functional would give reasonable A_{max} values because it was devised for predicting excitation energies. A plot of LB94 calculated versus experimentally determined A_{max} shows linearity (Figure A2.3, r = 0.930), which indicates good agreement between the actual and calculated values and verifies the reliability of the method.

TDDFT of Fluorescein I: Simulation of Absorption Spectra. The absorption and emission spectra of fluorescein vary significantly with pH as summarized in Table A2.3.[9] Fluorescein dianion exhibits an intense absorption band centered at 490 nm (ε = 76,900 $M^{-1}cm^{-1}$) with a shoulder at 475 nm and several distinct peaks in the UV-region. Protonation of the phenol group gives fluorescein monoanion, which is characterized by two weaker absorption bands of similar intensity (472, 453 nm, $\varepsilon \sim$ 29,000 $M^{-1}cm^{-1}$). The neutral quinoid shows A_{max} at 434 nm (ε = 11,000 $M^{-1}cm^{-1}$) and a shoulder at 475 nm (ε = 3,600 $M^{-1}cm^{-1}$). The neutral lactone does not absorb in the visible region. Fluorescein cation shows a relatively intense absorption band at 437 nm (ε = 56,000 $M^{-1}cm^{-1}$) and less intense features at 297 and 250 nm.

TDDFT was used to simulate the absorption spectra of the various isomers and protonation states of fluorescein and Table A2.3 includes the results from these calculations. Good agreement between experimentally determined and calculated A_{max} values was obtained and the correlation is shown in Figure A2.4 (slope = 0.90, r=0.97). The calculated oscillator strengths do not correlate well with the experimentally determined extinction coefficients; however, calculated oscillator strengths are generally considered to be unreliable and so this behavior was not unexpected.[14]

TDDFT on the neutral lactone form gives no absorption (data not shown), in agreement with experimental observation.

TDDFT of Fluorescein II. Assignment of Spectra. The molecular orbitals responsible for fluorescein absorption were analyzed. With the exceptions of the neutral zwitterion, which we exclude from this discussion because we found the quinoid to be energetically favored in solution, and the colorless lactone, the transients underlying fluorescein absorption are xanthene-based $\pi \rightarrow \pi^*$ transitions. In what follows, we focus our discussion on fluorescein dianion, which is the predominant species in solution at pH 7 and is symmetric, which facilitates the MO analysis. The donor and acceptor molecular orbitals assigned to fluorescein dianion absorption are given in Figure A2.5. The donor MO is the HOMO and has no C_1 character (see Figure A2.1 for atom numbering). In contrast, the acceptor orbital, which is the LUMO, has substantial C_1 character. This observation points to a key role for the C_1 π and π^* orbitals in fluorescein absorption, and offers a rationale for the colorless nature of the lactone form. Formation of the lactone ring involves nucleophilic addition of the carboxylate oxygen atom to C_1 of the xanthenone system. As a result of lactone formation, the C_1 π^* orbital is no longer available to accept an excited electron, and no absorption occurs in the visible region.

The observation that the benzoate moiety plays no role in fluorescein absorption was expected given the reported absorption spectra of several xanthenone-based compounds including 6-hydroxyxanthen-3-one,[15] **7**, and 6-hydroxy-9-phenylxanthen-3-one,[16] **8**, (Figure A2.6). In mixed aqueous/organic solvents, these species, which either lack the benzoate carboxylate functionality or the benzoate moiety altogether, have absorption spectra similar to that of fluorescein dianion ($A_{max} \sim 490$ nm). TDDFT on the anionic forms of **7** and **8** reproduces the experimentally observed spectra. Figure A2.7 shows the donor and acceptor molecular orbitals assigned to the absorption spectra of these two xanthenone species. These molecular orbitals are completely analogous to those responsible for fluorescein dianion absorption (Figure A2.5).

Molecular Orbital Analysis. The analyses described above suggest that elucidating the nature of the donor and acceptor molecular orbitals involved in fluorescein dianion absorption is possible through consideration of the xanthenone portion alone. As a result, an in depth analysis of the molecular orbitals of the anionic form of **7** was conducted. This compound contains a fused, three-ring system, which can be related to that of anthracene, $C_{14}H_{10}$. Unlike xanthenone chromopohores, however, anthracene exhibits no absorption in the visible region. This comparison indicates that the xanthenone oxygen atoms exert significant influence on the nature of the donor and/or acceptor molecular orbitals involved in its absorption. To understand the influence of these oxygen atoms, the π molecular orbitals in anthracene were correlated to those in the xanthenone framework by stepwise addition of the central and peripheral oxygen atoms. The resulting molecular orbital correlation diagram is depicted in Figure A2.8 (see Figures A2.9 – A2.11 for individual diagrams and representations of all MOs). Anthracene has 14 π electrons and the energies of its seven filled π molecular orbitals and its LUMO are presented in Figures A2.8 and A2.9. The HOMO-LUMO gap is 2.72 eV. Replacement of a central methylene group with an oxygen atom to afford xanthene perturbs the ordering and relative energies of the anthracene π molecular orbitals. The xanthene cation was used to conserve the 14 π electron count. The most striking change upon this substitution is the stabilization of the orbitals derived from 34a and 44a (left). These orbitals (29a and 29a, in middle) contain substantial C—O bonding character, and the energetic stabilization results from the fact that C—O bonds are inherently stronger than C—C bonds. The significant stabilization of the orbital derived from 44a (left) causes the orbital ordering to change (42a and 44a, middle, relative to 39a and 43a, left). Introduction of the central oxygen atom also results in increased aromatic character in the peripheral aryl rings. Finally, introduction of the central oxygen atom also stabilizes the frontier molecular orbitals and decreases the magnitude of the HOMO-LUMO gap

by ~0.7 eV and the amount of C_1 character in the LUMO increases upon introduction of the central oxygen atom.

The xanthenone framework can be obtained by replacing two peripheral hydrogen atoms with oxygen atoms. From a fragment molecular orbital perspective, this substitution can be considered by making bonding and antibonding combinations of the peripheral oxygen atom π molecular orbitals with the molecular orbitals of the xanthene system. The correlation diagram in Figure A2.8 depicts the results of this fragment analysis (see Figure A2.11 for all π molecular orbitals of the xanthenone anion). The fragment orbitals defined by the peripheral oxygen atoms form bonding and antibonding combinations with orbital 46a (middle), which results in one bonding (48a, right) and one antibonding (55a, right) combination. Formation of orbital 55a upon introduction of the peripheral oxygen atoms is critical since it results in alteration of the HOMO, the donor orbital, and further reduces the energy of the HOMO-LUMO gap (1.73 eV compared to 2.07 eV for central oxygen atom substitution and 2.71 eV for anthracene). It is also interesting to note that the resulting HOMO (55a, right) has no C_1 character as compared to HOMO 47a (middle) of the cationic species, which has some C_1 character. Destabilization of the LUMO also results due to gained antibonding interactions between the peripheral oxygen atom fragment and the fused ring fragment. Destabilization of 43a (middle, becomes 51a on right) results from a loss of bonding character in the peripheral aryl rings. Two orbitals (42a and 45a, right) are derived from molecular orbital 39a (middle), and 45a is relatively destabilized because of decreased bonding character across the bottom of the xanthenone moiety.

In summary, the main conclusions from this molecular orbital analysis are: (*i*) both the central and peripheral oxygen atoms are underlying contributors to xanthenone absorption, (*ii*) introduction of the central oxygen atom stabilizes both the HOMO and LUMO, and also causes the HOMO-LUMO gap to decrease by ~0.7 eV because of greater stabilization of the LUMO, (*iii*) the central oxygen atom causes an increase in the

contribution of C_1 to the LUMO, and (*iv*) introduction of the peripheral oxygen atoms alters the composition of the HOMO such that is has no C_1 character and further reduces the HOMO-LUMO gap.

Simulation and Assignment of Absorption Spectra for Protonated Fluorescein. The absorption spectra of anionic and neutral fluorescein have been simulated (Table A2.2) and preliminary molecular orbital assignments and analyses have been carried out. Figure A2.12 includes the molecular orbitals responsible for absorption of neutral fluorescein in addition to neutral **8**. Like fluorescein dianion, the transitions are completely xanthenone based $\pi \rightarrow \pi^*$ transitions and the acceptor orbitals have significant C_1 π character. In these systems, TDDFT generates two molecular orbital transitions of significant weight that contribute to fluorescein absorption. The dominant transition (weight = 0.742) originates from the HOMO-1 and the second transition comes from the HOMO-2 (weight = 0.204). Interestingly, the HOMO-1 has significant C_1 character and we speculate that this feature will play a critical role in explaining the differences in fluorescein dianion and monoanion absorption.

Summary and Perspectives

Theoretical investigations of fluorescein and some of its derivatives have been conducted. As a result of this work, we showed that the quinoid isomer, not the zwitterionic form, is energetically favored in solution. We established a protocol for calculating fluorescein pK_a values and reproduced the experimental pK_a results for 2',7'-dichlorofluorescein. Furthermore, our calculations indicate that the carboxylate moiety deprotonates first, in agreement with some experimental evidence and chemical intuition. A theoretical framework for using TDDFT to simulate and assign the absorption spectra of organic dyes was established and the absorption spectra of fluorescein in its various protonation states and isomeric forms investigated. These studies show that the donor/acceptor molecular orbital transitions responsible for

fluorescein (quinoid) absorption are all xanthenone-based and indicate that the empty π orbital on C_1 (acceptor orbital) is essential for fluorescein absorption. A molecular orbital analysis was conducted to ascertain how the central and peripheral oxygen atoms of the xanthenone unit influence absorption. These studies provide a solid foundation for investigations of more complicated systems, including fluorescein-based metal ion and NO sensors developed in our laboratory. Some preliminary steps toward this objective are included in Chapters 2 and 7.

References

(1)   Fabian, W. M. F.; Schuppler, S.; Wolfbeis, O. S. *J. Chem. Soc. Perkin Trans. 2* **1996**, 853-886.

(2)   Jang, Y.; Hwang, S.; Chung, D. S. *Chem. Lett.* **2001**, 1316-1318.

(3)   Ueno, T.; Urano, Y.; Setsukinai, K.-I.; Takakusa, H.; Kojima, H.; Kikuchi, K.; Ohkubo, K.; Fukuzumi, S.; Nagano, T. *J. Am. Chem. Soc.* **2005**, *127*, 4888-4894.

(4)   Marques, M. A. L.; Gross, E. K. U. *Annu. Rev. Phys. Chem.* **2004**, *55*, 427-455.

(5)   Markuszewski, R.; Diehl, H. *Talanta* **1980**, *27*, 937-946.

(6)   Anthoni, U.; Christophersen, C.; Nielsen, P. H.; Puschl, A.; Schaumburg, K. *Structural Chem* **1995**, *6*, 161-165.

(7)   Markuszewski, R.; Diehl, H. *Talanta* **1985**, *32*, 159-164.

(8)   Wang, L.; Roitberg, A.; Meuse, C.; Gaigalas, A. K. *Spectrochim. Acta A* **2001**, *57*, 1781-1791.

(9)   Sjöback, R.; Nygren, J.; Kubista, M. *Spectrochim. Acta A* **1995**, *57*, 1781-1791.

(10)   Leonhart, H.; Gordon, L.; Livingson, R. *J. Phys. Chem.* **1971**, *75*, 245-249.

(11)   Diehl, H.; Horchak-Morris, N.; Hefley, A. J.; Munson, L. F.; Markuszewski, R. *Talanta* **1986**, *33*,

         910-915.

(12)   Diehl, H.; Markuszewski, R. *Talanta* **1989**, *36*, 416-418.

(13)   Baik, M.-H.; Silverman, J. S.; Yang, I. V.; Ropp, P. A.; Szalai, V. A.; Yang, W.; Thorp, H. H. *J. Phys.

         Chem. B* **2001**, *105*, 6437-6444.

(14)   Baik, M.-H. *Personal communication.*

(15)   Shi, J.; Zhang, H.; Neckers, D. C. *J. Org. Chem.* **1992**, *57*, 4418-4421.

(16)   Lindqvist, L.; Lundeen, G. W.; Martin, M. *J. Chem. Phys.* **1971**, *55*, 3-4.

Table A2.1. Thermodynamic Data for Fluorescein Isomers[a]

	E(SCF)[b] (eV)	ΔG(solv)[c] (kcal/mol)	ZPE[d] (kcal/mol)	ΔS[e] (cal/mol-K)	ΔH$_{gas}$ (eV)	ΔG$_{gas}$ (eV)	ΔG$_{solution}$ (eV)
3	-31176.631	-16.58	172.96	140.091	-31169.131	-31170.942	-31171.661
1	-31176.590	-18.96	172.42	146.190	-31169.113	-31171.003	-31171.825
2	-31175.290	-34.60	173.13	16.586	-31167.782	-31169.445	-31170.945

[a] See Figure A2.1 for nomenclature. Geometries were optimized at the 6-31G** level. [b] Single point calculation performed at the ccpTVZ(-f) level of theory. [c] Solvation free energy calculated using a dielectric constant of 78.4 for water. [d] Calculated zero point energy. [e] Calculated entropy at 298.15 K. [f] Gas phase free enthalpy. [g] Gas phase free energy. [h] Solution phase free energy.

Table A2.2. Calculated and Experimental A_{max} for Selected Organic Compounds[a]

	BLYP (nm)	PW91 (nm)	PBE (nm)	LB94 (nm)	~Exp. (nm)
Coumarin	353	351	351	366	373
Dansyl Chloride	n.d.[b]	317	315	324	327
Acridine Orange	446	452	447	468	430
Phenolphthalein	n.d.	n.d.	n.d.	511	558
Indoaniline	488	489	489	413	525
Malachite Green	n.d.	531,	531,	552,	600,
	n.d.	473	452	453	435
Methylene Blue	535	538	538	561	609

[a] Geometries were optimized at the 6-31G** level of theory. [b] n.d. = not determined.

Table A2.3. TDDFT Results for Fluorescein Derivatives and Experimental Data[a]

Compound[b]	Absorption Exp. (nm)	Absorption LB94 (nm)	$\varepsilon \times 10^3$ ($M^{-1}cm^{-1}$)	Oscillator Strength LB94
6	490	471	76.9	0.322
	475	461		0.070
	322	328	9.5	0.032
	283	315	14.4	0.045
5	472	479	29.0	0.067
	453	464	29.0	0.116
	310	337	7.0	0.113
	273	301	17.0	0.158
1	475	476	3.6	0.135
	434	392	11.0	0.199
3		477		0.135
		453		0.272
4	437	422	53.0	0.300
	297	268	7.1	0.065
	250	259	33.0	0.440
DCF[2-]	515	483	101	0.405
DFF[2-]	490	472	92	0.311

[a] See Figure A2.1 for nomenclature. [b] Experimental data were taken from refs. 9, 10 and 14.
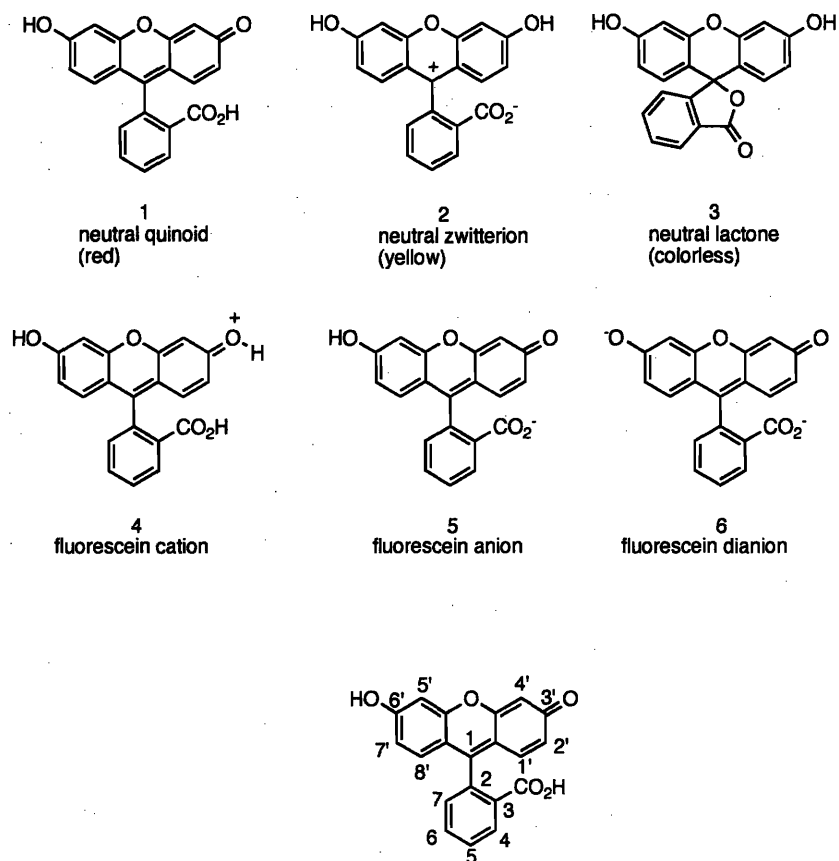
Figure A2.1. Fluorescein in its various isomeric forms and protonation states, and the numbering scheme for fluorescein and its derivatives. The cation, anion and dianion are represented with the quinoid structure. The dianion is responsible for fluorescein emission.
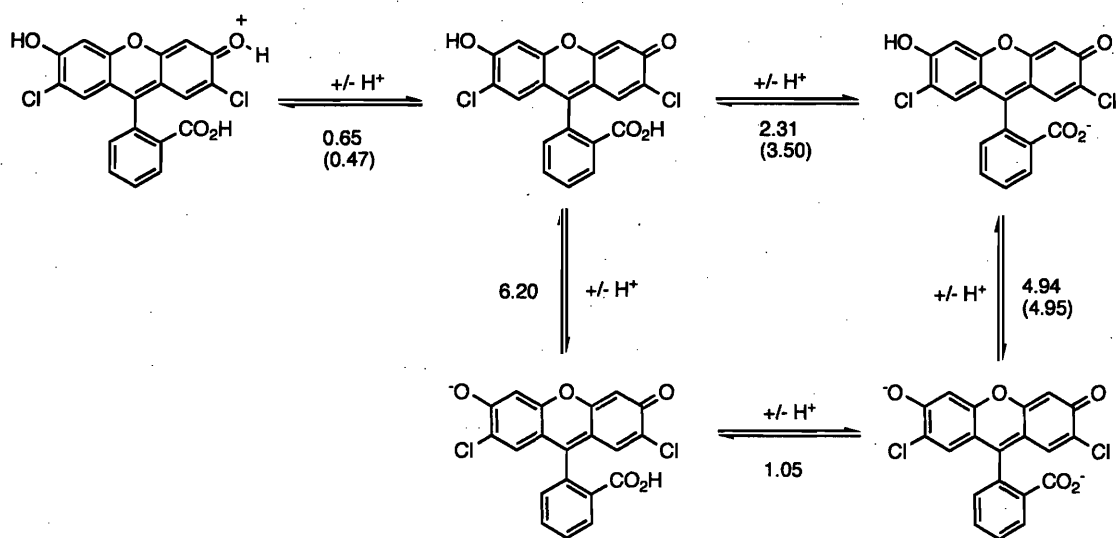
Figure A2.2. Calculated and experimental pK_a values for 2′,7′-dichlorofluorescein (DCF). The experimentally determined numbers are given in parantheses. Good correlation between the calculated and experimental values was obtained (slope = 0.9995, r = 0.546). Both experiment and theory agree that the carboxylate moiety deprotonates first.
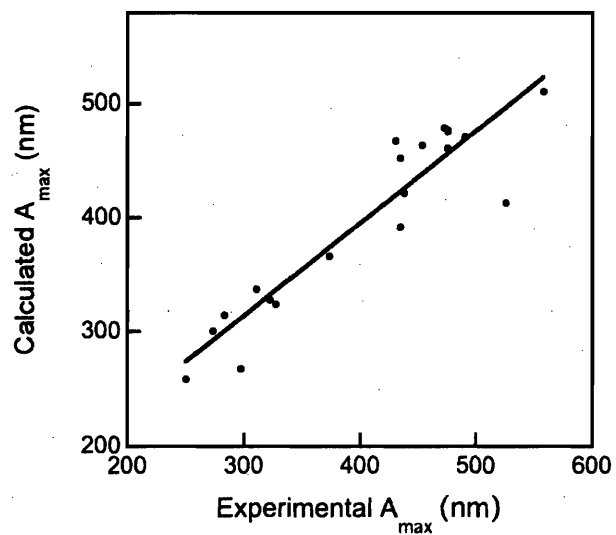
Figure A2.3. TDDFT calibration. Calculated vs. experimental A_{max} (slope = 0.809, r = 0.930). The data listed in Tables A2.1 and A2.2 are included in this plot.
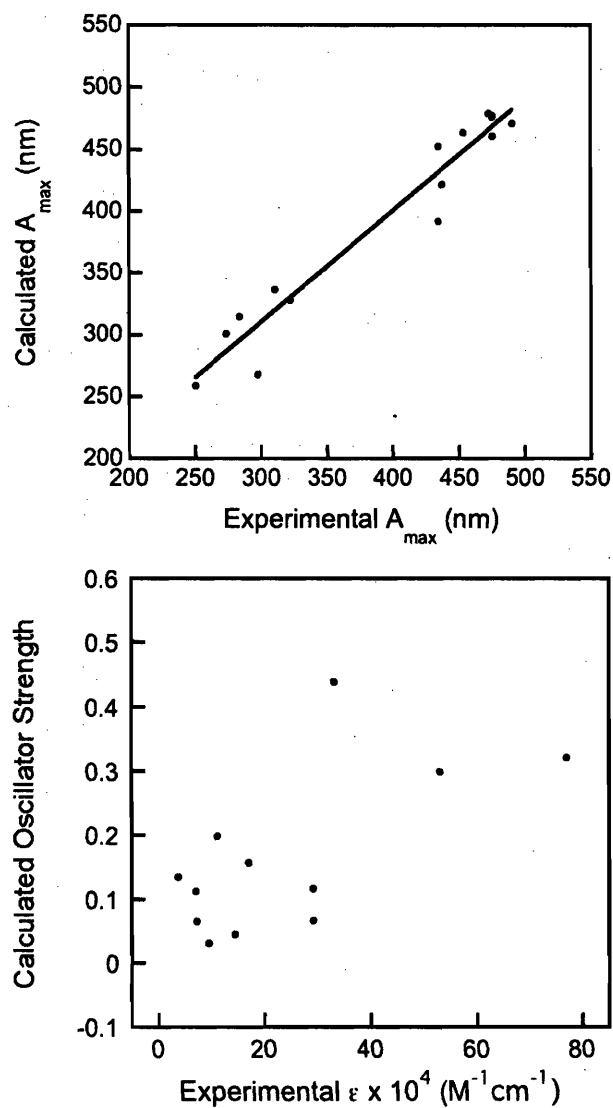
Figure A2.4. Top plot: Calculated vs. experimental A_{max} for fluorescein in its various forms (slope = 0.90, r = 0.972). Data are listed in Table A2.2. Bottom: Calculated oscillator strengths vs. experimentally determined extinction coefficients for fluorescein in its various forms. The poor agreement between the calculated oscillator strengths and extinction coefficients is expected since the former are considered unreliable.

(-2.32) —— LUMO

(-4.14) —— HOMO
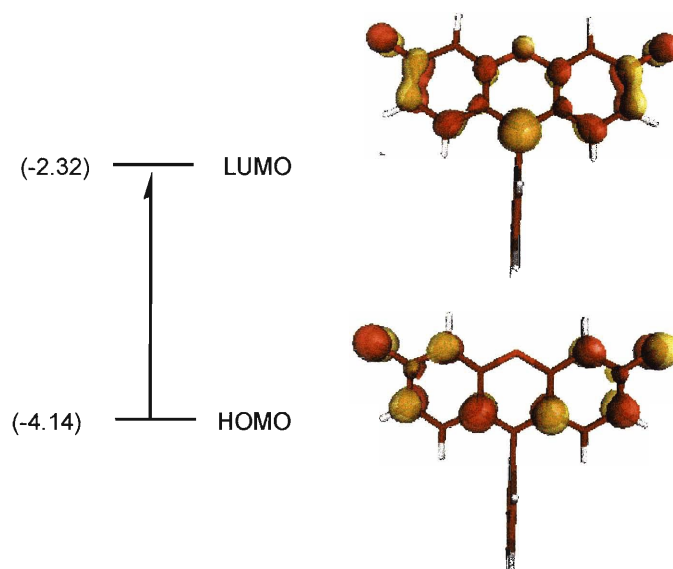
Figure A2.5. Molecular orbitals responsible for the dominant absorption band of fluorescein dianion based on TDDFT analysis. The experimental A_{max} is 490 nm and TDDFT predicts A_{max} of 471 nm. The transition is completely xanthenone-based. The donor orbital has no C_1- and the acceptor orbital has significant C_1-character. Energies are listed in eV.
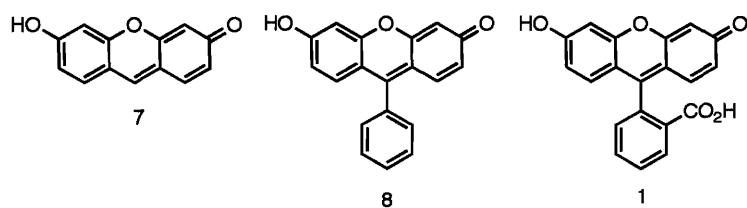
Figure A2.6. Xanthenone-based compounds **7** and **8** that exhibit absorption spectra similar to that of fluorescein, **1**, in mixed aqueous/organic solvents ($A_{max} \sim 490$ nm).

(-5.01) —— LUMO

(-6.74) —— HOMO

(-5.09) —— LUMO

(-6.80) —— HOMO
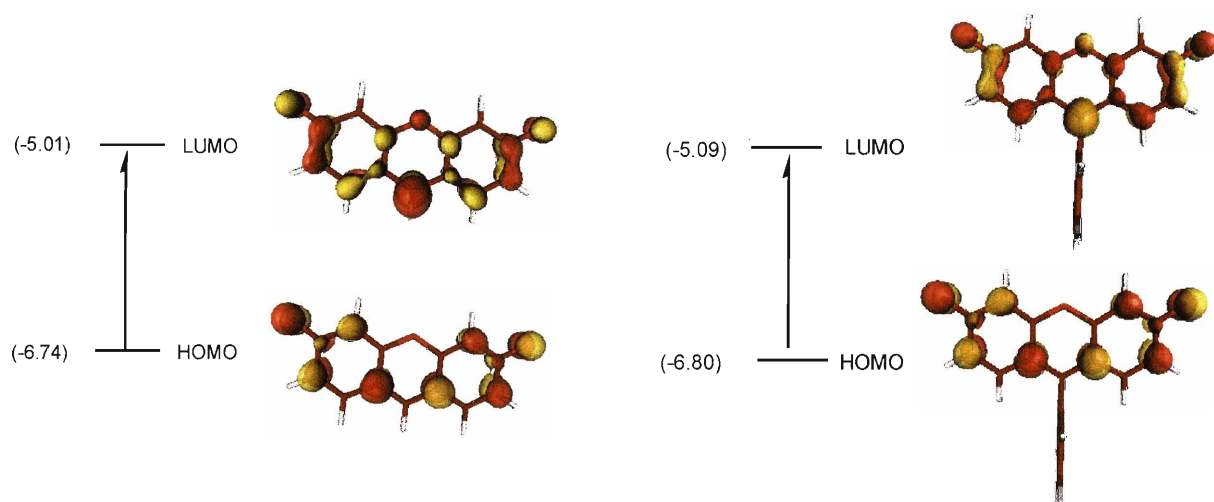
Figure A2.7. Molecular orbitals responsible for 6-hydroxyxanthen-3-one (**7**, left) and 6-hydroxy-9-phenylxanthen-3-one (**8**, right) absorption. In each case the transition is completely xanthenone-based. The donor orbital has no and the acceptor orbital has significant C_1 character. Energies are listed in eV.

48a (-7.89)
LUMO

56a (-5.01)
LUMO   56a

(-13.53) 48a
LUMO

55a (-6.74)
HOMO   55a

47a (-10.16)
HOMO

(-15.55)
47a

52a (-7.54)

46a

46a (-11.30)
45a (-11.60)

51a (-8.39)
50a (-8.75)

45a

44a (-12.55)
42a (-12.70)

(-17.37)
43a

48a (-10.04)

39a

45a (-10.70)

38a (-14.08)

42a (-11.58)
40a (-11.65)

(-18.89)
37a

34a (-14.98)

34a (-13.48)

(-21.63) 29a
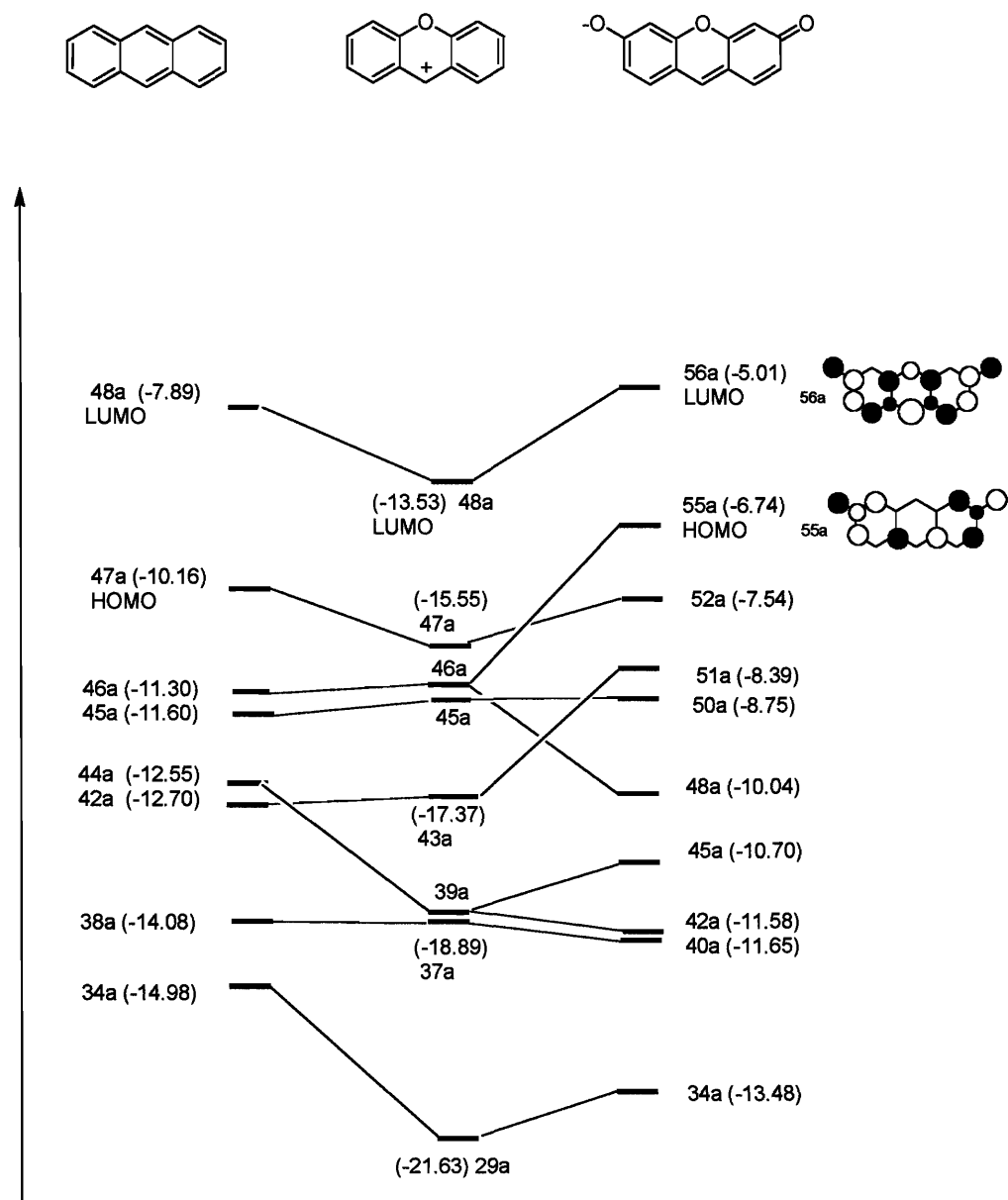
Figure A2.8. Molecular orbital correlation diagram for anthracene to the xanthenone anion. Energies are listed in eV. See Figures A2.9 to A2.11 for individual MO diagrams. See Figures A2.9 – A2.11 for individual MO diagrams.

——— (-7.89) LUMO 48a

——— (-10.16) HOMO 47a

——— (-11.30) 46a
═══ (-11.60) 45a

══ (-12.55, -12.70) 44a, 42a

——— (-14.08) 38a

——— (-14.98) 34a
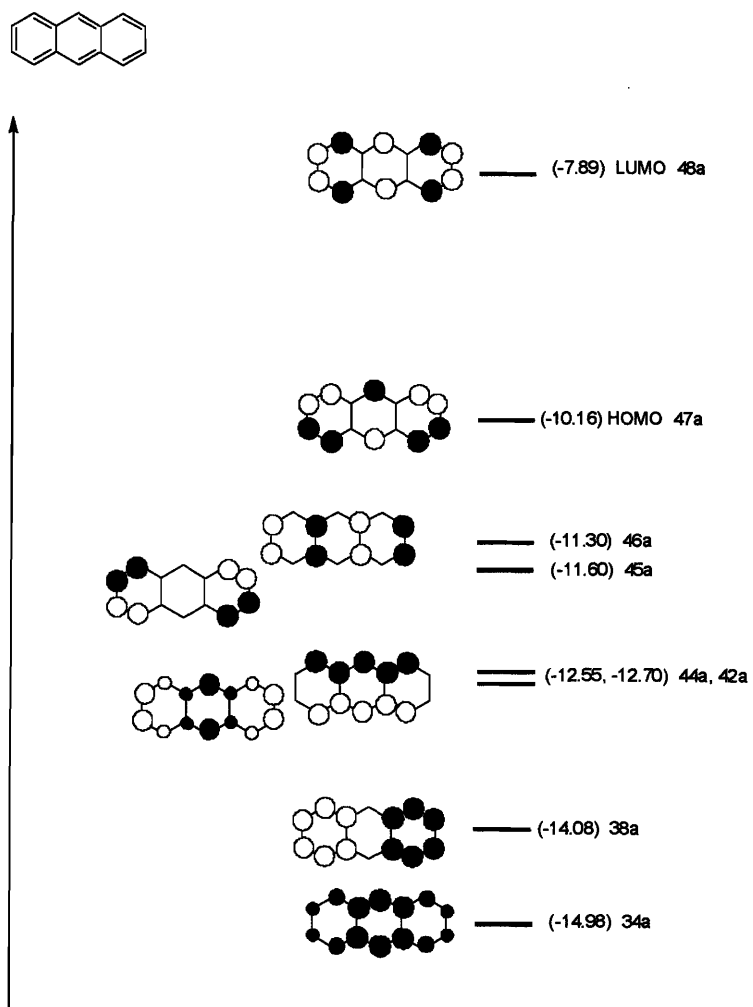
Figure A2.9. Molecular orbital diagram for anthracene. This diagram illustrates the seven filled π orbitals and the LUMO.
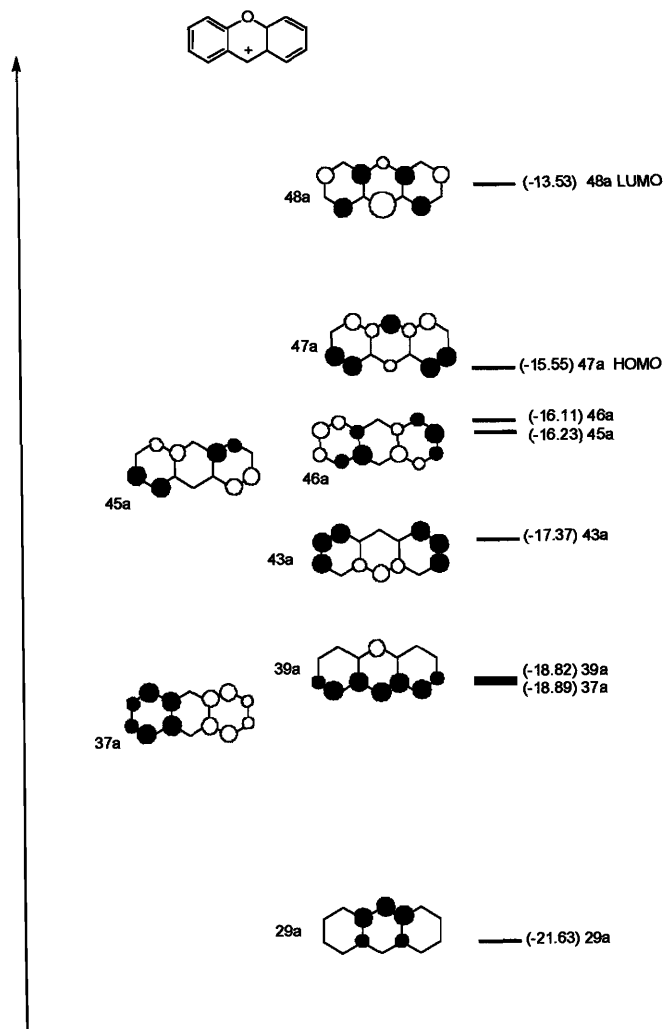
Figure A2.10. Molecular orbital diagram for the xanthene cation. This diagram illustrates the seven filled π orbitals and the LUMO.
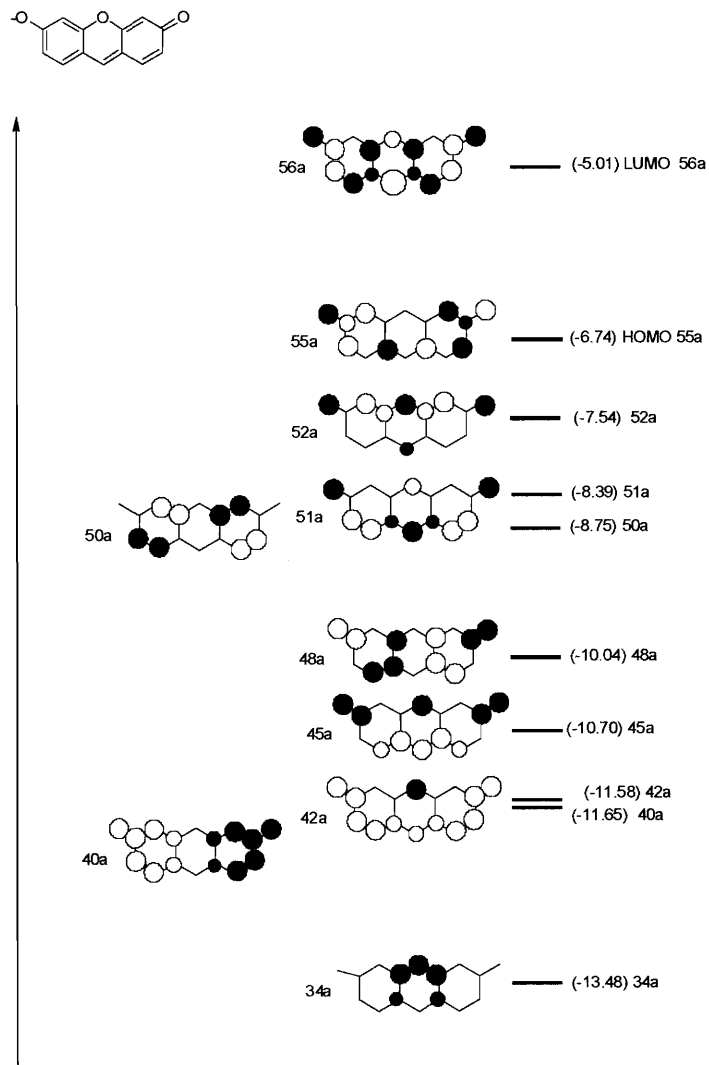
Figure A2.11. Molecular orbital diagram for 6-hydroxyxanthen-3-one, **7**, anion. This diagram includes the 9 filled π orbitals and the LUMO.
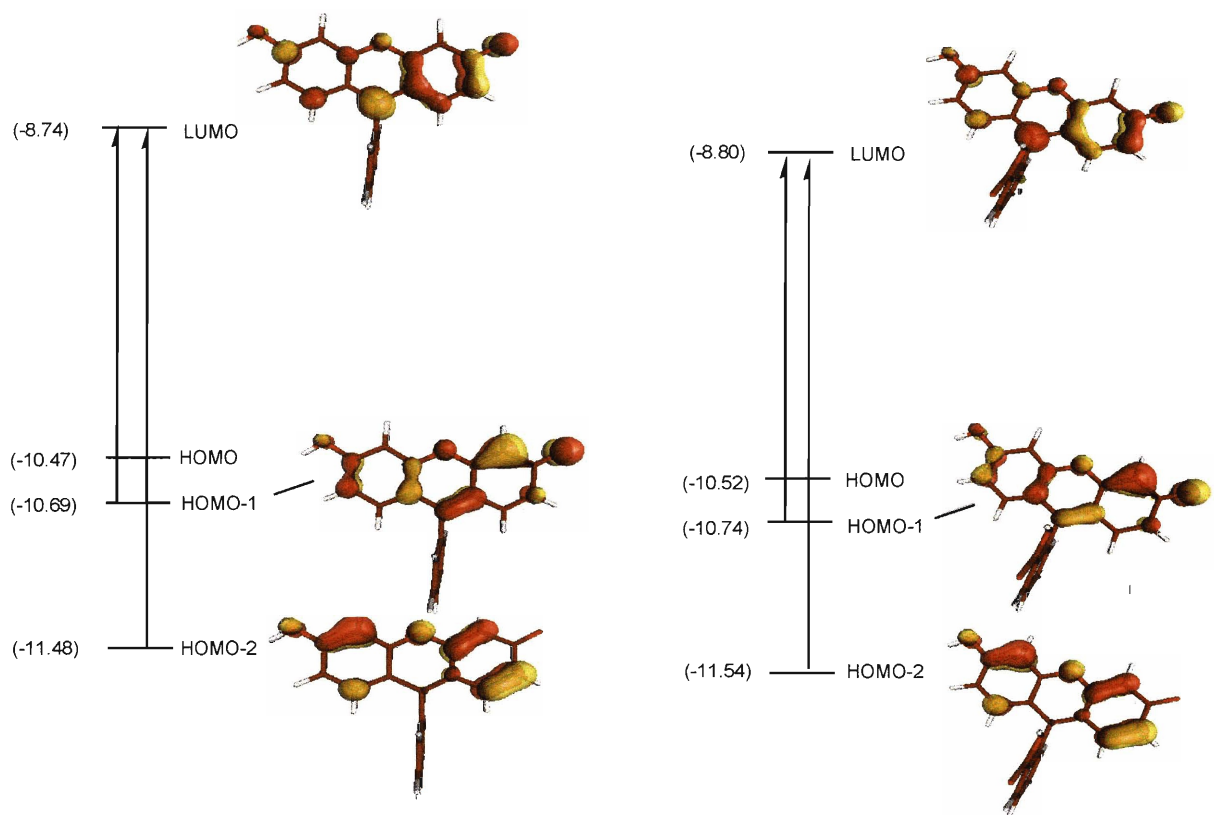
Figure A2.12. Molecular orbitals involved in the transitions responsible for absorption from neutral xanthenone species. The left diagram is for 6-hydroxy-9-phenylxanthen-3-one, **8**, and the right is for fluorescein, **1**. The donor orbitals in the HOMO-1 to LUMO transition have significant C_1 character.
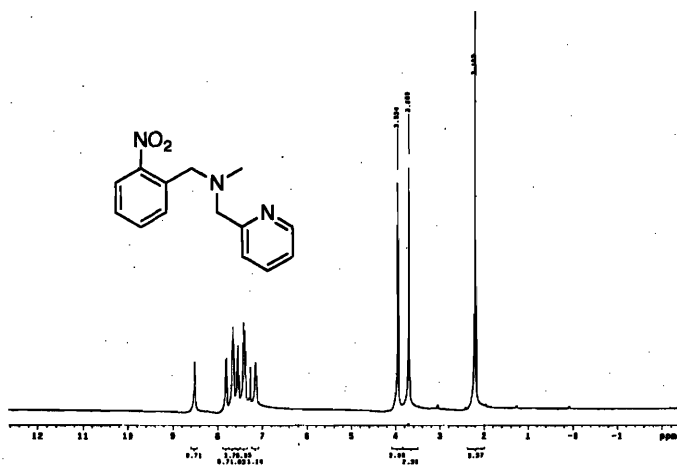
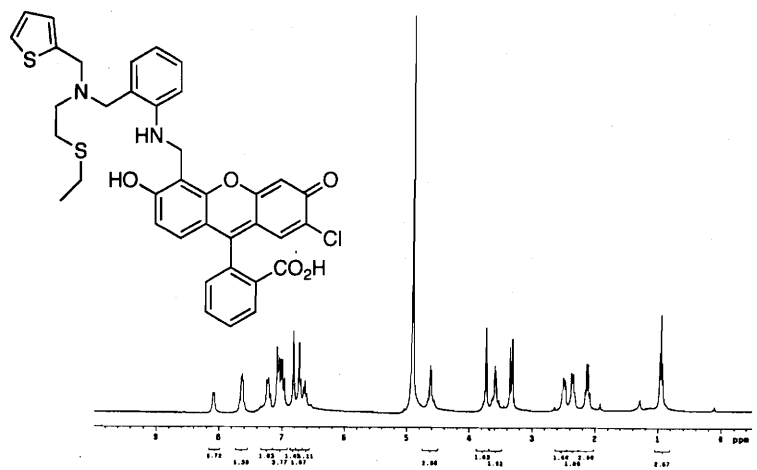# Appendix 3
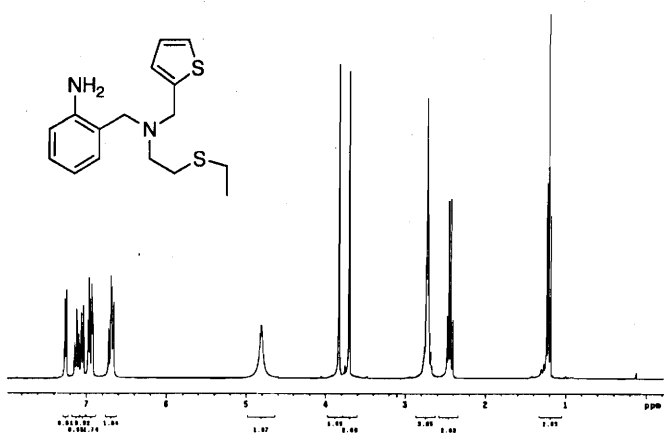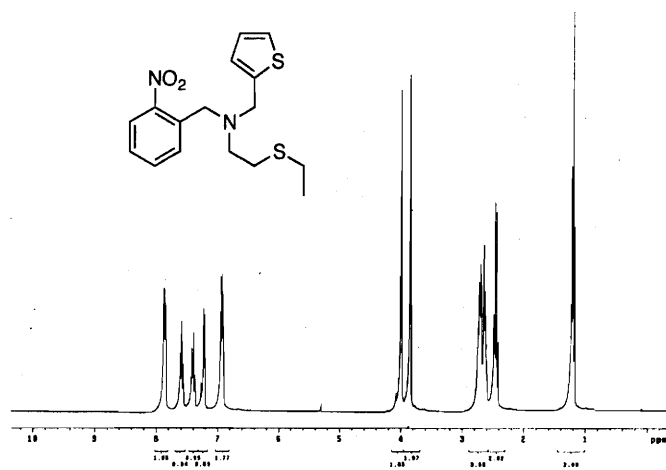
Miscellaneous NMR Spectra
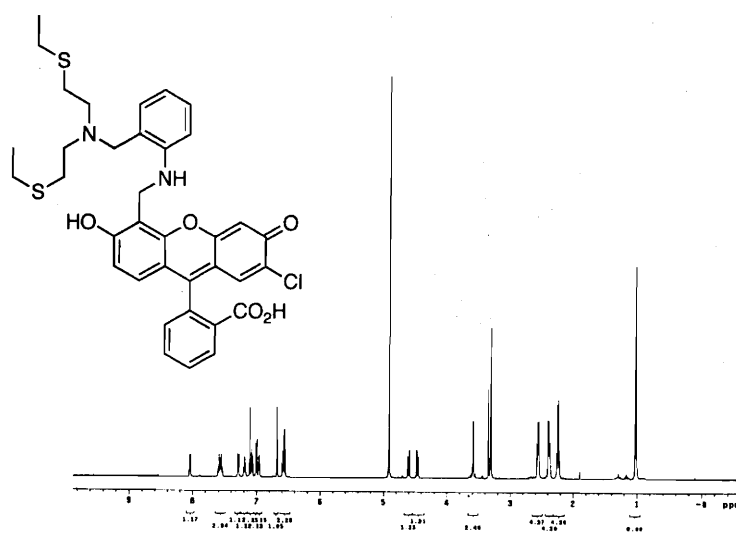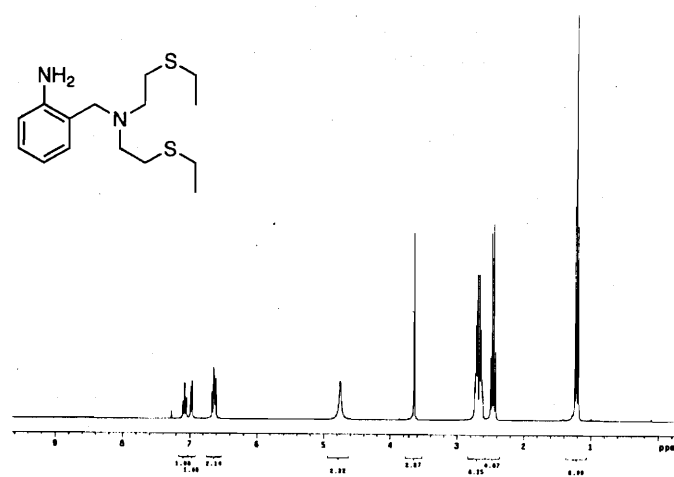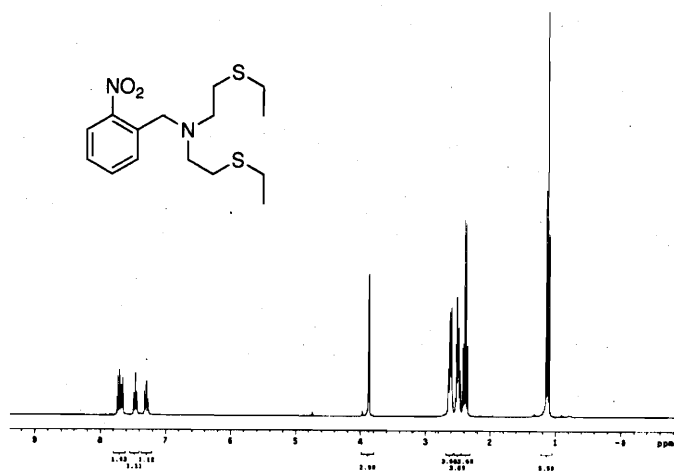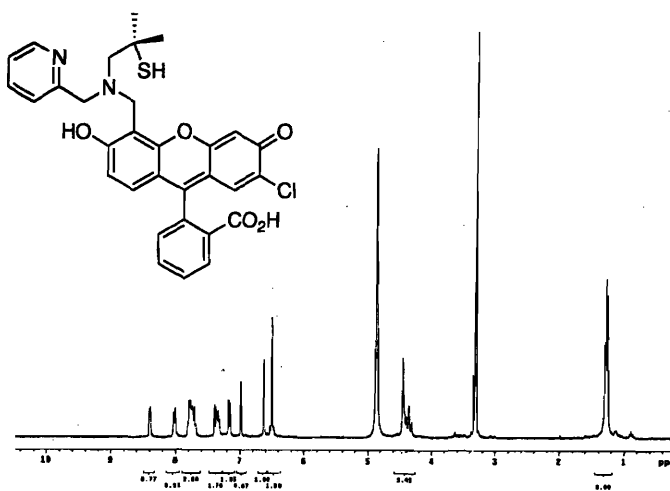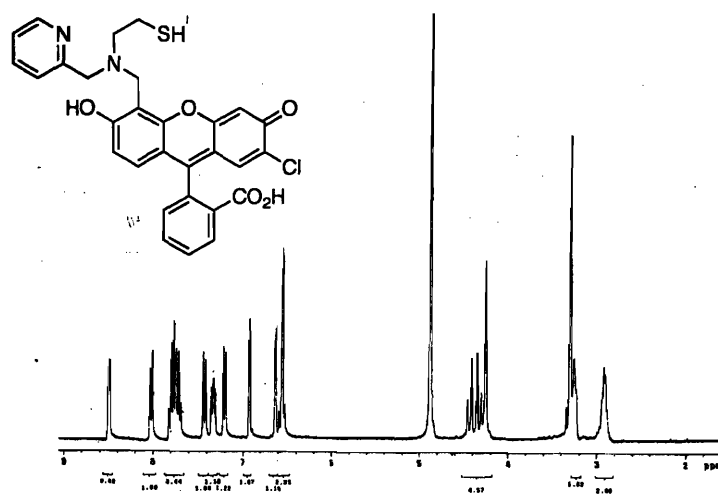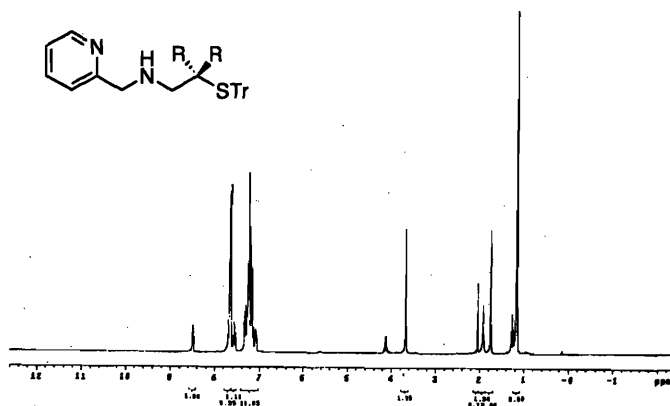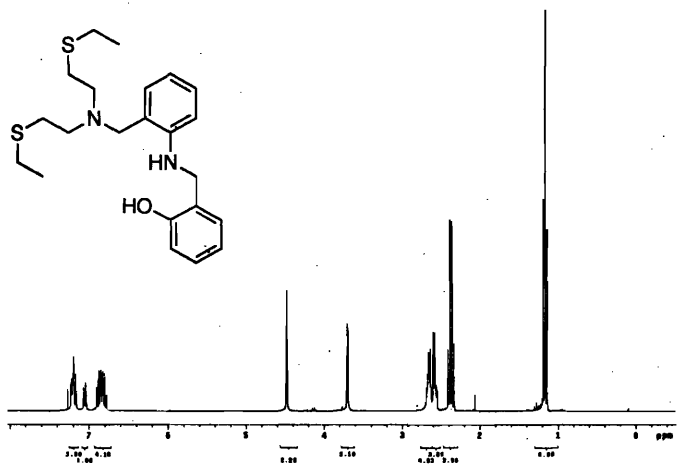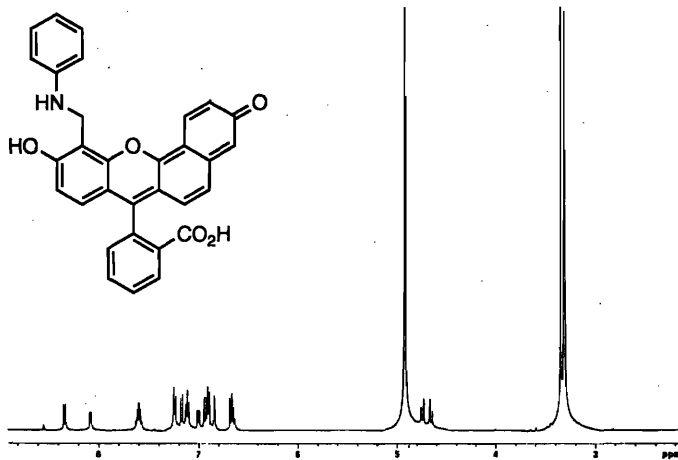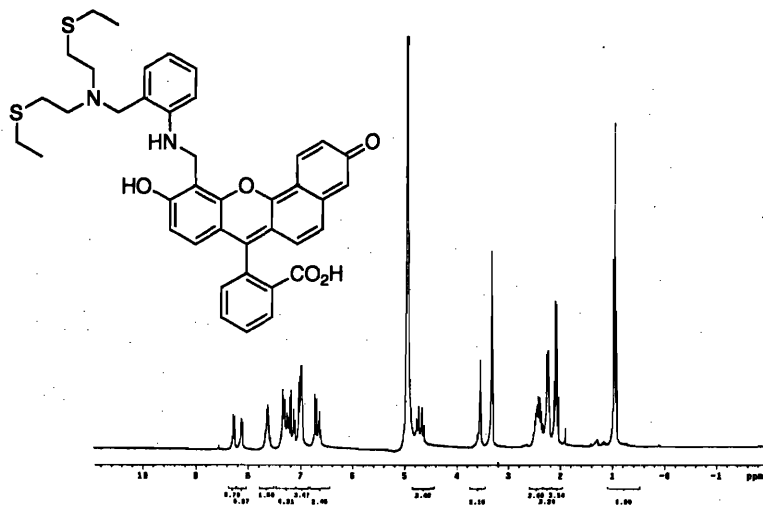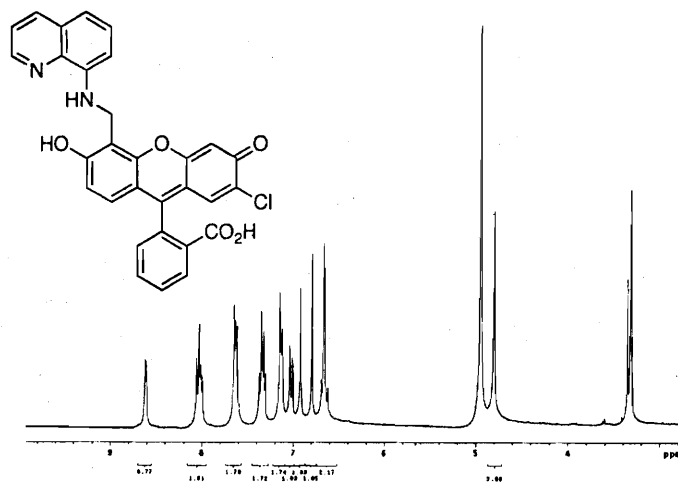
3, QZ1
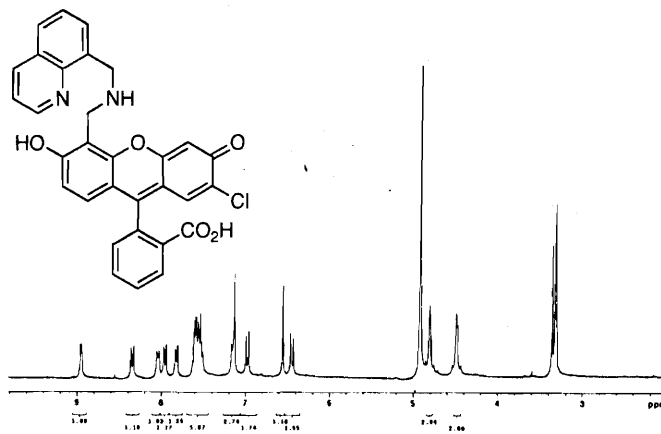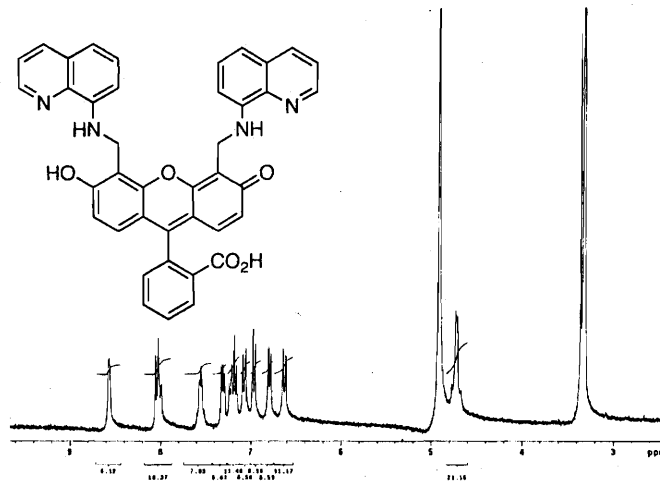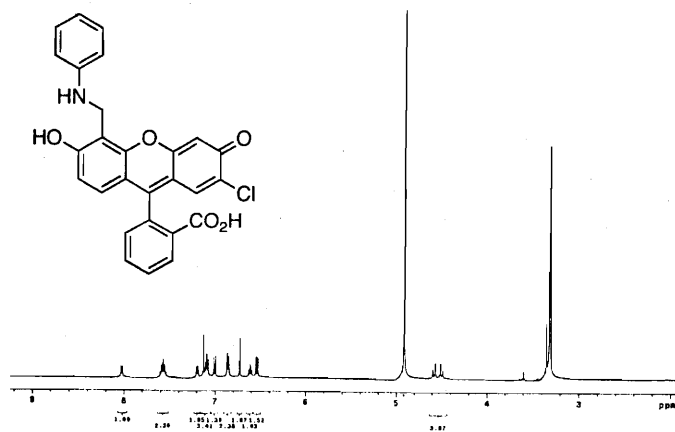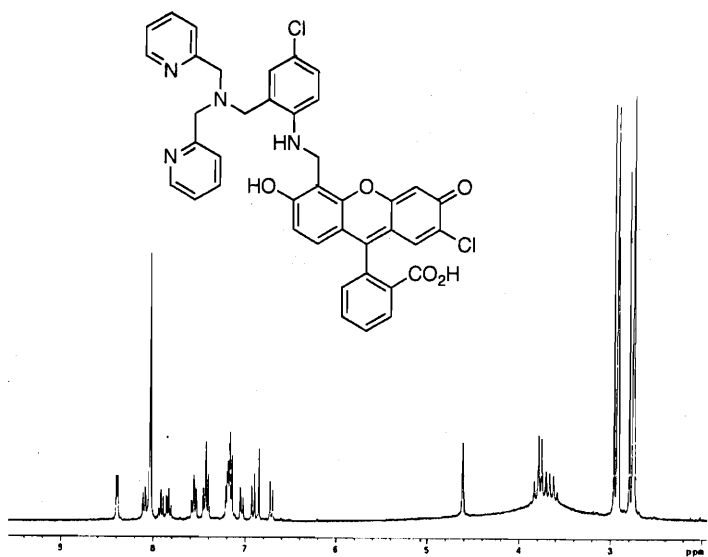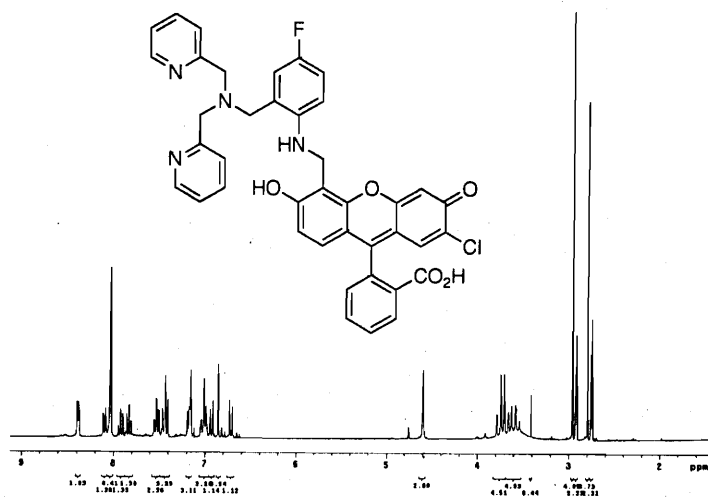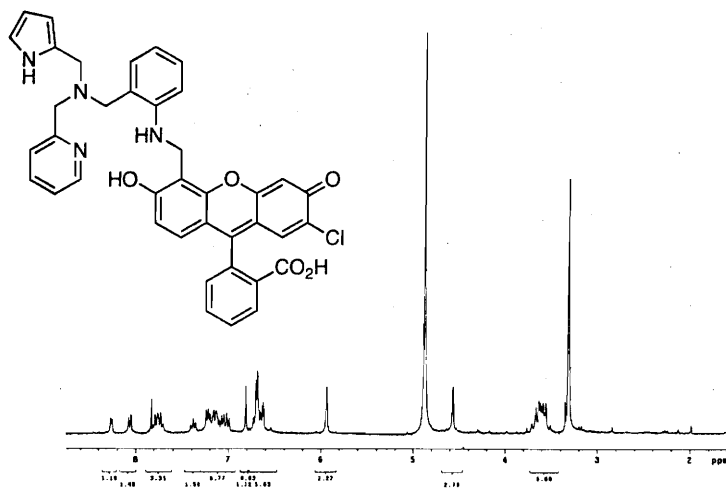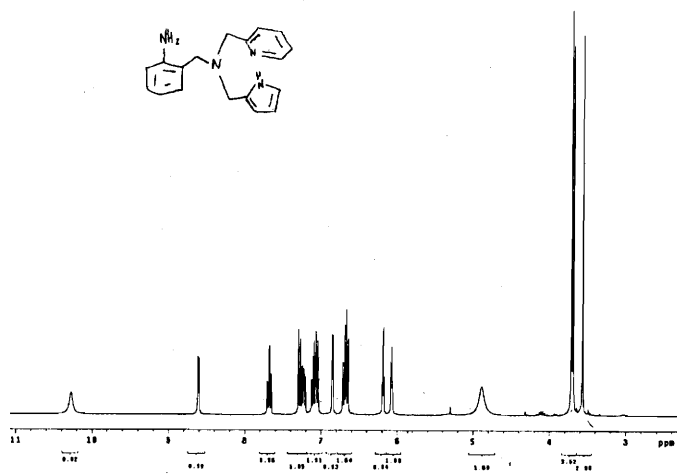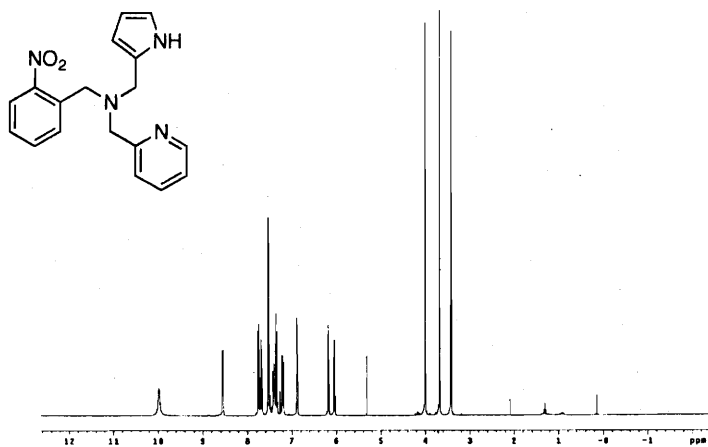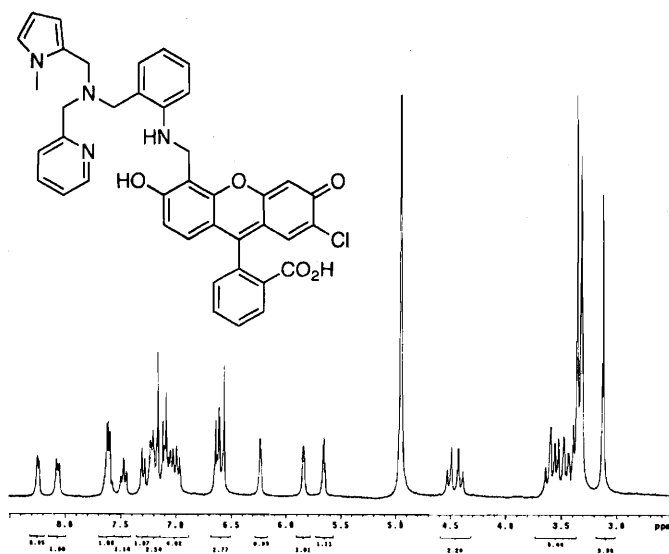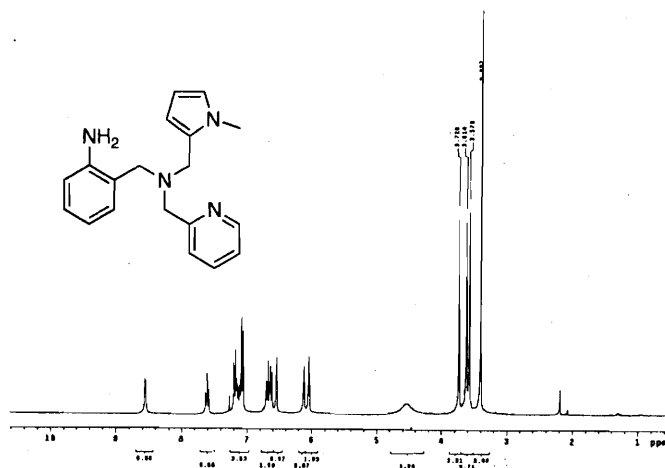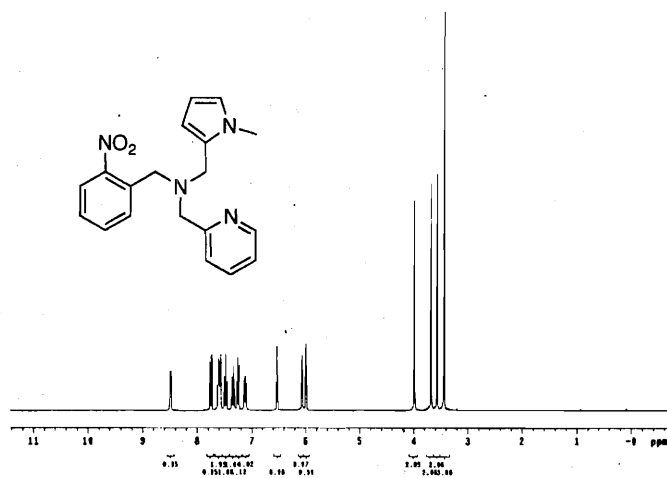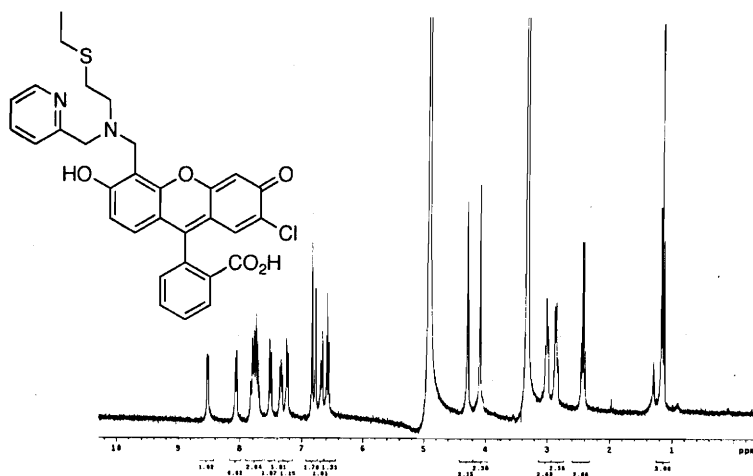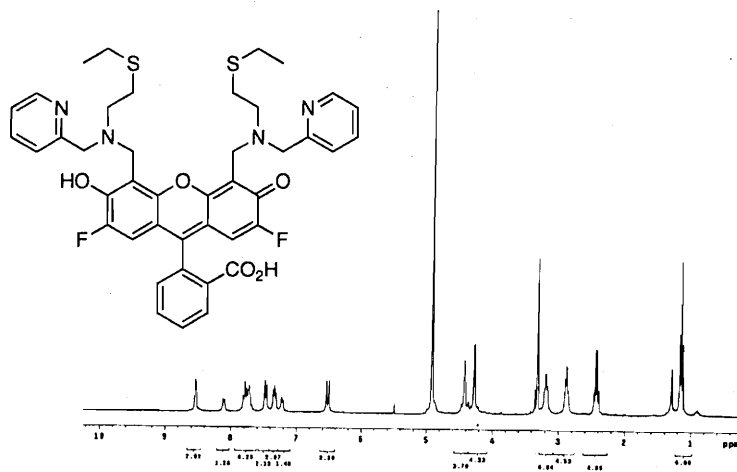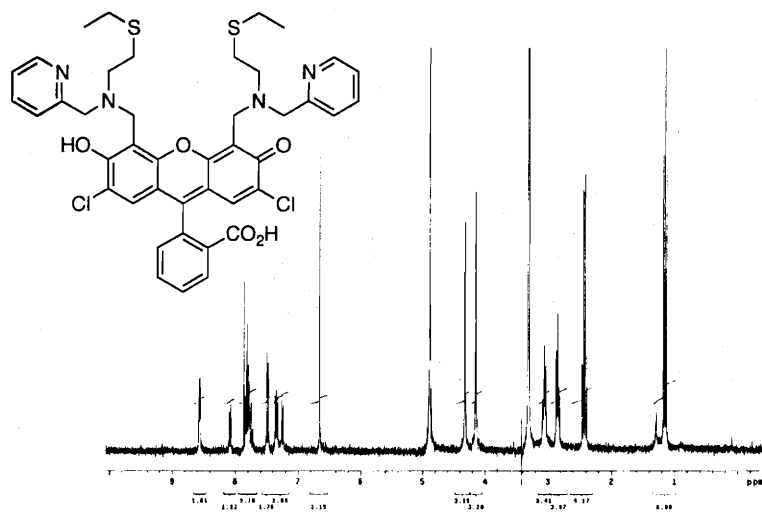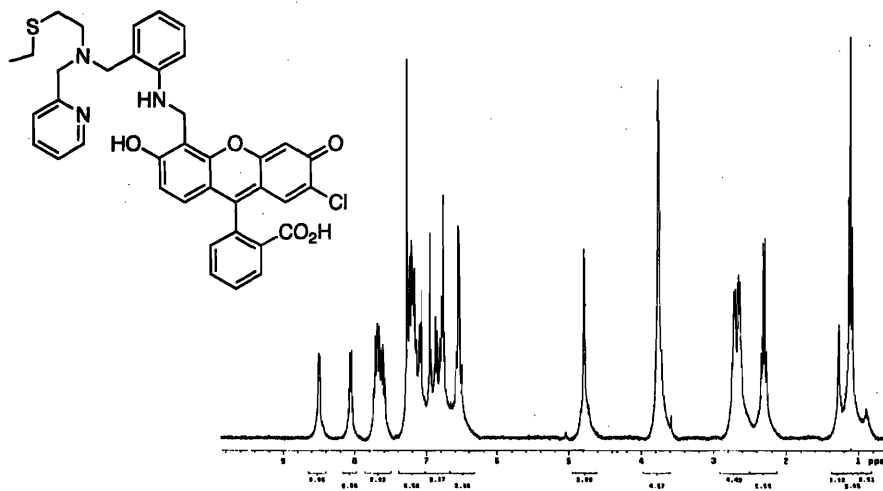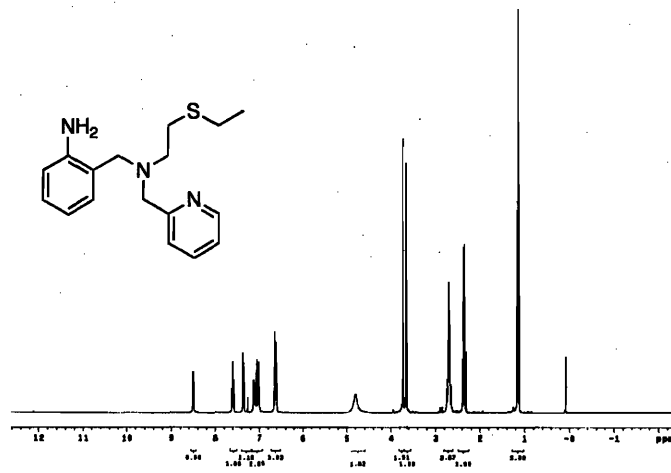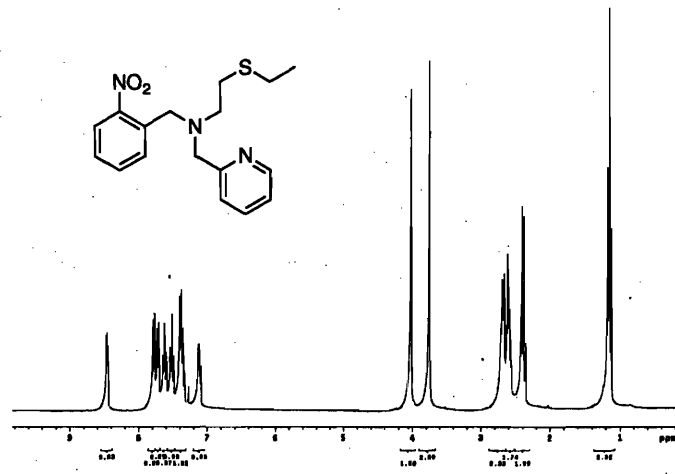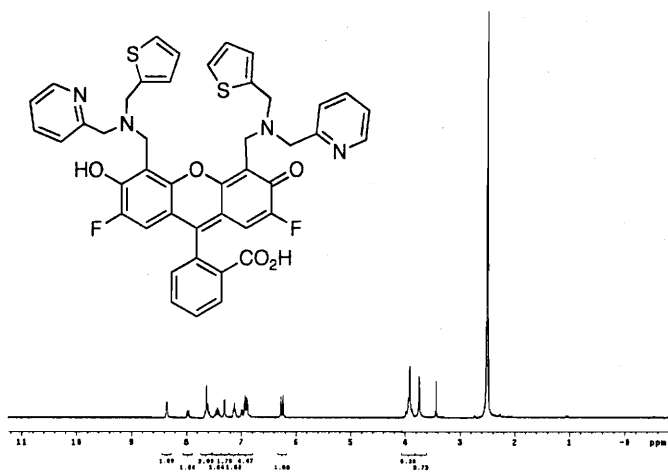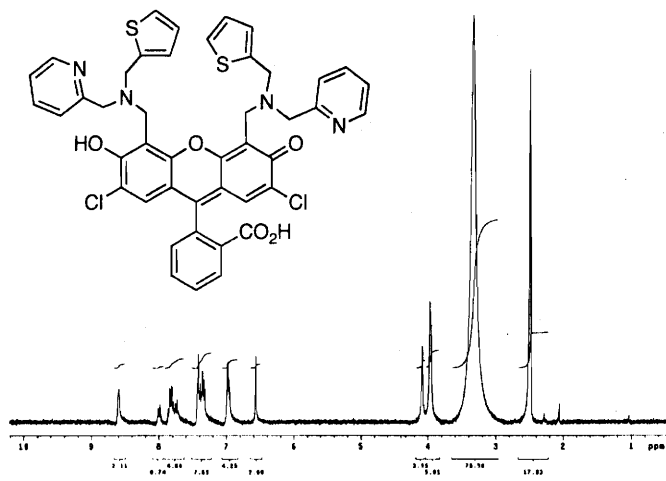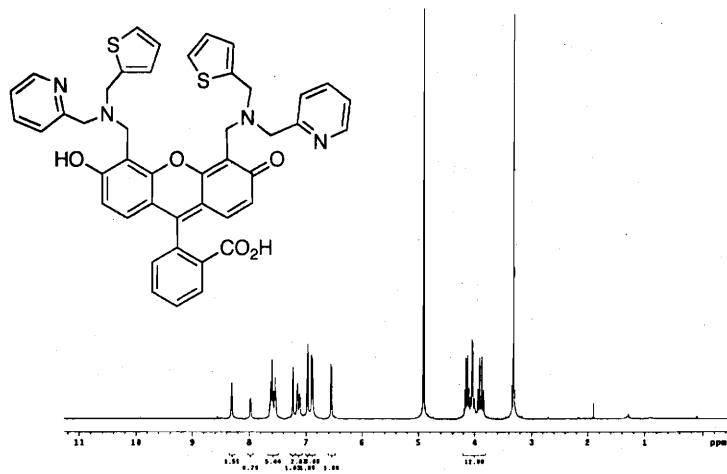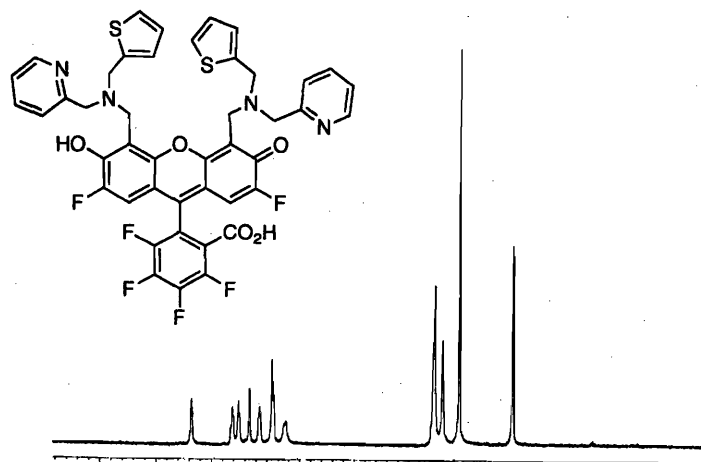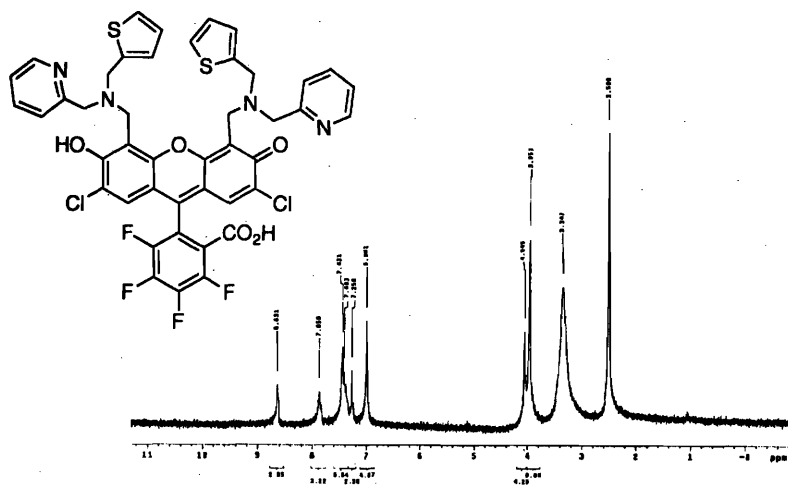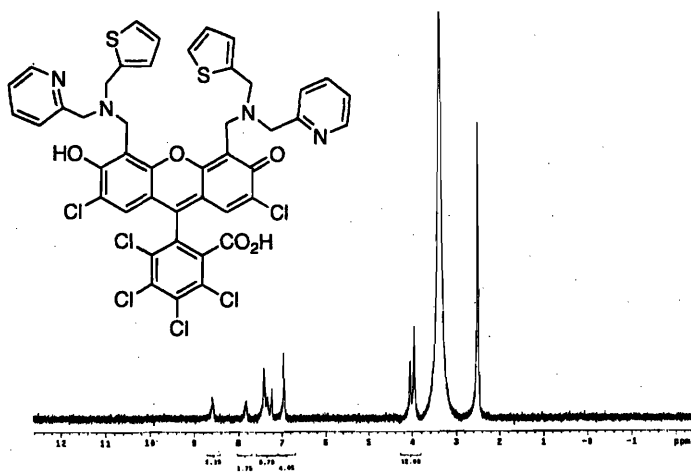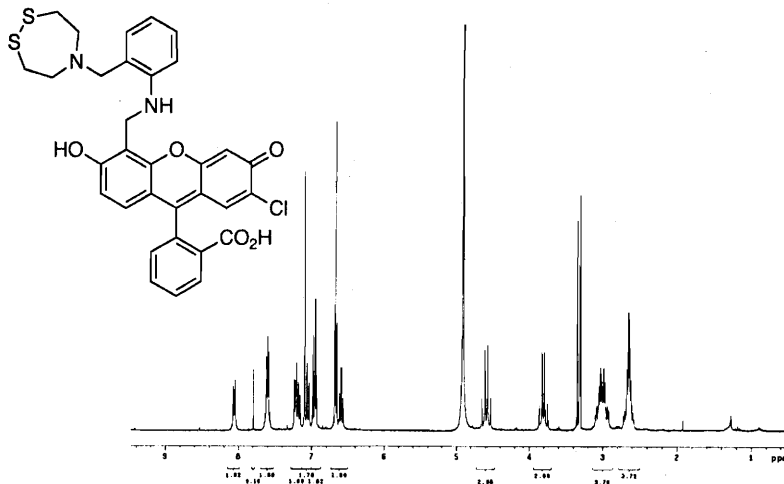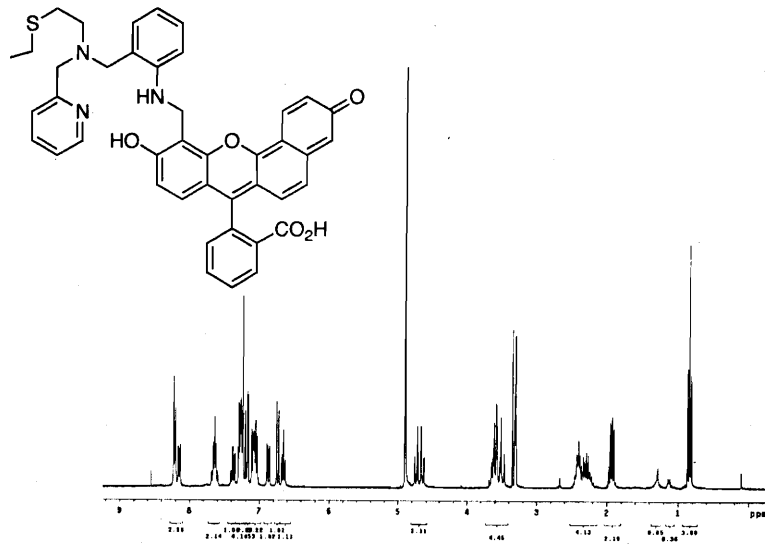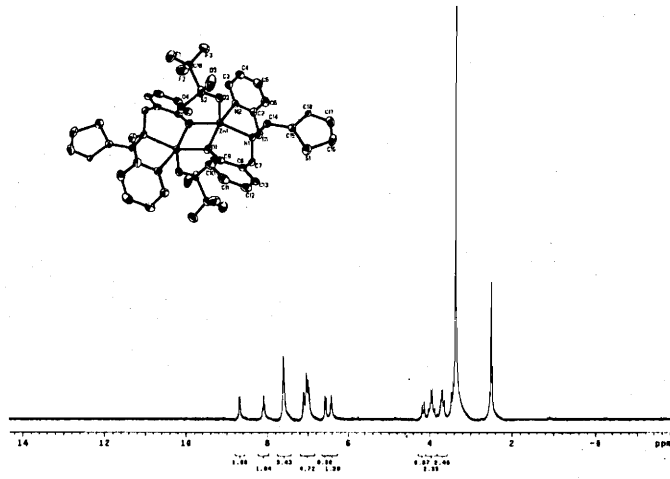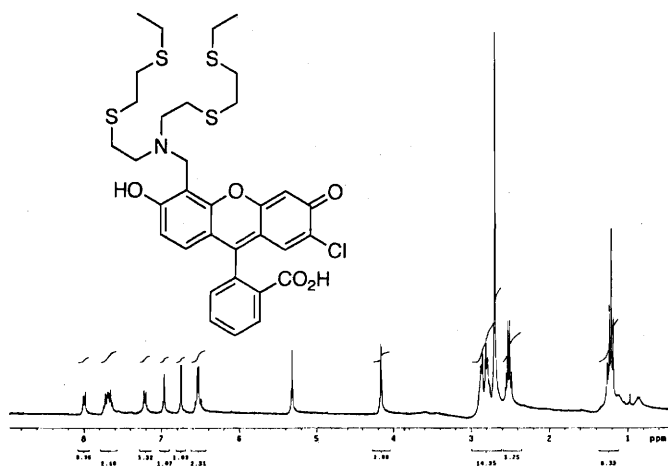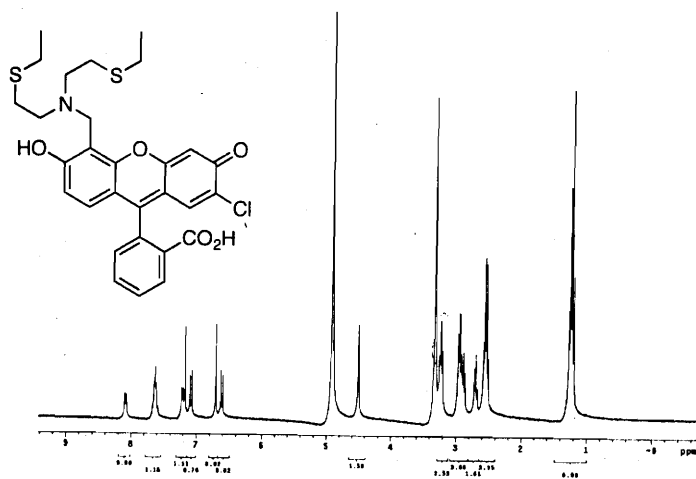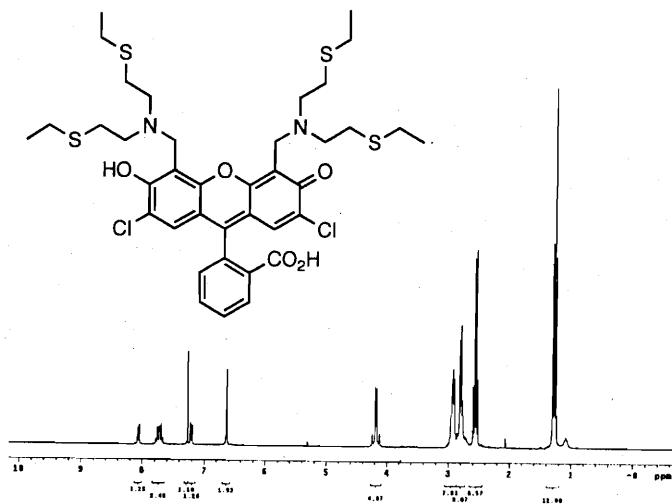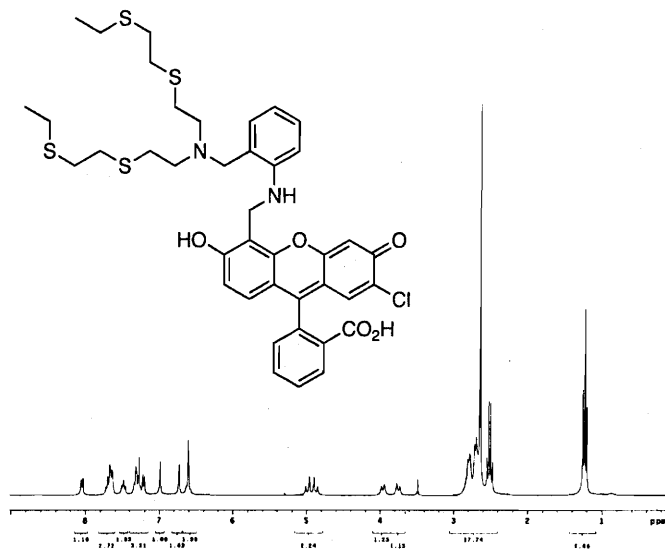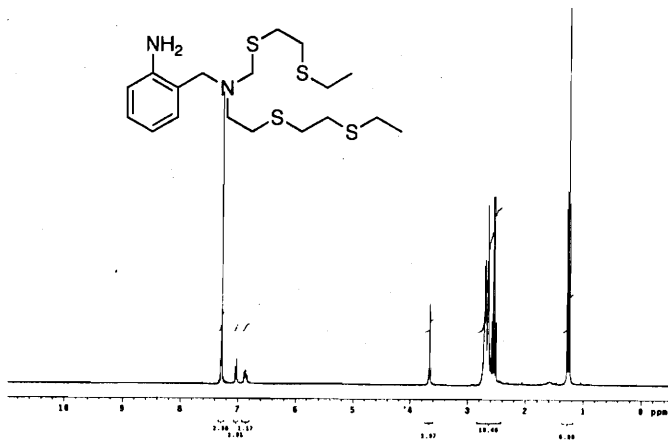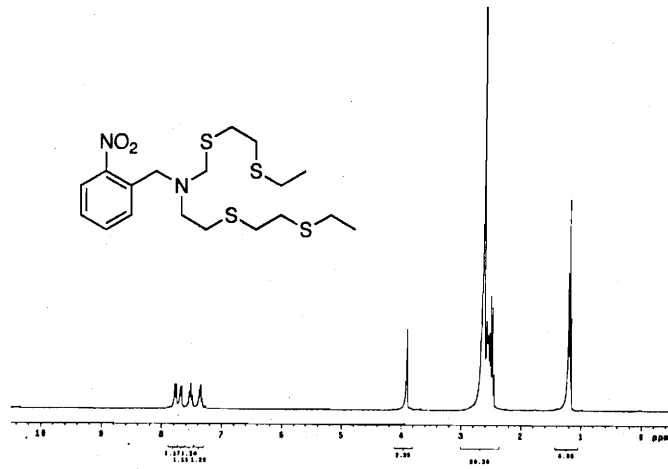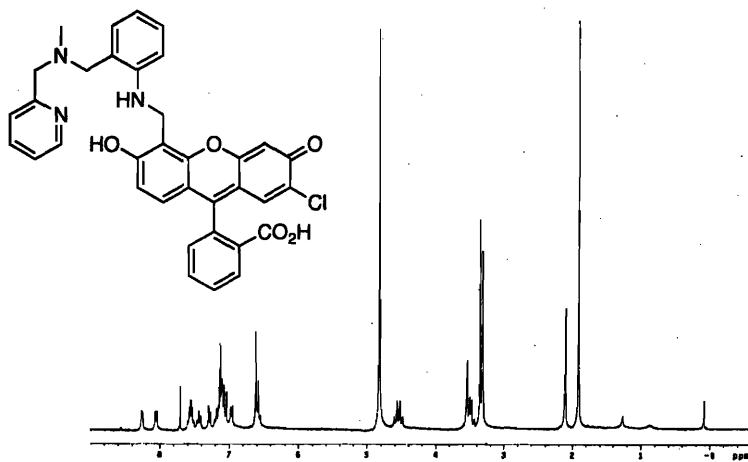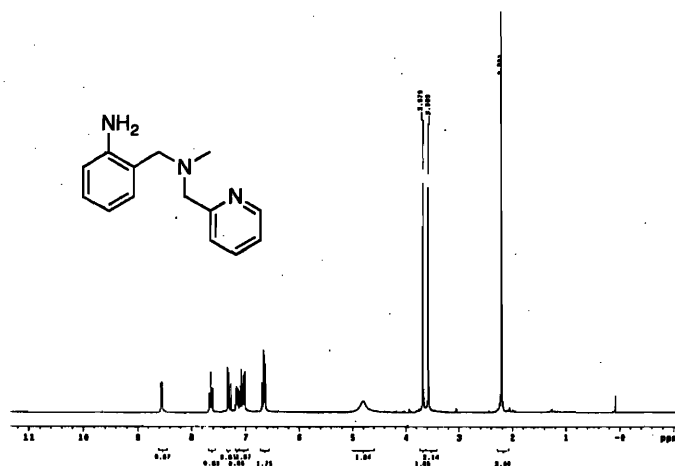
Biographical Sketch

The author was born in Albany, N.Y. in 1978 to Drs. John and Donna Nolan. She was raised in Niskayuna, N.Y. with her four siblings Bridgit, Catherine, John and Megan, and attended Niskayuna High School. In 2000, Liz graduated magna cum laude with Highest Honors in Chemistry and with a minor in Music from Smith College. During that time, she conducted computational chemistry research under the direction of Professor R. G. Linck. Her undergraduate honors thesis detailed investigations of stereoelectronic effects in substituted alkanes. Liz spent the 2000-2001 academic year in Strasbourg, France on a Fulbright Scholarship and received a NDSEG Graduate Fellowship before commencing her studies at MIT. As a graduate student in the laboratory of Professor Stephen J. Lippard, she was awarded a Whitaker Health Science Fund Fellowship and a National Young Investigator Award. After graduating from MIT, Liz will pursue post-doctoral research in the laboratory of Professor Christopher T. Walsh at Harvard Medical School.

Elizabeth M. Nolan

Education

Ph.D. Chemistry   Massachusetts Institute of Technology
2001-2006   Advisor: Professor Stephen J. Lippard

B.A. Chemistry   Smith College
1996-2000   Advisor: Professor R. G. Linck

Publications (11/12)

Elizabeth M. Nolan, Maryann E. Racine and Stephen J. Lippard, "Selective Hg(II) Detection in Aqueous Solution with Thiol Derivatized Fluoresceins," *Inorg. Chem.* **2006**, *45*, 2742-2749.

Elizabeth M. Nolan, Jacek Jaworski, Ken-Ichi Okamoto, Yasunori Hayashi, Morgan Sheng, and Stephen J. Lippard, "QZ1 and QZ2: Rapid, Reversible Quinoline-Derivatized Fluoresceins for Sensing Biological Zn(II)," *J. Am. Chem. Soc.* **2005**, *127*, 16812-16823.

Elizabeth M. Nolan and Stephen J. Lippard, "MS4, a seminaphthofluorescein-based chemosensor for the ratiometric detection of Hg(II)," *J. Mater. Chem.* **2005**, *27-28*, 2778-2783 (highlighted in the July 2005 issue of *Chemistry World*).

Elizabeth M. Nolan and Stephen J. Lippard, "The Zinspy Family of Fluorescent Zinc Sensors: Syntheses and Spectroscopic Investigations," *Inorg. Chem.* **2004**, *43*, 8310-8317.

Elizabeth M. Nolan, Shawn C. Burdette, Jessica J. Harvey, Scott A. Hilderbrand and Stephen J. Lippard, "Synthesis and Characterization of Zinc Sensors Based on a Monosubstituted Fluorescein Platform," *Inorg. Chem.* **2004**, *43*, 2624-2635.

Christopher J. Chang, Elizabeth M. Nolan, Jacek Jaworski, Shawn C. Burdette, Morgan Sheng, and Stephen J. Lippard, "Bright Fluorescent Chemosensor Platforms for Imaging Endogenous Pools of Neuronal Zinc," *Chem. Biol.* **2004**, *11*, 203-210.

Christopher J. Chang, Jacek Jaworski, Elizabeth M. Nolan, Morgan Sheng, and Stephen J. Lippard. "A Tautomeric Chemosensor for the Ratiometric Fluorescence Imaging of NO-Induced Release of Intracellular Zinc," *Proc. Natl. Acad. Sci. USA* **2004**, *101*, 1129-1134.

Elizabeth M. Nolan and Stephen J. Lippard, "A 'Turn-On' Fluorescent Sensor for the Selective Detection of Mercuric Ion in Aqueous Media," *J. Am. Chem. Soc.* **2003**, 125, 14270-14271 (highlighted in Thomson ESI Special Topics, June 2005).

Elizabeth M. Nolan and R. G. Linck, "Through Space Charge and Dipolar Effects in Substituted Ethanes and 1,1,1-Trifluoroethanes," *J. Phys. Chem. A.* **2002**, *106*, 533-543.

Elizabeth M. Nolan and R. G. Linck, "An Exploration of Long Range Electronic Effects in Substituted Alkanes," *J. Phys. Chem. A.* **2001**, *105*, 7297-7307.

Elizabeth M. Nolan and R. G. Linck, "Charges in Substituted Alkanes: Evidence for a Through Space Mechanism," *J. Am. Chem. Soc.* **2000**, *122*, 11497-11506.